12-2012

Flow Behavior Modeling and Process Control of Electrically-Assisted Forming (EAF) for Sheet Metals in Uniaxial Tension

Joshua Jones
Clemson University, joshj3088@gmail.com

FLOW BEHAVIOR MODELING AND PROCESS CONTROL OF ELECTRICALLY-ASSISTED FORMING (EAF) FOR SHEET METALS IN UNIAXIAL TENSION

A Dissertation
Presented to
the Graduate School of
Clemson University

In Partial Fulfillment
of the Requirements for the Degree
Doctor of Philosophy
Automotive Engineering

By
Joshua J. Jones
December 2012

Accepted by:
Dr. Laine Mears, Committee Chair
Dr. Fadi Abu-Farha
Dr. Randy Collins
Dr. Mica Grujicic

ABSTRACT

This work studies the influence of an applied electrical current on magnesium sheet metal and introduces models which are successful in predicting the deformation behavior (*i.e.* material flow stress, local material strain, and thermal response). Also, this work examined the theory of electroplasticity by studying prior proposed theories and by quantifying the prior theories potential for improved dislocation mobility. From this analysis, a single dominant mechanism is determined and the theory of electroplasticity is explained using this single mechanism. The theory discussed in this work is supported by experimental testing and microstructure analysis.

In addition to studying the exact electroplastic mechanism, the electrical energy added to the system results in a decrease in the material flow stress. The decrease in flow stress is due to the direct electrical effect (*i.e.* electroplasticity), bulk thermal softening from the temperature rise, and thermal expansion effects. Each of these effects are predicted by models and quantified in this work.

Aside from the theory and modeling aspects of this work, the applicability of Electrically-Assisted Forming (EAF) to unique processing techniques is performed. Specifically, control strategies of constant force forming, constant stress forming, and constant current density forming were envisioned and demonstrated. Thus, new class of control approaches is developed for EAF. Also, the applicability of the introduced EAF models are analyzed for use in model predictive control strategies.

DEDICATION

I dedicated this dissertation work to my family and friends who have inspired me to further my education and challenge myself. Specifically, I would like to thank my parents and my sister for their love, encouragement, and support throughout my time as a student. Last, I would like to dedicate this dissertation to all of my grandparents who helped make me who I am today.

ACKNOWLEDGEMENTS

I would like to thank and acknowledge the following people for their support of my dissertation work in addition to my committee members:

Dr. Laine Mears: I would like to thank Dr. Mears for the support, knowledge, and motivation he has provided over my time at Clemson University during both my studies and PhD research.

Dr. John Roth: I would like to acknowledge and thank John for the guidance and inspiration he provided me as an undergraduate student in both course/research work and for his continuous support of my professional development.

Dr. Cristina Bunget: I would like to acknowledge and thank Cristina for her advice on metal forming and feedback on my research work.

BMW Motor Company: I would like to acknowledge BMW Motor Company for providing the magnesium sheet material used in this dissertation work.

TABLE OF CONTENTS

LIST OF FIGURES

LIST OF TABLES

DEFINITIONS

AC – Alternating Current
AI – Analog Input
AMRL – Advanced Materials Research Lab
AO – Analog Output
BiW – Body-in-White
CCD – Constant Current Density
CGA – Circle Grid Analysis
CI – Confidence Interval
cRIO – CompactRIO
DAQ – Data Acquisition
DC – Direct Current
DIC – Digital Image Correlation
DOE – Design of Experiments
EAF – Electrically-Assisted Forming
EAM – Electrically-Assisted Manufacturing
EM – Electron Microscope
FE – Finite Element
FLC – Forming Limit Curve
FLD – Forming Limit Diagram
GUI – Graphical User Interface
H-N – Hutchinson-Neale
I/O – Input/Output
LDH – Limiting Dome Height
LVDT – Linear Variable Differential Transformer
MBC – Model Based Control
Mg – Magnesium
M-K – Marciniak-Kuczinski
NCCD – Non-constant Current Density
NI – National Instruments
OP – Oxide Polishing
PID – Proportional-Integral-Derivative
PS – Parameter Set
RT – Room Temperature
SCR – Silicon Controlled Rectifier
SiC – Silicon Carbide
SPF – Superplastic Forming
TWB – Tailor Welded Blanks

EXECUTIVE SUMMARY

One evolving method to help process and manufacture lightweight materials is Electrically-Assisted Forming (EAF). The process of EAF is defined as the application of a direct electrical current through the workpiece while being subject to deformation. From the late 1950's, this process has progressed, however, has not been adopted in industry as a result of the lack of fundamental knowledge on the processing mechanisms and limited modeling work. As a result of the limited modeling efforts since its inception, this process is not currently predictable and any attempts to manufacture materials using this technique would not be optimal (*e.g.* minimum energy forming of high strength materials or maximizing achievable elongation). As a result of not being able to provide optimal conditions for the processing of materials, it is still uncertain to manufacturers how feasible this technique is for industrial applications.

The current state-of-the-art work in this field is just beginning to model and describe how the addition of an electric current field affects the processing of metals from both a macroscopic and microscopic view. This work is primarily focused on the macroscopic or bulk characteristics of the deformation of metals and is directed toward the deformation behavior of sheets during EAF. In addition, the most modern theory of the electroplastic effect is discussed and this work explores first-principle physics models to understand the magnitude of various proposed direct electrical effects. Last, a new class of control approaches specific to EAF are created and demonstrated.

CHAPTER 1 - INTRODUCTION

1.1 - Introduction to Lightweight Materials Design and Manufacturing

In most manufactured goods today, consumers desire the highest functional and geometric-quality products with minimal cost. As a result of these demands, engineers and designers are turned toward more aggressive designs and materials to successfully compete. Along with these new designs are the associated challenges that companies must face to economically manufacture new designs. This trend has been observed in the automotive industry in the last few decades where consumers have had an increased demand for safety/comfort features and vehicle driving performance. As a result of these demands, they have led to a significant increase in the vehicle mass due to the added vehicle systems. More recently, these demands were tied with government issued fuel efficiency and emission reduction standards which created a major conflict between these two objectives [1.1]. Therefore, to balance these conflicting objectives, vehicle manufacturers have turned toward lightweight engineering, as this technique is capable of supporting all of these objectives in total. Other applicable methods could include advanced engine and drivetrain technology, however, these are often very costly and also increase the vehicle mass. Considering the impact of lightweight engineering on fuel consumption and emissions is relatively small and therefore the major benefit is enhanced driving performance. Yet, with lightweighting there is some physical effect which can be significant if examined from a life-cycle costing standpoint [1.2] or by considering the effects of mass-decompounding [1.3].

There are two main methods that designers/engineers use to achieve vehicle lightweighting. The first is to combine multiple parts within a system to a few single parts. This often leads to reduced fasteners and new designs that have a better optimized geometry to reduce the system mass. However, this method requires additional design/development time and is often hard to realize or discover within a vehicle. The second method is to adopt or incorporate metals with high strength-to-weight ratios such as titanium, magnesium, aluminum, or even high strength steels. Although these materials are lightweight in nature, they typically suffer with regards to manufacturability because of their unique intrinsic material properties or crystalline structure. Additionally, with many new materials being introduced into vehicles this complicates the assembly of the vehicle as jointing dissimilar materials can be challenging. Hence, new and alternative manufacturing processes must be explored for the successful implementation of these materials from both a functionality and cost standpoint. There are several methods that are commonly used in industry such as incremental forming, superplastic forming (SPF) and its variants, tailor welded blanks (TWB), hydroforming, and hot/warm working. These methods are described in detail in *Chapter 2*. Aside from these techniques, researchers are developing and advancing the science in new or evolving processing techniques.

1.2 - Introduction to Magnesium

Within this section the lightweight material magnesium which is of interest for this dissertation is discussed and compared to other lightweight materials.

1.2.1 - Material Properties

Magnesium is the 8th most common element on earth and the 11th most abundant element by mass in the human body [1.4]. The main source for magnesium production is sea water which holds great amounts of dissolved magnesium compounds [1.5]. Magnesium is considered the lightest structural engineering metal. However, in its pure state it is not very useful for any engineering/structural applications. As a result, it is commonly alloyed with other elements to improve its mechanical properties. When comparing this material to other common engineering materials, it is 36% lighter per unit volume than aluminum and 78% lighter per unit volume than steel. The properties of magnesium are compared with other engineering materials in Table 1.1. As seen the density is much lower compared to the other materials. However, the strength and modulus of elasticity are much less than the other materials. Also of note, is the formability of magnesium at cold working temperatures is significantly less than the other materials. As a result, wrought products must be formed at elevated temperatures which are not a typical requirement for aluminum or steel (depends on process and final component though) [1.6]. As a result, magnesium is a very attractive material for casting processes due to its low formability and low melting temperature. Another problem is the price of magnesium. The cost of magnesium is presently about 4 times the price of steel, and is approximately 1.5 times the price of aluminum. Also, the properties of magnesium suffer when exposed to elevated temperatures for longer durations (low creep resistance) [1.7]. Considering corrosion, magnesium readily oxidizes and forms a self-protecting layer of magnesium oxide on its surface. As the material performs a protective layer this

is somewhat beneficial, however if placed in a wear environment it easily loses this layer. Also with magnesium, it has a very high potential for galvanic corrosion [1.7]. Consequently, it is difficult to join this material to others and it is difficult to find appropriate fastening methods.

Table 1.1- Material Comparison **[1.8-1.10]**

Property	Magnesium	Aluminum	Steel	Titanium (G5)
Density (kg/m^3)	1740	2700	7850	4500
Yield Strength (MPa)	200-300	145-503	250-1000	950-1050
Modulus of Elasticity (GPa)	45	68	205	115
Fracture Elongation (%)	5	35	45	15
Melting Temperature (°C)	650	660	1536	1630
Cost Index	4	2.6	1	5.5

1.2.2 - Present /Potential Application Areas

In general, magnesium is used for such things as missile components, material handling equipment, portable power tools, bicycles, sporting goods, and where lightweighting is necessary [1.8]. When considering material selection in the transportation industry, the main factors that should be considered are the functionality of the material, the cost, the recyclability, and the overall environmental impact. Considering these, there are many applications or components that would benefit from the use of magnesium considering the required material properties, the benefit of magnesium being highly recyclable, and the benefit of the weight savings of fuel consumption and emissions. However, the main barrier that needs to be considered is the cost of the material and the associated manufacturing costs. Over the years, these factors have been considered and some components have been produced from magnesium.

Magnesium was heavily being used for aircraft production during WWII to lower the plane weight and increase its carrying capacity [1.10]. This material was used extensively in Germany and in their airplanes. After the war, the first main usage was in the Volkswagen (VW) Beetle which used a cast magnesium air cooled engine and gearbox [1.7]. To combat the issues of high temperatures in the combustion chamber, an Al-Steel sleeve was used. Specifically in 1972, VW used 30,000 tons of magnesium. The use of magnesium in other areas that did not use a casting process was showcased in vehicles such as the 1957 Corvette SS racecar which had magnesium body panels and the Porsche 962 racecar (magnesium frame and skin) [1.7].

The usage of magnesium increased in the 1970's, but as aluminum became a cheaper and an easier to manufacture material it caused a diminishing trend in the usage of magnesium in the 1980's. Mainly, although magnesium is 36% lighter than aluminum, it has a difficult time competing as aluminum is more formable and has better strength properties, in addition the cost is less (still present to date).

As of now, casting of magnesium really dominates over wrought products in automotive applications [1.11]. This is mostly because wrought products are harder to manufacture and increase the production costs which are a function of achievable/required production rate and the required manufacturing process. Ultimately it has to be decided if using magnesium to replace a component is beneficial from an economic standpoint as compared to the weight savings over time.

Despite the challenges with magnesium, there have been several production vehicles which have used magnesium components. In addition to the VW magnesium

engine, the US used magnesium for steering columns in the 1970's (GM in 73' and in Ford 78') [1.12]. In 1982, Ford used magnesium in the brake pedal brackets in its Ranger model [1.13]. In 1999, GM was using approximately 3.5kg of magnesium in their vehicles [1.13]. More recently, Ford's F150 used a magnesium front end radiator support which created a savings of 9.3 kg [1.13]. In 2006, BMW used a special high temperature alloy (A562A) to produce magnesium engine blocks for its 325i and 330i models [1.7]. Presently, cars on average have about 2.72 kg of magnesium [1.5]. Other applications where magnesium has been successfully implemented include seat structures, instrument panel frames, steering wheels (today, 85% of steering wheels are made from cast magnesium), cam covers, transmission cases, and intake manifolds [1.4]. The most common cast alloys used in the automotive industry is AM50 and other popular ones are AM60 and AZ91D [1.14]. The most common wrought alloy used for automotive and other applications is AZ31. When considering the names of these alloys, the letters usually represent the major alloying elements. For example in AM60 and AZ31, the "A" is for Aluminum, "M" is for manganese, and "Z" is for zinc.

For the future, one benefit that has high potential in using magnesium is the unsprung mass of the vehicle. One prospect is to make wheels from magnesium, however, current technology in this area is not suitable for high production and the cost would be too high for most consumer vehicles. The use of magnesium wheels has been used in the racing industry where extra cost is allowable. Also, the usage of magnesium extrusions could be implemented in space frame designs [1.13]. Below in Figure 1.1 to Figure 1.3 are magnesium components produced for automotive usage.

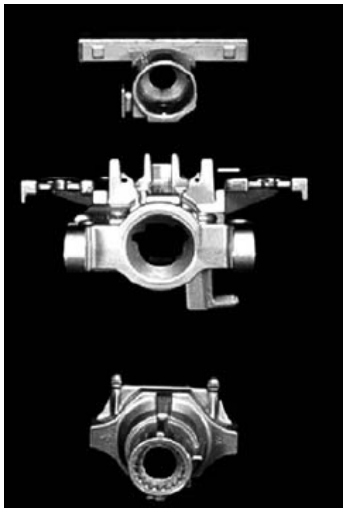

Figure 1.1- Magnesium Steering Column Components (Daimler Chrysler) **[1.14]**

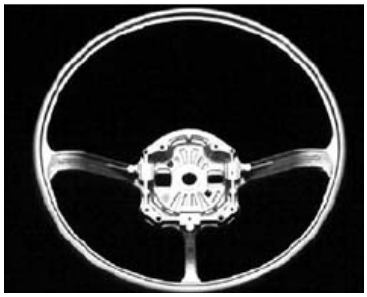

Figure 1.2 - Magnesium Steering Wheel Frame (Alfa Romeo) **[1.14]**

Figure 1.3 - Magnesium Dashboard for Testing **[1.15]**

1.2.3 - Potential Weight Savings

Considering the potential of weight savings, the use of magnesium has a significant advantage when just considering its very low density. Table 1.2 compares some current and potential uses of magnesium and the associated weight reductions. As can be seen for the replacement of a cast iron engine block, using magnesium could reduce the weight by 13 kg or 41%. Savings such as this would be extremely influential in reducing the fuel consumption and emissions of the vehicle over its lifetime. Even for replacing an aluminum alloy engine block, the weight savings would be approximately 19%. Also in this table are other scenarios for varying components. Overall, there is extreme potential for weight savings when incorporating magnesium alloys, however, the design/overall functionality must be met and the cost associated with both the material and manufacturing must be economical for the vehicle manufacturer. This is the main barrier today as current manufacturing technologies for magnesium production at high rates is limited and the cost of the material is higher than its closest competitor (aluminum) [1.11].

Table 1.2 - Weight Reduction Obtained with the use of Magnesium **[1.11]**

Material	Component				
	Engine block	Gearbox & clutch housing	Oil pan	Four road wheels	Engine cradle
Cast iron [kg]	32				
Steel [kg]				36	25
Al alloys [kg]	23.5	24.5	3	23	17.5
Mg alloy [kg]	19	18	2	18	15
Weight reduction [kg]	13/4.5	6.5	1	18/5	10/2.5
Weight reduction [%]	41/19	27	33	50/22	40/15

1.2.4 - Manufacturability

Considering the manufacturability of magnesium, the following sections discuss the types of raw forms available, the most common manufacturing processes used to produce magnesium components, the forming limits, and the joining and the availability of magnesium.

1.2.4.1 - Available Raw Forms

Magnesium is available in wrought form or could be cast into the net shape of the final component. The wrought form is available in extruded profiles (bars and varying shapes), as forgings, or as rolled plate/sheet [1.16]. The two main methods for production of magnesium (the metal) is by an electrolysis process or by a thermal reduction. Electrolysis reduces $MgCl_2$ to metal form and thermal reduction creates magnesium metal by subjecting magnesium oxides to high temperatures and pressures [1.12].

1.2.4.2 - Common Manufacturing Processes

To form the varying wrought products, magnesium alloys from cast ingots can be extruded, rolled, or press forged. During the rolling, extrusion, and forging of these magnesium alloys, it is critical that they be performed at elevated temperatures as a result of the poor formability at room temperature. This hot working of the material is typically done between temperatures of 300-500°C [1.6]. Also for these processes, it is commonly required to use a very low press rate to prevent material cracking/fracture [1.11].

When performing secondary processing of these materials such as machining or grinding, care must be taken as small/fine magnesium powders are highly flammable, however, these processes are very easily accomplished on this material [1.8]. When

secondary forming rolled sheet, this must also performed at elevated temperatures to mitigate the premature failure of the material [1.16]. The process of superplastic forming is a popular process to achieve enormous elongation increases in fine grained magnesium sheet. Obviously, the use of wrought products would be more ideal for automotive usage as they have better mechanical properties over cast magnesium components, however, the use of wrought components has not been used on a large scale in the automotive market.

Considering the casting of magnesium, this material can be sand and permanent molded (depending on the production rate and desired tolerances). For permanent molding, high pressure die casting is a common process used to achieve high productivity at relatively low costs. The most common die casting alloys include: AM50, AM60, AZ91D, ACM522, AXJ552, AS21X, AJ52X, and AJ62. Cold chamber machines are typically used when large castings are required and hot chamber machines are used for smaller components [1.11].

Overall for casting, magnesium is an ideal material as it has a low melting point, high fluidity, low specific heat, can handle high gate pressures (limit porosity), and has low solubility for Fe (does not cause die wear or react with steel dies) [1.5].

1.2.4.3 - Forming Limits

Magnesium forming requires elevated temperatures to enable different deformation mechanisms mostly due to its HCP crystal structure and the limited amount of slip systems [1.6]. For forming at room temperature which is commonly required for the high production of sheet metal components used in the automotive industry, this has significantly reduced the use of this material in wrought form (*i.e.* brittle behavior during

cold forming). Current research is exploring the use of magnesium wrought products and working to improve the manufacturability of the material. For example, superplastic forming (SPF) research has been focused on improving the formability of magnesium sheet and applying it to higher production scenarios [1.16]. An example of SPF of magnesium sheet metal is shown in Figure 1.4.

Figure 1.4 - Superplastic Forming of Magnesium at 400°C with Varying Strain Rates **[1.16]**

1.2.4.4 - Jointing Methods

Considering the joining of magnesium to itself, this can be performed using MIG or TIG welding, however TIG being the most popular [1.5]. During welding, it is necessary to have the appropriate gas shielding as the molten material will readily react with the environment and this can cause brittle areas or heavy oxidation which usually creates a weakened weld. For the joining of seams, the material can be spot and seam welded. However, joint bending is a significant problem with magnesium as the

achievable bend radius is very large (2-3 times) compared to other common automotive materials [1.8].

For the use of rivets/bolts/fasteners, this creates large problems with galvanic corrosion. Galvanic corrosion is caused from the interaction of metals that have different electrode potentials which causes the cathode metal to dissolve the anode metal. As a result, it is difficult to join magnesium to other materials without a protective barrier or coating. On the market, there are many suitable adhesives that could be used if applicable to the specific component. Also, research pertaining to Stir Friction Welding (SFW) of magnesium is being investigated for the joining of dissimilar metals (very popular method as a result of its low melting point).

1.2.4.5 - Material Availability

Magnesium is more difficult to obtain than to aluminum or steel. Really, there are only certain companies in the world that heavily produce magnesium products or stock. Most manufactures of magnesium stock and products are in Canada and Europe.

1.2.5 - Recyclability/Environmental Impact

The use of magnesium is excellent from a recycling point of view. This material is easily recyclable as a result of its low melting point and low specific heat, however, considering the automotive market there is not a very large recycling effort as a result of the low amount of material contained in the vehicles [1.17]. As of now, most recycling of magnesium from automobiles just gets mixed with the other non-ferrous materials (Al and Cu) after being sent through the car shredder. After being separated from the ferrous material, it is usually just used as alloying elements for other materials (*e.g.* aluminum)

[1.18]. Yet, with the increased use of magnesium in the automotive industry, this will increased the amount of recycled material and will open new avenues for magnesium separation from other non-ferrous materials and separation by magnesium alloy [1.19].

1.2.6 - Material Cost

Presently, one of the main barriers to heavy adoption of this material into the automotive market is cost. Today, automakers are viewing aluminum as a more suitable lightweight material even though magnesium is lower in density. This is mainly resulting from the better material properties (*i.e.* higher strength) and lower costs of aluminum. The relative cost of magnesium with other common vehicle engineering materials is compared in Table 1.1. Additionally, the magnesium market is much more susceptible to fluctuations in material price which creates additional concern for automotive manufacturers as they cannot reliably receive the same product as the same price [1.6]. This is extremely important in the automotive sector as most designs and manufacturing techniques are highly cost driven and the products have lower cost margins to other sectors.

1.2.7 - Potential/Barriers to Adoption

As of now, the use of magnesium is limited in the automotive industry and is only applied where it is economical for the manufacturer. However, with the escalating need for increased fuel economy and lower emissions, this material will definitely be a major player in the future. Listed below are some of the potential barriers that are prohibiting the use of magnesium on a large scale in the passenger vehicle market [1.6, 1.7, 1.11]:

- Material cost

- Poor high temperature strength
- Poor corrosion resistance (in general and high galvanic corrosion), needs coatings in many applications (does form self-oxidizing layer which protects itself)
- Difficult to bond/attach to different materials due to galvanic corrosion
- Low creep resistance
- High coefficient of thermal expansion which may be limiting it in certain applications
- Low modulus
- Low ductility at lower temperatures
- Low fatigue stability
- Heavy adoption would require investments in new specific equipment and research/development of alloys and manufacturing methods

Essentially, the present automotive industry is using magnesium in low amounts and where it has been proved in the past.

1.2.8 - Magnesium Conclusion

Overall, magnesium is a very attractive material to reduce the weight of a vehicle. The main factor in its limited use is the cost/market of the material and the difficulty in manufacturing of the wrought products. Nevertheless, magnesium has been successfully implemented in the vehicle where it has been found to be economically viable for the vehicle manufacturer.

1.3 - Motivation

One evolving method to help process and manufacture lightweight materials is Electrically-Assisted Forming (EAF). From the late 1950's, this process has progressed, however, has not been adopted in industry as a result of the lack of fundamental knowledge on the processing mechanisms and limited modeling work. As a result of the limited modeling efforts since its inception, this process is not currently predictable and any attempts to manufacture materials using this technique would not be optimal (*e.g.* minimum energy forming of high strength materials or maximizing achievable elongation). As a result of not being able to provide optimal conditions for the processing of materials, it is still uncertain to manufacturers how feasible this technique is for industrial applications.

The EAF process combines a direct electrical current with a deformation process such that the electrical current passes through a metal component during deformation to improve its plasticity. In addition, the EAF process has been shown to reduce forces required for deformation and remove the elastic recovery of the material (*i.e.* springback). A process schematic is shown in Figure 1.5 where a current source applies an electrical current through a metallic component and a machine applies deformation to the component. Feedback from the process includes force, displacement, temperature, voltage, and current.

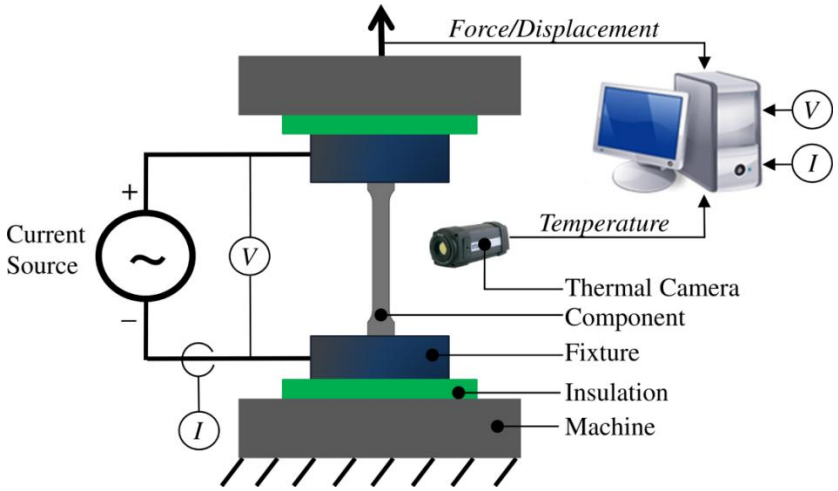

Figure 1.5 - Schematic of Electrically-Assisted Forming (EAF)

These process benefits show strong potential for easing the manufacturing difficulty of lightweight materials such as magnesium and hence this process is further researched from a fundamental standpoint in this dissertation.

When considering the applicability of EAF, this processing technique has a wide range of industries that could potentially benefit. Considering the automotive industry, most vehicles produced today have a vehicle architecture which is constructed from a unibody or body-in-white (BiW) which is primarily a collection of joined sheet metal components which have been bent and/or stamped (Figure 1.6). Considering the large amount of stamping and bending of sheet metal required, EAF has the potential to help improve the efficiency of these processes by allowing for more achievable deformation before material failure and for the application of springback reduction. With the potential for improved formability from current materials, this could provide a reduction of the number of components that need to be stamped and bent separately, thus reducing the required number of individual parts needed to construct the BiW. This would be

significant for manufacturers as this would lower the complexity of body assembly and it would reduce the time for the actual manufacturing or construction of the BiW.

The reduction in the number of components which typically promotes optimal geometry designs and the incorporation of lightweight materials is increasingly important today and in the future as vehicle fuel consumption, vehicle emissions, and the turn toward hybrid and electric vehicles requires the mass of the vehicle to be reduced. Additionally, the topic of lightweighting vehicles is becoming more important and consequently manufacturers of vehicles are turning to more effective designs which reduce unnecessary ("lazy") parts and toward the use of lightweight materials (Mg, Al, Ti, and composites). As these lightweight materials typically suffer in ductility (as a result of material properties and crystalline structure) for the high production rates required for the automotive industry, EAF could alleviate the issue of low fracture strain and allow for the materials to be used on a larger scale in production. Last, for automotive, the forming of the skin or panels of the body could utilize EAF to allow for sharper contours or new lightweight (usually less ductile materials) to be incorporated. Other industries that have the potential to be impacted from EAF include aerospace, medical, and sheet metal forming industries in general.

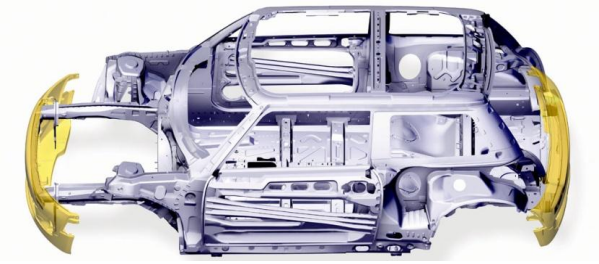

Figure 1.6 - Body in White (BiW) [1.20]

1.4- Research Objective

The objective of this research is to understand and model the deformation behavior of sheet metal in uniaxial tension subject to direct electrical current flow during deformation. Deformation behavior is defined as the material flow stress, local material strain, and thermal response of the material.

The model will incorporate mechanical, electrical, and thermal properties of the material, the attributes of the applied electrical current, and the processing parameters. The specific model inputs and outputs are shown in Table 1.3. The inputs in Table 1.3 were selected as they are necessary to obtain a model of deformation behavior under an applied electrical current and are critical parameters determined from other researchers and the PhD candidate in the field of Electrically-Assisted Forming (EAF) [1.21-1.40]. The model outputs relate directly to the research objective and allow for the deformation behavior to be characterized.

Table 1.3 - Model Inputs and Outputs for Electrically-Assisted Forming of Sheet Metals

Model Inputs				Model Outputs
Material	Mechanical	Strength Coefficients		Material Flow Stress
		Strain Hardening Exponent		
		Strain Rate Sensitivity Exponent		
		Yield Strength		
		Density		Local Material Strain
	Electrical	Electrical Resistivity		
	Thermal	Thermal Conductivity		
		Heat Capacity		
Process	Mechanical	Strain Rate		
	Electrical	Current Magnitude		Thermal Response
		Duty Cycle		
		Wave Shape		
	Thermal	Convection Coefficient		
		Initial Workpiece/Die Temperatures		

The target material for this research is magnesium sheet metal because of its industrial interest, low density, and low formability in common sheet forming processes. It should be noted that this work is specifically studying the deformation mode of uniaxial tension as this is a necessary and major research subject that must be understood before expanding this work to other strain paths or bi-axial loading conditions.

The process of EAF is defined as the application of a direct electrical current through the workpiece while being subject to deformation. Present experimental findings dating back to the late 1950's have shown that when a direct electrical current is applied during forming of a metallic material, the forming force or flow stress is reduced, the amount of achievable deformation before failure can be increased over traditional methods, and the amount of springback in the formed part can be reduced. This prior research has also shown that the applied electrical current not only increases the temperature of the workpiece, but also directly aids in the deformation process (named the "electroplastic effect"). The current state-of-the-art work in this field is just beginning to model and describe how the addition of an electric current field affects the processing of metals from both a macroscopic and microscopic view. This work is primarily focused on the macroscopic or bulk characteristics of the deformation of metals and is directed toward the deformation behavior of sheets during EAF. In addition, the most modern theory of the electroplastic effect is discussed and this work explores first-principle physics models to understand the magnitude of various proposed direct electrical effects.

The intellectual merit of this work is a model which predicts the deformation behavior (*i.e.* material flow stress, local material strain, and temperature distribution of

the material) for sheet metal subject to a direct electrical current field. This model is influential in that it will bring EAF to a feasible position for industry and advance the state of knowledge for sheet metal forming. Moreover, this work quantifies how the applied electrical current is divided into bulk material temperature rise and how much energy is directly imparted into the deformation process itself for sheet metal forming. Last, prior research in the field of EAF has been performed with an open-loop control architecture for controlling the process output. However, this work also incorporates a closed-loop system that can be utilized to control the process and its desired output. Thus, a new class of control approaches specific to EAF are developed and demonstrated.

The broader impact of this dissertation work lies in the potential for future adoption of the process of EAF in manufacturing industries such as automotive and aerospace. The potential for improved formability of lightweight materials at high production rates and for reduced process energy consumption could potentially save these industries millions of dollars in manufacturing costs. In addition, the ability to economically produce vehicles from lightweight materials will lower their fuel consumption and emissions over time. Moreover, with the future turning toward hybrid and electric vehicles, the reduction of vehicle mass is crucial; and for manufacturing of these lightweight materials, EAF could lead the way. Additionally, as most metal deformation processes are performed first by simulation to save time and reduce costs, the developed models and modeling methodologies of this work can also be incorporated into commercial Finite Element (FE) software for prediction of metal forming processes in varying industries.

1.5 - Organization of the Dissertation

Chapter 1 of this dissertation provides a brief background to lightweight materials which set the motivation and objective of this work. In *Chapter 2*, a comprehensive literature review is provided for *i)* the forming of metals, *ii)* prior work in the field of EAF, and *iii)* classical plasticity theory as it is the foundation for this work. Then, *Chapter 3* describes the overall EAF modeling approach used in this dissertation and the main factors incorporated into the models. *Chapter 4* introduces the thermal modeling approach for EAF in detail and the predictive capability of the model is demonstrated for a series of test cases. In *Chapter 5*, the material flow stress and local strains for EAF are modeled using results from the thermal modeling performed in *Chapter 4*. Subsequently in *Chapter 6*, the thermal model and flow/deformation models are combined to a multiphysics model which predicts the local strain, material stress, and temperature for the sheet metal. *Chapter 7* explores experimental EAF and elevated temperature forming results by analyzing the mechanical properties. Following, the microstructure of the formed samples from *Chapter 7* are examined in *Chapter 8*. *Chapter 9* introduces potential control approaches for EAF and several are demonstrated. In *Chapter 10*, the theory of electroplasticity is explored and the most up-to-date understanding of the electroplastic effect is provided. Finally, *Chapter 11* concludes the dissertation by providing a summary of the major contributions of this work.

1.6 - References for Chapter 1

[1.1] National Highway Traffic Safety Administration(NHTSA) (2010). "Light-Duty Vehicle Greenhouse Gas Emission Standards and Corporate Average Fuel Economy Standards; Final Rule." *Federal Register 40 CFR Parts 85, 86, and 600; 49 CFR Parts 531, 533, 536, et al.*, 75(88): 25324-25728.

[1.2] M. Kuttolamadom, J.J. Jones, L. Mears, J. Ziegert, and T. Kurfess "A Systematic Procedure for Integrating Titanium Alloys as a Lightweight Automotive Material Alternative," *SAE Technical Paper* 2011-01-0429, doi:10.4271/2011-0429, 2011.

[1.3] M. Verbrugge, T. Lee, P. Krajewski, A. Sachdev, C. Bjelkengren, R. Roth, and R. Kirchain "Mass Decompounding and Vehicle Light-weighting." *Materials Science Forum*, Vol. 618-619 pp. 411-418, 2009.

[1.4] "Automotive Uses of Magnesium Alloys: Part One." 11/1/2010, http://www.keystometal.com

[1.5] L. Gaines, R. Cuenca, F. Stodolsky, and S. Wu "Potential Applications of Wrought Magnesium Alloys for Passenger Vehicles," Argonne National Laboratory, Argonne, Illinois, 1995.

[1.6] L. Gaines, R. Cuenca, F. Stodolsky, and S. Wu "Potential Automotive Uses of Wrought Magnesium Alloys," *Automotive Technology Development*, Detroit, Michigan, 1996.

[1.7] "Automotive Uses of Magnesium Alloys: Part Two." 11/1/2010, http://www.keystometal.com

[1.8] S. Kalpakjian *Manufacturing Processes for Engineering Materials*, 3rd ed. Menlo Park, CA: Addison Wesley Longman Inc., 1997.

[1.9] "Mechanical Properties of Magnesium and Magnesium Alloys." 11/1/2010, http://www.keystometal.com

[1.10] Superform Aluminum "AZ31B: Automotive Material Data Sheet- Mechanical and Design Information for Superforming Alloys," www. superform-aluminum.com, 2010.

[1.11] E. Aghion, B. Bronfin , H. Friedrich and Z. Rubinovich "The Environmental Impact of New Magnesium Alloys on the Transportation Industry," *Magnesium Technology: The Minerals, Metals & Materials Society*, pp. 167-172, 2004.

[1.12] H. Watarai "Trend of Research and Development for Magnesium Alloys – Reducing the Weight of Structural Materials in Motor Vehicles." *Science and Technology Trends*, No. 18, pp. 84-97, 2006.

[1.13] "Magnesium use in vehicles in the U.S. (1972-2003)." 11/1/2010, http://www.magnesium.com

[1.14] F. Bergeron, and J. Audet Feasibility Study for the Development and Marketing of Magnesium Seats for Motor Coaches and Other Modes of Public Transportation," IC^2 Technologies, Prepared for the Transportation Development Centre of Transport Canada, 2004.

[1.15] J. Lin, S. Lanka, and T. Ruden "Physical and Virtual Prototyping of Magnesium Instrument Panel Structures," *2005 SAE World Congress,* 2005-01-0726, pp10, 2005.

[1.16] F.K. Abu-Farha, and M.K. Khraisheh "Mechanical Characteristics of Superplastic Deformation of AZ31Magnesium Alloy." *Journal of Materials Engineering and Performance*, Vol.16, No.2, pp. 192-199, 2007.

[1.17] M. Chen "End-of-Life Vehicle Recycling in China: Now and the Future," *JOM*. pp. 20-26, 2005.

[1.18] A. Gesing, and R. Wolanski "Recycling Light Metals from End-of-Life Vehicles," *JOM*, pp.21-23, 2001.

[1.19] R. Brown "Magnesium Recycling Yesterday, Today, and Tomorrow," *Recycling of Metals and Engineered Materials: The Minerals, Metals &Materials Society*. pp. 1317-1329, 2000.

[1.20] Mini, "New MINI: Preview images and info," 2006.

[1.21] C. Bunget, W. Salandro, L. Mears, and J.T. Roth "Energy-based Modeling of an Electrically-assisted Forging Process," *Transactions of the North American Manufacturing Research Institute of SME,* vol. 39, 2010.

[1.22] H. Conrad, "Effects of Electric Current on Solid State Transformations in Metals," *Materials Science & Engineering,* vol. A287, pp. 227-237, 2000.

[1.23] H. Conrad, "Electroplasticity in Metals and Ceramics," *Materials Science & Engineering,* vol. A287, pp. 276-287, 2000.

[1.24] H. Conrad, "Thermally Activated Plastic Flow of Metals and Ceramics with an Electric Field or Current," *Materials Science & Engineering,* vol. A322, pp. 100-107, 2002.

[1.25] J. J. Jones, and J.T. Roth, "Effect on the Forgeability of Magnesium AZ31B-O When a Continuous DC Electrical Current is Applied," in *ASME International Manufacturing Science and Engineering Conference*, West Lafayette, IN, 2009, p. 10.

[1.26] J. J. Jones, and L. Mears "Empirical Modeling of the Stress-Strain Relationship for an Upsetting Process Under Direct Electrical Current," *Transactions of the North American Manufacturing Research Institute of SME,* vol. 38, 2010.

[1.27] J. J. Jones, and L. Mears, "A Process Comparison of Simple Stretch Forming using Both Conventional and Electrically-Assisted Forming Techniques," in *ASME International Manufacturing Science and Engineering Conference*, Erie, PA, 2010, p. 9.

[1.28] J. J. Jones, and L. Mears, "Constant Current Density Compression Behavior of 304 Stainless Steel and Ti-6Al-4V during Electrically-Assisted Forming," in *ASME International Manufacturing Science and Engineering Conference*, Corvallis, OR, 2011, p. 9.

[1.29] T. A. McNeal, J.A. Beers, and J.T. Roth, "The Microstructural Effects on Magnesium Alloy AZ31B-O While Undergoing an Electrically-Assisted Manufacturing Process," in *ASME International Manufacturing Science and Engineering Conference*, West Lafayette, IN, 2009, p. 10.

[1.30] T. A. Perkins, T.J. Kronenberger, J.T. Roth, "Metallic Forging Using Electrical Flow as an Alternative to Warm/hot Working," *Journal of Manufacturing Science and Engineering,* vol. 129, pp. 84-94, 2007.

[1.31] C. D. Ross, D.B. Irvin, and J.T. Roth, "Manufacturing Aspects Relating to the Effects of DC Current on the Tensile Properties of Metals," *Journal of Engineering Materials and Technology,* vol. 129, pp. 342-347, 2007.

[1.32] C. D. Ross, T.J. Kronenberger, and J.T. Roth "Effect of dc on the Formability of Ti–6Al–4V," *Journal of Engineering Materials and Technology,* vol. 131, p. 11, 2009.

[1.33] J. T. Roth, I. Loker, D. Mauck, M. Warner, S.F. Golovashchenko, A. Krause, "Enhanced Formability of 5754 Aluminum Sheet Metal Using Electric Pulsing," *Transactions of the North American Manufacturing Research Institute of SME,* vol. 36, pp. 405-412, 2008.

[1.34] W. A. Salandro, J.J. Jones, T.A. McNeal, J.T. Roth, S.T. Hong, and M.T. Smith "Effect of Electrical Pulsing on Various Heat Treatments of 5xxx Series Aluminum Alloys," in *ASME International Manufacturing Science and Engineering Conference*, Evanston, IL, 2008, p. 10.

[1.35] W. A. Salandro, A. Khalifa, and J.T. Roth "Tensile Formability Enhancement of Magnesium AZ31B-O Alloy Using Electrical Pulsing," *Transactions of the North American Manufacturing Research Institute of SME,* vol. 37, 2009.

[1.36] W. A. Salandro, and J.T. Roth, "Formation of 5052 Aluminum Channels Using Electrically-Assisted Manufacturing (EAM)," in *ASME International Manufacturing Science and Engineering Conference*, West Lafayette, IN, 2009, p. 10.

[1.37] W. A. Salandro, C. Bunget, and L. Mears, "Modeling and Quantification of the Electroplastic Effect when Bending Stainless Steel Sheet Metal," in *ASME International Manufacturing Science and Engineering Conference*, Erie, PA, 2010, p. 10.

[1.38] W. A. Salandro, C. Bunget, and L. Mears, "Thermo-mechanical Investigations of the Electroplastic Effect," in *ASME International Manufacturing Science and Engineering Conference*, Corvallis, OR, 2011, p. 10.

[1.39] M. S. Siopis, and B.L. Kinsey "Experimental Investigation of Grain and Specimen Size Effects During Electrical-Assisted Forming," *Journal of Manufacturing Science and Engineering,* vol. 132, p. 7, 2010.

[1.40] M. S. Siopis, B.L. Kinsey, N. Kota, and O. Ozdoganlar "Effect of Severe Prior Deformation on Electrical-Assisted Compression of Copper Specimens," in *ASME International Manufacturing Science and Engineering Conference*, Erie, PA, 2010, p. 7.

CHAPTER 2 - THEORY AND LITERATURE REVIEW

Herein, a literature review is provided in the areas of metal forming, Electrically-Assisted Forming (EAF), and classical plasticity theory.

2.1 - Metal Forming

2.1.1 - Forming Techniques

In many industrial applications, manufactures utilize processing techniques which allow their products to be produced efficiently and to the correct specifications. Considering sheet metal operations, one obstacle still faced is the lack of formability certain materials exhibit when being formed to complex shapes. This is mostly exhibited by less ductile materials such as magnesium, titanium, and some high strength aluminum alloys. As a result, some components are required to be made in smaller sections then collectively jointed using a fastening technique. Accordingly, this increases the individual part cost and the possibility of error/variability during assembly of the part while still not producing the component from one structurally sound piece.

Considering these issues with formability, common methods undertaken by manufacturers to improve the plasticity of sheet metal materials include: *i)* hot working, *ii)* incremental forming, *iii)* superplastic forming, and the use of *iv)* tailor welded blanks. The following sections summarize these processes and discuss the benefits and drawbacks.

2.1.1.1 - Hot Working

Hot working is the process of metal deformation where the material is first heated to a temperature greater than its recrystallization temperature before forming. As a result

of the higher temperature, the strength of the material decreases and the formability increases. However, with this process there are several drawbacks which included the abundance of residual stresses remaining after forming, an increased amount of workpiece/die adhesion during forming, a decrease in forming lubricant effectiveness, and greater amounts of dimensional variability between parts [2.1].

2.1.1.2 - Incremental Forming

Formability of sheet metal can also be improved through the technique of incremental forming. With this process, the material is deformed a certain strain percentage and then the material is removed from the die to be heat treated, thus reducing the effects of cold work stored within the material [2.2]. Yet, with the constant removal and refixturing of the workpiece, this not only increases processing time, but introduces the possibility for part variation. A schematic of this process is shown in Figure 2.1 where the $\Delta\sigma$'s represent the reduction in strength from the process anneal.

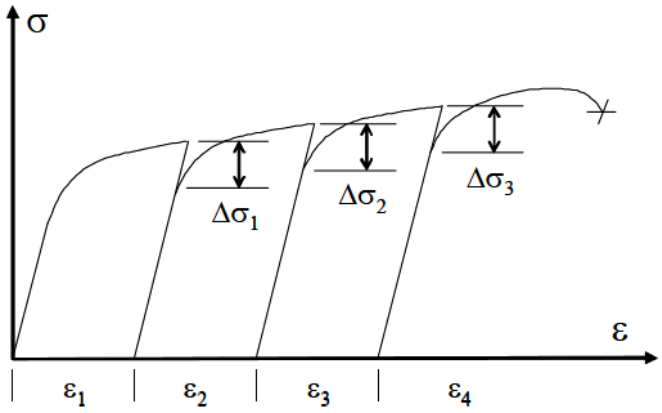

Figure 2.1 - Incremental Forming Process Schematic [2.2]

2.1.1.3 - Superplastic Forming (SPF)

The process of superplastic forming (SPF) occurs when the material is first heated to approximately two-thirds its melting temperature, then the forming process takes

place. This process differs from pure hot working in that it is commonly only for sheet components and the temperatures are slightly higher. The use of superplastic forming is extremely efficient in increasing the plasticity of the material. Specifically, elongation increases around 2000% can be attained in addition to the benefit of reduced flow stress during forming and low residual stresses once the process is complete [2.3]. However, this process is limited to only fine-grained materials as a result of the deformation mechanism present (grain boundary sliding) and the required strain rate is very low. Thus, this process is very time consuming and unfeasible for components which require high production rates due to vary large cycle times. An example SPF process for a fuel tank half manufactured from titanium is shown in Figure 2.2. Recent improvements to this process by Ford Motor Company have allowed for decreases in processing time (85% reduction) and for non-fine grained aluminum alloys to be used [2.4]. The process by Ford combines an initial hot stamping process, thus eliminating a large portion of the process which used to be only performed by gas forming.

Figure 2.2 - Superplastic Forming of Titanium Sheet [2.5]

2.1.1.4 - Tailor Welded Blanks (TWB)

Another method to help improve formability is to place material with the desired properties at the correct location on a component. This process is known as tailor welded blank (TWB) manufacturing [2.6]. Different materials in certain regions help to achieve the desired amount of formability or strength in specific areas. However, this process introduces extra processing time and cost in combining the materials and there may be variability from part to part due to the joining operation. An example of a TWB component used as a B-pillar in an automobile is shown in Figure 2.3.

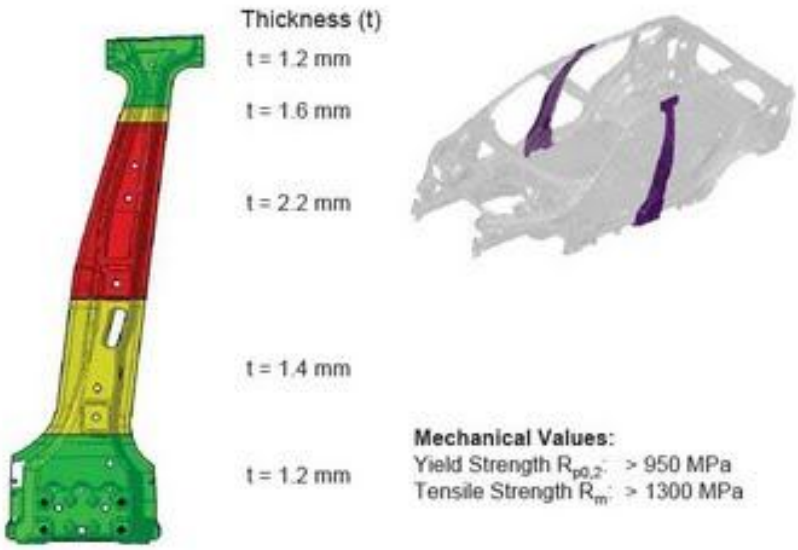

Figure 2.3 - Tailor Welded Blank [2.7]

2.1.1.5 - Electrically-Assisted Forming (EAF)

Considering an alternative processing technique which may alleviate or reduce some of these previously mentioned drawbacks would be significantly beneficial for manufacturers producing sheet metal components. One evolving technique is Electrically-Assisted Forming (EAF) which applies a direct electrical current through the workpiece concurrently while the material is being formed. At present, this technique has

only been studied on an experimental level in laboratory settings, and the heuristic results show increased fracture strain, reduced flow stress, and reduced springback; the enhanced process capability is beyond the range that would be expected from pure resistive heating effects [2.8]. A schematic of EAF is shown in Figure 1.5. Engineering materials that have been experimentally examined recently in a laboratory setting are listed in Table 2.1.

Table 2.1 - EAF Materials Examined

	Aluminum	Copper	Steel	Titanium	Magnesium
Alloy	2024 5052 5083 5754 6061 6111 7075	C11000 C22000 C26000 C27000 C36000 C46400	304 Stainless A2	Grade 2 (CP) Grade 5 (6Al-4V)	AZ31B

As an example, the improvement in material fracture strain for conventional forming compared with EAF in uniaxial tension is shown in Figure 2.4 for a magnesium alloy where the achievable elongation is approximately double that of the conventional process.

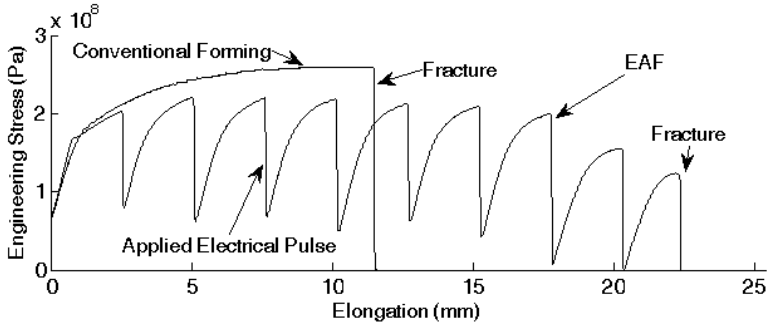

Figure 2.4 - Increased Elongation and Reduced Flow Stress for EAF of Magnesium Sheet Metal [2.9]

Although this processing technique shows promising benefits, there is a lack understanding of the physical dominant mechanisms during EAF and this process lacks predictive modeling, both empirical and first principle. Additionally, issues need to be addressed with the design and large scale feasibility of this processing technique.

2.1.2 - Deformation Theory of Metals

When considering metals at an atomic level, the metallic bond consists of ion cores (non-valence electrons and atomic nuclei) surrounded by valence electrons (electron cloud) which act as the medium to hold the ion cores together. Inside the electron cloud, there are typically one to three valence electrons per ion core and they are free to move within this region and are not restrained by any particular ion core. The ion cores vibrate rapidly about their present lattice position. With a rise in material temperature the average vibration energy of the ion core increases. At room temperature, a typical vibrational frequency is on the order of 10^{13} Hz with amplitudes around a few thousandths of a nanometer [2.10]. The concept of metallic bonding is simply illustrated in Figure 2.5.

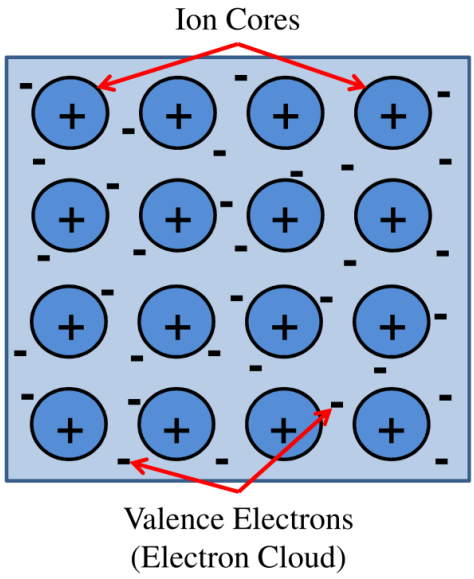

Figure 2.5 - Ion Cores Surrounded by Valence Electrons

Plastic deformation corresponds to the breaking and reforming of bonds that do not return to their original position once the stress is removed. The most common deformation mechanism is slip which occurs by dislocation creation/annihilation and motion. The crystallographic location that the dislocation moves on is called the slip plane which has the densest atomic packing for a particular crystal structure. On a slip plane there are certain preferred directions in which the dislocations move and these are defined by the directions having the greatest linear density. The dislocation density of a material is the total dislocation length per unit volume with units of mm/mm^3 or mm^{-2}. Example densities are $10^3 mm^{-2}$ for carefully solidified metals to 10^9 to $10^{10} mm^{-2}$ for heavily deformed metals [2.10]. For each dislocation within the metal's lattice there exists a strain field. When a metal is deformed, about 95% goes to heat whereas the remaining 5% is retained internally. Almost all of this 5% goes to strain energy associated with dislocations. The strain energy surrounding a dislocation causes interactions with

other defects and dislocations in the lattice. Two dislocations on the same slip plane with their strain fields aligned are repulsive. In contrast, two dislocations with opposite strain fields will attract and cause dislocation annihilation. The basic concept of plastic deformation is shown in Figure 2.6 where an edge dislocation is created.

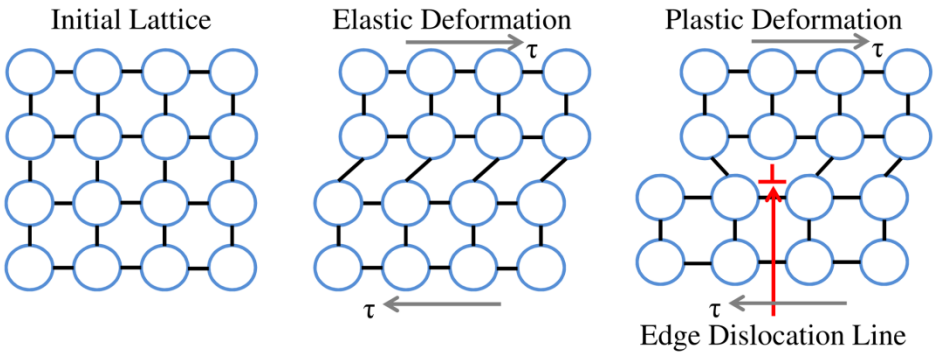

Figure 2.6 - Creation of an Edge Dislocation due to an Applied Stress

A dislocation can be classified as an internal defect that is caused by a metal's ion cores being misaligned, thus causing the bonds between the ion cores to be alternately stretched and compressed. There are three main categories or classifications of dislocations: edge, screw, and mixed which is a combination of an edge and screw dislocation. When discussing dislocation motion, it is known that a dislocation will move through the lattice on a slip plane. The number of slip planes within a material is determined by the metal's crystalline structure. When discussing the crystalline structure of the material in this dissertation, magnesium has a HCP crystal structure (3 slip systems) which has fewer slip systems (combination of slip plane and direction) in comparison to a BCC (12 or 24 slip systems) or a FCC (12 slip systems) crystal structure. Specifically for basal slip of magnesium which is active at room temperature, the slip plane is $\{0001\}$ with three different $\langle 11\bar{2}0\rangle$ directions, thus there are three basal slip

systems. Also in HCP magnesium there is $\{10\bar{1}0\}\langle 11\bar{2}0\rangle$ prismatic slip and $\{10\bar{1}1\}\langle 11\bar{2}0\rangle$ pyramidal slip, but these planes have larger critical resolved shear stresses and are harder to activate at lower temperatures. As a result, these materials tend to be less ductile due to their limited number of slip systems.

As the dislocations move through the lattice, they will interact with other internal flaws or defects. The flaws that a dislocation may interact with include: grain boundaries, phase boundaries, voids, cracks, impurity atoms, and other dislocations. To circumvent these obstacles, the dislocation may change direction, bend, bow, or slide around the internal lattice flaws. Alternatively, the material could continue deformation by twinning. This deformation mechanism is where the material does not deform by slip on its slip planes; instead, the lattice structure reorients itself such that the structure is mirrored on each side of the twinning plane.

Excluding twinning, as a material is deformed, the number of dislocations or dislocation density also continues to increase in the material. With this increase in dislocation density, the required flow stress increases due to the fact that most of the created dislocations within the lattice tend to be repulsive in nature, as well as, the abundance of the new dislocations being impeded by other lattice flaws. As a result of the impeded motion, the flow stress within the material increases, thus making the material more difficult to deform. This process is classified as strain hardening.

Another factor when considering plastic deformation is the strain rate which is imposed on the material. For most metals, an increased strain rate increases the force that is required to deform the material due to the strain rate hardening effect. Also, if the

strain rate is increased, the ductility of the material usually decreases in comparison to a slower strain rate. When considering how the strain rate affects the strength of a material, an important factor that needs to be considered is the temperature at which deformation is occurring. Since working a material at an elevated temperature with a certain strain rate usually decreases strength and increases ductility, this factor plays an important role in the strain rate/strength relationship. Normally, a material that is plastically deformed at room temperature has little to no strain rate sensitivity with respect to the material's strength. However, at elevated temperatures, the strength is highly dependent on the strain rate due to material anelasticity.

2.1.3 - Sheet Metal Formability

2.1.3.1 - Definition of Formability

The formability of a material can be generally defined as the ability of a material to plastically deform to a desired shape without the presence of defects. When considering the formability of a material there are many considerations or inputs to the forming process. These can be broken down into three main categories: process parameters, material attributes, and strain boundary criteria. These three groups are detailed in Table 2.2 with the most relevant parameters highlighted.

Table 2.2 - Factors that Influence Formability [2.12]

Formability	Process	Deformation Mode
		Applied Stress State
		Strain Rate
		Temperature
		Lubrication Regime
	Material	Normal Anisotropy
		Yield Strength
		Fracture Toughness
		Strain Hardening
		Strain Rate Sensitivity
		Grain Size and Shape
		Dislocation Density
		Texture
		Crystal Structure
	Strain Boundary Criteria	Wrinkling
		Surface Roughness
		Springback
		Strain Localization
		Tearing

For sheet stamping, work by Ford Motor Company has developed forming indices that classify possible defects resulting from a forming process [2.11]. The defects that are the basis of the indices are:

1) Splits in the stamping – mechanical damage on the stamping surface that develops into a local neck that eventually creates a split with continued deformation.
2) Splits on the stamping edge – burrs on the sheet edge under tensile stresses become regions where splitting can occur.

3) Wrinkling – a local area in the sheet suffers a compressive stress which leads to plastic instability and sheet waviness.
4) Shape change – during unload of the sheet elastic recovery or springback can occur.
5) Low stretch – low deformation of flat areas of the sheet can have less work hardening than other areas and suffer in dent resistance.
6) Soft surface – an uneven amount of deformation in a flat area of the sheet can cause unbalanced residual stresses such that a small force disturbance on the sheet after forming can cause elastic instability (*i.e.* oil canning).

For these defects, the first two are hard failures where the remaining defects are unacceptable during sheet forming. From these defects, six formability index terms have been derived corresponding to the above failure modes:

1) Anti-fracturability
2) Anti-edge-fracturability
3) Anti-wrinklability
4) Shape-fixability
5) Stretchability, and
6) Anti-buckability

Additionally, other formability parameters can include: the normal anisotropy, the limiting dome height (LDH), the hole expansion ratio, the forming limit diagram (FLD), and the uniaxial tensile test data. These aforementioned parameters are described below.

Normal Anisotropy – The normal anisotropy coefficient (r_n) can be used as a measure of formability as it defines the resistance of the material to thinning. It can be defined by the ratio of the strain in the width direction to the strain in the thickness direction. Thus, it is desirable to have a higher *r* value so that the material will be more resistive to thinning and delay material failure. The normal anisotropy relates to formability as the resistance to thinning is critical in sheet forming as the material fails from local thinning (necking). The mathematical relations are given in Equations (2.29) and (2.30).

Limiting Dome Height – The limiting dome height (LDH) is a measure of formability of sheet metal in that it collectively quantifies parameters such as the n-value, the m-value, and achievable elongation. This value is limited to the stretching mode and provides more realistic data as it includes die contact and friction. For the testing, various sheet specimen widths are tested (get varying strain paths) and the maximum height of the dome is the LDH value. Thus, the higher the LDH value, the higher the formability of the material.

Hole Expansion Ratio – The hole expansion ratio (λ value) is a formability measure that describes the formability of sheet metal near the edges of the part. This ratio is useful for determining how a material will form in relation to the edges of the blank to be formed. A larger ratio value is desired as there will be a higher capability for reaching higher strain without material failure. This ratio and the results are very sensitive to the quality of the edge and the microstructure of the material, thus testing should probably

replicate the same quality and microstructure that will be used for the actual forming process.

Forming Limit Diagram – The forming limit diagram (FLD) is a common conceptual tool used to represent the forming behavior for a given material while describing the onset of sheet necking for varying loading configurations. On an FLD, the forming limit curve (FLC) represents the maximum achievable major principle strains for a given minor principle strain (Figure 2.7). The strain paths shown in the figure from left to right are: pure shear, uniaxial tension, plane strain, stretching, and balanced bi-axial stretching. This concept was introduced by Keeler and Backofen in 1964 [2.13] for the positive minor strains and by Goodwin in 1986 [2.14] for negative minor strains.

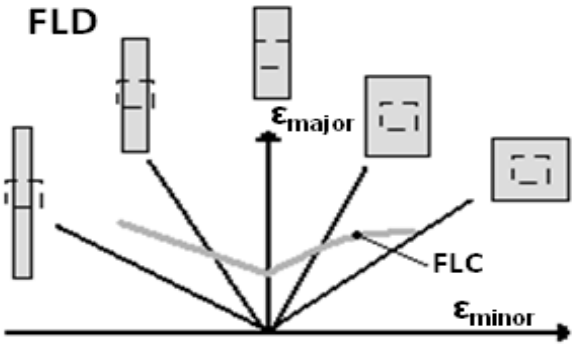

Figure 2.7 - Forming Limit Diagram (FLD) Schematic

Uniaxial Tensile Test – The uniaxial tensile test is the most common test for determining the flow characteristics and basic properties used for engineering analysis. Properties that are commonly derived from this test include: Young's modulus, yield strength, tensile strength, uniform elongation, total elongation, strain hardening value, and normal anisotropy.

2.1.3.2 - Theoretical Prediction of Formability

The assessment of forming limits is highly relevant in industrial forming operations, however, it is very tedious, expensive, and nearly impossible to experimentally determine the forming limits for every forming condition/material/process combination. Hence, theoretical and numerical methods of predicting the forming limits of materials are very relevant.

The first approach for the problem of tensile instability in uniaxial tension was approached by Considère in 1885. It was proposed that stable plastic straining occurred when the hardening influence was greater than the influence of a cross-section reduction and that unstable plastic straining occurred when the material hardening could not compensate for the reduction of the cross-section. Hence, this change from stable to unstable occurs when the force of deformation is a maximum. Or mathematically,

$$dF = 0 \tag{2.1}$$

where, F is force.

Knowing that,

$$F = \sigma A \tag{2.2}$$

where, σ is the stress and A is the cross-sectional area.

Upon differentiation,

$$\frac{dF}{d\varepsilon} = \sigma \frac{dA}{d\varepsilon} + A\frac{d\sigma}{d\varepsilon} = 0 \tag{2.3}$$

Or,

$$\frac{d\sigma}{\sigma} = -\frac{dA}{A} = \frac{dL}{L} = d\varepsilon \tag{2.4}$$

So,

$$\frac{d\sigma}{d\varepsilon} = \sigma \tag{2.5}$$

Using the power law ($\sigma = K\varepsilon^n$) to describe the flow stress behavior, Equation (2.5) becomes,

$$nK\varepsilon^{n-1} = K\varepsilon^n \tag{2.6}$$

Therefore,

$$\varepsilon = n \tag{2.7}$$

Hence, for the Considère condition, a material following the power law will start to neck when the strain is equal to the strain hardening coefficient.

In 1952 Swift applied the Considère condition to biaxial tension and arrived at an expression for the limiting strains [2.15]:

$$\begin{aligned}
\varepsilon_1 &= \frac{\sigma_1\left(\frac{\partial f}{\partial \sigma_1}\right)^2 + \sigma_2\left(\frac{\partial f}{\partial \sigma_2}\right)\left(\frac{\partial f}{\partial \sigma_1}\right)}{\sigma_1\left(\frac{\partial f}{\partial \sigma_1}\right)^2 + \sigma_2\left(\frac{\partial f}{\partial \sigma_2}\right)^2} n \\
\varepsilon_2 &= \frac{\sigma_2\left(\frac{\partial f}{\partial \sigma_1}\right)^2 + \sigma_1\left(\frac{\partial f}{\partial \sigma_1}\right)\left(\frac{\partial f}{\partial \sigma_2}\right)}{\sigma_1\left(\frac{\partial f}{\partial \sigma_1}\right)^2 + \sigma_2\left(\frac{\partial f}{\partial \sigma_2}\right)^2} n
\end{aligned} \tag{2.8}$$

where, *f* is the desired yield function and n is the strain hardening exponent. Therefore, by using different yield criteria, it is possible to evaluate the limiting strains for varying materials and parameters of the material.

For uniaxial tension, Hill proposed that a localized neck develops at an inclined angle to the loading direction which is coincident with the direction of zero-elongation [2.16]. The relations to the limiting strains according to Hill are:

$$\varepsilon_1 = \frac{\dfrac{\partial f}{\partial \sigma_1}}{\dfrac{\partial f}{\partial \sigma_1} + \dfrac{\partial f}{\partial \sigma_2}} n$$
$$\varepsilon_2 = \frac{\dfrac{\partial f}{\partial \sigma_2}}{\dfrac{\partial f}{\partial \sigma_1} + \dfrac{\partial f}{\partial \sigma_2}} n \tag{2.9}$$

where, f is the desired yield function and n is the strain hardening exponent.

In 1967, based on experimental testing, Marciniak suggested that necking is usually created by a structural or geometric non-homogeneity of the material [2.17]. A model was created based off of an analysis assuming a geometric imperfection. This model is commonly called the Marciniak-Kuczinski or M-K model and it incorporates a hardening law, yield criterion, and the associated flow rule. A representation is shown in Figure 2.8, where a sudden variation is geometry is assumed to simplify the model.

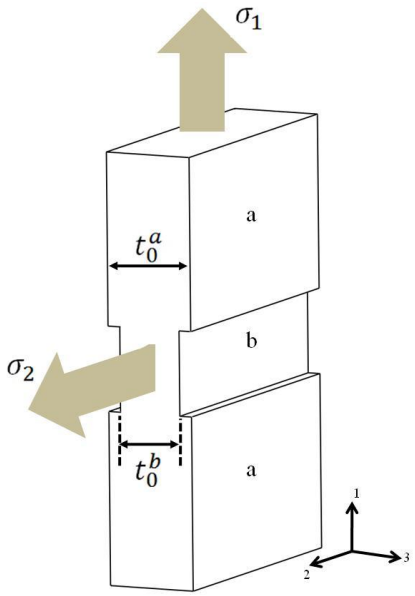

Figure 2.8 - M-K Geometric Model

The initial geometrical non-homogeneity can be described by:

$$f = \frac{t_o^b}{t_o^a} \tag{2.10}$$

where, t_0^i represents the thickness of each respective region. For this model, a biaxial stress state is applied ($\sigma_1 \; and \; \sigma_2 > 0$) and this causes the development of strain increments in both regions (a and b). It is assumed that compatibility and equilibrium equations are fulfilled across the imperfection and the major inputs to the model include a yield criterion and a material hardening law. As deformation continues the strain in the imperfection region (b) is greater than the strain in the nominal region (a); and at a certain ratio of strain ($\varepsilon_b/\varepsilon_a$), localization failure occurs in the groove. The maximum strain ratio is typically taken as 10 in practice, but is really infinite in theory [2.12].

Continued work using a sheet non-homogeneity model has shown that the assumption of the non-homogeneity being normal to the principle direction of loading

results in inaccurate prediction of forming limits in the minor strain region [2.18-2.20]. As a result, Hutchinson and Neale introduced a modified M-K analysis such that the groove was inclined at an angle (ψ) [2.18-2.20]. This model is commonly referred to as the H-N model and is depicted in Figure 2.9. The analysis is performed using the same methods as the M-K analysis, however, the imperfection angle is updated at each increment of plastic deformation based off of the principle strains in region *a*.

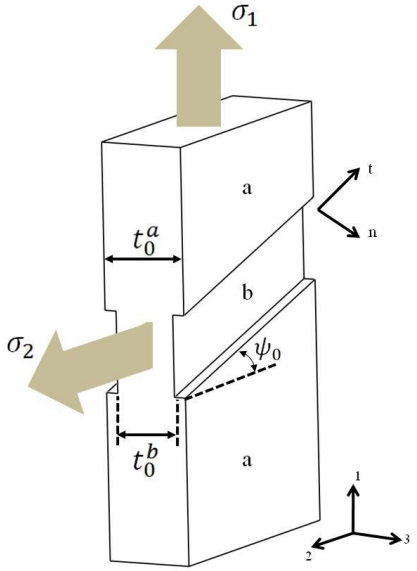

Figure 2.9 - H-N Geometric Model

2.2 - Electrically-Assisted Forming Prior Research

Considering the work that has been performed thus far in the field of EAF and after reviewing the literature, the amount of work has been divided into five main categories. The percentage of work performed in each category is displayed graphically in Figure 2.10. The following sections describe these categories and the major works performed by this PhD candidate and other contributors to the field of EAF.

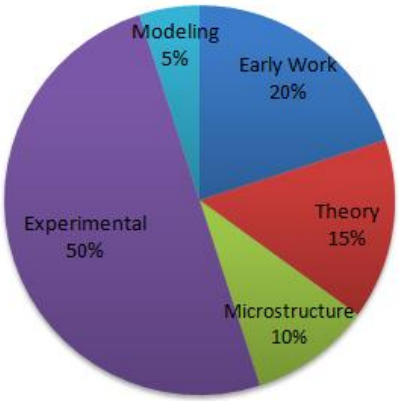

Figure 2.10 - Percent Breakdown of Prior Work in the Field of Electrically-Assisted Forming

2.2.1 - Early Work

The development of EAF has progressed since its inception by Machlin in 1959 [2.21]. In the work of Machlin, three-point bending tests and compression tests were performed on brittle rock salt (NaCl) and it was shown that the application of electrical current increased the ductility of the material by an order of magnitude and decreased the yield point of the material by one-third. Later in 1969, Troitskii examined the flow stress in compression and tensile testing of zinc materials using very short and high magnitude electrical pulses [2.22]. It was concluded in this work that larger magnitude current pulses caused larger decreases in flow stress and it was postulated that the applied electrical current caused motion of previously hindered dislocations within the material's lattice. Okazaki et al. published research in 1978 related to EAF, and through tensile testing of various materials it was shown that the flow stress reduction for short duration pulses was independent of the strain imposed on the material [2.23].

2.2.2 - Electroplastic Effect/Electrical Theory

In 1967, work by Nabarro suggested the interaction of the flow of electrons within a metal during a static condition will cause local scattering off of internal lattice flaws,

thus creating local areas of increased energy around the flaw [2.24]. This discussion of internal flaw interaction with material resistivity is the basis for the most current electrical theory. Work by Kravchenko defined the term "electroplasticity" as the portion of flow stress reduction that could not be explained by only thermal softening and stated that if the electrons are flowing faster than the dislocations, the electrons will impact and transfer energy to the dislocations and will "push" them through the material [2.25]. This movement of previously hindered dislocations speaks to the observed increase in material plasticity and lower forming forces. Further work by Brown specifically examined the electrical resistivity of grain boundaries in metals [2.26]. He determined that the electrical resistivity of the boundaries was mostly a function of the dislocations present at these sites/boundaries. Also, he suggested that the electron scattering within a material is a direct result of the interaction with the dislocation core and not the elastic strain field associated with the dislocation. This is suggestive that the grain size of the material will affect the achievable flow stress reduction when using EAF. This grain size effect was later shown to be true by Siopis [2.27, 2.28]. Considering these major works, Roth et al. developed a combined postulated three-part theory for the electroplastic effect [2.29]. The three core concepts which work in unison during EAF are centralized around the electrical current causing localized resistive heating at lattice flaws, the electrical current applying a force on the dislocations (*i.e.* the electron wind effect), and the electrical current assisting in bond breaking and reforming.

2.2.3 - Microstructure Work

In 1988, Xu et al. examined the microstructure of alpha-titanium subject to an applied electrical current during a recrystallization process [2.30]. From this work it was shown that an applied electrical current increased the recrystallization rate and promoted faster grain growth. Other work by McNeal et al. more recently related to microstructural alterations showed that the grain size of the material could be modified by varying EAF pulsing parameters for equivalent fracture elongations [2.31]. Additionally, works by Siopis et al. in 2010 examined how the flow stress reductions were altered for varying initial material grain sizes and how the effects of prior cold work imposed on the material effected the EAF flow stress reductions [2.27, 2.28]. From these works it was shown that smaller initial grain sizes created larger flow stress reductions compared to the same material with larger grain sizes. Additionally, specimens with prior cold work and thus higher dislocation densities created larger reductions in the flow stress during EAF for the same nominal current applied.

2.2.4 - Experimental Work

Presently, most research is focused on the applicability of this processing technique, such as applying it to varying other processes (*e.g.* rolling, extrusion, machining) [2.32]. In work by Andrawes et al., it was shown that EAF has the potential to drastically reduce process energy requirements [2.33]. In 2007, Perkins et al. studied the effect of a continuous current on the compression behavior of multiple materials (aluminum, copper, and steel alloys) [2.34]. The general results showed drastic reductions in the flow stress and increases in the fracture strain of the material. Also,

Perkins et al. also experimentally demonstrated that hot working the material at temperatures through isothermal testing above those reached in EAF tests on compression specimens did not create near the formability or flow stress reductions that were present in the EAF tests. In 2009, work by Jones et al. examined the compression behavior of a difficult to bulk process magnesium material [2.8]. It was deduced from this work that applying EAF to bulk forming of magnesium could be performed successfully by reducing the material flow stress and increasing the fracture strain by four times the baseline fracture strain. Also in 2009, Ross et al. examined the compression behavior of Ti-6Al-4V using EAF to portray the potential to use this technique for forging of high strength and brittle materials [2.35]. Other work by Ross et al. examined the tensile formability of several metallic materials in tension using EAF and continuously applied current [2.36]. The results from this work showed very low forming flow stress, but the material failed prematurely compared to baseline, and the predicted failure was determined to be from highly diffused necking and material instability from the high heat generation. To mitigate these effects, Roth et al. introduced the concept of applying square wave electrical pulses for a given duration at a given period [2.29]. Using a 5754 Aluminum Alloy and experimentation, Roth achieved total elongation increases of approximately 400% over that of the baseline test (*i.e.* no electricity). In 2010, Jones et al. examined how the current flow path and polarity affected the achievable forming depth for a simple stretch forming process [2.37]. The results showed that applying the current across the workpiece and from the tool to the workpiece was equivalent in terms of forming load and achievable forming depth, but the

current need for applying the current through the tool was double. Work by Salandro et al. further examined the formability of sheet metal (Mg AZ31B) in uniaxial testing using pulsed electrical current [2.9]. The results showed that the achievable elongation of the specimen could be doubled using EAF and that there was a linear relation between the current density and pulse duration for a given final specimen elongation. Considering springback, Green et al. performed flattening and shape retention tests and showed that using a single electrical pulse through the workpiece for a given duration could allow for the workpiece to retain its present shape (bent or flat) [2.38].

2.2.5 - Modeling Work

More recently, work regarding the modeling of the material flow stress during EAF has taken prominent steps. Work by Bunget et al. utilized an energy-based analytical approach to separate the mechanical power required for deformation and the input electrical power to predict the material flow stress for uniaxial compression using a numeric approach [2.39]. Additional work by Kronenberger et al. examined the use of FEA to predict the material flow stress during EAF; however, using only the resistive heating effects, the model was inadequate at predicting the EAF flow stress [2.40]. Work by Jones et al. in 2010 examined the use of an empirically derived flow stress predictor for EAF [2.41]. This work presented a model which accurately characterized the material flow stress for small and larger strains in magnesium and copper materials. Also in 2010, Salandro et al. examined air bending of 304 Stainless Steel sheet metal [2.42]. Using an analytical approach, a model of the forming load was constructed for conventional bending and electrically-assisted bending. The model incorporated both mechanical and

thermal effects which produced accurate approximations of the forming load during the process. In 2011, Jones et al. examined compression testing of 304 Stainless Steel and Grade 5 Titanium which applied a constant current density throughout the specimen for the first time during the test [2.43]. Thus, prior work only utilized an initial nominal current density which changed as a result of specimen shape change during deformation, however, in this work the current density was constant irrespective of specimen shape change. Using these flow curves which were more representative of the actual material response to an applied electrical current field, an observed flow stress modifier was created which accurately predicted the flow stress for the EAF tests knowing the material response under conventional forming conditions. In 2011, Salandro et al. performed thermal modeling of a uniaxial EAF compression process to study the effects of electrical energy input and its contribution to resistive heating or to aiding deformation [2.44]. The results of the thermal modeling showed a power law form for the amount of energy that went into aiding deformation as a function of strain.

2.3 - Classical Plasticity Theory

The theory of plasticity can be regarded as the mathematical study of the stress and strain relations in plastically deformed metal solids [2.45]. To describe the plastic behavior of a metallic material in any general stress state there are three main components that need to be defined. They are i) a yield criterion which describes the limits of elasticity under any possible combination of stresses, ii) an associated plastic flow rule which describes the relationships between the components of the strain rate and stress, and iii) a hardening rule which expresses the evolution of the material flow stress

over the forming process. Considering these three areas, the following sections describe the fundamental work and the basis for this research.

2.3.1 - Yield Criteria

The yield criterion for metals expresses the transition from the elastic to plastic state and the associated stress at this point. The yield point is commonly associated with a uniaxial tension/compression test where this value can be established from the stress-strain curve. However, in a multiaxial stress state it is more difficult to determine the transition from the elastic to plastic state. For this a mathematical expression in terms of the principle stresses in the material is required. This relation can be generally defined by:

$$f\left(S_{ij}\right) = C \tag{2.11}$$

where, *Sij* is the deviatoric stress tensor and *C* is a constant [2.46].

The general state of stress at a point or stress tensor is described by:

$$\sigma_{ij} = \begin{bmatrix} \sigma_{xx} & \tau_{xy} & \tau_{xz} \\ \tau_{yx} & \sigma_{yy} & \tau_{yz} \\ \tau_{zx} & \tau_{zy} & \sigma_{zz} \end{bmatrix} \tag{2.12}$$

where, σ represents the normal stresses and τ represents the shear stresses. A unit stress element with the corresponding normal and shear stresses is shown in Figure 2.11.

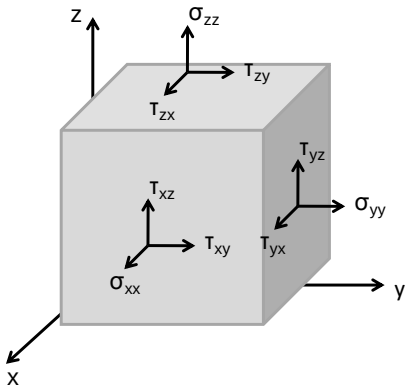

Figure 2.11 - Stress Element

Assuming that yielding in a metal is unaffected by hydrostatic pressure, the stress tensor can be broken down into the deviatoric stress tensor and the hydrostatic stress tensor. The hydrostatic stress tensor can be described as being responsible for elastic volume change where the deviatoric stress tensor is associated with plastic deformation shape change. The expansion of the general stress tensor is:

$$\sigma_{ij} = \begin{bmatrix} \sigma_{xx} & \tau_{xy} & \tau_{xz} \\ \tau_{yx} & \sigma_{yy} & \tau_{yz} \\ \tau_{zx} & \tau_{zy} & \sigma_{zz} \end{bmatrix} = \begin{bmatrix} \sigma_{xx} - \sigma_m & \tau_{xy} & \tau_{xz} \\ \tau_{yx} & \sigma_{yy} - \sigma_m & \tau_{yz} \\ \tau_{zx} & \tau_{zy} & \sigma_{zz} - \sigma_m \end{bmatrix} + \begin{bmatrix} \sigma_m & 0 & 0 \\ 0 & \sigma_m & 0 \\ 0 & 0 & \sigma_m \end{bmatrix} \quad (2.13)$$

or,

$$\sigma_{ij} = S_{ij} + \sigma_m \delta_{ij} \quad (2.14)$$

where, σ_m is the mean or hydrostatic stress and δ_{ij} is the Kronecker delta. The mean stress is given as:

$$\sigma_m = \frac{\sigma_{xx} + \sigma_{yy} + \sigma_{zz}}{3} \quad (2.15)$$

As the stress tensor is a physical quantity and is independent of the coordinate system chosen, there are certain invariants or properties of a system that do not change

under transformations which are associated with this tensor. As the stress tensor is a second rank tensor there are then three independent invariants. The invariants can be determined using linear algebra concepts by determining the determinate of the stress tensor:

$$\det\left(\sigma_{ij} - \lambda\delta_{ij}\right) = 0 \tag{2.16}$$

The determinate of this equation yields the general stress characteristic equation:

$$-\lambda^3 + I_1\lambda^2 - I_2\lambda + I_3 = 0 \tag{2.17}$$

where,

$$\begin{aligned} I_1 &= \sigma_{xx} + \sigma_{yy} + \sigma_{zz} \\ I_2 &= \sigma_{xx}\sigma_{yy} + \sigma_{yy}\sigma_{zz} + \sigma_{zz}\sigma_{xx} - \tau_{xy}^2 - \tau_{yz}^2 - \tau_{zx}^2 \\ I_3 &= \sigma_{xx}\sigma_{yy}\sigma_{zz} + 2\tau_{xy}\tau_{yz}\tau_{zx} - \sigma_{xx}\tau_{yz}^2 - \sigma_{yy}\tau_{zx}^2 - \sigma_{zz}\tau_{xy}^2 \end{aligned} \tag{2.18}$$

where, I_1, I_2, and I_3 are the invariants for the general stress tensor.

The same procedure can be performed for the deviatoric stress tensor.

$$\det\left(S_{ij} - \lambda\delta_{ij}\right) = 0 \tag{2.19}$$

The determinant of this equation yields the deviatoric stress characteristic equation:

$$-\lambda^3 + J_1\lambda^2 - J_2\lambda + J_3 = 0 \tag{2.20}$$

where,

$$\begin{aligned} J_1 &= 0 \\ J_2 &= \frac{1}{6}\left[\left(\sigma_{xx} - \sigma_{yy}\right)^2 + \left(\sigma_{yy} - \sigma_{zz}\right)^2 + \left(\sigma_{zz} - \sigma_{xx}\right)^2\right] - \tau_{xy}^2 - \tau_{yz}^2 - \tau_{zx}^2 \\ J_3 &= \frac{2}{27}I_1^3 - \frac{1}{3}I_1I_2 + I_3 \end{aligned} \tag{2.21}$$

where, J_1, J_2, and J_3 are the invariants for the deviatoric stress tensor.

The first two main yield criteria that have been proposed that incorporate the deviatoric stress are the Tresca and the von Mises criteria.

The Tresca criterion states that the material changes from an elastic state to a plastic state when the maximum shear stress in the material reaches a critical value [2.12]. The Tresca criterion is given by:

$$\max\left\{\left|\sigma_1-\sigma_2\right|,\left|\sigma_2-\sigma_3\right|,\left|\sigma_3-\sigma_1\right|\right\}=C \tag{2.22}$$

where, σ_1, σ_2, σ_3 are the principle stresses and C is a constant.

The von Mises criterion suggests that when J_2 reaches a critical value yielding occurs, thus the yield function did not involve J_3 [2.42]. The von Mises criterion is given by:

$$J_2=C=k^2 \tag{2.23}$$

where, k is the shear yield strength of the material.

Or,

$$J_2=\frac{1}{6}\left[\left(\sigma_{xx}-\sigma_{yy}\right)^2+\left(\sigma_{yy}-\sigma_{zz}\right)^2+\left(\sigma_{zz}-\sigma_{xx}\right)^2\right]-\tau_{xy}^2-\tau_{yz}^2-\tau_{zx}^2=k^2 \tag{2.24}$$

and, in terms of principle stresses,

$$J_2=\frac{1}{6}\left[\left(\sigma_1-\sigma_2\right)^2+\left(\sigma_2-\sigma_3\right)^2+\left(\sigma_3-\sigma_1\right)^2\right]=k^2 \tag{2.25}$$

Considering the case of simple tension where,

$$\sigma_2 \,\&\, \sigma_3 = 0$$

$$k = \frac{\sigma_1}{\sqrt{3}} \tag{2.26}$$

$$\frac{1}{6}\left[\left(\sigma_1-\sigma_2\right)^2+\left(\sigma_2-\sigma_3\right)^2+\left(\sigma_3-\sigma_1\right)^2\right]=\left(\frac{\sigma_1}{\sqrt{3}}\right)^2=\left(\frac{\sigma_o}{\sqrt{3}}\right)^2$$

Or,

$$\frac{1}{2}\left[\left(\sigma_1-\sigma_2\right)^2+\left(\sigma_2-\sigma_3\right)^2+\left(\sigma_3-\sigma_1\right)^2\right]=\sigma_o^2 \tag{2.27}$$

where, σ_o is the yield strength of the material in uniaxial tension.

In 1972, Holsford introduced a generalized form of an isotropic yield criterion [2.47]. The equation takes the form of:

$$\frac{1}{2}\left[\left(\sigma_1-\sigma_2\right)^m+\left(\sigma_2-\sigma_3\right)^m+\left(\sigma_3-\sigma_1\right)^m\right]=\sigma_o^m \tag{2.28}$$

where, m is a constant. The value of m can range from 1 to infinity. If m=1 the equation reduces to the Tresca yield criterion and if m=2 the equation becomes the von Mises yield criterion.

For the above yield criteria relations, these are based on the assumption that the properties are equal in all directions (*i.e.* isotropic). However, sheet metals usually exhibit directional properties as a result of the processing steps required to produce the sheet. Therefore, to account for the variation in plastic behavior with respect to direction, a coefficient of anisotropy was formally defined (commonly referred to as the Lankford parameter) [2.48]. The anisotropy coefficient is defined by:

$$r = \frac{\varepsilon_w}{\varepsilon_t} \tag{2.29}$$

$$r_n = \frac{r_0 + 2r_{45} + r_{90}}{4} \tag{2.30}$$

where, r is the anisotropy coefficient, ε_w is the strain in the width direction, ε_t is the thickness strain, r_n is the coefficient of normal anisotropy, and r_0, r_{45}, r_{90} are the anisotropy coefficients in varying in-plane directions which are denoted by the subscript angle.

To account for anisotropy, Hill proposed a yield criterion in 1948 which is expressed as a quadratic function with the form [2.49]:

$$F\left(\sigma_{yy} - \sigma_{zz}\right)^2 + G\left(\sigma_{zz} - \sigma_{xx}\right)^2 + H\left(\sigma_{xx} - \sigma_{yy}\right)^2 + 2L\tau_{yz}^2 + 2M\tau_{zx}^2 + 2N\tau_{xy}^2 = 1 \tag{2.31}$$

where, *F*, *G*, *H*, *L*, *M*, and *N* are specific constants to describe the anisotropy state of the material and *x*, *y*, and *z* are the principle anisotropic axes.

Where the principle stresses are in alignment with the principle anisotropic axes, the criterion can be simplified to:

$$\sigma_1^2 - \frac{2r_0}{1+r_0}\sigma_1\sigma_2 + \frac{r_0\left(1+r_{90}\right)}{r_{90}\left(1+r_0\right)}\sigma_2^2 = \sigma_o^2 \tag{2.32}$$

where, r_0 and r_{90} are the anisotropy coefficients in the rolling and transverse directions, respectively, and σ_o is the yield strength along the rolling direction.

Where the anisotropy coefficient is equivalent in all directions ($\bar{r} = r_0 = r_{90}$), the criterion can be reduced to:

$$\sigma_1^2 - \frac{2\bar{r}}{1+\bar{r}}\sigma_1\sigma_2 + \sigma_2^2 = \sigma_o^2 \tag{2.33}$$

where, $\bar{r}$ is the normal anisotropy independent of orientation and σ_o is the uniaxial yield strength.

Various other yield criteria models have been proposed such as the Hill 1990, Barlat, and the Karafillis-Boyce models [2.12]. Many other models exist, however, these are the main models that have been implemented in commercial programs as a result of their accuracy and simplicity. The main difficulty in using some of these criteria is that they require the need for more experimental data to be collected for a given material. For example, the Hill 1990 criterion requires knowledge of the equibiaxial yield strength and this requires a special testing machine. Therefore, the Hill 1948 yield criterion is popular as it does not require the equibiaxial yield strength and it is an accurate model for metals that exhibit anisotropy.

2.3.2 - Plastic Flow Rule

The flow rule describes the relationships between the components of the strain rate and stress for plastic deformation. In general the flow rule can be stated as,

$$d\varepsilon_{ij} = d\lambda \frac{\partial f}{\partial \sigma_{ij}} \tag{2.34}$$

where, $d\varepsilon_{ij}$ is the plastic strain increment, $d\lambda$ is an overstress function which may incorporate the dependence of the stress/strain behavior on the material properties and microstructural properties, and f is the function of σ_{ij} that describes yielding [2.45].

Using von Mises yield criteria in terms of principle stresses,

$$f = \frac{1}{2}\left[\left(\sigma_1 - \sigma_2\right)^2 + \left(\sigma_2 - \sigma_3\right)^2 + \left(\sigma_3 - \sigma_1\right)^2\right] - \sigma_o^2 \tag{2.35}$$

So,

$$\frac{\partial f}{\partial \sigma_1} = 2\sigma_1 - (\sigma_2 + \sigma_3)$$
$$\frac{\partial f}{\partial \sigma_2} = 2\sigma_2 - (\sigma_1 + \sigma_3) \tag{2.36}$$
$$\frac{\partial f}{\partial \sigma_3} = 2\sigma_3 - (\sigma_1 + \sigma_2)$$

This leads to the Levy-Mises equations,

$$\frac{d\varepsilon_1}{2\sigma_1 - (\sigma_2 + \sigma_3)} = \frac{d\varepsilon_2}{2\sigma_2 - (\sigma_1 + \sigma_3)} = \frac{d\varepsilon_3}{2\sigma_3 - (\sigma_1 + \sigma_2)} = d\lambda \tag{2.37}$$

where, the ratio of the strain increments will be the same as the ratio of deviatoric stresses [2.50].

Since,

$$\sigma_1^{'} = \sigma_1 - \sigma_m = \frac{1}{3}\left[2\sigma_1 - (\sigma_2 + \sigma_3)\right]$$
$$\sigma_2^{'} = \sigma_2 - \sigma_m = \frac{1}{3}\left[2\sigma_2 - (\sigma_1 + \sigma_3)\right] \tag{2.38}$$
$$\sigma_3^{'} = \sigma_3 - \sigma_m = \frac{1}{3}\left[2\sigma_3 - (\sigma_1 + \sigma_2)\right]$$

where, σ_i' is the deviatoric stress and σ_m is the mean stress in principle components.

Thus,

$$\frac{d\varepsilon_1}{\sigma_1^{'}} = \frac{d\varepsilon_2}{\sigma_2^{'}} = \frac{d\varepsilon_3}{\sigma_3^{'}} = d\lambda \tag{2.39}$$

Or, in plane stress conditions,

$$\frac{d\varepsilon_1}{2\sigma_1 - \sigma_2} = \frac{d\varepsilon_2}{2\sigma_2 - \sigma_1} = \frac{d\varepsilon_3}{-(\sigma_1 + \sigma_2)} = d\lambda \tag{2.40}$$

A similar procedure can be performed for differing yield criterion. For example, considering the Hill 1948 criterion in plane stress and for an anisotropy coefficient which is equivalent in all directions, Equation (2.33) can be described as,

$$f = \sigma_1^2 - \frac{2\bar{r}}{1+\bar{r}}\sigma_1\sigma_2 + \sigma_2^2 - \sigma_o^2 \tag{2.41}$$

So,

$$\begin{aligned} \frac{\partial f}{\partial \sigma_1} &= 2\sigma_1 - \frac{2\bar{r}}{1+\bar{r}}\sigma_2 \\ \frac{\partial f}{\partial \sigma_2} &= 2\sigma_2 - \frac{2\bar{r}}{1+\bar{r}}\sigma_1 \end{aligned} \tag{2.42}$$

Therefore,

$$\frac{d\varepsilon_1}{(1+\bar{r})\sigma_1 - \bar{r}\sigma_2} = \frac{d\varepsilon_2}{(1+\bar{r})\sigma_2 - \bar{r}\sigma_1} = d\lambda \tag{2.43}$$

2.3.3 - Hardening Rule

The hardening rule describes the evolution of the material stress during the forming process. This relation is commonly developed by the use of a tensile test and is commonly approximated using an empirical relation. Specifically, the deformation mechanisms present, whether the material is strain hardening, or if the material is strain rate sensitive influence the constitutive equations. Below are commonly used relations to model the effective flow stress [2.3].

For some materials there is little strain hardening, thus the flow stress can be approximated as a rigid perfectly plastic material where the flow stress is:

$$\bar{\sigma} = Y \tag{2.44}$$

where, Y is a strength constant.

Alternately, for a material with strain hardening, it could be approximated using a linear strain-hardening relation.

$$\bar{\sigma} = Y + P\bar{\varepsilon} \tag{2.45}$$

where, P is the slope representing the linear hardening and $\bar{\varepsilon}$ is the effective strain.

Following this, the most convenient and commonly used approximation utilizes a power law relation.

$$\bar{\sigma} = K\bar{\varepsilon}^{n} \tag{2.46}$$

where, K is a strength coefficient and n is the strain hardening exponent.

This model can be adapted to account for pre-strain (ε_o) imposed on the material and can be represented by:

$$\bar{\sigma} = K\left(\varepsilon_o + \bar{\varepsilon}\right)^{n} \tag{2.47}$$

Considering a material that exhibits strain rate sensitivity, the following relation can be used to incorporate the dependency of strain rate.

$$\bar{\sigma} = C\dot{\bar{\varepsilon}}^{m} \tag{2.48}$$

where, $\dot{\varepsilon}$ is the strain rate, and m is the strain rate sensitivity exponent.

Last, for a material that exhibits both strain hardening and strain rate sensitivity, the effective flow stress can be represented by:

$$\bar{\sigma} = C'\bar{\varepsilon}^{n}\dot{\bar{\varepsilon}}^{m} \tag{2.49}$$

where, C' is the strength coefficient. When examining this equation and its relationship to the flow stress of a material, the constants C', n, and m are all functions of temperature. Typically, if the material is worked at an elevated temperature, the constants C' and n are

decreased, while *m* is increased. Also, these values are affected by strain rate where the constants *m* and *n* decrease with an increased strain rate.

2.3.4 - Plastic Work

Since forming processes are irreversible, a portion of the energy is converted into the material deformation process while the remaining is converted into thermal energy [2.51]. The work for a particular element under a multi-axial stress state in terms of principle directions can be expressed as:

$$dW = \left(\sigma_1 d\varepsilon_1 + \sigma_2 d\varepsilon_2 + \sigma_3 d\varepsilon_3\right)V \tag{2.50}$$

where, V is the volume of the element [47]. For a given time step the instantaneous power is expressed as:

$$P = \frac{dW}{dt}\left(\sigma_1 \dot{\varepsilon}_1 + \sigma_2 \dot{\varepsilon}_2 + \sigma_3 \dot{\varepsilon}_3\right)V \tag{2.51}$$

The corresponding work during uniaxial deformation can be given by:

$$dW' = \left(\sigma_f d\bar{\varepsilon}\right)V' \tag{2.52}$$

Or,

$$P' = \left(\sigma_f \dot{\bar{\varepsilon}}\right)V' \tag{2.53}$$

where, σ_f is the flow stress, $\bar{\varepsilon}$ is the effective strain, $\dot{\bar{\varepsilon}}$ is the effective strain rate, and V' is the volume of the specimen.

If the material element and the material in uniaxial deformation possess the same flow resistance in a particular time interval, then:

$$\frac{dW}{V} = \frac{dW'}{V'} or \frac{P}{V} = \frac{P'}{V'} \tag{2.54}$$

Thus,

$$\sigma_f d\bar{\varepsilon} = \sigma_1 d\varepsilon_1 + \sigma_2 d\varepsilon_2 + \sigma_3 d\varepsilon_3 \tag{2.55}$$

This expression is useful in deriving the relation of the incremental effective strain to the three incremental principle strains [2.51].

2.3.5 - Effective Stress and Effective Strain

For the application of a uniaxial flow curves to be applied to multi-axial stress states there is a need to represent the multi-axial stresses as an effective value. Thus for the von Mises criterion, the effective flow stress can be given by:

$$\bar{\sigma} = \sqrt{\frac{1}{2}\left[\left(\sigma_1 - \sigma_2\right)^2 + \left(\sigma_2 - \sigma_3\right)^2 + \left(\sigma_3 - \sigma_1\right)^2\right]} \tag{2.56}$$

And for uniaxial tension,

$$\bar{\sigma} = \sigma_f \tag{2.57}$$

as σ_2 and σ_3 are zero.

The effective strain can be derived using an energy balance of plastic work while satisfying the yield criteria and associated flow rule [2.12].

From work equivalency (Equation (2.55)),

$$\bar{\sigma} d\bar{\varepsilon} = \sigma_1 d\varepsilon_1 + \sigma_2 d\varepsilon_2 + \sigma_3 d\varepsilon_3 \tag{2.58}$$

Or, for sheet metal forming which is typically plane stress ($\sigma_3 = 0$), thus,

$$\bar{\sigma} d\bar{\varepsilon} = \sigma_1 d\varepsilon_1 + \sigma_2 d\varepsilon_2 \tag{2.59}$$

Commonly, it is easier to represent and manipulate expression using stress and strain ratios [2.12].

Thus,

$$\alpha = \frac{\sigma_2}{\sigma_1} and \beta = \frac{d\varepsilon_2}{d\varepsilon_1} \tag{2.60}$$

Hence Equation (2.59) becomes,

$$d\bar{\varepsilon} = d\varepsilon_1 \left(\frac{\sigma_1}{\bar{\sigma}} \right) (1 + \alpha\beta) \tag{2.61}$$

Using the Levy-Mises flow rules,

$$\beta = \frac{d\varepsilon_2}{d\varepsilon_1} = \frac{2\sigma_2 - \sigma_1}{2\sigma_1 - \sigma_2} = \frac{2\alpha - 1}{2 - \alpha} \tag{2.62}$$

Or,

$$\alpha = \frac{1 + 2\beta}{2 + \beta} \tag{2.63}$$

Then substituting Equation (2.63) into Equation (2.61) yields,

$$d\bar{\varepsilon} = d\varepsilon_1 \left(\frac{\sigma_1}{\bar{\sigma}} \right) \left[1 + \beta \left(\frac{1 + 2\beta}{2 + \beta} \right) \right] = d\varepsilon_1 \left(\frac{\sigma_1}{\bar{\sigma}} \right) \left[\frac{2\left(\beta^2 + \beta + 1\right)}{\beta + 2} \right] \tag{2.64}$$

For plane stress ($\sigma_3 = 0$), the von Mises expression becomes,

$$\bar{\sigma} = \sqrt{\sigma_1^2 + \sigma_2^2 - \sigma_1\sigma_2} \tag{2.65}$$

Or,

$$\bar{\sigma} = \sigma_1 \sqrt{\alpha^2 - \alpha + 1} \tag{2.66}$$

Substitution of Equation (2.63) into Equation (2.66) yields,

$$\frac{\sigma_1}{\bar{\sigma}} = \frac{2 + \beta}{\sqrt{3}} \sqrt{\frac{1}{\beta^2 + \beta + 1}} \tag{2.67}$$

Incorporating Equation (2.67) into Equation (2.64) gives,

$$d\bar{\varepsilon} = \frac{2d\varepsilon_1}{\sqrt{3}}\sqrt{\beta^2+\beta+1} \tag{2.68}$$

Substituting β from Equation (2.60) into Equation (2.68) produces,

$$d\bar{\varepsilon} = \frac{2}{\sqrt{3}}\sqrt{d\varepsilon_1^2 + d\varepsilon_2^2 + d\varepsilon_1 d\varepsilon_2} \tag{2.69}$$

Assuming volume constancy,

$$\varepsilon_1 + \varepsilon_2 + \varepsilon_3 = 0 or\, d\varepsilon_1 + d\varepsilon_2 + d\varepsilon_3 = 0 \tag{2.70}$$

Thus,

$$d\varepsilon_1^2 + d\varepsilon_2^2 + d\varepsilon_3^2 = d\varepsilon_1^2 + d\varepsilon_2^2 + \left(-d\varepsilon_1 - d\varepsilon_2\right)^2 = 2\left(d\varepsilon_1^2 + d\varepsilon_2^2 + d\varepsilon_1 d\varepsilon_2\right) \tag{2.71}$$

Using the relations in Equation (2.71), Equation (2.69) becomes,

$$d\bar{\varepsilon} = \frac{2}{\sqrt{3}}\sqrt{\frac{d\varepsilon_1^2 + d\varepsilon_2^2 + d\varepsilon_3^2}{2}} = \sqrt{\frac{2}{3}\left(d\varepsilon_1^2 + d\varepsilon_2^2 + d\varepsilon_3^2\right)} \tag{2.72}$$

For proportional straining (constant ratio between $d\varepsilon_1$, $d\varepsilon_2$, and $d\varepsilon_3$), the total effective strain can be expressed in terms of the total strains as,

$$\bar{\varepsilon} = \sqrt{\frac{2}{3}\left(\varepsilon_1^2 + \varepsilon_2^2 + \varepsilon_3^2\right)} \tag{2.73}$$

A similar procedure can be performed considering varying yield criterion and their associated plastic flow rules.

2.4 - References for Chapter 2

[2.1] M. P. Groover, *Fundamentals of Modern Manufacturing*, 3 ed. Hoboken, NJ: Wiley & Sons, 2007.

[2.2] S. F. Golovashchenko, A. Krause, and A.J. Gillard "Incremental Forming for Aluminum Automotive Technology," in *ASME - International Mechanical Engineering Congress and Exposition*, 2005, p. 7.

[2.3] S. Kalpakjian *Manufacturing Processes for Engineering Materials*, 3rd ed. Menlo Park, CA: Addison Wesley Longman Inc., 1997.

[2.4] Y. Luo, S.G. Luckey, P.A. Friedman, and Y. Peng "Development of an Advanced Superplastic Forming Process Utilizing a Mechanical Pre-forming Operation," *International Journal of Machine Tool and Manufacture*, vol. 48, pp. 1509-1518, 2008.

[2.5] Orbiter, "Shaping a transition from rocket fuel to oil rigs," 2011.

[2.6] B. L. Kinsey, and J. Cao, "An Analytical Model for Tailor Welded Blank Forming," *Journal of Manufacturing Science and Engineering*, vol. 125, pp. 344-351, 2003.

[2.7] Smitty, "BMW X5 B-Pillar UHSS - Where would you make your cut?," 2009.

[2.8] J. J. Jones, and J.T. Roth, "Effect on the Forgeability of Magnesium AZ31B-O When a Continuous DC Electrical Current is Applied," in *ASME International Manufacturing Science and Engineering Conferenc*e, West Lafayette, IN, 2009, p. 10.

[2.9] W. A. Salandro, A. Khalifa, and J.T. Roth "Tensile Formability Enhancement of Magnesium AZ31B-O Alloy Using Electrical Pulsing," *Transactions of the North American Manufacturing Research Institute of SME*, vol. 37, 2009.

[2.10] D.R. Askeland, and P.P Phule, *The Science and Engineering of Materials*, 4 ed. Australia: Brooks/Cole – Thomson Learning, 2003.

[2.11] Y. Xu, "Universal Formability Technology and Applications," *Materials Processing and Technology*, vol. 151, pp. 119-125, 2004.

[2.12] D. Banabic, H.J. Bunge, K. Pohlandt, and A.E. Tekkaya, *Formability of Metallic Materials*. London: Springer, 2000.

[2.13] S. P. Keeler, and W.A. Backofen, "Plastic Instability and Fracture in Sheets Stretched Over Rigid Punches," *ASM Transactions Quarterly*, vol. 56, 1964.

[2.14] G. M. Goodwin, "Application of Strain Analysis to Sheet Metal Forming Problems in the Press Shop," in *SAE*, 1968.

[2.15] H. W. Swift, "Plastic Instability under Plane Stress," *Mechanics and Physics of Solids*, vol. 1, pp. 1-18, 1952.

[2.16] R. Hill, "On Discontinuous Plastic States, with Special Reference to Localized Necking in Thin Sheets" *Mechanics and Physics of Solids*, vol. 1, pp. 19-30, 1952.

[2.17] Z. Marciniak, and K. Kuczynski "Limit Strains in the Process of Stretch-Forming Sheet Metal," *International Journal of Mechanical Sciences*, vol. 9, pp. 609-620, 1967.

[2.18] J. W. Hutchinson, K.W. Neale, and A. Needleman, "Sheet Necking - I. Validity of Plane Stress Assumptions of the Long-wavelength Approximation," in *Mechanics of Sheet Metal Forming*, D. P. Koistinen, and N. Wang, Ed. New York: Plenum Publishing Corporation, 1978.

[2.19] J. W. Hutchinson, and K.W. Neale, "Sheet Necking - II. Time-Independent Behavior," in *Mechanics of Sheet Metal Forming*, D. P. Koistinen, and N. Wang, Ed. New York: Plenum Publishing Corporation, 1978.

[2.20] J. W. Hutchinson, and K.W. Neale, "Sheet Necking - III. Strain-Rate Effects," in *Mechanics of Sheet Metal Forming*, D. P. Koistinen, and N. Wang, Ed. New York: Plenum Publishing Corporation, 1978.

[2.21] E. S. Machlin, "Applied Voltage and the Plastic Properties of “Brittle” Rock Salt," *Journal of Applied Physics*, vol. 30, pp. 1109-1110, 1959.

[2.22] O. A. Troitskii, "Electromechanical Effect in Metals," *Pis’ma Zhurn. Experim. Teoret. Fiz.*, vol. 10, pp. 118-22, 1969.

[2.23] K. Okazaki, M. Kagwa, and H. Conrad "A Study of the Electroplastic Effects in Metals," *Scripta Metallurgica*, vol. 22, pp. 187-190, 1978.

[2.24] F. R. N. Nabarro, *Theory of Crystal Dislocations*: Clarendon Press, 1967.

[2.25] V. Kravchenko, "Influence of Electrons in Delaying Dislocation in Metals," *JETP (USSR)* vol. 51, 1966.

[2.26] R. A. Brown, "A Dislocation Model of Grain Boundary Electrical Resistivity," *Journal of Physics F: Metal Physics*, vol. 7, pp. 1477-1488, 1977.

[2.27] M. S. Siopis, and B.L. Kinsey "Experimental Investigation of Grain and Specimen Size Effects During Electrical-Assisted Forming," *Journal of Manufacturing Science and Engineering*, vol. 132, p. 7, 2010.

[2.28] M. S. Siopis, B.L. Kinsey, N. Kota, and O. Ozdoganlar "Effect of Severe Prior Deformation on Electrical-Assisted Compression of Copper Specimens," in *ASME International Manufacturing Science and Engineering Conference*, Erie, PA, 2010, p. 7.

[2.29] J. T. Roth, I. Loker, D. Mauck, M. Warner, S.F. Golovashchenko, A. Krause, "Enhanced Formability of 5754 Aluminum Sheet Metal Using Electric Pulsing," *Transactions of the North American Manufacturing Research Institute of SME*, vol. 36, pp. 405-412, 2008.

[2.30] Z. S. Xu, Z.H. Lai, and Y.X. Chen "Effect of Electric Current on the Recrystallization Behavior of Cold Worked Alpha-Ti," *Scripta Metallurgica*, vol. 22, pp. 187-190, 1988.

[2.31] T. A. McNeal, , J.A. Beers, and J.T. Roth "The Microstructural Effects on Magnesium Alloy AZ31B-O While Undergoing an Electrically-Assisted Manufacturing Process," in *ASME International Manufacturing Science and Engineering Conference*, West Lafayette, IN, 2009, p. 10.

[2.32] W. Zhang, *Intelligent Energy Field Manufacturing: Interdisciplinary Process Innovations*, 2010.

[2.33] J. S. Andrawes, T.J. Kronenberger, J.T. Roth, and R.L. Warley "Effects of DC Current on the Mechanical Behavior of AlMg1SiCu," *Materials and Manufacturing Processes*, vol. 22, pp. 91-101, 2007.

[2.34] T. A. Perkins, T.J. Kronenberger, J.T. Roth, "Metallic Forging Using Electrical Flow as an Alternative to Warm/hot Working," *Journal of Manufacturing Science and Engineering*, vol. 129, pp. 84-94, 2007.

[2.35] C. D. Ross, T.J. Kronenberger, and J.T. Roth "Effect of dc on the Formability of Ti–6Al–4V," *Journal of Engineering Materials and Technology*, vol. 131, p. 11, 2009.

[2.36] C. D. Ross, D.B. Irvin, and J.T. Roth, "Manufacturing Aspects Relating to the Effects of DC Current on the Tensile Properties of Metals," *Journal of Engineering Materials and Technology*, vol. 129, pp. 342-347, 2007.

[2.37] J. J. Jones, and L. Mears, "A Process Comparison of Simple Stretch Forming using Both Conventional and Electrically-Assisted Forming Techniques," in *ASME International Manufacturing Science and Engineering Conference*, Erie, PA, 2010, p. 9.

[2.38] C. R. Green, T.A. McNeal, and J.T. Roth, "Springback Elimination for Al-6111 Alloys Using Electrically-Assisted Manufacturing (EAM)," *Transactions of the North American Manufacturing Research Institute of SME*, vol. 37, 2009.

[2.39] C. Bunget, W. Salandro, L. Mears, and J.T. Roth "Energy-based Modeling of an Electrically-assisted Forging Process," *Transactions of the North American Manufacturing Research Institute of SME*, vol. 39, 2010.

[2.40] T. A. Kronenberger, D.H. Johnson, and J.T. Roth "Coupled Multifield Finite Element Analysis Model of Upsetting Under an Applied Direct Current," *Journal of Manufacturing Science and Engineering*, vol. 131, p. 8, 2009.

[2.41] J. J. Jones, and L. Mears "Empirical Modeling of the Stress-Strain Relationship for an Upsetting Process Under Direct Electrical Current," *Transactions of the North American Manufacturing Research Institute of SME*, vol. 38, 2010.

[2.42] W. A. Salandro, C. Bunget, and L. Mears, "Modeling and Quantification of the Electroplastic Effect when Bending Stainless Steel Sheet Metal," in *ASME International Manufacturing Science and Engineering Conference*, Erie, PA, 2010, p. 10.

[2.43] J. J. Jones, and L. Mears, "Constant Current Density Compression Behavior of 304 Stainless Steel and Ti-6Al-4V during Electrically-Assisted Forming," in *ASME International Manufacturing Science and Engineering Conference*, Corvallis, OR, 2011, p. 9.

[2.44] W. A. Salandro, C. Bunget, and L. Mears, "Thermo-mechanical Investigations of the Electroplastic Effect," in *ASME International Manufacturing Science and Engineering Conference*, Corvallis, OR, 2011, p. 10.

[2.45] R. Hill, *The Mathematical Theory of Plasticity*. Oxford: Clarendon Press, 1950.

[2.46] W. F. Hosford, and R.M. Caddell, *Metal Forming: Mechanics and Metallurgy*, 2 ed. Englewood Cliffs, NJ: Prentice Hall, 1993.

[2.47] W. F. Hosford, "A Generalized Isotropic Yield Criterion," *Journal of Applied Mechanics*, vol. 39, pp. 607-609, 1972.

[2.48] W. T. Lankford, S.C. Snyder, and I.A. Bauscher, "New Criteria for Predicting the Press Performance of Deep Drawing Sheet," *Transactions of the American Society for Metals*, vol. 42, pp. 1197-1232, 1950.

[2.49] R. Hill, "A Theory of the Yielding and Plastic Flow of Anisotropic Metals," Proceedings of the Royal Society of London. Series A, *Mathematical and Physical Sciences*, vol. 193, pp. 281-297, 1948.

[2.50] Z. Marciniak, J.L. Duncan, and S.J. Hu, *Mechanics of Sheet Metal Forming*. Oxford: Butterworth Heinemann, 2002.

[2.51] K. Lange, *Handbook of Metal Forming*. New York: Mc Graw Hill, 1985.

CHAPTER 3 - MODELING METHODOLOGY FOR EAF

3.1 - Global Modeling Methodology

For successful implementation of EAF in manufacturing industries, one area that needs to be addressed is the predictability or material response at a bulk level. This predictability can partially be provided by process modeling of a tensile sample under an applied electric current field. From the understanding and knowledge gained in examining uniaxial tension, this then can be translated to other deformation modes or bi-axial loading conditions which are commonly utilized by manufacturers. The main methodology for bulk process modeling is shown in Figure 3.1.

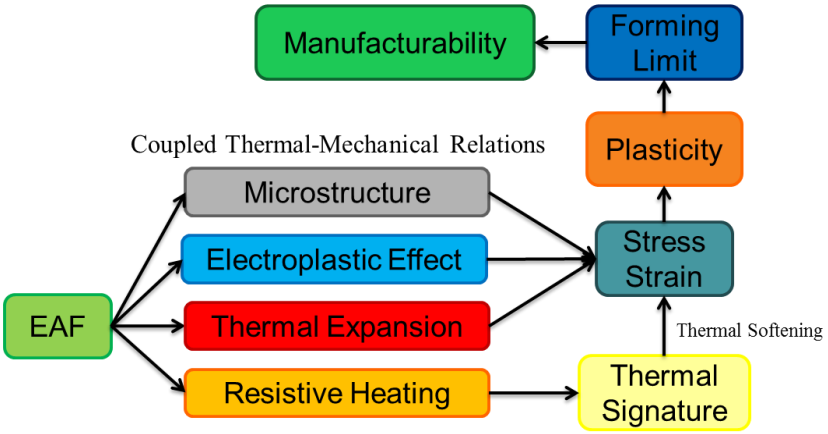

Figure 3.1 - EAF's Coupled Thermal-Mechanical Relations and how EAF translates to Manufacturability

As shown in Figure 3.1, the EAF process has a direct relation to the local strains and stress state within a material through coupled thermal-mechanical relations. These include the initial material microstructure, electroplastic effect, thermal expansion, and bulk resistive heating. For this work, these relations are incorporated except for the initial material microstructures influence on the resultant stress and strain. Although not incorporated, it has been shown that varying initial microstructures in an annealed

material can create differences in flow stress reductions for the same electrical parameters (note, there has not been any analysis of temperature in prior work in this area, thus it may only be bulk resistive heating effects since all grain sizes have approximately the same dislocation density) [3.1]. Nevertheless, this effect is suggestive of modified electron scattering at grain boundaries which may influence the bulk temperature rise of the material. The electroplastic effect or electroplasticity is the amount of applied energy that goes directly into aiding in deformation and not to bulk joule heating. There are several proposed mechanisms that this effect is attributed to which include: localized heating at defects, the electron wind effect (*i.e.* momentum transfer), and reduced bonding energies. For the process modeling in this work, the contribution of electroplasticity will be developed from the variation in thermal energy observed from experimental results to a model result that attributes temperature rise only from Joule heating. In addition, the thermal expansion of the material during the application of electric current has an effect on the stress response and this has not been incorporated in previous EAF works. As a result, this work includes this effect and determines its magnitude on the material stress. Last, as a consequence of passing electrical current through a metal, the metal's temperature will rise due to bulk resistive heating. As the temperature of the material increases, the material softens which directly translates to a modification in the material stress. Hence, this work combines for the first time the electroplastic effect, thermal expansion, and bulk thermal softening to predict the stress and strain response for a material subject to EAF. This concept is illustrated in Figure 3.2

where the percent contribution for each effect will be determined for the reduction in force or flow stress of the material.

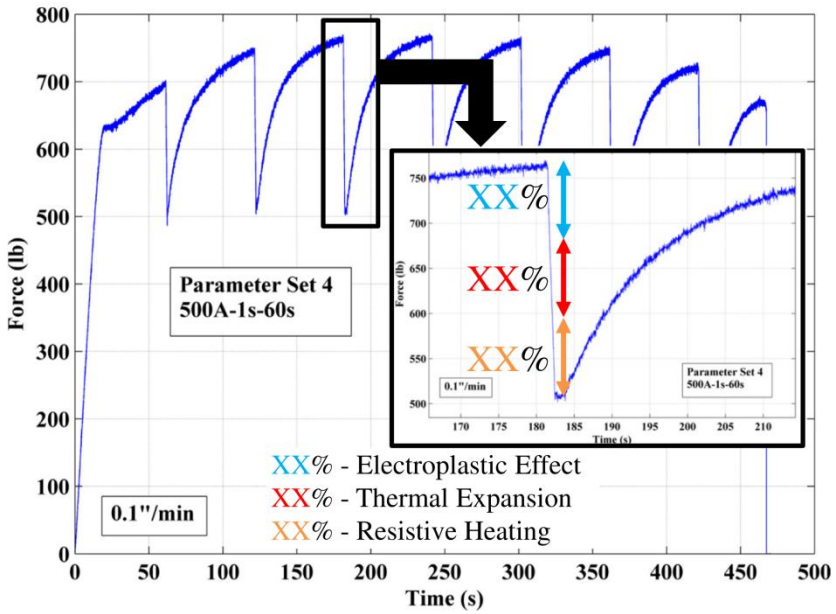

Figure 3.2 - Concept for Superposition of Thermal-Mechanical Effects on Flow Stress Reduction

Once the local strain and stress state within the material is known, these results can be related to how the material plastically flows and to the amount of achievable deformation before failure. These forming limits then convert to the ability of the material to be deformed to produce a component with a complex shape. Thus, the macro process modeling in this work relates the deformation of a metal subject to an electric current field to the material's forming limit which is a parameter of the material's manufacturability.

3.2- The Electroplastic Effect

The electroplastic effect is the portion of the applied electrical current that goes directly toward aiding in deformation. Hence, a main question is the division of the

electrical energy applied to bulk resistive heating and the electroplastic effect. This is simply shown in Figure 3.3.

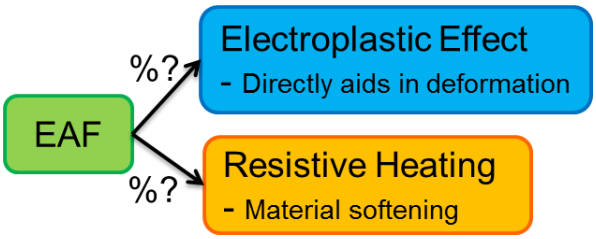

Figure 3.3 - The Major Question Regarding how the Applied Electrical Current is Partitioned

Aside from using bulk observations to quantify this phenomenon, this work uses physics-based models to determine the significance of the present electroplastic theories. Specifically, the transient energy provided to the dislocation core and that transferred to the surrounding lattice are compared and quantified. A schematic is shown in Figure 3.4 (left) where an edge dislocation is represented by a cylindrical dislocation core. Figure 3.4 (right) depicts a snapshot of a fundamental transient response of Joule heating as a result of the greater dislocation core electrical resistance. The dislocation core has geometric properties of diameter *D* and length *L*.

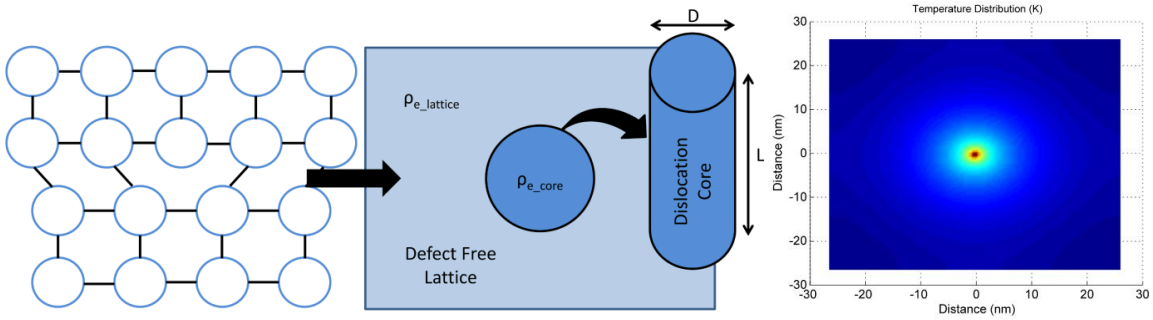

Figure 3.4 - Left shows an Edge Dislocation Represented as a Cylindrical Dislocation Core Surrounded by a Defect Free Lattice and Right shows the Principle Joule Heating Response for a Dislocation Core versus the Defect Free Lattice

The two primary theories for electroplasticity are localized heating at lattice defects and the electron wind effect. The localized heating is a result of increased scattering at defects which create areas of greater atomic vibrations or "hot spots", whereas the electron wind effect is based on actual momentum transfer to the dislocation core. The localized Joule heating effect can be quantified as a temperature rise by:

$$\Delta T = \frac{J^2 \rho_e}{\rho c} \Delta t \tag{3.1}$$

where, ΔT is the temperature rise, J is the current density, ρ_e is the electrical resistivity, Δt is the change in time, ρ is the density, and c is the specific heat. It is hypothesized that these local "hot spots" ease dislocation movement through the lattice and allow for them to pass by other unmovable lattice defects. The analysis of this model determines if the excess temperature rise or energy at the dislocation core is significant to allow for enhanced atomic motion.

Conversely, the energy imparted to the dislocation core from the electron wind is:

$$E_{ew\_core} = Z^* e \rho_e JNb \tag{3.2}$$

where, E_{ew_core} is the electron wind energy imparted to the dislocation core, Z^* is the effective charge number, e is the charge of an electron, N is the number of equivalent atoms per dislocation core, and b is an atomic distance [3.2]. It is suggested that the momentum transfer from the electric field directly assists the dislocation movement within the metal's lattice. This model is evaluated by examining the added energy to the dislocation core as a result of momentum transfer and its influence on improved atomic motion of the dislocation core.

3.3- Thermal Effects

For the thermal effects which influence the stress state of the material, the two main factors are the thermal expansion and bulk resistive heating. For an EAF process, the temperature increases as a result of bulk heating and this then creates a thermal expansion stress on the material which is linearly related to the material stiffness and coefficient of thermal expansion. As a result, this work incorporates this effect and evaluates its magnitude on the observed stress reduction when electrical current is applied. Also, for bulk resistive heating the material softens and an observed stress reduction is quantified. For determination of local temperatures during EAF modeling, governing equations which include the 1st law of thermodynamics, Joule's 1st law for heat generation, Fourier's law for conduction, and Newton's law of cooling for convection are applied. Where the fist law of thermodynamics is given by,

$$E_{in} - E_{out} = \Delta E_{system} \tag{3.3}$$

where, E_{in} is the total energy entering the system, E_{out} is the total energy leaving the system, and ΔE_{system} is the change in the total energy of the system. Joule's 1st law for heat generation is,

$$Q_{gen} = I^2 R t \tag{3.4}$$

where, Q_{gen} is the heat generated, I is the electrical current, R is the electrical resistance, and t is the time. Fourier's law for 1-D conduction is,

$$\dot{Q}_{cond} = -kA\frac{dT}{dx} \tag{3.5}$$

where, $\dot{Q}_{cond}$ is the rate of heat conduction, k is the thermal conductivity, A is the conduction area, and $\frac{dT}{dx}$ is the temperature gradient along the dimension x. Last, Newton's law of cooling is given by,

$$\dot{Q}_{conv} = hA_s\left(T_s - T_\infty\right) \tag{3.6}$$

where, $\dot{Q}_{conv}$ is the rate of heat convection, h is the convection heat transfer coefficient, A_s is the surface area, T_s is the surface temperature, and T_∞ is the fluid temperature far from the surface.

3.4 - References for Chapter 3

[3.1] M. S. Siopis, and B.L. Kinsey "Experimental Investigation of Grain and Specimen Size Effects During Electrical-Assisted Forming," *Journal of Manufacturing Science and Engineering*, vol. 132, p. 7, 2010.

[3.2] Z. Suo, Reliability of Interconnect Structures, pp.265-324 in Volume 8: Interfacial and Nanoscale Failure (W. Gerberich, W. Yang, Editors), Comprehensive Structural Integrity (I. Milne, R.O. Ritchie, B. Karihaloo, Editors-in-Chief), Elsevier, Amsterdam, 2003.

CHAPTER 4 - THERMAL MODELING OF SHEET METALS DURING EAF

An important aspect of understanding how an applied direct electrical current influences the flow stress and formability is to determine the thermal profile response and resistive heating during the process. Thus, the objective of this chapter is to model the thermal response of sheet metals subject to EAF which will allow for a greater understanding and characterization of the electroplastic effect. The presented model predicts the thermal behavior of the sheet metal under the assumption that all of the input electrical energy is converted to heat generation through Joule heating. As a result, the response can be compared to experimental EAF results to determine if a portion of the applied energy aided in deformation. This work examines the thermal response of Mg AZ31 as a result of its industrial use, low density, and overall low formability in common sheet forming processes.

This work varies as compared to other thermal research in EAF as this work is considering geometrically larger specimens which have large thermal gradients present. Therefore, this work cannot consider a lumped mass approach in the analysis of the component subject to EAF.

4.1 - Model Development

In the following two sections the development of the thermal stationary model for process variable identification and the thermal deformation model for verification of the electroplastic effect are presented.

4.1.1 - Stationary Model

The stationary model was created for a stationary test (*i.e.* no deformation) of an ASTM tensile specimen subjected to an applied direct electrical current. This model is used for process variable identification and overall modeling methodology and construction validation. The key process variables to be identified were the heat transfer convection coefficient, initial component and clamping die temperatures, the power supply efficiency and its associated losses, and effective clamping die conduction length in the clamped region. As this model is the basis for the subsequent thermal deformation model, it is described in detail. A limited set of results are presented in this chapter, however, a full set of results are given in *Appendix A*.

The constructed 1D transient finite difference thermal model is of a standard 12.5mm wide ASTM tensile specimen [4.1] that is to be used for the uniaxial testing of EAF and the model contains equally spaced nodes along the length of the specimen (Figure 4.1). The model accounts for:

- Heat conduction throughout the specimen
- Heat conduction to the dies in the clamping region
- Heat convection to the environment in the testing region
- Joule heating of the specimen and dies when the direct electrical current is applied (corresponds to varying wave shapes, magnitudes of current, and duty cycles)
- Temperature dependent material properties of the sheet material (density, electrical resistivity, thermal conductivity, and heat capacity) [4.2]

The model is based on the following assumptions:

- The temperatures across the width and thickness of the specimen are uniform and the temperature only varies along the length of the specimen (*i.e.* it is assumed

that the thermal gradient in the thickness and width direction are relatively small as compared to the gradient along the length of the specimen).

- The material is homogeneous and isotropic.
- The geometric model does not incorporate the fillets which link the testing region to the clamping region of the specimen.
- The clamping dies are analyzed as a lumped mass to conserve the 1D nature of the model.
- The radiation heat transfer is incorporated into the convection coefficient (*i.e.* $h_{combined}$ and it is just denoted as h in the below equations for simplicity).
- The electrical resistivity and specific heat of the clamping dies is not temperature dependent (There is not a large temperature change of the clamping die so this is an accurate assumption).

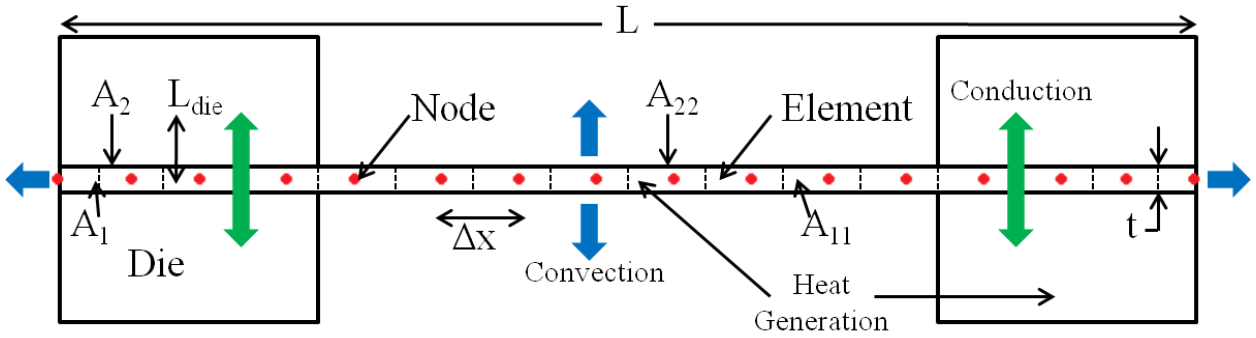

Figure 4.1 - Stationary Thermal Model Schematic

The general expression to characterize the balance of energy for the system given in terms of power is,

$$\sum_{All\ Sides} \dot{Q} + \dot{E}_{generation} = \frac{\Delta E_{System}}{\Delta t} \tag{4.1}$$

where, $\dot{Q}$ is the respective rate of heat transfer into all of the system sides depending on the boundary conditions (*i.e.* conduction or convection), $\dot{E}_{generation}$ is the heat generated

within the specimen from resistive heating, ΔE_{System} is the change of internal energy associated with the system, and Δt is the change in time.

Considering only one element,

$$\sum_{Element\ Sides} \dot{Q} + \dot{E}_{gen,element} = \frac{\Delta E_{Element}}{\Delta t} \tag{4.2}$$

In constructing the model, there are three separate areas which had varying boundary conditions. These include the interior nodes in contact with the clamping die interface, the two nodes at each end of the specimen, and the exterior nodes in the testing region exposed to the environment.

For an interior node in contact with the clamping die interface, the power balance can be written as:

$$\frac{kA_1\left(T_{m-1}^i - T_m^i\right)}{\Delta x} + \frac{kA_1\left(T_{m+1}^i - T_m^i\right)}{\Delta x} + 2\left[\frac{k_{a2}A_2\left(T_{die}^i - T_m^i\right)}{L_{die}}\right] + \dot{e}_{gen,clamp}A_1\Delta x = \rho A_1 \Delta x c \frac{T_m^{i+1} - T_m^i}{\Delta t} \tag{4.3}$$

where, k is the thermal conductivity of the sheet, A_1 is the element conduction area of the sheet in the clamping die region, Δx is the nodal spacing, T_{m-1}^i is the present temperature at the node to the left of the node being analyzed, T_m^i is the temperature of the node being analyzed, T_{m+1}^i is the present temperature at the node to the right of the node being analyzed, k_{a2} is the thermal conductivity of the clamping die made from A2 Steel, A_2 is the element conduction area into the dies, T_{die}^i is the present temperature of the clamping die, L_{die} is the die conduction length, $\dot{e}_{gen,clamp}$ is the heat generation per unit volume for the sheet in the clamping region, ρ is the density of the sheet metal, c is the heat

capacity of the sheet, $T_m^{i+1} - T_m^i$ is the temperature change of the node being analyzed from the present time to the future time, and Δt is the time step.

For the two nodes at each end of the specimen,

$$\frac{kA_1\left(T_{m+1}^i - T_m^i\right)}{\Delta x} + 2\left[\frac{k_{a2}\frac{\Delta x}{2}w\left(T_{die}^i - T_m^i\right)}{L_{die}}\right] + htw\left(T_\infty - T_m^i\right) + \dot{e}_{gen,clamp}A_1\frac{\Delta x}{2} = \rho A_1\frac{\Delta x}{2}c\frac{T_m^{i+1} - T_m^i}{\Delta t} \quad (4.4)$$

where, w is the sheet width in the clamping region, h is the convection coefficient, t is the sheet thickness, and T_∞ is the atmospheric temperature.

For a node in the testing region exposed to the environment,

$$\frac{kA_{11}\left(T_{m-1}^i - T_m^i\right)}{\Delta x} + \frac{kA_{11}\left(T_{m+1}^i - T_m^i\right)}{\Delta x} + 2\left[hA_{22}\left(T_\infty - T_m^i\right)\right] + \dot{e}_{gen,test}A_{11}\Delta x = \rho A_1\Delta xc\frac{T_m^{i+1} - T_m^i}{\Delta t} \quad (4.5)$$

where, A_{11} is the element conduction area of the sheet in the testing region, A_{22} is the element convection area in the test region, and $\dot{e}_{gen,test}$ is the heat generation per unit volume for the sheet in the testing region. And the material properties were updated at each time step as a function of temperature,

$$k, k_{a2}, \rho, c = f\left(T_m^i\right) \quad (4.6)$$

in all the above equations [19].

Using an explicit solution approach, Equations (4.3)-(4.5) can be solved to determine the new nodal temperature after a given time step.

Thus, for an interior node in contact with the die interface,

$$T_m^{i+1} = T_m^i + \Delta t\left[\frac{kT_{m-1}^i}{\Delta x^2\rho c} + \frac{2k_{a2}A_2T_{die}^i}{L_{die}\rho A_1\Delta xc} - \left(\frac{2k}{\Delta x^2\rho c} + \frac{2k_{a2}A_2}{L_{die}\rho A_1\Delta xc}\right)T_m^i + \frac{kT_{m+1}^i}{\Delta x^2\rho c} + \frac{\dot{e}_{gen,clamp}}{\rho c}\right] \quad (4.7)$$

For the nodes at each end of the specimen,

$$T_m^{i+1} = T_m^i + \Delta t \left[\frac{kT_{m+1}^i}{\frac{\Delta x^2}{2}\rho c} - \left(\frac{k}{\frac{\Delta x^2}{2}\rho c} + \frac{2k_{a2}w}{L_{die}\rho A_1 c} + \frac{htw}{\rho A_1 \frac{\Delta x}{2} c} \right) T_m^i + \frac{2k_{a2}wT_{die}^i}{L_{die}\rho A_1 c} + \frac{htwT_\infty}{\rho A_1 \frac{\Delta x}{2} c} + \frac{\dot{e}_{gen,clamp}}{\rho c} \right] \quad (4.8)$$

For the nodes in the testing region,

$$T_m^{i+1} = T_m^i + \Delta t \left[\frac{kT_{m-1}^i}{\Delta x^2 \rho c} - \left(\frac{2k}{\Delta x^2 \rho c} + \frac{2hA_{22}}{\rho A_{11} \Delta x c} \right) T_m^i + \frac{kT_{m+1}^i}{\Delta x^2 \rho c} + \frac{2hA_{22}T_\infty}{\rho A_{11} \Delta x c} + \frac{\dot{e}_{gen,test}}{\rho c} \right] \quad (4.9)$$

As the electrical current will be passing through the die and heat will be transferred from the sheet metal to the die, the die temperature will also change as a function of time. To conserve the 1D nature of this analysis, the die is considered to be a lumped mass with a uniform temperature. This is an accurate assumption as the Biot number is less than 0.1 for the die geometry and heat transfer properties [4.3].

Thus, the power balance for the dies are given by,

$$hA_{s,die}\left(T_\infty - T_{die}^i\right) + \frac{2k_{a2}A_3\left(T_{avg,mg\ clamp}^i - T_{die}^i\right)}{L_{die}} + \dot{e}_{gen,die}V_{die} = \rho_{a2}V_{die}c_{a2}\frac{T_{die}^{i+1} - T_{die}^i}{\Delta t} \quad (4.10)$$

where, $A_{s,die}$ is the die surface area, T_{die}^i is the present die temperature, A_3 is the full conduction area between the sheet and the die, $T_{avg,mg\ clamp}^i$ is the average temperature at the clamping region for the sheet, V_{die} is the volume of the die, ρ_{a2} is the density of the die material (A2 Steel) which is a function of temperature, c_{a2} is the heat capacity of the die material, and $T_{die}^{i+1} - T_{die}^i$ is the temperature change of the die from the present time to the future time.

Additionally, the average temperature at the clamping region for the sheet is defined by,

$$T^{i}_{avg,mg\,clamp} = \frac{1}{b}\sum_{1}^{b} T^{i}_{m,clamp\,region,b} \tag{4.11}$$

where, b is the number of nodes in the clamping region.

Using an explicit solution approach, Equation (4.10) can be written as,

$$T^{i+1}_{die} = T^{i}_{die} + \Delta t\left[\frac{hA_{s,die}T_{\infty}}{\rho_{a2}V_{die}c_{a2}} + \frac{2k_{a2}A_3T^{i}_{avg,mg\,clamp}}{\rho_{a2}V_{die}c_{a2}L_{die}} - \left(\frac{hA_{s,die}}{\rho_{a2}V_{die}c_{a2}} + \frac{2k_{a2}A_3}{\rho_{a2}V_{die}c_{a2}L_{die}}\right)T^{i}_{die} + \frac{\dot{e}_{gen,die}}{\rho_{a2}c_{a2}}\right] \tag{4.12}$$

Thus, Equations (4.7), (4.8), (4.9) and (4.12) are the generic nodal solutions which constitute the thermal model.

To characterize the resistive heating, Joule's first law is used,

$$\dot{E}_{gen} = \dot{e}_{gen}V \tag{4.13}$$

Thus,

$$\dot{e}_{gen} = \frac{\dot{E}_{gen}}{V} = \frac{I^2R}{V} = \frac{I^2R}{Lwt} \tag{4.14}$$

where, V is the volume of interest, I is the current in amps, R is the resistance in ohms, and $L, w, and\ t$ are the length, width, and thickness of interest, respectively.

For a rectangular cuboid geometry the resistance can be defined by,

$$R = \rho_e\frac{L}{A} = \rho_e\frac{L}{wt} \tag{4.15}$$

where, ρ_e is the electrical resistivity of the material of interest and A is the area of interest.

Thus by substitution of Equation (4.15) into Equation (4.14),

$$\dot{e}_{gen} = \frac{I^2 \rho_e}{w^2 t^2} \tag{4.16}$$

Then, using Equation (4.16) along with the corresponding electrical resistivity, geometric width, and geometric thickness, the magnitude of the heat generated per unit volume can be determined for each element. Equation (4.16) is therefore used to calculate the magnitude of the heat generation per unit volume of each element in the sheet metal in the clamping region, the testing region, as well as the die using the appropriate dimensions and material properties. Applying this magnitude with varying wave shapes and duty cycles represents the present testing methods for EAF in tensile applications. The solution schematic for solving the model is given in Figure 4.2.

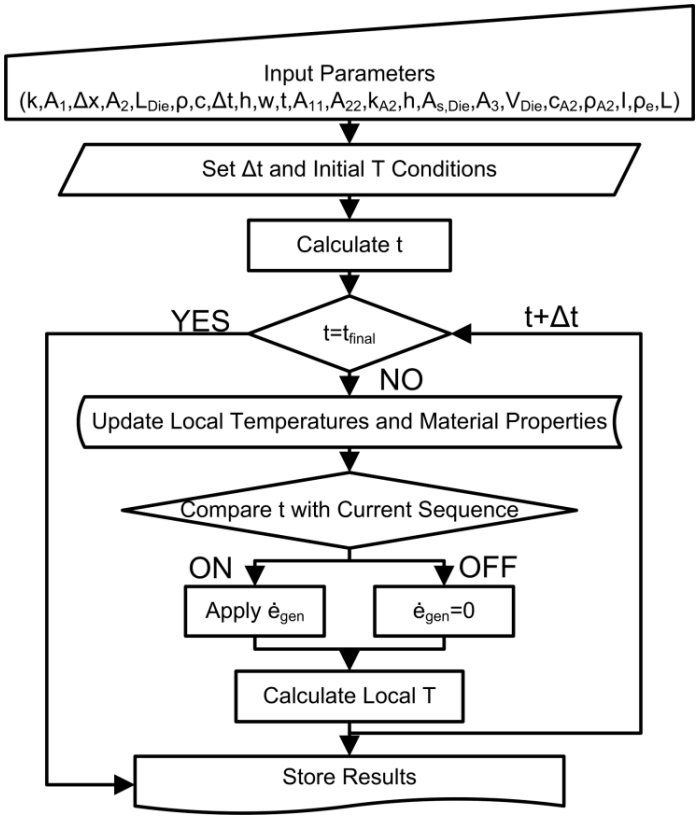

Figure 4.2 - Stationary Model Solution Schematic

4.1.2 - Deformation Model

A model was created for a deformation test subject to an applied direct electrical current and this can used to determine if a portion of the energy from the applied electric current went directly into aiding deformation and not to Joule heating. For the deformation modeling, two variants were created. The first considers the deformation to be uniform, therefore the elements in the test region are equal in size and change shape as deformation is imposed. The second accounts for diffuse necking during deformation and at present the diffuse neck is predicted using experimental Circle Grid Analysis (CGA) results obtained from experimentation. The diffuse model was created as in prior EAF testing a diffuse neck was found to be apparent during uniaxial tension [4.4, 4.5].

For the case with uniform deformation, there are several variables that do not remain constant as in the case of stationary testing. The factors that had to be accounted for were the shape change of the elements in the testing region of the sheet and the heat generation per unit volume as a result of specimen shape change (note: it is a function of sheet width and thickness as described in Equation (4.16)).

The deformation in the length direction of the specimen (Δs) can be calculated as:

$$\Delta s = t\dot{s} \tag{4.17}$$

where, t is the present time in the test and $\dot{s}$ is the platen speed.

Therefore, as there are a fixed number of elements ($Elements_{test}$) in the test region, the displacement of each element can be determined by,

$$\Delta s_{Elements} = \frac{\Delta s}{Elements_{test}} \tag{4.18}$$

The strain in the elements in the length direction can be calculated using,

$$\varepsilon_L = \ln\left(\frac{\Delta s + L_{initial,test}}{L_{initial,test}}\right) \tag{4.19}$$

where, $L_{initial,test}$ is the initial length of the entire test region and assuming isotropy the width and thickness strain is,

$$\varepsilon_w = \varepsilon_t = -0.5\varepsilon_L \tag{4.20}$$

The instantaneous size of the elements is determined using:

$$\Delta x_{uniform} = \Delta s_{Elements} + \Delta x \tag{4.21}$$

$$t_{uniform} = te^{\varepsilon_t} \tag{4.22}$$

$$w_{uniform} = w_{test}e^{\varepsilon_w} \tag{4.23}$$

where, $\Delta x_{uniform}$ is the length of the element, $t_{uniform}$ is the thickness of the sheet under uniform deformation, t is the initial thickness of the sheet, $w_{uniform}$ is the width of the sheet under uniform deformation, and w_{test} is the initial width of the sheet in the testing region. As a result of the uniform deformation assumption, all elements have equal lengths, widths, and thicknesses. Additionally, the conduction areas and convection areas are determined from the new element sizes by,

$$A_{11\_uniform} = A_{11}\frac{\Delta x}{\Delta x_{uniform}} \tag{4.24}$$

$$A_{22\_uniform} = \Delta x_{uniform} w_{uniform} \tag{4.25}$$

where, $A_{11\_uniform}$ is the new conduction area in the test region of the sheet and $A_{22\_uniform}$ is the new convection area in the sheet for each element.

Last, the heat generated from the applied current now varies as a function of deformation as the resistance of the sheet increases with elongation. The heat generated can now be given as,

$$\dot{e}_{gen\_uniform} = \frac{I^2 R_{uniform}}{t_{uniform} w_{uniform} \left(\Delta s + L_{initial,test} \right)} \tag{4.26}$$

where,

$$R_{uniform} = \rho_e \frac{\left(\Delta s + L_{initial,test} \right)}{t_{uniform} w_{uniform}} \tag{4.27}$$

Thus,

$$\dot{e}_{gen\_uniform} = \frac{I^2 \rho_e}{t_{uniform}^2 w_{uniform}^2} \tag{4.28}$$

For the case with diffuse deformation, the model considers that the length, width, and thickness of the elements in the testing region are non-uniform. The present element size is calculated using experimental strain measurements at failure which were assumed to be a linear function from zero strain to the fracture strain. Thus, the length of the element and width of the element can be calculated using,

$$\Delta x_{m,diffuse} = \Delta x e^{\varepsilon_{m,L}} \tag{4.29}$$

$$w_{m,diffuse} = w e^{\varepsilon_{m,w}} \tag{4.30}$$

where, $\varepsilon_{m,L}$ and $\varepsilon_{m,w}$ are the length and width strains for each element.

The strain in the thickness direction is calculated by,

$$\varepsilon_{m,t} = -\left(\varepsilon_{m,L} + \varepsilon_{m,w} \right) \tag{4.31}$$

Thus the sheet thickness is give as,

$$t_{m,diffuse} = te^{\varepsilon_{m,t}} \tag{4.32}$$

The heat transfer dimensions of the model can be calculated for each element as,

$$A_{11,m,diffuse} = t_{m,diffuse} w_{m,diffuse} \tag{4.33}$$

$$A_{22,m,diffuse} = \Delta x_{m,diffuse} w_{m,diffuse} \tag{4.34}$$

where, $A_{11,m,diffuse}$ is the new conduction area in an element and $A_{22,m,diffuse}$ is the new convection area for an element.

Finally, the heat generated from the applied current now varies as a function of the element size as the resistance of the element increases with elongation. The heat generated can now be given as,

$$\dot{e}_{m,gen\_diffuse} = \frac{I^2 R_{m,difuse}}{t_{m,diffuse} w_{m,diffuse} \Delta x_{m,diffuse}} \tag{4.35}$$

where,

$$R_{m,diffuse} = \rho_e \frac{\Delta x_{m,diffuse}}{t_{m,diffuse} w_{m,diffuse}} \tag{4.36}$$

Thus,

$$\dot{e}_{m,gen\_diffuse} = \frac{I^2 \rho_e}{t_{m,diffuse}^2 w_{m,diffuse}^2} \tag{4.37}$$

For determination of the strain present in each element at a certain time (for diffuse model), experimental analysis of the local strains at failure (summarized in Table 4.1 for the center of the specimen) were linearized from time zero to the time at which the fracture occurred. Figure 4.3 (left) shows the averaged strain in the length, width, and

thickness directions from the experimental testing results at failure for Parameter Set 4, which is defined in Table 4.2 of the subsequent Experimental Setup section. In Figure 4.3 (right), the corresponding strain input for the length strain is depicted as an example.

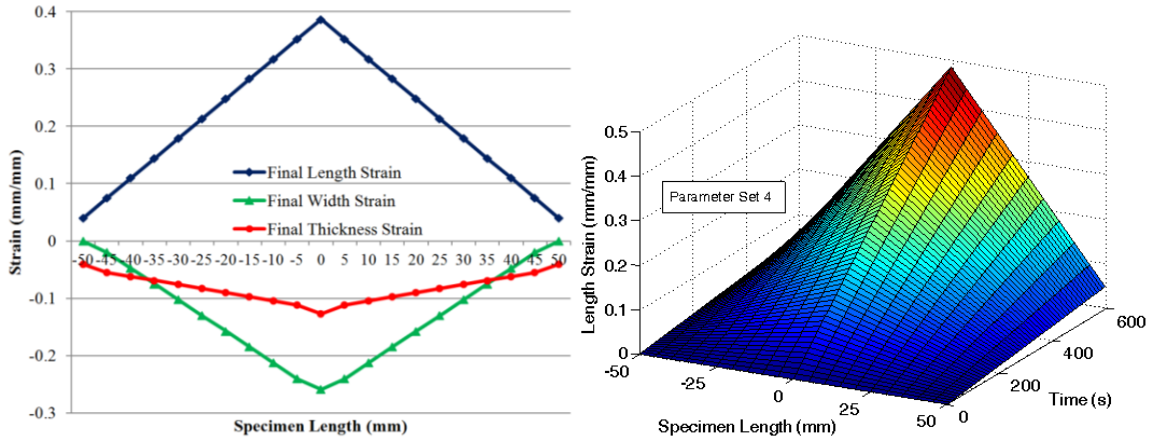

Figure 4.3 - Linearized Experimental Strain Data for Parameter Set 4 at Failure (Left) and Corresponding Input Length Strain Surface (Right)

Table 4.1 - Fracture Strains for Specimen Center

Center of Specimen	Final Length Strain	Final Width Strain	Final Thickness Strain
Parameter Set 1	0.35	-0.27	-0.08
Parameter Set 2	0.43	-0.32	-0.11
Parameter Set 3	0.30	-0.22	-0.08
Parameter Set 4	0.39	-0.26	-0.13

4.2 - Experimental Setup

To validate and examine the results from the derived models, experimental tests were performed with varying test conditions using a square wave input as this will create transient thermal periods for robust model validation. The testing conditions are listed in Table 4.2. As can be seen, two current densities were examined (increased during test), three pulse durations were used, and the pulse period was held constant. For the conditions in Table 4.2 (Parameter Sets 1-4), both stationary (*i.e.* no deformation) and deformation tests with a platen speed of 2.54mm/min (corresponds to an initial true strain

rate of $0.0004s^{-1}$) were performed with two replications. As a result of the repeatability of the test results (force/thermal) this replication number was deemed sufficient. The maximum thermal difference was less than 3°C for all thermal tests and the average force difference was 5MPa. Parameter Set 0 represents conventional room temperature forming.

Table 4.2 - Testing Conditions

Parameter Set	Current Magnitude	Initial Current Density	Pulse Duration	Pulse Period	Duty Cycle	Wave Shape
0	0A	$0A/mm^2$	n/a	n/a	n/a	n/a
1	800A	$64A/mm^2$	0.3s	60s	0.50%	Square
2	800A	$64A/mm^2$	0.5s	60s	0.83%	Square
3	500A	$40A/mm^2$	0.5s	60s	0.83%	Square
4	500A	$40A/mm^2$	1.0s	60s	1.67%	Square

The experimental setup of the testing is shown in Figure 4.4. An Instron hydraulic testing machine with specialized tensile grips to isolate the electricity from the testing equipment was used to deform the tensile specimens. For the mechanical response, force and displacement (resolution of 0.0254mm) was collected and this allowed for the mechanical strain and stress to be calculated. The tensile specimens started as 20x200mm sheet strips and were prepared according to ASTM Standard B557M [4.1]. A thin layer of ceramic paint was applied on one side to reduce emissivity issues for thermal response measurements while the other side of the specimen was acid etched with a strain grid for (CGA). The material tested in this study was Mg AZ31B warm rolled sheet and the test region had a cross-section of 1mm thick by 12.5mm wide per ASTM Standard B557M [4.1]. To measure the thermal response during the test, a

FLIR A40M thermal camera (upper temperature capacity: 550°C, temperature resolution: 0.1°C, and frame rate: 12.5/s) was used (not shown in Figure 4.4).

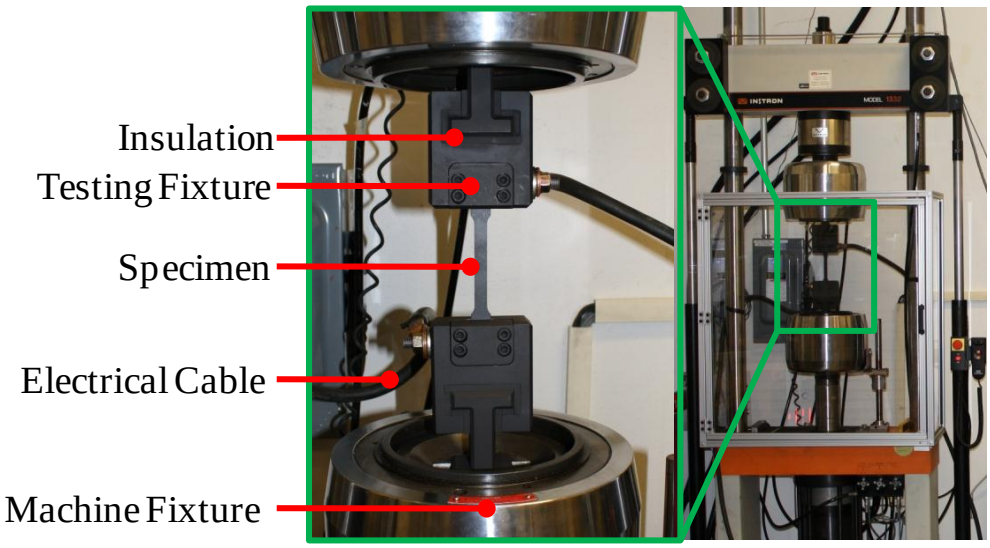

Figure 4.4 - Experimental Testing Setup

An example thermal response of a stationary test over one period is shown in Figure 4.5 (settings correspond to Parameter Set 4). For this test case, the maximum temperature is reached at 1s as this is where the applied current is discontinued and the remaining three profiles (20s, 40s, and 60s) display the cooling of the tensile specimen. Also by observation, the thermal gradient in the width direction is small as compared to the length direction (less than 3°C) and it is assumed that the thickness gradient is even smaller, therefore the assumption of a 1D model is sufficient.

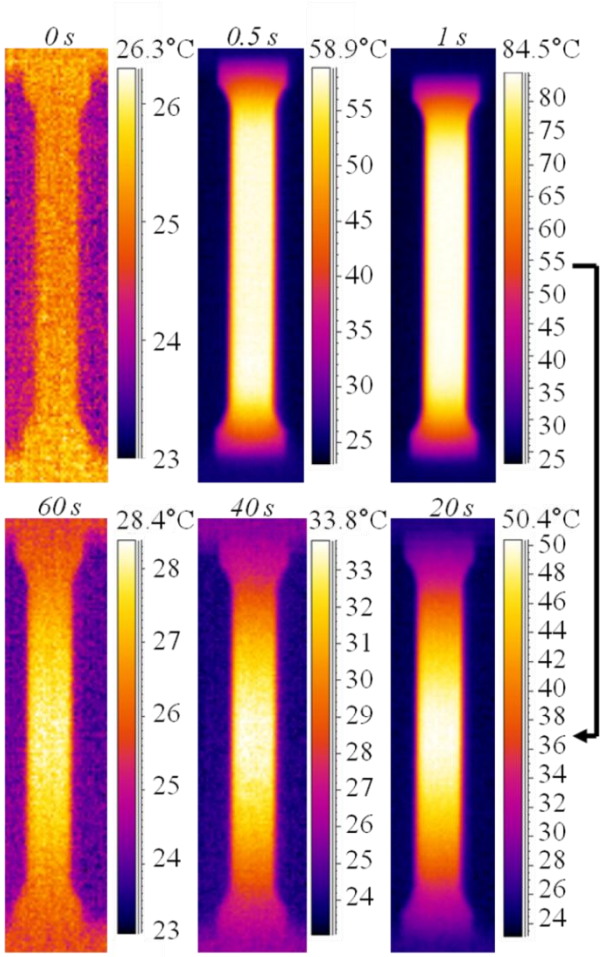

Figure 4.5 - Stationary Test Thermal Sequence over one Period for Parameter Set 4

4.3 - Results and Discussion

In the following section, the stationary and deformation models (uniform and diffuse) are compared to the experimental results obtained from the experimental testing. Additionally, the diffuse thermal model sensitivity to the experimental strain input is examined. For experimental results, the average of the test replications is displayed.

It should be noted that when using the explicit solution approach the time step should be chosen carefully as the solution is not unconditionally stable. Hence, if the time step is not sufficiently small, the solutions may oscillate uncontrollably or diverge from

the actual solution. To choose a time step, a stability criterion can be established based on the second law of thermodynamics. For this, the coefficients of the prior time step must be greater or equal to zero for all nodes when explicitly solved for the next time step. As a result of different nodes having varying boundary conditions, the most restrictive time step should be used. For this analysis, the most restrictive condition was the nodes in the test region of the specimen. Taking into consideration the thermal conductivity, density, specific heat, conduction/convection coefficients, and the mesh properties, the upper limit on the time step was 0.30 seconds for the uniform deformation case. In this analysis, a time step of 0.01 seconds was used and there appeared to be no issues with the solution stability. For the deformation cases, the same time step of 0.01 seconds was used and from analysis of the results there was maintained stability of the solution and the second law of thermodynamics was not violated during analysis of the data. Therefore, even with fast temperature changes and changing element shapes the time step used in these simulations was deemed appropriate.

4.3.1 - Thermal Model Comparison

For the stationary model, one parameter set was used to define/establish the key process variables (heat transfer convection coefficient, initial component and die temperatures, the power supply efficiency and its associated losses, and effective die conduction length in the clamped region) and to validate the overall model construction. Once the variable identification was complete, the key process variables were held constant for the remaining simulations for both the stationary and deformation models. Hence, when comparing the stationary models to the experimental results, the only

variable input was the electrical input parameters (Table 4.2). In the following results, Parameter Set 4 was chosen to display in detail the model results as compared to experimental data; all the developed trends were similar for all of the testing conditions. A full summary of results and the establishment of the process variables (heat transfer convection coefficient, initial component and die temperatures, the power supply efficiency and its associated losses, and effective die conduction length in the clamped region) can be seen in *Appendix A*.

To evaluate the stationary model there are two major criteria to be assessed. These include the maximum temperature observed with respect to test time and the distribution of the temperature along the length of the specimen as a function of time. Figure 4.6 displays the maximum temperature profile for the stationary experimental and model results.

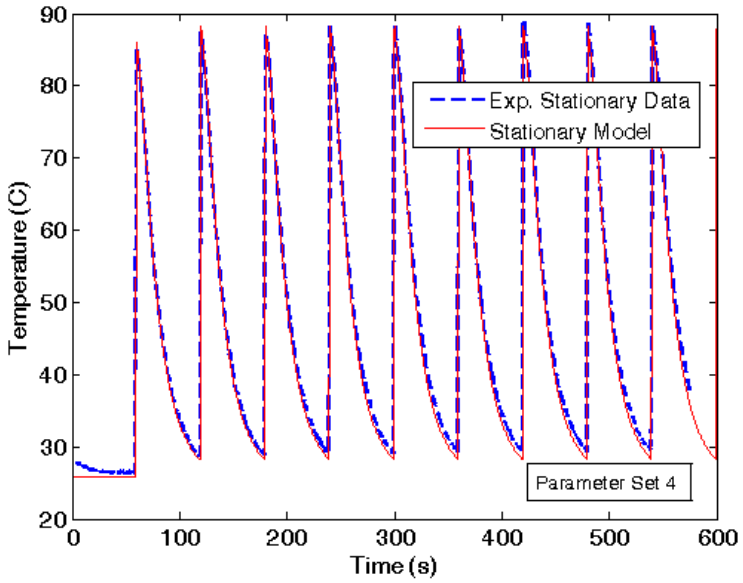

Figure 4.6 - Stationary Maximum Temperature Response of Experimental and Model Results for Parameter Set 4

As can be seen, there is agreement with the experimental data and the model such that the maximum error is 3°C. As shown the temperature rises quickly during the current application and cools fairly fast as the specimen acts like a large fin (illustrated in Figure 4.5).

Another metric to consider in the successful prediction of the stationary response is the temperature along the length of the specimen. Figure 4.7 shows the temperature along the length of the specimen for varying times during one pulse sequence. As can be seen there is a small variation in the model result at 1s where the model overpredicts the experimental data. Also, in the fillet regions of the specimen there is a larger thermal profile difference in the experimental and model results. This can be explained from the model assumption that the fillet region is not included in the model, but may have had an effect on the temperature distribution (see Figure 4.5 near die interface). Thus, as the fillet region has a larger cross-section than assumed, the model predicts this region to have a slightly higher heat generation and thus a higher temperature.

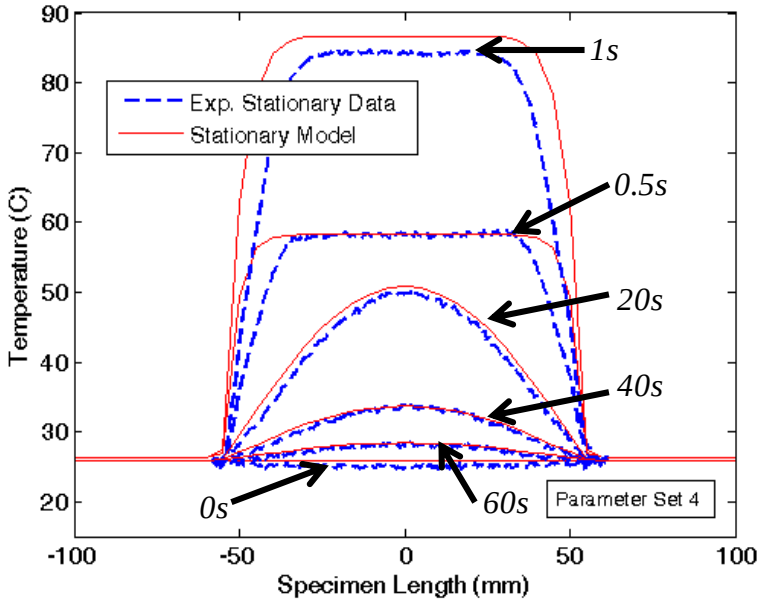

Figure 4.7 - Stationary Axial Length Temperature Profile of Experimental and Model Results for Parameter Set 4

The remaining stationary maximum temperature profiles for the other parameters sets are summarized in Figure 4.8 to display the validity of the established process variables that were held constant while only modifying the electrical input parameters. As can be seen in the figure, the model was capable of matching the experimentally observed thermal response (maximum error is less than 2°C). Also, the maximum temperatures reached can be observed for the varying electrical conditions and the higher current with the middle pulse duration produced the largest temperature.

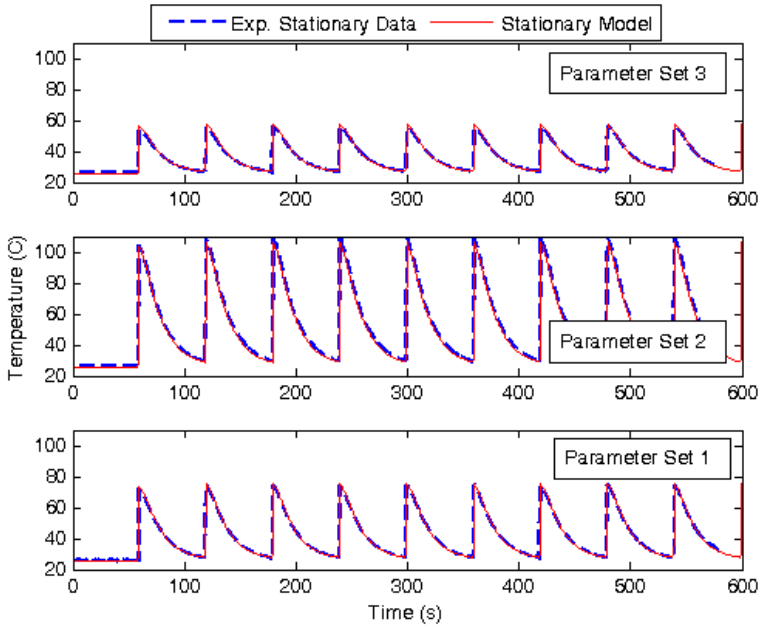

Figure 4.8 - Stationary Maximum Temperature Response of Exp. and Model Results for Remaining Parameter Sets

Upon validation of the stationary model, the thermal response for the case with deformation was examined. The maximum thermal profile for an experimental stationary and deformation test are displayed in Figure 4.9. As can be seen, the stationary curve maintains a constant maximum temperature whereas the deformation curve response increases as time progresses. This increase in the maximum temperature is a result of the elongation and shrinking cross-sectional area which modifies the resistance of the sheet and thus the heat generation per unit volume. Additionally, with deformation the heat transfer conduction area decreases and convection area increases which influence the cooling during and after the applied electrical current.

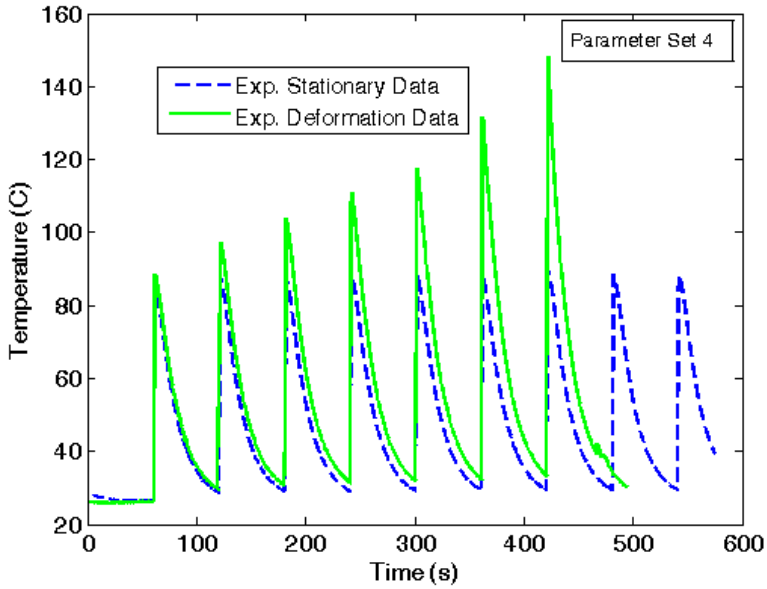

Figure 4.9 - Experimental Maximum Temperature Response of Stationary and Deformation Results for Parameter Set 4

The models created to account for deformation are compared to the experimental results in Figure 4.10 for Parameter Set 4. As can be seen the uniform model underpredicts the thermal response as a result of the assumption that only uniform deformation occurs during the process even though it assumes that all of the input electrical energy goes into resistive heating. However, in EAF uniaxial testing, diffuse necking is present as a result of the specimen geometry and the high cooling rate into the die regions which leaves the center of the specimen at higher elevated temperatures for a longer duration. The diffuse model which assumes that all of the input electrical energy goes into resistive heat and which uses the actual strain from experimental testing overpredicts the thermal response of the experimental data. This overprediction of temperature is suggestive that some energy of the applied electrical current may have gone directly to aiding in deformation (*i.e.* electroplastic effect) and not toward Joule heating.

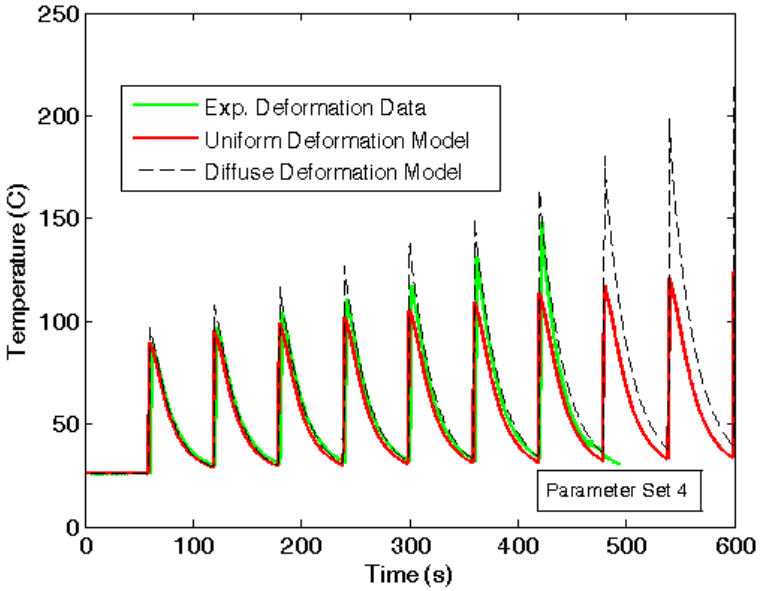

Figure 4.10 - Maximum Temperature Comparison of Deformation Models to Experimental Results for Parameter Set 4

The experimental deformation model response over the length of the specimen is displayed in Figure 4.11 for the sixth pulse and the subsequent cooling period before the seventh pulse. The results in this figure more clearly portray the overprediction of the diffuse deformation model where the variation in the thermal response would represent the applied electrical energy that went directly into aiding deformation and not Joule heating.

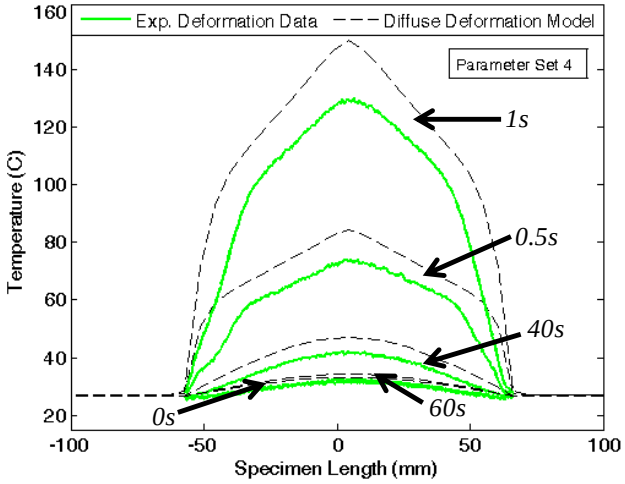

Figure 4.11 - Axial Comparison of Deformation Model to Experimental Results for Parameter Set 4

Figure 4.12 depicts the thermal response of the deformation models and experimental data over the entire data set to see the complete response shape. As observed, the uniform model's overall temperature increases with time, however it does not show an increased temperature at the specimen center as the diffuse model and the experimental data.

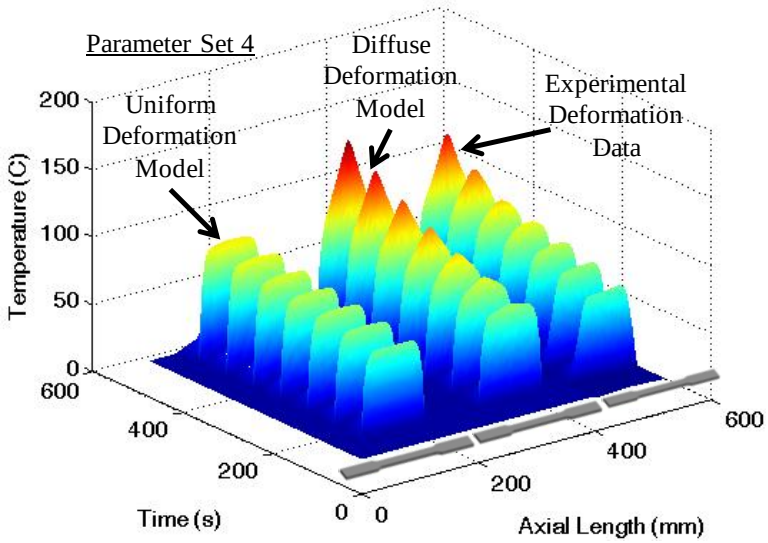

Figure 4.12 - Thermal Response Surface for Deformation Models and Experimental Data as a Function of Time

4.3.2 - Thermal Model Sensitivity

To examine the sensitivity of the experimental strain measurements from the CGA to the output temperature of the diffuse deformation model, several model simulations were performed where the original experimental strain data was mathematically transformed. To transform the strain data, it was reduced by multiplying it by a percentage. This was performed to verify that the difference from the all-heating thermal model was not greater or equal when compared to the experimental data as a result of strain input sensitivity. To compare the results, the center temperature of the specimen is examined (corresponds to the maximum temperature of the specimen). For the analysis, Parameter Set 4 was examined to show the general trends. The simulation runs performed are given in Table 4.3.

Table 4.3 - Strain Sensitivity Runs Performed

	% Decrease in Strain	% of Original Exp. Data
Diffuse Deformation Model	0%	100%
Diffuse Def. Model (10%)	10%	90%
Diffuse Def. Model (20%)	20%	80%
Diffuse Def. Model (40%)	40%	60%

An example of the decrease in strain is shown in Figure 4.13 where the maximum 40% decrease is depicted.

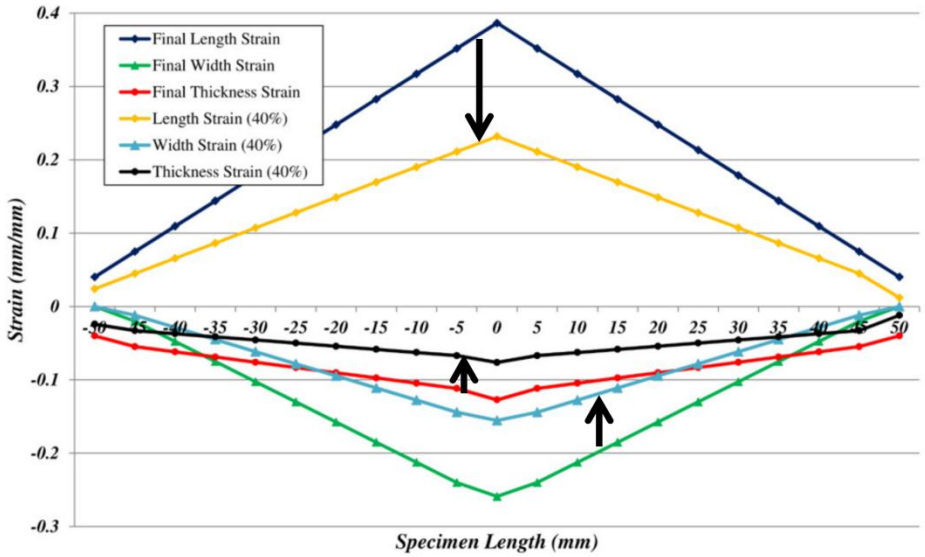

Figure 4.13 - Original and Modified (40% Decrease) Linearized Experimental Strain Data for Parameter Set 4 at Failure

The following figures show an enlarged portion of the thermal response at several times during the test to depict the varying thermal responses from the model results as compared to the experimental data. Figure 4.14 shows the different model responses and experimental results during the first application of electricity. As seen with a decreasing strain input to the diffuse model, this correlates to a lower thermal profile. This is expected as the cross-sectional area is greater and it has an inverse correlation to the heat generated within the specimen (*i.e.* larger cross-sectional area means less heat generation as described in Equation (4.16)). As shown, the experimental results are still less than all of the models, and this is a result of the deformation still being quite uniform for the experimental test at this point.

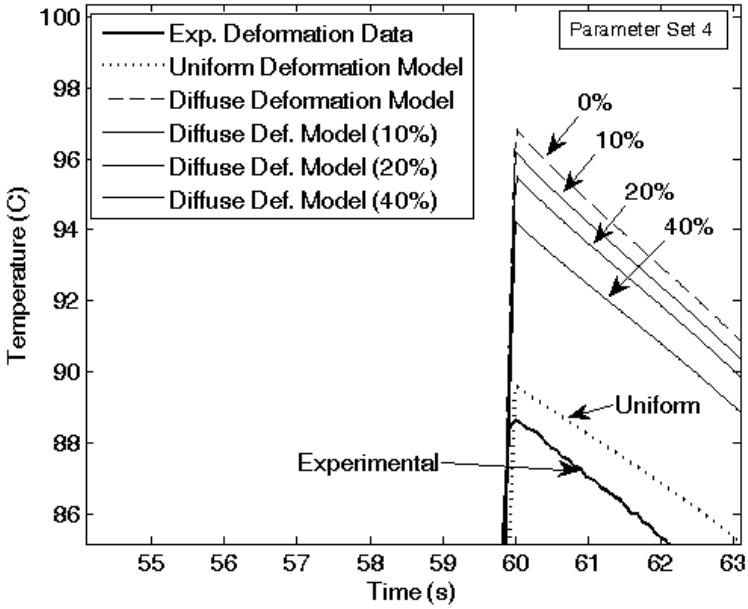

Figure 4.14 - Strain Input Sensitivity for Diffuse Deformation Model versus Experimental Results at First Application of Current (60s)

In Figure 4.15, the same results are seen, however, the experimental results are equivalent to the diffuse deformation model at a 40% decrease. This is a result of the experimental test having a greater amount of diffuse deformation. For the experimental test, the deformation along the axial length is diffuse and may not be linearly distributed from one end of the specimen to the center or at the center point. Thus, the peak temperature may not increase linearly. However, for the model this is an assumption that was used when taking the fracture strain measurements from the circle grid analysis.

Similar results are presented in Figure 4.16, but the experimental result is now at the diffuse deformation model at 20% reduction in strain.

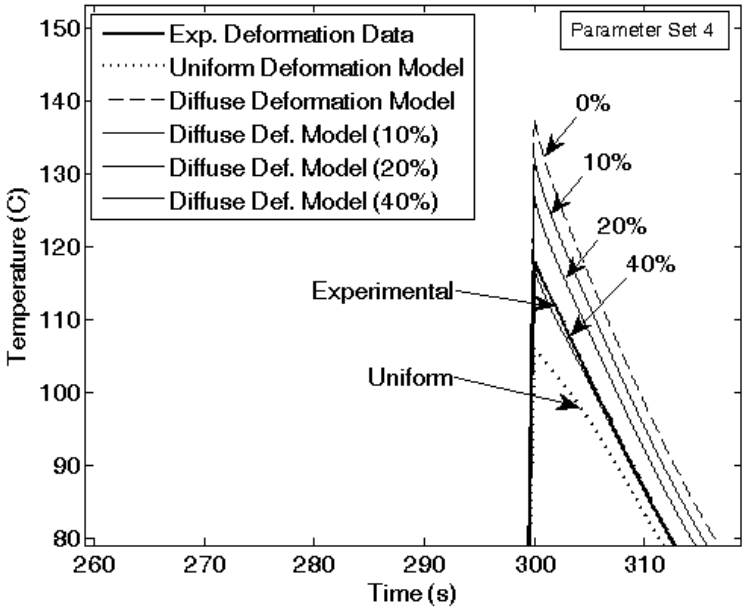

Figure 4.15 - Strain Input Sensitivity for Diffuse Deformation Model versus Experimental Results at Fifth Application of Current (300s)

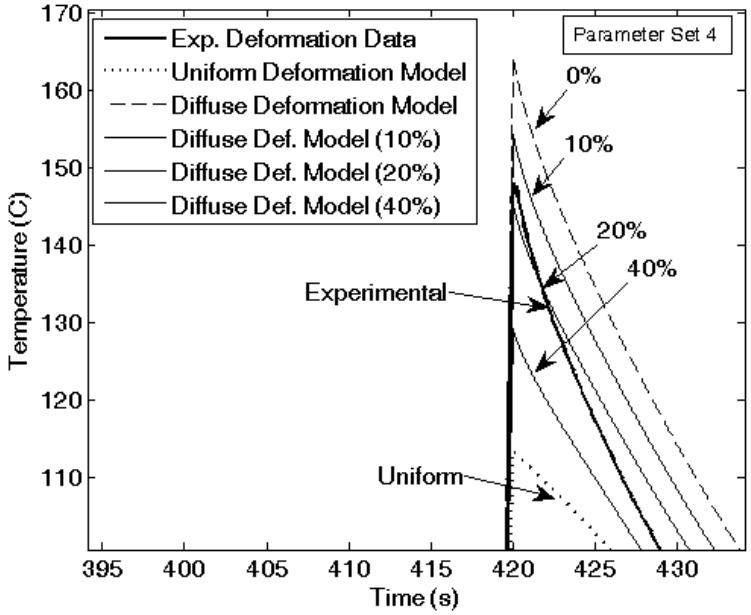

Figure 4.16 - Strain Input Sensitivity for Diffuse Deformation Model versus Experimental Results at Seventh Application of Current (420s)

The overall conclusion from this analysis is that the sensitivity of the strain input is not the reason for seeing a larger thermal response from the model that considers all of the electrical energy is transformed into joule heating. This is since at the end of the deformation test (*i.e.* experimental result is near failure) the experimental result is only at the diffuse deformation model at 20% reduction in strain which is a large variation from the original experimental measured strain data. Thus, this confirms that the observed variation in the thermal responses from the diffuse deformation model to the experimental result is due to energy going into directly aiding in deformation (*i.e.* electroplasticity).

4.4 - Thermal Model Conclusions

The thermal response is an important aspect to consider during EAF as this is a coupled thermal-mechanical process. As a result, this chapter examined and successfully modeled the thermal response of sheet metal subject to EAF and established models that can predict the response for stationary tests as well as deformation tests for varying electrical testing conditions. It was shown that there is good agreement with the model as compared to the stationary response with an applied electrical current. However, for consideration of deformation during the process, the diffuse model suggests that a portion of the applied current goes directly into aiding deformation and not to Joule heating. Thus, this chapter is suggestive that the electroplastic effect is significant, and causes the applied current to directly aid in deformation as has been previously described. Additional figures of the model results versus the experimental results are shown in *Appendix A*.

Overall, the output of this chapter is the creation of accurate thermal response models for EAF. These models will be later used for coupled thermo-mechanical modeling and then toward the prediction of failure strain modeling.

4.5 - References for Chapter 4

[4.1] ASTM B557M – 10: Standard Test Methods for Tension Testing Wrought and Cast Aluminum- and Magnesium-Alloy Products (Metric), 2010.

[4.2] United States Department of Defense (1998). "Department of Defense Handbook: Metallic Materials and Elements for Aerospace Vehicle Structures, MIL-HDBK-5H."

[4.3] Y.A. Cengel, *Heat and Mass Transfer: A Practical Approach*, 3 ed. Boston: McGraw Hill, 2007.

[4.4] W.A. Salandro, J.J. Jones, T.A. McNeal, J.T. Roth, S.T. Hong, and M.T. Smith (2009) "Formability of Al 5xxx Sheet Metals Using Pulsed Current for Varying Heat Treatments," *J. of Manuf. Science and Eng.*, Vol. 132, pp.051016-1-11.

[4.5] W.A. Salandro, A. Khalifa, and J.T. Roth "Tensile Formability Enhancement of Magnesium AZ31B-O Alloy Using Electrical Pulsing," *Transactions of the North American Manufacturing Research Institute of SME*, vol. 37, 2009.

CHAPTER 5 - DEFORMATION/STRENGTH MODELING OF SHEET METALS DURING EAF

This chapter introduces the strength modeling and local strain modeling for EAF of sheet metals in uniaxial tension. The results displayed in *Chapter 4* are used as an input to the model to provide the thermal variation axially along the specimen and with respect to time. The deformation/strength model created here will be further combined with the thermal model from *Chapter 4* to produce the multiphysics model in *Chapter 6*.

5.1 - Sheet Deformation Model with Structural/Geometric Non-homogeneity

The deformation/strength model allows for understand and prediction of the deformation behavior of sheet metals in uniaxial tension during EAF. The model considers both a structural and geometric non-homogeneity as a result of a non-uniform temperature distribution (structurally related) and diffuse necking (geometrically related) observed during EAF testing. A schematic is presented in Figure 5.1 where the tensile sample is divided into a number of elements with each capable of having different strength properties and dimensional sizes. The basis for the model is that force equivalency must be maintained throughout the tensile sample, but the stress and area can vary along the length of the specimen. Also, the model is solved incrementally, where the input is a given displacement (d) that creates the elements to plastically deform. As the displacement is imposed, the other continuity condition is that the summation of the individual element displacements adds to the total imposed displacement.

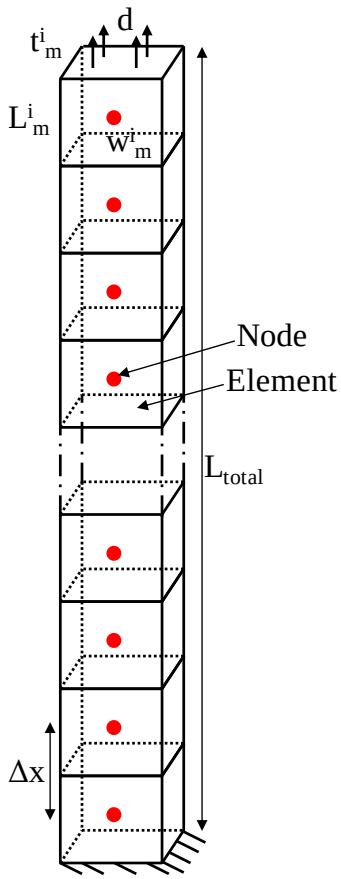

Figure 5.1 - Deformation Model Schematic

5.1.1 – Deformation/Strength Model Derivation

This section contains the derivation of the deformation/strength model. The derivation is written for a time step (*i*). Thus at a given time step *i*, force equivalency gives:

$$F = F_m = F_{m+1} \quad for\ m = \{1...(m-1)\} \tag{5.1}$$

where, *F* is the force and *m* is the number of nodes/elements in the model.

The force can be written in terms of stress and area by:

$$\sigma_m A_m = \sigma_{m+1} A_{m+1} \tag{5.2}$$

Or,

$$\sigma_m t_m w_m = \sigma_{m+1} t_{m+1} w_{m+1} \tag{5.3}$$

where, *t* and *w* are thickness and width, respectively.

Knowing that,

$$t = t_o e^{\varepsilon_t} \tag{5.4}$$

$$w = w_o e^{\varepsilon_w} \tag{5.5}$$

where, t_o is the initial thickness, ε_t is the thickness strain, w_o is the initial width, and ε_w is the width strain. This yields,

$$\sigma_m t_{o,m} w_{o,m} e^{\varepsilon_{t,m}} e^{\varepsilon_{w,m}} = \sigma_{m+1} t_{o,m+1} w_{o,m+1} e^{\varepsilon_{t,m+1}} e^{\varepsilon_{w,m+1}} \tag{5.6}$$

Or,

$$\sigma_m t_{o,m} w_{o,m} e^{\varepsilon_{t,m}+\varepsilon_{w,m}} = \sigma_{m+1} t_{o,m+1} w_{o,m+1} e^{\varepsilon_{t,m+1}+\varepsilon_{w,m+1}} \tag{5.7}$$

Since volume is conserved,

$$\varepsilon_t + \varepsilon_w + \varepsilon_L = 0 \text{ or } \varepsilon_t + \varepsilon_w = -\varepsilon_L \tag{5.8}$$

where, ε_L is the incremental strain in the length direction (*i.e.* along axial length). Incremental strain is the strain in each individual element over one time step. The incremental strain accrues over time to the accumulative strain of each element.

This gives,

$$\sigma_m t_{o,m} w_{o,m} e^{-\varepsilon_{L,m}} = \sigma_{m+1} t_{o,m+1} w_{o,m+1} e^{-\varepsilon_{L,m+1}} \tag{5.9}$$

Or,

$$\sigma_m A_{o,m} e^{-\varepsilon_{L,m}} = \sigma_{m+1} A_{o,m+1} e^{-\varepsilon_{L,m+1}} \tag{5.10}$$

Manipulating,

$$\frac{\sigma_m A_{o,m}}{\sigma_{m+1} A_{o,m+1}} = \frac{e^{-\varepsilon_{L,m+1}}}{e^{-\varepsilon_{L,m}}} \tag{5.11}$$

$$\frac{\sigma_m A_{o,m}}{\sigma_{m+1} A_{o,m+1}} = e^{\left(\varepsilon_{L,m} - \varepsilon_{L,m+1}\right)} \tag{5.12}$$

$$\ln\left(\sigma_m A_{o,m}\right) - \ln\left(\sigma_{m+1} A_{o,m+1}\right) - \varepsilon_{L,m} + \varepsilon_{L,m+1} = 0 \tag{5.13}$$

Where the stress (σ) is defined by a modified power law relation (see developed phenomenological constitutive equation in *Section 7.4*):

$$\sigma_m\left(\varepsilon_{L,m,total}, T_m\right) = K_m \varepsilon_{L,m,total}^{n_m} e^{\varepsilon_{L,m,total} s_m} \tag{5.14}$$

$$\sigma_{m+1}\left(\varepsilon_{L,m+1,total}, T_{m+1}\right) = K_{m+1} \varepsilon_{L,m+1,total}^{n_{m+1}} e^{\varepsilon_{L,m+1,total} s_{m+1}} \tag{5.15}$$

And,

$$\varepsilon_{L,m,total} = \varepsilon_{L,m,acc}^{i-1} + \varepsilon_{L,m} \tag{5.16}$$

$$\varepsilon_{L,m+1,total} = \varepsilon_{L,m+1,acc}^{i-1} + \varepsilon_{L,m+1} \tag{5.17}$$

where, $\varepsilon_{L,m,total}$ and $\varepsilon_{L,m+1,total}$ are the total accumulative strain in element *m* and *m+1* developed during forming at time step *i*, respectively. $\varepsilon_{L,m,acc}^{i-1}$ and $\varepsilon_{L,m+1,acc}^{i-1}$ represent the total accumulative strain in element *m* and *m+1* from the start of forming to the prior time step (*i-1*). $\varepsilon_{L,m}$ and $\varepsilon_{L,m+1}$ are the incremental strain occurring during time step *i* for elements *m* and *m+1*, respectively.

Such that *K*, *n*, and *s* are:

$$K := \begin{cases} T \le 25°C : K = K_{RT} \\ 25°C < T < 150°C : K = K_1 T + K_2 \\ T \ge 150°C : K = K_3 \exp\left(K_4 T\right) \end{cases} \tag{5.18}$$

$$n := \begin{cases} T \le 25°C : n = n_{RT} \\ 25°C < T < 150°C : n = n_1 T + n_2 \\ T \ge 150°C : n = n_3 T + n_4 \end{cases} \quad (5.19)$$

$$s := \begin{cases} T < 120°C : s = 0 \\ 120°C \le T \le 327°C : s = s_1 T^2 + s_2 T + s_3 \\ T > 327°C : s = 0 \end{cases} \quad (5.20)$$

where, the coefficients are given in Table 5.1. For more detail on the phenomenological constitutive equation refer to *Section 7.4*.

Table 5.1 - Conventional Room and Elevated Temperature Model Coefficients for Mg AZ31B

Constant	Value
K_{RT}	457.72
K_1	-1.9529
K_2	500.68
K_3	931.06
K_4	-0.01
n_{RT}	0.1818
n_1	-0.0004
n_2	0.1909
n_3	-0.0009
n_4	0.2713
s_1	0.00008
s_2	-0.0357
s_3	3.1162

Thus,

$$\ln\left(K_m \varepsilon_{L,m,total}^{n_m} e^{\varepsilon_{L,m,total} s_m} A_{o,m}\right) - \ln\left(K_{m+1} \varepsilon_{L,m+1,total}^{n_{m+1}} e^{\varepsilon_{L,m+1,total} s_{m+1}} A_{o,m+1}\right) - \varepsilon_{L,m} + \varepsilon_{L,m+1} = 0 \quad (5.21)$$

Or,

$$\ln\left(\frac{K_m}{K_{m+1}}\right) + \ln\left(\varepsilon_{L,m,total}^{n_m}\right) - \ln\left(\varepsilon_{L,m+1,total}^{n_{m+1}}\right) + \varepsilon_{L,m,total} s_m - \varepsilon_{L,m+1,total} s_{m+1} + \ln\left(\frac{A_{o,m}}{A_{o,m+1}}\right) - \varepsilon_{L,m} + \varepsilon_{L,m+1} = 0 \quad (5.22)$$

Finally,

$$\ln\left(\frac{K_m}{K_{m+1}}\right)+\ln\left(\frac{A_{o,m}}{A_{o,m+1}}\right)+n_m\ln\left(\varepsilon_{L,m,acc}^{i-1}+\varepsilon_{L,m}\right)-n_{m+1}\ln\left(\varepsilon_{L,m+1,acc}^{i-1}+\varepsilon_{L,m+1}\right)+\varepsilon_{L,m}\left(s_m-1\right)-\varepsilon_{L,m+1}\left(1-s_{m+1}\right)+\varepsilon_{L,m,acc}^{i-1}s_m-\varepsilon_{L,m+1,acc}^{i-1}s_{m+1}=0 \quad (5.23)$$

Using Equation (5.23), this leads to a system of *m-1* equations for $m=\{1...(m-1)\}$ where *m* is the number of nodes/elements.

It should be noted that the terms $A_{o,m}$ and $A_{o,m+1}$ change independently from each other from the time step *i* to *i+1*, thus simulating a varying cross-sectional area along the specimen length.

This leads to a system of *m-1* implicit non-linear equations with *m* unknowns. Thus, the final condition required is:

$$\Delta d=\sum_{1}^{m}\Delta L_m \quad (5.24)$$

where, Δd is the imposed input displacement and ΔL_m is the change in length of an element. This expression states that the summation of the element displacements is equal to the overall imposed displacement.

Knowing,

$$\varepsilon_{L,m}=\ln\left(\frac{L_{o,m}+\Delta L_m}{L_{o,m}}\right) \quad (5.25)$$

Or,

$$\Delta L_m=L_{o,m}\left(e^{\varepsilon_{L,m}}-1\right) \quad (5.26)$$

Hence,

$$\Delta d = \sum_{1}^{m} L_{o,m}\left(e^{\varepsilon_{L,m}} - 1\right) \tag{5.27}$$

Finally,

$$\boxed{\sum_{1}^{m} L_{o,m}\left(e^{\varepsilon_{L,m}} - 1\right) - \Delta d = 0} \tag{5.28}$$

It should be noted that $L_{o,m}$ can vary along the length of the specimen per each element and it is the initial length of the element from the prior time step (i-1) as a result of Δd being defined as an increment (*i.e.* constant).

Therefore, using Equations (5.23) and (5.28), the strain in each element in the axial direction can be determined by solving the system of equations. These strains can then be used to determine the strain in the other directions for each element using an associated flow rule and the new dimensions of the elements can be determined. Since the corresponding stress and area in each element relate to an overall equivalent force, this force can be determined and used with the displacement given to produce a force and displacement profile (just as would occur for an experimental test).

5.1.2 – Deformation/Strength Model Solution Method

There are several numerical methods to find the roots of this non-linear implicit system of equations. The Newton-Raphson method is efficient and converges quickly given good initial approximations of the variables. The method is given by [5.1] for a system of non-linear equations:

$$\begin{aligned} f_1(x_1, x_2, \ldots, x_n) &= 0 \\ f_2(x_1, x_2, \ldots, x_n) &= 0 \\ f_3(x_1, x_2, \ldots, x_n) &= 0 \end{aligned} \tag{5.29}$$

For each equation a multivariable 1st order Taylor series expansion is written. For example, for the k^{th} equation:

$$f_{k,i+1} = f_{k,i} + \left(x_{1,i+1} - x_{1,i}\right)\frac{\partial f_{k,i}}{\partial x_1} + \left(x_{2,i+1} - x_{2,i}\right)\frac{\partial f_{k,i}}{\partial x_2} + \ldots + \left(x_{n,i+1} - x_{n,i}\right)\frac{\partial f_{k,i}}{\partial x_n} \tag{5.30}$$

where, the first subscript (k) represents the equation of unknown and the second subscript denotes whether the value or function is at the present value (i) or at the next value ($i+1$).

By setting $f_{k,i+1}$ to zero this means that we are looking for the roots of the system of equations. This then gives:

$$-f_{k,i} + x_{1,i}\frac{\partial f_{k,i}}{\partial x_1} + x_{2,i}\frac{\partial f_{k,i}}{\partial x_2} + \ldots + x_{n,i}\frac{\partial f_{k,i}}{\partial x_n} = x_{1,i+1}\frac{\partial f_{k,i}}{\partial x_1} + x_{2,i+1}\frac{\partial f_{k,i}}{\partial x_2} + \ldots + x_{n,i+1}\frac{\partial f_{k,i}}{\partial x_n} \tag{5.31}$$

By examining Equation (5.31), the only unknowns are the $x_{k,i+1}$ terms on the right-hand side of the equation as all other quantities are known at the present value (i). This now provides a system of linear equations that can be solved. Matrix notation is used to simplify the expression. The partial derivatives can be expressed by:

$$[J] = \begin{bmatrix} \frac{\partial f_{1,i}}{dx_1} & \cdots & \frac{\partial f_{1,i}}{dx_n} \\ \vdots & \ddots & \vdots \\ \frac{\partial f_{n,i}}{dx_1} & \cdots & \frac{\partial f_{n,i}}{dx_n} \end{bmatrix} \tag{5.32}$$

where, J is commonly called the Jacobian matrix.

The initial and final values in vector form are:

$$\{X_i\}^T = \left[x_{1,i} \ldots x_{n,i} \right] \tag{5.33}$$

And,

$$\{X_{i+1}\}^T = \left[x_{1,i+1} \ldots x_{n,i+1} \right] \tag{5.34}$$

The function values in vector form are:

$$\{F_i\}^T = \left[f_{1,i} \ldots f_{n,i} \right] \tag{5.35}$$

Thus, the linear system can be expressed in the standard form:

$$Ax = b \tag{5.36}$$

Or,

$$[J]\{X_{i+1}\}^T = -\{F_i\}^T + [J]\{X_i\}^T \tag{5.37}$$

This system can be solved using a technique such as Gauss elimination. The process can be repeated iteratively to obtain refined estimates of the unknown variables. For the simulations performed in this work, the Newton-Raphson method was repeated until the norm (*i.e.* vector length) of the root vector was very small (*i.e.* less than 1×10^{-10}).

Once the strains in each element are known is the axial direction, the strain in the width and thickness direction can be determined using a material flow rule. Presently, it is proposed to assume the von Mises yield criterion and material isotropy (note: other yield criterion or anisotropy could be applied here as well). This results in the Levy-Mises equations:

$$\frac{d\varepsilon_1}{2\sigma_1} = \frac{d\varepsilon_2}{-\sigma_1} = \frac{d\varepsilon_3}{-\sigma_1} \tag{5.38}$$

where, $d\varepsilon_p$ is the incremental strain in the primary three directions and σ_1 is the stress applied along the length axis.

This results in:

$$\varepsilon_{w,m} = \varepsilon_{t,m} = -\frac{1}{2}\varepsilon_{L,m} \tag{5.39}$$

After determining the strain in each direction (length, width, and thickness), the new element geometry can be determined by:

$$\begin{aligned} L_m^{i+1} &= L_{o,m} e^{\varepsilon_{L,m}} \\ w_m^{i+1} &= w_{o,m} e^{\varepsilon_{w,m}} \\ t_m^{i+1} &= t_{o,m} e^{\varepsilon_{t,m}} \end{aligned} \tag{5.40}$$

Where, L_m^{i+1}, w_m^{i+1}, and t_m^{i+1} are the new length, width, and thickness of the element, respectively. The new cross-sectional area (A_m^{i+1}) of the elements can be calculated using the new width and thickness by:

$$A_m^{i+1} = w_m^{i+1} t_m^{i+1} \tag{5.41}$$

The stress for each element can be given by:

$$\sigma_m\left(\varepsilon_{L,m,total}, T_m\right) = K_m \varepsilon_{L,m,total}^{n_m} e^{\varepsilon_{L,m,total} S_m} \tag{5.42}$$

where, the constants are calculated from Equations (5.18)-(5.20) and the total strain in the axial direction of the element is used. The force is calculated (equal for each element) as:

$$F = A_m^{i+1} \sigma_m \tag{5.43}$$

The force at each time step can be paired with the imposed displacement at that time step to produce a corresponding force and displacement curve. This profile can be

converted to true strain and stress by the assumption of uniform deformation for comparison to experimental results.

5.2 - Deformation/Strength Model Results

In the following sections, the model results are presented for the application of both uniform temperature distributions and EAF temperature distributions during tensile deformation.

5.2.1 - Uniform Temperature Distribution

The uniform temperature distribution inputs are summarized in this section. Detailed results (*e.g.* incremental strain, accumulative strain, stress, and force) are presented for the room temperature (22°C) test and the other temperatures are summarized by comparing the force output.

5.2.1.1 - Results at 22°C (Room Temperature)

The incremental strains to predict the deformation behavior of magnesium sheet are shown in Figure 5.2 for the simulation performed at 22°C. The incremental strain is equal for each element due to the temperature distribution applied each element being equal and constant throughout the entire simulation.

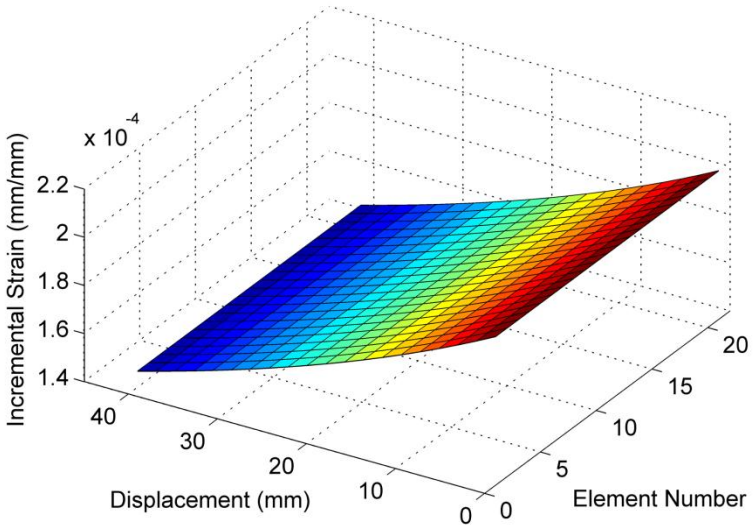

Figure 5.2 - Incremental Strain Results for a Uniform Temperature Input of 22C

The incremental strains are small for each time step (*i.e.* displacement increment) as a result of the time step being small (0.5s) with a deformation rate of 2.54mm/min. Thus, at each time step there is not a significant amount of strain imposed to the entire material. The incremental strain decreases over time as a result of the ratio between the final length of each element and the initial length of each element decreasing with time. This can be seen in Equation (5.44) where ΔL remains constant for each time step and L_o increases with each time step as deformation is imposed. Thus, the quantity in the natural logarithm decreases which causes the incremental strain to decrease over time.

$$\varepsilon_L = \ln\left(\frac{L_f}{L_o}\right) = \ln\left(1+\frac{\Delta L}{L_o}\right) \tag{5.44}$$

The error in force as a function total imposed displacement is given in Figure 5.3.

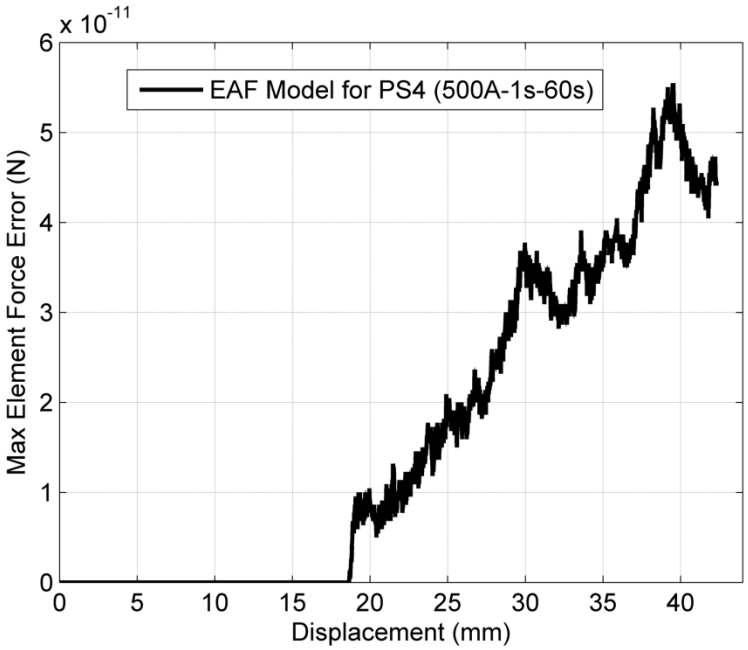

Figure 5.3 - Element Force Error for a Uniform Temperature Input of 22C

The maximum element force error is the difference between the element with the highest derived force and the element with the lowest derived force at every time step. The error is lower than $6x10^{-11}$N, which is very small. Thus, this concludes that the simulation solution method was effective in solving the model with very little error and Equation (5.1) remained satisfied during the simulation.

Also, the other imposed condition was that the summation of the change in element length at a given time step is equal to the imposed total displacement (Equation (5.24)). The element displacement error is given in Figure 5.4 where the error represents the difference between the simulated total displacement of all elements and the imposed total displacement. As shown, the error is extremely small ($<12x10^{-13}$mm). Thus, the condition given by Equation (5.24) was upheld during the simulation.

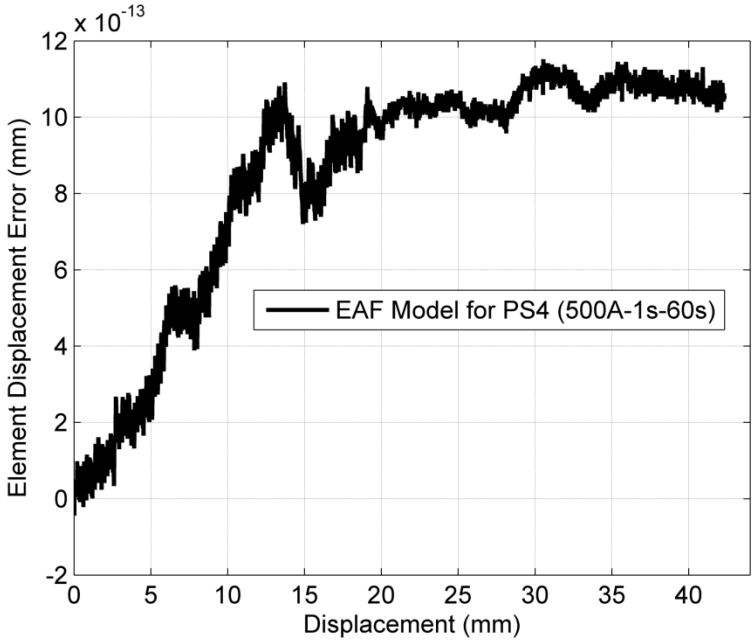

Figure 5.4 - Element Displacement Error for a Uniform Temperature Input of 22C

From the incremental strain solution, the accumulation of these small increments over time provides the total accumulative strain in each element. The total accumulative strain for each element is given in Figure 5.5.

Figure 5.6 shows the element length change with respect to the total imposed displacement. As seen, the length of each element increases in length by 2mm during the simulation. Again, the length increase for each element is equivalent as the temperature of each element is the same throughout the simulation.

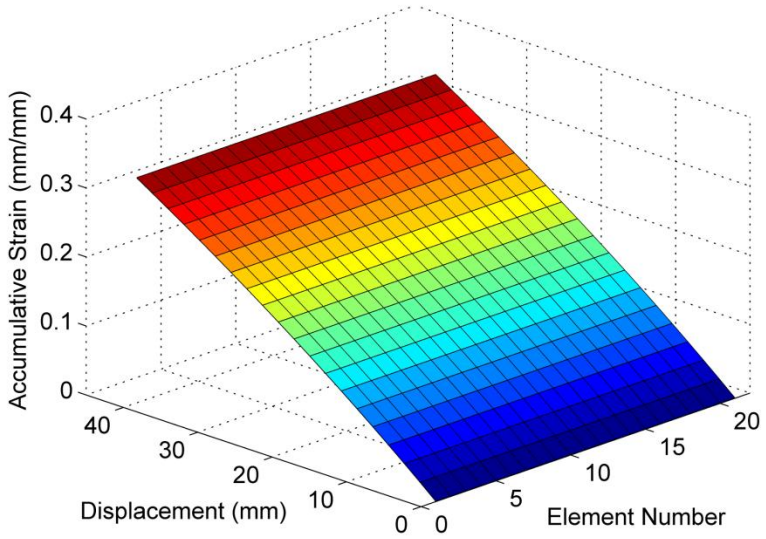

Figure 5.5 - Accumulative Strain Results for a Uniform Temperature Input of 22C

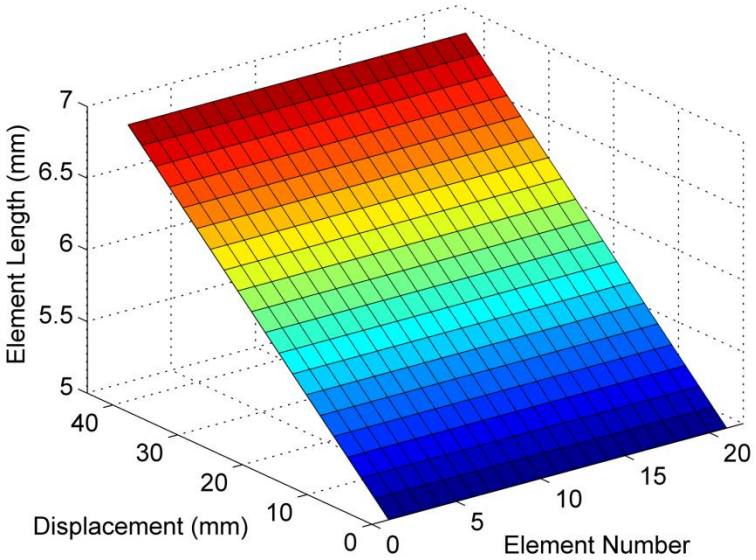

Figure 5.6 - Element Length Results for a Uniform Temperature Input of 22C

Corresponding to the increase in length, Figure 5.7 displays the reduction in area for each element based on conservation of volume. The area is reduced from 12.5mm^2 to approximately 9mm^2.

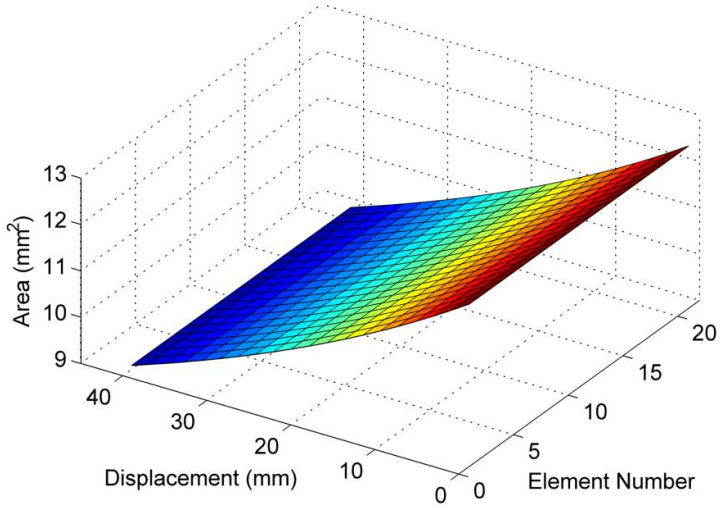

Figure 5.7 - Element Area Results for a Uniform Temperature Input of 22C

The stress required for deformation during the simulation is given in Figure 5.8. As seen, the true stress required to deform the sample increases with imposed displacement. This is a result of the material strain hardening at this temperature (22°C).

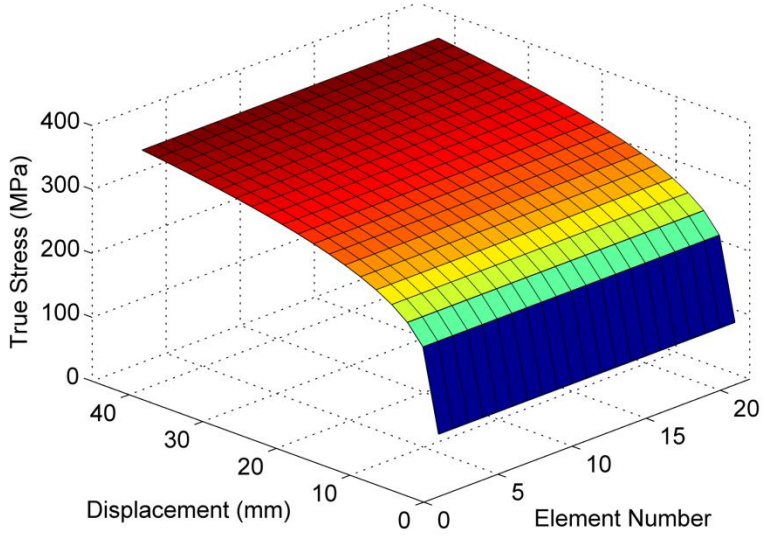

Figure 5.8 - True Stress Results for a Uniform Temperature Input of 22C

The forming force from the simulation is given in Figure 5.9.

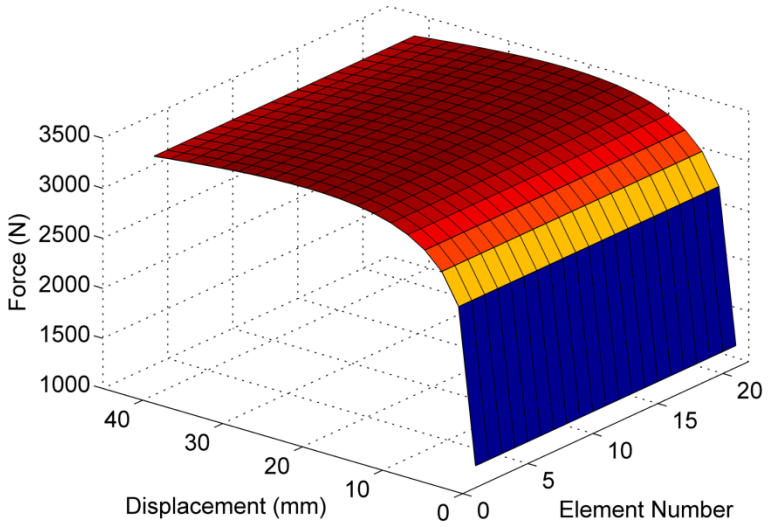

Figure 5.9 - Force Results for a Uniform Temperature Input of 22C

As seen, the force increases and reaches a maximum force at approximately 21mm of displacement and then the force begins to decreases. The decrease in force indicates a material instability point where the material does not have perfect uniform elongation (i.e. indication of localized necking). However, localized necking was not incorporated in the model and that is why the incremental strain solutions were equal throughout the entire simulation. To better visualize the instability point, the force profile is plotted in Figure 5.10.

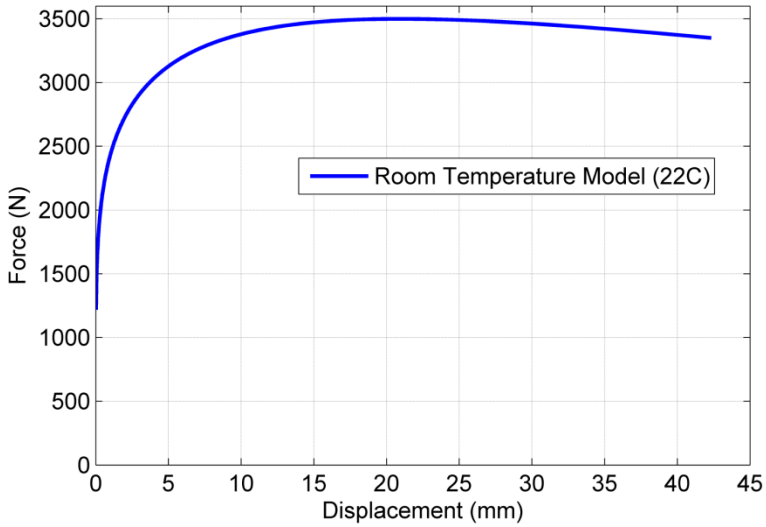

Figure 5.10 - Force Results Plot for a Uniform Temperature Input of 22C

Using Equation (7.12), the predicted point of instability for a uniform temperature input of 22°C should occur at:

$$\varepsilon^* = \frac{n}{1-s} = \frac{.1818}{1-0} = .1818 \tag{5.45}$$

where, the strain hardening exponent (n) is equal to 0.1818 and the softening coefficient (s) is zero at 22°C.

The instability strain can be converted to a displacement by:

$$L_{instability} = L_o\left(e^* - 1\right) = \left(105mm\right)e^{.1818} - 105mm = 20.93mm \tag{5.46}$$

where, the gauge length (*i.e.* region where deformation occurs) is 105mm. Thus, comparing this result to Figure 5.10, it is shown that the model predicts that instability occurs at the same displacement (*i.e.* maximum force corresponds to 20.93mm).

To verify the output of the model, Figure 5.11 shows the true stress/strain response versus the experimental data. As seen, the model accurately predicts the experimental result. The model extends past the fracture point of the experimental result

as the model does not incorporate any failure criteria that would indicate that the point at which the material will fail.

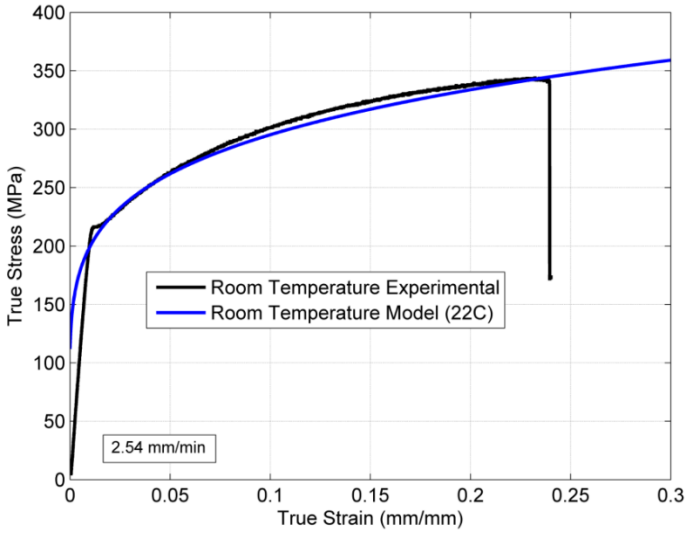

Figure 5.11 - True Stress Plot for a Uniform Temperature Input of 22C (Experiment vs. Simulation)

5.2.1.2 - Results at Elevated Temperatures

The results from additional simulations are provided in Figure 5.12 where the force is proved as a function of total imposed displacement. As seen, the model predicts the required forming force to decrease with increasing temperature.

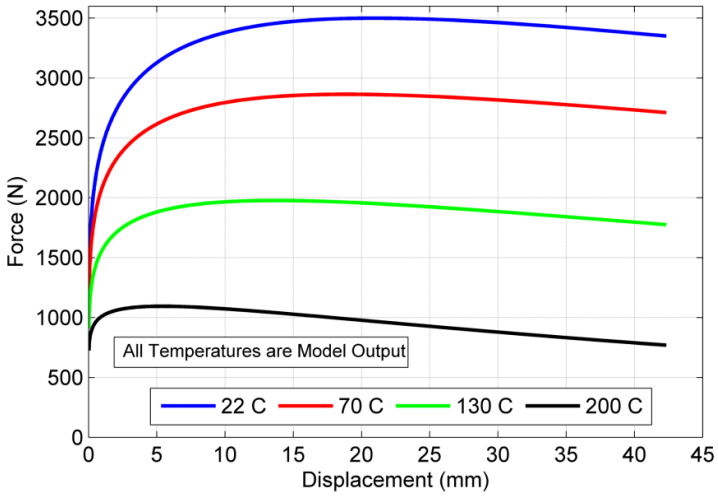

Figure 5.12 - Force Results Plot for a Uniform Temperature Input of 22C, 70C, 130C and 200C

Additionally, the prediction of instability was calculated using Equation (7.12) and the results are provided in Table 5.2. As seen, the model results from the simulation were capable of predicting the instability point (*i.e.* maximum force) for each temperature simulated.

Table 5.2 - Summary of Instability Strain and Displacement Predictions

	22C	70C	130C	200C
Strain Hardening Exponent (n)	0.1818	0.1654	0.1436	0.0913
Softening Coefficient (s)	0	0	-0.1728	-0.8238
Instability Strain (mm/mm)	0.1818	0.1654	0.12244	0.05006
Instability Displacement (mm)	20.93	18.89	13.68	5.39

Figure 5.13 compares the elevated temperature responses (*i.e.* 200°C and 250°C) from the model to the actual experimental data. As shown, the model accurately predicts the response until greater strains (>0.3) are reached. This deviation is a result of severe non-uniform elongation in the gauge region of the experimental test. This non-uniform elongation is where the material begins to fail and as a result of the model not incorporating any failure criteria, this response is not modeled.

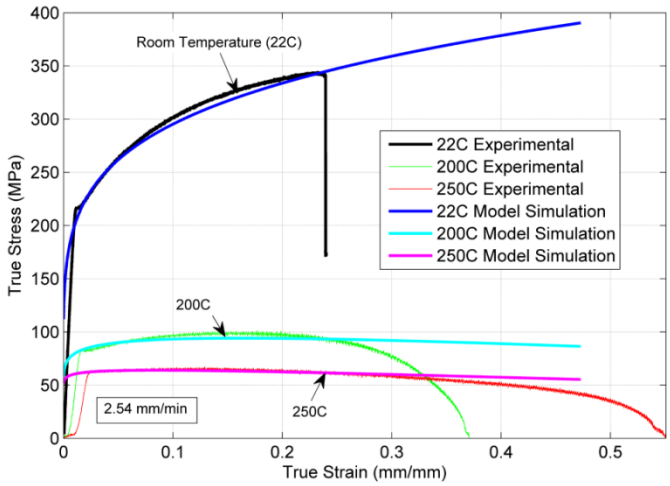

Figure 5.13 - True Stress Plot for a Uniform Temperature Input of 22C, 200C, and 250C (Experiment vs. Simulation)

Thus, this section shows the ability of the model to predict the strain in each element and the required force to deform all of the elements at varying temperatures. Additionally, the simulations using the derived models matched the experimental data.

5.2.2- Non-uniform Temperature Distribution Input

For EAF, *Chapter 4* has shown that large thermal gradients can exist along the length of a tensile sample during forming. As a result, the capability of this deformation/strength model allows for the prediction of local strain in each element and the overall forming force to deform the material.

5.2.2.1 - EAF Diffuse Thermal Model Results (Parameter Set 4)

To simulate EAF forming conditions, the temperature distribution output from the diffuse deformation model in *Chapter 4* is used to be the input to the deformation/strength model in this chapter. The results below are presented for Parameter Set 4 (500A for 1s every 60s) to maintain consistency with the results presented in *Chapter 4*. The thermal input to the model is given in Figure 5.14 where the temperature increases quickly as the current is applied and then cools after the current is discontinued. Each of the temperature rises on the figure represents an applied electrical pulse. Also, since the thermal model assumed a diffuse geometry from experimental measurement, the temperature is greater for the center elements over time as a result of a reduced cross-sectional area in these elements.

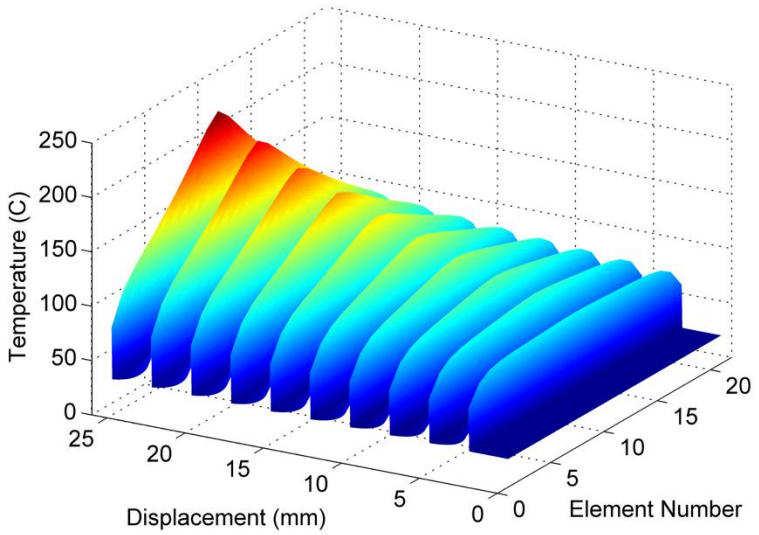

Figure 5.14 - Temperature Distribution (EAF Diffuse Thermal Model Output for PS 4)

The solution to the simulation is presented in Figure 5.15 which displays the incremental strain results.

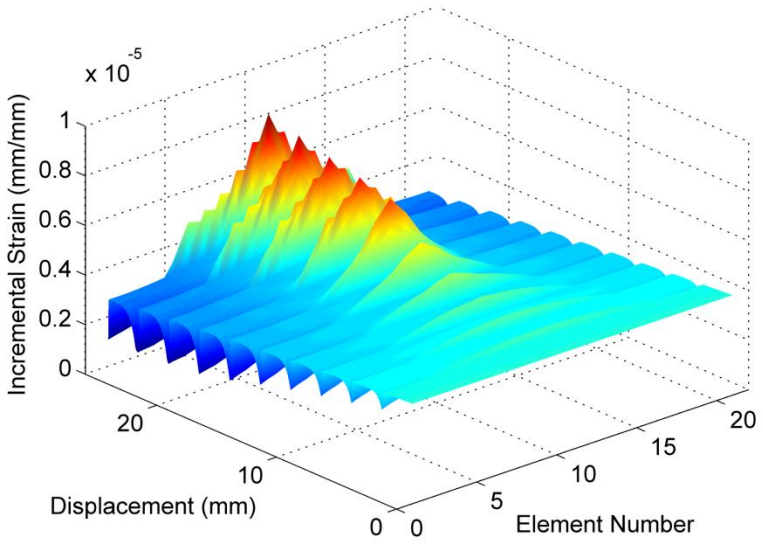

Figure 5.15 - Incremental Strain Results for EAF Diffuse Thermal Model Input for PS 4

As seen, during a temperature rise, the incremental strain can now vary from element to element. This is seen during the current application as the elements with a greater temperature (*i.e.* near center) have a greater incremental strain as compared to the

elements at a lower temperature (*i.e.* near ends). Also, as the material cools after the electrical pulse, it is shown that the incremental strain for each element approach each other as the strength properties become similar.

From the simulation results, the force error is given in Figure 5.16.

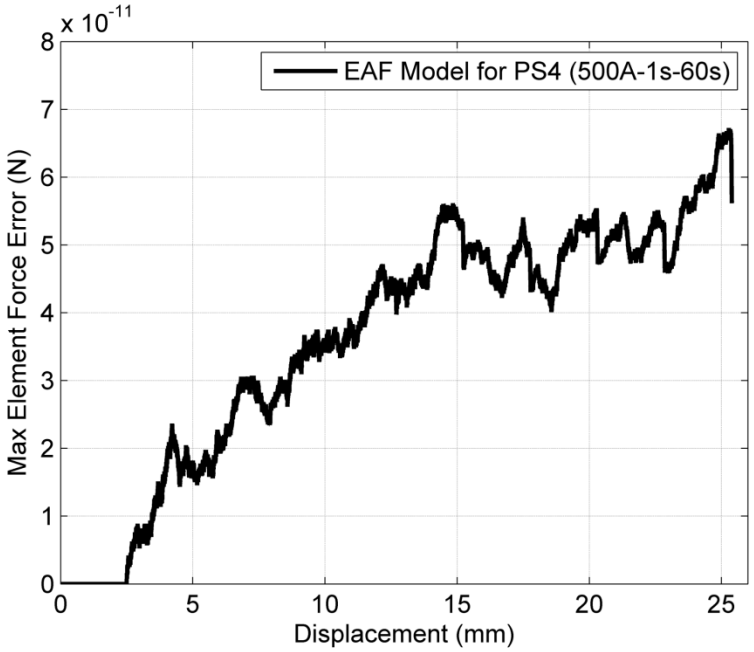

Figure 5.16 - Element Force Error for EAF Diffuse Thermal Model Input for PS 4

The maximum element force error is the difference between the element with the highest derived force and the element with the lowest derived force at every time step. The error is lower than $8x10^{-11}$N. Thus, this concludes that the simulation solution method was effective in solving the model with very little error and Equation (5.1) remained satisfied during the simulation.

Also, the other imposed condition was that the summation of the change in element length at a given time step is equal to the imposed total displacement (Equation (5.24)). The element displacement error is given in Figure 5.17 where the error represents

the difference between the simulated total displacement of all elements and the imposed total displacement. As shown, the error is extremely small (<$4x10^{-12}$mm). Thus, the condition given by Equation (5.24) was upheld during the simulation.

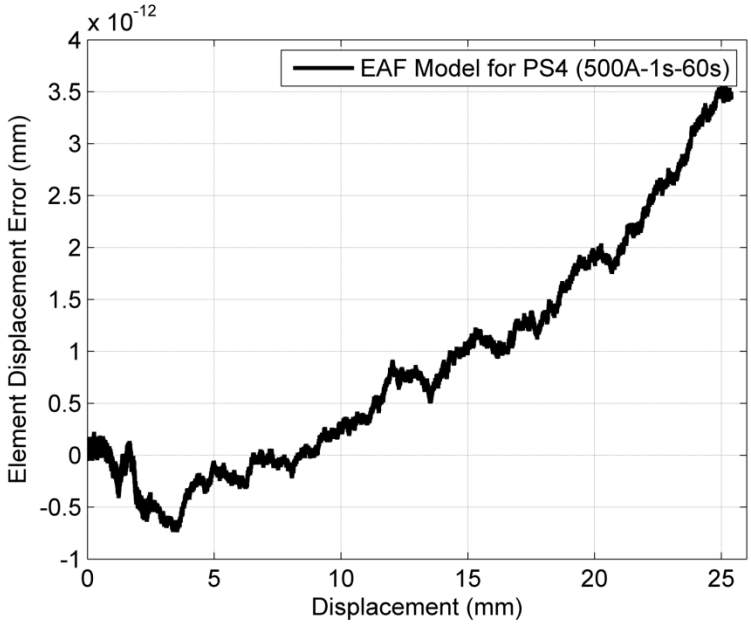

Figure 5.17 - Element Displacement Error for EAF Diffuse Thermal Model Input for PS 4

As a result of varying incremental strain results from the simulation, the accumulative strain over time will not be equal for each element. The accumulative strain for each element is presented in Figure 5.18. As seen, the center elements with greater incremental strain have a larger amount of strain imposed over time (*i.e.* accumulative strain). Also, the simulation solution does not begin to show a significant amount of localized straining until near the end of the simulation. This can be attributed directly to the input temperature distribution where there is a much larger thermal gradient along the length at the end (*i.e.* >15mm of total imposed displacement).

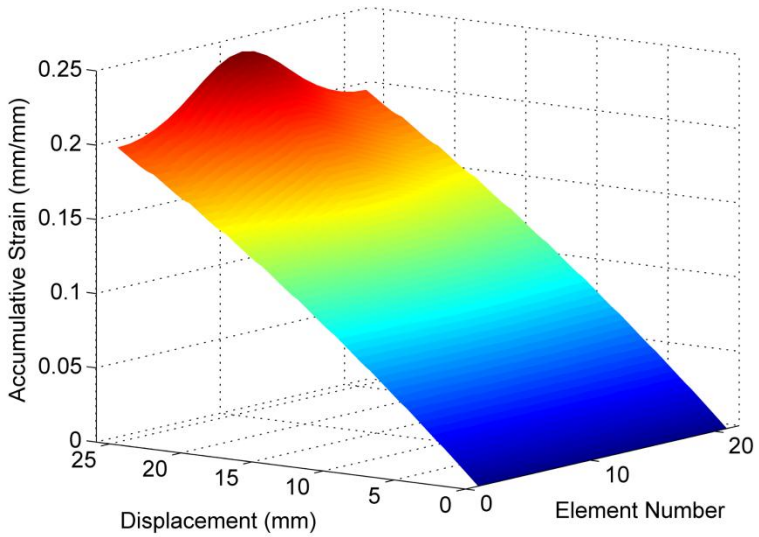

Figure 5.18 - Accumulative Strain Results for EAF Diffuse Thermal Model Input for PS 4

Due to the diffuse accumulative strain, the length and area of each element with vary at a given total input displacement. These results for element length and area are presented in Figure 5.19 and Figure 5.20, respectively. The element length is directly derived from the accumulative strain, thus the overall profile is the same.

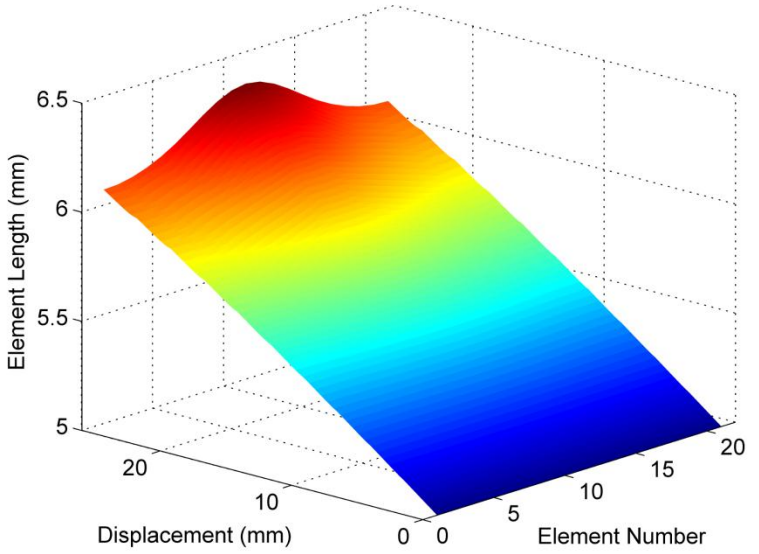

Figure 5.19 - Element Length Results for EAF Diffuse Thermal Model Input for PS 4

For the area, the elements with more strain (*i.e.* center) have a smaller cross-sectional area due to the length of the element being greater.

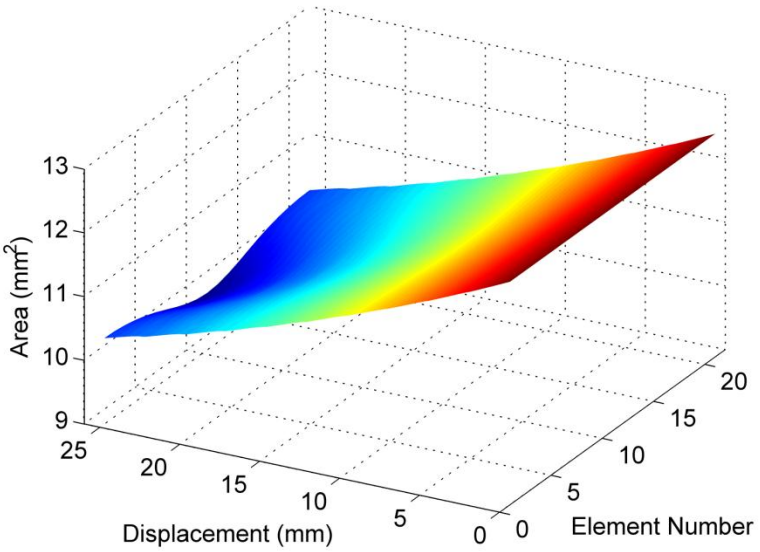

Figure 5.20 - Element Area Results for EAF Diffuse Thermal Model Input for PS 4

The stress response from the simulation is given in Figure 5.21. As seen, during the application of current (*i.e.* temperature rise), the true stress of the material significantly decreases as a result of the material being in a weaker state.

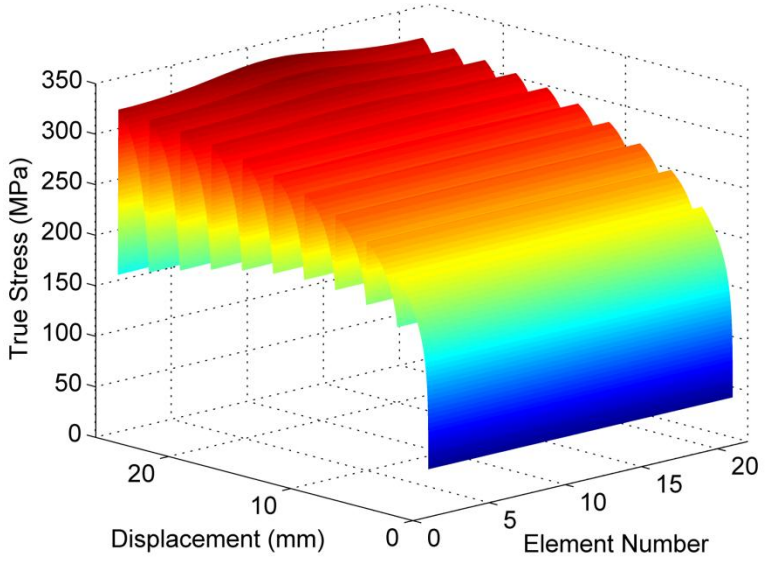

Figure 5.21 - True Stress Results for EAF Diffuse Thermal Model Input for PS 4

The stress response for each element at a given time step may not be equal due to the elements having different cross-sectional areas. This is seen where the elements with a smaller cross-sectional area (*i.e.* center) have a greater stress than the elements with a larger cross-sectional area (*i.e.* ends).

The force required for deformation is given in Figure 5.22 where the force is equal in each element (verified by Figure 5.16). As the current is applied, the force required for deformation is reduced.

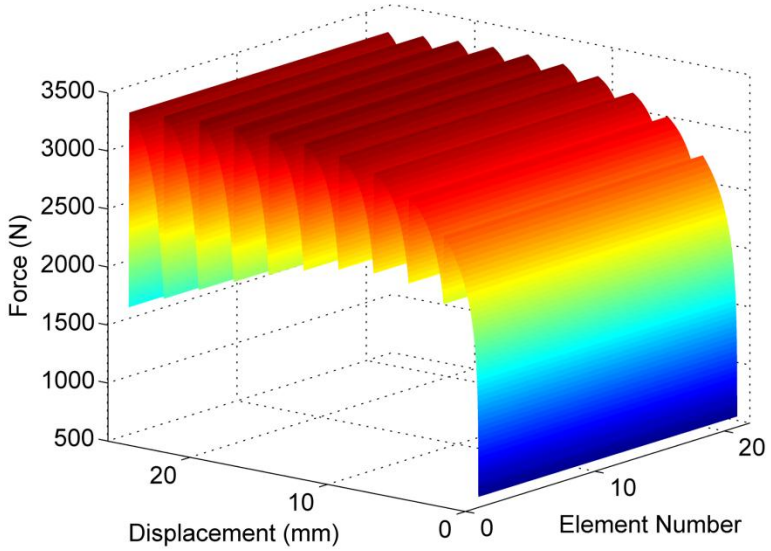

Figure 5.22 - Force Results for EAF Diffuse Thermal Model Input for PS 4

To better visualize the force response, Figure 5.23 displays the forming force versus the imposed overall displacement. The force is reduced during the current application and then increases as a result of the material decreasing in temperature. Also, it is shown that the decrease in force increases with respect to displacement. This is a result of the material being deformed and the cross-sectional area continuously decreasing with imposed displacement. As the cross-sectional area is reduced, this results

in greater temperatures which induce a greater amount of material softening. Hence, the decrease in force increases over time.

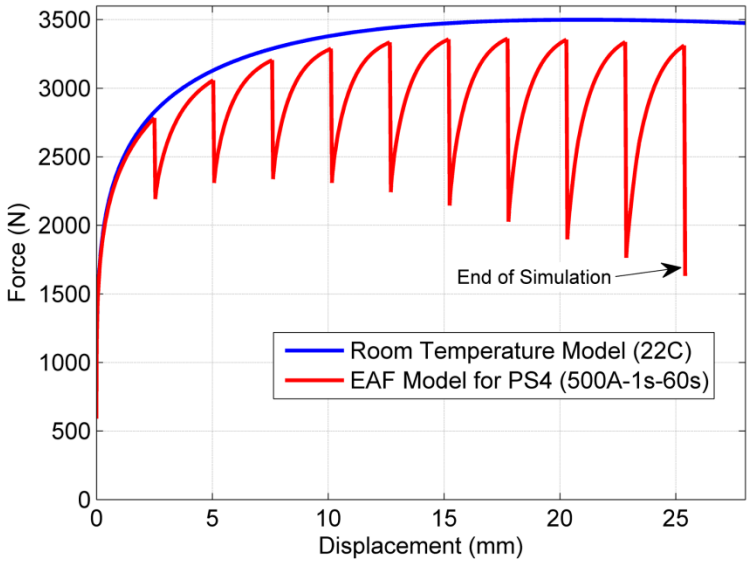

Figure 5.23 - Force Results Plot for EAF Diffuse Thermal Model Input for PS 4

The simulation of the model for Parameter Set 4 versus the experimental data is given in Figure 5.24.

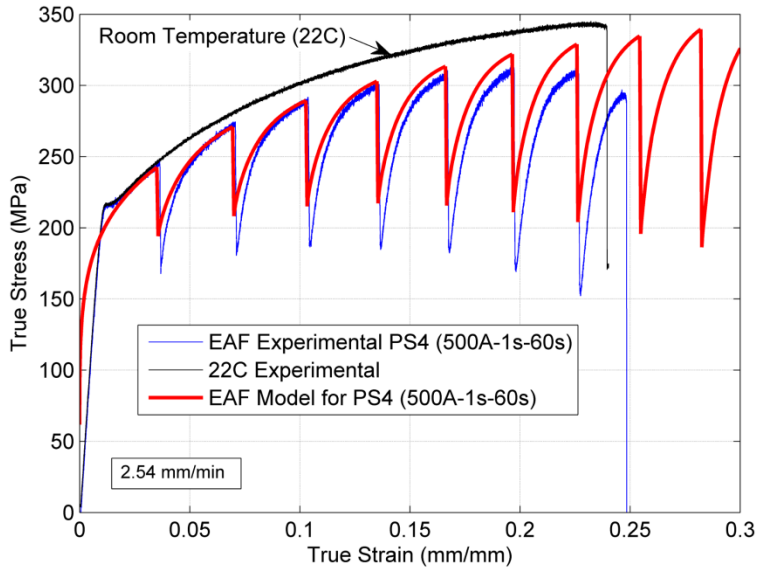

Figure 5.24 - True Stress Plot for EAF Diffuse Thermal Model Input for PS 4 (Experiment vs. Model Simulation)

As seen, the model accurately predicted the true stress/strain response until the first application of electrical current. During the first application of current (*i.e.* first pulse) and the subsequent applications, the model underpredicted the flow stress reduction. The temperature input to the model assumed that the entire quantity of electrical energy went to only Joule heating. Thus, the drop in stress is due to bulk thermal softening and the electroplastic effect. For this model, it does not separate direct electrical effects against bulk heating effects as a result of the diffuse thermal output from *Chapter 4* being used. The division of bulk heating and the electroplastic effect will be accounted for in *Chapter 6*. Additional error may be due to the initial linear strain input used in the diffuse deformation thermal model in *Chapter 4* to produce the thermal response applied here in *Chapter 5*. To physically quantify the difference in flow stress reduction, Figure 5.25 displays the difference in the flow stress reduction between the experimental result and the model result. The difference in the flow stress reduction is nearly constant for each electrical pulse with an average of 27MPa. Thus, it is assumed to be a result of thermal expansion stress which was not considered in this model. The flow stress reduction due to thermal expansion is incorporated in the multiphysics model in *Chapter 6*. As a result of thermal expansion not being incorporated in the model, the simulation predicts a greater material flow stress as compared to the experimental result. The model exceeds the point at which the experimental result failed due to the lack of failure criteria applied to the model simulation.

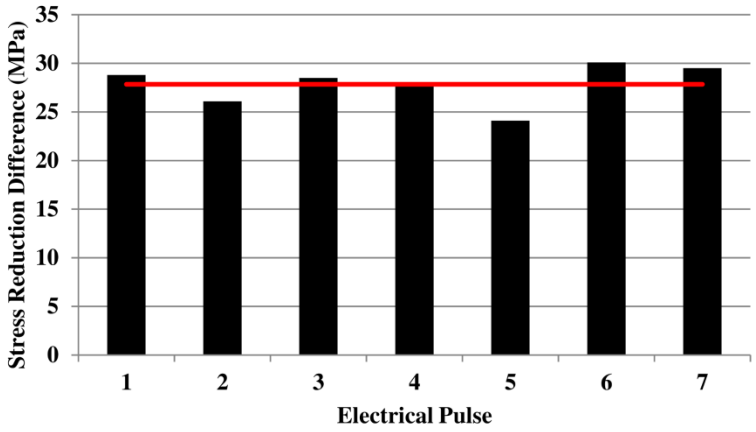

Figure 5.25 - Stress Reduction Difference during Current Application between Experiment and Model Simulation for PS4

5.2.2.2 - Additional EAF Diffuse Thermal Model Results

This section summarized the remainder of the results for Parameter Sets 1-3. Accordingly, the experimental results and the EAF model results are given in Figure 5.26 for Parameter Set 1.

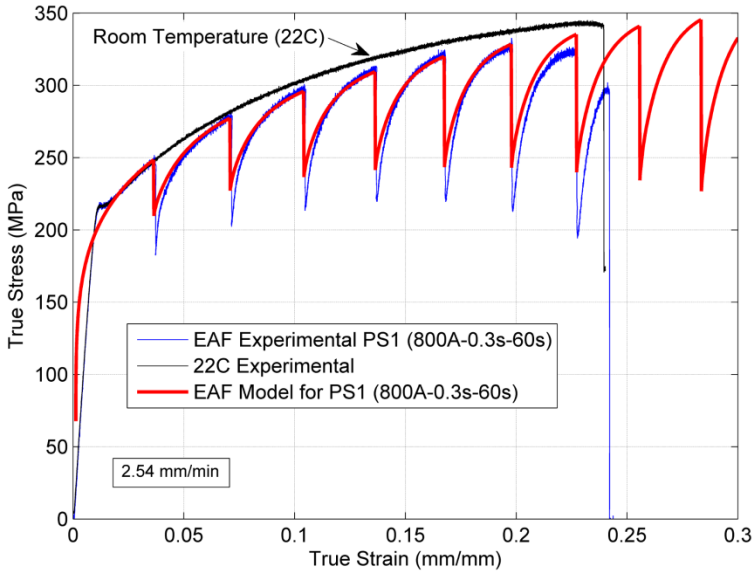

Figure 5.26 - True Stress Plot for EAF Diffuse Thermal Model Input for PS 1 (Experiment vs. Model Simulation)

In comparing the model versus the experimental result, the model is accurate in predicting the general hardening behavior after the applied electrical pulses. However, the

model underpredicts the flow stress reduction during the time the electrical current is applied. This is again assumed to be due to the lack of thermal expansion stress reduction in the material flow stress.

The results for Parameter Set 2 are given in Figure 5.27. Again, the flow stress reduction during the applied current is lower than that for the experimental results. This can be attributed to the model not incorporating the thermal expansion stress. Also, this parameter set has larger flow stress reductions as compared both Parameter Set 1 and 4. This is a result of Parameter Set 2 having the largest amount of electrical energy per unit resistance applied to the sheet metal.

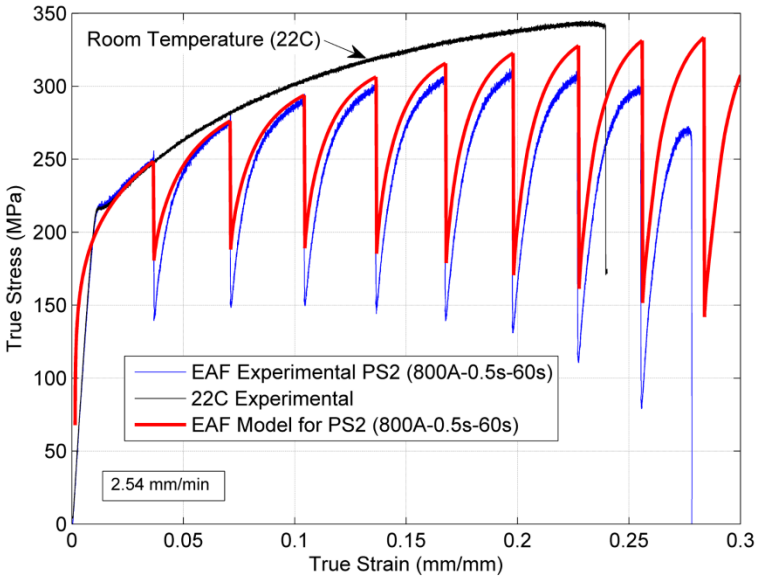

Figure 5.27 - True Stress Plot for EAF Diffuse Thermal Model Input for PS 2 (Experiment vs. Model Simulation)

Parameter Set 3 is presented in Figure 5.28 where the model predicts the experimental data well during the hardening portion of the curve, however, the model underpredicts the flow stress reduction while the current is applied. This can again be attributed to the thermal expansion stress not included in the model.

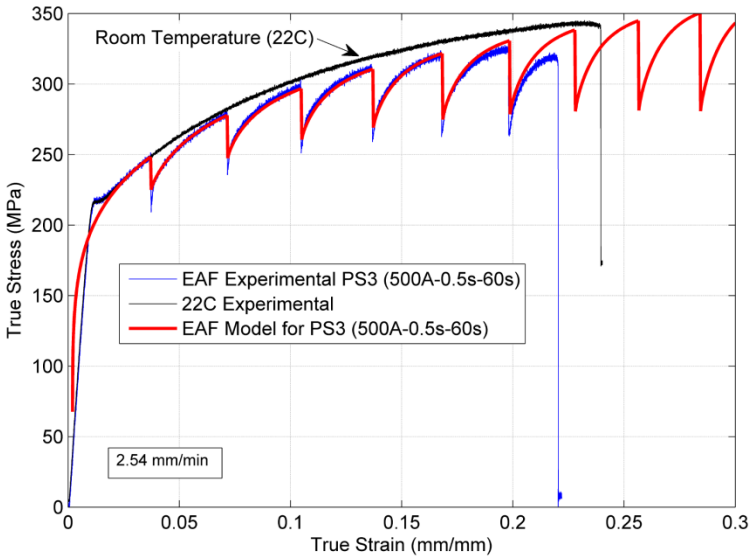

Figure 5.28 - True Stress Plot for EAF Diffuse Thermal Model Input for PS 3 (Experiment vs. Model Simulation)

5.3 - References for Chapter 5

[5.1] S.C. Chapra and R.P. Canale, *Numerical Methods for Engineers*, 5th ed. Boston: McGraw Hill, 2006.

CHAPTER 6 - MULTIPHYSICS EAF MODEL OF SHEET METALS

In this chapter, the local material strain, flow stress, and thermal profile are predicted for EAF of sheet metal in uniaxial tension. This is accomplished by combining the thermal model introduced in *Chapter 4* with the deformation/strength model of *Chapter 5*. Additionally, thermal expansion effects are incorporated as they also introduce stress to the material. The division of electrical energy applied to the workpiece during EAF is also divided between bulk thermal softening and direct electrical effects in this chapter.

6.1 - Model Overview and Solution Scheme

The multiphysics EAF model incorporates bulk thermal softening effects, direct electrical effects (i.e. electroplasticity), and thermal expansion effects to predict the local material strain, flow stress, and thermal response of sheet metal during EAF. The multiphysics model incorporates the models introduced and derived in *Chapters 4* and *5* that predict the temperature and deformation/strength response, respectively. The model solution scheme is given in Figure 6.1. First, the initial conditions are set for the sheet metal which include the geometric and strength properties. Again, the sheet metal in uniaxial tension is divided into elements along the length such that the geometry and strength of the elements can vary spatially and with time. The simulation runs by determining if the desired total displacement to the sheet is applied. When not fully deformed to the desired amount, a displacement of Δd is imposed on the sheet metal. Using the relationships in *Chapter 5* (Equation (5.1) and (5.24)), the incremental element strains are calculated. Using the incremental strains, the element shapes are updated

corresponding to the amount of imposed strain in each element. After, the element temperatures are calculated by using Equations (4.7) - (4.9) and Equation (4.12). The time step is compared with the electrical current application sequence during this step to determine if there is local heat generation due to Joule heating. After the temperatures are determined, the element temperatures are stored and each element has its temperature updated for the next iteration. As the temperatures are updated, new strength and thermal properties are calculated for each element. Following, the process repeats until the desired total displacement of the sheet is reached.

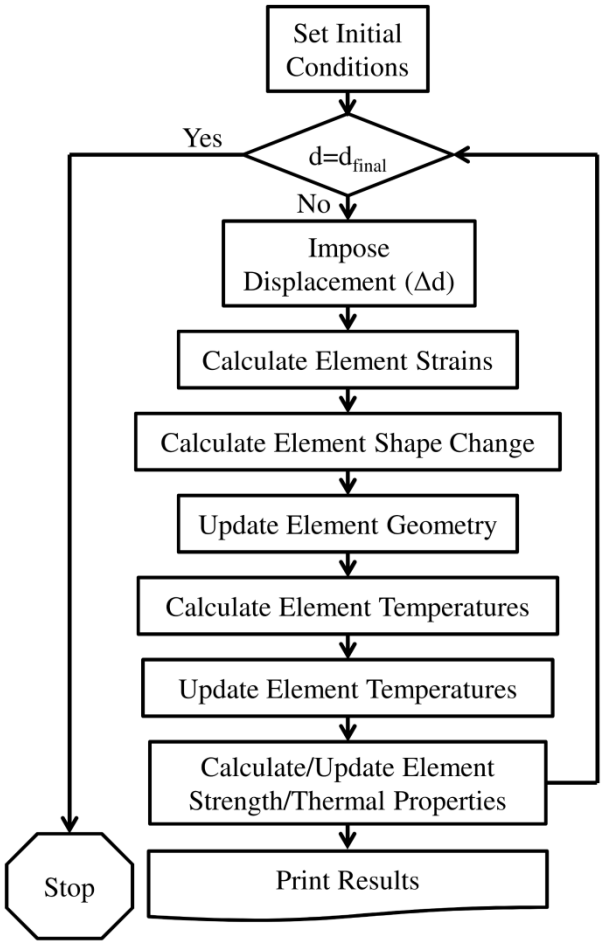

Figure 6.1 - Multiphysics EAF Model Solution Scheme

6.2 - Thermal Expansion Stress

As there is a temperature distribution during EAF both along the specimen and as a function of time, the elevated temperatures can impact the observed force due to thermal expansion. As a result, this effect is incorporated into the model to determine its corresponding effects.

For an element *m* at time *i*, the coefficient of thermal expansion can be given by:

$$CTE = A\left(T_{mean}^{B}\right)[=]\frac{1}{K} \tag{6.1}$$

where,

$$T_{mean} = \frac{1}{2}\left(T_m^{i-1} + T_m^i\right)[=]K \tag{6.2}$$

and, such that for Mg AZ31B [6.1],

$$\begin{aligned} A &= 8.7218x10^{6} \\ B &= 0.17979 \end{aligned} \tag{6.3}$$

The modulus of elasticity can be given by:

$$E = xT_{mean}^3 + yT_{mean}^2 + zT_{mean} + w[=]GPa \tag{6.4}$$

And, such that for Mg AZ31B [6.1],

$$\begin{aligned} x &= 2x10^{-6} \\ y &= -0.0022 \\ z &= 0.8791 \\ w &= -68.205 \end{aligned} \tag{6.5}$$

Thus, assuming a fixed-fixed end with no buckling, the thermal stress developed in the element is given by:

$$\Delta\sigma_{TE} = 1000\left(E\right)\left(CTE\right)\left(T_m^i - T_m^{i-1}\right)[=]MPa \tag{6.6}$$

This thermal stress is applied to the element during each time step such that the effects of thermal expansion are incorporated.

6.3 - Model Results

The model simulation results are presented in this section for Parameter Set 4 using the derived EAF multiphysics model. The incremental strain (left) and accumulative (right) are given in Figure 6.2.

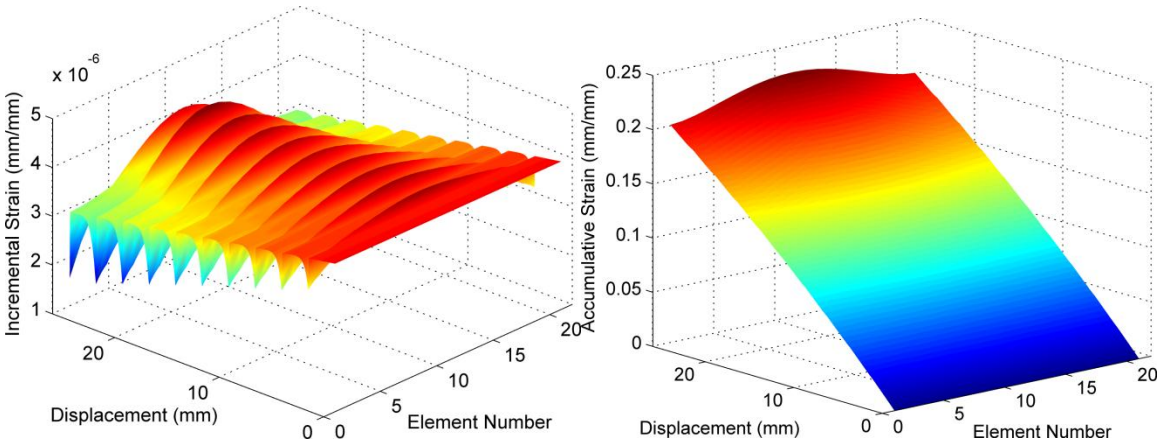

Figure 6.2 - Incremental Strain (left) and Accumulative Strain (right) Results from EAF Multiphysics Model for PS 4

As shown, the incremental strains are greater for elements that are at higher temperatures as compared to the elements with lower temperatures. The accumulative strain increases with time and the elements in the center have a greater overall strain due to the elements having greater temperatures.

From the solution to the simulation, the associated errors for force equilibrium and displacement continuity are given in Figure 6.3, respectively. Again, the small values from these results verify that the conditions of force equilibrium and displacement continuity are upheld during the simulation.

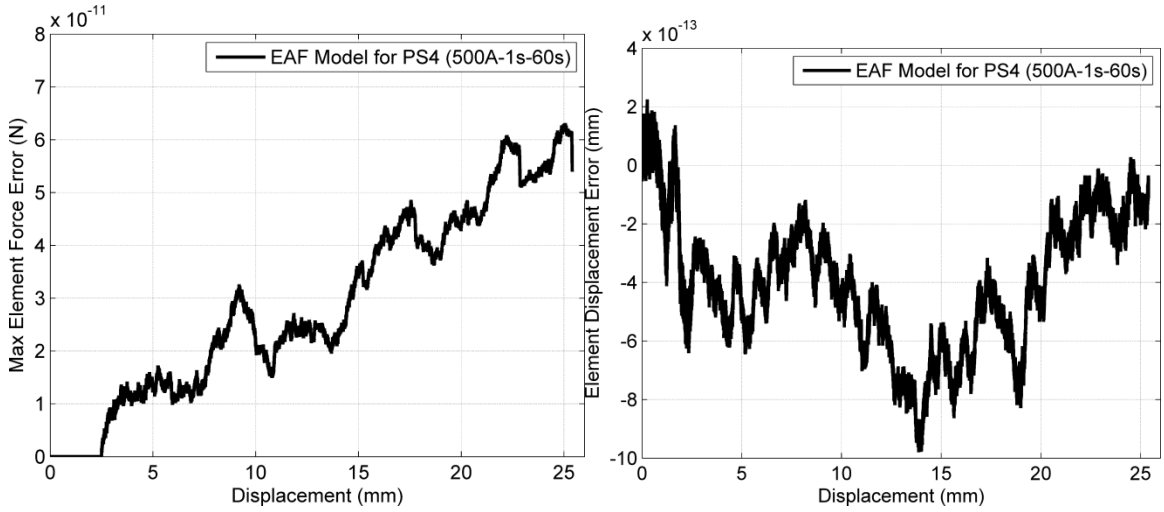

Figure 6.3 - Element Force (left) and Displacement (displacement) Errors from EAF Multiphysics Model for PS 4

From the accumulative strains, the element length and element areas are calculated. These results are presented in Figure 6.4, where increased element length results in a smaller cross-sectional area.

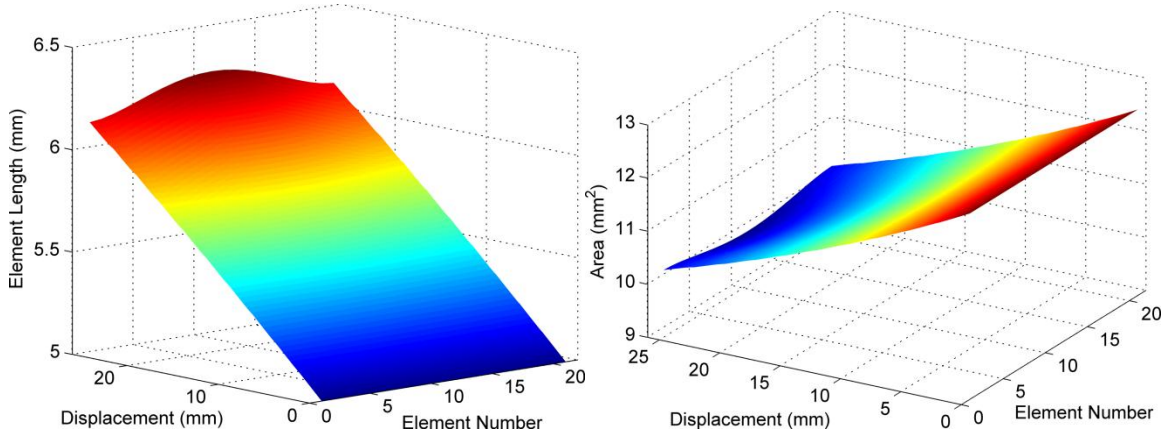

Figure 6.4 - Element Length (left) and Element Area (right) Results from EAF Multiphysics Model for PS 4

As a result of the EAF multiphysics model incorporating a thermal aspect, the temperature distribution is calculated at each time step. The temperature distribution is

given in on the left of Figure 6.5, and the maximum temperature with respect to time from the model and experimental results are displayed on the right of Figure 6.5.

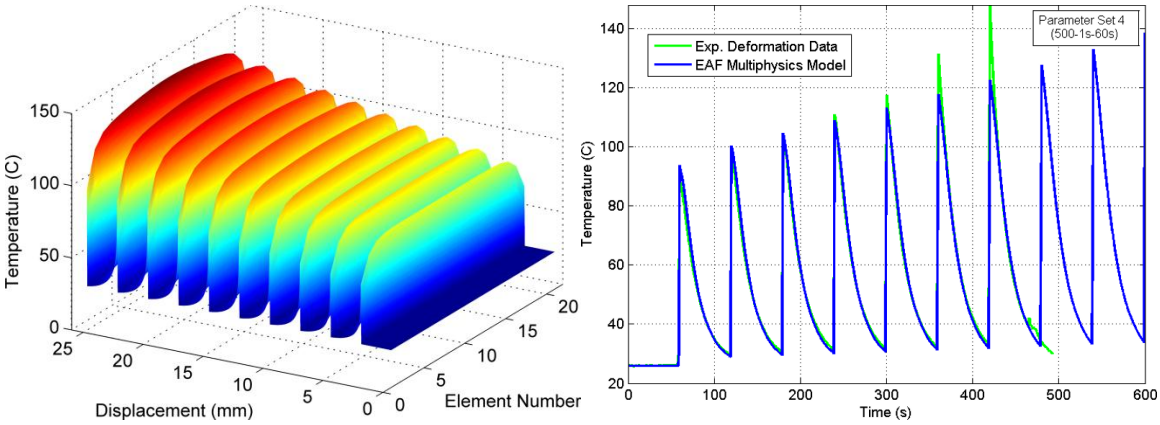

Figure 6.5 - Temperature Distribution (left) and Maximum Temperature versus Experimental Results (right) for PS 4

As seen, the thermal response increases during the application of the electrical current and decreases once the current is discontinued. Also, the temperature increases over time and the element with the most strain (*i.e.* center element) is at the highest temperature. The maximum temperature response from the model shows good agreement with the experimental result, however, the last three pulses of electrical current produce a greater temperature rise for the experimental result. This is a result of the actual experimental specimen probably having a larger amount of localized necking at the center of the sample as compared to the prediction of the model. The maximum thermal error is on the last pulse and is approximately 20°C.

The force to deform the sample is also provided from the EAF multiphysics model output. The force is given in Figure 6.6 and it is seen that the current application is predicted by a decrease in the material force. The increase in force increases as a function of displacement due to the cross-sectional area of the sample decreasing.

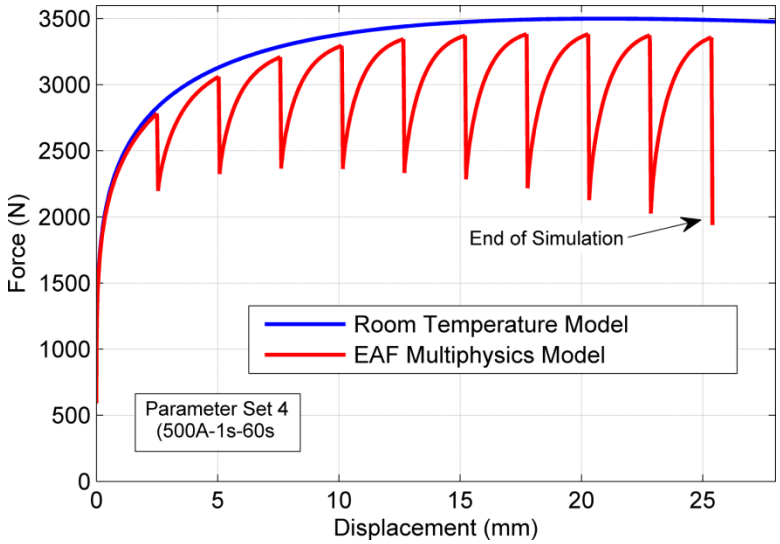

Figure 6.6 - Force Results Plot from EAF Multiphysics Model for PS 4

The most valuable output from the model is the accurate prediction of the material flow stress. The material flow stress output with no thermal expansion effects is given by the left plot in Figure 6.7.

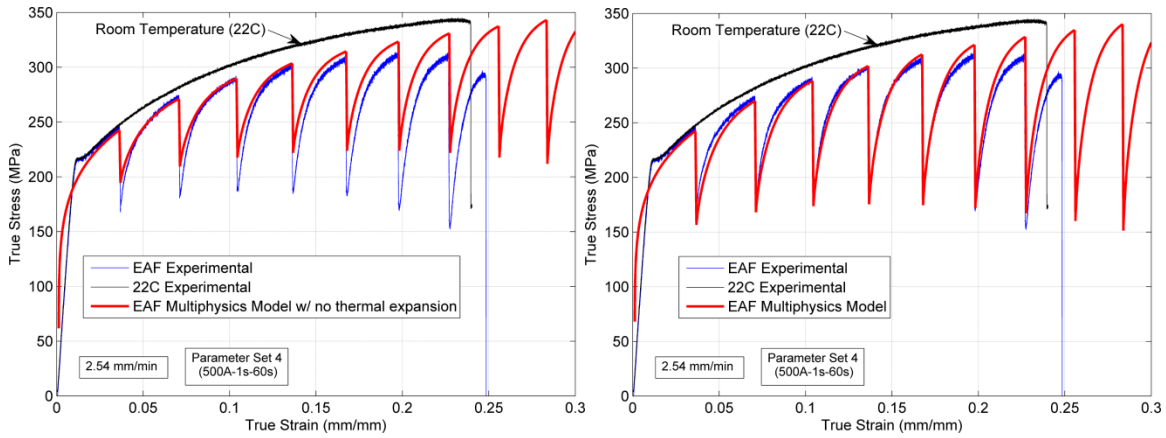

Figure 6.7 - True Stress Plot for the EAF Multiphysics Model for PS4 where Left does not Include Thermal Expansion and Right Includes Thermal Expansion Effects

As shown, the model displays similar results to the output from *Chapter 5* where the full reduction in stress during current application is not modeled. However, including the stress reduction from thermal expansion (right in Figure 6.7) allows for a greater prediction of the material flow stress when comparing the model and simulation result.

Thus, it is shown that a good portion of the stress reduction is due to thermal expansion effects. This is studies in more detail in the next section.

6.4 - Division of Thermal Expansion, Thermal Softening, and Direct Electrical Effects

One of the main outcomes from this work was to understand what the actual mechanisms are that reduce the material strength when applying an electric current field. Thus, what portion of the electrical energy reduces the material flow stress from thermal expansion, bulk thermal softening, and the electroplastic effect. The thermal expansion stress effect could be directly calculated (Equation (6.6)) and compared to the overall predicted reduction in material flow stress. This results in a percentage or contribution to the overall stress reduction. It was found that the thermal expansion stress accounts for approximately 30% of the total reduction. The main question is what portion is from direct electrical effects (*i.e.* electroplastic effect) and from bulk thermal softening. To answer this question, the thermal response was analyzed for each flow stress reduction due to the applied current. Using the thermal response and the corresponding material strain at that time, the flow stress reduction due to purely thermal effects was calculated. The calculation was performed using a constitutive equation that predicts the material stress response at varying temperatures for this material. This equation is developed and detailed in *Section 7.4*. Once the stress reduction due purely to bulk thermal heating was determined; it was compared to the result in Figure 6.7 (left). The percentage of the total reduction was found to be approximately 60%. Thus, including thermal expansion, this leaves the remaining 10% to direct electrical effects or electroplasticity. These

calculations are summarized in Figure 6.7. As seen, there is some variation, but the overall trend attributes the most to bulk thermal softening, and then thermal expansion. The smallest contribution is due to direct electrical effects. These direct electrical effects are described in detail in *Chapter 10*. The larger contribution from the electroplastic effect for pulse 7 is not presently known.

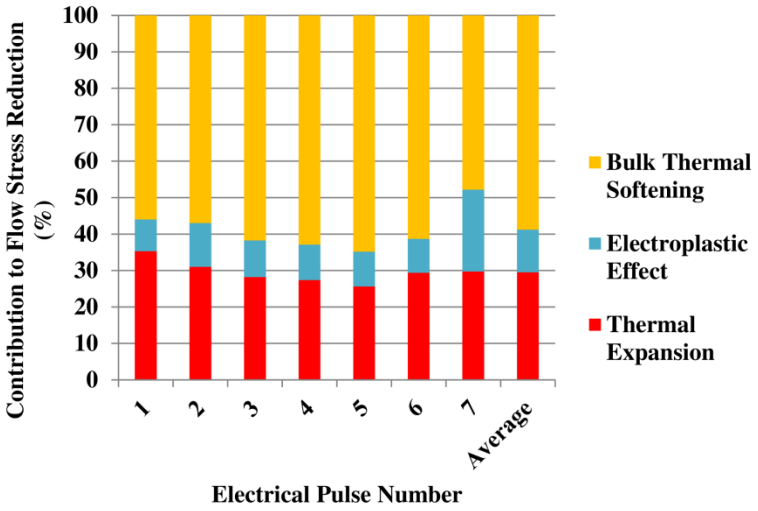

Figure 6.8 - Division of Thermal Expansion, Bulk Thermal Softening, and the Electroplastic Effect for EAF

6.5- References for Chapter 6

[6.1] International Magnesium Association, McLean, VA, and MIL-HDBK-5H, 1 Dec 1998, p4-11.

CHAPTER 7 - EXPERIMENTAL MECHANICAL INVESTIGATION OF SHEET METALS DURING EAF/ELEVATED TEMPERATURE FORMING

In this chapter, the deformation behavior of magnesium sheet is analyzed through experimental testing using EAF and room/elevated temperature testing. The results presented in this chapter are used in *Chapters 4*, *5*, and *6* for model construction and to act as independent data sets for model validation. Additionally, select samples tested in this chapter are subsequently examined in *Chapter 8* with respect to microstructure to determine the influence of an applied electrical current. Last, the tests performed in this chapter are used to study the influence of an applied electrical current on the mechanical properties and how these mechanical strength changes relate to the theory of electroplasticity.

7.1 - Testing Setup

There are two types of experimental setups utilized in this work to examine the mechanical behavior of the magnesium sheet metal. These include: room temperature/EAF testing and elevated temperature testing. The setup and systems used for the tests are described below.

7.1.1 - Room Temperature and EAF Testing

The testing setup for the room temperature and EAF tests are shown in Figure 7.1. For the tests, a platen velocity of 2.54mm/min or 25.4mm/min was used depending on the desired rate. The faster rate of 25.4mm/min was only used to examine the strain rate sensitivity of the material for both room temperature and EAF tests. An Instron hydraulic testing machine with specialized tensile grips to isolate the electricity from the testing

equipment was used to deform the tensile specimens. To measure the thermal response during the test, a FLIR A40M thermal camera (maximum temperature: 550°C, temperature resolution: 0.1°C, and frame rate: 12.5/s) was used (not shown in Figure 7.1). The power supply used in the testing can provide 0-4kA with varying wave shapes and duty cycles. For complete information regarding power supply control and a waveform study of the output refer to *Appendix D*. The test samples for the room temperature and EAF tests were prepared according to ASTM B557M [7.1] and more details are provided in *Appendix B*. To ensure repeatability and minimize variability in the test results, duplicate tests were performed and the testing order was randomized.

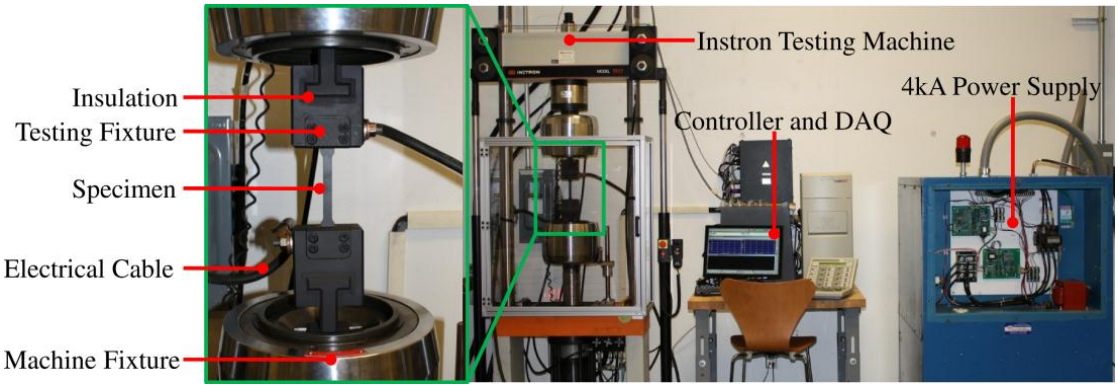

Figure 7.1 - Room Temperature and EAF Testing Setup

7.1.2 - Elevated Temperature Testing

For the elevated temperature tests, an environmental chamber was used to maintain isothermal conditions for the varying temperatures tested. The testing speed was consistent with the room temperature and EAF tests at the slower platen speed (2.54mm/min). For the testing, sufficient soak time was allowed such that the specimen reached the desired temperature. The setup is shown in Figure 7.2 and details on

specimen geometry are provided in *Appendix B*. The temperatures tested were 150°C, 200°C, 250°C, and 300°C and duplicate tests were performed to ensure consistent results.

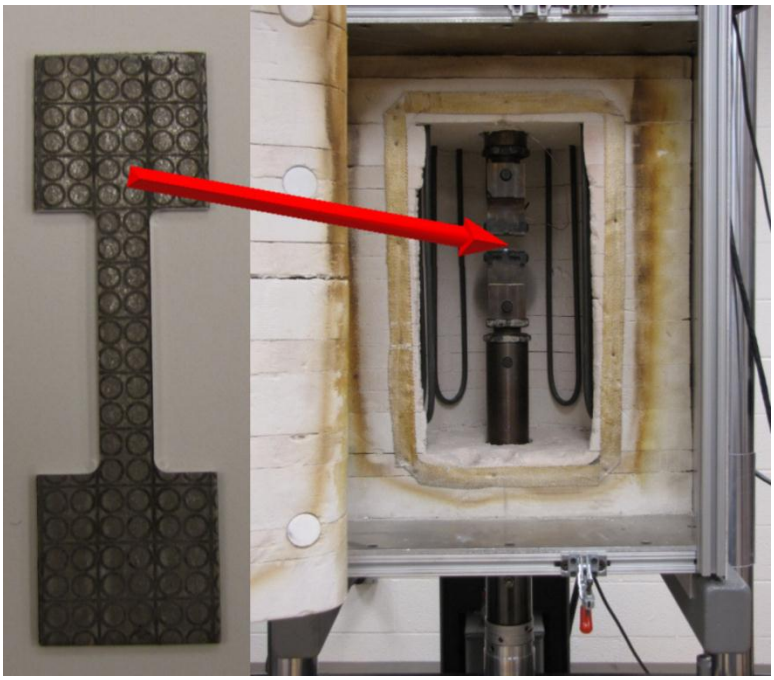

Figure 7.2 - Elevated Temperature Testing Setup

7.2- Mechanical Testing

The following sections explore the mechanical properties of the magnesium sheet for room temperature, elevated temperatures, and EAF.

7.2.1 - Room Temperature Mechanical Properties

The tensile stress-strain response of this magnesium material is shown in Figure 7.3. The result is an average of several tests such that a representative average flow stress curve is presented. The observed yield strength is approximately 220MPa and this is consistent with published values for this alloy and grain size [7.2]. It should be noted that the elastic region was not corrected for machine/fixture compliance and this is not critical in this research as the analysis is only comparative. Although the result is an average of

several tests (5 tests), it should be noted that some tests displayed variability in the material yield strength and hardening behavior (one standard deviation is shown in Figure 7.4 to quantify). This difference is likely a result of the material texture varying within the sheet or the test samples being produced from two sheets (pre-sheared samples were provided by BMW). The texture of the material is important in that it influences the strength and deformation behavior as a result of grains having preferred orientations instead of a random orientation. The concept of a textured material becomes more important in HCP crystal structures as a result of the limited number of slip systems the dislocations have to travel on and the alignment of these slip systems at the grain boundaries (*i.e.* having preferred and not random grain boundary angles). Thus, with certain textures the ease of dislocation motion can be enhanced or reduced across grain boundaries.

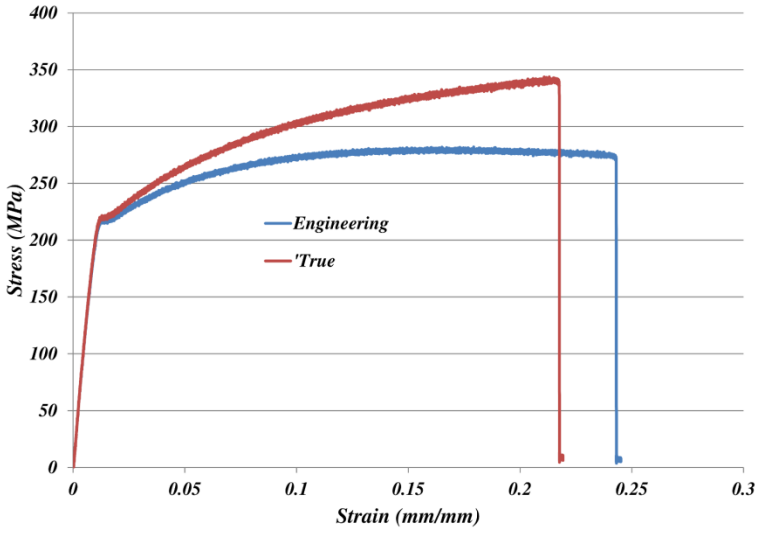

Figure 7.3 - Mechanical Response under Room Temperature Conditions

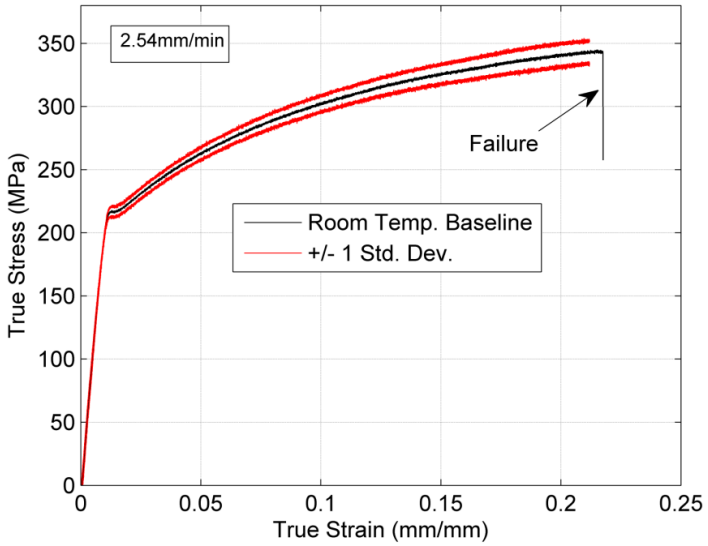

Figure 7.4 - Variation in Mechanical Response under Room Temperature Conditions

Additionally, the mechanical responses for the two platen velocities are compared in Figure 7.5. It is noted that the yield strength is slightly greater for the faster platen velocity and it also had an average reduced total elongation before material failure. Overall, it can be concluded that this material has a low strain rate sensitivity given the velocities tested and room temperature forming conditions.

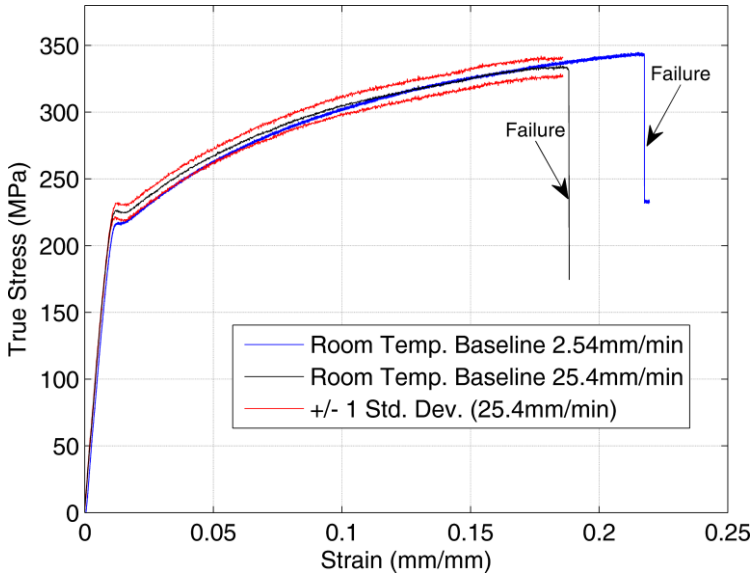

Figure 7.5 – Variation in Mechanical Response under Room Temperature Conditions at a Faster Platen Velocity (25.4mm/min)

7.2.2 - Elevated Temperature Mechanical Properties

For the elevated temperature tests, the flow curves are presented in Figure 7.6. As observed, with an increasing temperature, the yield strength of the material is reduced and in general more elongation before fracture is achievable. The observed lower yield strength is a result of the added thermal energy to the material lattice allowing for material slip or plastic deformation to occur at a lower stress level. The enhanced ductility is due to the added thermal energy in the material lattice which helps to facilitate dislocation motion and lower stress concentrations within the lattice which eventually lead to material crack initiation. A model to predict the observed flow stress behavior for varying temperatures was derived from this data and is presented in *Section 7.4*. Also, it is seen for all the elevated temperature tests that there is a large region of non-uniform deformation (*i.e.* necking). This non-uniform deformation can be visualized by the amount of material strain beyond the point where the maximum stress is reached for each respective curve. This is the opposite of what is observed with the room temperature test (22°C) where the stress reaches a maximum value and failure occurs very shortly after that point (*i.e.* very localized necking at fracture location).

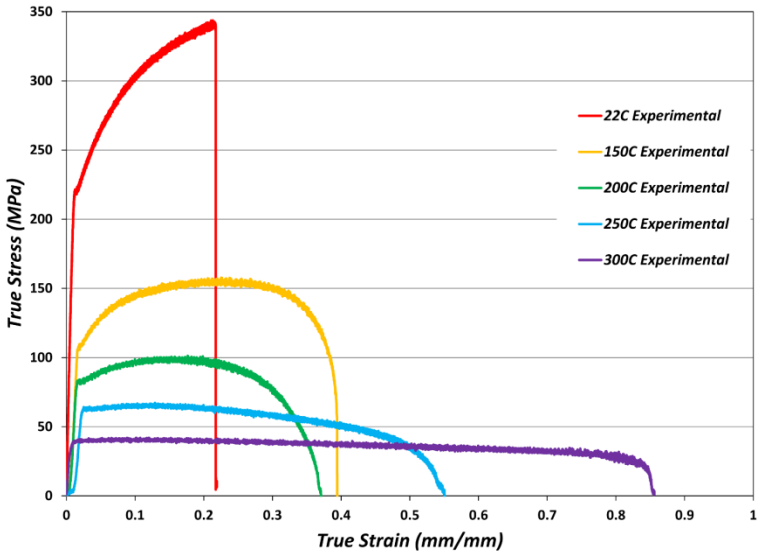

Figure 7.6 - Mechanical Response under Elevated Temperature Conditions

A photograph of the deformed specimens at fracture for varying temperatures is shown in Figure 7.7 to show the large amount of necking present. The large neck region is a result of the specimen geometry and the material being in a softened state. As a result, the majority of the deformation is non-uniform and this results in a large diffuse neck. The quantification of the neck region was performed by circle grid analysis (CGA) in *Section 7.3* and all the results are presented in *Appendix A*.

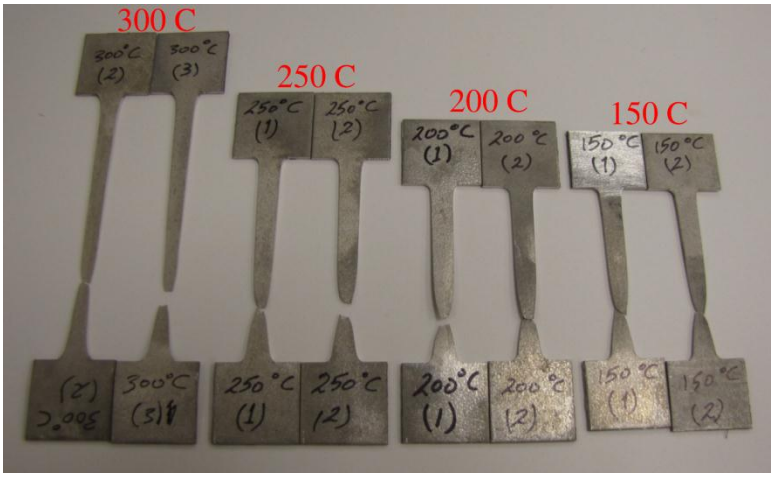

Figure 7.7 - Fractured Specimens for Elevated Temperature Conditions

7.2.3 - EAF Mechanical Properties

The subsequent sections display experimental results for various EAF tests that allow for a deeper understanding of the deformation mechanisms present during EAF and the electroplastic theory.

7.2.3.1 - EAF with Square Wave Current Application

For the testing performed under EAF conditions using a square wave current application, several parameter sets were tested with several replications to examine the influence of an applied electrical current. The present design space explored is listed in Table 7.1 and these do not necessarily represent optimal parameters for improved formability with this material. For all of the EAF tests in this section, the electrical current was applied using a square wave shape with a given duration and period (as listed in Table 7.1). Also, the magnitude of the applied square wave corresponds to the current magnitude listed in the table. A schematic of the application scheme is given in Figure 7.8. For Parameter Sets 1-8, EAF deformation tests were performed and the average result is presented. Also, for Parameter Sets 1-4, stationary electrical tests with the same square wave conditions were performed and the samples were then tested under room temperature conditions to failure. The results of these tests will be compared to the deformation behavior of the as-received material to see if the stationary electrical testing had any influence on the mechanical response. It should be noted that Parameter Set 5 was manually varied within the bounds listed in the table such that an approximate steady forming force was achieved. Also, for the EAF test figures presented in this chapter it

should be noted that the observed stress discontinuities are representative of the period the electrical current was applied.

Table 7.1 - EAF Square Wave Testing Conditions

Parameter Set	Current Magnitude	Pulse Duration	Pulse Period	Duty Cycle	Wave Shape	Platen Velocity
1	800A	0.3s	60s	0.50%	Square	2.54mm/min
2	800A	0.5s	60s	0.83%	Square	2.54mm/min
3	500A	0.5s	60s	0.83%	Square	2.54mm/min
4	500A	1.0s	60s	1.67%	Square	2.54mm/min
5	Varying 500-1000A	0.1s	Varying 4-6s	Varying	Square	2.54mm/min
6	500A	0.5s	30s	1.67%	Square	2.54mm/min
7	1000A	0.5s	30s	1.67%	Square	2.54mm/min
8	800A	0.5s	30s	1.67%	Square	2.54mm/min

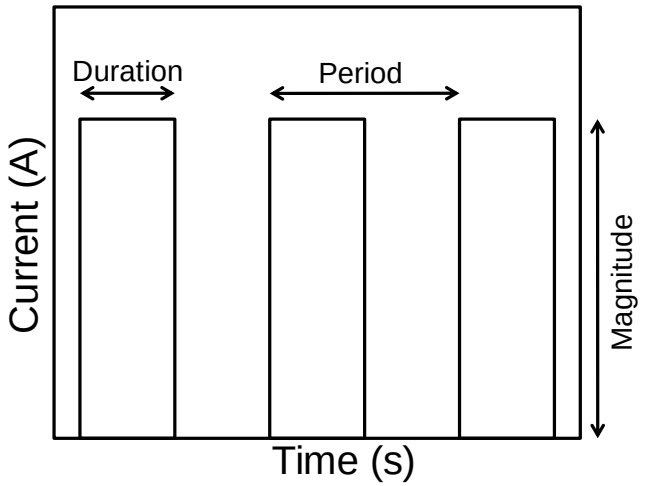

Figure 7.8 - EAF Square Wave Electrical Current Application Scheme

For Parameter Sets 1-4, these testing conditions were for model construction and to act as independent data sets for model validation in *Chapters 4, 5,* and *6*. As a result, these tests were performed with varying electrical current magnitudes and pulse durations. The results for Parameter Sets 1-4 are displayed in Figure 7.9 to Figure 7.12. As shown in all of the figures, the applied electrical current decreased the material's flows stress as a result of bulk heating, thermal expansion, and electroplasticity as

explained in *Chapter 3*. After the application of the electrical current was removed the temperature decreased and the material strengthened until the next application of electrical current. Also, the overall fracture strain was not significantly affected with these applied electrical conditions as compared to the results presented in Figure 2.4.

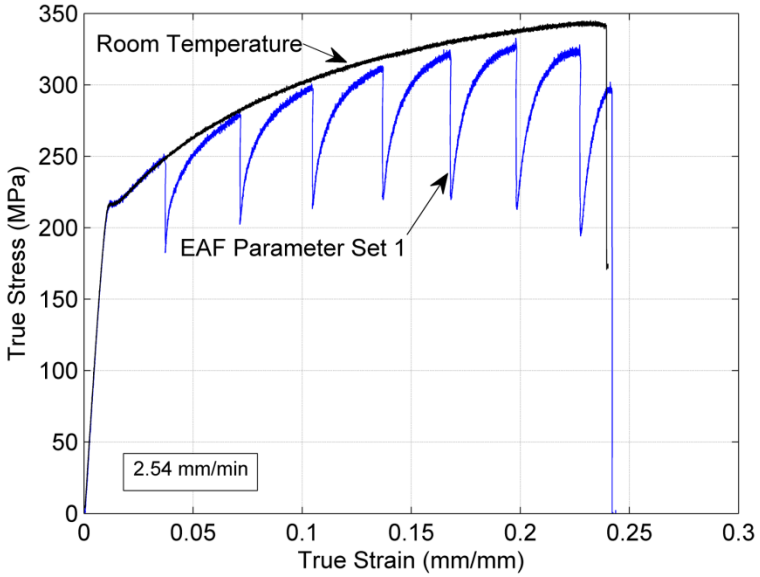

Figure 7.9 - Experimental EAF Flow Stress Results (Parameter Set 1)

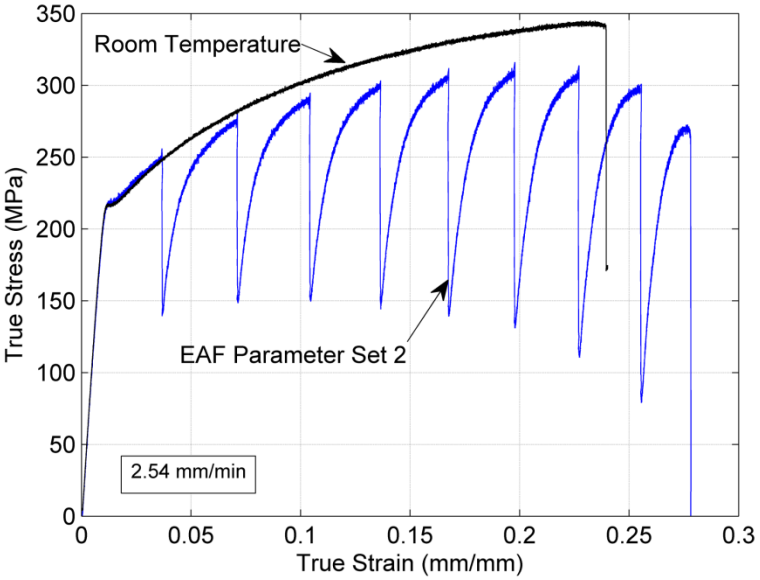

Figure 7.10 - Experimental EAF Flow Stress Results (Parameter Set 2)

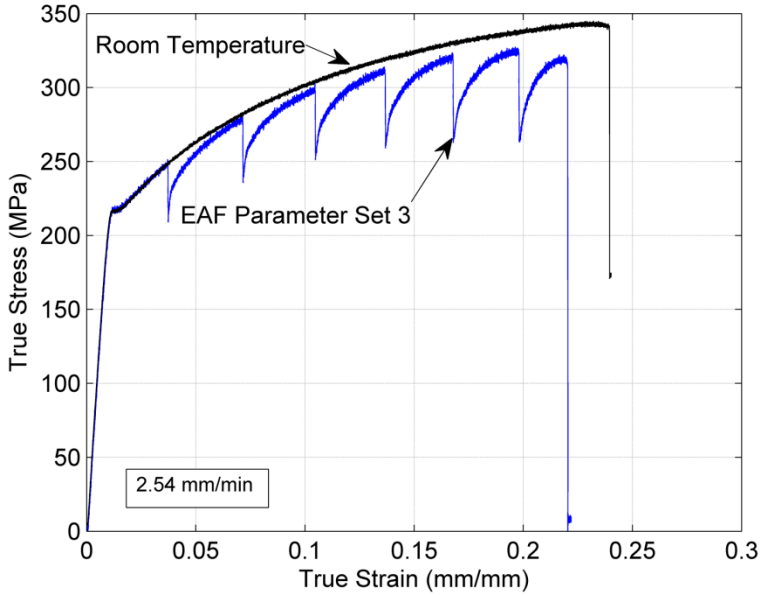

Figure 7.11 - Experimental EAF Flow Stress Results (Parameter Set 3)

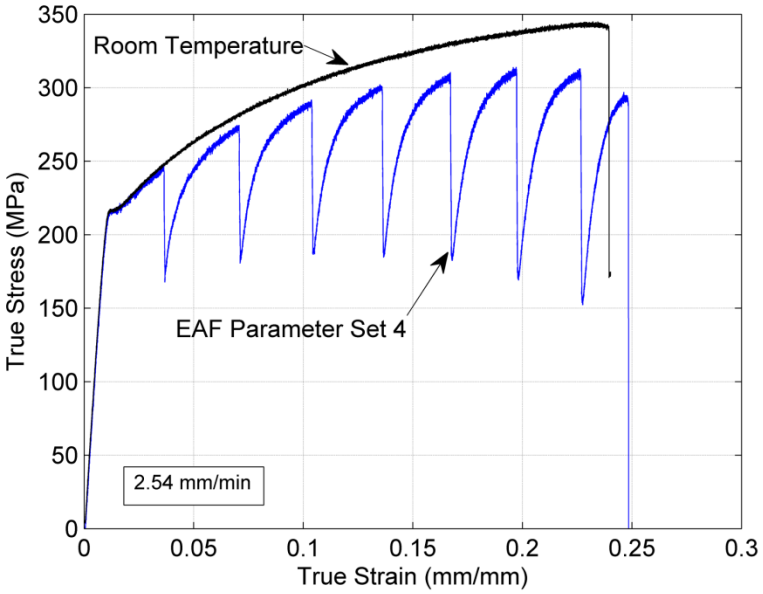

Figure 7.12 - Experimental EAF Flow Stress Results (Parameter Set 4)

To summarize Parameter Sets 1-4, Figure 7.13 shows the flow stress reduction as a function of strain and input electrical energy per unit resistance. As shown, higher electrical energy input resulted in larger stress reductions and the constructed surface of these testing conditions is almost planar. Also, it should be noted that with increasing

electrical energy input, this directly relates to higher peak temperatures throughout the material. The maximum temperature reached spatially and over time for Parameter Set 2, Parameter Set 4, Parameter Set 1, and Parameter Set 3 are 224°C, 148°C, 108°C, and 77°C, respectively. These measurements of temperature were recorded using the procedure in *Section 4.2*.

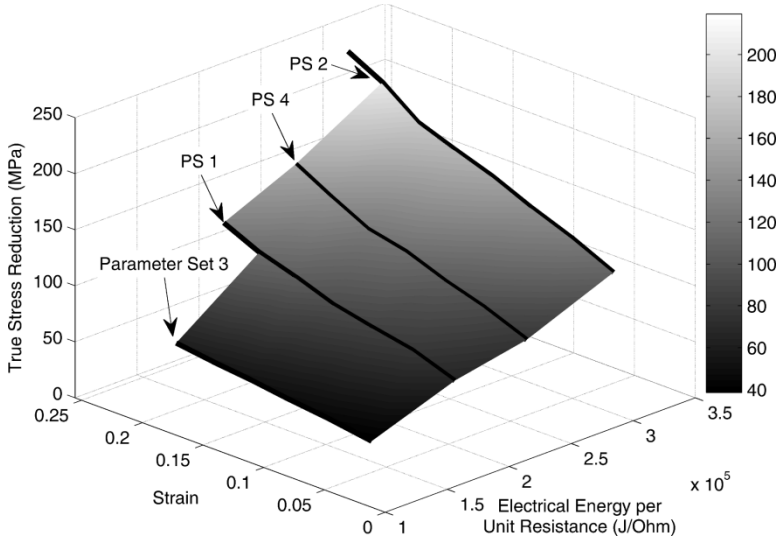

Figure 7.13 - Stress Reduction Surface for PS1-PS4 at Varying Strain Levels

In addition to the EAF testing of Parameter Sets 1-4, stationary tests were conducted at the same electrical conditions, however, no deformation was imposed during the application of current. After performing the stationary electrical testing, the specimens were cooled to room temperature conditions and deformed to failure at room temperature. The results from this testing are presented in Figure 7.14 for Parameter Sets 1-4 along with the average room temperature baseline with a ±3 standard deviation bound. Statistically, the average room temperature baseline and its ±3 standard deviations represent 99.73% of the normally distributed spread for all baseline tests. It is assumed that the mechanical response follows a normal distribution due to the variation in the

sheets samples being random. As shown, all of the room temperature tests fall within the ±3 standard deviation bounds and can be considered to not be outliers from the data set. As a result, it can be concluded that significant modifications did not occur from the application of current which alter the strength response of the material. It should be noted that there is some variation (<16MPa) and this may be a result of some dislocation annihilation due to temperature rise or dislocation wind effects or possibly small amounts of grain growth from elevated temperatures. The reason for this variation is studied in *Chapter 10*. Since the material was warm rolled it is basically in a recrystallized state off of the rolling mill and would have a fairly low dislocation density. Also, it is not expected that the material recrystallized since the recrystallization procedure is to hold at 205°C for one hour after 15% cold work, while the maximum temperature reached for a short time (a few seconds) was 224°C from all parameter sets [7.2]. Additionally, the temperatures reached were well below the annealing temperature of 345°C and the hot working range of 230°C-425°C. Thus, it can be concluded that stationary electrical treating did not significantly alter the mechanical response, however, some dislocation annihilation or grain growth may have occurred. *Chapter 8* examines these effects at a microstructure level.

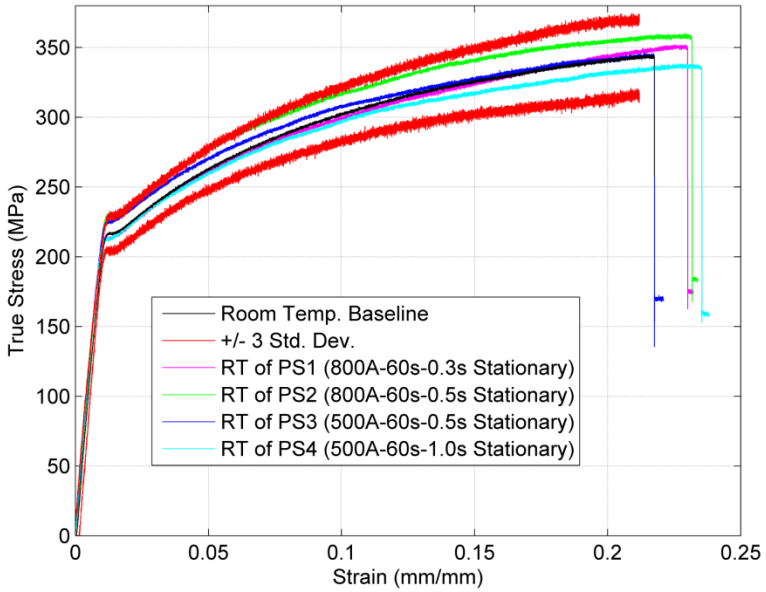

Figure 7.14 - Experimental Flow Stress Results of Room Temperature Behavior for Preceding Stationary Electrical Testing

Parameter Set 5 was manually controlled and the magnitude and period were varied throughout the testing. As can be seen in Figure 7.15 the material flow stress can be significantly modified as a result of the applied current. With the observed results seen for Parameter Set 5, it is suggested that the material flow stress can be controlled with the application of electrical current. This type of process control technique is discussed in *Chapter 9* of this work where constant forming force and constant stress forming are designed and implemented during uniaxial forming.

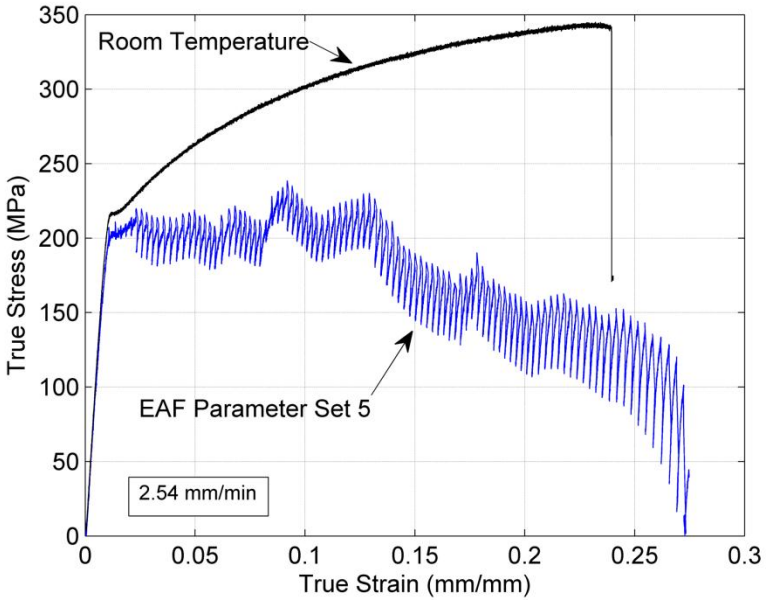

Figure 7.15 - Experimental EAF Flow Stress Results (Parameter Set 5)

In contrast to Parameter Sets 1-4, Parameter Sets 6-7 show experimental results with a shorter pulse periods which translate to a greater amount of electrical power being supplied to the sample with respect to time. The results for Parameter Set 6 and 7 are shown in Figure 7.16 and Figure 7.17, respectively. Upon comparing the results from Parameter Set 3 to Parameter Set 6, it is seen that the stress reductions at the same strain level are equivalent, however, Parameter Set 6 has slightly greater elongation on average before failure (4.32%).

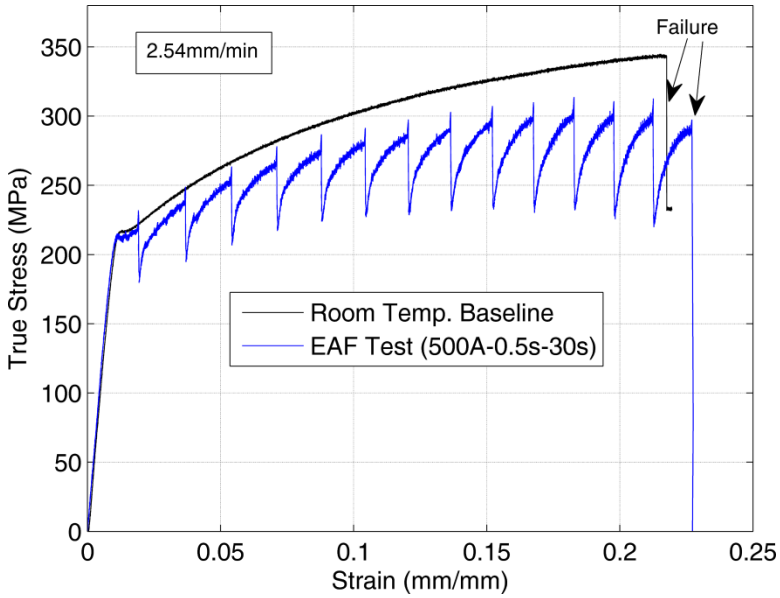

Figure 7.16 - Experimental EAF Flow Stress Results (Parameter Set 6)

Comparing Parameter Set 7 to Parameter Set 6 gives a significanly different flow stress response where doubling the applied current did not double the observed stress reduction. This is expected as the electrical power is proprotion to the square of the applied current. For Parameter Set 7, the current was discontinued around a strain of 0.17 as a result of the stress approaching zero, so the remainder of the test continued without current to material fracture. It is interesting to note that the material was capable of hardening such that the stress reached approximately 275MPa while the prior stress state of the material was near zero.

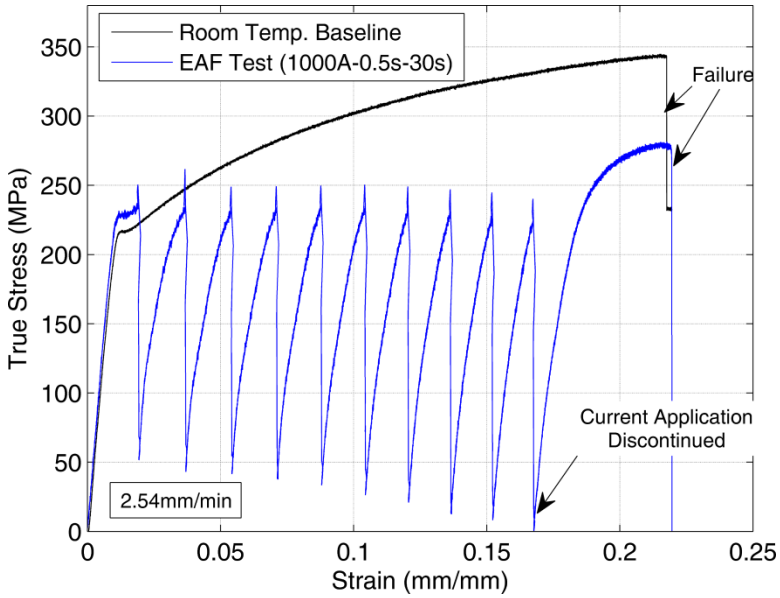

Figure 7.17 - Experimental EAF Flow Stress Results (Parameter Set 7)

The results in Figure 7.18 compare Parameter Set 8 without and with air cooling applied uniformly to the specimen during EAF testing. The results show significantly different flow stress responses where the test with cooling had rapid increases in strength after the application of electrical current was discontinued and lower flow stress reductions as compared to the non-cooled test. The rapid increase in strength is a result of enhanced heat transfer (*i.e.* a reduced sample temperature and thus a lower amount of thermal softening) resulting from forced convection rather than only natural convection. This type of processing may be advantageous to reduce thermal loads on the workpiece while also allowing for the benefits of EAF. Additionally, an adaptation could be to track regions where the material begins to neck and apply cooling to these regions to mitigate material failure and allow for more uniform deformation. This could be accomplished with in process Digital Image Correlation (DIC) data and a control system for the cooling application.

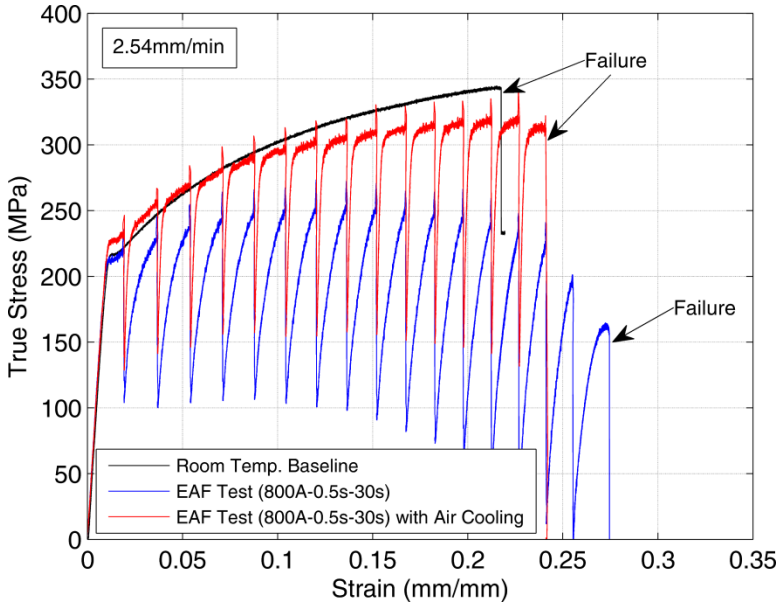

Figure 7.18 - Experimental EAF Flow Stress Results (Parameter Set 8) and Effect of Specimen Cooling during EAF

To better understand the lower flow stress reductions of the cooled test as compared to the non-cooled test, Figure 7.19 summarizes the stress reductions. As seen in the figure, there is an average difference of 9MPa in stress reduction comparing the cooling and non-cooling tests. This lower stress reduction for the cooling test is suggested to be a result of a reduction in the amount of temperature rise during the application of current which leads to a reduced amount of thermal softening. Although the exact temperatures were not recorded for these set of tests, it may be stated that a difference of 9MPa is quite small compared to the overall stress reduction while an assume temperature difference might be quite large by examining the quick increase in material strength after the discontinuation of electrical current. This would then suggest that a larger portion of the overall stress reduction is a result of electroplasticity and not bulk thermal softening. Thus, this is an area that can further be explored as an ideal EAF test would be performed without any bulk temperature rise (*i.e.* cooling application technique

that would suppress bulk joule heating) such that the observed reduction in stress would be purely due to electroplasticity.

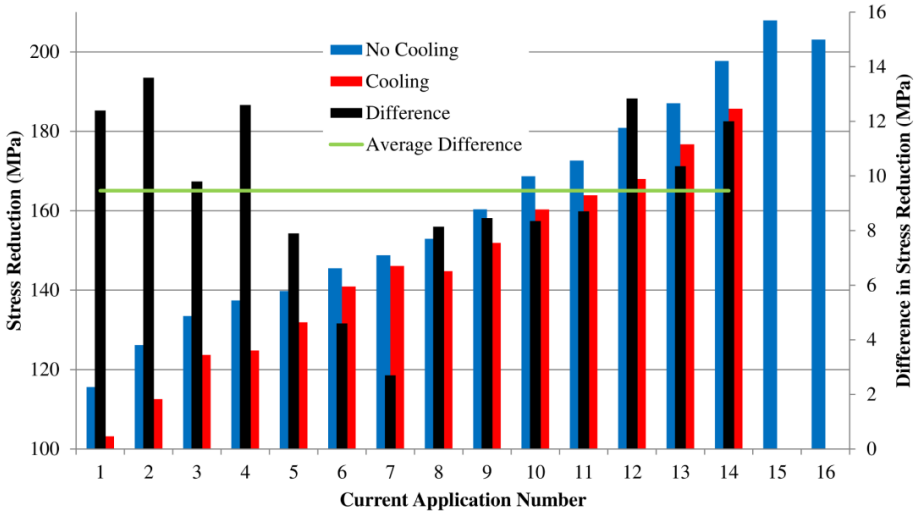

Figure 7.19 - Summary of Stress Reductions for Parameter Set 8 with and without Specimen Cooling

7.2.3.2 - EAF with Continuous Current Application

The influence of electrical current during deformation with a continuous wave was also examined in this work. These tests (summarized in Table 7.2) were performed with two testing velocities to examine the effect of strain rate and with varying current magnitudes.

Table 7.2 - EAF Continuous Wave Testing Conditions

Test Name	Current Magnitude	Wave Shape	Platen Velocity
100A Continuous EAF	100A	Continuous	2.54mm/min
150A Continuous EAF	150A	Continuous	2.54mm/min
200A Continuous EAF	200A	Continuous	2.54mm/min
100A Continuous EAF	100A	Continuous	25.4mm/min
150A Continuous EAF	150A	Continuous	25.4mm/min
200A Continuous EAF	200A	Continuous	25.4mm/min

The results are presented in Figure 7.20 for the slow platen speed of 2.54mm/min at room temperature forming and EAF with a continuous current at 100A, 150A, and 200A. The current application was applied at the beginning of the test while the material was still being elastically deformed (*i.e.* prior to the material yield point). As seen, with an increasing current magnitude the yield strength of the material decreases. The observed decrease in the yield point can be a result of two possible phenomenon. The first is that an increased bulk temperature due to Joule heating adds thermal energy to the material lattice which allows for plastic deformation to occur at a reduced level of stress. This is very similar to the effects observed and discussed for the elevated temperature testing of the magnesium sheet in *Section 7.2.2*. To quantify the temperatures during the test, Figure 7.21 shows the maximum temperature profile with respect to test time. As shown, there is a significant difference in the initial temperatures when comparing the 100A to the 200A test (100°C at the yield point). The second effect is from electroplasticity where the electrical current flow directly interacts with the material lattice to reduce the stress as which material slip begins to occur. This concept is not clearly visible in these tests, but the interaction with electrical current and the yield point is clearly shown in *Section 7.2.3.3*.

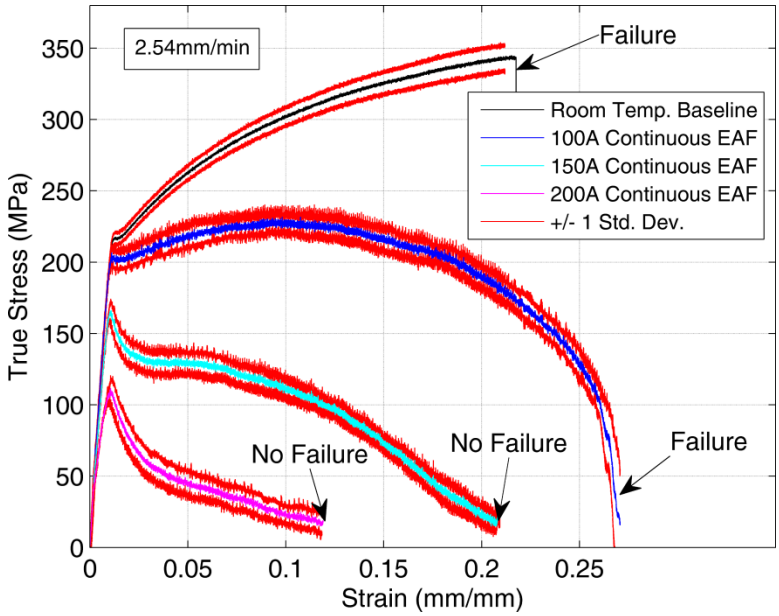

Figure 7.20 - Experimental EAF Flow Stress Results for Continuous Application of Electrical Current at 2.54mm/min

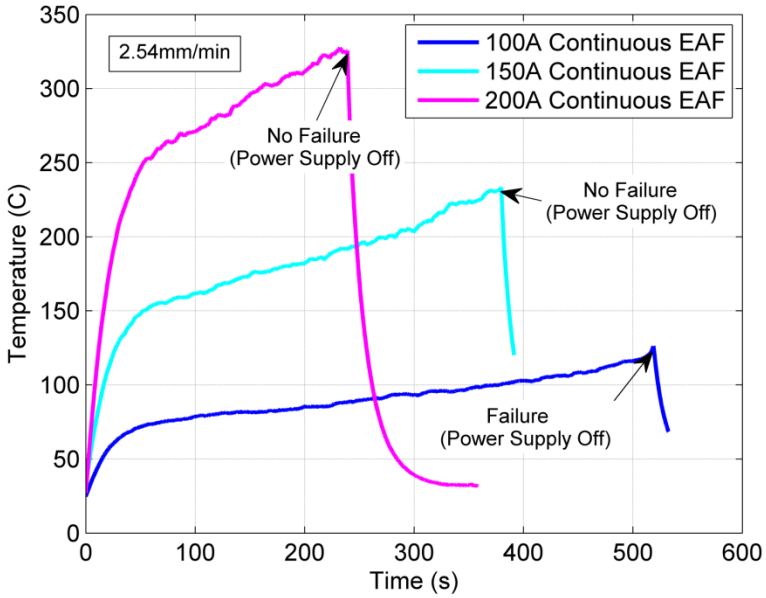

Figure 7.21 - Maximum Temperature Response for Continuous Current Application of Electrical Current at 2.54mm/min

Figure 7.22 examines an individual continuous EAF test where a current of 200A is applied to the material, and when an extremely low stress level is reached (corresponds to 50N forming load) the current application is discontinued. After the applied current is stopped, the material then begins to cool and the material begins to harden to approximately the initial yield strength of the as-received material. This result from this test is important as this could be a processing strategy that could be used in industrial applications. For example, the material can be formed under very low stress conditions using EAF which is desirable and then the material could be formed a small amount of the total strain to significantly increase the strength of the material. The final strength of the material is critical as this is the strength properties that the material will have in service unless additional post-forming thermal treatments are performed.

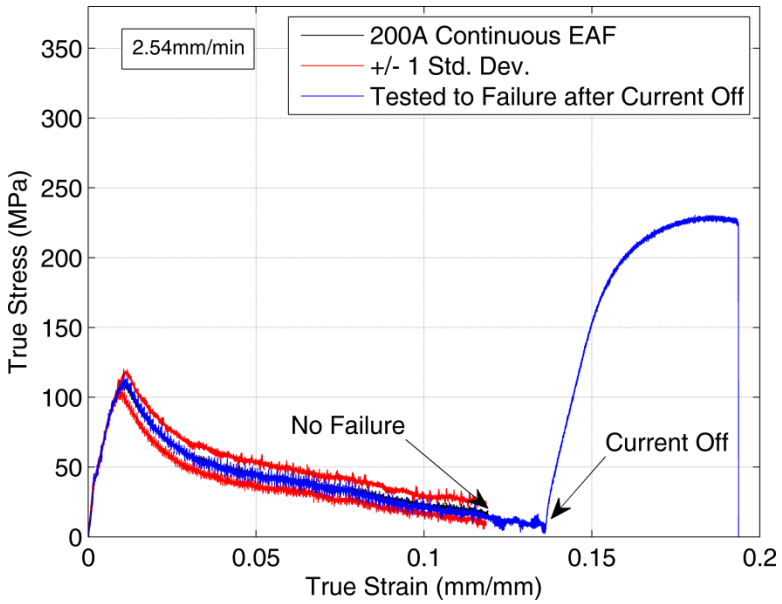

Figure 7.22 - Experimental EAF Flow Stress Results for 200A of Continuous Electrical Current at 2.54mm/min with Discontinuation near End of Test

In addition, a faster platen velocity (10 times the initial velocity) was tested for the continuous EAF tests, and the results are presented in Figure 7.23. The results show similar trends, however, the yield strength of the material is not affected to the extent of the slower platen velocity. This can be described again by examining the thermal response of the tests (Figure 7.24) where the maximum temperatures are much lower at the point where yielding occurs. It should be noted that the maximum temperatures observed for the faster platen speed reach higher peak temperatures (most notably for the 200A test). This can be explained as a result of a faster platen speed which creates an accelerated diffuse necking geometry. Due to the diffuse neck, a smaller cross-sectional area is present and this creates an area with higher heat generation which leads to a higher peak temperature. The relation of area to heat generation is given in Equation (4.16).

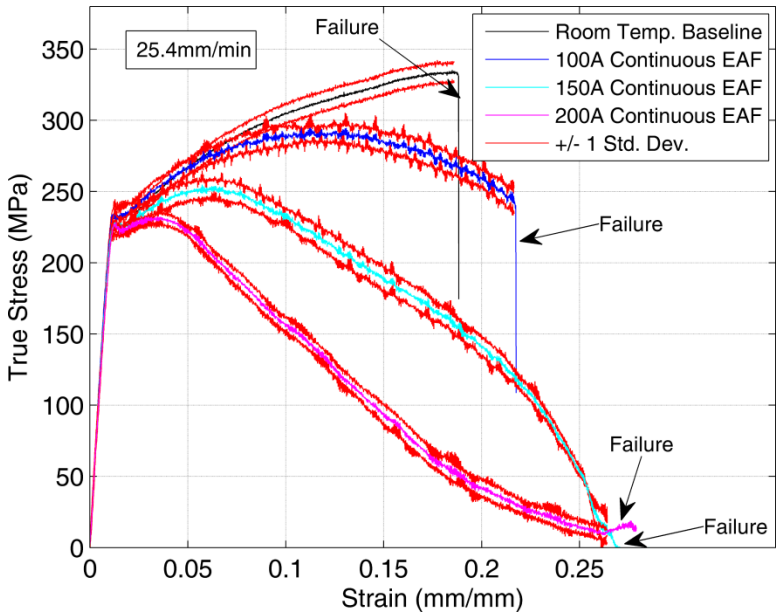

Figure 7.23 - Experimental EAF Flow Stress Results for Continuous Application of Electrical Current at 25.4mm/min

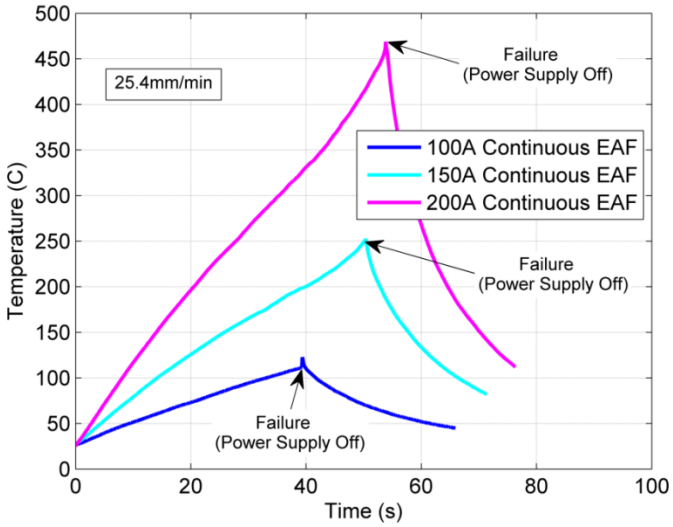

Figure 7.24 - Temperature Response for Continuous Current Application of Electrical Current at 25.4mm/min

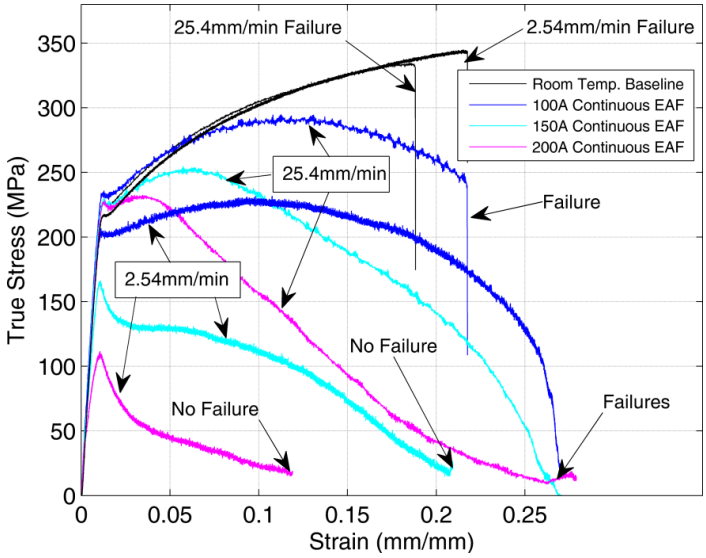

Figure 7.25 - Experimental EAF Flow Stress Results for Continuous Application of Electrical Current at 2.54mm/min and 25.4mm/min

To compare the results from the two platen velocities, Figure 7.25 displays all of the flow stress curves on one single figure. As seen the yield point is significantly affected for the slower platen velocity and there is very little change for the faster tests. Also, both platen velocities show reduced material flow stress with the slow platen velocity having larger reductions in stress.

To specifically compare the maximum temperature at yield, the experimental thermal results were analyzed and the observed temperatures are given in Figure 7.26.

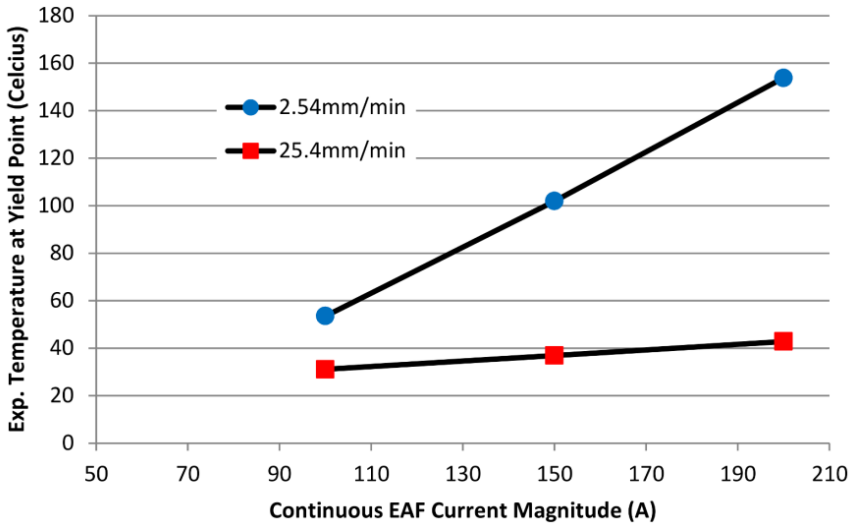

Figure 7.26 - Experimental Temperature at Material Yield Stress for Continuous Application of Electrical Current at 2.54mm/min and 25.4mm/min

It can be seen that with increasing continuous current magnitudes, the experimental temperature at yielding increases. Also, the main difference is the slope for each of the platen velocities. Thus, the significantly reduced yield point for the slower platen speed can be partially due to the much higher temperatures observed at the time of material yielding. It is interesting to note that the observed temperature measurements at material yield are nearly linear for each platen velocity. The significance or influence of this result is an area where more exploration is warranted.

7.2.3.3 - EAF with Incremental Current Application

In addition to examining the material flow stress response under square and continuous wave applications, this section examines the use of EAF in an incremental manner. The term incremental means the electrically is applied to the sample, but not

during deformation. Additionally, the sample is allowed to cool to room temperature before any deformation is imposed to the sample. The first experimental result is given in Figure 7.27 where room temperature deformation occurred to a strain level of 0.07mm/mm (corresponds to 5.08mm of deformation) and then an applied electrical pulse of 1000A for 1 second was applied while the sample was still loaded, but no deformation was occurring. After the applied electrical pulse, the sample was unloaded and allowed to cool to the room temperature. The sample continued to be deformed at room temperature in steps of 5.08mm until failure (17% increase over room temperature).

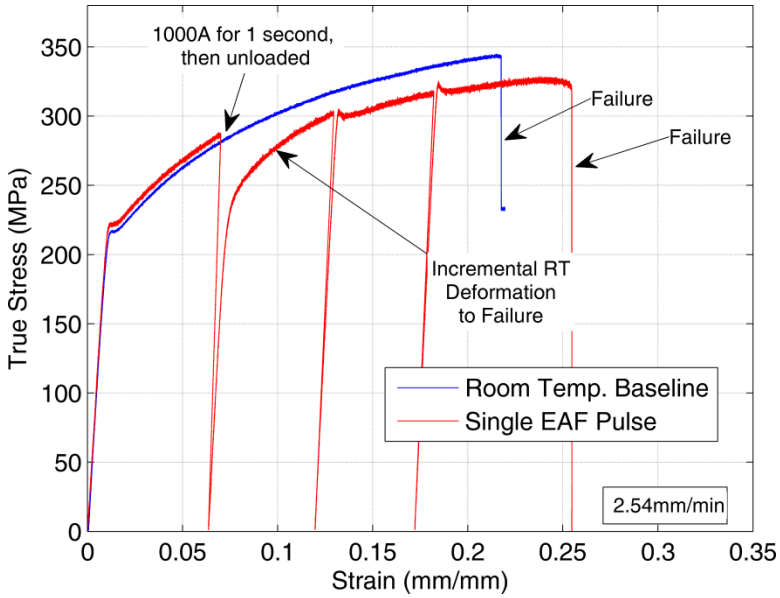

Figure 7.27 - Experimental EAF Flow Stress Results for Single Pulse Application of Electrical Current during Incremental Forming

The main observation from this test is the modified yield point of the material after the applied electrical current application. Since the material was stationary during this time and only a load was applied, the bulk temperature effects are expected to be small as a result of the maximum temperature only reaching 338°C for a very short period of time (Figure 7.28).

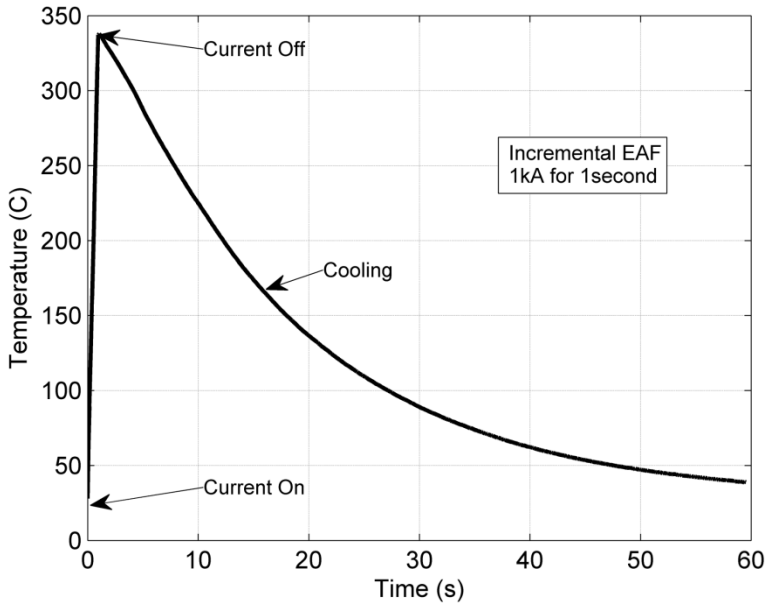

Figure 7.28 - Temperature Response for Single Pulse Application of Electrical Current during Incremental Forming

Again, for this material, the recrystallization temperature is 205°C for one hour with approximately 15% cold work and the annealing temperature for this material is 345°C. Thus, this suggests that the applied electrical current had a direct influence on the material's yield strength and the material was not annealed or recrystallized pure from thermal effects. This observed effect could be a result of the applied electrical current directly modifying the dislocation density of the material and thus allowing for an instantaneous stress relief with the use of a single pulse of electrical current. This is analogous to traditional incremental forming where a conventional purely thermal process anneal treatment would be used to reduce the material strength or remove some effects of cold work during processing (see Figure 2.1). The theory behind the modification of the yield point is fully described in *Chapter 10*. In addition, as the stress of the material is reduced this then suggests a decrease in the dislocation density of the

material. As a result, the amount of dislocation annihilated during this application allowed for the material to deform to a greater extent over the room temperature baseline.

From a processing or economic standpoint this technique could be incorporated directly in the forming equipment instead of having to remove the workpiece to place in external annealing equipment which also has additional energy and capital costs. After the incremental EAF pulse, the material was deformed under ambient temperature conditions until failure. It is shown that without the application of current the material returns to its prior flow stress before entering the plastic deformation regime.

The second experiment also applied EAF in an incremental format where the material is only deformed under room temperature conditions and the current application is applied at intervals where the specimen is loaded, but deformation is not occurring. The results for this method and incremental room temperature forming without any annealing are displayed in Figure 7.29. As seen, the EAF incremental test reduced the material flow stress after each electrical pulse and also modified the material yield strength. It should be noted that for the room temperature incremental test the material yielded at the prior flow stress which was reached before the unloading occurred. This is a result of the material being strengthened from cold work imposed on the material and the material having this strength upon unloading. Also, using this technique allowed for the specimen to have uniform elongation as a result of the deformation only occurring at room temperature and without a temperature gradient in the specimen (EAF tests with deformation display large thermal gradients along the length axis of the specimen). This is beneficial as uniform strain is present and the application of electrical current during

the periods where deformation is halted helps to reduce the material flow stress and reduce the dislocation density of the material. Last, using this technique allowed for greater uniform strain before fracture as compared to the room temperature and square wave EAF tests. The increased amount of elongation can be attributed to the reduced strength of the material (*i.e.* dislocation density reduction) which in turn reduces the local stresses at pinned dislocation. The reduced local stresses in the lattice reduce the occurrence of microvoid formation and cracking.

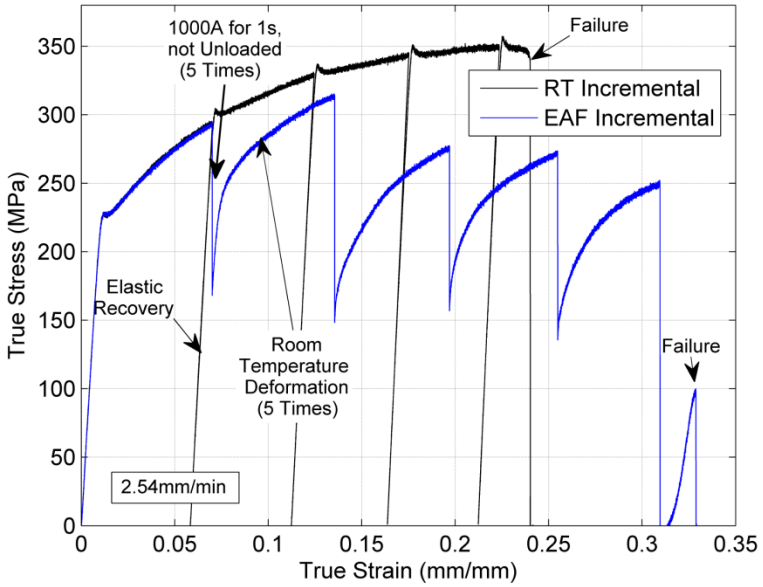

Figure 7.29 - Experimental Flow Stress Results Comparing RT and EAF Incremental Forming

7.3 - Post Forming Strain Examination using Circle Grid Analysis (CGA)

Following the testing, the chemically applied strain grids were analyzed for select tests. An example image to be used in image analysis software is shown in Figure 7.30.

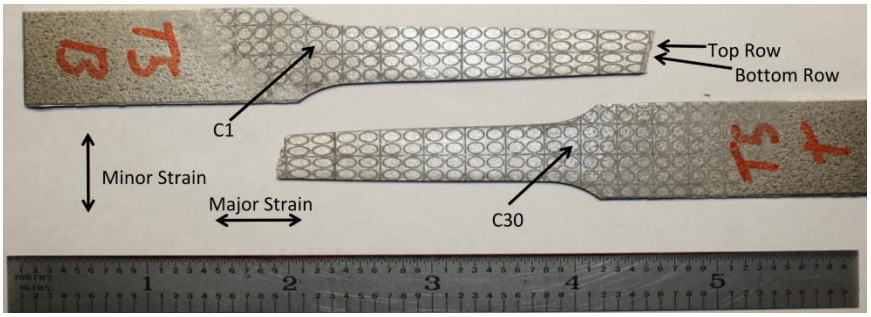

Figure 7.30 - Photograph of Fractured Specimen for CGA (Parameter Set 4)

Using the image analysis software, the major and minor strain along the length of the specimen is measured and an example output is given in Figure 7.31 for Parameter Set 4. The thickness strain was calculated under the assumption of volume constancy.

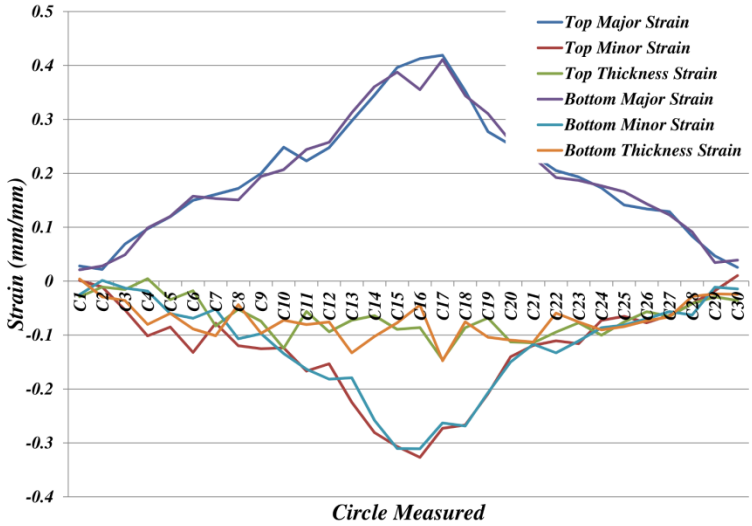

Figure 7.31 - Circle Grid Results (Parameter Set 4)

For the models introduced in *Chapter 4*, this EAF CGA data was linearized to use as a model input. An example is given in Figure 7.32 where the data shows the strain at the point of material failure. For the models in *Chapter 4* this linear data was extrapolated linearly from zero strain through the results in Figure 7.32 and this then results in the surface profiles given in Figure 7.33.

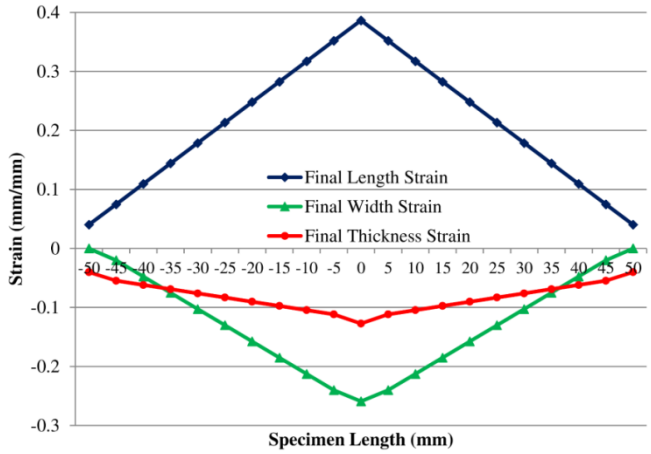

Figure 7.32 - Linear Model for CGA (Parameter Set 4)

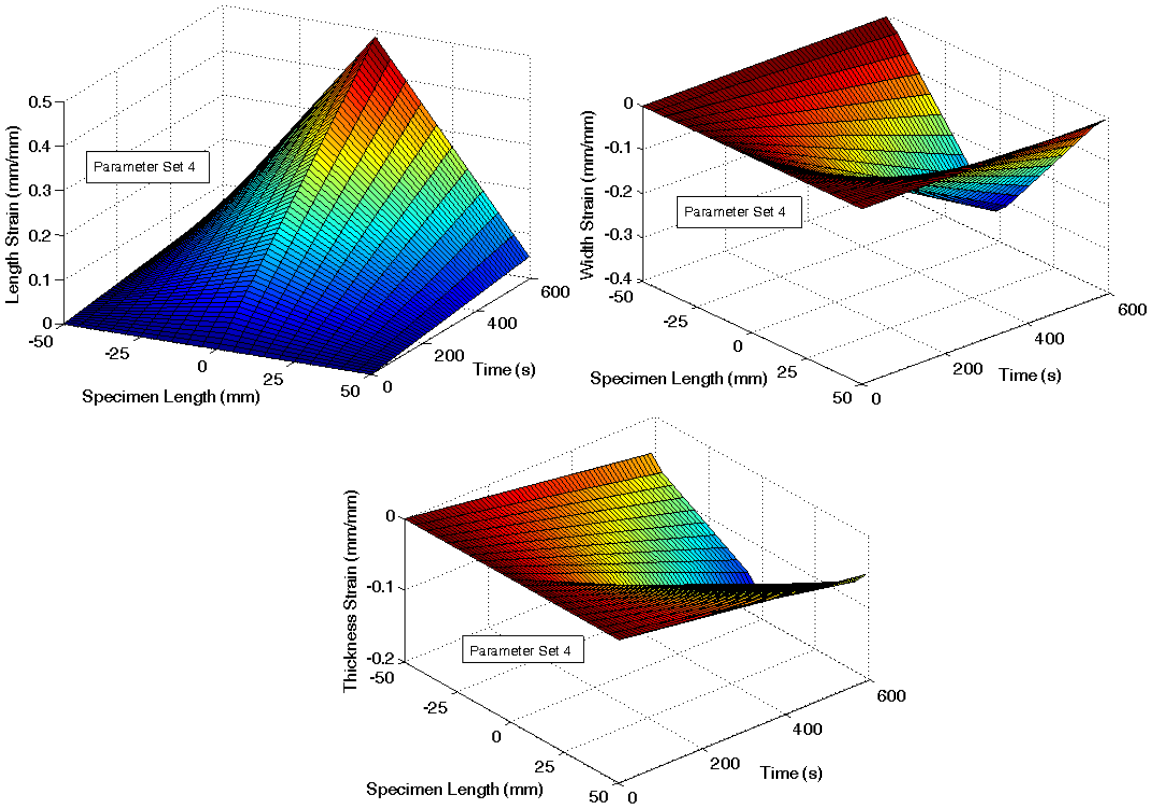

Figure 7.33 - Diffuse Model Strain Inputs for Parameter Set 4

Additionally, the local strain was measured for the elevated temperature results using the same procedure and an image used to analyze the strains is displayed in Figure 7.34.

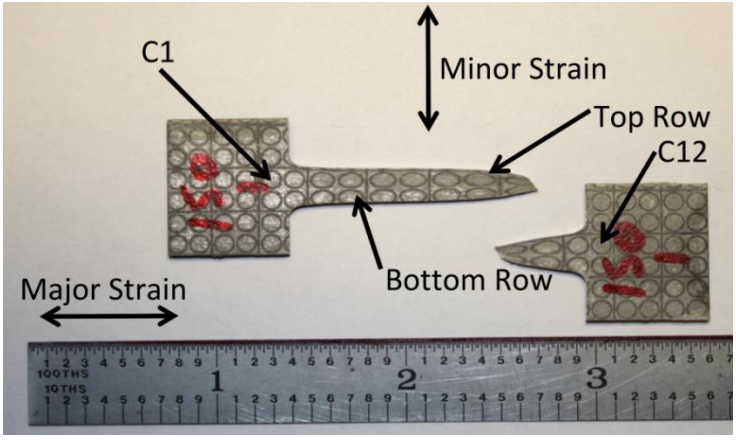

Figure 7.34 - Photograph of Fractured Specimen for CGA (150C Elevated Temperature)

An example output is displayed for the 150C test where it is seen that there is a diffuse neck throughout the specimen and then highly localized strains near the fracture location. This profile is different in comparison to the electrical profile in Figure 7.31 as the electrical test has a maximum temperature at the center for the specimen which relates to the most strain being concentrated in this region. For the elevated temperature test, the localized strains near the failure region are dictated by crack initiation due to a defect in the material.

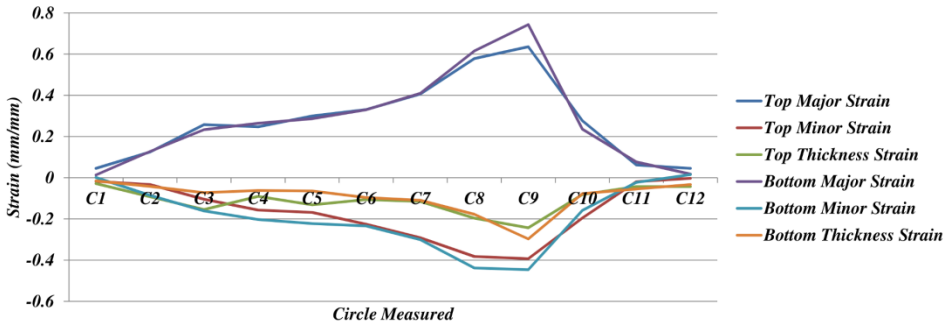

Figure 7.35 - Circle Grid Results (150C Elevated Temperature)

Also, the results collected using this technique are used in *Chapter 6* to compare the predicted local strains with the measured experimental results. Additional CGA results are displayed in *Appendix A*.

7.4 - Conventional Room/Elevated Temperature Phenomenological Flow Stress Model

For the room temperature and elevated temperature data, a phenomenological constitutive equation was developed to predict the flow stress behavior under conventional forming conditions at varying temperatures. This was derived such that the effects of temperature could be related to material flow stress and bulk thermal softening in the models created in this work. The expression is given generally in Equation (7.1) and the constants as a function of temperature are given in Equations (7.2)-(7.4).

$$\sigma_f = K\varepsilon^n \exp(\varepsilon s) \tag{7.1}$$

$$K := \begin{cases} T \le 25°C : K = K_{RT} \\ 25°C < T < 150°C : K = K_1 T + K_2 \\ T \ge 150°C : K = K_3 \exp(K_4 T) \end{cases} \tag{7.2}$$

$$n := \begin{cases} T \le 25°C : n = n_{RT} \\ 25°C < T < 150°C : n = n_1 T + n_2 \\ T \ge 150°C : n = n_3 T + n_4 \end{cases} \tag{7.3}$$

$$s := \begin{cases} T < 120°C : s = 0 \\ 120°C \le T \le 327°C : s = s_1 T^2 + s_2 T + s_3 \\ T > 327°C : s = 0 \end{cases} \tag{7.4}$$

where, σ_f is the flow stress, K is a strength coefficient, ε is strain, n is the strain hardening exponent, and s is a softening term. The term $\exp(\varepsilon s)$ represents the softening

potential of the material for higher temperatures. The strength coefficient (K) is constant at room temperature and increases linearly to 150°C where it then decays exponentially with an increasing temperature, n has a linear decrease with temperature as related to two temperature ranges, and s has a parabolic form such that at lower temperatures and higher temperatures there is no softening, but is a maximum at a moderate temperatures. The lower effect of s at a higher temperature may be a result of other possible deformation mechanisms or dynamic recrystallization and at lower temperatures there is not much material softening. The best fit coefficients given in Table 7.3 were determined using least squares regression.

The model results are compared to the experimental results in Figure 7.36. Also shown, is the predicted model result for 100°C. To visually depict the response of this function, Figure 7.37 displays the corresponding true stress over varying temperatures and strains.

Table 7.3 - Conventional Room and Elevated Temperature Model Coefficients for Mg AZ31B

Constant	Value
K_{RT}	457.72
K_1	-1.9529
K_2	500.68
K_3	931.06
K_4	-0.01
n_{RT}	0.1818
n_1	-0.0004
n_2	0.1909
n_3	-0.0009
n_4	0.2713
s_1	0.00008
s_2	-0.0357
s_3	3.1162

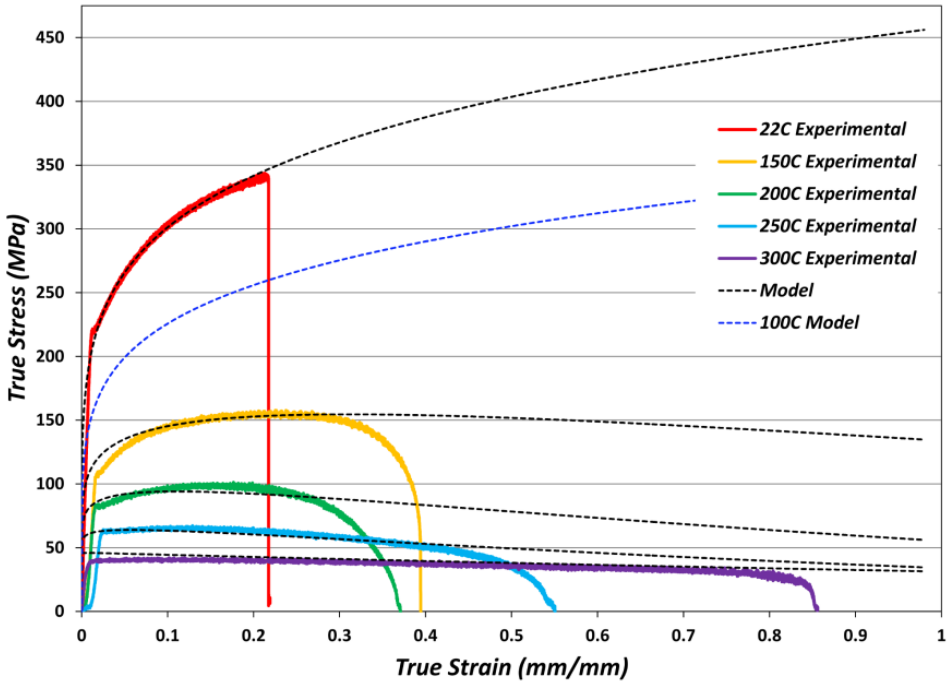

Figure 7.36 - Conventional Room and Elevated Temperature Flow Stress Model Comparison

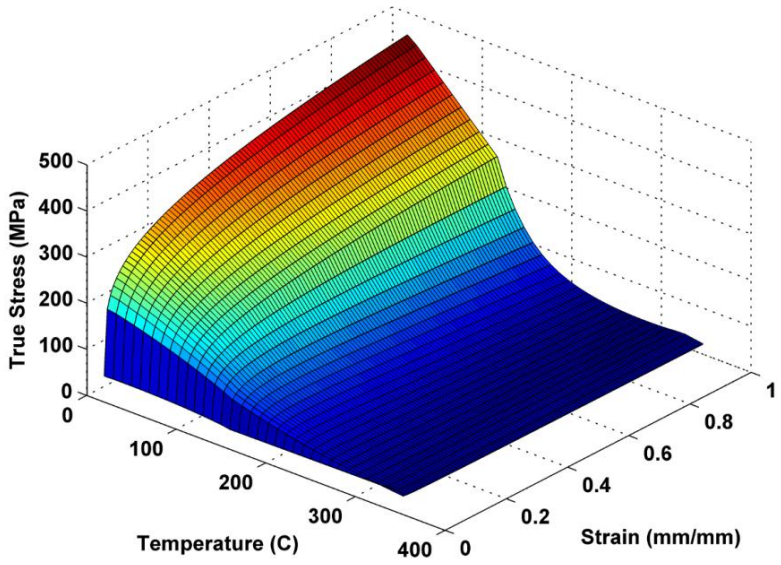

Figure 7.37 - Conventional Flow Stress Response Surface for Room Temperature to Elevated Testing Temperatures over Varying Strain Levels

7.5 - Failure for Conventional Room/Elevated Temperature Flow Stress Model

The tensile instability approach by Considère in 1885 stated that instability occurs when,

$$dF = 0 \tag{7.5}$$

where, F is the force during deformation.

Knowing that,

$$F = \sigma A \tag{7.6}$$

where, σ is stress and A is the area, and upon differentiation,

$$\frac{dF}{d\varepsilon} = \sigma \frac{dA}{d\varepsilon} + A\frac{d\sigma}{d\varepsilon} = 0 \tag{7.7}$$

Or,

$$\frac{d\sigma}{\sigma} = -\frac{dA}{A} = \frac{dL}{L} = d\varepsilon \tag{7.8}$$

Hence,

$$\frac{d\sigma}{d\varepsilon} = \sigma \tag{7.9}$$

Using the derived constitutive model for this magnesium material (see phenomenological constitutive equation in *Section 7.4*),

$$\sigma_f = K\varepsilon^n e^{\varepsilon s} \tag{7.10}$$

Applying Equation (7.9) to Equation (7.10) yields:

$$Ks\varepsilon^n e^{\varepsilon s} + Kn\varepsilon^{n-1} e^{\varepsilon s} = K\varepsilon^n e^{\varepsilon s} \tag{7.11}$$

Therefore, the instability can be predicted as:

$$\varepsilon^* = \frac{n}{1-s} \tag{7.12}$$

7.6 - Experimental Analysis Conclusions

The main conclusions drawn from this experimental testing are:

- The room temperature behavior of this material was consistent with published literature on this alloy with respect to yield strength and the strain hardening exponent/strength coefficient.
- The elevated temperature tests showed reduced yield strength and increased elongation with increasing temperature. Also, all elevated temperature tests displayed non-uniform deformation throughout the gauge length.
- The EAF square wave tests decrease material flow stress during the application of current. This decrease is a result of thermal softening from bulk heating, thermal expansion, and electroplasticity. Also, the fracture

strain was not significantly affected by electrical parameters examined in this work.

- The electrical pretreating samples which were deformed at room temperature conditions displayed only a small variation in mechanical response (<16MPa). Thus, it is suggested that the variation is a result of the dislocation density being altered from electrical pretreating.
- The EAF square wave test with in-process manual control of the flow stress level suggested that the material deformation force or flow stress could be controlled, especially with a formal control strategy. This is investigated in *Chapter 9*.
- The EAF square wave tests that applied cooling with air showed that the stress rapidly increased after the current was discontinued as compared to the non-cooled test. Also, it was suggest that this technique could be used to reduce thermal loads and possibly track and cool the local neck region during EAF. When comparing the EAF cooled vs. non-cooled test, there is an average difference of 9MPa in stress reduction. This lower stress reduction for the cooling test is suggested to be a result of a reduction in the amount of temperature rise during the application of current which leads to a reduced amount of thermal softening. Although the exact temperatures were not recorded for these set of tests, it may be stated that a difference of 9MPa is quite small compared to the overall stress reduction while an assume temperature difference might be quite large by

examining the quick increase in material strength after the discontinuation of electrical current. This would then suggest that a larger portion of the overall stress reduction is a result of electroplasticity and not bulk thermal softening.

- The continuous current tests were performed at two platen velocities where both showed reduced material flow stress, however, the slow velocity displayed larger reductions. Also, the slow platen velocity showed a significant decrease in the material yield point as compared to the faster velocity. This was a result of the material temperature being much greater for the slower platen speed at the point where yielding occurred.
- The EAF testing using an incremental method showed that the yield point of the material was reduced after the applied electrical pulse. It should be noted that the observed temperature increase from the electrical current was very unlikely to cause the material to recrystallize or anneal from purely thermal effects because of the measured temperature magnitude and the duration at an elevated temperature. Last, this method allowed for uniform elongation during deformation with additional flow stress reductions.
- Post forming analysis was performed to measure the local strains for select samples which are used as model inputs (*Chapter 4*) and for model validation (*Chapter 5* and *Chapter 6*).

- A room temperature and elevated temperature phenomenological flow stress model was created for this material. The model form was a modified power law which incorporated thermal material softening effects.

7.7 - References for Chapter 7

[7.1] ASTM B557M – 10: Standard Test Methods for Tension Testing Wrought and Cast Aluminum- and Magnesium-Alloy Products (Metric), 2010.

[7.2] ASM: General Engineering Properties of Wrought Products – AZ31B/C, 1999.

CHAPTER 8 - MICROSTRUCTURE EXAMINATION OF SHEET METALS DURING EAF

Bulk properties such as strength or ductility of a metal can be empirically obtained from material testing. However, to fully understand these observed macro-properties the underlying material microstructure must be examined. Therefore for the subject alloy of this dissertation, this chapter studies the microstructure of the as-received material, the material deformed at room temperature, and materials deformed using EAF. To examine the material, a detailed procedure was developed as given in *Appendix C*. As the microstructure may vary in different orientations or spatially due to processing, several locations and orientations on the ASTM tensile samples were examined. The possible locations and orientations examined are shown in Figure 8.1 where L1 to L4 represent the possible mounting locations (select areas were chosen depending on the desired comparisions) and 1-3 represent the different orientations at a given location.

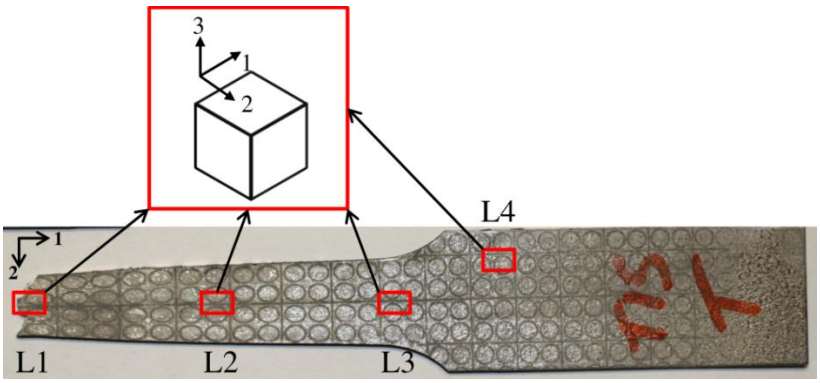

Figure 8.1 - Sample Mounting Locations and Orientations

Direction 1 is oriented such that the micrograph is showing a plane perpendicular to the rolling direction where the roll direction is parallel to the specimen length axis. Direction 2 is oriented to provide a micrograph that examines a plane parallel to the rolling direction. Direction 3 is oriented orthogonal to direction 1 and direction 2 such

that the micrograph is in plane with the top surface of the sheet. In order to specify these orientations during mounting, different color specimen clips were used. Thus, in the below results which label the sample, a capital letter "R" denotes orientation 1, "B" or "K" denote orientation 2, "NONE" denotes orientation 3, and additional letters and numbers represents the image number. As an example, "S1Rb2" means Sample 1 showing Orientation 1 and the image number is b2.

8.1 - As-received Material Microstructure

The as-received material was first examined to evaluate grain size and to understand the distribution of the grain size measurements. A polished surface prior to etching is shown in Figure 8.2 and the etched image is given in Figure 8.3. As seen, the applied etchant reacted with the surface of the material and the grain boundaries are revealed. The grain boundaries become visible due to a greater rate of material erosion at the boundaries as a result of the additional lattice energy present from the misalignment at the grain surfaces. Although not as prevalent as with a polarized lens, the individual grain shade depicts different grain orientations. To quantify the grain size, approximately 100 grains were fit by an ellipse for each micrograph. From the ellipse geometry, the area of each measured grain could be calculated. Using the calculated area, the equivalent circular grain diameter was determined and this value is presented to represent the grain size in the micrographs. More detail on grain size measurements are provided in *Appendix C*. The grain size of the as-received material in orientation 3 is 4.93μm with a standard deviation of 1.71μm which is typical for this Mg alloy and for a warm rolled sheet. Also, since this sheet was warm rolled there should not be an abundance of cold

work instilled into the material. This is visually verified as the micrographs do not appear to display much or any significant amount of twinning. A twin boundary would appear similar to that of a grain boundary, but it would slicing through the grain linearly.

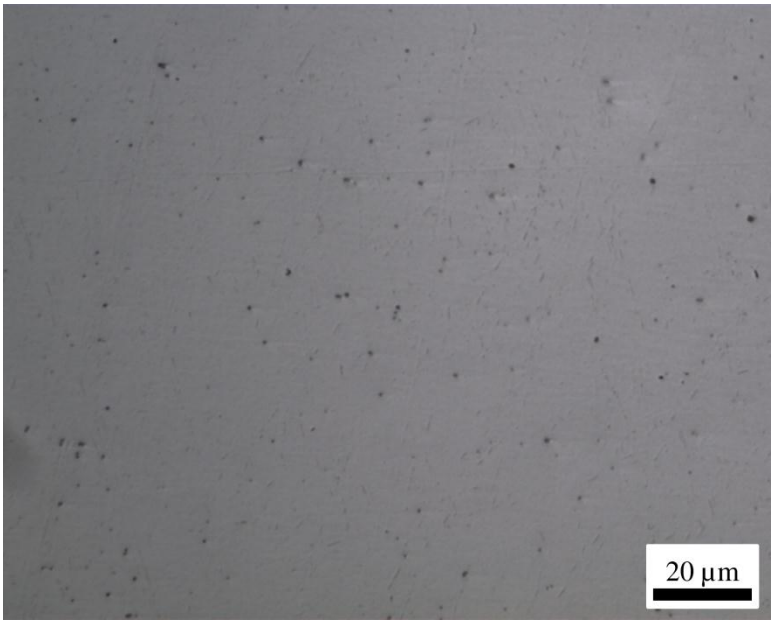

Figure 8.2 - Polished Material Surface before Etching

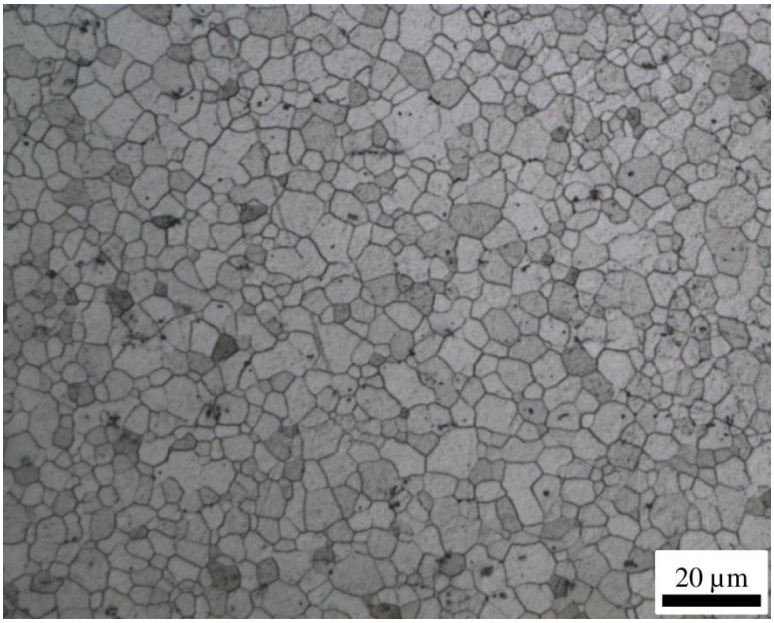

Figure 8.3 - Microstructure of As-received Material (Sample 1) in Orientation 3

From the numerous measurements taken on each micrograph, this allowed for a distribution of measurements to be generated as shown in Figure 8.4 for the as-received material in orientation 3. From examining the distribution, the data set appeared to follow a lognormal distribution. This type of distribution was verified by constructing a lognormal distribution test and the results are presented in Figure 8.5. As shown, a p-value of 0.961 resulted from the test which is highly suggestive that the data set of grain sizes is represented well by a lognormal distribution.

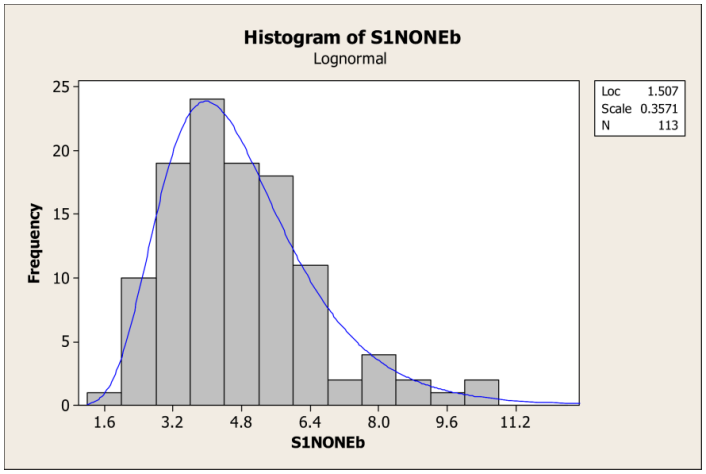

Figure 8.4 - Lognormal Histogram of Equivalent Circular Grain Size for the As-received Material in Orientation 3

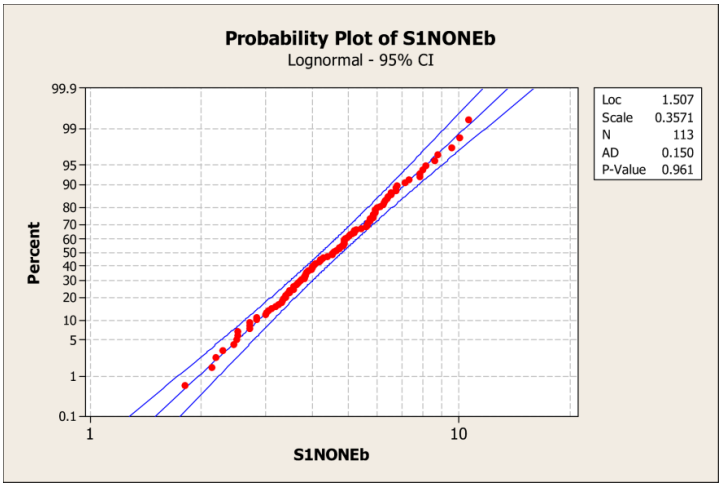

Figure 8.5 - Lognormal Probability Plot of Equivalent Circular Grain Size for the As-received Material in Orientation 3

To confirm the lognormal distribution, the natural logarithm of the data set was taken to verify the distribution was normal. A histogram and a normality test of the natural logarithm of the data set are present in Figure 8.6 and Figure 8.7, respectively.

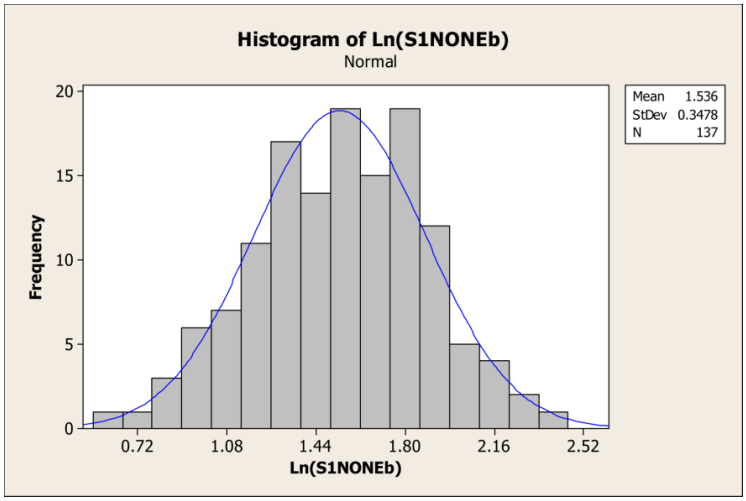

Figure 8.6 - Normal Histogram of the Natural Logarithm of Equivalent Circular Grain Size for the As-received Material in Orientation 3

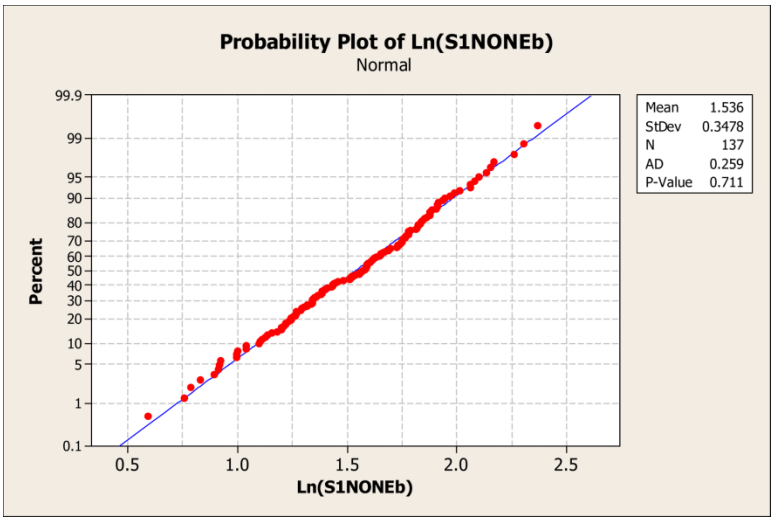

Figure 8.7 - Normal Probability Plot of the Natural Logarithm of Equivalent Circular Grain Size for the As-received Material in Orientation 3

As shown, the histogram physical displays a normally distributed data set and the normality test suggests that the probability of the data set being normal is very high (*i.e.* p-value of 0.711).

In addition to examining the distribution of the data set, several micrographs were taken on the same sample in the same orientation to ensure that the results were equivalent. This was performed as each micrograph is only displaying a small portion of the actual mounted sample. This analysis was performed and it was concluded that the micrograph image location on a given orientation did not have an influence on the measured results. The analysis was performed on the as-received material in orientation 3. The average equivalent circular grain size for image a, b, and c are shown in Figure 8.8 along with a 95% lognormal confidence interval (CI).

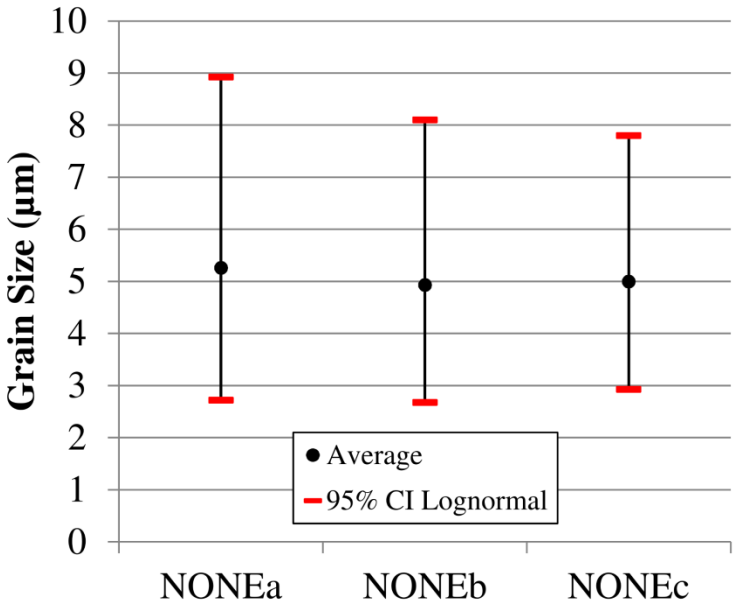

Figure 8.8 - Average and 95% Lognormal Confidence Interval of Equivalent Circular Grain Size at Three Locations for the As-received Material in Orientation 3

From Figure 8.8 it appears that the average and CI are very similar. To visualize the actual distributions, a lognormal fit was given to each data set (Figure 8.9). Once again, the results for each image appear to be very close.

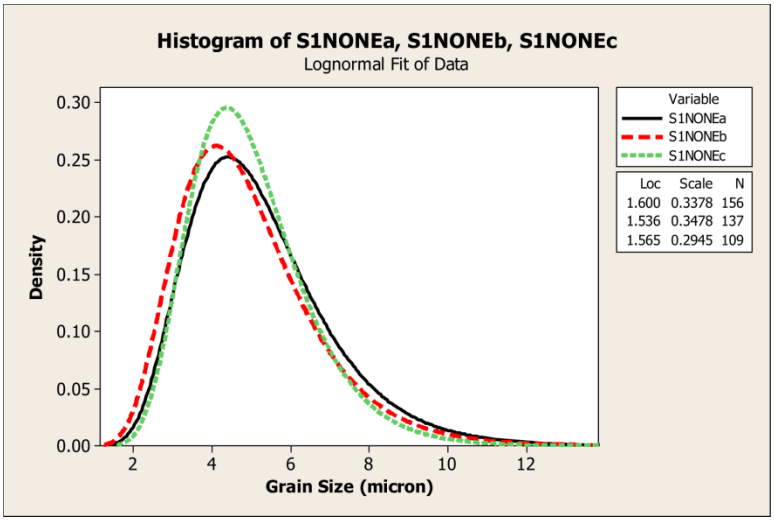

Figure 8.9 - Lognormal Fit of Equivalent Circular Grain Size at Three Locations for the As-received Material in Orientation 3

To specifically determine if there is a statistical difference between the data sets, two different test methods were used. To perform the tests, the data was first transformed to normal by taking the natural logarithm of the data sets such that the tests performed would be valid (tests require assumption of normally distributed data sets). After performing the tests, the results would then infer if the original data sets were equivalent.

The first was a two sample t-test with unequal sample sizes and variances (Welch's t-test) to verify if the population means are equal. The test provides a p-value which can be compared to a level of significance. The p-value for this test is calculated by using the Student's t distribution where the probability is given by,

$$P\left(X_0 \le x \le X_1\right) where\, X \sim T\left(t, d.f.\right) \tag{8.1}$$

Such that,

$$t = \frac{\overline{X}_1 - \overline{X}_2}{s_{\overline{X}_1 - \overline{X}_2}} \tag{8.2}$$

and,

$$s_{\overline{X}_1-\overline{X}_2} = \sqrt{\frac{s_1^2}{n_1} + \frac{s_2^2}{n_2}} \tag{8.3}$$

$$d.f. = \frac{\left(\frac{s_1^2}{n_1} + \frac{s_2^2}{n_2}\right)^2}{\frac{\left(\frac{s_1^2}{n_1}\right)^2}{n_1 - 1} + \frac{\left(\frac{s_2^2}{n_2}\right)^2}{n_2 - 1}} \tag{8.4}$$

where, P is the probability, T represents the Student's t distribution, t is the t statistic, s is the standard deviation of each data set, n is the number of measurements of each data set, and *d.f.* is the degrees of freedom [8.1].

The second test is to examine the variance of two data sets to verify that they are equal. To perform this, both a Levene test and a Bartlett test were performed and the average result is provided. The Bartlett test was designed for a nearly normal distribution where the distribution does not affect the result of the Levene test [8.2]. To calculate the probability of the variances being equal built in Excel functions were utilized.

The results of the two sample t-test for multiple images of the as-received material in orientation 3 are presented in Table 8.1. As seen, assuming 95% confidence or an alpha value of 5%, the p-value results are all greater when comparing the three images.

Table 8.1 - Two Sample t-test Results for Equivalent Circular Grain Size at Three Locations for the As-received Material in Orientation 3

	Sample 1 (p-value in percent)		
	NONEa	NONEb	NONEc
NONEa	-	17.2	45.6
NONEb	17.2	-	53.0
NONEc	45.6	53.0	-

The average results of the Levene and Bartlett tests are given in Table 8.2 where the p-values are greater than 5% for all cases. Thus, it can be concluded that the mean grain size and variance of each image is equivalent and it is not necessary to examine multiple images for a given sample and orientation.

Table 8.2 - Average of Levene and Bartlett Results for Equivalent Circular Grain Size at Three Locations for the As-received Material in Orientation 3

	Sample 1 (p-value in percent)		
	NONEa	NONEb	NONEc
NONEa	-	57.3	18.2
NONEb	57.3	-	6.0
NONEc	18.2	6.0	-

The above analysis for the as-received material in orientation 3 was performed for all the additional micrographs to ensure the data had a lognormal distribution. The remainder orientations for the as received material are given in Figure 8.10 and Figure 8.11 for orientation 1 and orientation 2, respectively. For orientation 1, the average grain size is 6.34µm with a standard deviation of 2.46µm and orientation 2 has an average grain size of 6.35µm and a standard deviation of 2.15µm. Again, since this sheet was warm rolled there is no signs of residual cold work in these orientations as verified by the lack of twin boundaries.

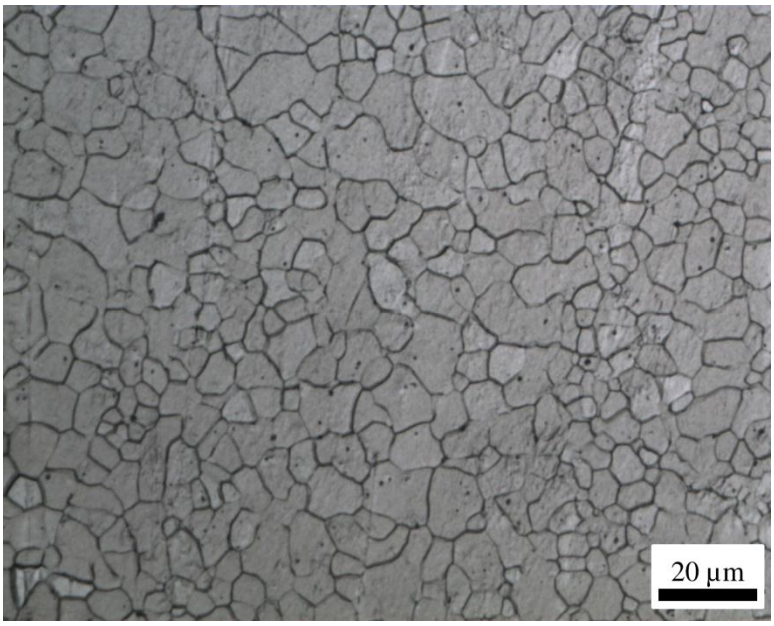

Figure 8.10 - Microstructure of As-received Material (Sample 1) in Orientation 1

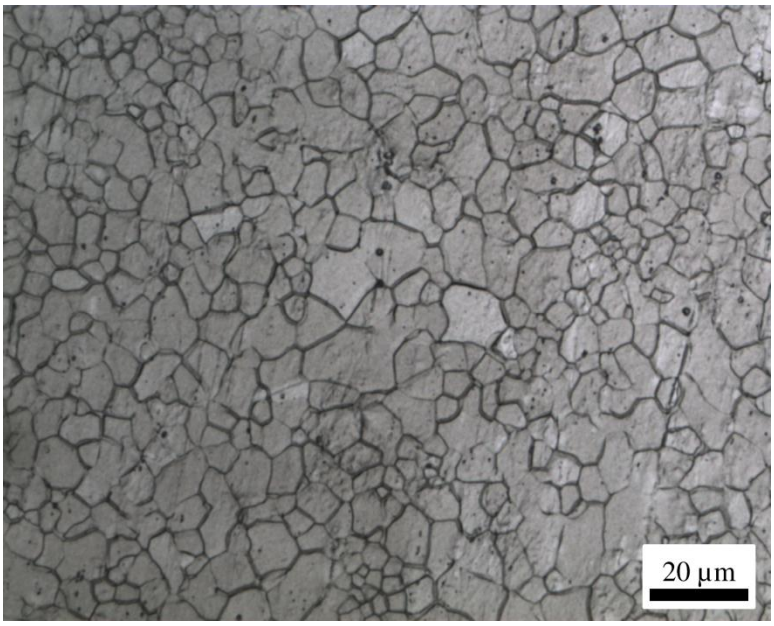

Figure 8.11 - Microstructure of As-received Material (Sample 1) in Orientation 2

To summarize this section examining the as-received material, Figure 8.12 displays a 3D representation of the material microstructure along with the three material orientations.

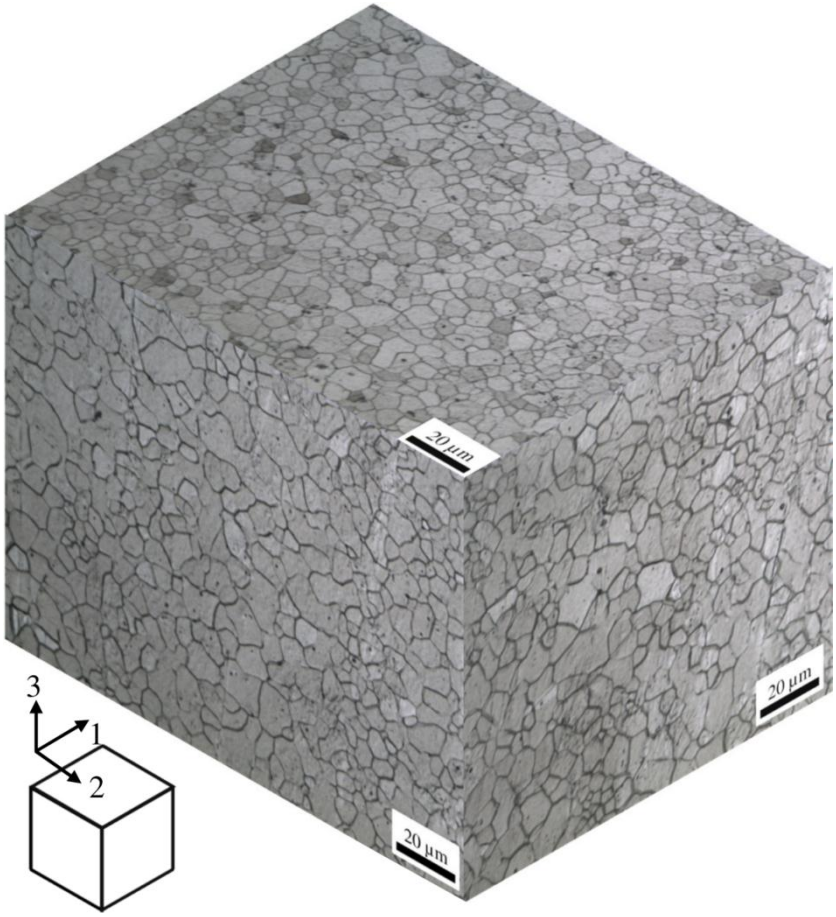

Figure 8.12 - 3D Microstructure of As-received Material (Sample 1) showing Orientations 1, 2, and 3

8.2 - Summary of Statistical Analysis of Micrographs

This section provides a statistical comparison between all the samples studied in this work and a summary of the samples examined are provided in Table 8.3. As seen there are a total of 18 samples which contain microstructure images for the as-received material, room temperature deformation, EAF square wave testing, EAF continuous wave testing, and incremental EAF tests. To compare the micrographs, the 2 sample t-test is

used to determine if the measured means are statistically equivalent and the Levene/Bartlett tests are used to conclude if the grain size measurements have equal variances. The results from these tests are summarized for all samples although not all samples are directly comparable (*i.e.* specific comparisons are made for select samples in the below discussion). When comparing the micrographs of the samples, orientation 1 and 2 was examined as orientation 2 and 3 have the same axial elongation. Hence, orientation 1 and orientation 2 are compared across all samples separately.

Table 8.3 - Summary of Samples Examined

Sample #	*Orientation*			*Location*	*Deformation*	*Wave Shape*	*Current Magnitude*	*Pulse Duration*	*Pulse Period*	*Notes*
	1	*2*	*3*							
Sample 1	Rb	Bc	NONEb	n/a	NO	n/a	n/a	n/a	n/a	As-received Material
Sample 2	Rb2	Bc2	n/a	L1	YES	n/a	n/a	n/a	n/a	Room Temperature Deformation
Sample 3	Ra	Bc	n/a	L1	YES	Square	500A	1s	60s	EAF Square Wave (500A/1s/60s)
Sample 4	Rc	Bb	n/a	L4	NO	Square	500A	1s	60s	Stationary Electrical Test
Sample 5	Rb2	Bb2	n/a	L1	YES	n/a	n/a	n/a	n/a	Electrically Treated Deformation Test
Sample 6	Rc2	Ba	n/a	L1	YES	Continuous	200A	n/a	n/a	Continuous EAF (200A)
Sample 7	Ra	Bc	n/a	L2	YES	Continuous	200A	n/a	n/a	Continuous EAF (200A)
Sample 8	Ra	Bb	n/a	L3	YES	Continuous	200A	n/a	n/a	Continuous EAF (200A)
Sample 9	Ra	Bc	n/a	L1	YES	n/a	n/a	n/a	n/a	Room Temperature Deformation to 5.08mm
Sample 10	Rc2	Bb	n/a	L1	YES	Square	1000A	1s	n/a	Room Temperature Deformation to 5.08mm and Single Pulse
Sample 11	Rb2	Bb2	n/a	L1	YES	Continuous	150A	n/a	n/a	Continuous EAF (150A)
Sample 12	Ra2	Ba2	n/a	L2	YES	Continuous	150A	n/a	n/a	Continuous EAF (150A)
Sample 13	Ra	Ba	n/a	L3	YES	Continuous	150A	n/a	n/a	Continuous EAF (150A)
Sample 14	Rb	Bc	n/a	L1	YES	Square	800A	0.5s	60s	EAF Square Wave (800A/.5s/60s)
Sample 15	Rb	Bc	n/a	L2	YES	Square	800A	0.5s	60s	EAF Square Wave (800A/.5s/60s)
Sample 16	Rc2	Bb2	n/a	L3	YES	Square	800A	0.5s	60s	EAF Square Wave (800A/.5s/60s)
Sample 17	Ra2	Kc2	n/a	L1	YES	Continuous	200A	n/a	n/a	Continuous EAF (200A) with Current Discontinuation
Sample 18	Rb	Kc	n/a	L1	YES	Square	500A	0.5s	60s	EAF Square Wave (500A/.5s/60s)

The average equivalent circular grain size for all samples in orientation 1 is given in Figure 8.13 along with a 95% lognormal confidence interval. As seen, there is not a great difference in the average grain size (3.82-7.48μm) or variance (2.41-8.45μm^2).

The results for the statistical tests are given in Table 8.4 and Table 8.5 for orientation 1. The values from the tests which are lower than 5% are highlighted in green to show the samples which do not provide statistical equality assuming a 95% confidence level.

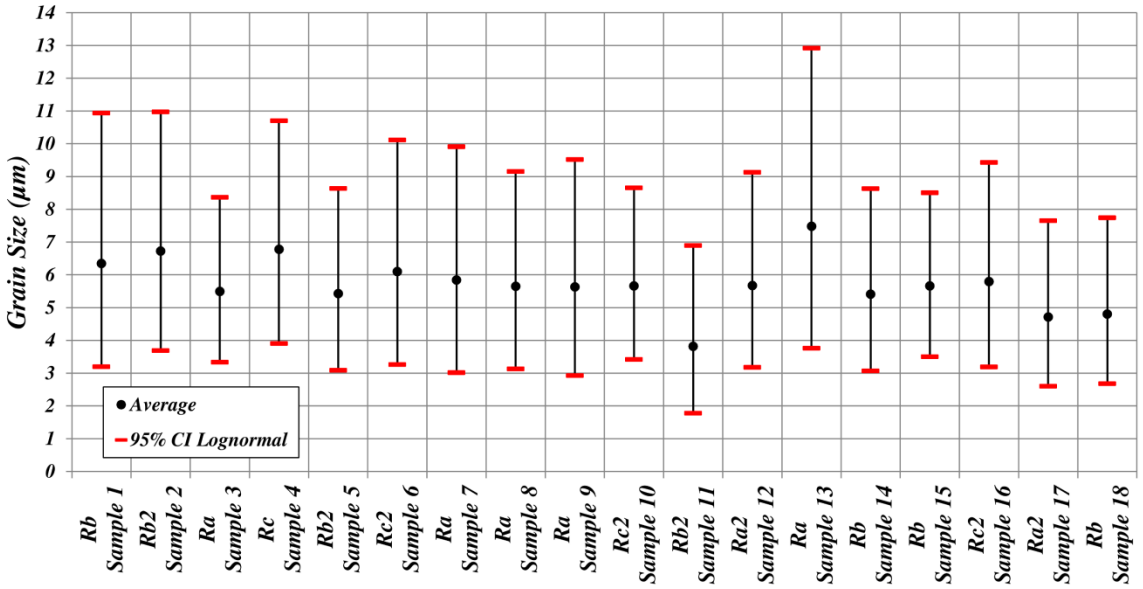

Figure 8.13 - Average and 95% Lognormal Confidence Interval for All Microstructure Samples in Orientation 1

Table 8.4 - Two Sample t-test Results for All Microstructure Samples in Orientation 1

		p-value from 2 Sample t-test (Welch's t-test)																	
		Sample 1 Rb	Sample 2 Rb2	Sample 3 Ra	Sample 4 Rc	Sample 5 Rb2	Sample 6 Rc2	Sample 7 Ra	Sample 8 Ra	Sample 9 Ra	Sample 10 Rc2	Sample 11 Rb2	Sample 12 Ra2	Sample 13 Ra	Sample 14 Rb	Sample 15 Rb	Sample 16 Rc2	Sample 17 Ra2	Sample 18 Rb
Sample 1	Rb	-	14.04	1.67	6.54	0.60	57.45	11.85	4.56	2.91	8.79	0.00	6.12	0.15	0.51	8.51	13.29	0.00	0.00
Sample 2	Rb2		-	0.00	72.52	0.00	3.21	0.13	0.02	0.02	0.07	0.00	0.04	5.93	0.00	0.04	0.15	0.00	0.00
Sample 3	Ra			-	0.00	59.84	5.69	41.77	74.43	98.06	48.58	0.00	63.27	0.00	54.16	39.63	37.13	0.01	0.04
Sample 4	Rc				-	0.00	1.07	0.02	0.00	0.00	0.01	0.00	0.01	10.68	0.00	0.00	0.03	0.00	0.00
Sample 5	Rb2					-	2.16	20.68	42.07	65.99	24.43	0.00	34.18	0.00	93.15	18.09	17.86	0.13	0.40
Sample 6	Rc2						-	29.61	13.25	8.54	23.41	0.00	17.09	0.01	1.84	23.82	32.68	0.00	0.00
Sample 7	Ra							-	64.53	45.86	90.02	0.00	74.89	0.00	18.25	96.38	94.22	0.00	0.01
Sample 8	Ra								-	75.56	73.06	0.00	88.68	0.00	37.81	64.74	59.16	0.01	0.03
Sample 9	Ra									-	52.38	0.00	65.61	0.00	60.63	44.80	41.55	0.07	0.21
Sample 10	Rc2										-	0.00	84.10	0.00	21.60	92.76	84.11	0.00	0.01
Sample 11	Rb2											-	0.00	0.00	0.00	0.00	0.00	0.00	0.00
Sample 12	Ra2												-	0.00	30.52	76.10	69.24	0.01	0.02
Sample 13	Ra													-	0.00	0.00	0.00	0.00	0.00
Sample 14	Rb														-	15.76	15.71	0.20	0.57
Sample 15	Rb															-	90.06	0.00	0.00
Sample 16	Rc2																-	0.00	0.00
Sample 17	Ra2																	-	65.14
Sample 18	Rb																		-

Less than 5%

Mirrored

Table 8.5 - Average of Levene and Bartlett Results for All Microstructure Samples in Orientation 1

		Average p-value from Levene and Bartlett Tests																	
		Sample 1 Rb	Sample 2 Rb2	Sample 3 Ra	Sample 4 Rc	Sample 5 Rb2	Sample 6 Rc2	Sample 7 Ra	Sample 8 Ra	Sample 9 Ra	Sample 10 Rc2	Sample 11 Rb2	Sample 12 Ra2	Sample 13 Ra	Sample 14 Rb	Sample 15 Rb	Sample 16 Rc2	Sample 17 Ra2	Sample 18 Rb
Sample 1	Rb	-	41.57	3.67	27.78	44.44	91.17	75.17	65.95	86.32	5.09	87.57	34.23	67.71	33.56	0.78	38.08	39.83	11.89
Sample 2	Rb2		-	19.65	77.70	85.44	47.42	58.78	69.66	41.06	22.70	33.04	89.70	20.63	86.08	5.99	77.37	78.01	46.30
Sample 3	Ra			-	32.51	15.77	4.18	5.89	8.13	2.98	97.26	2.76	23.14	0.84	23.17	51.82	19.81	18.63	56.19
Sample 4	Rc				-	73.14	32.20	40.62	50.45	27.77	35.79	21.27	87.55	12.56	82.01	12.01	73.97	74.66	66.22
Sample 5	Rb2					-	50.34	62.70	73.30	42.41	18.36	35.95	84.42	21.33	83.06	3.84	89.89	92.54	42.57
Sample 6	Rc2						-	83.82	73.70	89.52	5.67	78.74	39.17	58.81	38.25	0.82	43.09	45.02	14.22
Sample 7	Ra							-	88.70	74.49	7.85	62.82	49.46	43.90	48.57	1.26	54.40	56.71	18.64
Sample 8	Ra								-	64.51	10.16	54.98	59.48	36.89	58.09	1.68	63.97	66.39	25.66
Sample 9	Ra									-	4.09	82.19	32.93	67.51	31.55	0.48	35.17	36.93	11.91
Sample 10	Rc2										-	4.03	26.17	1.36	26.02	53.09	22.37	21.05	59.02
Sample 11	Rb2											-	27.01	79.94	26.73	0.63	30.85	32.38	8.44
Sample 12	Ra2												-	15.48	93.37	6.77	84.51	85.09	54.51
Sample 13	Ra													-	14.71	0.11	16.92	18.06	4.15
Sample 14	Rb														-	6.41	90.99	90.28	55.83
Sample 15	Rb															-	4.98	4.57	23.94
Sample 16	Rc2																-	97.37	51.10
Sample 17	Ra2																	-	48.99
Sample 18	Rb																		-

Less than 5%

Mirrored

The average equivalent circular grain size for all samples in orientation 2 is given in Figure 8.14 along with a 95% lognormal confidence interval. Again, there is not a great difference in the average grain size (4.18-7.01μm) or variance (1.66-5.77μm^2) for all the samples examined in this work.

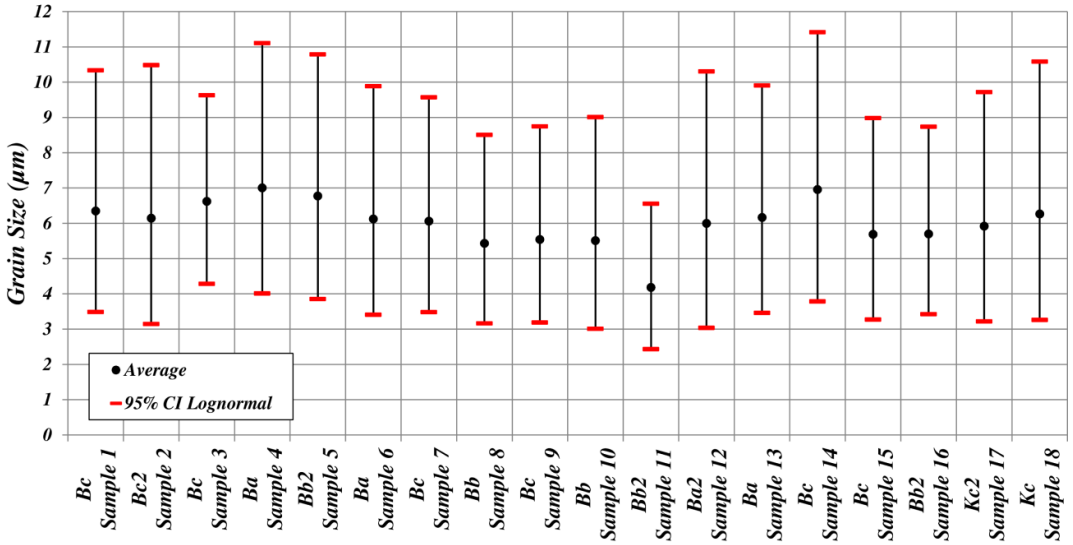

Figure 8.14 - Average and 95% Lognormal Confidence Interval for All Microstructure Samples in Orientation 2

The results for the statistical tests (t-test and Levene/Bartlett tests) are given in Table 8.6 and Table 8.7 for orientation 2. The values from the tests that are lower than 5% are highlighted in green to show the samples which are not statistical equivalent assuming a 95% confidence level.

Table 8.6 - Two Sample t-test Results for All Microstructure Samples in Orientation 2

	p-value from 2 Sample t-test (Welch's t-test)																	
	Sample 1 Bc	Sample 2 Bc2	Sample 3 Bc	Sample 4 Ba	Sample 5 Bb2	Sample 6 Ba	Sample 7 Bc	Sample 8 Bb	Sample 9 Bc	Sample 10 Bb	Sample 11 Bb2	Sample 12 Ba2	Sample 13 Ba	Sample 14 Bc	Sample 15 Bc	Sample 16 Bb2	Sample 17 Kc2	Sample 18 Kc
Sample 1 Bc	-	36.42	11.27	2.07	15.34	51.70	38.08	0.09	0.47	0.27	0.00	15.17	57.49	7.97	4.36	3.31	17.29	64.73
Sample 2 Bc2		-	1.34	0.19	2.67	84.63	90.82	2.87	7.89	4.91	0.00	60.66	69.72	1.24	27.33	29.17	62.29	66.14
Sample 3 Bc			-	33.99	93.22	3.89	0.82	0.00	0.00	0.00	0.00	0.26	2.55	62.08	0.04	0.00	0.47	4.50
Sample 4 Ba				-	46.91	0.73	0.10	0.00	0.00	0.00	0.00	0.03	0.35	75.75	0.00	0.00	0.07	0.75
Sample 5 Bb2					-	5.80	2.17	0.00	0.00	0.00	0.00	0.71	4.88	71.74	0.13	0.05	1.02	7.10
Sample 6 Ba						-	91.90	2.55	6.57	4.16	0.00	49.83	87.35	2.94	22.15	23.40	51.57	82.85
Sample 7 Bc							-	1.03	3.84	2.27	0.00	50.05	76.02	0.96	19.40	19.15	52.33	71.77
Sample 8 Bb								-	66.75	92.35	0.00	11.07	0.53	0.00	35.68	18.97	13.15	0.72
Sample 9 Bc									-	76.11	0.00	23.66	2.11	0.00	59.48	40.21	26.16	2.49
Sample 10 Bb										-	0.00	15.72	1.24	0.00	43.30	26.67	17.82	1.49
Sample 11 Bb2											-	0.00	0.00	0.00	0.00	0.00	0.00	0.00
Sample 12 Ba2												-	35.23	0.31	55.99	63.84	99.97	34.12
Sample 13 Ba													-	2.28	12.47	11.52	37.70	94.18
Sample 14 Bc														-	0.06	0.02	0.46	3.51
Sample 15 Bc															-	84.95	57.65	12.64
Sample 16 Bb2																-	65.64	12.09
Sample 17 Kc2																	-	36.37
Sample 18 Kc																		-

Less than 5%

Mirrored

Table 8.7 - Average of Levene and Bartlett Results for All Microstructure Samples in Orientation 2

		Average p-value from Levene and Bartlett Tests																	
		Sample 1	Sample 2	Sample 3	Sample 4	Sample 5	Sample 6	Sample 7	Sample 8	Sample 9	Sample 10	Sample 11	Sample 12	Sample 13	Sample 14	Sample 15	Sample 16	Sample 17	Sample 18
		Bc	Bc2	Bc	Ba	Bb2	Ba	Bc	Bb	Bc	Bb	Bb2	Ba2	Ba	Bc	Bc	Bb2	Kc2	Kc
Sample 1	Bc	-	35.66	0.36	37.01	45.90	83.66	59.19	13.15	47.33	67.90	41.34	16.47	85.08	41.15	36.06	8.59	63.20	76.99
Sample 2	Bc2		-	0.02	7.61	12.54	35.87	14.48	1.53	10.64	18.63	8.46	65.90	26.72	10.46	9.25	0.94	21.10	32.20
Sample 3	Bc			-	4.28	7.04	1.76	1.58	14.55	3.26	1.36	3.19	0.00	0.65	7.23	9.05	24.37	4.85	1.40
Sample 4	Ba				-	74.90	53.94	70.95	55.54	82.85	63.94	92.50	2.57	48.13	80.26	87.76	40.93	72.93	49.83
Sample 5	Bb2					-	59.08	77.48	56.21	90.96	70.16	76.93	5.84	56.00	94.56	87.91	42.32	82.28	54.35
Sample 6	Ba						-	75.77	24.25	62.94	83.13	58.57	19.92	86.99	54.90	49.86	17.06	75.80	95.26
Sample 7	Bc							-	29.78	78.77	86.47	71.96	6.55	79.05	67.95	60.62	20.65	70.98	72.87
Sample 8	Bb		Less than 5%						-	35.54	22.07	40.85	0.39	15.07	50.13	58.78	88.32	33.32	14.31
Sample 9	Bc									-	77.41	86.68	4.36	60.70	84.71	77.02	30.30	85.49	59.31
Sample 10	Bb										-	69.93	7.90	81.94	65.03	58.44	18.75	82.77	79.39
Sample 11	Bb2											-	2.88	53.26	82.54	83.09	34.91	74.17	54.01
Sample 12	Ba2												-	11.91	4.57	3.93	0.27	10.93	16.50
Sample 13	Ba													-	51.03	45.26	12.27	74.51	80.23
Sample 14	Bc			Mirrored											-	92.26	45.40	77.80	50.17
Sample 15	Bc															-	53.29	71.56	45.83
Sample 16	Bb2																-	30.79	13.17
Sample 17	Kc2																	-	72.03
Sample 18	Kc																		-

8.3 - Room Temperature Deformation Microstructure

The microstructure of the room temperature deformation (Sample 1) was examined in orientation 1 and 2 at the fracture location (L1). The room temperature test had approximately 22% strain imposed at material failure. The amount of strain imposed is significant on the final grain distortion from the original state. The micrographs are presented in Figure 8.15 and Figure 8.16 for orientation 1 and 2, respectively. As seen in Figure 8.15 the micrograph shows signs of material deformation by the change in the grain shape and the abundance of twin boundaries. The average grain size of the room temperature deformation microstructure in orientation 1 is 6.73µm with a standard deviation of 2.29µm. A few of the twin boundaries are denoted in Figure 8.15. Statistically, the mean grain size and variance is the same compared to the as-received material (Table 8.4 and Table 8.5). This can be physically explained by the deformation

altering the shape of the grains to be less equiaxed, but the grain area is still the same. Hence, the equivalent circular grain size and variance is statistically equal.

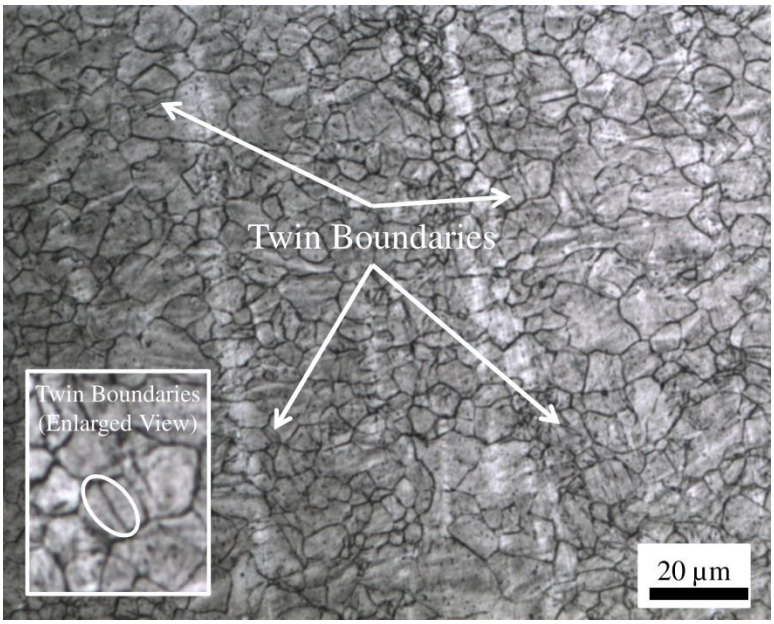

Figure 8.15 - Microstructure of Room Temperature Deformation (Sample 2) in Orientation 1 at L1

For orientation 2, it is noted that the grain shape is more changed which is represented by the jagged appearance of the grains and the grains being less equiaxed. Also, since this orientation is in line with the direction of loading, there is a significantly greater amount of twin boundaries present. A few of the boundaries are shown in the figure for reference. The average grain size of the room temperature deformation microstructure in orientation 2 is 6.15µm with a standard deviation of 2.33µm. Again, statistically, these values are equivalent in terms of equivalent grain size and variance to the as-received material. This can physically be explained by the grains still having the same area after deformation.

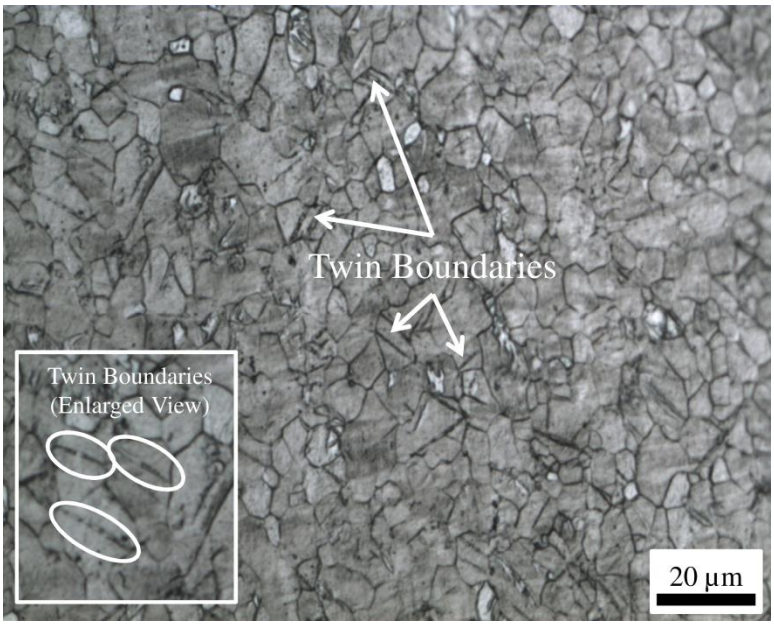

Figure 8.16 - Microstructure of Room Temperature Deformation (Sample 2) in Orientation 2 at L1

Overall, the microstructure of the room temperature deformation sample shows a less equiaxed grain structure with a significant amount of twinning. The presence of twinning is due to the limited number of slip systems active at room temperature for this material.

8.4 - EAF Microstructure

In the following sections various EAF micrographs are compared to the as-received material and to room temperature deformation micrographs in order to gain a better understand of material deformation during EAF.

8.4.1 - Stationary Electrical Square Wave Current Application

To examine the influence of an applied electrical square wave without any deformation, a test was performed where 500A was passed through the sample every 60s for a duration of 1s. This square wave was applied to the specimen for nine minutes

which equates to nine electrical pulses ($2.25x10^6$ J/Ω). The micrograph for orientation 1 is given in Figure 8.17 where a visual analysis suggests no alterations to the microstructure when it is compared to the as-received material.

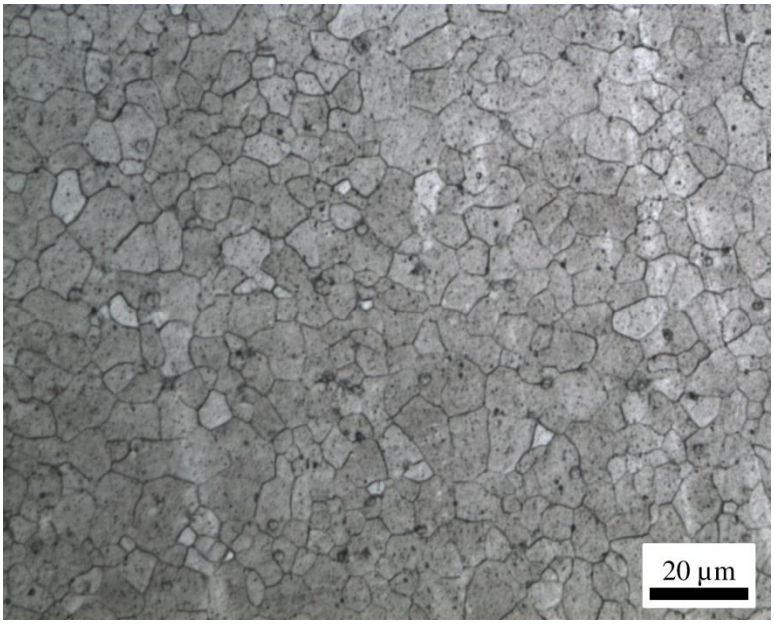

Figure 8.17 - Microstructure of Stationary Electrical Test (Sample 4) in Orientation 1 at L4

This sample was compared to the as-received material as no deformation was imposed. The average grain size for Sample 4 in orientation 1 is 6.78µm with a standard deviation of 2.13µm. From the statistical analysis, the visual results are confirmed in that the mean grain size and variance are equal.

The micrograph for orientation 2 is shown in Figure 8.18 where the average grain size is 7.01µm with a standard deviation of 2.22µm.

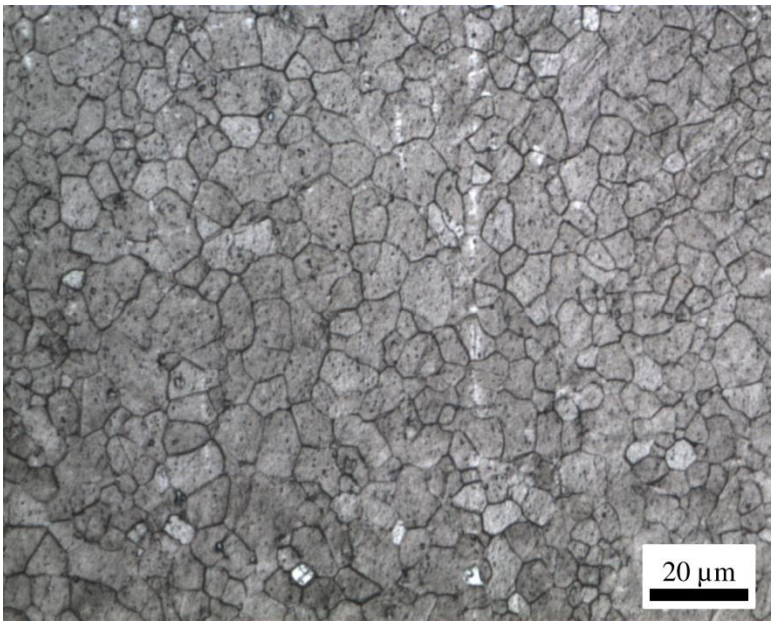

Figure 8.18 - Microstructure of Stationary Electrical Test (Sample 4) in Orientation 2 at L4

From a visual inspection, there appears to be no difference as compared to the as-received material in this orientation, however, the statistical analysis suggests that the means are not equal. However, the Levene/Bartlett tests suggest that the variances of the images are equivalent. The grain size in orientation 2 is slightly larger as compared to the as-received material and the reason for this may be due to a temperature rise of the material which allowed for a slight amount of grain growth which could have been favored in this orientation. Yet, there is no indication of a direct electrical effect on the material's grain size under stationary testing. From the mechanical testing in *Chapter 7* it was concluded that stationary electrical treating did not significantly alter the mechanical response. This is confirmed from this microstructure analysis as the material after electrical treating is mostly equivalent to the as-received material at this level of analysis. However, some dislocation annihilation may have occurred to the as-received material due to the applied electrical current. This type of analysis would need an additional study

to quantify the dislocation density before and after electrical treating. As a result of the grain sizes being mostly equal (orientation 2 is slightly larger in equivalent average grain size), the variation in *Chapter 7* would be attributed to the annihilation of dislocations or a change in dislocation density within the material's lattice (Figure 7.14).

After completing this test, another sample was tested where the same electrical treatment was performed and then the sample was deformed at room temperature to failure. This result is compared to the room temperature deformation sample (Sample 2). The micrographs for the electrically treated deformed sample in orientation 1 and 2 are shown in Figure 8.19 and Figure 8.20, respectively.

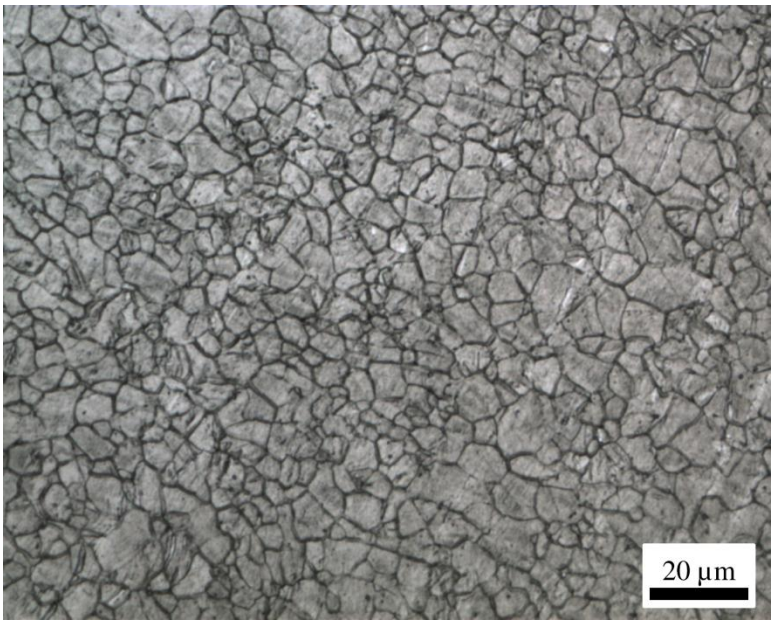

Figure 8.19 - Microstructure of Electrically Treated Deformation Test (Sample 5) in Orientation 1 at L1

From a visual comparison of orientation 1, the grain size of the electrically treated sample deformed at room temperature appears to have a smaller average grain size with approximately an equal amount of twinning. From the statistical analysis, it is said that

the means are not equivalent, but the variances are the same. The average equivalent grain size of the stationary electrical test in orientation 1 is 5.43µm with a standard deviation of 1.74µm as compared to 6.73µm with a standard deviation of 2.29µm for the deformation test of the as-received material in orientation 1

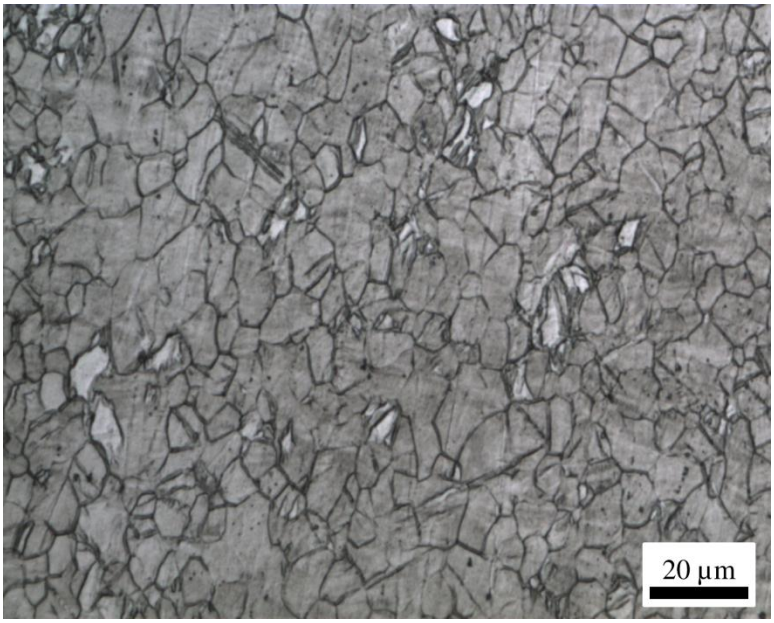

Figure 8.20 - Microstructure of Electrically Treated Deformation Test (Sample 5) in Orientation 2 at L1

. For orientation 2, a visual analysis suggests that grain size is slightly larger and the grains have become more elongated. The statistical analysis concluded that the means are not equal, but the variances are the same. The average equivalent grain size of the stationary electrical test in orientation 2 is 6.78µm with a standard deviation of 2.13µm as compared to 6.15µm with a standard deviation of 2.33µm for the deformation test of the as-received material in orientation 2. The variation in the mean and grain shape as compared to the as-received deformation sample (Sample 2) may be a result of the additional strain that was imposed on the material before failure (approximately 24%)

which is greater than that of Sample 2. This additional deformation could explain the greater amount of grain elongation and directional alignment shown in orientation 2 (Figure 8.20). As a result of the grains in orientation 2 becoming elongated more, the grains in orientation 1 reduced in grain size to maintain approximately the same grain volume. Thus, this additional amount of deformation could explain the observed micrograph differences despite the stationary electrical pretreating not altering the grain size/shape as described above.

8.4.2 - EAF with Square Wave Current Application

To examine the influence on an applied electrical current during EAF testing with a square wave current application, different electrical conditions were tested and analyzed. This section varies from the prior section in that the electrical square wave is applied during deformation.

The first test applied 800A at intervals of 60s for a duration of 0.5s and this application was continued until the specimen fractured. In addition to examining the microstructure at the fracture location (L1), this section examines a section at the middle of the specimen (L2), and a section from the region near the specimen fillet (L3). This was performed to determine if a microstructure gradient is present as a result of non-uniform local strains present during EAF (see *Chapter 5*). The resultant micrographs for orientation 1 are given in Figure 8.21 to Figure 8.23 for L3 to L1, respectively. From visual examination, there is a significant change from location L3 to L1 where the grain size decreases and is smallest at the fracture location (L1). This is in agreement with the prior results where the grain size decreases with greater amounts of strain. This gradient

in microstructure is observed here as the amount of local strain increases from L3 to L1 and in this orientation the grain decreases in overall diameter.

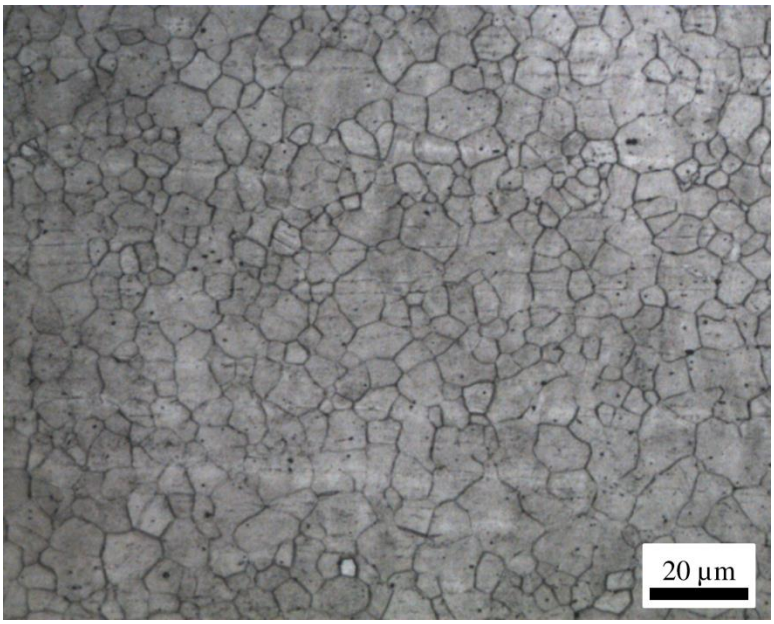

Figure 8.21 - Microstructure of EAF (800A-0.5s-60s) Test (Sample 16) in Orientation 1 at L3

The average grain size for the EAF (800A-0.5s-60s) test in orientation 1 at L3 is 5.80µm with a standard deviation of 1.96µm. For the same test at L2 the average grain size is 5.66µm with a standard deviation of 1.55µm and at L3 the average grain size is 5.41µm with a standard deviation of 1.74µm. Although the two sample t-test equates these three average grain sizes, it is clearly visible that the shape varies along the length of the test specimen. Again, this is physically due to the thermal gradients present during EAF which results in localized strains that vary along the length as compared to uniform room temperature deformation. It is also noted that there is a lower number of twin boundaries present in these micrographs as compared to the room temperature deformation micrograph.

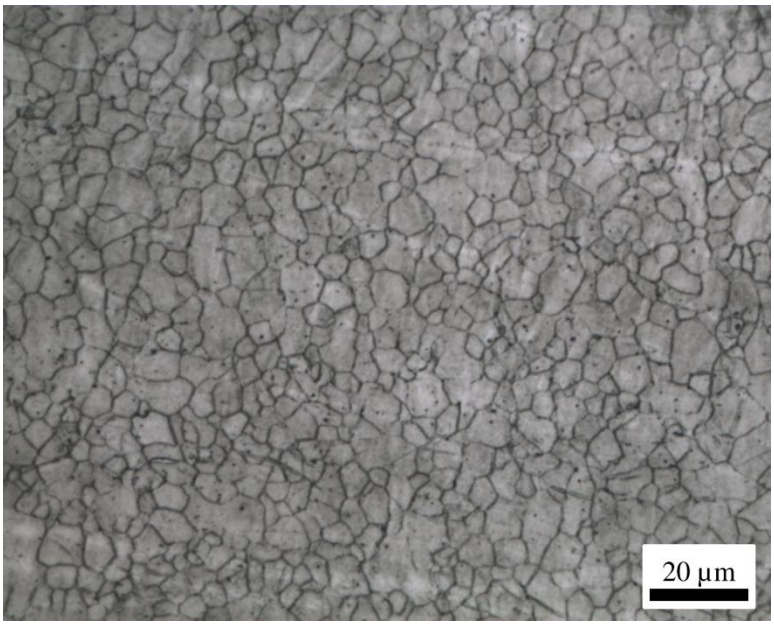

Figure 8.22 - Microstructure of EAF (800A-0.5s-60s) Test (Sample 15) in Orientation 1 at L2

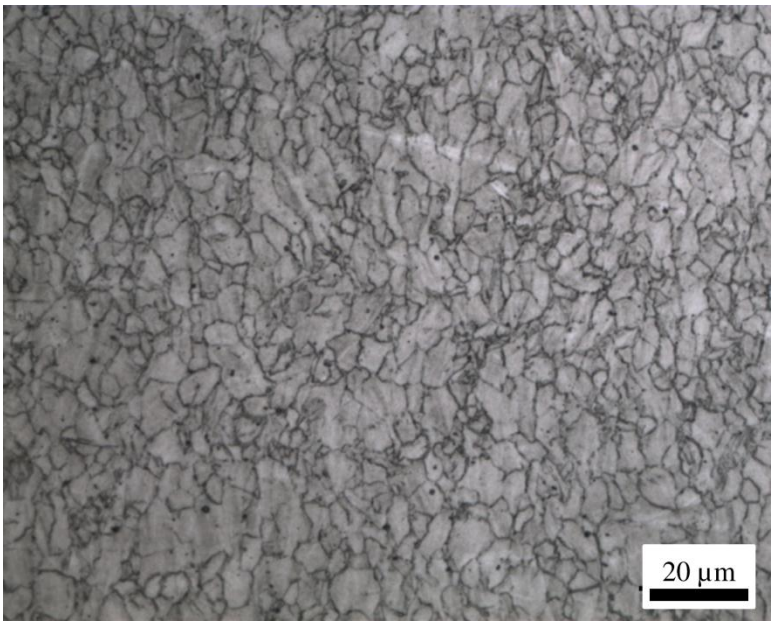

Figure 8.23 - Microstructure of EAF (800A-0.5s-60s) Test (Sample 14) in Orientation 1 at L1

Upon comparing these microstructure results (orientation 1) to the test deformed at room temperature in orientation 1 it is statistically observed that the mean is not equivalent even when comparing the results at L1. This is mainly a result of the difference in strain of these regions. In the test deformed at room temperature, the

material strain is uniform throughout its gauge section until localized necking occurs whereas the EAF test displays diffuse necking. Last, it is noted that the variances were statistically equivalent to the test deformed at room temperature (Sample 2) even though the grain size was not. Last, the EAF (800A-0.5s-60s) test displayed a reduce amount of material twinning which may be a result of the applied electrical current aiding in deformation by a temperature rise (Joule heating) and/or by direct electrical effects. This observance is discussed in more detail during the explanation of the electrical theory in *Chapter 10*.

A similar analysis was performed for orientation 2 and the micrographs are presented in Figure 8.24 to Figure 8.26 for the EAF (800A-0.5s-60s) test. From a visual analysis it is evident that a microstructure gradient exists within the test sample for this orientation as well. This is seen where the grains become less equiaxed from L3 toward L1 and the grain boundaries are more jagged indicating a greater amount of strain. The average grain size for the EAF (800A-0.5s-60s) test in orientation 2 at L3 is 5.7μm with a standard deviation of 1.66μm. For the same test and orientation at L2, the average grain size is 5.69μm with a standard deviation of 1.79μm and L1 has a grain size of 6.96μm with a standard deviation of 2.40μm. From the statistical analysis, the average grain size of L2 (Sample 15) and L3 (Sample 16) was equivalent, but L1 (Sample 14) was different from both L2 and L3. However, the variances for L1-L3 were equal. Again, it is noted that this orientation had a reduced amount of twin boundaries as compared to the micrographs of the room temperature deformation test.

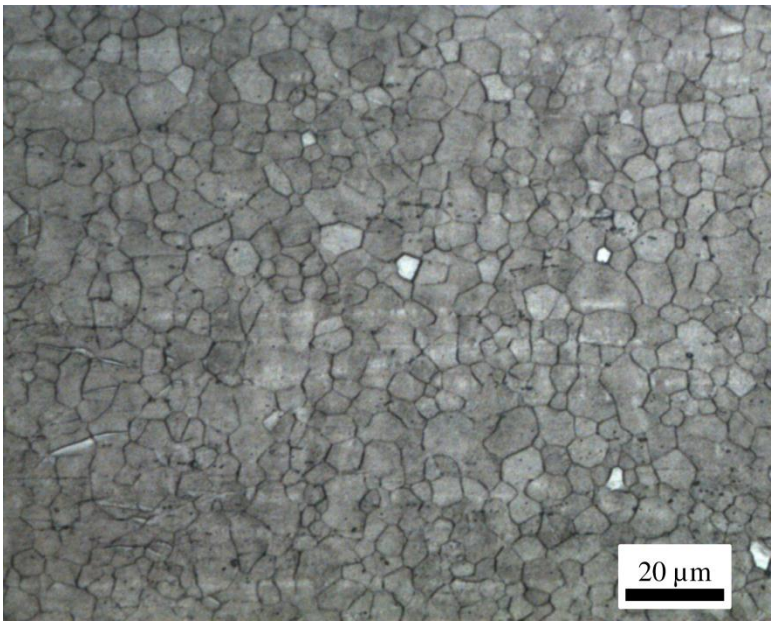

Figure 8.24 - Microstructure of EAF (800A-0.5s-60s) Test (Sample 16) in Orientation 2 at L3

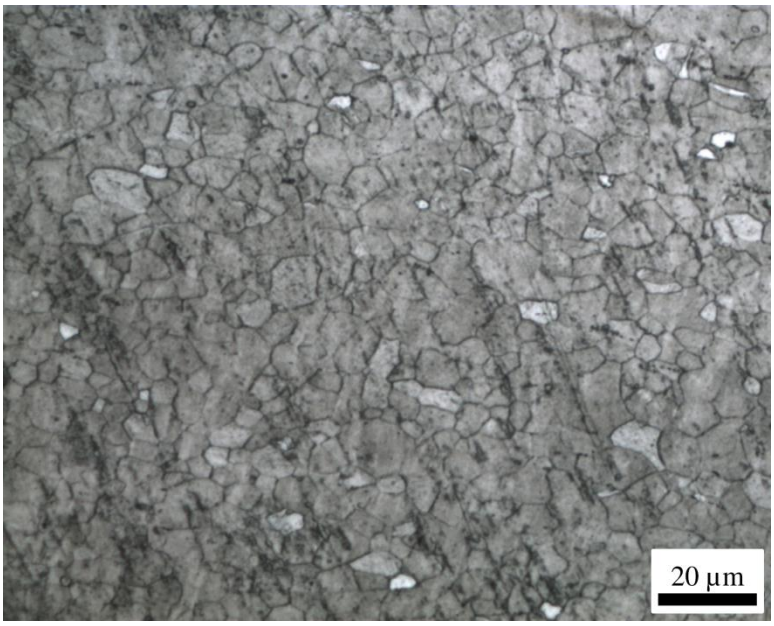

Figure 8.25 - Microstructure of EAF (800A-0.5s-60s) Test (Sample 15) in Orientation 2 at L2

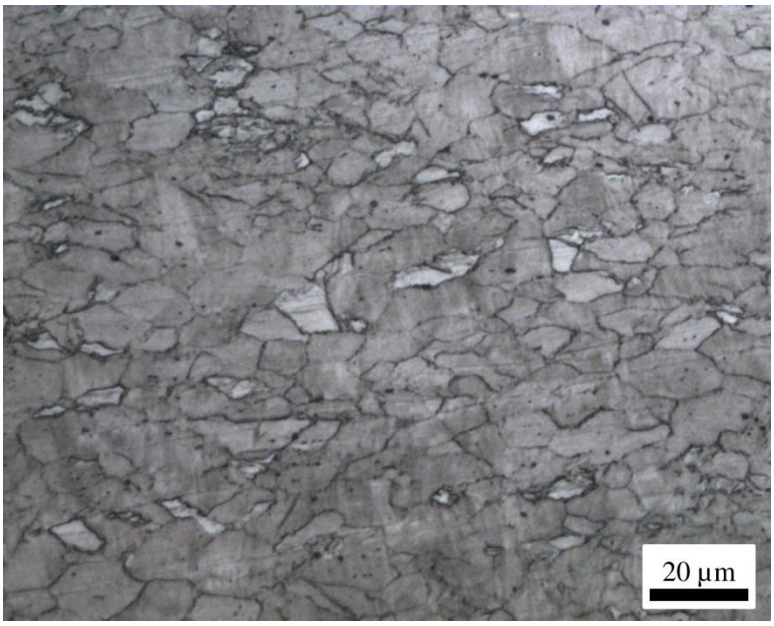

Figure 8.26 - Microstructure of EAF (800A-0.5s-60s) Test (Sample 14) in Orientation 2 at L1

To compare the EAF (800A-0.5s-60s) test to the room temperature deformation test (Sample 2) in orientation 2, it is statistically shown that the average grain size is different at the fracture region (L1). Again, this is a result of the strain difference due to the room temperature deformation having uniform strain with local necking and the EAF test having diffuse necking with non-uniform strain.

In addition to the EAF (800A-0.5s-60s) test, two other parameter sets were examined at L1. The results are presented for the 500A test with a pulse duration of 0.5s and a pulse period of 60s in Figure 8.27 and Figure 8.28 for orientation 1 and 2, respectively. Thus, only the current magnitude of the square wave is different as compared to the prior EAF test results.

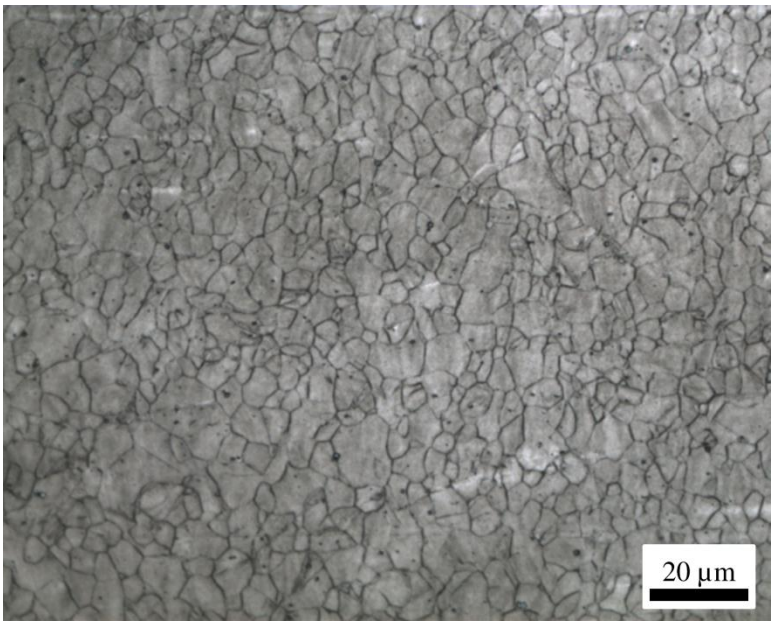

Figure 8.27 - Microstructure of EAF (500A-0.5s-60s) Test (Sample 18) in Orientation 1 at L1

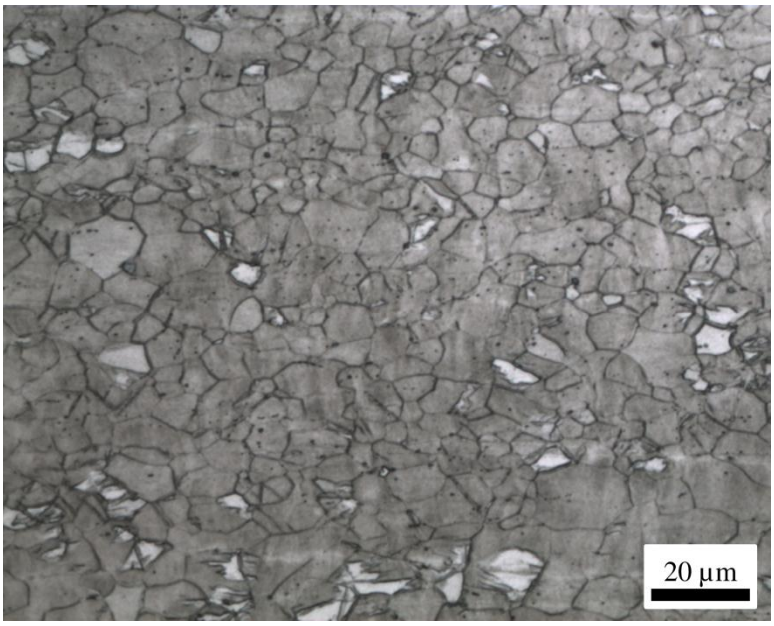

Figure 8.28 - Microstructure of EAF (500A-0.5s-60s) Test (Sample 18) in Orientation 2 at L1

The average grain size for the EAF (500A-0.5s-60s) test in orientation 1 is 4.80µm with a standard deviation of 1.59µm. In comparison to the EAF (800A-0.5s-60s) test, the grain size is smaller for the test with the lower current. Also, the statistically analysis shows that the grain sizes are not equivalent, but the variances are equal. It

should be noted that the shape of the grains are visually different between the 500A and 800A test where the 800A test has more jagged grain boundaries. This may be due to the difference in the amount of deformation imposed on the material before failure which affects the grain boundary appearance as a result of more slip planes being exposed on the surface of the grain boundary. In the 800A test the strain was approximately 27% as compared to the 500A test with a fracture strain of 22%. Again, the statistical analysis shows the average grain size is different as compared to the room temperature deformation test at L1 due to non-uniform strain for the EAF test. In addition, the EAF micrograph again displayed a reduced amount of twin boundaries as compared to the room temperature deformation test.

For orientation 2, the (500A-0.5s-60s) had an average grain size of 6.27μm with a standard deviation of 2.32μm at L1. This grain size is lower and statistically different than the 800A test (Sample 14), but the variances were statistically the same. This result is easily visualized and the additional amount of deformation for the 800A test is easily seen by the more elongated grains as compared to the 500A micrograph. In comparing the 500A test to the room temperature deformation test, the average grain size and variation is statistically equivalent. However, there was a reduced amount of twin boundaries present in the EAF test.

The third EAF square wave test was performed with a 500A current magnitude at a period of 60s with a 1s pulse duration until material failure. These electrical parameters are the same as the last test, however the pulse duration is doubled. The micrographs for

the 500A-1s-60s test for orientation 1 and 2 are given in Figure 8.29 and Figure 8.30, respectively.

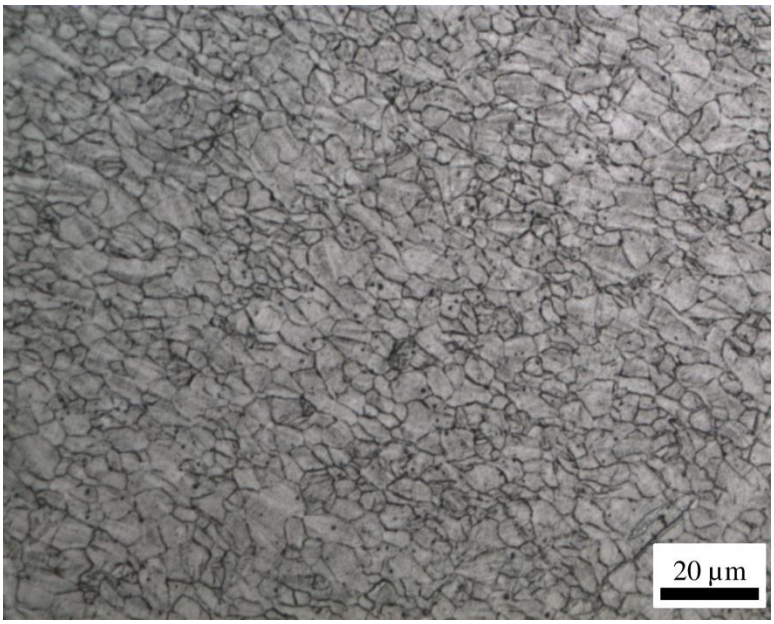

Figure 8.29 - Microstructure of EAF (500A-1s-60s) Test (Sample 3) in Orientation 1 at L1

The average grain size for the EAF (500-1s-60s) test in orientation 1 at L1 is 5.50µm with a standard deviation of 1.57µm. For comparison of this micrograph with the prior EAF testing conditions, it visually appears that the microstructure is similar to the EAF (800-0.5s-60s) test and is not the same as the EAF test with the same current magnitude (500A) with a shorter pulse duration (0.5s). This is statistically verified where Sample 3 has the same average grain size as compared to Sample 14, but not Sample 18. This may be a result of the inverse relation between the current magnitude and pulse duration where a smaller pulse duration coupled with a large current magnitude can produce a similar microstructure to a larger pulse duration with a smaller current magnitude. Comparing this EAF test with the room temperature baseline shows that the

statistical average grain size is different. Also, there appears to be a reduce amount of twin boundaries present in this EAF sample.

For orientation 2 of the EAF (500A-1s-60s) test at L1, the average grain size is 6.62μm with a standard deviation of 1.66μm. The statistical analysis shows that Sample 3 (500-1s-60s) is again equivalent to Sample 14 (800A-0.5s-60s), but not Sample 18 (500A-0.5s-60s) in terms of average grain size. Also, the grain size of Sample 3 is statistically different as compared to the room temperature deformation test as a result of the non-uniform deformation behavior of the EAF test. Moreover, there is a reduced amount of twinning present as was seen for the other EAF tests.

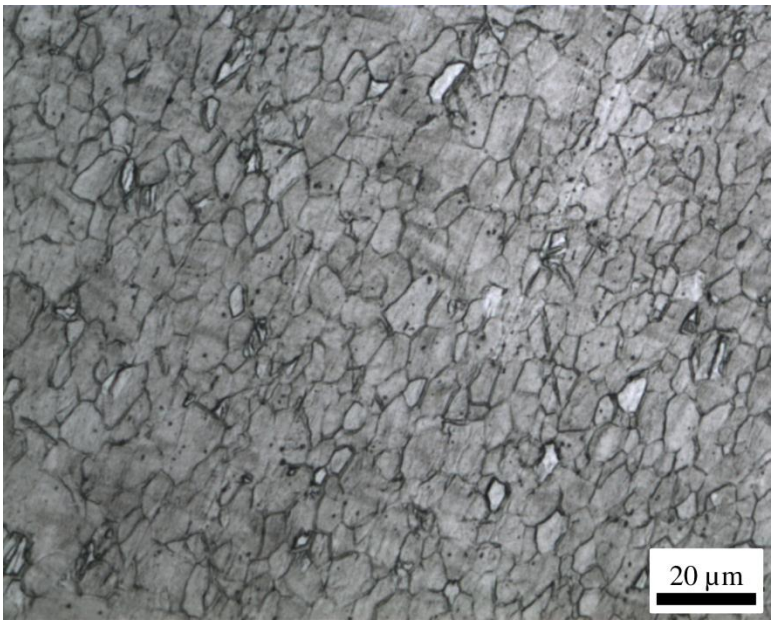

Figure 8.30 - Microstructure of EAF (500A-1s-60s) Test (Sample 3) in Orientation 2 at L1

8.4.3 - EAF with Continuous Wave Current Application

In this section the microstructure of EAF tests with a continuous wave are compared. Specifically, two current magnitudes (150A and 200A) are examined and the results are given at L1, L2, and L3 for each orientation. Also, a test where 200A is

applied for a set strain and then the material is deformed under conventional conditions (see Figure 7.22) is studied.

The micrographs are presented for the 150A continuous test (Figure 7.20) in orientation 1 at L3 to L1 in Figure 8.31 to Figure 8.33, respectively. From a visual examination, the grain size appears to decrease from the fillet region (L3) toward the fracture region (L1). From the statistical analysis, it is also confirmed that the grain sizes are different from L3, L2, and L1. For orientation 1, the average grain size at L3 is 7.49μm with a standard deviation of 2.91μm. For L2, the average grain size is 5.68μm with a standard deviation of 1.87μm; whereas, L1 has an average grain size of 3.82μm and a standard deviation of 1.64μm.

This microstructure gradient is suggested to be a result of the temperature and deformation gradient along the specimen length. A summary of the temperature results for the 150A test at L1, L2, and L3 with respect to time is shown in Figure 8.34. The temperature is greatest for L1 and is least for L3 as a result of the heat transfer of the testing setup. For the 150A continuous test (Figure 7.20), the stress and strain response of the test is suggestive of dynamic recrystallization due to the decreasing stress response after a peak stress is reached. This type of behavior has been noted in works performing elevated temperature forming of magnesium [8.3, 8.4]. The difference in this dissertation is that the temperature rise is a result of Joule heating within the material as compared to external heating in a chamber. Also, unlike external heating methods, a temperature gradient is present along the length of the specimen. Consequently, this allows for a variation in deformation behavior along the specimen length which corresponds to the

observed variation in microstructure. The localized deformation behavior is illustrated in Figure 8.35 where there is an extreme amount of localized deformation at L1. From a visual perspective it appears that L3 and L2 only have a small amount of deformation and the deformation is concentrated at L1. Also, it appears that dynamic recrystallization has occurred during forming at L1. This is a result of the higher temperature and additional strain which increases the internal energy of the lattice. Recrystallization is a process where strain free grains are nucleated and grain growth continues until the boundaries are impinged. The orientation 1 micrograph at L1 is suggestive of dynamic recrystallization due to a large quantity of smaller grains surrounded by a few coarse grains.

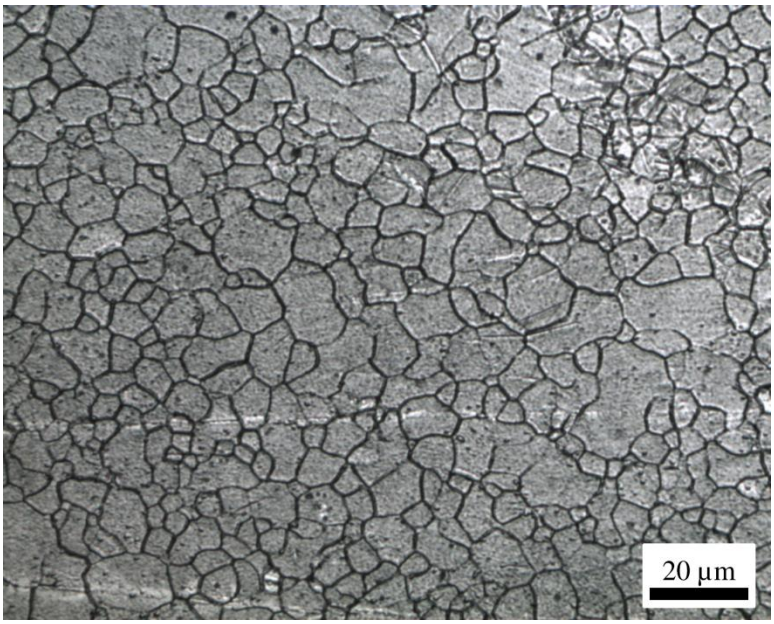

Figure 8.31 - Microstructure of Continuous EAF (150A) Test (Sample 13) in Orientation 1 at L3

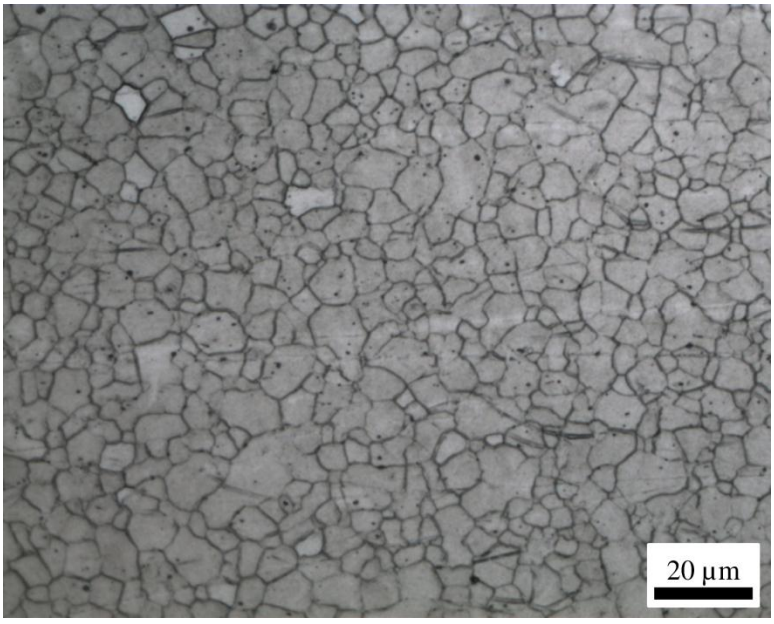

Figure 8.32 - Microstructure of Continuous EAF (150A) Test (Sample 12) in Orientation 1 at L2

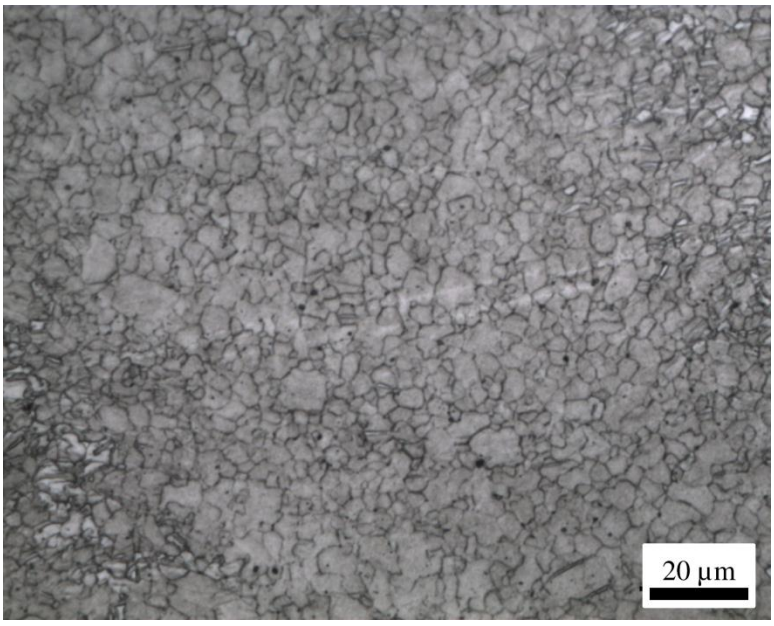

Figure 8.33 - Microstructure of Continuous EAF (150A) Test (Sample 11) in Orientation 1 at L1

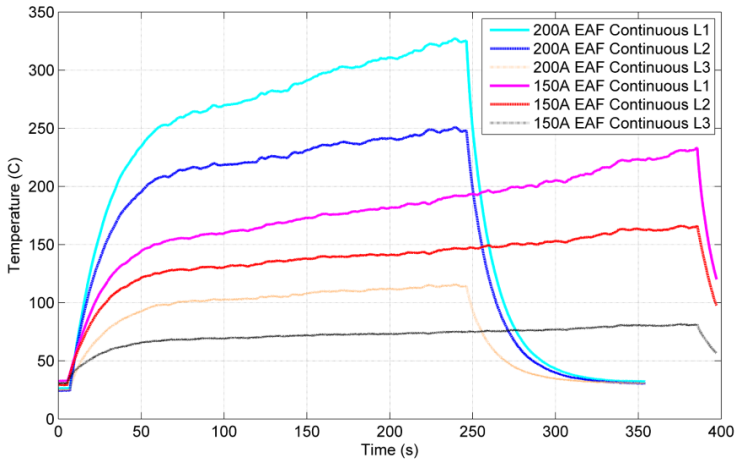

Figure 8.34 - Temperature Response for Continuous Current Application at L1, L2, and L3

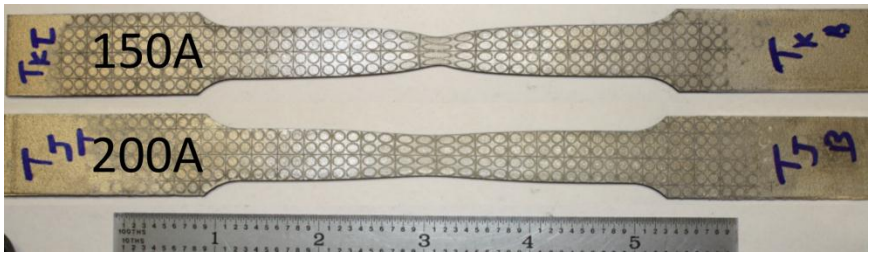

Figure 8.35 - Continuous EAF Tensile Specimens Tested at 150A and 200A

For orientation 2 of the 150A test, similar results are seen for the three locations. Again, L3 and L2 have larger grains with a small amount of deformation whereas L1 displays a recrystallized structure. From the statistical analysis, this is shown where Sample 11's average grain size is different from Sample 12 and Sample 13. The average grain size of Sample 13 (L3) and Sample 12 (L2) in orientation 2 is 6.16µm with a standard deviation of 2.02µm and 6.00µm with a standard deviation of 2.31µm, respectively. In comparison, Sample 11 (L1) in orientation 2 has an average grain size of 4.18µm with a standard deviation of 1.29µm.

Since this micrograph orientation depicts the microstructure along the deformation axis, a non-recrystallized structure would be extremely elongated in this axis (*e.g.* Figure 8.26). However, this is not the case and the grain structure is refined.

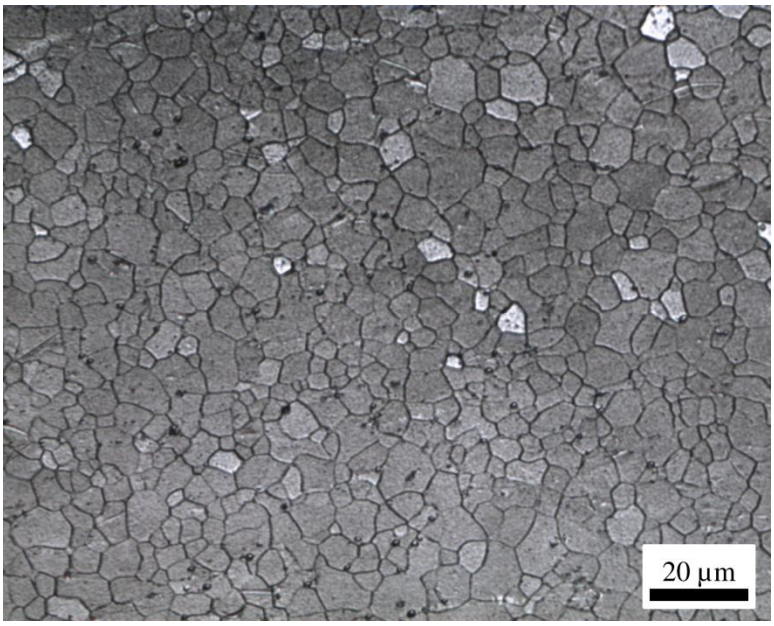

Figure 8.36 - Microstructure of Continuous EAF (150A) Test (Sample 13) in Orientation 2 at L3

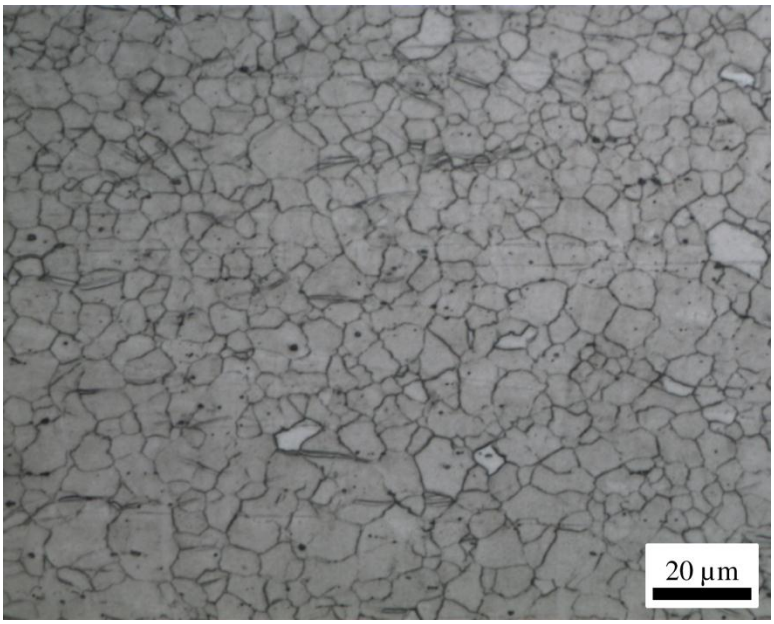

Figure 8.37 - Microstructure of Continuous EAF (150A) Test (Sample 12) in Orientation 2 at L2

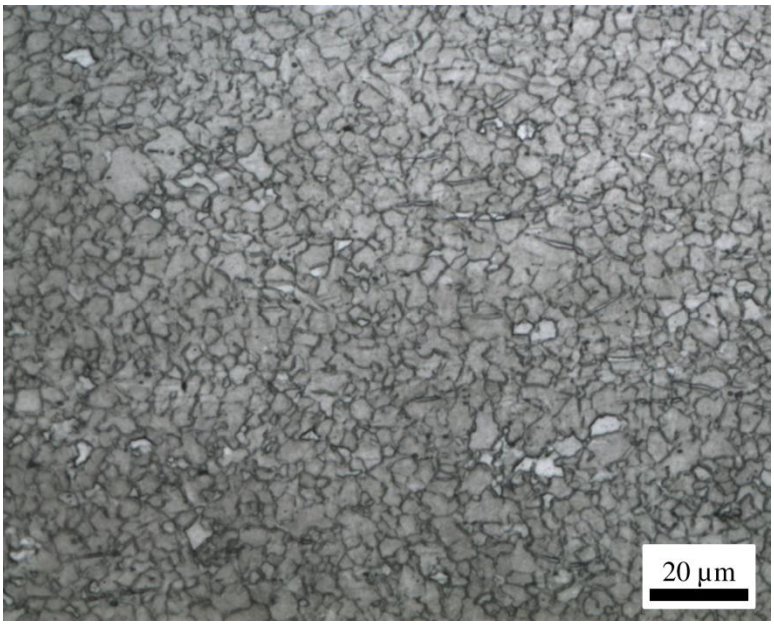

Figure 8.38 - Microstructure of Continuous EAF (150A) Test (Sample 11) in Orientation 2 at L1

The micrographs are presented for the 200A continuous test (Figure 7.20) in orientation 1 at L3 to L1 in Figure 8.39 to Figure 8.41, respectively. The average grain size for Sample 8 (L3) and Sample 7 (L2) in orientation 1 is 5.65µm with a standard deviation of 1.89µm and 5.84µm with a standard deviation of 2.18µm. Sample 6 (L1) has an average grain size of 6.10µm with a standard deviation of 2.16µm in orientation 1.

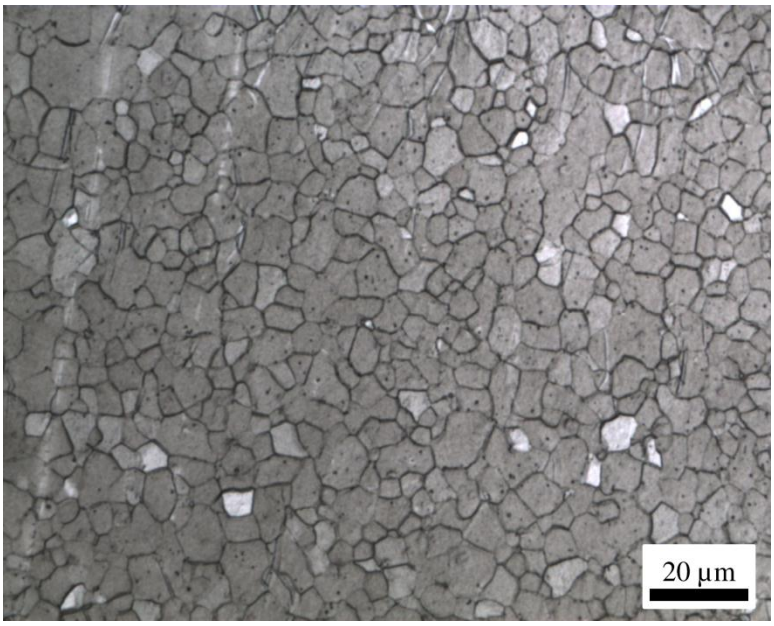

Figure 8.39 - Microstructure of Continuous EAF (200A) Test (Sample 8) in Orientation 1 at L3

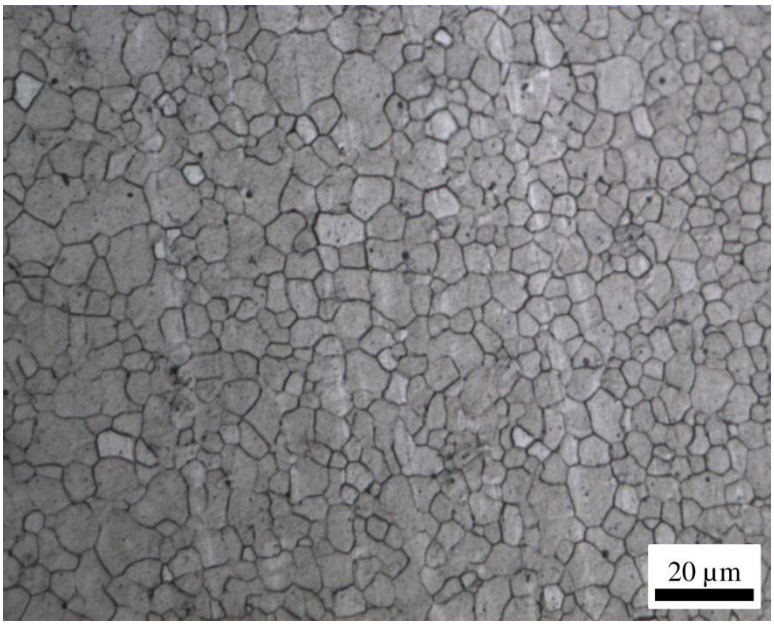

Figure 8.40 - Microstructure of Continuous EAF (200A) Test (Sample 7) in Orientation 1 at L2

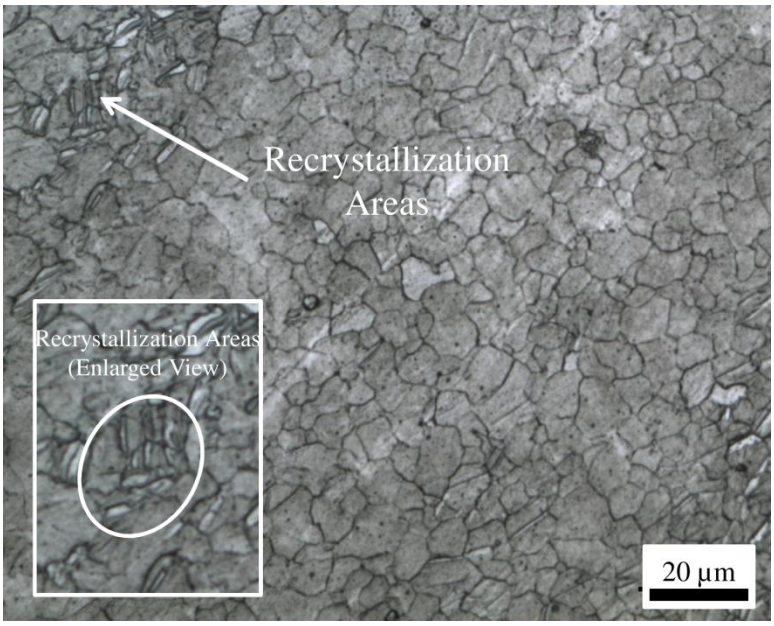

Figure 8.41 - Microstructure of Continuous EAF (200A) Test (Sample 6) in Orientation 1 at L1

As seen, similar trends are seen from this set of micrographs as compared to the 150A test (Sample 11-13). However, it is noted that the material has not recrystallized at L1 as small equiaxed grains are not present. Although the temperature is greater (Figure 8.34), it is reached for a shorter period of time and there is less localized deformation at L1 (Figure 8.35). However, there appears to be regions were the recrystallization process has started. This can be seen in the top left corner of Figure 8.41, however, the material has not completely recrystallized. It is also noted by the box containing an enlarged view. From the statistical analysis the average grain size and variance are all equivalent in this orientation for the 200A test. This is somewhat expected due to the low amount of strain imposed on the material (approximately 12%). This low amount of strain is a result of the test being terminated by the testing control system as the lower stress limit set by the controller was reached.

The results for orientation 2 of the 200A tests at L3 to L1 are given in Figure 8.42 to Figure 8.44, respectively. The average grain size for Sample 8 (L3) and Sample 7 (L2) in orientation 2 is 5.43µm with a standard deviation of 1.67µm and 6.06µm with a standard deviation of 1.91µm, respectively. Sample 6 (L1) has an average grain size of 6.12µm with a standard deviation of 2.03µm in orientation 2.

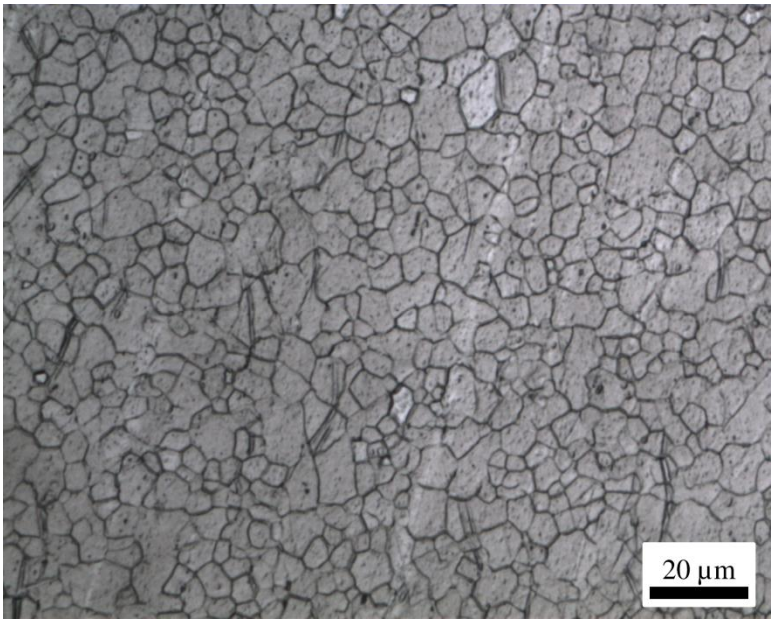

Figure 8.42 - Microstructure of Continuous EAF (200A) Test (Sample 8) in Orientation 2 at L3

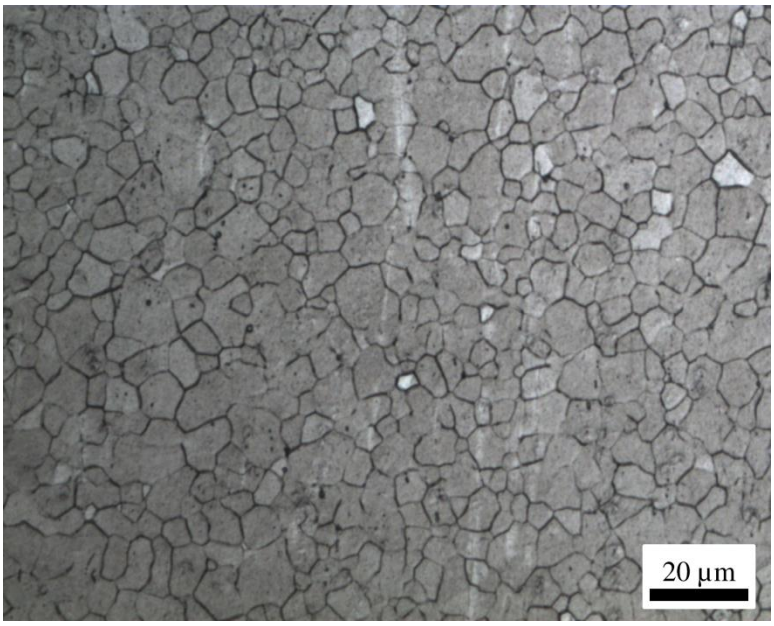

Figure 8.43 - Microstructure of Continuous EAF (200A) Test (Sample 7) in Orientation 2 at L2

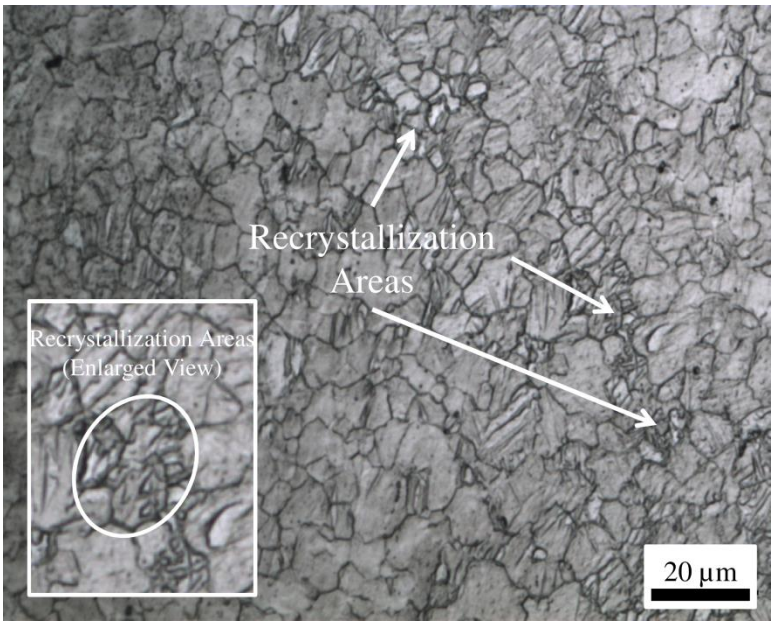

Figure 8.44 - Microstructure of Continuous EAF (200A) Test (Sample 6) in Orientation 2 at L1

The results are similar to the 150A test in orientation 2, but the micrograph at L1 is not fully recrystallized. This is in agreement with the results presented for orientation 1 at 200A at L1. As seen in Figure 8.44, there are regions where the material is beginning to recrystallize, but the material is not fully recrystallized as seen in the 150A test. This is

again is a result of the lower amount of strain imposed in addition to being subject to elevated temperatures for a shorter duration.

The last EAF continuous sample examined (Sample 17) was a test performed at 200A until a strain of 13.5% is reached, where the current was discontinued and the sample was then deformed to failure (Figure 7.22). The micrographs for this test at L1 are given in Figure 8.45 and Figure 8.46 for orientation 1 and orientation 2, respectively. The average grain size in orientation 1 is 4.71μm with a standard deviation of 1.59μm. For orientation 2, the average grain size is 5.92μm with a standard deviation of 2.05μm. From a visual perspective, it is shown that the grain diameter is reduced in orientation 1 and the grains are elongated in orientation 2 as compared to the as-received material. The aspect ratio (*i.e.* ratio of grain length to width) of Sample 17 is 1.87 on average, as compared to the as-received material with a value of 1.48. In comparison to the 200A continuous test without any additional deformation (Sample 6), orientation 1 shows a smaller average grain diameter due to the increased amount of strain which decreases the average grain size in this direction as a result of elongation in orientation 2. This is shown by the statistics where the mean grain size is not equivalent. For orientation 2, the test with additional deformation (Sample 17) shows elongated and jagged edge grains which indicate deformation at a lower temperature as compared to the 200A continuous test without any additional deformation (Sample 6). Also, it is seen in Figure 8.46 that there are twin boundaries as a result of additional deformation at lower temperatures.

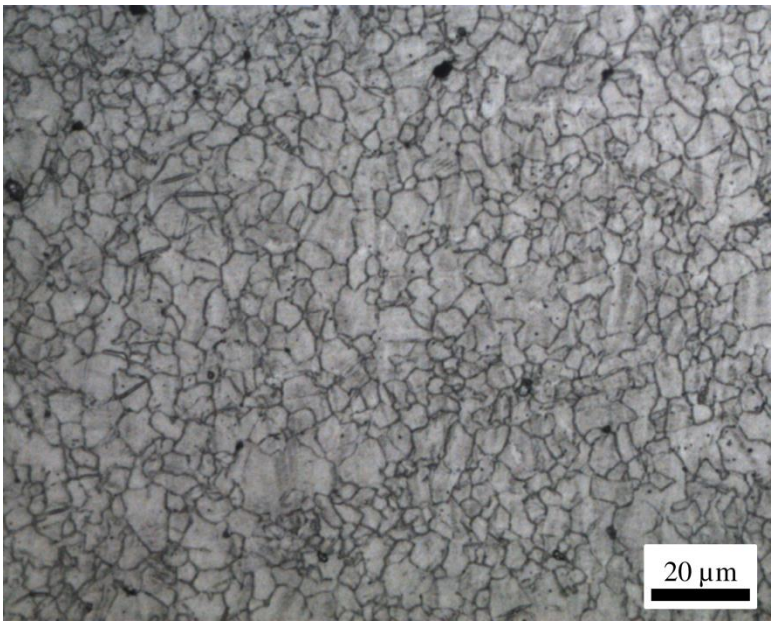

Figure 8.45 - Microstructure of Continuous EAF (200A) Test with Current Discontinuation (Sample 17) in Orientation 1 at L1

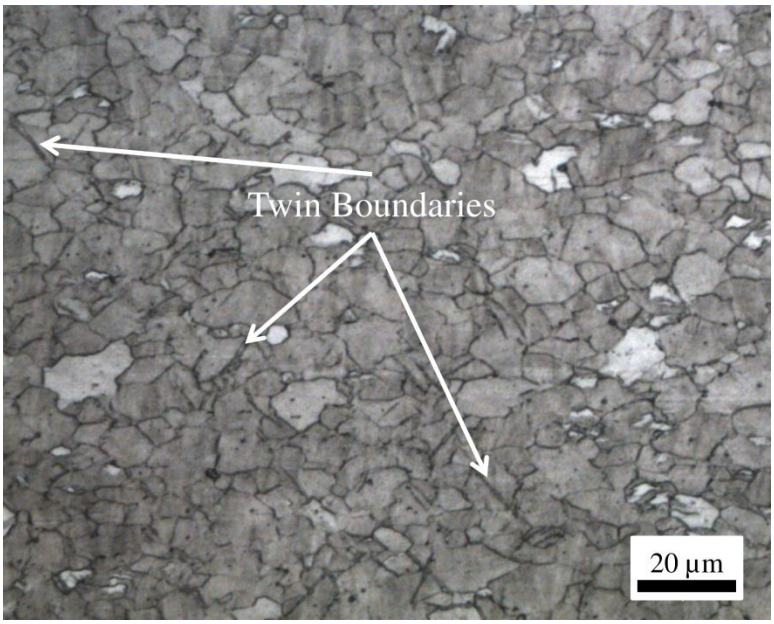

Figure 8.46 - Microstructure of Continuous EAF (200A) Test with Current Discontinuation (Sample 17) in Orientation 2 at L1

8.4.4 - EAF with Incremental Current Application

This section compares two samples where both are conventionally formed at room temperature a given displacement (5.08mm), however, one sample is supplied a pulse of current (1000A) for 1s prior to the sample's force being unloaded. The other sample is just unloaded. From *Chapter 7* it was seen that the sample with the applied current had a modified yield point after the sample was loaded with force (Figure 7.27). Thus, this section examines these two samples to determine if microstructural alterations (grain size/shape) were the cause of the reduced yield point.

The micrographs of the sample with only 5.08mm of deformation are given in Figure 8.47 and Figure 8.48 for orientation 1 and orientation 2, respectively. The average grain size in orientation 1 for Sample 9 is 5.63μm with a standard deviation 2.09μm; where, the grain size for Sample 9 in orientation 2 is 5.54μm with a standard deviation of 1.74μm. From a visual analysis, twin boundaries are present in both micrographs with a greater amount present in orientation 2.

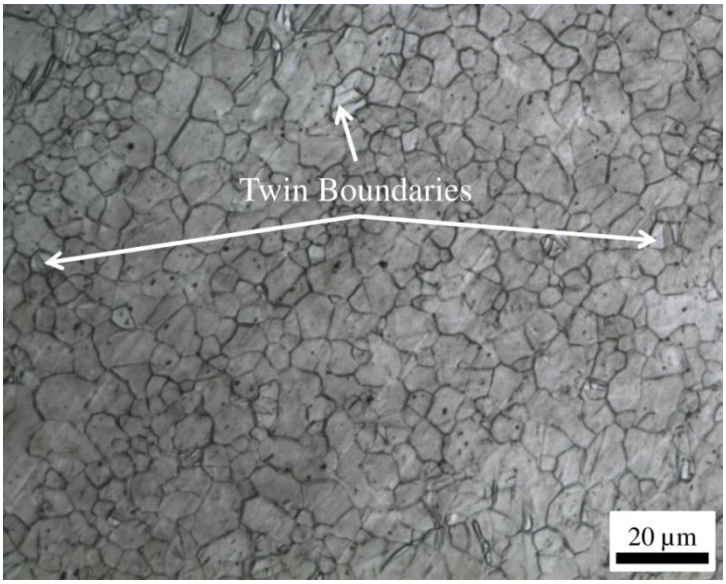

Figure 8.47 - Microstructure of Room Temperature Deformation to 5.08mm (Sample 9) in Orientation 1 at L1

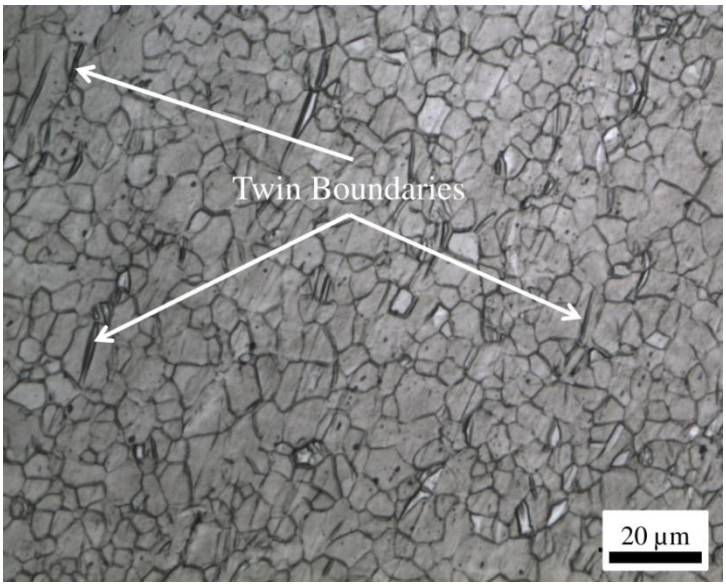

Figure 8.48 - Microstructure of Room Temperature Deformation to 5.08mm (Sample 9) in Orientation 2 at L1

The micrographs for the deformation test (5.08mm) with a single pulse of 1000A for 1s are given in Figure 8.49 and Figure 8.50 for orientation 1 and orientation 2, respectively. The average grain size of Sample 10 in orientation 1 is 5.66µm with a standard deviation of 1.63µm; where, orientation 2 has an average grain size of 5.51µm

with a standard deviation of 1.89μm. As seen, the results are very similar to the deformed test (Sample 9) with no electrical current application (grain size and amount of twinning). This is also statistically verified by the two sample t-test where the grain size means are equivalent for both orientations. However, the variances are only equivalent for orientation 2. Thus, it is suggestive that the reduced yield point (Figure 7.27) is a result of the interaction of heat generation/electroplasticity within the material lattice and not an alteration of the material grain size/shape. This interaction with the lattice is suggested to be a modification of the dislocation density within the material. Additional discussion and theory conclusions on this observance are given in *Chapter 10*.

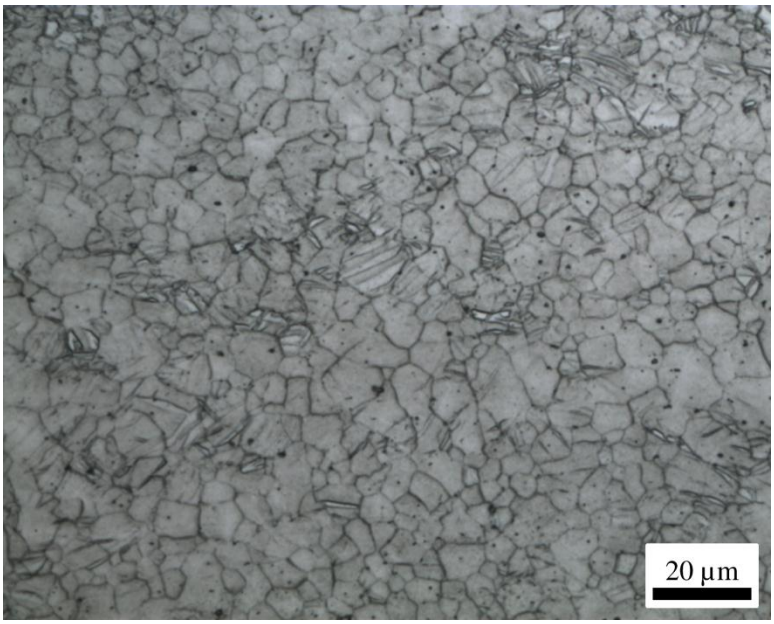

Figure 8.49 - Microstructure of Room Temperature Deformation to 5.08mm (Sample 10) with Single Electrical Pulse in Orientation 1 at L1

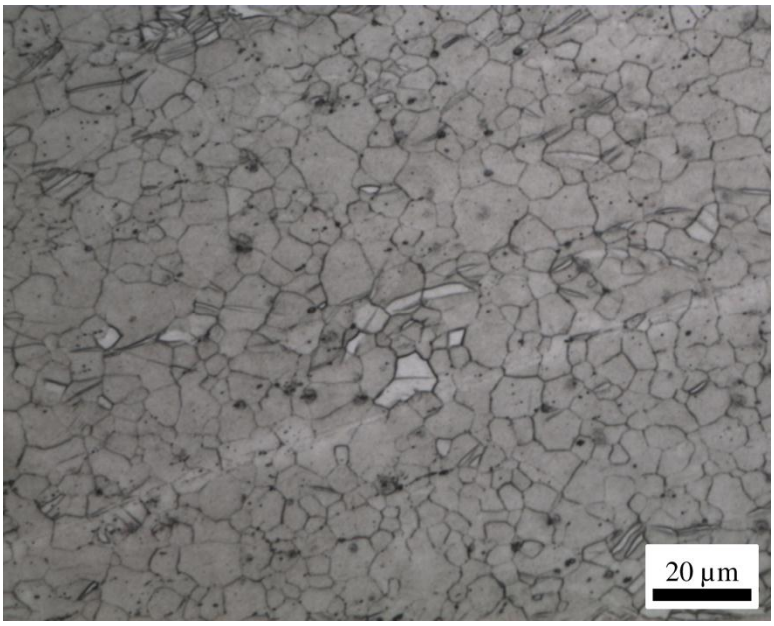

Figure 8.50 - Microstructure of Room Temperature Deformation to 5.08mm (Sample 10) with Single Electrical Pulse in Orientation 2 at L1

8.5 - Microstructure Analysis Conclusions

The main conclusions drawn from the analysis in this chapter are:

- The as-received material had an average grain size that is in agreement with literature. Also, this material was free from twin boundaries as a result of the material being warm rolled.
- The room temperature forming microstructure showed a deformed structure (non-equiaxed grains) and the presence of a large number of twin boundaries which were a result of the limited number of slip systems active at room temperature.
- The stationary electrical square wave (electrical treating) showed no indication of a direct electrical effect at the grain level. Consequently, the observed variation in the mechanical response is suggested to be a result of the applied current altering the dislocation density of the material.

- The square wave electrical tests all showed similar microstructures to the room temperature forming test, but the amount of twinning appeared to be reduced. This could be a consequence of the electrical current allowing for pinned dislocations to be freed thus reducing the necessity of twin boundary formation for continued deformation. Also, there was a microstructure gradient present due to the diffuse necking of the specimen (non-uniform strain). This non-uniform strain is a result of the thermal gradient in the specimen due to forming setup geometry. Overall for these tests, the grain size was affected by the amount of deformation imposed on the material and the current magnitude and pulse duration did not appear to modify the grain size to any significant level. Thus, this suggests that the microstructure is not affected by pulsed current, but the acting mechanism (thermal/electroplastic) for force reduction is occurring only at the atomic level (in the material's lattice).
- The continuous EAF tests also displayed a microstructure gradient along the specimen length due to non-uniform strain. Also, dynamic recrystallization was present at some locations and was dependent on the amount of strain, the temperature, and time at the elevated temperature.
- The EAF applied in an incremental manner is in agreement with the square wave electrical tests where the single pulse did not alter the grain size. As a result, the observed mechanical variation in the yield point is

suggested to be from heat/electroplastic contributions on the dislocation density of the material.

Overall, this study showed that EAF with various electrical conditions can alter the final microstructure, but it was more related to the local strain present as a result of the Joule heating causing thermal distributions within the sample. Thus, it is concluded that the observed bulk forming relations seen with EAF (reduced flow stress/increased elongation) is more connected with the interaction of dislocations which were not visible at the present scale examined. Although this work only considered one initial grain size, it is expected that starting initial grain size will influence the heat generated (Joule heating contribution) and thus the flow stress reduction by thermal softening. A reduced grain size will create a greater quantity of interactions between electrons and grain boundaries (*i.e.* greater electrical resistance), thus creating regions of greater atomic vibration or more heat generation. These local regions of greater heat generation will translate to a greater bulk temperature.

8.6- References for Chapter 8

[8.1] G.D. Ruxton (2006) "The Unequal Variance t-test is an Underused Alternative to the Student's t-test and the Mann-Whitney U test," *Behavioral Ecology*, Vol. 17, pp. 688-690.

[8.2] NIST-SEMATECH (2012) "Levene and Bartlett Tests," Engineering Statistics Handbook.

[8.3] T. Al-Samman and G. Gottstein (2008) "Dynamic Recrystallization during High Temperature Deformation of Magnesium," *Materials Science and Engineering*, Vol. 490, pp. 411-420.

[8.4] S.E. Ion, F.J. Humphreys, and S.H. White (1982) "Dynamic Recrystallization and the Development of Microstructure during the High Temperature Deformation of Magnesium," *Acta Metall.*, Vol. 30, pp. 1909-1919.

CHAPTER 9 - PROCESS CONTROL FOR EAF OF SHEET METALS

In this chapter, several control approaches are described for forming a metal under an electrical current field. In addition, the approaches are demonstrated and potential applications for these control schemes are discussed. The specific examples where closed-loop control is used to determine the process output is for constant force forming, constant stress forming, and constant current density forming. Last, the feasibility toward model based control (MBC) is discussed for the models developed in *Chapters 4-6*.

9.1- Constant Force Forming

The concept for constant force forming was realized from experimental testing where the current was manually modulated such that the forming force could be regulated to some extent (see Figure 7.15). Thus, a formal control strategy was envisioned that could regulate or maintain the force during forming at a specific set-point value. To achieve this, a block diagram (Figure 9.1) was first constructed to understand the flow of information and relationships. $F_{desired}$ is the desired force set point, *Force* is the force feedback from the process, ΔF is the force error, and V_{feed} is a feed voltage that the current source uses to output current I to the process.

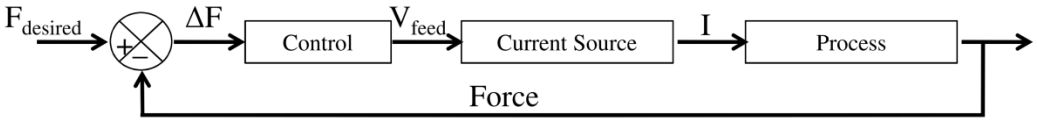

Figure 9.1 - Block Diagram for Constant Force Forming (No Force Correction)

To realize the goal of constant force forming, a Darrah Silicon Controlled Rectifier (SCR) with a current output of 0-4kA was used to supply the process with direct electrical current. To control the power supply, an external remote was built using a

National Instruments (NI) CompactRIO (cRIO) integrated controller/chassis containing various I/O modules programmed with NI LabVIEW software. A control schematic is presented in Figure 9.2, where a linear variable differential transformer (LVDT) provides displacement data (*d*) and a load cell provides the force data (*F*) to the analog input (AI) on the cRIO. Additionally, the measured current ($I_{measured}$) is collected using the AI on the cRIO. The cRIO interfaces with a computer which also records thermal data (*T*). The cRIO controls the power supply output (*I*) by applying a feed voltage (V_{feed}) from the analog output (AO).

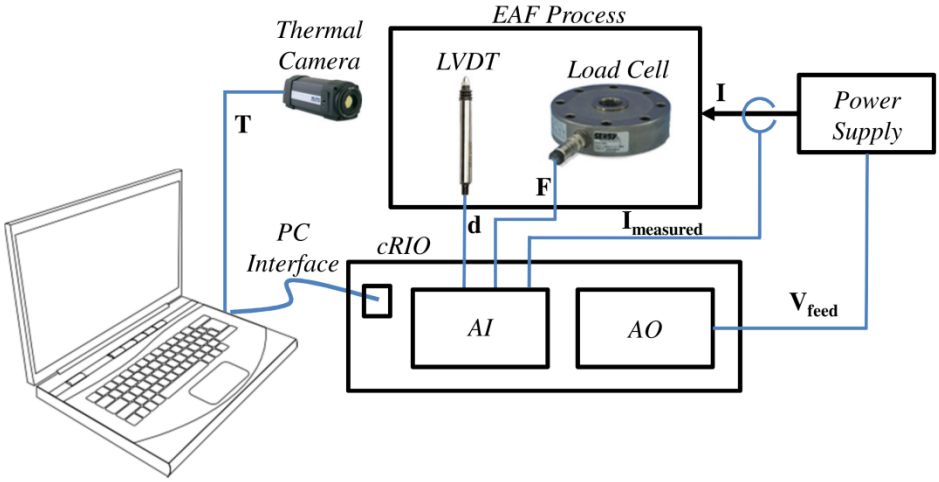

Figure 9.2 - Control Schematic using cRIO

For the current supply to provide the correct output to the process, a feed voltage with a linear relationship was established (See *Appendix D*). The feed voltage was used to communicate to the power supply to set the desired current output. Once the power supply control was established, the LabVIEW software was modified to specifically include a proportional-integral-derivative (*PID)* control block. A *PID* controller is a general controller which calculates an error between the set point value and the measured

result. Using this calculated error, the controller adjusts the process inputs to try to minimize the error. The controller has three terms (*P*, *I*, *D*) where *P* is dependent on the present error, *I* on the summation of past errors, and *D* is a prediction of future effort. For this control application, the gains for the integral (*I*) and derivative (*D*) were set to zero. Specific details on the graphical user interface (GUI) and LabVIEW control block diagram are given in *Appendix D*. For constant force forming, three force set points were tested to show the robustness of the control application.

The force results for constant force forming at 1334N (300lb), 1779N (400lb), and 2224N (500lb) are presented in Figure 9.3 along with the filtered result.

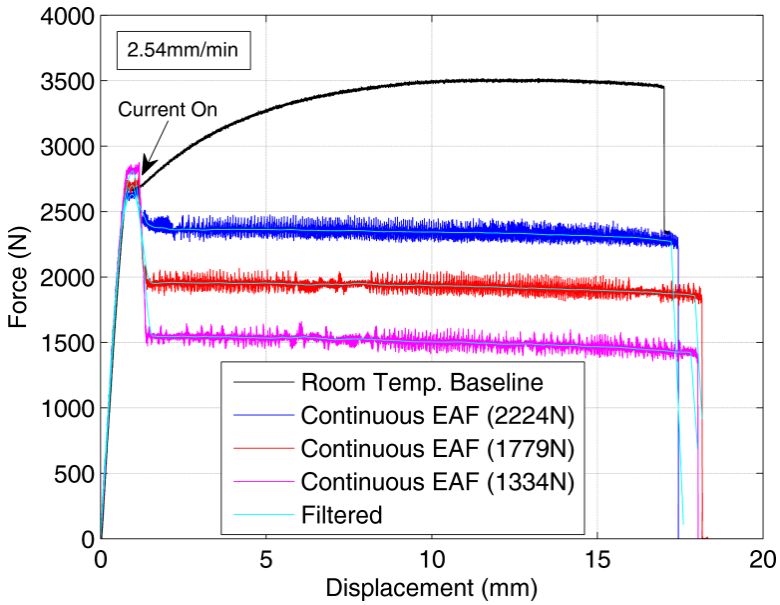

Figure 9.3 - Constant Force Forming at varying Set Points (No Force Correction)

As the control system is turned on just after the material's yield point, the applied current quickly drives the force to the desired set point. After reaching the desired set point value, the controller is capable of accurately modulating the applied current to maintain constant force forming until the specimen fractures. The conversion of the

constant force results to stresses are presented in Figure 9.4 where the true stress increases linearly as a result of the force maintaining a constant value. For this transformation, it was assumed that all the elongation was uniform.

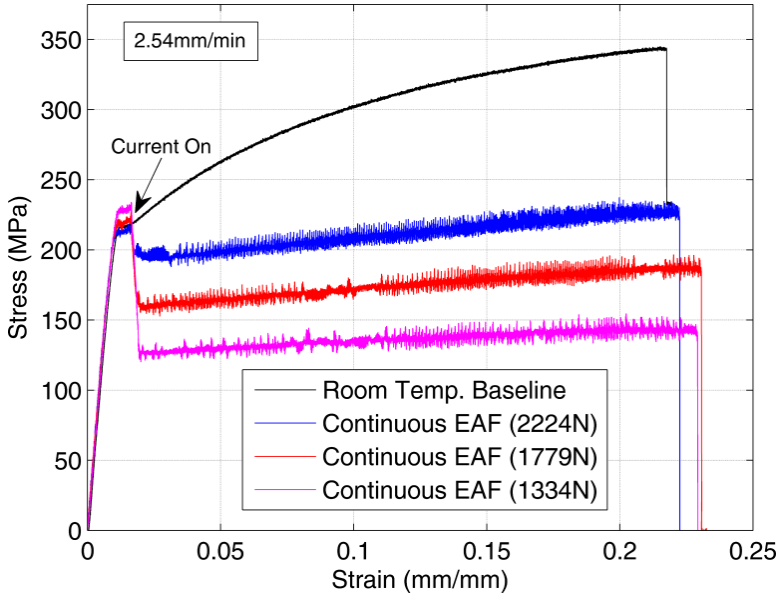

Figure 9.4 - Stress Response for Constant Force Forming (No Force Correction)

The current applied during the process is summarized in Figure 9.5 where a maximum allowable current was set (300A). As seen, the current quickly increases to the maximum allowable current value and then shortly decrease as the forming force is quickly reduced. After this initial spike, the current is modulated by the controller such that a constant force is maintained.

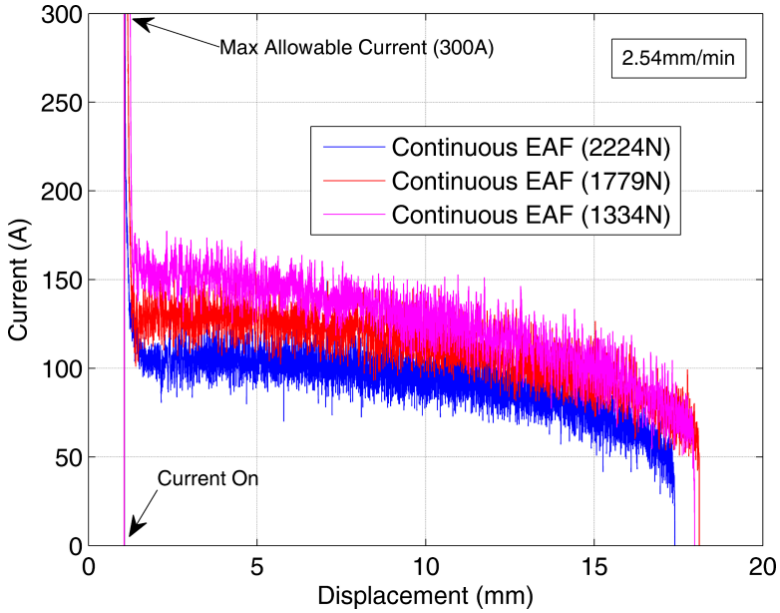

Figure 9.5 - Current Application during Constant Force Forming (No Force Correction)

Upon studying the actual steady state values in Figure 9.3, the experimental force output is greater than the set point value. This variation is a result of only using a proportional (*P*) controller as a non-zero error is needed to drive the controller. Hence, a *P* controller typically operates with a steady-state error or droop. To compensate for the droop of the controller, an additional correction factor or the integral portion of the *PID* controller can be added. The integral portion can be added to move the current process output to the desired set point by minimize the steady-state error. However, for this application, a simple correction factor was implemented such that the possibility of overshoot from the integral term was not presented. The modified block diagram for constant force forming is given in Figure 9.6. As seen, the process force output is corrected ($F_{corrected}$) prior to determining the error that gets provided to the controller.

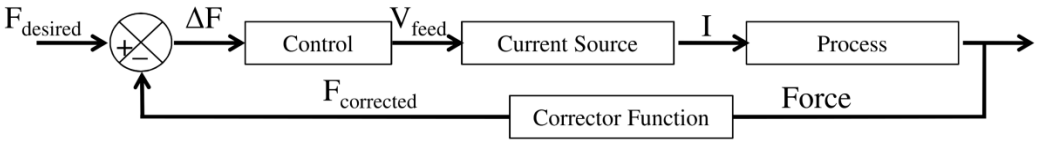

Figure 9.6 - Block Diagram for Constant Force Forming

The correction factor was determined from examining the results in Figure 9.3 and a linear fit was used to represent the correction. This correction is given in Figure 9.7 where the correction factor is a function of the desired set point.

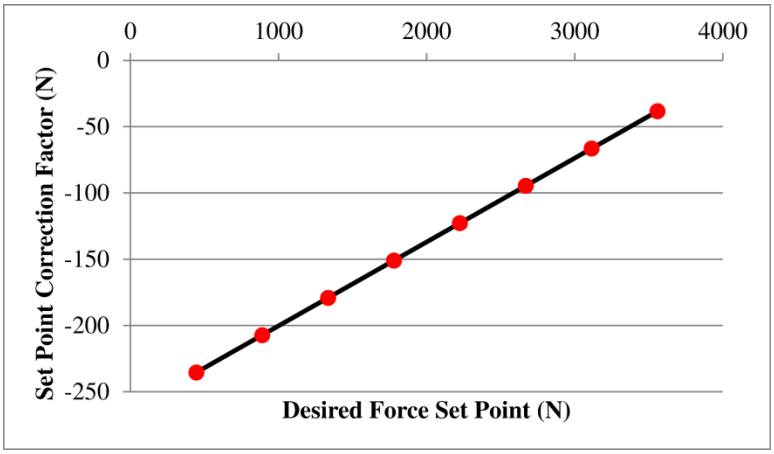

Figure 9.7 - Constant Force Forming Correction Factor

The correct constant force forming results are shown in Figure 9.8 and a filtered response is given in Figure 9.9.

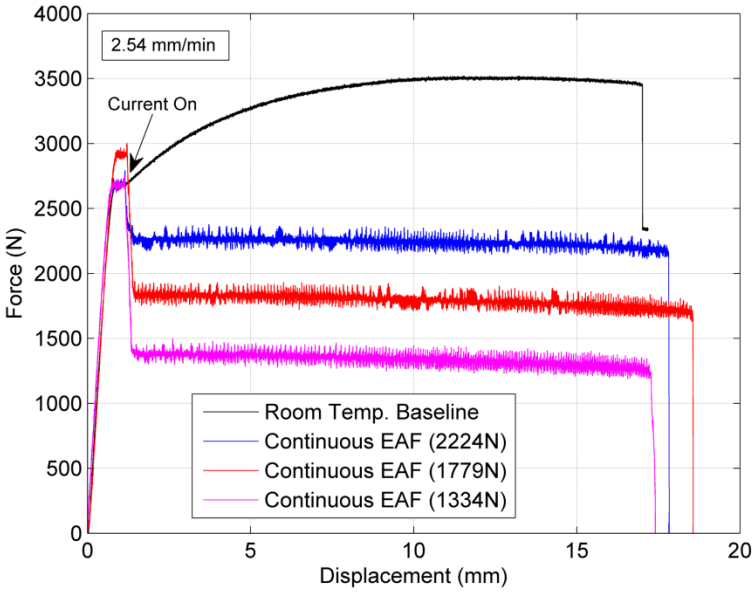

Figure 9.8 - Constant Force Forming at varying Set Points

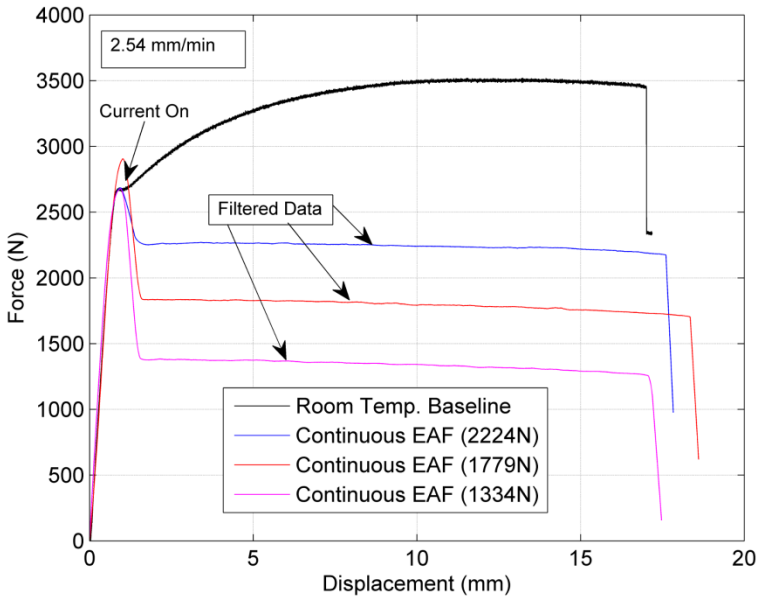

Figure 9.9 – Filtered Constant Force Forming Data

Figure 9.10 provides the force profiles converted to true stress and strain profiles for the constant force forming. Again, the true stress increases linearly as a result of the forming load being constant. A filtered response of the stress-strain relation is given by Figure 9.11.

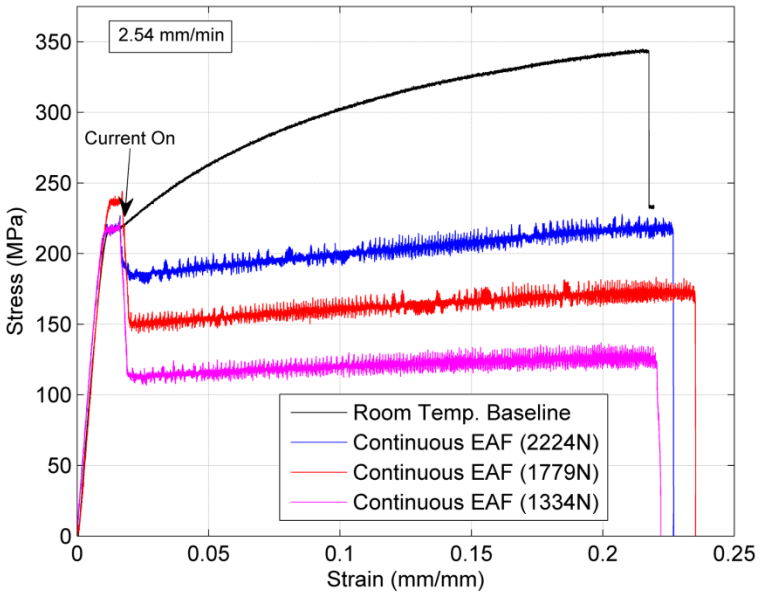

Figure 9.10 - Stress Response for Constant Force Forming

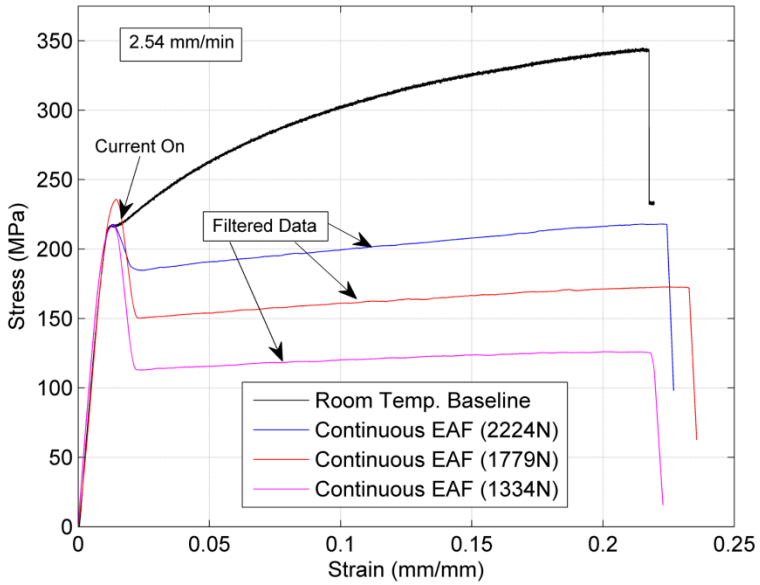

Figure 9.11 - Filtered Stress Response for Constant Force Forming

The final results of the current applied to achieve constant force forming are displayed in Figure 9.12 where the overall current application shape is similar to Figure 9.5.

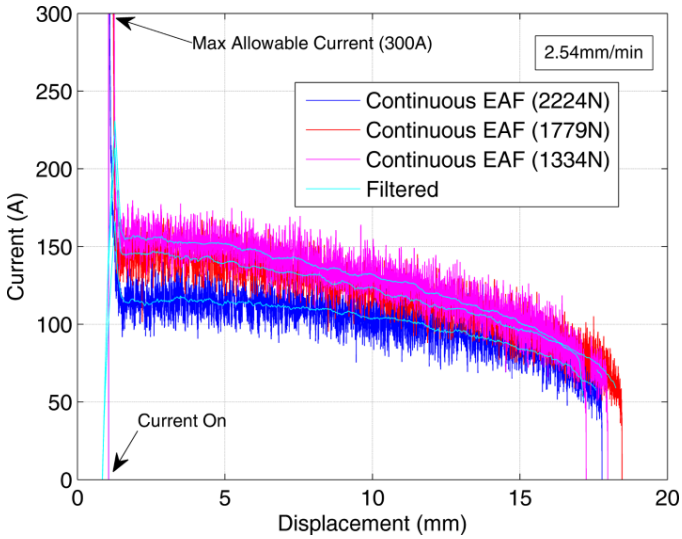

Figure 9.12 - Current Application during Constant Force Forming

In addition, the thermal response of the tests were recorded and the maximum temperature of the sample with respect to time is displayed. As the current is applied the temperature quickly increases and then the rate of change of temperature begins to decrease as the material reaches the desired force set point (lower current level to maintain force). As the test continues, the temperature follows the same trend as the electrical current which decreases until the specimen fractures. The thermal response is present here as this could represent another possible area for control. Specifically, the temperature during forming could be controlled by modulating the electrical current applied if real-time temperature data was available. A similar approach has been presented for stationary heating using an electrical current before performing a Kolsky Bar test [9.1], but not for sheet forming during deformation.

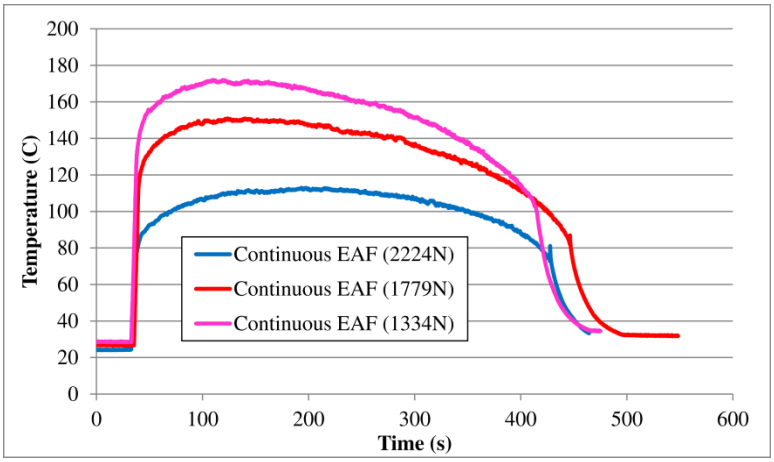

Figure 9.13 - Thermal Response for Constant Force Forming Tests

The significance of constant force forming allows for the forming force to now be specified as a control parameter and not just monitored as a process output. As a result, this technique could allow for lower capacity (*i.e.* smaller force) machines which often have smaller capital investments to form high strength materials. Additionally, with having the capability to form a greater range of material on a lower capacity machine, this reduces the number of individual machines that a company may require.

9.2 - Constant Stress Forming

Constant stress forming was also performed using a similar method as described for the constant force forming. The block diagram for constant stress forming is presented in Figure 9.14 where $\sigma_{desired}$ is the true stress set point, σ_{true} is the observed true stress from the process, and $\Delta\sigma$ is the stress error. The true stress was calculated by:

$$\sigma_{true} = \frac{F_{corrected} L}{A_o L_o} \tag{9.1}$$

where, $F_{corrected}$ is the instantaneous corrected force, L is the instantaneous gauge length, A_o is the initial cross-sectional area, and L_o is the initial gauge length.

To correct for droop due to only using a proportional control term the same corrector function derived for the constant force forming was applied. Specific details on the GUI and LabVIEW control block diagram are given in *Appendix D*.

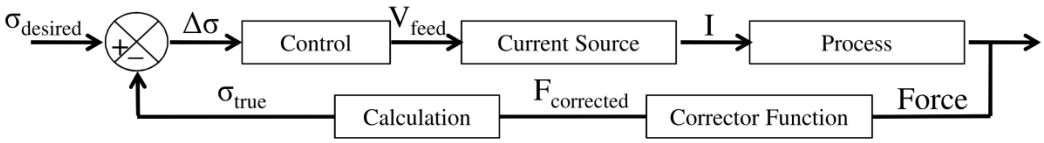

Figure 9.14 - Block Diagram for Constant Stress Forming

The force results are shown in Figure 9.15 for the constant stress forming tests. As seen, the force is immediately reduced to the desired stress level and the force decreases linearly over the length of the test to maintain a constant flow stress.

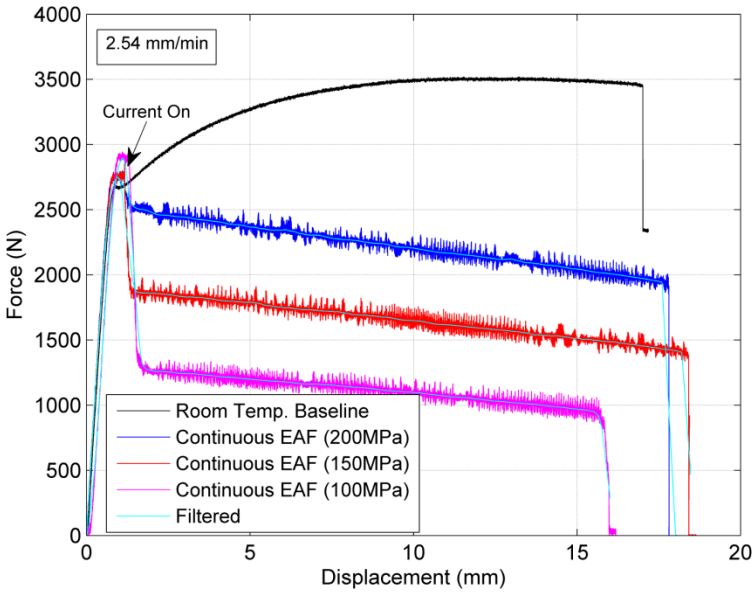

Figure 9.15 - Force Response for Constant Stress Forming

The flow stress results are given in Figure 9.16 and the true stress during forming is constant at the correct set point values of 100MPa, 150MPa, and 200MPa.

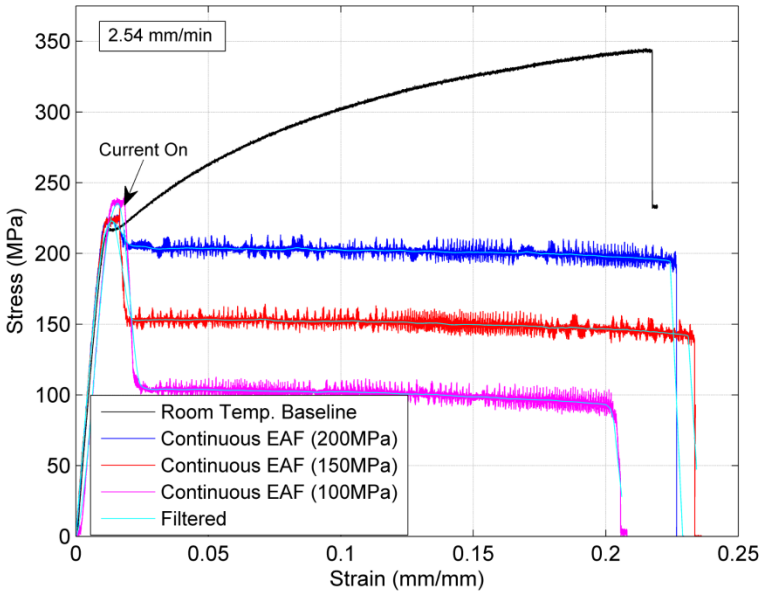

Figure 9.16 - Constant Stress Forming at varying Set Points

The current supplied to the process is summarized in Figure 9.17 for three test cases performed (100MPa, 150MPa, and 200MPa). The current quickly increases to the maximum allowable current once the controller is applied and quickly decreases at the point where the material reaches the desired stress state. Once the stress state is reached, the current slowly decreases till the specimen fractures.

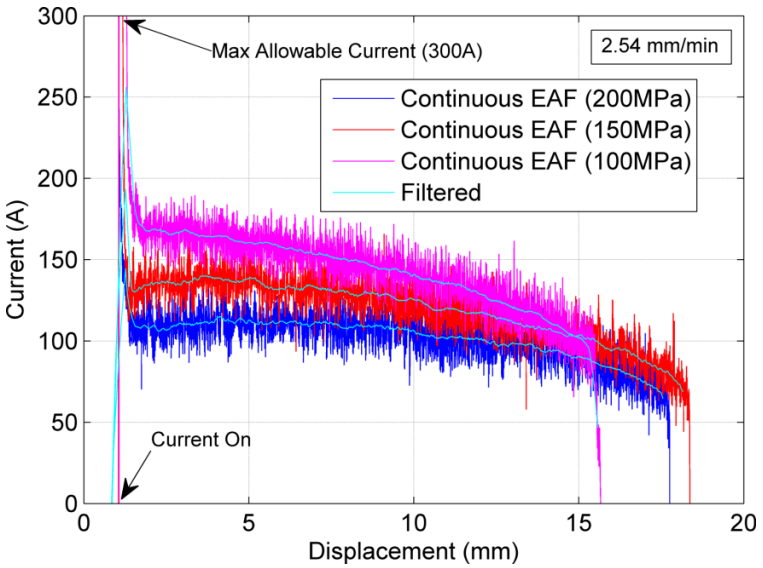

Figure 9.17 - Current Application during Constant Stress Forming

For the constant stress forming results an assumption of constant uniform strain was assumed for the entire test length. However, as a result of the testing setup, there is a thermal gradient within the test samples which causes diffuse necking during the test (see Figure 9.18). Due to the diffuse necking this modifies the actual local stresses within the material due to the presence of an area gradient along the sample length. Consequently, the presented response is an averaging of the true stress within the sample and it can be seen that the experimental response decreases slightly near the end of the tests due to larger amounts of diffuse necking present just prior to fracture.

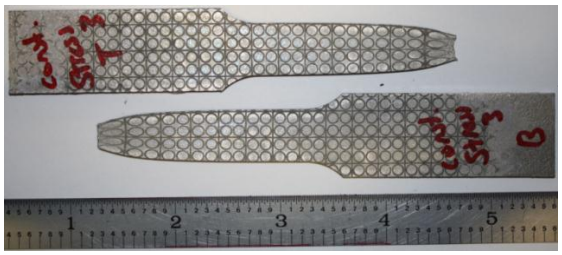

Figure 9.18 - Constant Stress Forming Sample

With the introduction of constant stress forming, this opens additional areas of research for determining the desired or optimal material flow stress response during forming for a given material/process combination. Additionally, this demonstration also leads to the opportunity for present forming machine architectures/designs to be modified with the goal of becoming more flexible which is highly desirable in industry.

9.3 - Constant Current Density Forming

Constant current density (CCD) forming has been performed for uniaxial compression upsetting (Figure 9.19) for both 304 Stainless Steel and Grade 5 Titanium (Ti-6Al-4V). The internal block diagram for the overall control of the current scheme is shown in Figure 9.20.

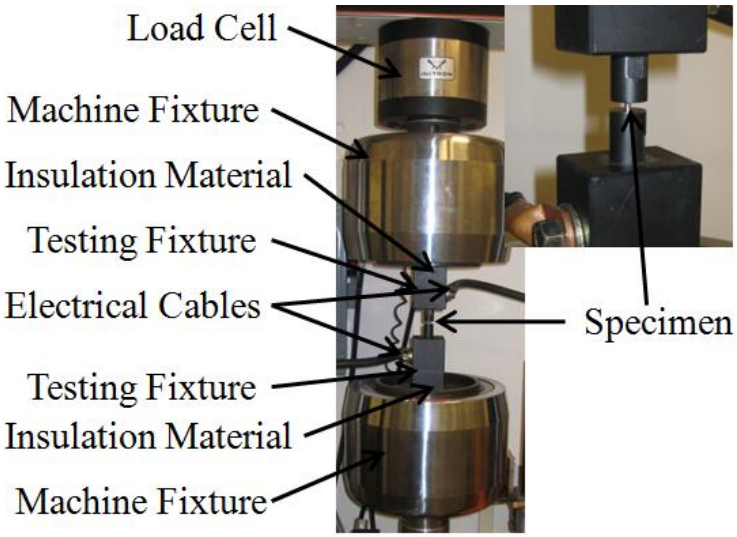

Figure 9.19 - Constant Current Density Forming Setup

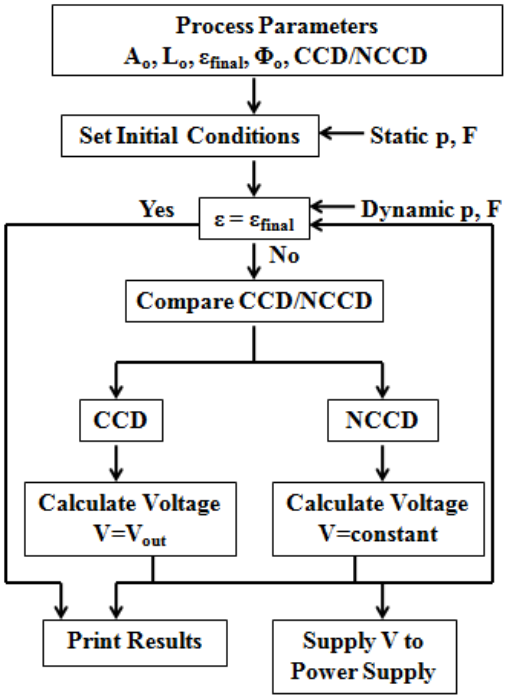

Figure 9.20 - Internal Block Diagram for Control of NCCD and CCD Processes

In the block diagram, the initial state of the force and load is set to use as a reference point. Then, depending on the desired process (NCCD or CCD), the controller calculates the feed voltage that gets supplied to the current source. The current source reads the feed voltage and outputs a corresponding electrical current to the forming process. This process is repeated until the desired amount of material strain is reached. For the NCCD tests, the supplied current is constant and the shape change makes the current density decrease with time (compression tests). For the CCD tests, the supplied current is increased with time to maintain a constant current density irrespective of specimen shape change.

The variation in the material flow stress by taking into consideration component shape change during the forming process is shown in Figure 9.21 and Figure 9.22 for 304 Stainless Steel and Grade 5 Titanium, respectively. As seen, by modulating the current during the test, the material flow response is altered as compared to using only a nominal current value. As a note, for compression forming the current is applied continuously during the entire forming process. These results provide a better representation of the actual material stress due to an applied current as specimen shape is not a factor.

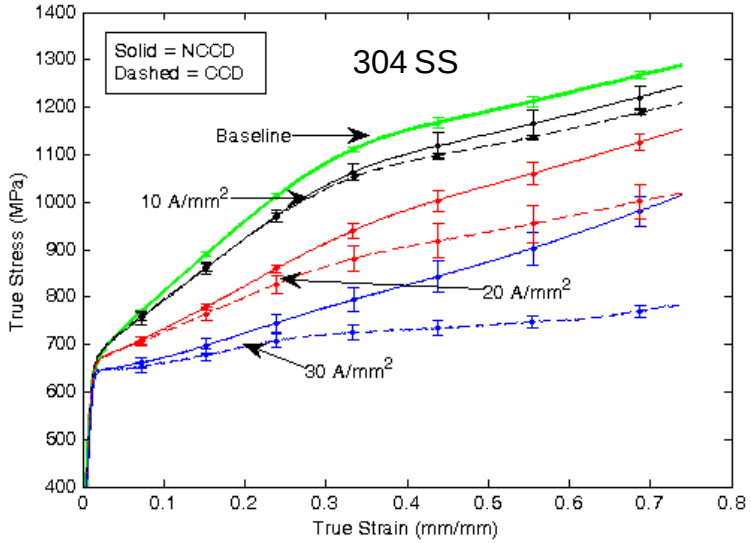

Figure 9.21 - Flow Curves for 304 Stainless Steel: Comparing Non-Constant Current Density (NCCD) vs. Constant Current Density (CCD)

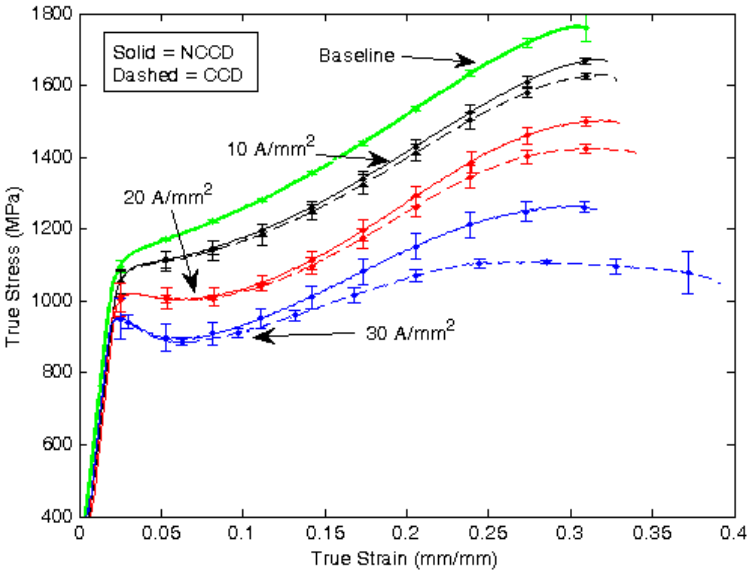

Figure 9.22 - Flow Curves for Grade 5 Titanium: Comparing Non-Constant Current Density (NCCD) vs. Constant Current Density (CCD)

Last, the measured current during the process was compared to the theoretical current to maintain a constant current density during forming and this is shown graphically in Figure 9.23.

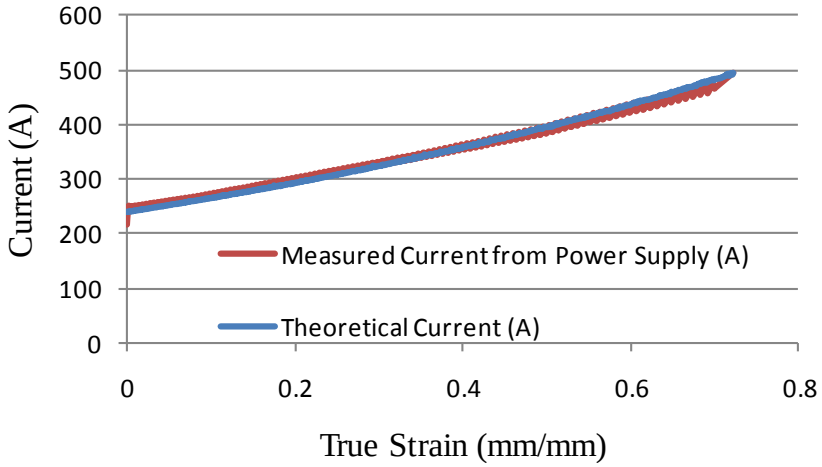

Figure 9.23 - Theoretical and Experimental Data of Electrical Current Output for Constant Current Density Forming

In summary, this work introduced the first constant current density (CCD) tests to examine the actual material flow stress while subject to an EAF process. As a result of CCD testing, the shape change of the specimen during the process did not influence the effect that the electrical current had on the material strength. Accordingly from CCD testing, it was shown that the flow stress is further reduced as a result of the increased current applied to the material with increasing strain. Moreover, increases in flow stress reductions were increased by approximately 30% in certain cases. Additional experimental results and data driven modeling for both NCCD and CCD profiles are given by the PhD candidate in [9.2].

From an applications standpoint, this type of control technique could be used to help maintain consistent material flow and strength levels through components with

varying cross-sections such that the resulting output is a formed part with more uniform strain/strength properties.

9.4 - Model Based Control (MBC) Feasibility

Model Based Control (MBC) is a control method where the control system incorporates a process model in the control algorithm. Within MBC, there have been numerous approaches developed and this work focuses on Model Predictive Control (MPC). In MPC, the model of the process is used to estimate the response of the system to apply control action instead of waiting for feedback from the process. Specifically in MPC, a weighted objection function is defined, the response of the system to the inputs is predicted over a finite time horizon, the performance of the system is optimized with respect to the objective function using design variables as system inputs, and the system is driven toward the optimized state [9.3]. This type of strategy has two main advantages over traditional control in that it *1)* betters the performance as a result of an understanding of the system physics instead of reactive compensation, and *2)* the process output can be optimized to any parameter(s) while the underlying model may contain uncertainty [9.4]. A general MPC architecture is shown in Figure 9.24.

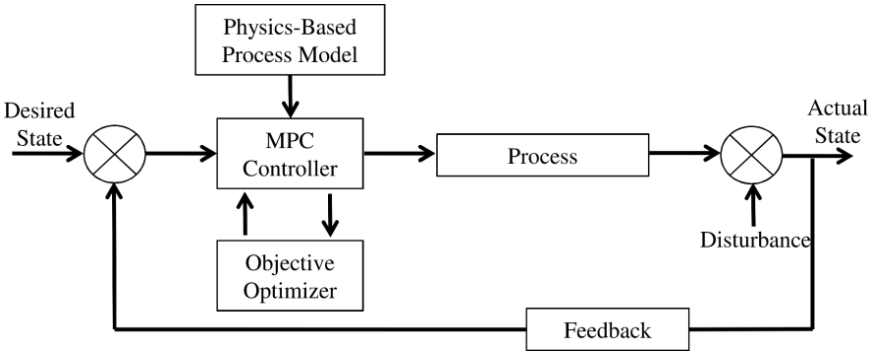

Figure 9.24 - General MPC Block Diagram

When considering this control strategy for EAF, the previous sections used a *PID* controller which employed a compensation strategy instead of predictive action. Additionally, the desired state was directly measurable or capable of being directly calculated from the actual state of the process. For advanced control of EAF processes, the incorporation of MPC and physics-based models could allow for immeasurable process outputs to be controlled by the use of measurable processes feedback. From the models created in this work, the required force or stress, local strain, and temperature profile of the tensile sample could be calculated. As a result, one strategy using the thermo-mechanical process model for EAF developed in this work could allow for the temperature of the formed tensile sample to be controlled. Although the temperature is a measurable output, there are difficulties in measuring the entire thermal response (*i.e.* large thermal gradients during EAF sheet forming) as a result of image/data processing. Hence, real time feedback may be limited to point measurements on the tensile sample. The forming process could be controlled such that the temperature does not exceed a certain value or the part is formed in a certain temperature range. In addition, the input electrical energy to the process could be minimized while still maintaining the constraints for temperature. The block diagram is shown in Figure 9.25 where the process measurements could include temperature (most likely point measurements), current, force, and displacement. The thermo-mechanical process model would allow for temperature prediction such that the control actions could be set before the actual feedback or past output measurements are provided. Again, the MPC is shown providing

a feed voltage (V_{feed}) which the current source translates to direct electrical current to the physical process.

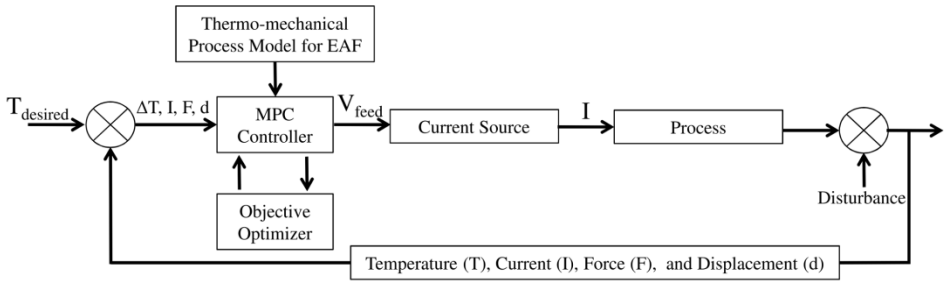

Figure 9.25 - MPC Block Diagram for Temperature Control during EAF

Additional strategies could include maximizing the elongation before failure or providing a desired elongation while minimizing the amount of electrical energy applied to the component. Also, with further work in microstructure analysis of EAF samples, this could allow for grain size control using current and the deformation rate as the control variables.

9.5 - Process Control Conclusions

The main conclusions drawn from this chapter are:

- Several control approaches were envisioned, created, and demonstrated for forming using an electric current field.
- The first examples of constant force forming and constant stress forming using modulation of electric current flow through the workpiece were demonstrated.
- The constant force forming and constant stress forming applications utilized only the proportional gain of a *PID* controller and a resulting steady state error was present. As a result, a correction factor was applied

to remove this steady state error. It is also noted that the integral portion of the controller could have been used to drive the steady state error to zero.

- The constant force forming control approach using a correction function was successfully capable of forming at three different force set points.
- The constant force forming control approach allows for the forming force to be a specified process input and not just an output of the process. This can allow for lower capacity machines to be used on a wider range of materials with various strength properties.
- The constant stress forming was successfully demonstrated for three flow stress set points. With this introduced capability there are now additional areas where future research could be performed. For example, the desired or optimal stress response when forming a material using a certain process could be a possible area. Additionally, this also leads to the opportunity for forming machine architectures/designs to be modified to allow for more flexibility in material deformation which is highly desirable in industry.
- The constant current density forming introduced the first material response under electrical current irrespective of material shape change. As a result, the true response of the material due to the electrical current field was visualized. This technique is applicable in that it could allow for more consistent material flow and strength levels in components with varying cross-sections.

- Model Based Control (MBC) has potential applications for controlling EAF processes using derived physics-based models. Specifically, this work concentrated on Model Predictive Control (MPC) which is a subset of MBC. In MPC, the model of the process is used to estimate the response of the system to apply control action instead of waiting for feedback from the process. One control application was presented using the thermo-mechanical process model for EAF such that the temperature during forming could be controlled.

9.6 - References for Chapter 9

[9.1] S.P. Mates, R. Rhorer, E. Whitenton, T. Burns, and D. Basak "A Pulse-Heated Kolsky Bar Technique for Measuring the Flow Stress of Metals at High Loading and Heating Rates," *Experimental Mechanics*, vol. 48, pp. 799-807, 2008.

[9.2] J. J. Jones, and L. Mears, "Constant Current Density Compression Behavior of 304 Stainless Steel and Ti-6Al-4V during Electrically-Assisted Forming," in *ASME International Manufacturing Science and Engineering Conference*, Corvallis, OR, 2011, p. 9.

[9.3] P. Mehta, and L. Mears, "Model Based Prediction and Control of Machining Deflection Error in Turning Slender Bars," in *ASME International Manufacturing Science and Engineering Conference*, Corvallis, OR, p. 9, 2011.

[9.4] L. Mears, P. Mehta, M. Kuttolamadom, C. Montes, J.J. Jones, W. Salandro, and D. Werner, "Manufacturing Process Modeling and Application to Intelligent Control." *Journal of the South Carolina Academy of Science*, Vol. 10, pp. 6, 2011.

CHAPTER 10 - ELECTROPLASTIC THEORY

The scientific contributions of this work are outlined in this chapter with respect to the theory of electroplasticity. The first contribution is the finding that the main cause attributed to the observed effects from an applied electrical current during deformation is due to internal heat generation, and not direct electron momentum transfer as previously supposed. The second contribution is a thermo-mechanical model of the effects of the electrical current on the deformation behavior (*i.e.* material flow stress, local material strain, and thermal response of the material) of sheet metals, based in first principle models. Experimental and microstructural findings are used to support the presented theories. Additionally, physics-based models are applied to determine the significance of prior electroplastic theories.

The major findings from the modeling work (*Chapter 4-6*), experimental testing (*Chapter 7*), and microstructure analysis (*Chapter 8*) help build and support the theory presented in this chapter with respect to the application of a direct electrical current to a metallic material under deformation. From the Modeling work in *Chapters 4-6* and *Chapter 7*, it was shown that a decrease in material flow stress is observed during current application due to electroplasticity, thermal softening, and thermal expansion. The electroplastic contribution is clearly explained in this chapter. Also, electrically pretreating the material before deformation created small variations in the room temperature material response without grain level microstructure changes. Moreover, a reduced yield point was observed in the EAF incremental tests where there were no grain size alterations as compared to the non-pulsed material (*i.e.* room temperature

deformation). The EAF incremental test only applied electrical current while the material was stationary and deformation only occurred once the material cooled to room temperature. Last, the EAF square wave testing provided similar microstructure results as the non-pulse material (*i.e.* room temperature deformation), however, there was a reduced amount of twinning present. The EAF square wave tests apply a pulse of electrical current for a set duration at a given interval while the material is being deformed. These above phenomena are all described by the theory presented in this chapter.

10.1- Deformation of Metals

To summarize *Section 2.1.2*, metals have metallic bonds where the bonds consist of ion cores surrounded by valence electrons, which act as the medium to hold the ion cores together. The ion cores oscillate rapidly about their present lattice position, and temperature changes modify the average vibrational energy of the ion core. Within the material lattice, linear defects classified as dislocations exist and these are important for material deformation. Material slip and twin boundary formation are the two major mechanisms of plastic deformation. Material slip involves the creation/annihilation and motion of dislocations on slip systems within the material lattice. The slip system consists of a *slip plane* and a *slip direction*, the plane/directions having the highest planar/linear density within the crystal structure. During deformation by slip, the dislocations reach obstacles such as grain boundaries, voids, cracks, impurity atoms, and other dislocations that cause their movement to be impeded. To overcome these obstacles, dislocations are able to continue motion by: changing direction, bowing, sliding, or bending. As the amount of plastic deformation is increased, dislocations will pile up against each other

which create regions of high dislocation density. Consequently, the difficulty of the dislocations to begin moving again is amplified. In doing so, the required force to continue deformation is increased. This strain hardening behavior is commonly modeled using expressions such as that given by Equation (2.46) where the hardening is described by a strain hardening exponent (n). Twin boundary formation occurs when one part of the crystal lattice reorients so that it becomes the crystallographic mirror image of the initial crystal. The crystallographic plane of symmetry where the reorientation occurs is called the twin plane and twinning differs from slip in that every plane of atoms suffers some movement. This movement of every plane is significant for plastic deformation in that the changes in plane orientation may allow for additional material deformation to occur by slip on the reoriented planes. The additional slip on the reoriented crystal structure will only easily occur if the crystal has a favorable slip system to the applied external load. However, twinning only occurs when material slip is restricted as the critical resolved shear stress to initiate twinning is greater than that of slip.

10.2 - Electrical Current

When an electric field is applied to a material, there is a force exerted on the free electrons (*i.e.* valance) such that they experience acceleration in the direction opposite to the electrical field as a result of their negative charge. Ideally, the electrons would continuously accelerate such that the current would always increase over time. However, internal friction forces (*i.e.* collisions with ion cores) within the material limit the electron acceleration, which settles at some constant current value. These collisions in the lattice make up the electrical resistivity (*i.e.* volume-specific) of the material. The electrical

resistivity of a material is characterized by the atomic structure, spacing, and bonding. However, the electrical resistivity is increased by the number dislocations, point defects, and interfacial defects (grain boundaries, cracks, voids) within the lattice. The total electrical resistivity can be described by Matthiessen's Rule:

$$\rho_{e\_total} = \rho_o + \rho_i + \rho_d \tag{10.1}$$

where, ρ_{e_total} is the total electrical resistivity, ρ_o is the ideally pure and perfect crystal resistivity which includes the influence of thermal vibration contribution, ρ_i is the contribution due to impurities in the lattice, and ρ_d is the contribution from plastic deformation [10.1]. Also, it is assumed that the scattering mechanisms act independently within the material.

As the electrical field is applied, the electrons accelerate and scatter off of the above listed defects and the vibrating ion cores themselves. The localized scattering on the defects causes the electrons to lose kinetic energy and to change their direction. Yet, the electrons still have a net movement (*i.e.* current) in the opposite direction of the applied field. This net movement can be described by the electron drift velocity, which is the average electron velocity in the direction of the applied force. The electron drift velocity is given as:

$$v_d = \frac{I}{n|e|A} \tag{10.2}$$

where, I is the current magnitude, n is the number of valence electrons per unit volume, e is the charge of an electron, and A is the cross-sectional area that the current passes

through [10.1]. The drift velocity is on the order of a few mm/s for the electrical current magnitudes examined in this work.

The concept of electrons scattering off of the material defects and the ion cores is known as Joule or resistive heating. As the electrons are accelerated by the electric field, they accelerate and only reach a velocity that is usually below the Fermi velocity (~1,800,000 m/s) and well below the speed of light (299,792,458 m/s), as a result of collisions with the material lattice. The Fermi velocity is the fastest possible velocity of an electron in a metal that is cooled to near zero Kelvin. Thus, at zero Kelvin, the Fermi velocity of an electron is derived from the kinetic energy equal to the Fermi energy. During the collisions, the electrons transfer kinetic energy to the ion cores, which increases the ion cores vibrational energy. This increase in vibrational energy causes the material to increase in temperature. Thus, when considering a larger portion of the material, ion cores around the material defects will have greater vibrational energy (*i.e.* greater temperature) due to lattice distortions and a greater frequency of electron/ion core interaction. There is a greater frequency of electron/ion core interaction due to the misalignment of the ion cores. In comparison, the defect free lattice regions will have a smaller vibrational energy increase due to the same applied electron flux through the lattice. Although the flux is the same, the defect region will not incur as many electron/ion core interactions due to the aligned lattice structure. As a result, the energy increases will be less. In addition, the vibrational energy gained in each of the regions (*i.e.* defect and defect free) will provide or gain energy from its neighboring ion cores in a transient manner. This creates vibrational energy gradients or thermal gradients at the ion

core level. From a lattice perspective, this translates to an average vibration energy of the individual ion cores within a grain (*i.e.* mean grain temperature). Overall, the collection of mean grain temperatures and heating at grain boundaries relates to the macro observed temperature. This macro or bulk temperature is what is typically measured during experimental testing, however, there are higher peak temperatures (*i.e.* vibrational energy) around defects within the material lattice.

When comparing Joule heating to raising the temperature of a material by convection (*e.g.* in an oven), the average vibrational energy of the ion cores in the lattice would increase. However, the vibrational energy would not have areas with greater amounts of energy around the defect sites as there is not a direct interaction as with the electrical flow. Thus, heating by convection will provide a transient wave of vibrational energy from the exterior surface. However, once the material is completely heated and soaked at the elevated temperature, the vibrational energy will be uniform within the material's lattice. This is one beneficial aspect to using EAF over conventional elevated temperature forming.

Aside from using bulk observations to quantify this phenomenon [10.2-10.4], this work uses physics-based models to determine the significance of the present electroplastic theories. Specifically, the transient energy provided to the dislocation core and that transferred to the surrounding lattice are compared and quantified. A schematic is shown in Figure 10.1 where an edge dislocation is represented by a cylindrical dislocation core. The core geometry is characterized by a right circular cylinder with a

diameter (D) and length (L). The diameter used in this work provides an equivalent area to the actual dislocation core area which has an elliptical cross-section.

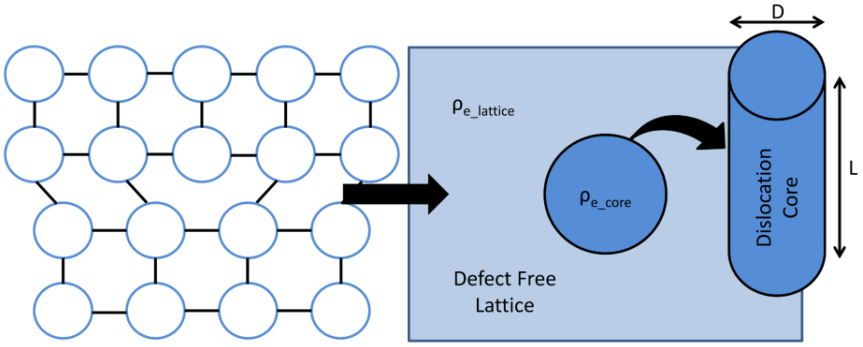

Figure 10.1 - Edge Dislocation Represented as a Cylindrical Dislocation Core Surrounded by a Defect Free Lattice

10.3 - Evaluation of Previous Electroplastic Theories

The two primary theories for electroplasticity are localized heating at lattice defects [10.5-10.7] and the electron wind effect [10.8-10.10]. The most recent work on electroplastic theory tersely stated that the two theories occur simultaneously when an electric current is applied during deformation [10.4]. This work compares the energy magnitude of these two as related to the movement of a dislocation core in a metal's lattice.

10.3.1 - Localized Lattice Heat from Joule Effect

The localized heating is a result of increased scattering at defects, which creates areas of greater atomic vibrations or "hot spots" (*i.e.* the Joule heating effect increased at defect sites), whereas the electron wind effect is based on actual momentum transfer to the dislocation core. In the following two sections, a case study is performed for each theory assuming that a current density (J) of 100 A/mm^2 is applied to a pure magnesium

metal such that the magnitude of influence can be determined. Critical material and lattice parameters are given in Table 10.1.

Table 10.1 - Magnesium Material and Lattice Parameters [10.1, 10.11-10.13]

ρ_o (Defect Free Lattice)	4.101	μΩcm
ρ_d (Dislocation Core)	28.707	μΩcm
ρ	1740	kg/m^3
D	0.587	nm
A	0.271	nm^2
L	6000	nm
V	1623.743	nm^3
n	$4.309x10^{28}$	$Atoms/m^3$
N_{core}	69921	Atoms
Q	135	KJ/mol
Z^*	-2	
e	$-1.602x10^{-19}$	C
b	$3.209x10^{-10}$	m

The localized energy provided to the dislocation core due to the Joule heating effect is given by:

$$E_{Joule} = J^2 \rho_d V \Delta t \tag{10.3}$$

where, J is the current density, ρ_d is the electrical resistivity of the dislocation core, V is the core volume, and Δt is the time the current is applied. It is hypothesized that these local "hot spots" ease dislocation movement through the lattice and allow for them to pass by other unmovable lattice defects. Using a current density of 100 A/mm^2 applied for one second, this results in $4.657x10^{-15}$ J or 29,069 eV of energy being applied to the dislocation core. The dislocation core electrical density was determined to be approximately six to eight times the electrical resistance of the defect free lattice [10.14].

This was determined by Kino et al. where careful experiments were performed to measure samples with varying dislocation densities [10.14]. For this analysis, a factor of seven was used during the calculations as it is the mean of the results published by Kino et al. The importance of a quantifiable amount of energy applied to the core is that it can be compared to the activation energy (Q) for lattice diffusion in magnesium. The lattice diffusion activation energy is the required energy to move an ion core from one lattice site to another during deformation. Thus, the activation energy for magnesium is approximately 1.4 eV/atom and this equates to an activation energy of 97,867 eV for an entire dislocation core. Therefore, the calculated additional energy due to Joule heating at the dislocation core is slightly less than 1/3 the total activation energy required to move the dislocation core one atomic distance. From a magnitude standpoint, this would have a significant effect on the mobility of the core and reduce the mechanical stress required to displace the dislocations in the material's lattice. It should be noted that the entire dislocation core does not move all at one time, but regions of the core advance through the lattice over time. This does not affect the results presented as they are examining the magnitude between Joule heating and the electron wind effect.

In addition, the localized Joule heating effect can be quantified as a temperature rise by:

$$\Delta T = \frac{J^2 \rho_e}{\rho c} \Delta t \tag{10.4}$$

where, ΔT is the temperature rise, J is the current density, ρ_e is the electrical resistivity of the area of interest, Δt is the change in time, ρ is the density, and c is the specific

heat. Due to the difference in electrical resistivity between the defect free lattice and dislocation core, the temperature magnitude is linearly scaled from the variation in resistivity (*i.e.* dislocation core is seven time hotter than the defect free lattice) as per Equation (10.4). To characterize this effect, a simplified model which includes transient conductive heat transfer from a 2D nodal mesh is shown in Figure 10.2.

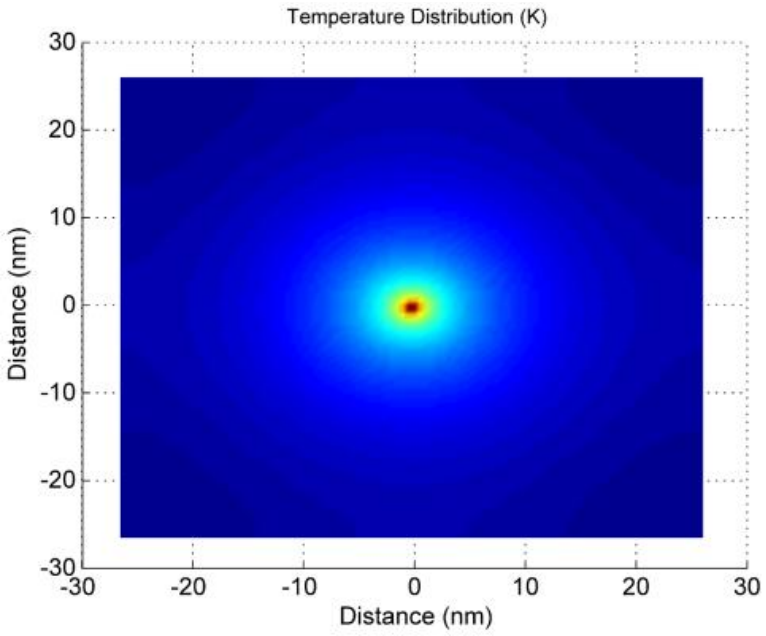

Figure 10.2 - Snapshot of Transient Response of Joule Heating as a result of the Greater Dislocation Core Electrical Resistance

This model was produced to understand the heat generation and dissipation during Joule heating around a dislocation core. As seen, the dislocation core in the center generates the greatest heat and is dissipated outward from the core center. Future use of this model could allow for the inclusion of additional defects (dislocations, point defects, and interfacial defects) such that a mean or bulk temperature could be calculated over a larger area. This bulk temperature from the model would allow for a comparison to experimental thermal results. Additionally, as deformation is imposed newly formed

dislocations could be incorporated to the model with some dislocation distribution to quantify the addition of new dislocations on the heat transfer response.

10.3.2 - Electron Wind Force Effect

Conversely, the energy imparted to the dislocation core from the electron wind is:

$$E_{wind} = Z^* e \rho_e J N_{core} b \tag{10.5}$$

where, E_{wind} is the electron wind energy imparted to the dislocation core, Z^* is the effective charge number, e is the charge of an electron, N_{core} is the number of equivalent atoms per dislocation core, and b is an atomic distance [10.12]. It is suggested that the momentum transfer from the electric field directly assists the dislocation movement within the metal's lattice. This model is evaluated by examining the added energy to the dislocation core as a result of momentum transfer. Using the values in Table 10.1, the total energy imparted on an individual atom for a current density of 100 A/mm^2 is 1.842x10^{-8} eV. This equates to 1.29x10^{-3} eV per dislocation core. This result is significantly less than that calculated due to Joule heating on the dislocation core (225 million times less). As a result, this effect is extremely small as compared to the energy required to allow for the dislocation core to diffuse in the material's lattice. Overall, it is concluded that this effect is not substantial in aiding dislocation movement within the metals lattice. It should be noted that the electron wind force or electromigration has been seen in semiconductor interconnects and integrated electric circuits. However, this involves larger current densities (~1,000 A/mm^2) and only individual ion cores are moved over time such that voids form in the circuit [10.12]. The void formation then opens the

circuit which causes the interconnect to fail. A failed interconnect is shown in Figure 10.3 where void growth and stress caused the interconnect to fail.

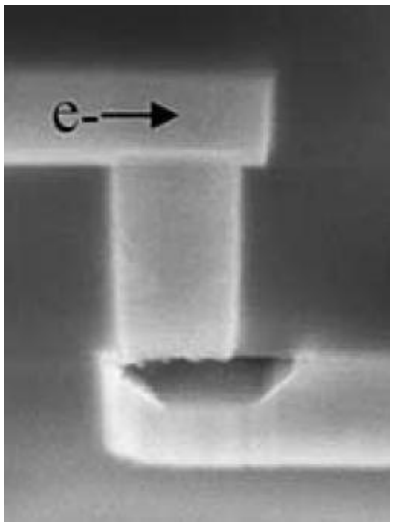

Figure 10.3 - Failed Interconnect by Electromigration [10.15]

Hence, from the prior analysis, it is concluded that the main contribution toward the observed electrical effects are due to localized areas of increased vibrational energy from electron scattering (*i.e.* Joule heating) and not a direct momentum effect on the dislocation cores themselves. Therefore, the concept of localized areas of greater vibrational energy is discussed below for the interaction of these "hot spots" and dislocations without and with deformation being imposed on the material. This proposed theory is different in that it only attributes the observed effect (flow stress reduction and improved formability) to one single phenomenon and that the theory is described from a material science viewpoint.

10.4 - Electroplastic Theory

In the following section the electroplastic theory is explained from a material science view such that a single physical contribution due to Joule heating explains the

observed effects of an applied current on the mechanical properties of a metal. The influence the applied current has on the material with no deformation, during deformation, and the currents influence on material formability are presented.

10.4.1 - Electrical Current Application without Deformation

When a metal is stationary (*i.e.* no deformation being imposed) and an electric current is applied, Joule heating occurs which creates local regions of greater atomic vibrations (*i.e.* temperatures) around defects within the material as compared to defect free regions. These areas with greater temperature can be called "hot spots" within the material's lattice. Thus, it is theorized that the "hot spots" allow for a rapid decrease in the stored energy of the material by facilitating dislocation annihilation. The motion to reduce the number of dislocations is a direct result of the enhanced atomic diffusion due to the "hot spots". This method of reducing the residual stress by removing dislocation is expected to be faster than by the conventional stress relief anneal using an oven. This is due to the difference of bulk convection heating and heating locally with an electric current field. The bulk convection heating requires energy input that has to heat the entire material to allow for the dislocations to diffuse to a sink (*e.g.* grain boundary); whereas, the electric current provides a greater amount of energy directly at the dislocation presumably in a faster manner. As a result of the removal of residual stresses and the annihilation of dislocations, the yield strength is expected to decrease. The yield strength is classically related to the grain size by the Hall-Petch:

$$\sigma = \sigma_o + kd^{-\frac{1}{2}} \tag{10.6}$$

where, σ is the yield strength, σ_o is the frictional stress (*i.e.* equivalent to yield stress of very-course grained polycrystal), *k* is constant which can be thought of as the source strength for dislocations, and *d* is the mean grain size [10.16]. Assuming that a dislocation moves on average $\bar{x}$ per unit strain, then:

$$\bar{x} = \beta d \tag{10.7}$$

where, β is a fraction of the grain size (β <1). Then the strain can be said to be:

$$\varepsilon = \rho \vec{b} \bar{x} \tag{10.8}$$

where, ρ is the dislocation density and $\vec{b}$ is the Burger's vector. Thus, the dislocation density is:

$$\rho = \frac{\varepsilon}{\vec{b}\bar{x}} = \frac{\varepsilon}{\vec{b}\beta d} \tag{10.9}$$

The dislocation density relation to strength was derived by Kocks [10.17] as:

$$\sigma = \sigma_o + \alpha G \vec{b} \rho^{\frac{1}{2}} \tag{10.10}$$

where, α is a constant, G is the shear modulus. Upon substitution of Equation (10.9) into Equation (10.10), this yields:

$$\sigma = \sigma_o + \alpha G \vec{b} \left(\frac{\varepsilon}{\vec{b}\beta d} \right)^{\frac{1}{2}} \tag{10.11}$$

Upon comparing Equation (10.11) to the Hall-Petch equation (Equation (10.6)) it can be seen that the constant *k* is equivalent to:

$$k = \alpha G \vec{b} \left(\frac{\varepsilon}{\vec{b}\beta} \right)^{\frac{1}{2}} \tag{10.12}$$

which, shows the interaction between grain size and dislocation density.

In summary, the material strength can be described as a function of grain size or dislocation density, where a smaller grain size or larger dislocation density provides greater strength. As a result, with a decrease in dislocation density due to local "hot spots" from the electrical current, the yield strength is expected to decrease.

These types of results were observed from the experimental testing and microstructure analysis performed in *Chapters 7-8*. For example, the electrical pretreating tests (Figure 7.14) showed variation in their mechanical response with no difference in the microstructure as compared to the as-received material. This is in agreement as no recrystallization occurred from electrically-treating the material, but the mechanical response has some variation. Since the as-received material was annealed from processing, it is expected that the dislocation density was fairly low and there was no cold work imposed on the material. Thus, the low amount of lattice strain coupled with the local "hot spots" at dislocation did not have a sufficient energy to drive a large quantity of dislocations to sinks. As a result, this was seen by the material yield strength not being significantly affected by electrical pretreating, however, some difference was observed once dislocation motion began. Additionally, the EAF incremental tests also agree with this effect. As shown in Figure 7.27 and Figure 7.29, the application of current had a significant effect on the yield strength of the material without affecting the microstructure. This directly aligns with the theory of localized "hot spots" which allow for dislocation annihilation as a result of enhanced diffusion directly surrounding the dislocation. This is in contrast to the electrical pretreating where there was little effect on

the material yield point. For the EAF incremental tests, there was a much greater driving force for dislocation annihilation due to the increased amount of lattice strain present. Thus, a larger amount of dislocations were removed and the stress of the material was reduced which equates to the reduced yield point.

10.4.2 - Electrical Current Application with Deformation

A similar theory is presented for the application of an electrical current during the deformation of a metal. As the current is applied during deformation, the local "hot spots" created from greater electron scattering at defects significantly enhance the vibrational energy in the surrounding area of the dislocation. This greater energy surrounding the dislocation allows for enhanced mobility along the slip plane as it can pass by lattice obstacles with less resistance. Thus, the dislocation has a greater quantity of energy and can move under a lower required stress (*i.e.* external required force for deformation is reduced). The lower required stress is what is observed on a macro scale when forming using an applied electric current. Also, for the other defects within the material (point and interfacial defects), they have an increased vibrational energy surrounding them as a result of larger amount of electron scattering. As a result, if dislocations interact or become piled-up at these defects, this additional energy from scattering may allow the dislocation to pass by the obstacle, where it otherwise would have remained pinned.

Aside from the local "hot spots" at dislocations and defects, the surrounding defect free lattice and the overall material temperature is rising. This overall bulk temperature rise translates to traditional elevated temperature effects on material deformation (*i.e.* thermal softening).

The reduction in material strength was observed in the square wave EAF tests in *Chapter 7* where the material stress was significantly reduced during the application of the current. From the theory, it is proposed that the main effect is a result of localized "hot spots" which significantly increase the mobility of the dislocations. Additionally, some dislocation annihilation may occur during the time the current is applied. From the microstructure analysis, it was noted that the EAF tests had a reduced amount of twinning. This may be from the applied current providing excess energy to dislocation or pinned dislocations such that they could continue the process of slip. As a result, this reduced the necessity for twin boundary formation, which was necessary for the room temperature deformation test to continue. Hence, the current application supplied energy directly to the regions of high stress or the areas with very high dislocation densities. Also, for the tests where cooling was compared to non-cooling (Figure 7.18), a small difference in flow stress reduction was noted while the cooled test quickly increased in strength after the application of the current. This is in agreement with the "hot spots" improving the mobility of the dislocations while the remainder of the material was not at such an elevated temperature. Once the current was discontinued, the electrical energy imparted to the dislocations was removed and the strength quickly increased as shown experimentally (*e.g.* Figure 7.9).

Moreover, this theory is also in agreement with Perkins et al. where isothermal tests were performed at temperature greater than were reached in the electrical tests [11.18]. The results from this work showed that the isothermal testing did not create near

the flow stress reductions or the increases in fracture strain as compared to the electrical tests. The results are given in Figure 10.4.

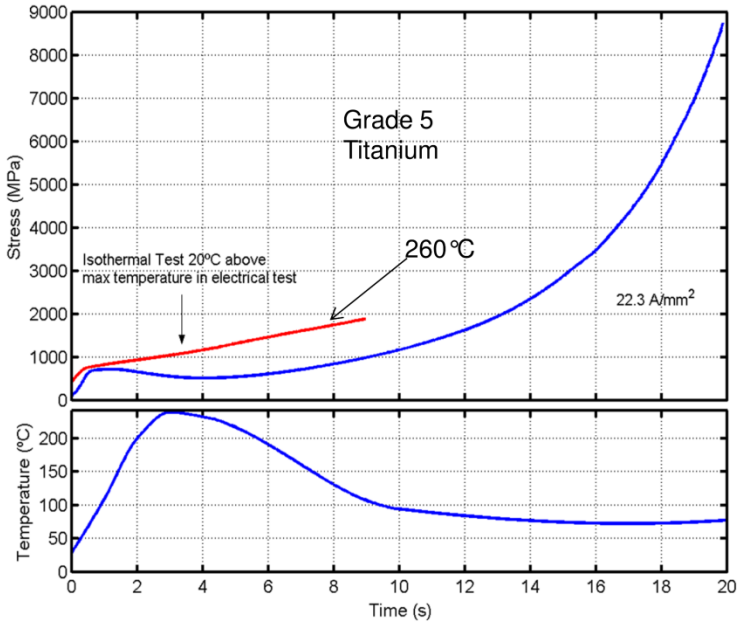

Figure 10.4 - Isothermal versus EAF Testing of Grade 5 Titanium [11.16]

This work directly speaks to the aforementioned difference between heating by external convection and with a direct electrical current; where the convection does not allow for localized "hot spots" within the lattice. Additionally, early works in EAF using very short duration pulses produced large flow stress reductions with very small bulk temperature increases [10.19, 10.20]. Thus, this works also coincides with the theory in that the short duration pulse allowed for high local temperatures at defects while the bulk of the lattice remained at a reduced temperature.

10.4.3- Electrical Current Application Effects on Formability

In regards to material formability, ductile fracture is usually transgranular such that failure occurs through the grains. Ductile fracture begins by the nucleation, growth,

and coalescence of microvoids. The microvoids are formed when a high stress induces separation of the material at grain boundaries or at small impurity particles (B in Figure 10.5). As the local stress in the material increases, the microvoids grow and coalesce into larger voids (C in Figure 10.5). Over time crack initiation begins at the void and the crack grows till the material ultimately fractures.

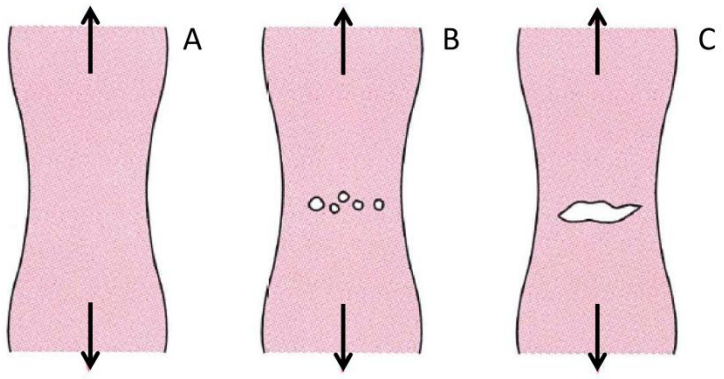

Figure 10.5 - Ductile Fracture Stages [10.1]

The high stresses within the material that cause microvoids to form can be a result of pinned dislocations within the lattice. As a result of the applied current providing energy to the dislocations, the added energy can allow for pinned or stuck dislocations to continue moving again. Consequently, this reduces the local stresses within the material's lattice and delays the process of void formation and fracture. This theorized ability of the electric current to supply sufficient energy to allow for pinned dislocations to be mobile can explain the observed effects seen in experimental testing [10.6, 10.21].

10.5 - Electroplastic Theory Conclusions

The main conclusions drawn from this chapter are:

- The flow of electrical current or the movement of valance electrons within the material is limited by the electrical resistivity. The resistivity is derived

from the atomic structure, bond type, atomic spacing, and the material defects present in the lattice. As a result of electron scattering within the lattice, areas of greater vibrational energy exist around defects due the increased amount of electron/ion core interaction. Additionally, the defect free lattice has some resistance to electric flow and the entire material begins to heat. This phenomenon is known as Joule heating.

- Joule heating differs from conventional convection heating of a material (*i.e.* in an oven). This is due to the convection heating only providing a uniform increase in vibrational energy throughout the lattice (*i.e.* both defect and defect-free regions). In contrast, Joule heating creates areas of increased vibrational energy at defects as compared to the defect free region. Thus, the energy is more directed to the critical areas (*i.e.* dislocations and defects) in the lattice for material deformation.
- Two primary theories for electroplasticity are compared by examining the magnitude of energy they impart on a dislocation core. The first theory is based off of Joule heating and the localized heat generated at the dislocation core. The second theory analyzed is from direct momentum transfer on the dislocation core due to the electron wind effect. To perform the comparison, a current density of 100 A/mm^2 is applied to a pure magnesium metal and the energy transferred to the core is calculated. The importance of a quantifiable amount of energy applied to the core is that it can be compared to the activation energy for lattice diffusion in

magnesium. The activation energy to move an ion core is approximately 1.4 eV/atom and this equals an activation energy of approximately 98 keV for the entire core. Of note is that the entire dislocation core does not move all at one time, but regions of the core advance throughout the lattice over time. Nevertheless, this does not affect the results as they examine the magnitude between Joule heating and the electron wind effect. From the analysis, the Joule heating creating local “hot spots” at defects was shown to provide a significant amount of energy (~29 keV) to the core which would have a significant effect on the dislocations mobility. Also, this amount of energy would significantly help to reduce the mechanical stress required to displace the dislocation. In contrast, the electron wind effect produced a very small amount of additional energy to the dislocation core (1.29×10^{-3} eV). The energy results are summarized in Table 10.2.

Table 10.2 - Summary of Energy Analysis for Electroplastic Theories

Theory	Local "Hot Spots" from Joule Heating	Electron Wind Force
Energy Provided to Dislocation Core	29 keV	1.29×10^{-3} eV
Required Activation Energy by Dislocation Core	98 keV	

As a result, it is expected that the electron wind effect will have little effect in aiding or increasing the mobility of the dislocation. In conclusion, the contribution toward the observed electrical effects are due to localized

areas of increased atomic vibration from electron scattering (*i.e.* Joule heating) and not direct momentum transfer on the dislocation cores themselves.

- The electroplastic theory is explained from a material science viewpoint with a single physical contribution due to Joule heating explaining the observed effects of an applied current on the mechanical properties of a metal. The influence the applied current has on the metal with no deformation, during deformation, and the currents influence on formability are provided.
- In the case of stationary electrical current application (*i.e.* no deformation), the local areas of increased atomic vibration allow for a rapid decrease in the stored energy of the material by facilitating dislocation motion and annihilation. The local "hot spots" provide the driving energy to allow the dislocations to move to a sink such that the overall lattice energy is reduced. In addition, if the material has been worked (*i.e.* additional lattice strain present), this increases the driving force for the movement of the dislocations. Thus, larger effects on the dislocation density are expected. This theory was supported by the observed mechanical and microstructure effects seen by the electrical pretreating and incremental EAF tests.
- For electrical current application during deformation, the local "hot spots" created from greater electron scattering at defects significantly enhance

the vibrational energy in the surrounding area of the dislocation. This greater energy surrounding the dislocation allows for enhanced mobility along the slip plane as it can pass by lattice obstacles with less resistance. Thus, the dislocation has a greater quantity of energy and can move under a lower required stress (i.e. external required force for deformation is reduced). Also, for the other defects within the material (point and interfacial defects), they have an increased vibrational energy surrounding them as a result of larger amount of electron scattering. As a result, if dislocations interact or become piled-up at these defects, this additional energy from scattering may allow the dislocation to pass by the obstacle, where it otherwise would have remained pinned. This theory is supported by the EAF square wave and cooling vs. non-cooling tests in this work. In addition, prior EAF tests with large currents coupled with short pulse durations and isothermal tests are also in agreement with this theory.

- With respect to increased elongation before failure, it is theorized that the applied current provides a sufficient energy to pinned or stuck dislocation within the lattice such that it allows for the dislocations to continue moving again. As a result, this reduces the local stress within the material's lattice and delays the process of void formation and fracture.

10.6 - References for Chapter 10

[10.1] W.D. Calister, Jr., *Materials Science and Engineering an Introduction*, 5th ed. New York: Wiley & Sons, 2000.

[10.2] J. J. Jones, and L. Mears "Empirical Modeling of the Stress-Strain Relationship for an Upsetting Process Under Direct Electrical Current," *Transactions of the North American Manufacturing Research Institute of SME*, vol. 38, 2010.

[10.3] W. A. Salandro, C. Bunget, and L. Mears, "Thermo-mechanical Investigations of the Electroplastic Effect," in *ASME International Manufacturing Science and Engineering Conference*, Corvallis, OR, 2011, p. 10.

[10.4] W.A. Salandro, “Thermo-Mechanical Modeling of the Electrically-Assisted Manufacturing (EAM) Technique during Open Die Forging,” PhD dissertation, Clemson University, 2012.

[10.5] W. A. Salandro, J.J. Jones, T.A. McNeal, J.T. Roth, S.T. Hong, and M.T. Smith "Effect of Electrical Pulsing on Various Heat Treatments of 5xxx Series Aluminum Alloys," in *ASME International Manufacturing Science and Engineering Conference*, Evanston, IL, 2008, p. 10.

[10.6] J. J. Jones, and J.T. Roth, "Effect on the Forgeability of Magnesium AZ31B-O When a Continuous DC Electrical Current is Applied," in *ASME International Manufacturing Science and Engineering Conference*, West Lafayette, IN, 2009, p. 10.

[10.7] J. T. Roth, I. Loker, D. Mauck, M. Warner, S.F. Golovashchenko, A. Krause, "Enhanced Formability of 5754 Aluminum Sheet Metal Using Electric Pulsing," *Transactions of the North American Manufacturing Research Institute of SME,* vol. 36, pp. 405-412, 2008.

[10.8] V. Kravchenko, "Influence of Electrons in Delaying Dislocation in Metals," *JETP (USSR)* vol. 51, 1966.

[10.9] H. Conrad, "Electroplasticity in Metals and Ceramics," *Materials Science & Engineering,* vol. A287, pp. 276-287, 2000.

[10.10] H. Conrad, "Thermally Activated Plastic Flow of Metals and Ceramics with an Electric Field or Current," *Materials Science & Engineering,* vol. A322, pp. 100-107, 2002.

[10.11] D.R. Askeland, and P.P. Phule, *The Science and Engineering of Materials*, 4th ed. Australia: Brooks/Cole, 2003.

[10.12] Z. Suo, Reliability of Interconnect Structures, pp.265-324 in Volume 8: Interfacial and Nanoscale Failure (W. Gerberich, W. Yang, Editors), Comprehensive Structural Integrity (I. Milne, R.O. Ritchie, B. Karihaloo, Editors-in-Chief), Elsevier, Amsterdam, 2003.

[10.13] R.S. Seth and S.B. Woods, “Electrical Resistivity and Deviations from Matthiessen’s Rule in Dilute Alloys of Aluminum, Cadmium, Silver, and Magnesium,” *Physical Review B*, Vol. 2, No. 8, 1970.

[10.14] T. Kino, T. Endo, and S. Kawata, “Deviations from Matthiessen’s Rule of the Electrical Resistivity of Dislocations in Aluminum,” *Journal of the Physical Society of Japan*, Vol. 36, No. 3, 1974.

[10.15] C.S. Hau-Rieg, “An Introduction to Cu Electromigration,” Microelectronics Reliability, Vol. 44, 2004.

[10.16] E.O. Hall, *Proc. Phys. Soc*., B64, 1951.

[10.17] U.F. Kocks, “A Statistical Theory of Flow Stress and Work Hardening, *Phil. Mag.*, Vol. 13, 1966.

[10.18] T.A. Perkins, T.J. Kronenberger, and J.T. Roth, “Metallic Forging Using Electrical Flow as an Alternative to Warm/hot Working.” *Journal of Manufacturing Science and Engineering*, Vol.129, No.1, pp.84-94, 2007.

[10.19] O.A. Troitskii, “Electromechanical Effects in Metals.” *Pis’ma Zhurn. Experim. Teoret. Fiz.*, No. 10, p. 118, 1969.

[10.20] K. Okazaki, M. Kagwa, and H. Conrad, “A Study of the Electroplastic Effects in Metals,” *Scripta Metallurgica*, Vol. 12, pp. 1063-1068, 1978.

[10.21] W. A. Salandro, A. Khalifa, and J.T. Roth "Tensile Formability Enhancement of Magnesium AZ31B-O Alloy Using Electrical Pulsing," *Transactions of the North American Manufacturing Research Institute of SME,* vol. 37, 2009.

CHAPTER 11 - CONCLUSION AND FUTURE WORK

11.1 - Conclusion

The work performed in this dissertation is summarized in Figure 11.1.

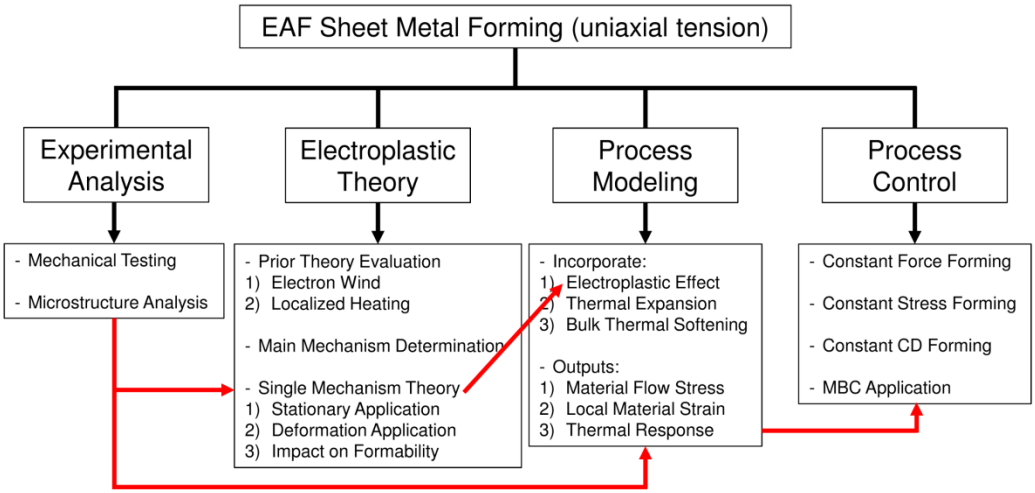

Figure 11.1 - Summary of Research

This work examined the theory of electroplasticity by studying prior proposed theories and by quantifying the prior theories potential for improved dislocation mobility. Prior work has suggested that there may be multiple electroplastic mechanisms that act in unison during deformation with a direct electrical current. As a result, this has introduced a significant amount of discussion and questions on the exact mechanism. Hence, this work analyzed these two theories to determine the most dominant mechanism. The two specific theories were localized heating at lattice defects as a result of Joule heating and the Electron Wind effect which is due to direct momentum transfer to the dislocations cores. From the analysis, it was shown that the localized heating effect at defects has a much greater influence for potential assistance of dislocation core motion as compared to the electron wind effect. Consequently, the theory of electroplasticity was explained in this work from a material science point of view with localized heating at defects being

the single mechanism. This theory was explained for the application of current without deformation (*i.e.* stationary) and during deformation. Also, the influence from this mechanism is discussed with respect to the observed formability improvements seen during EAF. The theory discussed in this work is supported by experimental testing and microstructure analysis.

In addition to studying the exact electroplastic mechanism, the electrical energy added to the system results in a decrease in the material flow stress. The decrease in flow stress is due to the direct electrical effect (*i.e.* electroplasticity), bulk thermal softening from the temperature rise, and thermal expansion effects. To understand and quantify the significance of each of these effects, models were created to predict the deformation behavior of sheet metals in uniaxial tension during EAF. The deformation behavior is the flow stress required for deformation, the local material strain in the specimen, and the thermal response from the applied electrical current. From the models, it is shown that approximately 30% of the flow stress reduction is a result of thermal expansion stresses and about 60% is a result of bulk thermal softening. The remaining 10% reduction is due to the electroplastic effect. The model results were verified by independent data from experimental testing.

Aside from the theory and modeling work, the applicability of this process to unique processing techniques was analyzed and performed. Specifically, control strategies of constant force forming, constant stress forming, and constant current density forming were envisioned and demonstrated. Thus, new class of control approaches was

developed for EAF in this work. Also, the applicability of the introduced models where analyzed for use in model predictive control strategies.

11.2- Intellectual Merit

The research objective was to understand the electroplastic mechanism present during EAF and to combine this effect with deformation behavior modeling of sheet metal in uniaxial tension. The following list presents the scientific contributions from this work:

- Physics-based models were applied (*Chapter 10*) to determine the significance of prior electroplastic theories (local heating at defects and the Electron Wind effect). From the analysis of this work, the electroplastic effect was deemed to be a result of only localized heating at lattice defects as a result of the Electron Wind effect not having a significant influence on the mobility of a dislocation.
- From the analysis of prior electroplastic effect theories, a new electroplastic theory is presented (*Chapter 10*) in this work which describes the influence of an electrical current on a material while stationary and during deformation. Additionally, the effect of the electrical current on the material formability is explained from a material science viewpoint. The theory presented is also supported by experimental testing (*Chapter 7*) and microstructure examination (*Chapter 8*).

- A modeling methodology was established for the EAF of sheet metals in uniaxial tension (*Chapter 3*). The methodology was used to create models that successfully predict the deformation behavior (*i.e.* material flow stress, local material strain, and thermal distribution) of sheet metals in uniaxial tension during EAF (*Chapters 4-6*). The models were independently validated by experimental EAF testing (*Chapter 7)*.
- The modeling work combined the influence of bulk thermal softening, thermal expansion stresses, and the electroplastic effect for the first time in EAF modeling research (*Chapter 6*). Using these models, the contribution of each of these effects was derived for the first time. The bulk thermal softening accounts for approximately 60% of the flow stress reduction, whereas the thermal expansion stress accounts for 30%. The remaining 10% in stress reduction is due to the electroplastic effect.
- This work introduces a new class of control approaches for EAF (*Chapter 9*). This work uses closed-loop control to allow for constant force, constant stress, and constant current density forming.

11.3 - Broader Impacts

The broader impact of this dissertation work lies in the potential for future adoption of the process of EAF in manufacturing industries such as automotive and aerospace. The models created allow for the determination of material flow stress to be determined given the input electrical conditions. Using these flow stress results, they could be incorporated into commercial finite element (FE) software to predict the

deformation behavior in other forming conditions. Also, the models and modeling methodology could be directly incorporated in the commercial FE software such that an electrically assisted forming module could be created. This would allow for companies to perform simulations to determine if applying EAF may be beneficial for their specific process. The adoption of the models is significant for EAF in that most metal deformation processes are performed first by simulation to save time and reduces costs.

The new control approaches developed in this work can also have a large impact on current forming methods. For example, the constant force/stress forming control approach allows for the forming force/stress to be a specified process input and not just an output of the process. This can allow for lower capacity machines to be used on a wider range of materials with various strength properties. Additionally, this also leads to the opportunity for forming machine architectures/designs to be modified to allow for more flexibility in material deformation which is highly desirable in industry.

On a larger scale, the potential for improved formability of lightweight materials at high production rates and for reduced process energy consumption could potentially save the forming industry millions of dollars in manufacturing costs. In addition, the ability to economically produce vehicles from lightweight materials will lower their fuel consumption and emissions over time. Moreover, with the future turning toward hybrid and electric vehicles, the reduction of vehicle mass is crucial; and for manufacturing of these lightweight materials, EAF could lead the way.

11.4 - Future Work

From the knowledge gained in this work for sheet forming during EAF, this work has also introduced future areas where a greater detail of fundamental research could be concentrated.

- First, the models in this work are examining uniaxial deformation and these models could be extended to other deformation modes. For example, the application of electrical current under a biaxial loading could be studied and modeled.
- This work also introduced a preliminary dislocation core heating model (Figure 10.2) which calculates the heat generated from the application of current at the dislocation and the surrounding area. Future work could expand this model to introduce additional dislocation cores and faze them in over time to study their interaction with respect to heat transfer between dislocation cores. Also, additional lattice defects such as grain boundaries could be incorporated.
- This work detailed the electrical theory in regard to the reduction in material flow stress and increased formability; however, a clear explanation of the removal of springback using EAF is still unclear.
- This work also introduced three main control strategies for EAF; however, additional control strategies for other applications could be developed. The addition of the derived models of this work could be incorporated in future MPC strategies; however, this work did not formally apply and test the

model capabilities. Also, for constant stress forming, the desired stress profile for forming a part could be an area of research where the stress profile could be optimized to achieve a desired objective (*i.e.* low quantity of residual stresses).

- From the analysis of the power supply response used in this work (*Appendix D*) it was shown that there is an AC component in addition to the DC component. With this AC component and its frequency this can create skin effects where a majority of the current will flow only near the surface of the conductor. As a result, the current flux will not be uniform throughout the cross-sectional area. Future work can study the influence of this AC component on the material response and its effect on the models introduced in this work.

APPENDICES

Appendix A

A.1 - Testing Conditions

Table A.1 shows the test conditions used for the thermal model development.

Table A.1 - Testing Conditions

Parameter Set	Current Magnitude	Initial Current Density	Pulse Duration	Pulse Period	Duty Cycle	Wave Shape
0	0A	0A/mm^2	n/a	n/a	n/a	n/a
1	800A	64A/mm^2	0.3s	60s	0.50%	Square
2	800A	64A/mm^2	0.5s	60s	0.83%	Square
3	500A	40A/mm^2	0.5s	60s	0.83%	Square
4	500A	40A/mm^2	1.0s	60s	1.67%	Square

A.2 - Power Supply Efficiency Determination

Figure A.1 shows the results for the determination of the power supply efficiency (note: convection coefficient (h) = 20W/m^2-K) which mainly affects the overshoot of the temperature at the end of the electrical current application (Parameter Set 1 was used). From this analysis a value of 70% was chosen as it best represented the experimental data.

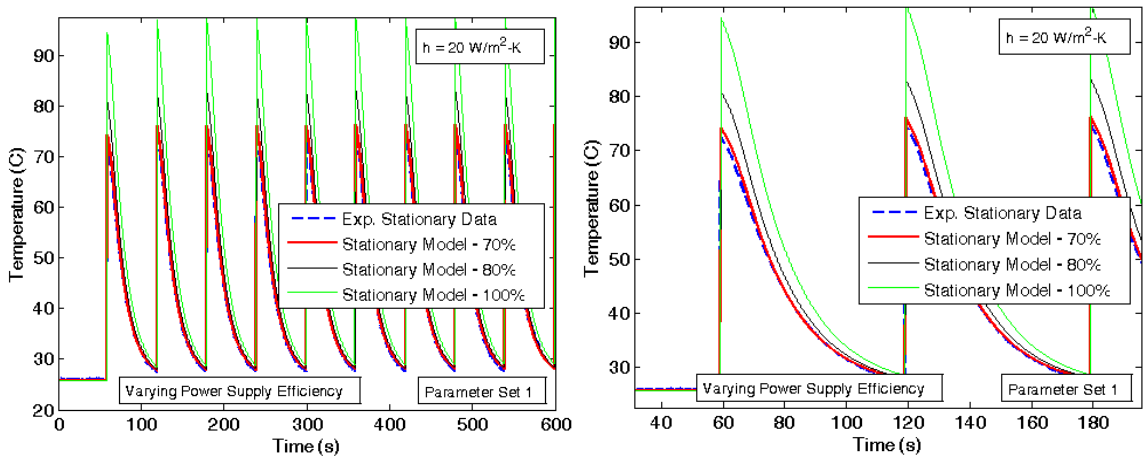

Figure A.1 - Power Supply Efficiency Comparison. Left is full view of simulation vs. experimental result and right is zoomed in view of simulation vs. experimental result.

A.3 - Convection Coefficient Determination

The results below compare various convection coefficients (using Parameter Set 1) so that a satisfactory coefficient is determined for the model (note: power supply efficiency = 70%). The convection coefficient determined (20W/m^2-K) was used throughout the model results for the other parameter sets.

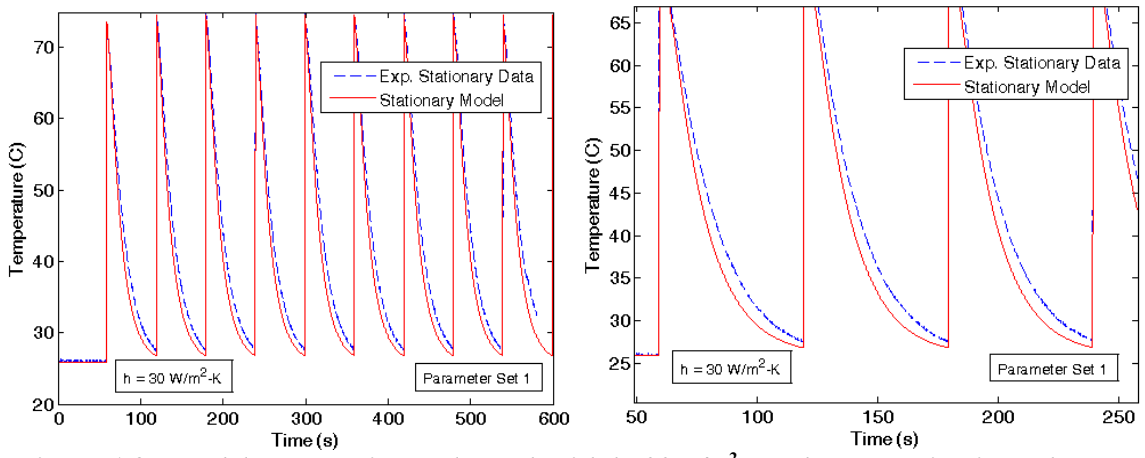

Figure A.2 - Model vs. Experimental Result with h=30W/m^2-K. The convection is too large as the model cools faster than the experimental results.

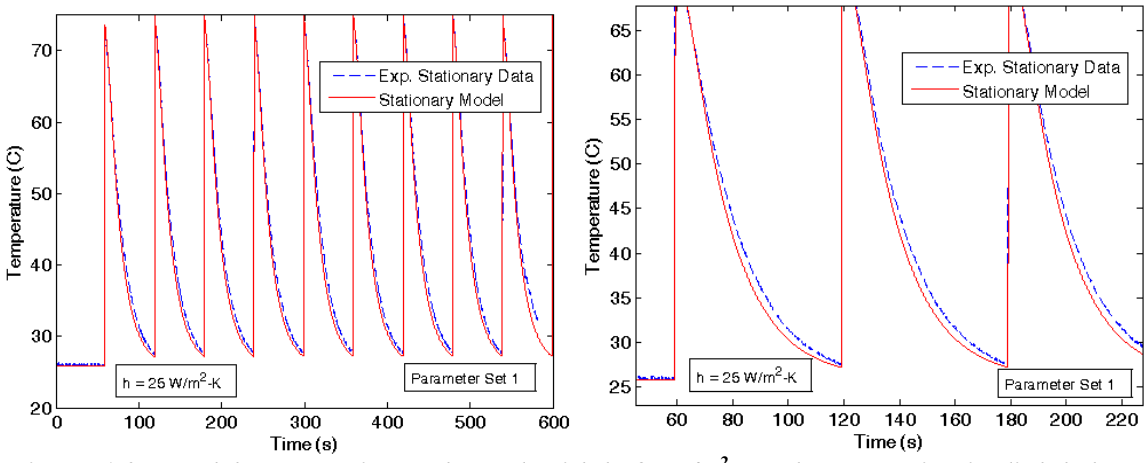

Figure A.3 - Model vs. Experimental Result with h=25W/m^2-K. The convection is slightly large as the model cools faster than the experimental results.

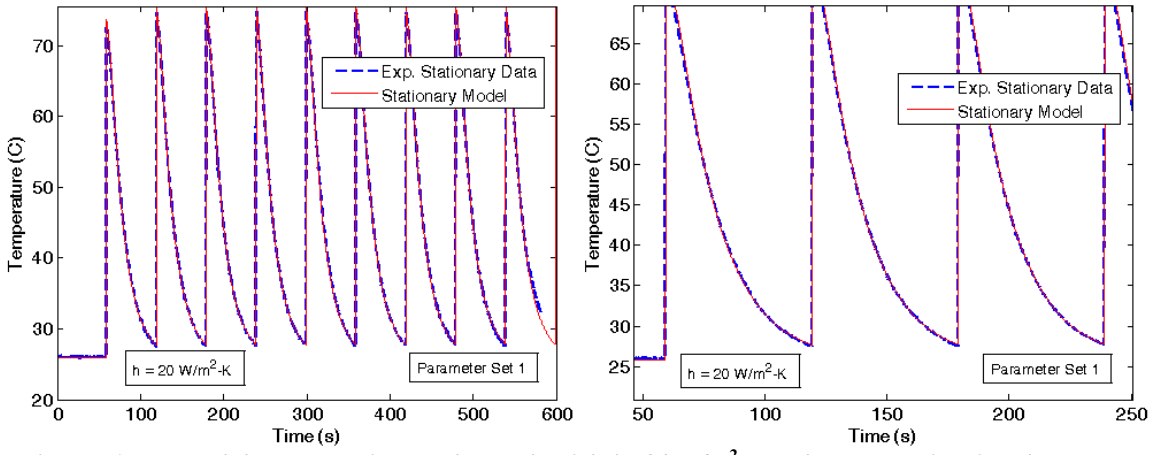

Figure A.4 - Model vs. Experimental Result with h=20W/m^2-K. The convection is adequate to describe the cooling response of the experimental results.

A.4 - All Model Results Summary

The model results vs. experimental results are shown in detail in the following sections.

A.4.1 - Parameter Set 1

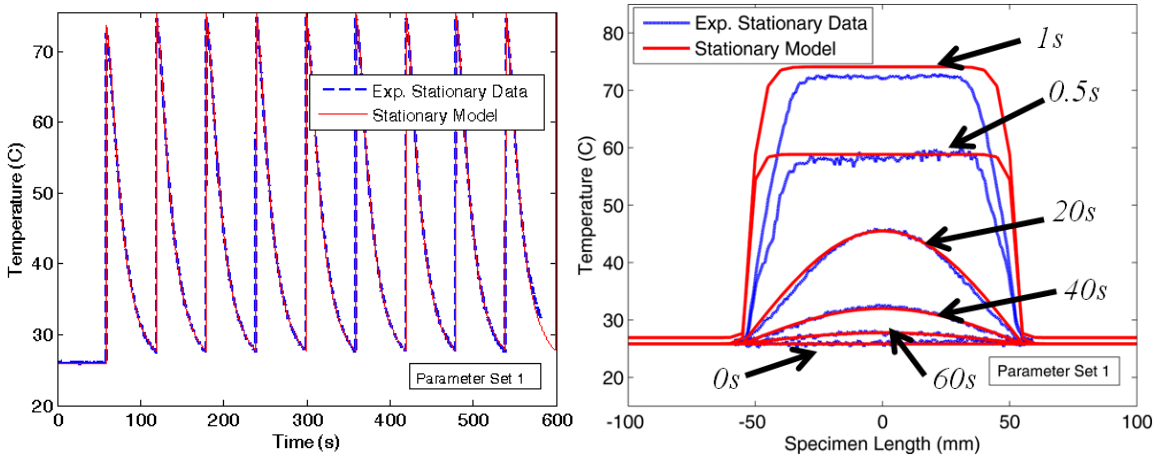

Figure A.5 - Left show Stationary Maximum Temperature Response of Experimental and Model Results for Parameter Set 1 and Right shows Stationary Axial Length Temperature Profile of Experimental and Model Results for Parameter Set 1

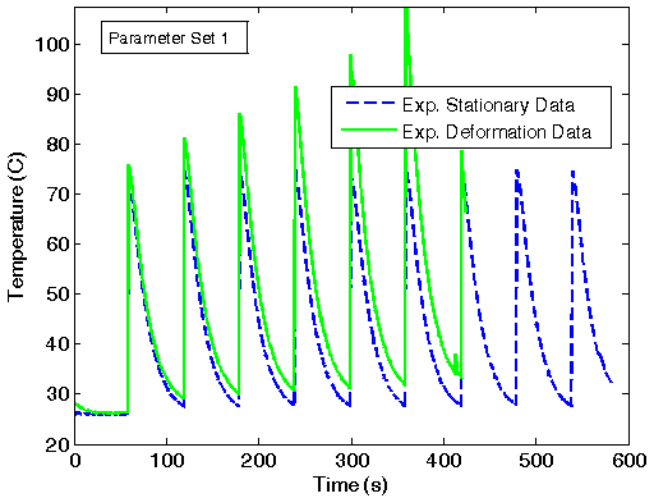

Figure A.6 - Experimental Maximum Temperature Response of Stationary and Deformation Results for Parameter Set 1

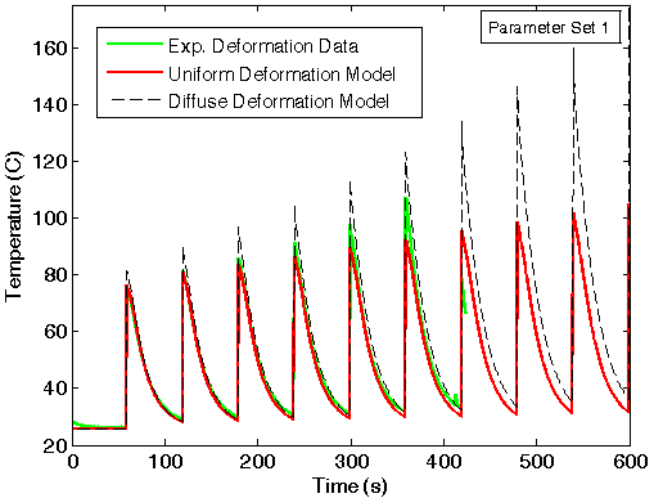

Figure A.7 - Maximum Temperature Comparison of Deformation Models to Experimental Results for Parameter Set 1

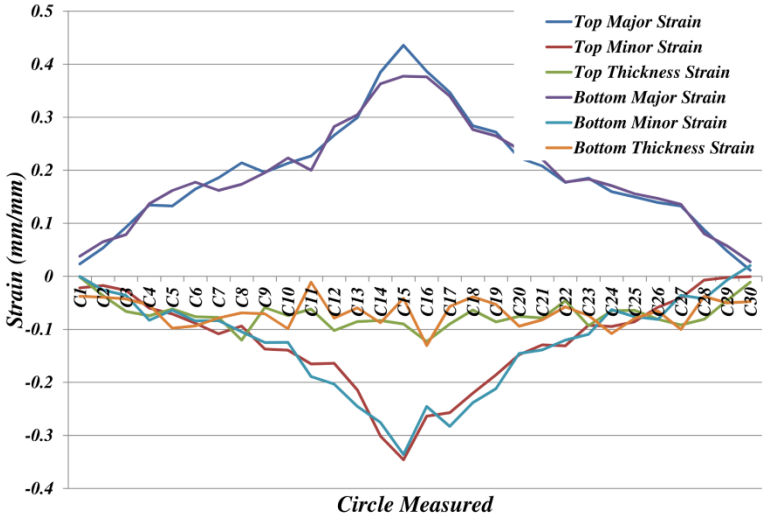

Figure A.8 - Experimental Strain Data for Parameter Set 1 at Failure

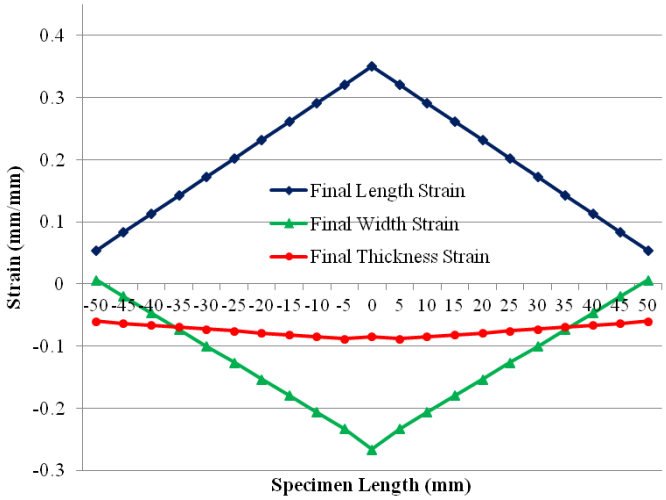

Figure A.9 - Linearized Experimental Strain Data for Parameter Set 1 at Failure

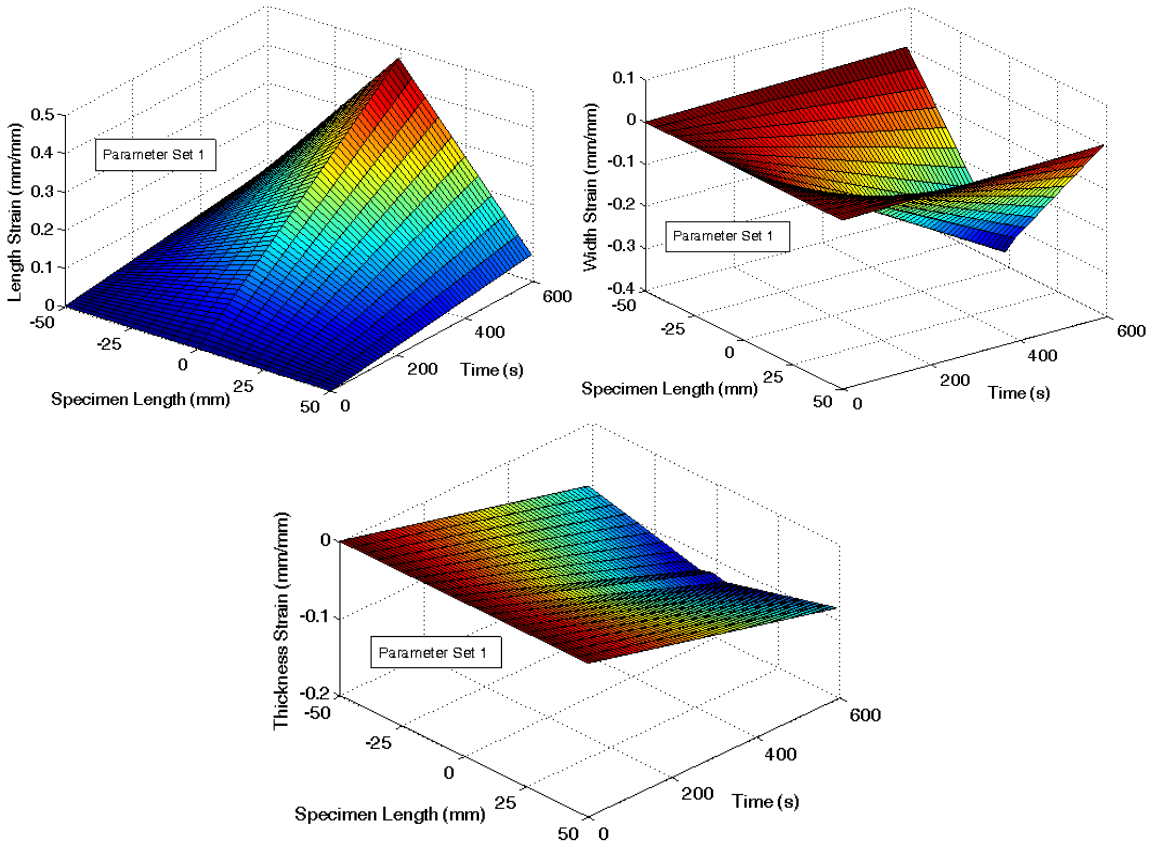

Figure A.10 - Diffuse Model Strain Inputs for Parameter Set 1

A.4.2 - Parameter Set 2

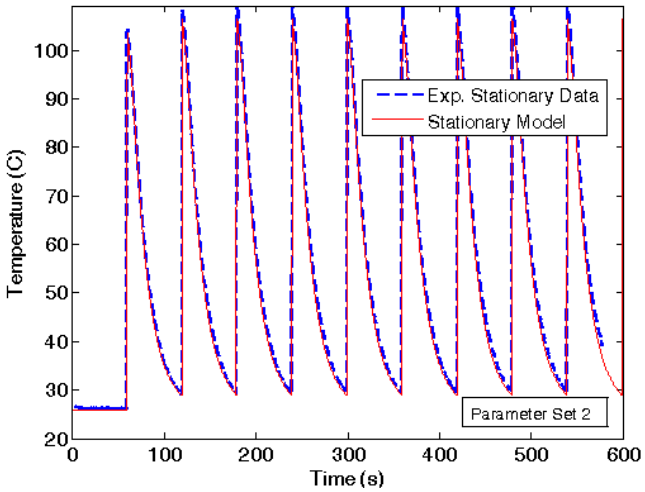

Figure A.11 - Stationary Maximum Temperature Response of Experimental and Model Results for Parameter Set 2

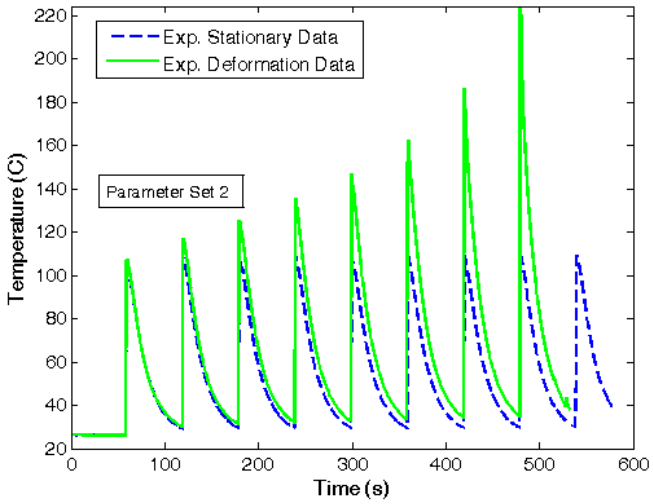

Figure A.12 - Experimental Maximum Temperature Response of Stationary and Deformation Results for Parameter Set 2

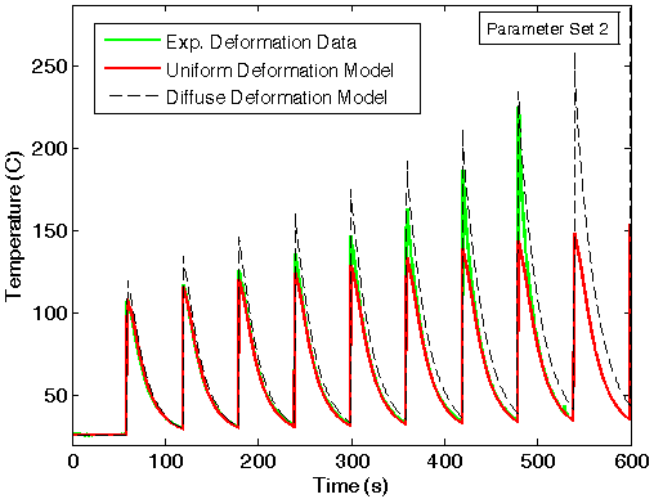

Figure A.13 - Maximum Temperature Comparison of Deformation Models to Experimental Results for Parameter Set 2

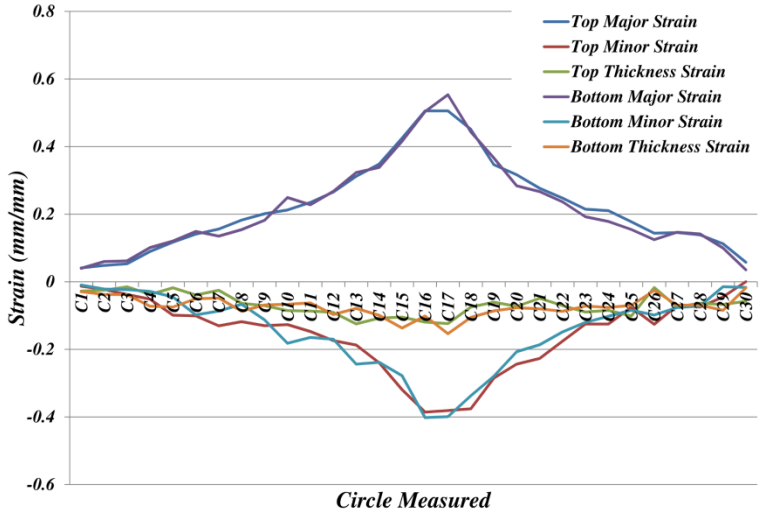

Figure A.14 - Experimental Strain Data for Parameter Set 2 at Failure

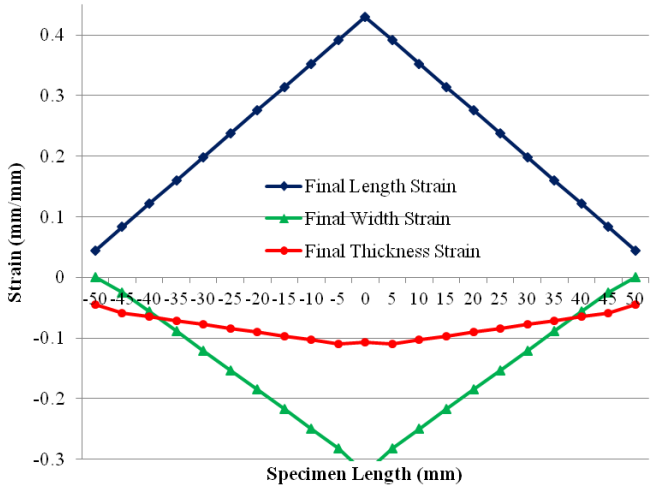

Figure A.15 - Linearized Experimental Strain Data for Parameter Set 2 at Failure

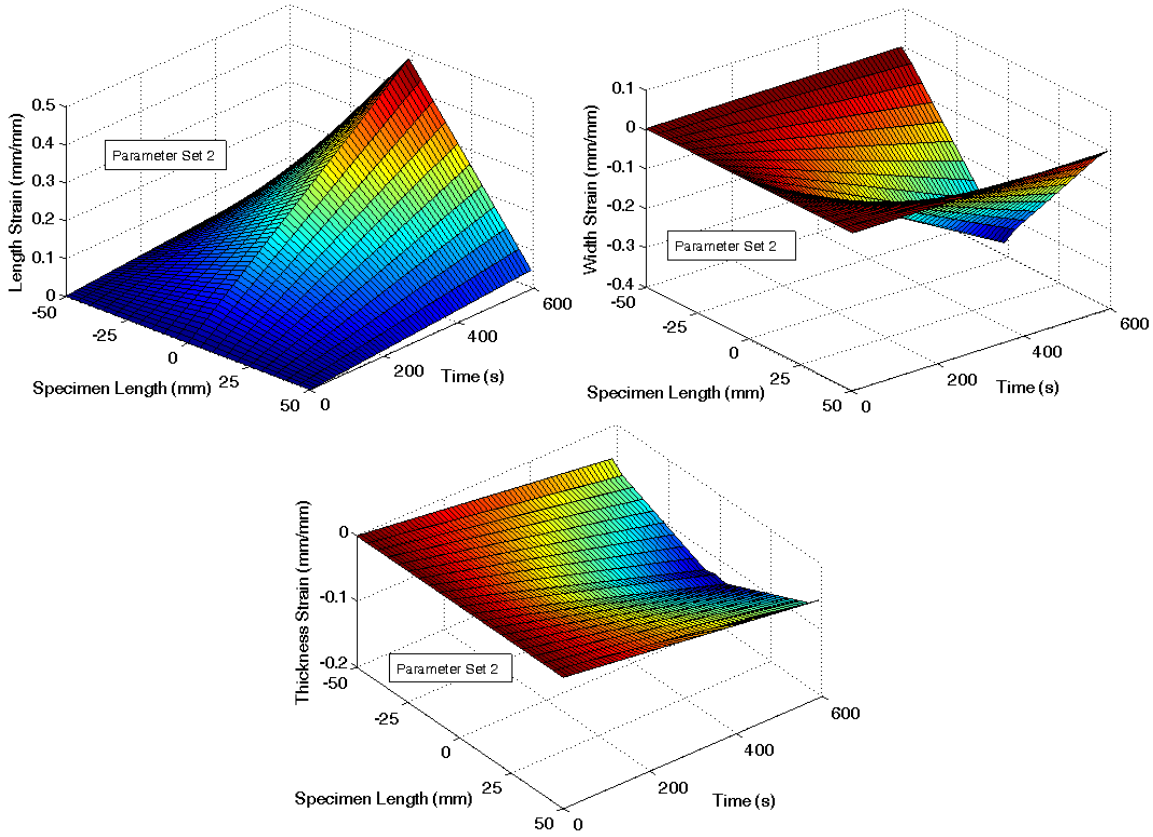

Figure A.16 - Diffuse Model Strain Inputs for Parameter Set 2

A.4.3 - Parameter Set 3

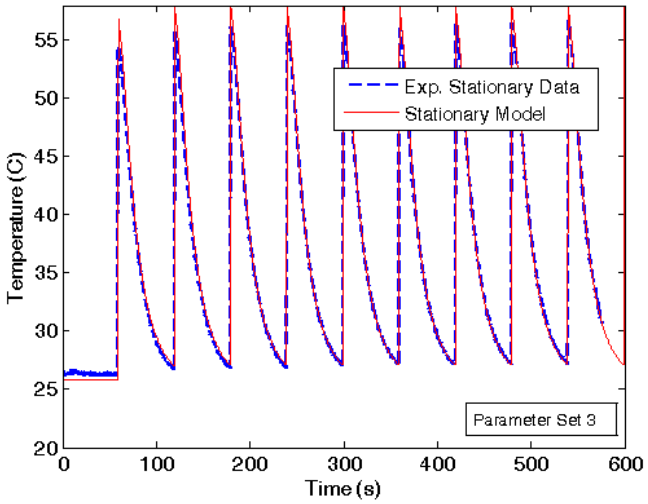

Figure A.17 - Stationary Maximum Temperature Response of Experimental and Model Results for Parameter Set 3

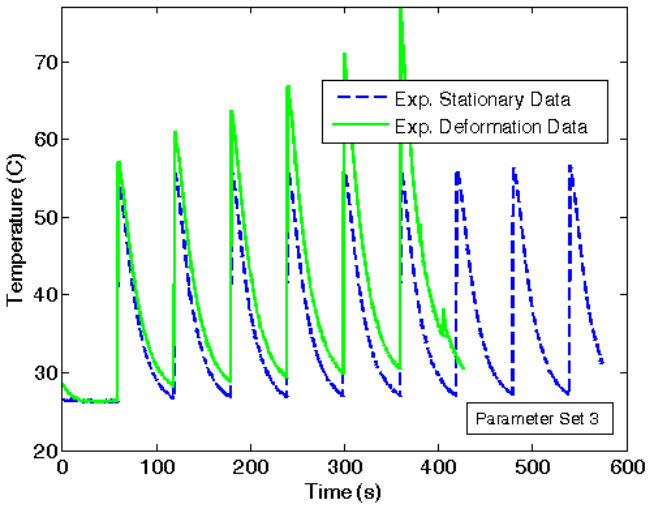

Figure A.18 - Experimental Maximum Temperature Response of Stationary and Deformation Results for Parameter Set 3

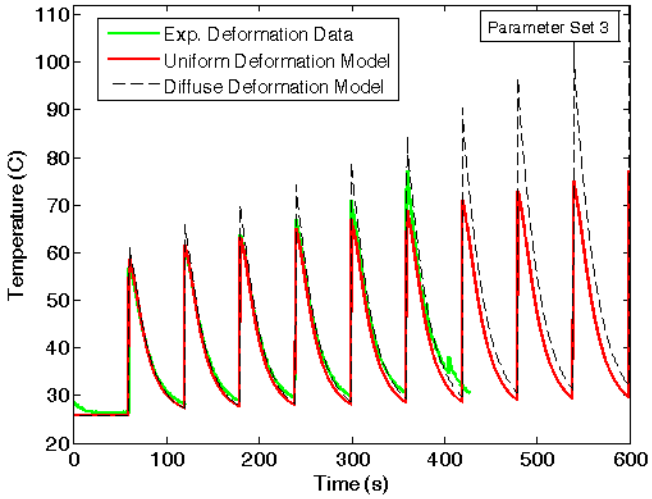

Figure A.19 - Maximum Temperature Comparison of Deformation Models to Experimental Results for Parameter Set 3

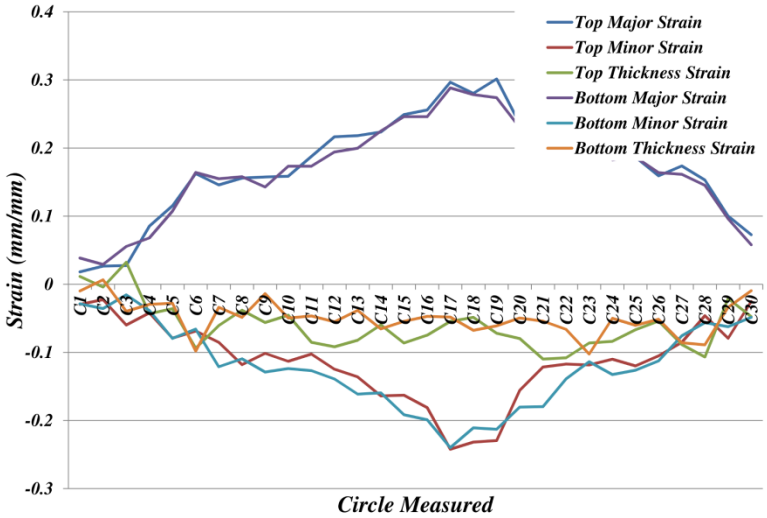

Figure A.20 - Experimental Strain Data for Parameter Set 3 at Failure

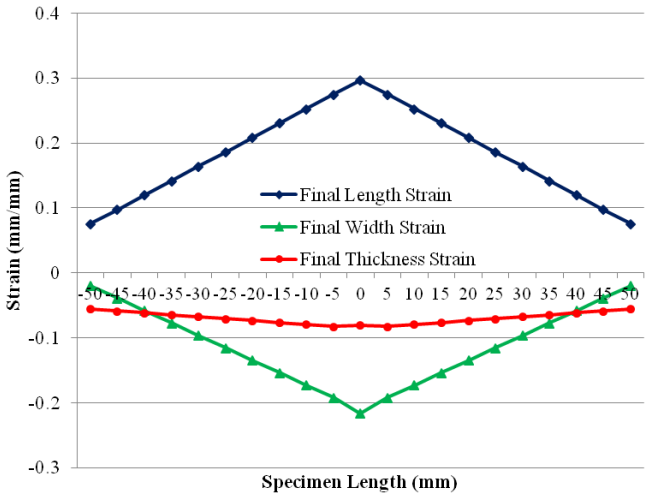

Figure A.21 - Linearized Experimental Strain Data for Parameter Set 3 at Failure

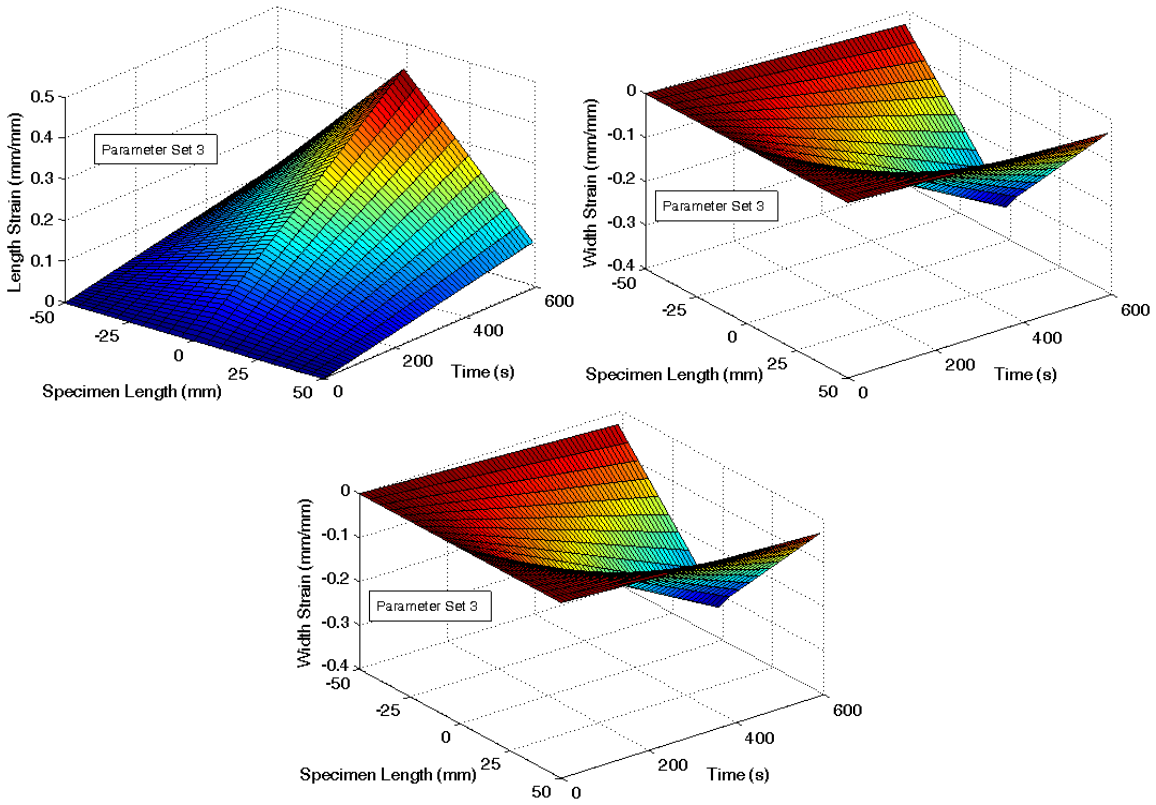

Figure A.22 - Diffuse Model Strain Inputs for Parameter Set 3

A.4.4 - Parameter Set 4

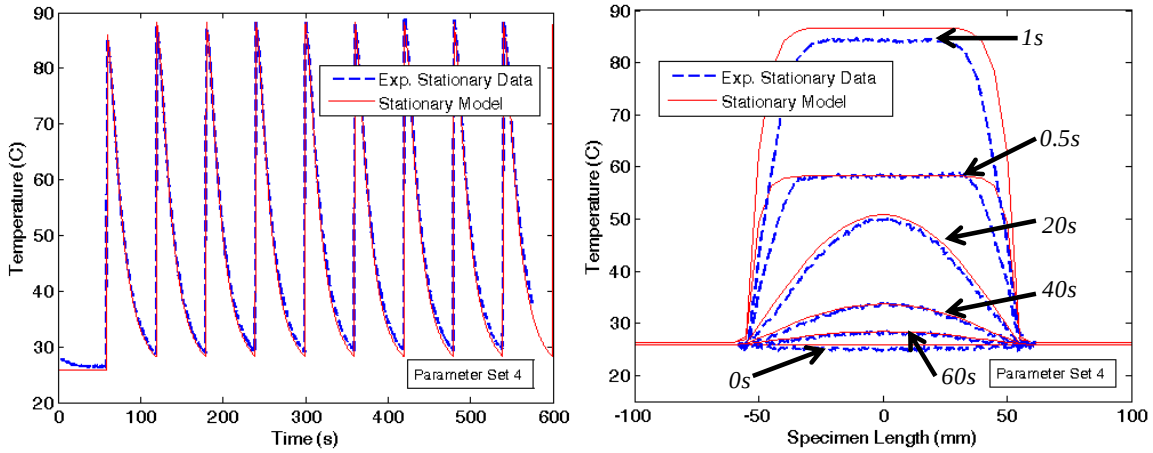

Figure A.23 - Left show Stationary Maximum Temperature Response of Experimental and Model Results for Parameter Set 4 and Right shows Stationary Axial Length Temperature Profile of Experimental and Model Results for Parameter Set 4

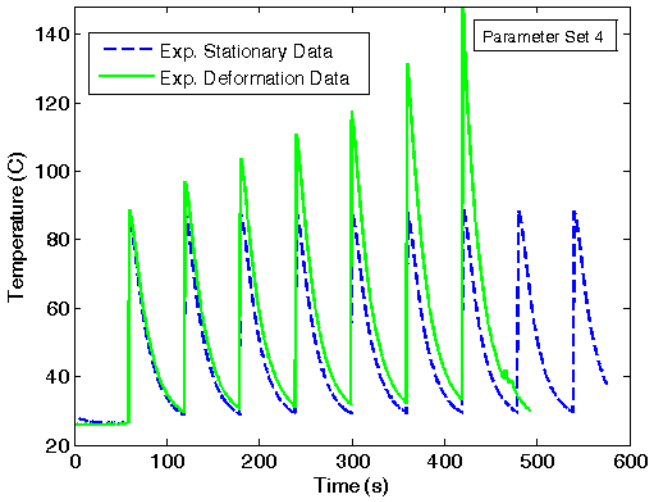

Figure A.24 - Experimental Maximum Temperature Response of Stationary and Deformation Results for Parameter Set 4

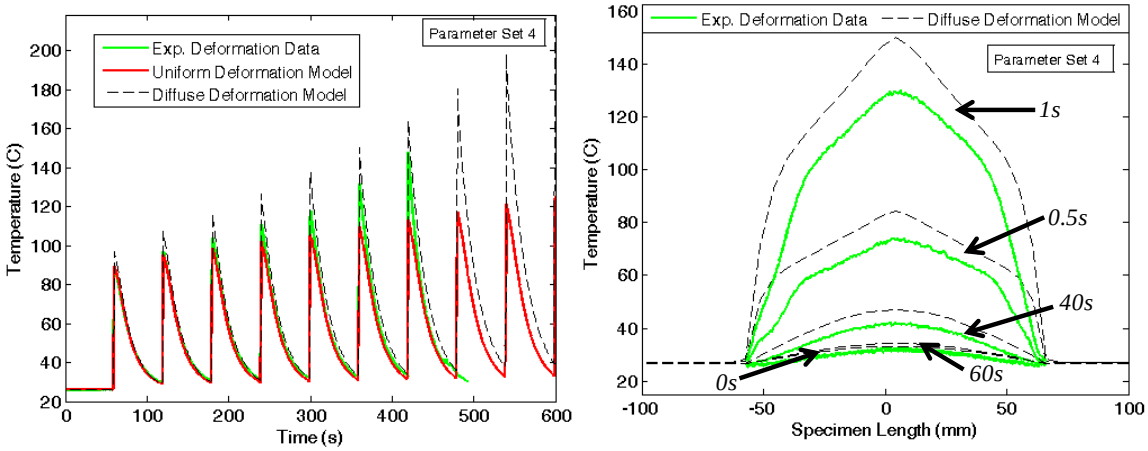

Figure A.25 – Left shows Maximum Temperature Comparison of Deformation Models to Experimental Results for Parameter Set 4 and Right shows Axial Comparison of Diffuse Deformation Model to Experimental Results for Parameter Set 4

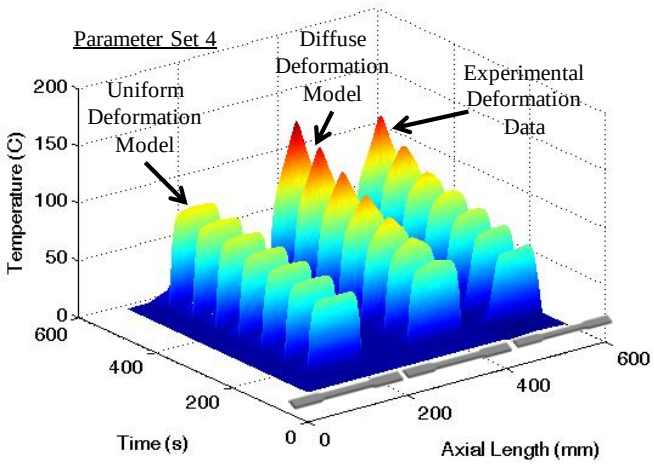

Figure A.26 - Thermal Response Surface for Deformation Models and Experimental Data as a Function of Time for Parameter Set 4

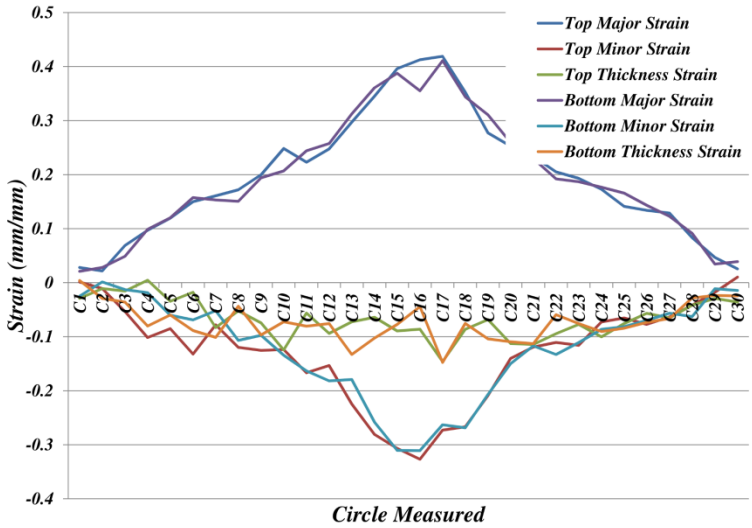

Figure A.27 - Experimental Strain Data for Parameter Set 4 at Failure

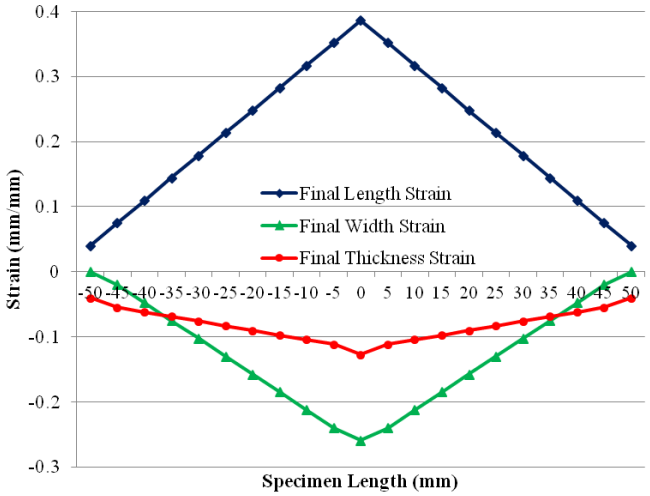

Figure A.28 - Linearized Experimental Strain Data for Parameter Set 4 at Failure

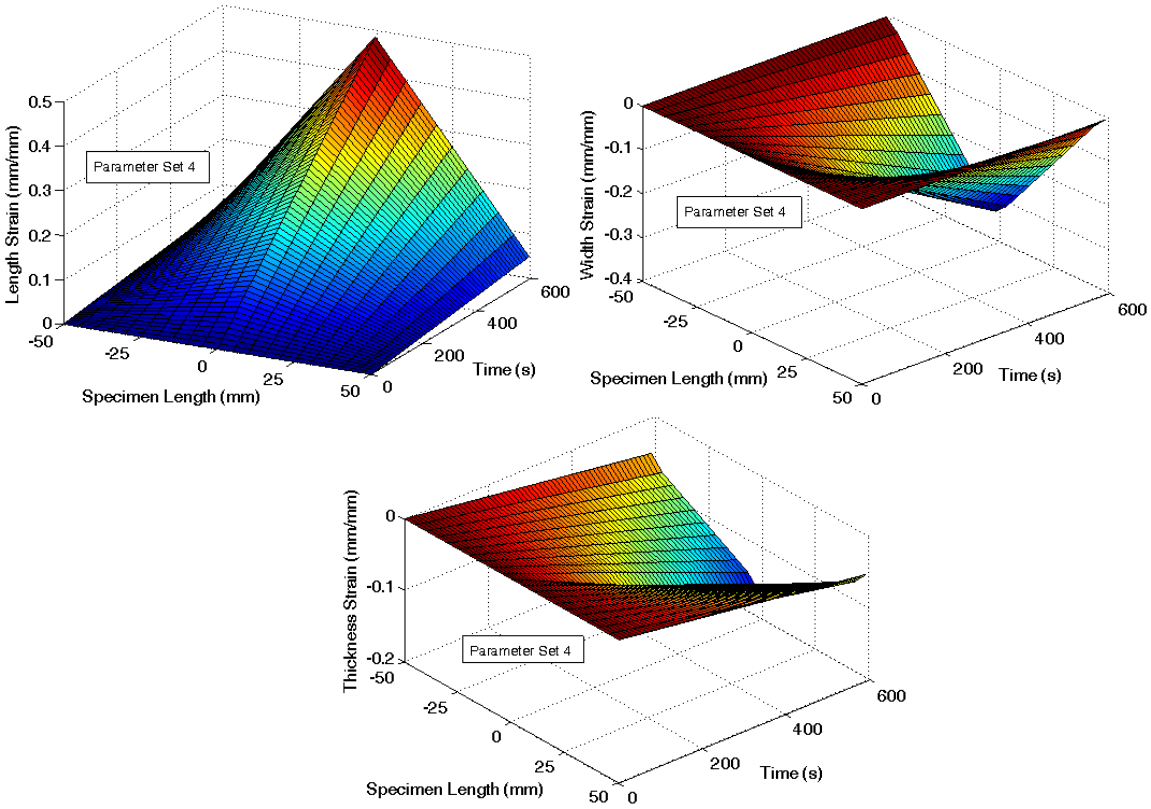

Figure A.29 - Diffuse Model Strain Inputs for Parameter Set 4

A.5 - Circle Grid Analysis Results at Elevated Temperatures

The below results summarize the measurements of the CGA for the elevated temperature testing.

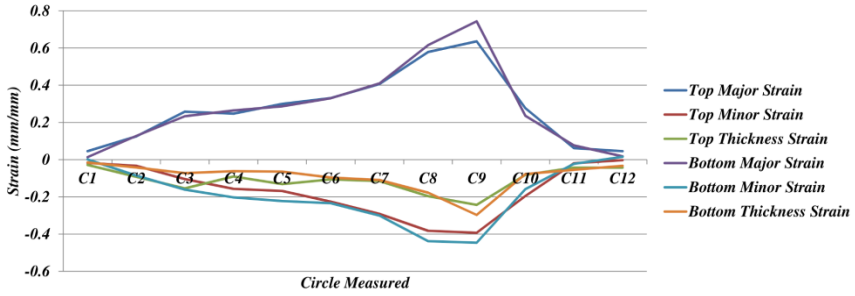

Figure A.30 - Circle Grid Results (150C Elevated Temperature)

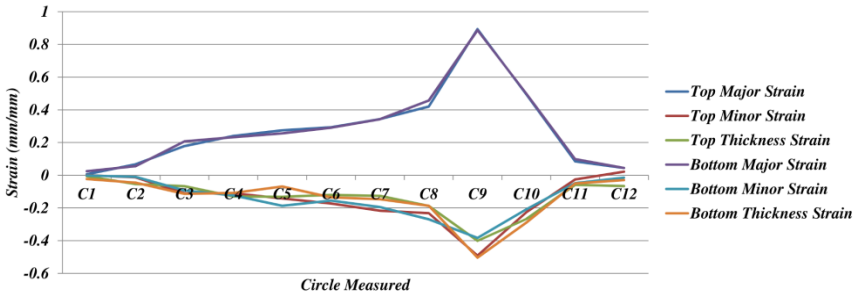

Figure A.31 - Circle Grid Results (150C Elevated Temperature)

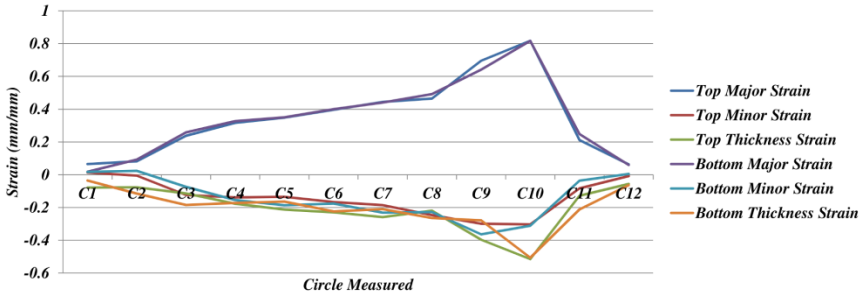

Figure A.32 - Circle Grid Results (150C Elevated Temperature)

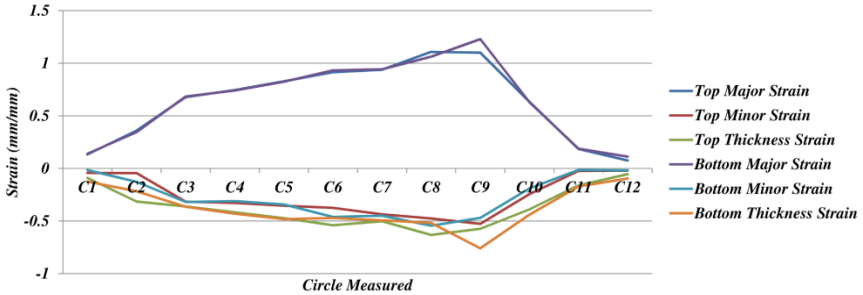

Figure A.33 - Circle Grid Results (150C Elevated Temperature)

Appendix B

B.1 - Sample Preparation

For sample preparation, two types of samples were created from the received warm rolled Mg AZ31B sheet. For the first type of specimen, the sheared 1mm thick sheet strips with dimensions of 20x200mm were machined according to ASTM B557M [B.1]. Afterward, a strain grid was chemically etched on one surface so that the local strain could be measured after deformation through Circle Grid Analysis (CGA). Additionally, the other side of the sheet was coated with a thin layer of ceramic paint to reduce emissivity issues during infrared imaging. This specimen type is used for conventional room temperature testing and EAF testing. The machining fixture and final specimen are shown in Figure B.1. For the elevated temperature tests conducted, the specimen geometry varied as a result of the available fixturing. The specimen geometry used in the elevated temperature tests is shown in Figure B.2 along with the applied strain grid.

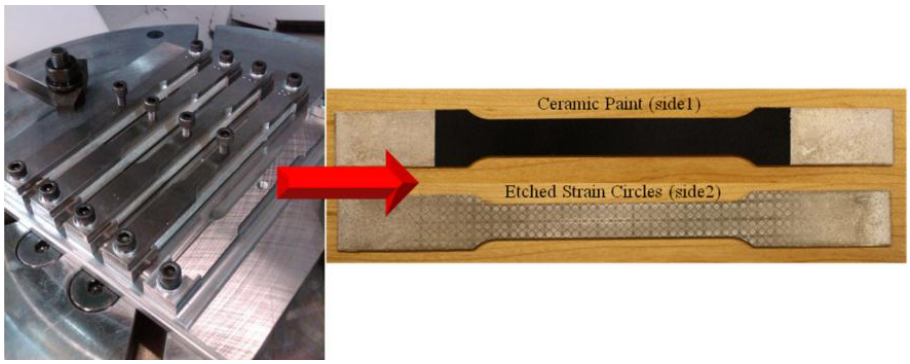

Figure B.1 - Room Temperature and EAF Testing Specimen Preparation

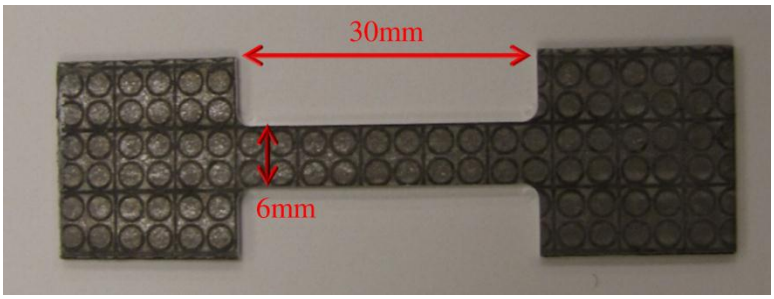

Figure B.2 - Elevated Temperature Specimen

B.2 - References for Appendix B

[B.1] ASTM B557M – 10: Standard Test Methods for Tension Testing Wrought and Cast Aluminum- and Magnesium-Alloy Products (Metric), 2010.

Appendix C

C.1 - Microstructure Examination Procedure

For examination of the magnesium microstructure the below procedure was used and was found to work the best for this alloy (Mg AZ31B).

C.1.1 - Mounting

The use of an epoxy cold mounting system with a cure time of approximately 8 hours is recommended and it is best to let the mounts cure overnight. For magnesium, plastic clips should be used to hold smaller specimens in the mount. An example of a mount is shown in Figure C.1 for a sample after being etched and imaged.

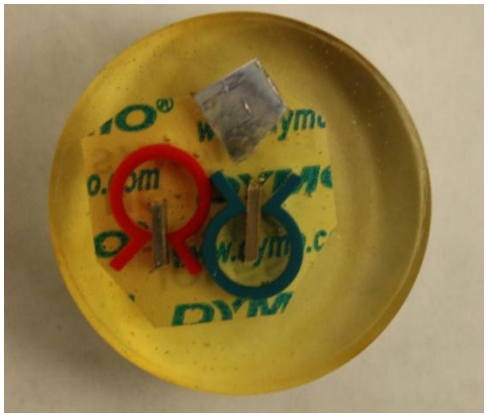

Figure C.1 - Microstructure Sample Preparation Station

C.1.2 - Grinding/Polishing

Three grinding steps are recommended before polishing. These include using disposable SiC paper at levels of 320, 600, and 1200 grit. Water must be used during grinding and the mounts should be rinsed with sufficient water/soap after each step so that any particles do not transfer to the next grinding step. To grind and polish the samples a Buehler automatic polisher with an automatic head was used. The setup is shown in Figure C.2.

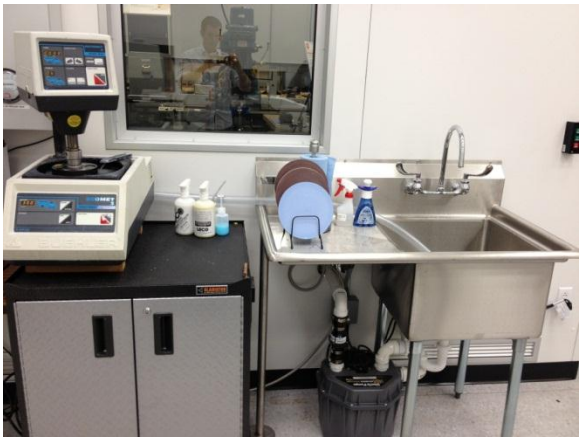

Figure C.2 - Microstructure Sample Preparation Station

Three polishing steps are recommended after completing the grinding steps. For fine polishing, first use a 3 micron monocystalline diamond suspension with an appropriate polishing cloth. Then a 1 micron monocystalline diamond suspension with an appropriate polishing cloth is used. Water is not to be used during these two polishing steps. For very fine polishing or oxide polishing (OP), 0.05 micron suspension of Colloidal Silica should be used along with an appropriate polishing pad. For very fine polishing, the polishing cloth can be wetted with water, but should not be applied during polishing. A detailed procedure is given in Table C.1.

Table C.1 - Recommended Grinding and Polishing Procedure

	Grit Size	***Time (min)***	***Load (lb)***	***RPM***	***Direction***	***Comments***
Step 1	320	Till Plane	6	300	Contra	
Step 2	600	3	6	300	Contra	
Step 3	1200	3	6	300	Contra	
Step 4	3µm	5	6	150	Contra	
Step 5	1µm	5	6	150	Contra	
Step 6	0.05µm	1.5	5	130	Contra	Last 5 sec: Water

C.1.3 - Etching

Following the polishing of the samples the surface needs to be etched to reveal the grain structure. The type of etchant used is highly dependent on the alloy and some

etchants may work better than others for some materials. The etchant can be applied using a cotton swab and the specimen surface can be rubbed gently with the cotton swab under appropriate hooding and ventilation. However, some alloys etch better using immersion. After applying the etchant (for a few seconds) you need to rinse with alcohol to stop the etching process. The alcohol can be blown away after that with an air jet (otherwise the alcohol might leave some residue).

For Mg AZ31, the most efficient etchant to reveal the grain structure was Acetic Picral Etchant #8 found in the ASM Specialty Handbook for Mg [1]. The etchant composition is given in Table C.2.

Table C.2 - Acetic Picral Etchant Number 8 from ASM Handbook [C.1]

10mL Acetic Acid
4.2g Picric Acid
10mL H_20
70mL Ethanol (95%)

It should be noted that the etchant containing picric acid should be handled and stored with care as dehydrated picric acid is very explosive.

C.1.4 - Imaging

To image the microstructure of the samples optical imaging was used. For this research the images were taken using a Zeiss Axiovert 25 microscope with Buehler OmniMet software at Clemson University's Electron Microscope (EM) Facility at the Advanced Materials Research Lab (AMRL).

C.1.5 - Detailed List of Consumables

Listed in Table C.3 is a detailed list of consumables used to prepare the microstructure samples.

Table C.3 - Detailed Consumables Listing for Microstructure Examination

Mounting
- Struers SpeciFix-20
- Leco Plastic Sample Clips
Grinding
- Leco 320 Premium Silicon Carbide Paper
- Leco 600 Premium Silicon Carbide Paper
- Leco 1200 Premium Silicon Carbide Paper
Polishing
- Leco Final Polishing Cloth (Lecloth) for Diamond Suspension
- Leco Final Polishing Cloth (Imperial) for OP Suspension
- Leco 3 micron Monocystalline Diamond Suspension
- Leco 1 micron Monocystalline Diamond Suspension
- Leco Diamond Lapping Oil for Diamond Suspension Extension
- Leco 0.05 micron OP Suspension (Colloidal Silica)
Etching
-10mL Acetic Acid
-4.2g Picric Acid
-10mL H_20
-70mL Ethanol (95%)

C.2 - Grain Size Measurement Procedure

To measure the grain size in each micrograph, two methods were used. The first is the line intercept method where the number of intersections is counted along a line of known length. Using the number of intersects and the line length this results in an average grain size for the image. The lines can be applied in a circular or grid pattern on the image. An example grid in shown in Figure C.3 where there are vertical and horizontal lines applied. This technique is limited such that it only gives an average size

and does not allow for the aspect ratio of the grain to be examined or the distribution of grain sizes to be determined. The second technique was to use imaging software (ImageJ) to fit an ellipse to grains within the micrograph. To gain a good representation of the population, approximately 100 grains were measure and analyzed. The measured characteristics were the major and minor axis of the ellipse and the total ellipse area. The major and minor dimensions of the ellipse were used to examine the aspect ratio of the grains and the area was used to calculate an equivalent circular grain diameter. The ellipse measurements taken for an example micrograph are also shown in Figure C.3.

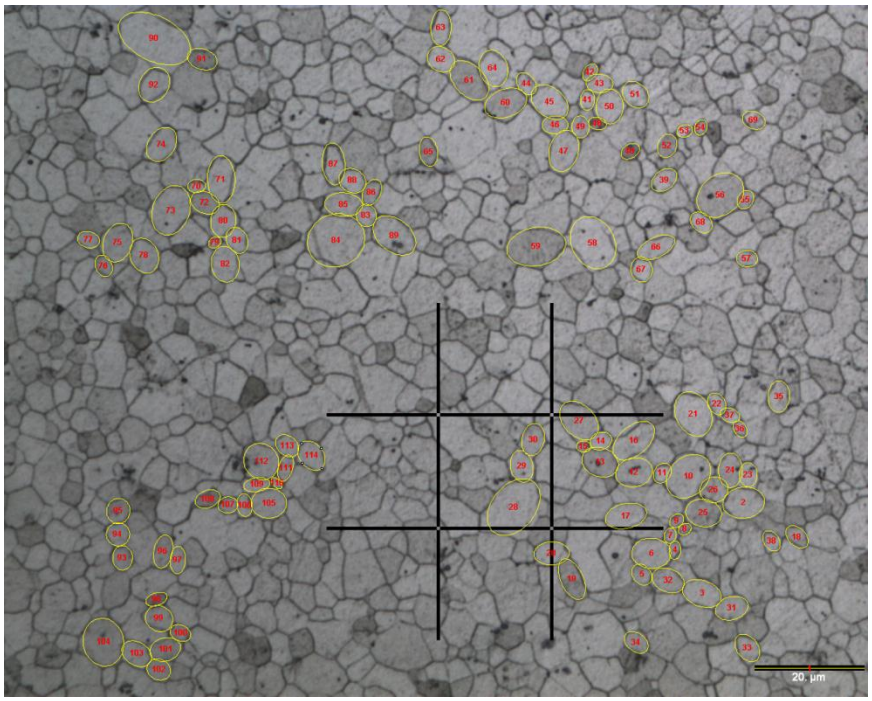

Figure C.3 - Grain Size Measurement Techniques

C.3 - References for Appendix C

[C.1] Avedesian, M.M. and H. Baker (1999). Magnesium and Magnesium Alloys - ASM Specialty Handbook, Second Edition, ASM International, Materials Park, OH.

Appendix D

D.1 - 4kA Power Supply Control

For the process of Electrically-Assisted Forming (EAF), the use of a power source to supply the direct electrical current to the process is required. For this research a Darrah Silicon Controlled Rectifier (SCR) with a current output from 0A to 4000A was used to supply the electric current to the forming process. In order to have control of the power supply, an external remote was built using a National Instruments (NI) CompactRIO (cRIO) integrated controller/chassis with varying I/O modules programmed with NI LabVIEW software. To have the power supply produce a current output, a feed voltage was provided to the power supply. For this, a relationship between feed voltage and current output was established. Follow the characterization of this relation, varying control techniques or programs were produced to supply current to the process.

D.1.1 - Characterization of Current Control

The first step in controlling the power supply was to determine a relationship between the input feed voltage and the output current from the power supply. This was manually performed by sending set feed voltages to the power supply and recording the current output using a clamp-on ammeter. The data collected along with a linear trend is shown in Figure D.1. As seen the relationship is exactly linear and is described mathematically by Equation D.1.

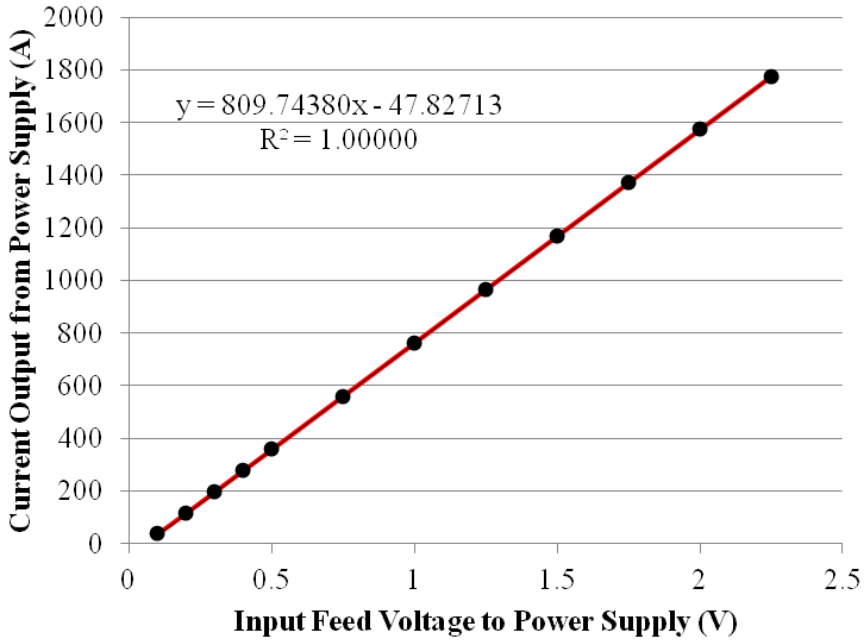

Figure D.1 - Feed Voltage and Current Output Relationship

$$V_{feed} = \frac{I+47.82713}{809.7438} \tag{D.1}$$

where, V_{feed} is the feed voltage required by the power supply and I is the desired direct current output.

For the process of EAF, it is also desirable to know the mechanical process outputs which are mainly the position and force of the forming process. To incorporate this information into the control of the power supply the Instron DAQ system was interfaced with the cRIO to provide real-time position and force measurements. The main process parameter flow schematic is shown in Figure D.2, where p is position, F is force, I is current, and V is voltage. As seen, the EAF process is position controlled and the corresponding force and position data was provided to the cRIO to communicate with the power supply which provided a current to the EAF process using a feed voltage.

Additionally, the cRIO can receive a measurement of the current output to have closed-loop control.

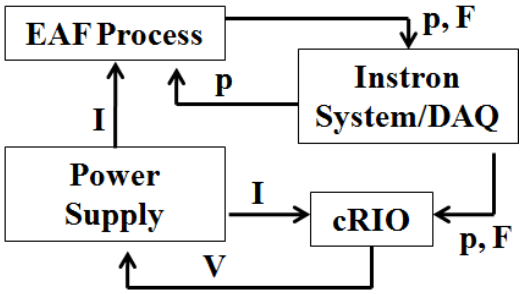

Figure D.2 - Information Flow Schematic for Control of Power Supply

To control the applied current during the forming process, five main control schemes were used. The first two schemes allows for a square wave input with varying duty cycles during deformation and without deformation (i.e. stationary), respectively. The third scheme allows for a continuous current to be applied during deformation. The fourth and fifth control scheme used real-time feedback for constant force and stress forming, respectively.

D.1.2 - Control System for Square Wave EAF Testing

To precisely control the current applied to the EAF process, a control scheme was programmed in LabVIEW. The general control system for EAF testing allowed for a square wave application of current to be applied. The graphical user interface (GUI) is shown in Figure D.3 where the user can input the magnitude of the electrical current square wave along with the pulse duration and period (which combine to produce the duty cycle) before testing. Also, inputs for the specimen dimensions are given (can be further used to provide inputs for constant current density forming). Once the initial conditions are given, the program is set to start the application of current once a preset

load is reached (*e.g.* 100 lb). After this point the material deformation continues along with the application of current until the user stops the test or the material fails. If the material fails the program is set to discontinue the application of current and turn off the power supply. Additionally, the program saves time, position, and force data to be used for later analysis. Also on the GUI are real-time force and position measurements along with the signal sent to the power supply. Additional test information such as time and total deformation are displayed as well.

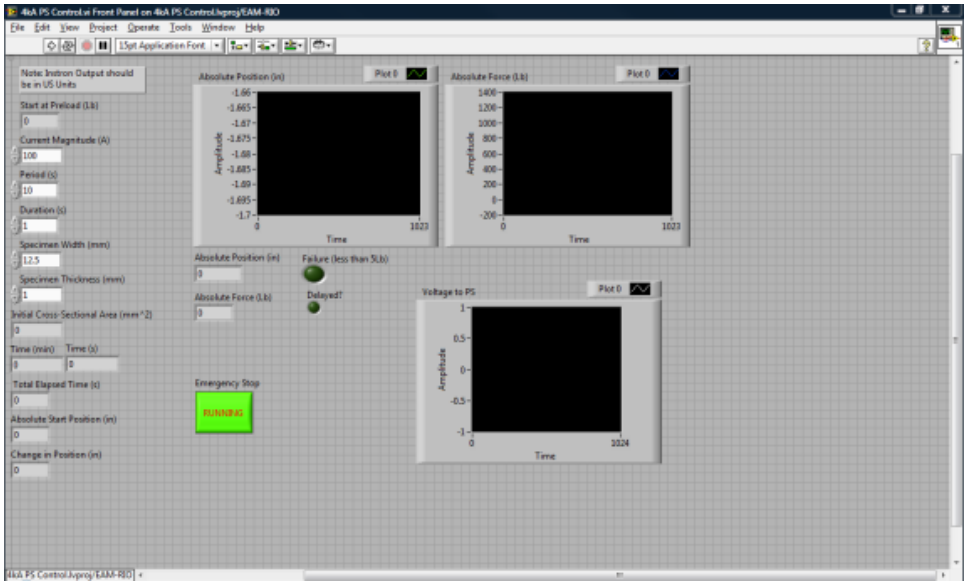

Figure D.3 - Front Panel of Control System for Square Wave EAF Testing

The block diagram is shown in Figure D.4 where a flat sequence structure is used. In the first sequence this is where the initial values are obtained by the user and sequence one ends when the preset force value is reached. The second sequence is where a wave generator is used to apply a feed voltage to the power supply with the set conditions given by the user in the first sequence. Also, the test time, force, and position values are

stored in arrays. The third sequence turns off the power supply and saves the collected data once the test is stopped by the user or the material fails.

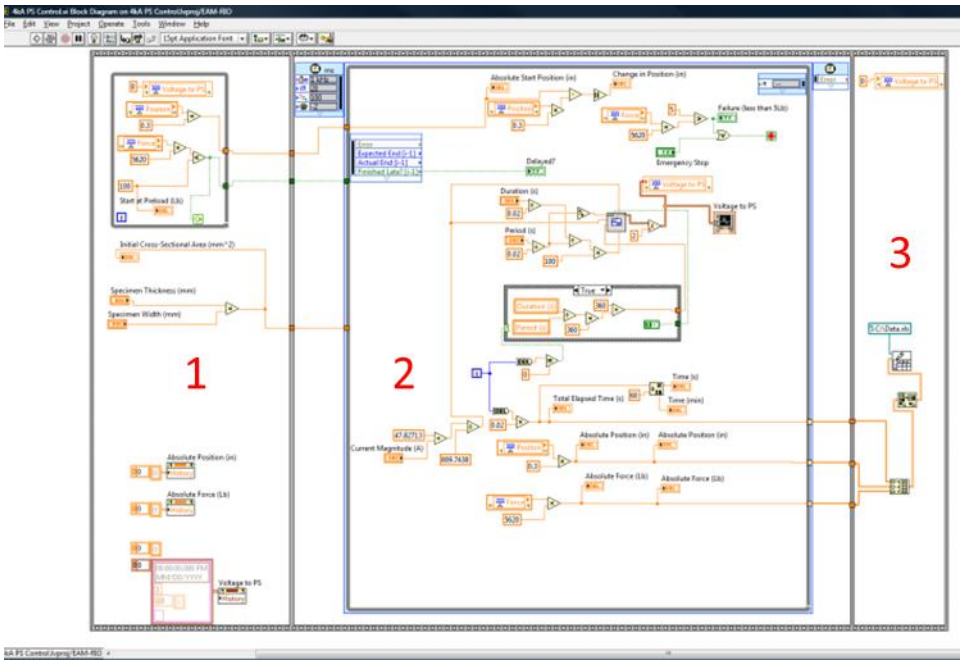

Figure D.4 - Block Diagram of Control System for Square Wave EAF Testing

D.1.3 - Control System for Stationary EAF Testing

For stationary EAF testing this program allows the user to input square wave characteristics (i.e. electrical current magnitude and duty cycle) and manually start the application of current to the test specimen. This type of control is used for only examining the thermal response of the material subject to an electric current field. The GUI (Figure D.5) is similar to the square wave EAF testing control; however, the application of current is started by the user.

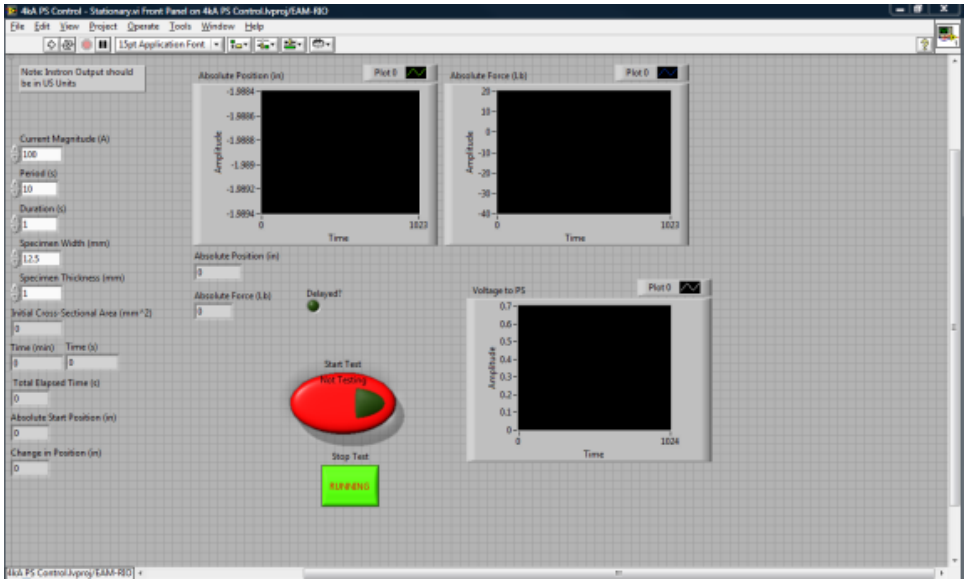

Figure D.5 - Front Panel of Control System for Stationary EAF Testing

The block diagram is shown in Figure D.6 and there are three sequences in a flat sequence structure. The configuration is very similar except that sequence two is not started by a preset load, but started by the user.

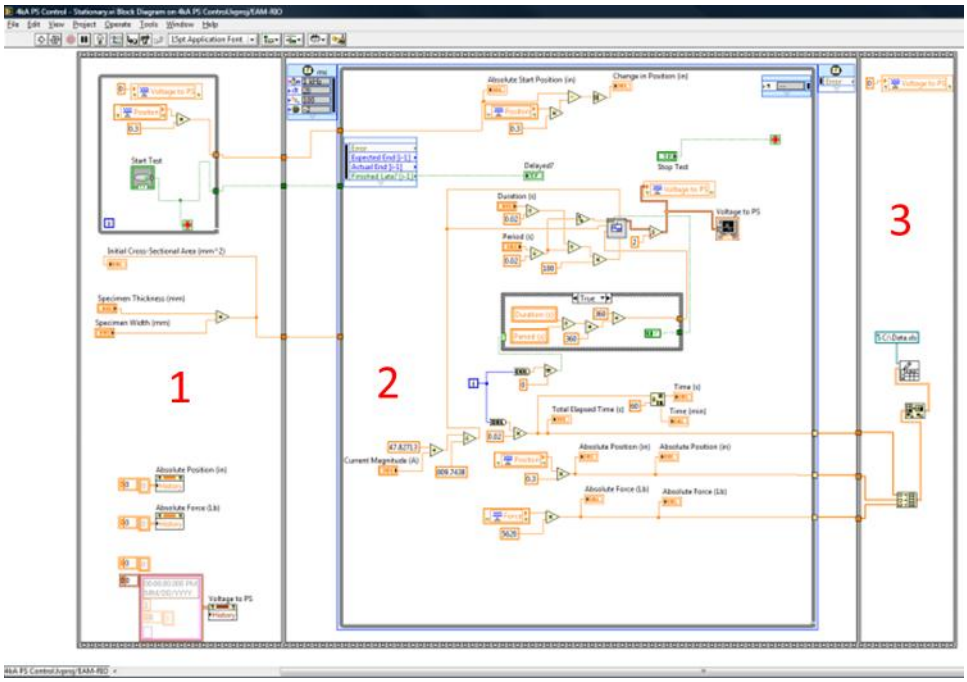

Figure D.6 - Block Diagram of Control System for Stationary EAF Testing

D.1.4 - Control System for Continuous EAF Testing

To test the material characteristics under a continuous current field this program allows the user to apply a continuous current until the user stops the current or a set load is reached (*e.g.* 10 lb) which indicates material failure. The inputs include geometric dimensions of the specimens and the current magnitude desired for the test. The current application is started once a given preset load is reached (*e.g.* 100 lb). The GUI is shown in Figure D.7 where the real-time load, position, and feed voltage to the power supply can be monitored by the user.

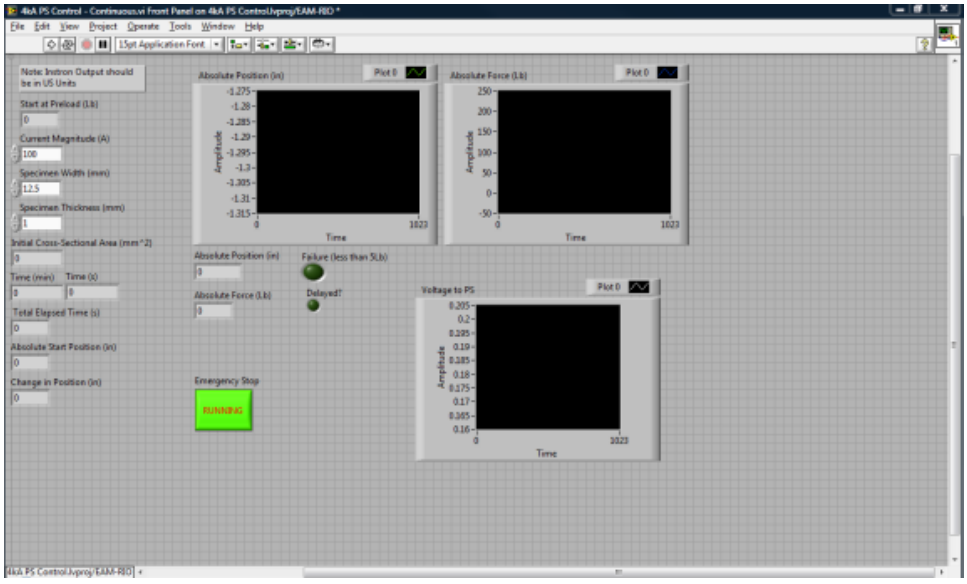

Figure D.7 - Front Panel of Control System for Continuous EAF Testing

The corresponding block diagram is presented in Figure D.8 and the use of a flat sequence structure is once again used. Sequence 1 is where the inputs are taken from the user and sequence 2 starts when the preset load is reached. Sequence 2 applies the current to the process and continues until the preset load is reached (*i.e.* indicating material failure) or the user stops the current application. In sequence 3 the time, force, and position data is stored and the power supply is shut off.

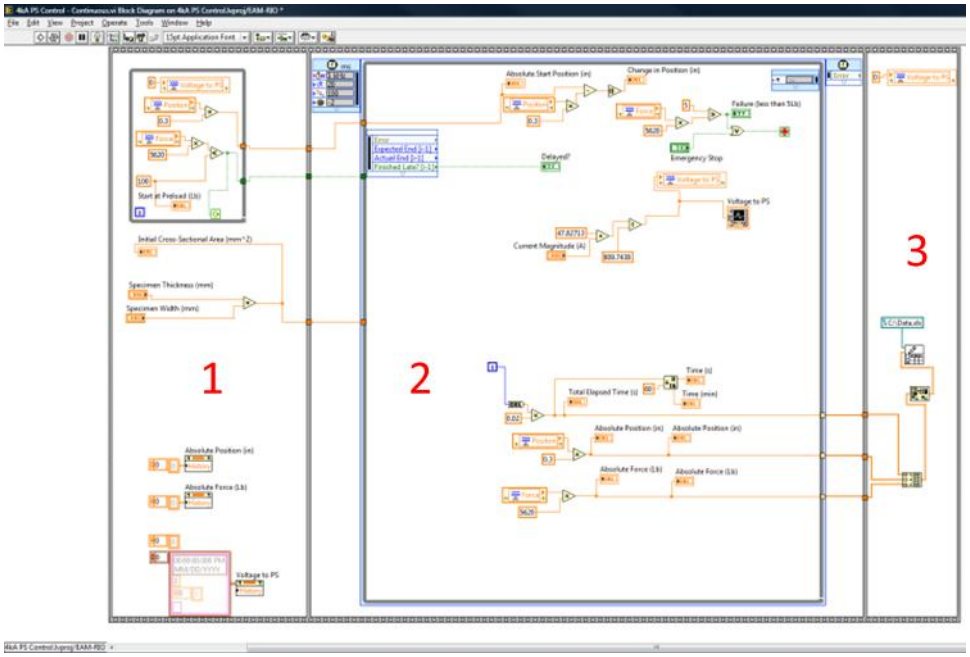

Figure D.8 - Block Diagram of Control System for Continuous EAF Testing

D.1.5 - Control System for Constant Force Forming

To allow for material forming under a constant force, the control system for continuous EAF testing was modified to incorporate a *PID* control block where the *I* and *D* gains were zero. Thus, only the proportional component was used. The GUI is shown in Figure D.9 where material dimensions are set along with the *PID* controller gains and the desired set point. Additionally, limits were imposed such that a maximum amount of current was allowed to be applied to the process for material flow alteration. The limit in this research was set to allow a maximum of 300A and the *P* control gain was set at a value of three. The *P* control gain was experimentally varied until an appropriate response of force modification by electrical current was achieved (*i.e.* fast response in force change relative to overall process time). The control block diagram is shown in Figure D.10 where the *PID* block was used in section 2 of the flat time sequence. Last, it should be noted that there was a correction factor used to remove the initially observed

steady-state error or droop. It is known that this additional correction factor could have been unnecessary if the use of the integral term was used in the control of the process. However, for this work it was not necessary as the goal was not to perfectly tune the system but to display EAF control architectures. Additional process control blocks and results are presented in *Chapter 9*.

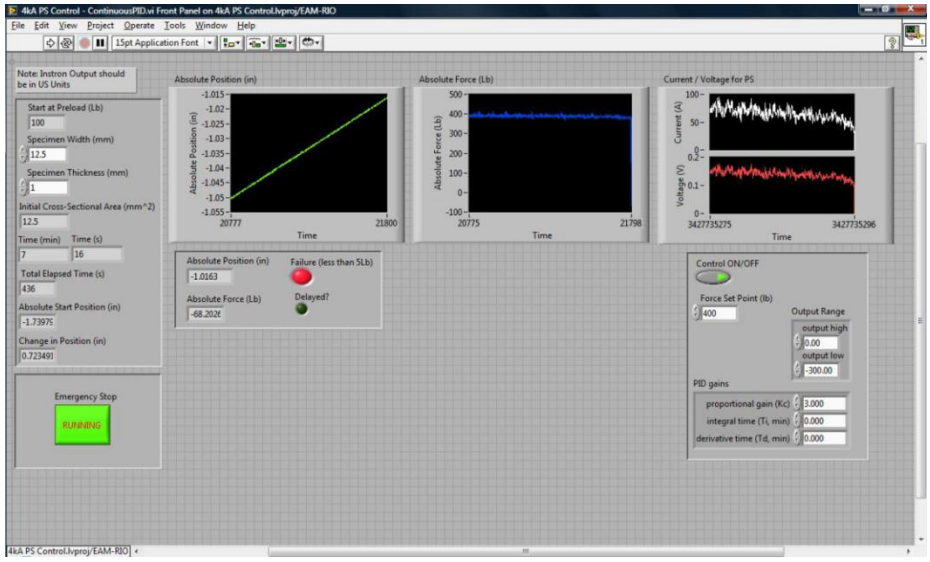

Figure D.9 - Front Panel of Control System for Constant Force Forming

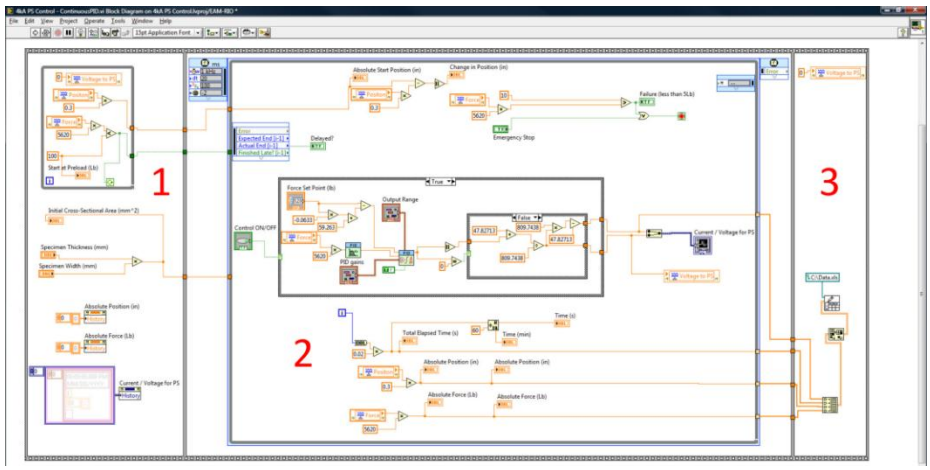

Figure D.10 - Block Diagram of Control System for Constant Force Forming

D.1.6 - Control System for Constant Stress Forming

The forming of a material under a constant stress was also demonstrated in this work and the control system was very similar to the constant force forming program. However, it was necessary to convert the force feedback to a true stress value such that this could be given to the *PID* control block along with the desire stress set point. Again, the droop present was corrected in the program. The GUI and control block diagram are given in Figure D.11 and D.12, respectively. Additional process control blocks and results are presented in *Chapter 9*.

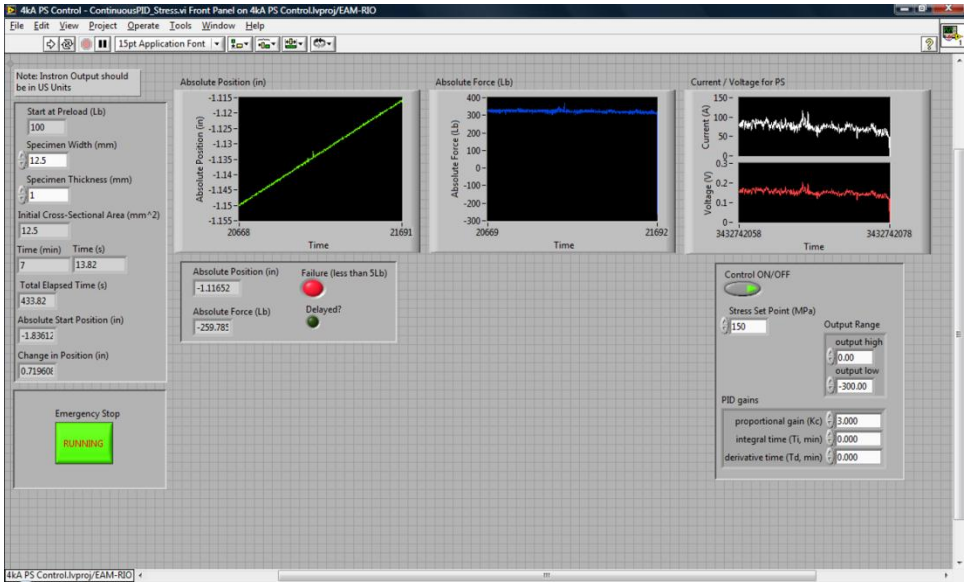

Figure D.11 - Front Panel of Control System for Constant Stress Forming

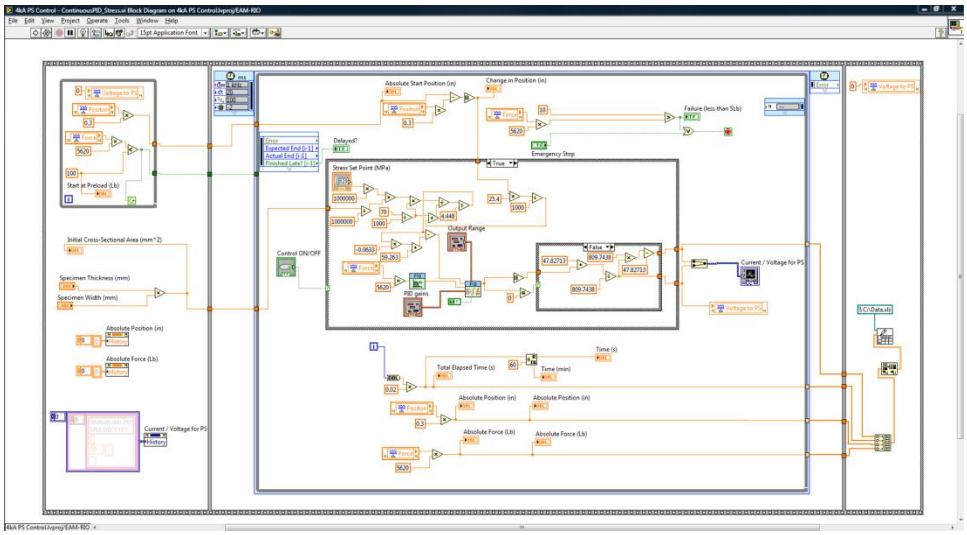

Figure D.12 - Block Diagram of Control System for Constant Stress Forming

D.2 - 4kA Power Supply Waveform Study

To quantify the quality and response of the power supply used in this research, several varying testing conditions were examined from the experimental tests performed in this work. There were three measurement sets taken which include the feed voltage given to the power supply to produce a current output, the power supply voltage across the output terminals under a load, and the voltage output from a clamp-on ammeter which can be converted to a current measurement. To examine the responses, a continuous and a square wave form was used with nominal current values at 0A, 500A, 800A, and 1000A. The results were measured using a Tektronix TDS420 Oscilloscope.

To summarize the findings, the feed voltage to the power supply provided a good approximation of a square wave with a fast rise time, little or no overshoot, and a very fast settling time. For the voltage signal measured across the power supply terminals, the waveform had a frequency slightly less than 360Hz and had considerable noise or fluctuation in the measurement. This noise in the waveform is an AC component on the

steady state DC current. As a result of the AC component, this may result in current flow on the exterior of the specimen. This is commonly known as the skin effect. For the skin effect, the current does not flow uniformly throughout the cross-section, but instead flows mostly on the surface of the specimen. This is commonly seen in high voltage transmission lines using AC current. In addition, for the higher nominal current values there was a significant overshoot. The rise and settling time of the responses was 130ms on average. Similar results were obtained using the clamp-on ammeter, however, there was less noise in the measurement results (filtered in the clamp-on ammeter). Also, the total rise and settling time was slightly larger on average at 160ms. Last, with increasing nominal current values the overshoot value increased. Thus, when considering these results and their impact to the process of EAF, it can alter the initial material response if the overshoot is too large. This can be a negative effect if the material temperature is desired to not exceed a give range. Also, for modeling efforts this could add noise to the system which could degrade or hinder the model results from accurately predicting the response due to the model assumptions. Also, it was noted for the continuous current that there was a frequency of material hardening and material softening that could have been due to the 360Hz fluctuation of the AC component on the steady state DC component. This hardening and softening effect at the observed high frequency is an additional area of study.

D.2.1 - Power Supply Feed Voltage

The feed voltage given to the power supply was produced by a NI cRIO programmed with NI LabVIEW software. This waveform was examined to determine the quality of the signal given to the power supply controller.

Figure D.13 displays the feed voltage when the desired current output is 0A and Figure D.14 shows the input signal corresponding to a 500A pulse with a 1s duration. As seen, there the wave has good characteristics of a square wave (ie. fast rise time, little or no overshoot, and settles very quickly). Figure D.15 shows a magnified input signal from the CompactRIO. Also, D.16 and Figure D.17 show similar results, however, the input signal corresponds to a 1000A pulse with a 1s duration. Is should be noted that there is some apparent noise in all the signals fed to the power supply.

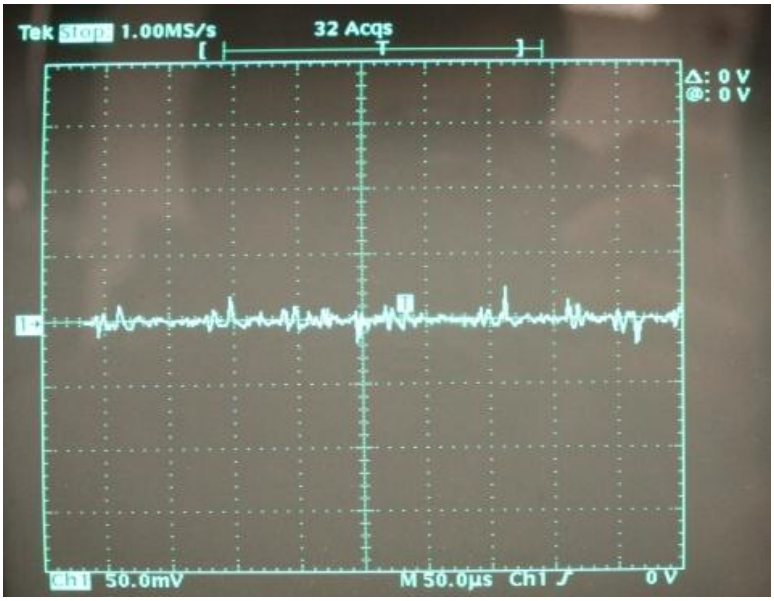

Figure D.13 - Power Supply Feed Voltage at 0A Output

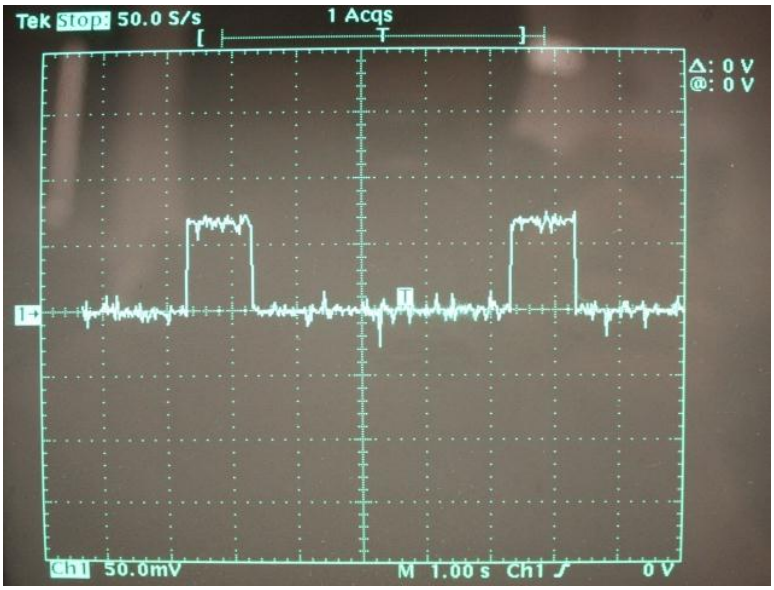

Figure D.14 - Power Supply Feed Voltage at 500A Output for a Square Wave with a 1s Pulse Duration

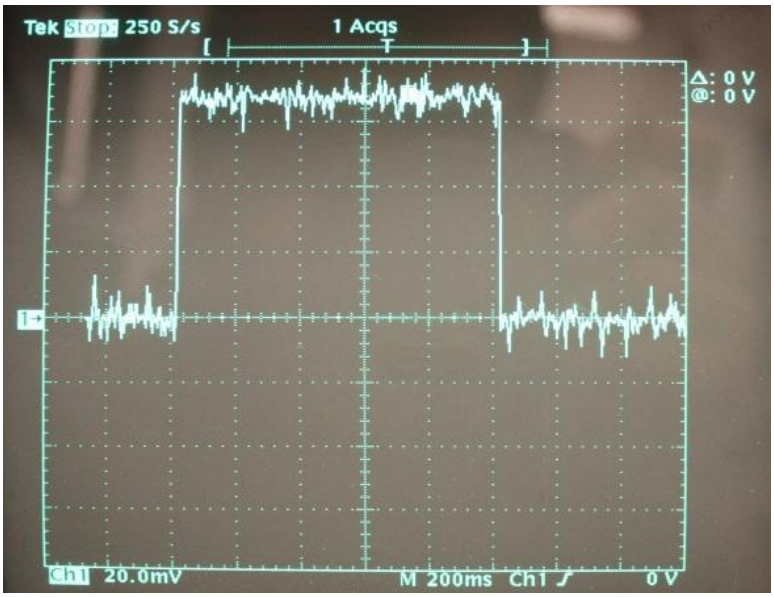

Figure D.15 - Magnified Power Supply Feed Voltage at 500A Output for a Square Wave with a 1s Pulse Duration

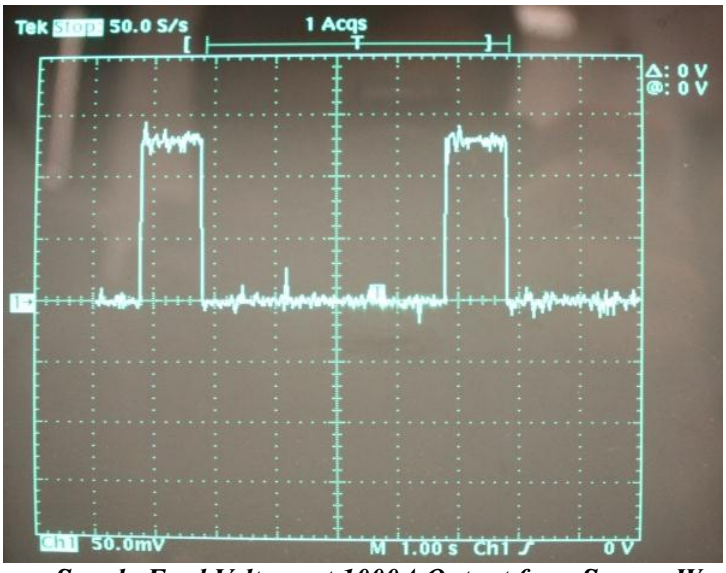

Figure D.16 - Power Supply Feed Voltage at 1000A Output for a Square Wave with a 1s Pulse Duration

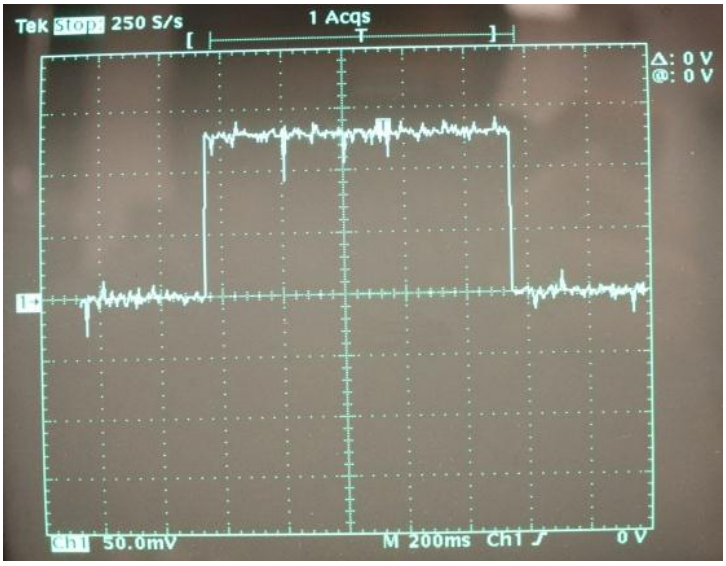

Figure D.17 - Magnified Power Supply Feed Voltage at 1000A Output for a Square Wave with a 1s Pulse Duration

D.2.2 - Power Supply Voltage Output across Terminals

To examine the output from the power supply, the voltage across the power supply terminals were measured with a load applied to the power supply. The following images are measures of the voltage and assuming an ohmic relation this directly relates to the current signal from the power supply. Table D.1 summarizes the findings from this

study where the measured voltage values were converted to current measurements. The main findings were that a there was a significant range of current values due to a oscillating frequency of slightly less than 360Hz when the application of current applied. This oscillation on the DC component is an AC component as the power supply does not provide a true DC signal to the process. The AC component may result in some of the current only traveling on the exterior of the specimen. This is known as the skin effect; where the current does not flow uniformly throughout the cross-section, but instead flows near the surface. This type of behavior is known to be present in high voltage transmission lines which carry AC current. For all the testing (both square wave and continuous) the frequency changed a small enough amount that it can be considered stable for all the tests. Comparing the 500A and 1000A square wave, the 500A wave had less overshoot but took a longer time to settle to a steady state value as compared to the 1000A waveform. Overall, once the square wave became steady state, it was approximately the same as the continuous waveform.

Table D.1 - Wave Shape Summary for PS Voltage Output across Terminals

	Square Wave		Continuous Wave	
Nominal Current (A)	500	1000	500	1000
Pulse Duration (s)	1	1	n/a	n/a
Min (A)	372	828	371	802
Max (A)	628	1172	629	1198
Range (A)	257	345	258	396
Overshoot (A)	775	1924	n/a	n/a
Mean (A)	500	1000	500	1000
Frequency (Hz)	351	354	356	358
Rise Time (ms)	33	46	n/a	n/a
Settling Time (ms)	121	59	n/a	n/a
Shut-off Time (ms)	44	46	n/a	n/a

Three magnifications of the 500A case are shown in Figure D.18 to Figure D.20 and the 500A continuous wave is displayed in Figure D.21. Figure D.22 presents the 1000A square wave signal where the larger overshoot and faster settling time are observed.

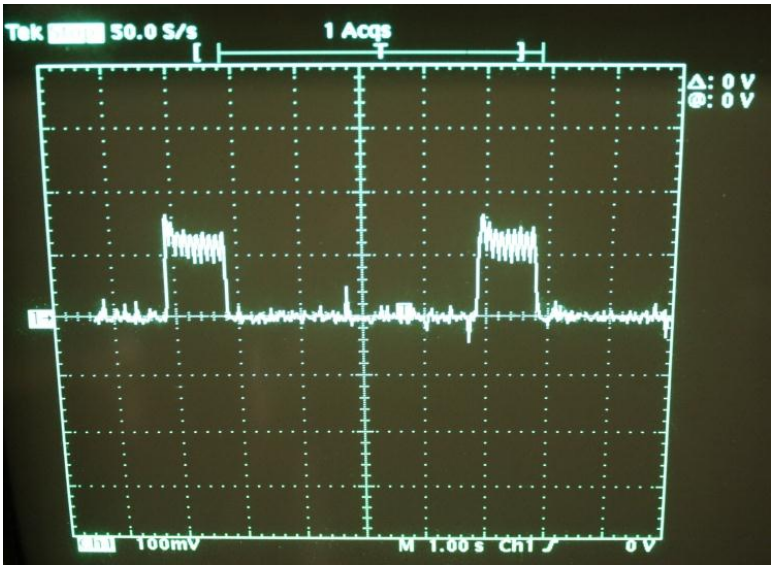

Figure D.18 - Power Supply Voltage across Terminals at 500A Output for a Square Wave with a 1s Pulse Duration

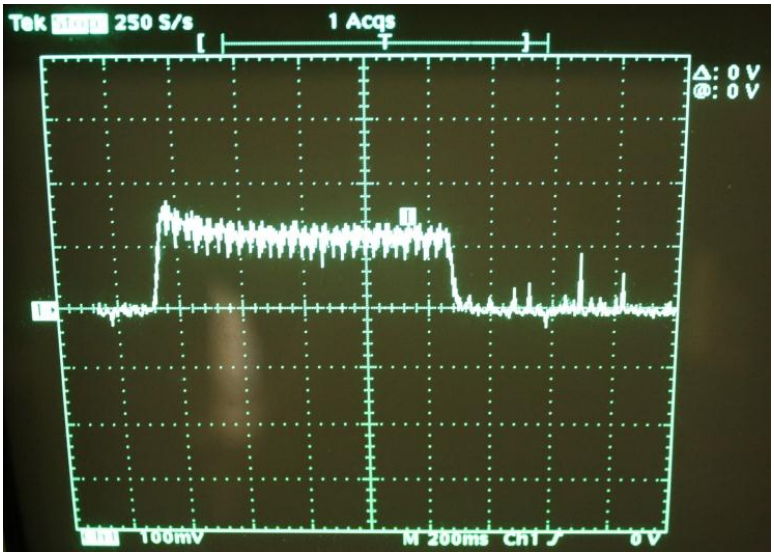

Figure D.19 - Magnified Power Supply Voltage across Terminals at 500A Output for a Square Wave with a 1s Pulse Duration

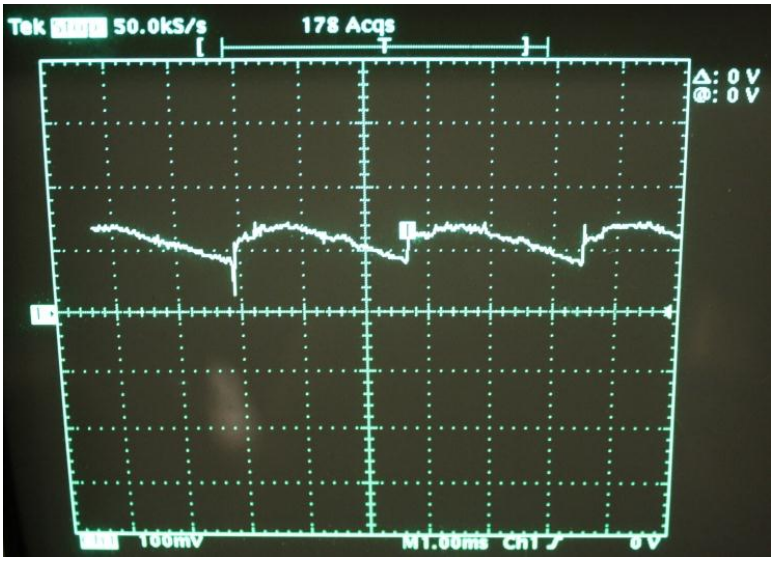

Figure D.20 - Magnified Steady State Power Supply Voltage across Terminals at 500A Output for a Square Wave with a 1s Pulse Duration

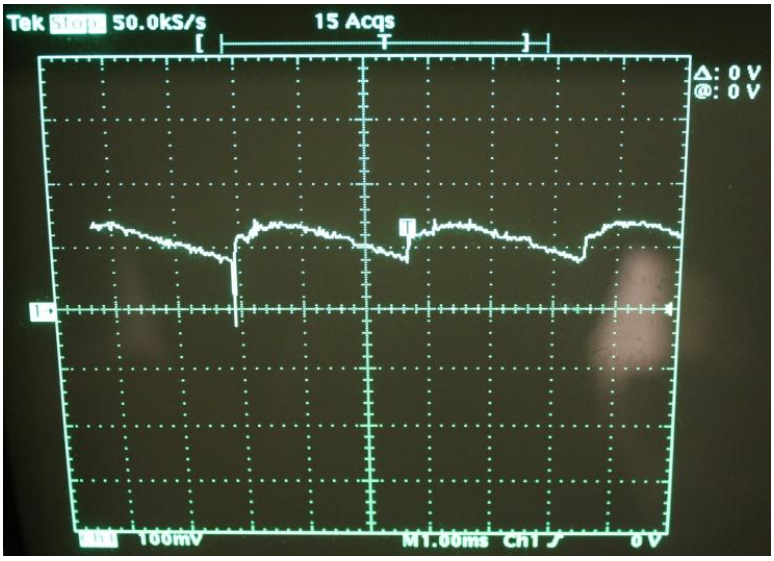

Figure D.21 - Power Supply Voltage across Terminals at 500A Output for a Continuous Waveform

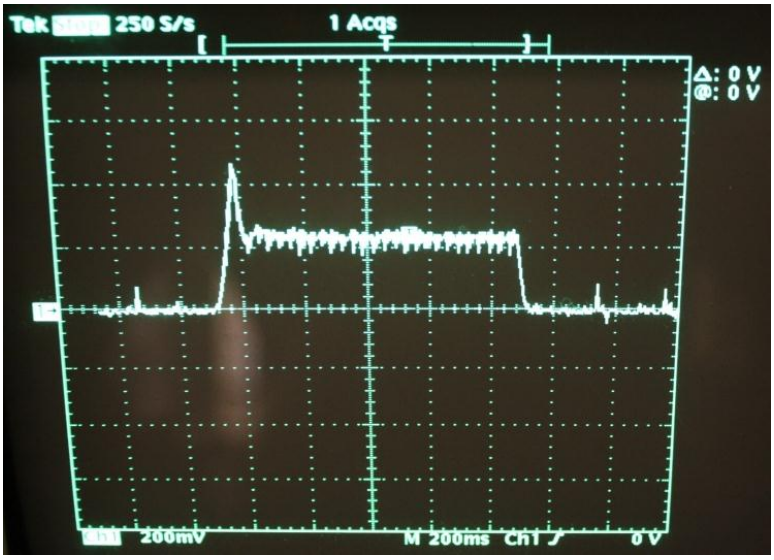

Figure D.22 - Power Supply Voltage across Terminals at 1000A Output for a Square Wave with a 1s Pulse Duration

The presented AC component on the steady state DC waveform can cause to a current density gradient throughout the cross-section. This gradient can be defined as the skin effect where a large percentage of the current flows between the surface and the skin depth. The skin depth can be calculated by:

$$\delta = \sqrt{\frac{2\rho}{\omega\mu}}$$

where, ρ is the electrical resistivity, ω is the angular frequency, and μ is the absolute magnetic permeability of the material. For the material in this work, the magnetic permeability can be considered one and the frequency is 360Hz (*i.e.* multiple of 60Hz). The skin depth is a caused by circulating eddy currents created from the AC current which act to cancel the current flow in the center of the conductor and strengthen it near the surface. The skin depth calculated as a function of temperature is given in Figure D.23.

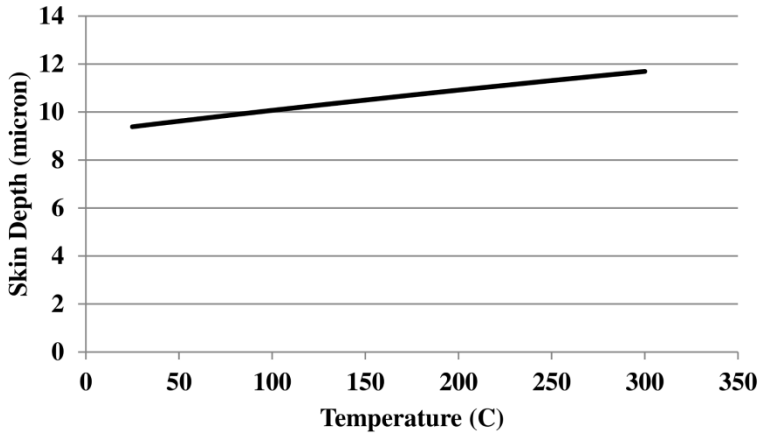

Figure D.23 - Skin Depth versus Temperature for AC Power Supply Component

The skin depth ranges from approximately 9 to 12 micron. Thus, when comparing this value to the sample's rectangular cross-section of 1mm by 12.5mm it is considerable less. This would then create some skin effects from the AC component. The current density from the AC component will decrease exponentially from the surface as shown in Figure D.24. Thus at the skin depth (*i.e.* one), the current density is about 37% of the original value.

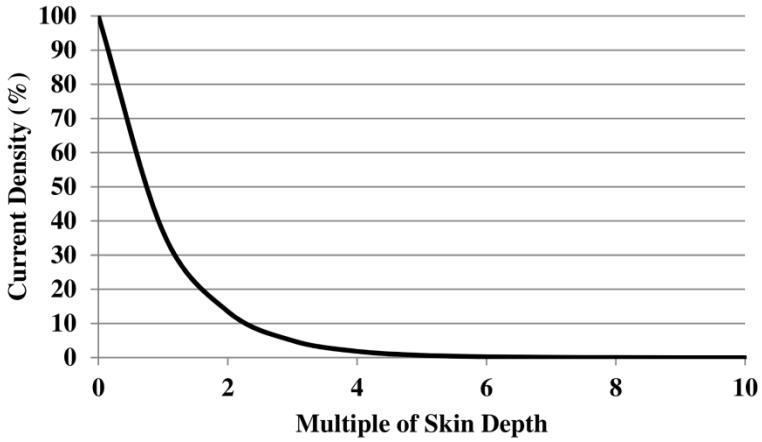

Figure D.24 - Current Density versus Skin Depth for AC Power Supply Component

Overall, the large DC current will create a uniform current flow through the cross-section and the AC component will induce some skin effects which will increase the current density near the specimen surface.

D.2.3 - Clamp-on Ammeter Output

The output of the power supply was also examined by using a Fluke i1010 AC/DC current clamp which provides a millivolt signal that can be converted to a current reading. The results from this analysis are summarized in Table D.2. On average the measured current was within 13A of the nominal value excluding the 500A/0.1s test. Also, it appeared that the overshoot increased as the nominal current value increased, however, there did not appear to be a trend relating the nominal current/pulse duration and the rise/settling time.

Table D.2 - Wave Shape Summary for Clamp-on Ammeter Output

	Square Wave							
Nominal Current (A)	500			800		1000		Average
Pulse Duration (s)	0.1	0.5	1	0.3	0.5	0.5	1	
Mean (A)	638	506	496	840	810	990	992	n/a
Overshoot (A)	638	680	668	1290	1290	1880	1910	n/a
Rise Time (ms)	47	57	65	50	46	58	66	56
Settling Time (ms)	n/a	158	161	42	49	122	81	102
Shut-off Time (ms)	142	74	88	53	50	48	51	72

Figure D.25 displays the results using a current of 500A applied for only a 0.1s pulse. As seen, this output did not follow a traditional square wave shape and appeared to be triangular in shape where the maximum was over the 500A value. This is probably due to the pulse duration being small for the system where the pulse duration was

approaching or smaller than the rise and settling time for the system to reach and settle at 500A.

Figure D.26 to Figure D.31 show the remaining tests and their corresponding waveforms.

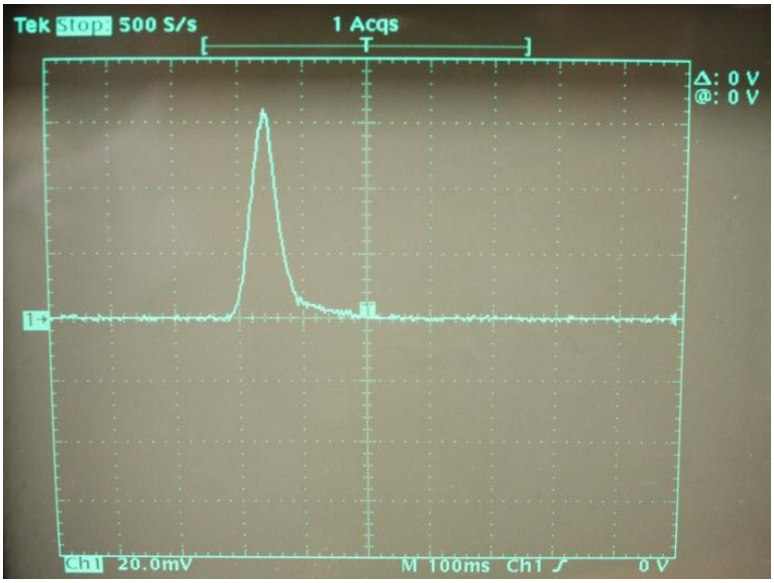

Figure D.25 - Clamp-on Ammeter Output for 500A Square Wave with a 0.1s Pulse Duration

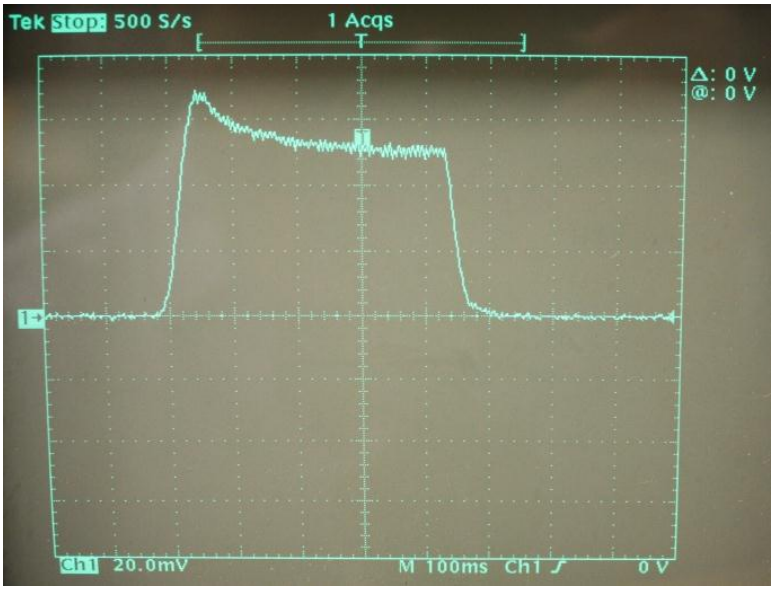

Figure D.26 - Clamp-on Ammeter Output for 500A Square Wave with a 0.5s Pulse Duration

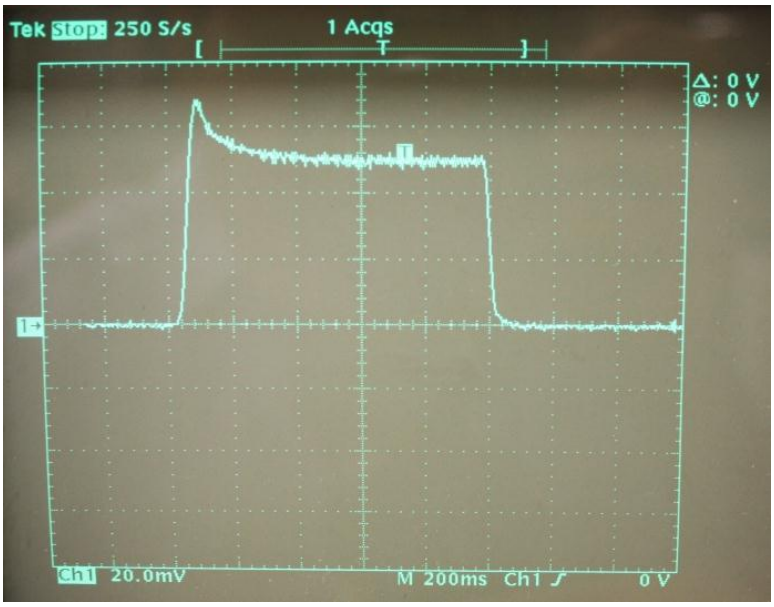

Figure D.27 - Clamp-on Ammeter Output for 500A Square Wave with a 1s Pulse Duration

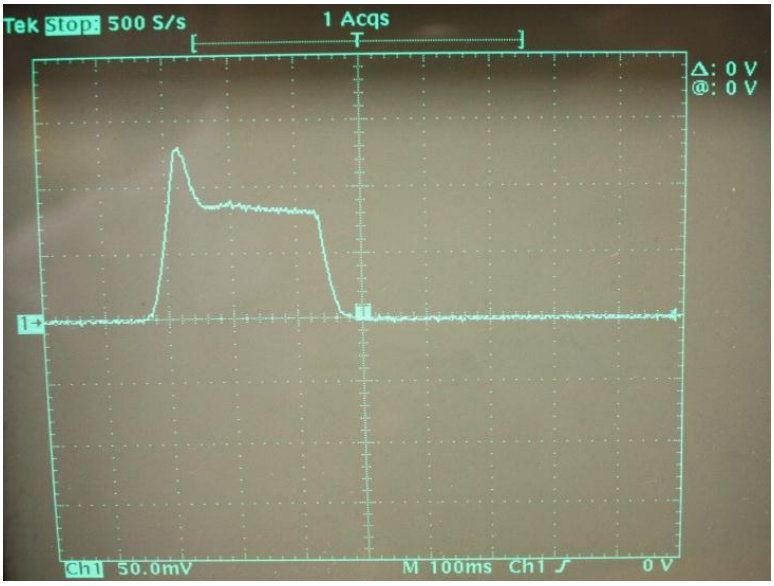

Figure D.28 - Clamp-on Ammeter Output for 800A Square Wave with a 0.3s Pulse Duration

Figure D.29 - Clamp-on Ammeter Output for 800A Square Wave with a 0.5s Pulse Duration

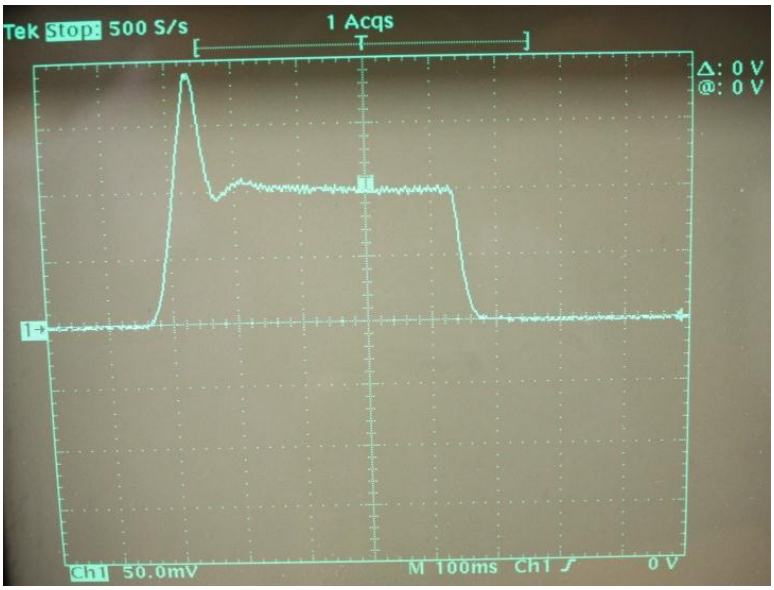

Figure D.30 - Clamp-on Ammeter Output for 1000A Square Wave with a 0.5s Pulse Duration

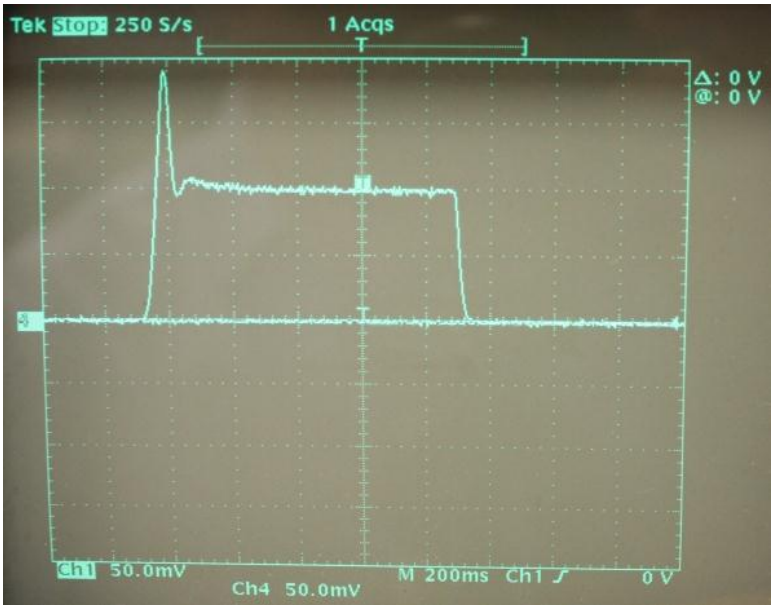

Figure D.31 - Clamp-on Ammeter Output for 1000A Square Wave with a 1s Pulse Duration

Appendix E

E.1 - Thermal Model Codes

E.1.1 - Thermal Model No Deformation

```
%1D transient finite difference model of sheet metal dogbone
temperature profile
%Includes: joule heating, conduction to dies, and convection to
environment

%Assumptions
%1)1D model and HT is equal across specimen thickness and width
%2)There are 41 nodes across the length of the specimen (spacing = 5mm)
%3)The material is homogeneous and isotropic
%5)Electrical resistivity of the dies is not temperature dependent*
%6)Specific heat of the dies is not temperature dependent*
%7)The environmental properties are an assumption (h value)
%8)Radiation effects is lumped into the convection coefficient - h
combined
%9)Sheet metal dogbone does not account for fillets from the test
region to the grip region
%10).........

%*not a large temperature chance in dies so it is a good approximation

%Notes
%1)Left side of specimen is node 1
%2)Right side of specimen is node 41
%3)Center of specimen is node 21
%4)Nodes 1-10 and 32-41 are in the clamping region - conduct directly
into dies
%5)Nodes 1 and 41 have convection effects on the end edge of the
specimen
%6)Nodes 11-31 have convection effects to environment
%7)All nodes are linked by conduction
%8)The thermal conductivity, heat capacity, and density of the sheet
are temperature dependent in the model
%9)The dies increases in temperature over time from joule heating when
current is applied - analyzed as a lumped mass
%10)47.5 of the specimen is clamped @ each end

%=========================================================================

%Variables
%=========================================================================

%environment properties
Tinf=273+26;                              %room temperature [=] K
h=20;                                   %convection coefficient [=] W/m^2-K
```

```
Tinitial=273+26;                          %initial material temperature
[=] K

%sheet geometry (Mg)
L=200/1000;                               %specimen length [=] m
Ld=(47.5/1000)*2;                         %specimen length under dies [=] m
Lt=L-Ld;                                  %specimen length in test region [=]
m
w=20/1000;                                %specimen width in grip region [=]
m
w1=12.5/1000;                             %specimen width in test region [=]
m
t=1/1000;                                 %specimen thickness [=] m

%sheet material properties (Mg)
rho=-0.1414*Tinitial+1821.9;              %density of MgAZ31B [=] kg/m^3
k=0.1011*Tinitial+49.557;                 %thermal conductivity of MgAZ31B
[=] W/m-K
c=0.779*Tinitial+777.64;                  %heat capacity [=] J/kg-K
rhoe=(2*10^-10)*Tinitial+(4*10^-8);       %electrical resistivity of MgAZ31B
[=] ohm-m

%die geometry (A2)
As_die=0.029832;                          %die surface area [=] m^2
V_die=0.000305837;                        %die volume [=] m^3

%die material properties (A2)
rho_a2=-0.3032*Tinitial+7951.5;           %density of A2 [=] kg/m^3
k_a2=0.0058*Tinitial+24.252;              %thermal conductivity of A2 dies
[=] W/m-K
c_a2=460;                                 %heat capacity
rhoe_a2=6*10^-7;                          %electrical resistivity of A2 [=]
ohm-m

%element properties
delta_x=(L/40);                           %node spacing [=] m
A1=t*w;                                   %conduction area in die region [=]
m^2
A11=t*w1;                                 %conduction area in test region [=]
m^2
A2=delta_x*w;                             %conduction area into dies [=] m^2
A22=delta_x*w1;                           %convection area in test region [=]
m^2
A3=w*(47.5/1000);                         %full conduction area into dies [=]
m^2
L_die=t/2;                                %die conduction length

%=========================================================================

%Internal Energy Generation
%=========================================================================
```

```
%pulsing parameters
I=500;                      %applied current magnitude (square wave)[=] A
PSeff=.7;                       %Power Supply effiency
period=60;                       %period for pulsing [=] s
duration=1;                      %length of pulse [=] s
duty=(duration/period)*100;     %duty cycle in percent

%specimen resistance (sheet)
R_clamp=rhoe*Ld/(w*t);                  %specimen resistance in clamp
region [=] ohm
R_test=rhoe*Lt/(w1*t);                  %specimen resistance in test
region [=] ohm

%joule heating (sheet)
egen_clamp_initial=((I^2)*R_clamp)/(Ld*w*t);    %heat generation per
unit volume in clamp region [=] W/m^3
egen_test_initial=((I^2)*R_test)/(Lt*w1*t);     %heat generation per
unit volume in test region [=] W/m^3

%joule heating (A2 die)
L1=0.04445;                             %height of section current flow
goes into die [=] m
L2=0.0381;                              %width of section current flow
goes into die [=] m
egen_die_initial=((I^2)*rhoe_a2)/((L1*L2)^2);   %heat generation per
unit volume in die [=] W/m^3

%=========================================================================

%Explicit Solution - Node Equations
%=========================================================================

%time step
delta_t=.01;                        %time step [=] s

%simulation length
length_t=10*60;                      %simulation length [=] s

%preallocate arrays for performance and memory allocation
Temperature=zeros(length_t/delta_t,41);
Die_temp=zeros(length_t/delta_t,1);
Density=zeros(length_t/delta_t,41);
Conductivity=zeros(length_t/delta_t,41);
H_capacity=zeros(length_t/delta_t,41);
Resistivity=zeros(length_t/delta_t,41);
Die_dens=zeros(length_t/delta_t,1);
Die_conduct=zeros(length_t/delta_t,1);
Time=zeros(length_t/delta_t,1);
T=zeros(41,1);
RHO=zeros(41,1);
K=zeros(41,1);
C=zeros(41,1);
```

```
RHOE=zeros(41,1);


%set initial conditions (room temperature)

%node temperatures (row1=node1 ... row 41=node41)
for u=1:1:41
    T(u,:)=Tinitial;
end

%density (sheet) (row1=node1 ... row 41=node41)
for mm=1:1:41
    RHO(mm,:)=rho;
end

%thermal conductivity (sheet) (row1=node1 ... row 41=node41)
for uu=1:1:41
    K(uu,:)=k;
end

%heat capacity (sheet) (row1=node1 ... row 41=node41)
for rr=1:1:41
    C(rr,:)=c;
end

%electrical resistivity (sheet) (row1=node1 ... row 41=node41)
for ss=1:1:41
    RHOE(ss,:)=rhoe;
end

%die temperature
Tdie=Tinitial;

%nodal solution
i=1;     %temperature array index
bb=1;    %time remaining display index
for j=delta_t:delta_t:length_t

    %joule heating arrays applied
    egen_clamp=egen_clamp_initial*egen_clamp_array(i,:)*PSeff;
    egen_test=egen_test_initial*egen_test_array(i,:)*PSeff;
    egen_die=egen_die_initial*egen_die_array(i,:)*PSeff;

    %die temperature calculations as a function of joule heating and
conduction back into dies (die temperature changes)

    %average Mg specimen temperature under dies for conduction into
dies
    Tavg_mg=mean([T(1,:) T(2,:) T(3,:) T(4,:) T(5,:) T(6,:) T(7,:)
T(8,:) T(9,:) T(10,:) T(32,:) T(33,:) T(34,:) T(35,:) T(36,:) T(37,:)
T(38,:) T(39,:) T(40,:) T(41,:)]);
```

```
    %calculate new die temperature

Tdien=Tdie+delta_t*(((h*As_die*Tinf)/(rho_a2*V_die*c_a2))+((2*k_a2*A3*T
avg_mg)/(rho_a2*V_die*c_a2*L_die))-
(((h*As_die)/(rho_a2*V_die*c_a2))+((2*k_a2*A3)/(rho_a2*V_die*c_a2*L_die
)))*Tdie+(egen_die/(rho_a2*c_a2)));

    %node 1

T1n=T(1,:)+delta_t*(((K(1,:)*T(2,:))/(((delta_x^2)/2)*RHO(1,:)*C(1,:)))
-
((K(1,:)/(((delta_x^2)/2)*RHO(1,:)*C(1,:)))+((2*k_a2*w)/((L_die)*RHO(1,
:)*A1*C(1,:)))+((h*t*w)/(RHO(1,:)*A1*(delta_x/2)*C(1,:))))*T(1,:)+((2*k
_a2*w*Tdien)/((L_die)*RHO(1,:)*A1*C(1,:)))+((h*t*w*Tinf)/(RHO(1,:)*A1*(
delta_x/2)*C(1,:)))+(egen_clamp/(RHO(1,:)*C(1,:))));

    %node 2

T2n=T(2,:)+delta_t*(((K(2,:)*T(1,:))/((delta_x^2)*RHO(2,:)*C(2,:)))+((2
*k_a2*A2*Tdien)/((L_die)*RHO(2,:)*A1*delta_x*C(2,:)))-
(((2*K(2,:))/((delta_x^2)*RHO(2,:)*C(2,:)))+((2*k_a2*A2)/((L_die)*RHO(2
,:)*A1*delta_x*C(2,:))))*T(2,:)+((K(2,:)*T(3,:))/((delta_x^2)*RHO(2,:)*
C(2,:)))+(egen_clamp/(RHO(2,:)*C(2,:))));

    %node 3

T3n=T(3,:)+delta_t*(((K(3,:)*T(2,:))/((delta_x^2)*RHO(3,:)*C(3,:)))+((2
*k_a2*A2*Tdien)/((L_die)*RHO(3,:)*A1*delta_x*C(3,:)))-
(((2*K(3,:))/((delta_x^2)*RHO(3,:)*C(3,:)))+((2*k_a2*A2)/((L_die)*RHO(3
,:)*A1*delta_x*C(3,:))))*T(3,:)+((K(3,:)*T(4,:))/((delta_x^2)*RHO(3,:)*
C(3,:)))+(egen_clamp/(RHO(3,:)*C(3,:))));

    %node 4

T4n=T(4,:)+delta_t*(((K(4,:)*T(3,:))/((delta_x^2)*RHO(4,:)*C(4,:)))+((2
*k_a2*A2*Tdien)/((L_die)*RHO(4,:)*A1*delta_x*C(4,:)))-
(((2*K(4,:))/((delta_x^2)*RHO(4,:)*C(4,:)))+((2*k_a2*A2)/((L_die)*RHO(4
,:)*A1*delta_x*C(4,:))))*T(4,:)+((K(4,:)*T(5,:))/((delta_x^2)*RHO(4,:)*
C(4,:)))+(egen_clamp/(RHO(4,:)*C(4,:))));

    %node 5

T5n=T(5,:)+delta_t*(((K(5,:)*T(4,:))/((delta_x^2)*RHO(5,:)*C(5,:)))+((2
*k_a2*A2*Tdien)/((L_die)*RHO(5,:)*A1*delta_x*C(5,:)))-
(((2*K(5,:))/((delta_x^2)*RHO(5,:)*C(5,:)))+((2*k_a2*A2)/((L_die)*RHO(5
,:)*A1*delta_x*C(5,:))))*T(5,:)+((K(5,:)*T(6,:))/((delta_x^2)*RHO(5,:)*
C(5,:)))+(egen_clamp/(RHO(5,:)*C(5,:))));

    %node 6

T6n=T(6,:)+delta_t*(((K(6,:)*T(5,:))/((delta_x^2)*RHO(6,:)*C(6,:)))+((2
```

```
*k_a2*A2*Tdien)/((L_die)*RHO(6,:)*A1*delta_x*C(6,:)))-
(((2*K(6,:))/((delta_x^2)*RHO(6,:)*C(6,:)))+((2*k_a2*A2)/((L_die)*RHO(6
,:)*A1*delta_x*C(6,:))))*T(6,:)+((K(6,:)*T(7,:))/((delta_x^2)*RHO(6,:)*
C(6,:)))+(egen_clamp/(RHO(6,:)*C(6,:))));

    %node 7

T7n=T(7,:)+delta_t*(((K(7,:)*T(6,:))/((delta_x^2)*RHO(7,:)*C(7,:)))+((2
*k_a2*A2*Tdien)/((L_die)*RHO(7,:)*A1*delta_x*C(7,:)))-
(((2*K(7,:))/((delta_x^2)*RHO(7,:)*C(7,:)))+((2*k_a2*A2)/((L_die)*RHO(7
,:)*A1*delta_x*C(7,:))))*T(7,:)+((K(7,:)*T(8,:))/((delta_x^2)*RHO(7,:)*
C(7,:)))+(egen_clamp/(RHO(7,:)*C(7,:))));

    %node 8

T8n=T(8,:)+delta_t*(((K(8,:)*T(7,:))/((delta_x^2)*RHO(8,:)*C(8,:)))+((2
*k_a2*A2*Tdien)/((L_die)*RHO(8,:)*A1*delta_x*C(8,:)))-
(((2*K(8,:))/((delta_x^2)*RHO(8,:)*C(8,:)))+((2*k_a2*A2)/((L_die)*RHO(8
,:)*A1*delta_x*C(8,:))))*T(8,:)+((K(8,:)*T(9,:))/((delta_x^2)*RHO(8,:)*
C(8,:)))+(egen_clamp/(RHO(8,:)*C(8,:))));

    %node 9

T9n=T(9,:)+delta_t*(((K(9,:)*T(8,:))/((delta_x^2)*RHO(9,:)*C(9,:)))+((2
*k_a2*A2*Tdien)/((L_die)*RHO(9,:)*A1*delta_x*C(9,:)))-
(((2*K(9,:))/((delta_x^2)*RHO(9,:)*C(9,:)))+((2*k_a2*A2)/((L_die)*RHO(9
,:)*A1*delta_x*C(9,:))))*T(9,:)+((K(9,:)*T(10,:))/((delta_x^2)*RHO(9,:)
*C(9,:)))+(egen_clamp/(RHO(9,:)*C(9,:))));

    %node 10

T10n=T(10,:)+delta_t*(((K(10,:)*T(9,:))/((delta_x^2)*RHO(10,:)*C(10,:))
)+((2*k_a2*A2*Tdien)/((L_die)*RHO(10,:)*A1*delta_x*C(10,:)))-
(((2*K(10,:))/((delta_x^2)*RHO(10,:)*C(10,:)))+((2*k_a2*A2)/((L_die)*RH
O(10,:)*A1*delta_x*C(10,:))))*T(10,:)+((K(10,:)*T(11,:))/((delta_x^2)*R
HO(10,:)*C(10,:)))+(egen_clamp/(RHO(10,:)*C(10,:))));

    %node 11

T11n=T(11,:)+delta_t*(((K(11,:)*T(10,:))/((delta_x^2)*RHO(11,:)*C(11,:)
))-
(((2*K(11,:))/((delta_x^2)*RHO(11,:)*C(11,:)))+((2*h*A22)/(RHO(11,:)*A1
1*delta_x*C(11,:))))*T(11,:)+((K(11,:)*T(12,:))/((delta_x^2)*RHO(11,:)*
C(11,:)))+((2*h*A22*Tinf)/(RHO(11,:)*A11*delta_x*C(11,:)))+(egen_test/(
RHO(11,:)*C(11,:))));

    %node 12

T12n=T(12,:)+delta_t*(((K(12,:)*T(11,:))/((delta_x^2)*RHO(12,:)*C(12,:)
))-
(((2*K(12,:))/((delta_x^2)*RHO(12,:)*C(12,:)))+((2*h*A22)/(RHO(12,:)*A1
1*delta_x*C(12,:))))*T(12,:)+((K(12,:)*T(13,:))/((delta_x^2)*RHO(12,:)*
```

```
C(12,:)))+((2*h*A22*Tinf)/(RHO(12,:)*A11*delta_x*C(12,:)))+(egen_test/(
RHO(12,:)*C(12,:)));

    %node 13

T13n=T(13,:)+delta_t*(((K(13,:)*T(12,:))/((delta_x^2)*RHO(13,:)*C(13,:)
))-
(((2*K(13,:))/((delta_x^2)*RHO(13,:)*C(13,:)))+((2*h*A22)/(RHO(13,:)*A1
1*delta_x*C(13,:))))*T(13,:)+((K(13,:)*T(14,:))/((delta_x^2)*RHO(13,:)*
C(13,:)))+((2*h*A22*Tinf)/(RHO(13,:)*A11*delta_x*C(13,:)))+(egen_test/(
RHO(13,:)*C(13,:)));

    %node 14

T14n=T(14,:)+delta_t*(((K(14,:)*T(13,:))/((delta_x^2)*RHO(14,:)*C(14,:)
))-
(((2*K(14,:))/((delta_x^2)*RHO(14,:)*C(14,:)))+((2*h*A22)/(RHO(14,:)*A1
1*delta_x*C(14,:))))*T(14,:)+((K(14,:)*T(15,:))/((delta_x^2)*RHO(14,:)*
C(14,:)))+((2*h*A22*Tinf)/(RHO(14,:)*A11*delta_x*C(14,:)))+(egen_test/(
RHO(14,:)*C(14,:)));

    %node 15

T15n=T(15,:)+delta_t*(((K(15,:)*T(14,:))/((delta_x^2)*RHO(15,:)*C(15,:)
))-
(((2*K(15,:))/((delta_x^2)*RHO(15,:)*C(15,:)))+((2*h*A22)/(RHO(15,:)*A1
1*delta_x*C(15,:))))*T(15,:)+((K(15,:)*T(16,:))/((delta_x^2)*RHO(15,:)*
C(15,:)))+((2*h*A22*Tinf)/(RHO(15,:)*A11*delta_x*C(15,:)))+(egen_test/(
RHO(15,:)*C(15,:)));

    %node 16

T16n=T(16,:)+delta_t*(((K(16,:)*T(15,:))/((delta_x^2)*RHO(16,:)*C(16,:)
))-
(((2*K(16,:))/((delta_x^2)*RHO(16,:)*C(16,:)))+((2*h*A22)/(RHO(16,:)*A1
1*delta_x*C(16,:))))*T(16,:)+((K(16,:)*T(17,:))/((delta_x^2)*RHO(16,:)*
C(16,:)))+((2*h*A22*Tinf)/(RHO(16,:)*A11*delta_x*C(16,:)))+(egen_test/(
RHO(16,:)*C(16,:)));

    %node 17

T17n=T(17,:)+delta_t*(((K(17,:)*T(16,:))/((delta_x^2)*RHO(17,:)*C(17,:)
))-
(((2*K(17,:))/((delta_x^2)*RHO(17,:)*C(17,:)))+((2*h*A22)/(RHO(17,:)*A1
1*delta_x*C(17,:))))*T(17,:)+((K(17,:)*T(18,:))/((delta_x^2)*RHO(17,:)*
C(17,:)))+((2*h*A22*Tinf)/(RHO(17,:)*A11*delta_x*C(17,:)))+(egen_test/(
RHO(17,:)*C(17,:)));

    %node 18

T18n=T(18,:)+delta_t*(((K(18,:)*T(17,:))/((delta_x^2)*RHO(18,:)*C(18,:)
))-
```

```
(((2*K(18,:))/((delta_x^2)*RHO(18,:)*C(18,:)))+((2*h*A22)/(RHO(18,:)*A1
1*delta_x*C(18,:))))*T(18,:)+((K(18,:)*T(19,:))/((delta_x^2)*RHO(18,:)*
C(18,:)))+((2*h*A22*Tinf)/(RHO(18,:)*A11*delta_x*C(18,:)))+(egen_test/(
RHO(18,:)*C(18,:))));

    %node 19

T19n=T(19,:)+delta_t*(((K(19,:)*T(18,:))/((delta_x^2)*RHO(19,:)*C(19,:)
))-
(((2*K(19,:))/((delta_x^2)*RHO(19,:)*C(19,:)))+((2*h*A22)/(RHO(19,:)*A1
1*delta_x*C(19,:))))*T(19,:)+((K(19,:)*T(20,:))/((delta_x^2)*RHO(19,:)*
C(19,:)))+((2*h*A22*Tinf)/(RHO(19,:)*A11*delta_x*C(19,:)))+(egen_test/(
RHO(19,:)*C(19,:))));

    %node 20

T20n=T(20,:)+delta_t*(((K(20,:)*T(19,:))/((delta_x^2)*RHO(20,:)*C(20,:)
))-
(((2*K(20,:))/((delta_x^2)*RHO(20,:)*C(20,:)))+((2*h*A22)/(RHO(20,:)*A1
1*delta_x*C(20,:))))*T(20,:)+((K(20,:)*T(21,:))/((delta_x^2)*RHO(20,:)*
C(20,:)))+((2*h*A22*Tinf)/(RHO(20,:)*A11*delta_x*C(20,:)))+(egen_test/(
RHO(20,:)*C(20,:))));

    %node 21

T21n=T(21,:)+delta_t*(((K(21,:)*T(20,:))/((delta_x^2)*RHO(21,:)*C(21,:)
))-
(((2*K(21,:))/((delta_x^2)*RHO(21,:)*C(21,:)))+((2*h*A22)/(RHO(21,:)*A1
1*delta_x*C(21,:))))*T(21,:)+((K(21,:)*T(22,:))/((delta_x^2)*RHO(21,:)*
C(21,:)))+((2*h*A22*Tinf)/(RHO(21,:)*A11*delta_x*C(21,:)))+(egen_test/(
RHO(21,:)*C(21,:))));

    %node 22

T22n=T(22,:)+delta_t*(((K(22,:)*T(21,:))/((delta_x^2)*RHO(22,:)*C(22,:)
))-
(((2*K(22,:))/((delta_x^2)*RHO(22,:)*C(22,:)))+((2*h*A22)/(RHO(22,:)*A1
1*delta_x*C(22,:))))*T(22,:)+((K(22,:)*T(23,:))/((delta_x^2)*RHO(22,:)*
C(22,:)))+((2*h*A22*Tinf)/(RHO(22,:)*A11*delta_x*C(22,:)))+(egen_test/(
RHO(22,:)*C(22,:))));

    %node 23

T23n=T(23,:)+delta_t*(((K(23,:)*T(22,:))/((delta_x^2)*RHO(23,:)*C(23,:)
))-
(((2*K(23,:))/((delta_x^2)*RHO(23,:)*C(23,:)))+((2*h*A22)/(RHO(23,:)*A1
1*delta_x*C(23,:))))*T(23,:)+((K(23,:)*T(24,:))/((delta_x^2)*RHO(23,:)*
C(23,:)))+((2*h*A22*Tinf)/(RHO(23,:)*A11*delta_x*C(23,:)))+(egen_test/(
RHO(23,:)*C(23,:))));

    %node 24
```

```
T24n=T(24,:)+delta_t*(((K(24,:)*T(23,:))/((delta_x^2)*RHO(24,:)*C(24,:)
))-
(((2*K(24,:))/((delta_x^2)*RHO(24,:)*C(24,:)))+((2*h*A22)/(RHO(24,:)*A1
1*delta_x*C(24,:))))*T(24,:)+((K(24,:)*T(25,:))/((delta_x^2)*RHO(24,:)*
C(24,:)))+((2*h*A22*Tinf)/(RHO(24,:)*A11*delta_x*C(24,:)))+(egen_test/(
RHO(24,:)*C(24,:))));

    %node 25

T25n=T(25,:)+delta_t*(((K(25,:)*T(24,:))/((delta_x^2)*RHO(25,:)*C(25,:)
))-
(((2*K(25,:))/((delta_x^2)*RHO(25,:)*C(25,:)))+((2*h*A22)/(RHO(25,:)*A1
1*delta_x*C(25,:))))*T(25,:)+((K(25,:)*T(26,:))/((delta_x^2)*RHO(25,:)*
C(25,:)))+((2*h*A22*Tinf)/(RHO(25,:)*A11*delta_x*C(25,:)))+(egen_test/(
RHO(25,:)*C(25,:))));

    %node 26

T26n=T(26,:)+delta_t*(((K(26,:)*T(25,:))/((delta_x^2)*RHO(26,:)*C(26,:)
))-
(((2*K(26,:))/((delta_x^2)*RHO(26,:)*C(26,:)))+((2*h*A22)/(RHO(26,:)*A1
1*delta_x*C(26,:))))*T(26,:)+((K(26,:)*T(27,:))/((delta_x^2)*RHO(26,:)*
C(26,:)))+((2*h*A22*Tinf)/(RHO(26,:)*A11*delta_x*C(26,:)))+(egen_test/(
RHO(26,:)*C(26,:))));

    %node 27

T27n=T(27,:)+delta_t*(((K(27,:)*T(26,:))/((delta_x^2)*RHO(27,:)*C(27,:)
))-
(((2*K(27,:))/((delta_x^2)*RHO(27,:)*C(27,:)))+((2*h*A22)/(RHO(27,:)*A1
1*delta_x*C(27,:))))*T(27,:)+((K(27,:)*T(28,:))/((delta_x^2)*RHO(27,:)*
C(27,:)))+((2*h*A22*Tinf)/(RHO(27,:)*A11*delta_x*C(27,:)))+(egen_test/(
RHO(27,:)*C(27,:))));

    %node 28

T28n=T(28,:)+delta_t*(((K(28,:)*T(27,:))/((delta_x^2)*RHO(28,:)*C(28,:)
))-
(((2*K(28,:))/((delta_x^2)*RHO(28,:)*C(28,:)))+((2*h*A22)/(RHO(28,:)*A1
1*delta_x*C(28,:))))*T(28,:)+((K(28,:)*T(29,:))/((delta_x^2)*RHO(28,:)*
C(28,:)))+((2*h*A22*Tinf)/(RHO(28,:)*A11*delta_x*C(28,:)))+(egen_test/(
RHO(28,:)*C(28,:))));

    %node 29

T29n=T(29,:)+delta_t*(((K(29,:)*T(28,:))/((delta_x^2)*RHO(29,:)*C(29,:)
))-
(((2*K(29,:))/((delta_x^2)*RHO(29,:)*C(29,:)))+((2*h*A22)/(RHO(29,:)*A1
1*delta_x*C(29,:))))*T(29,:)+((K(29,:)*T(30,:))/((delta_x^2)*RHO(29,:)*
C(29,:)))+((2*h*A22*Tinf)/(RHO(29,:)*A11*delta_x*C(29,:)))+(egen_test/(
RHO(29,:)*C(29,:))));
```

```
    %node 30

T30n=T(30,:)+delta_t*(((K(30,:)*T(29,:))/((delta_x^2)*RHO(30,:)*C(30,:)
))-
(((2*K(30,:))/((delta_x^2)*RHO(30,:)*C(30,:)))+((2*h*A22)/(RHO(30,:)*A1
1*delta_x*C(30,:))))*T(30,:)+((K(30,:)*T(31,:))/((delta_x^2)*RHO(30,:)*
C(30,:)))+((2*h*A22*Tinf)/(RHO(30,:)*A11*delta_x*C(30,:)))+(egen_test/(
RHO(30,:)*C(30,:))));

    %node 31

T31n=T(31,:)+delta_t*(((K(31,:)*T(30,:))/((delta_x^2)*RHO(31,:)*C(31,:)
))-
(((2*K(31,:))/((delta_x^2)*RHO(31,:)*C(31,:)))+((2*h*A22)/(RHO(31,:)*A1
1*delta_x*C(31,:))))*T(31,:)+((K(31,:)*T(32,:))/((delta_x^2)*RHO(31,:)*
C(31,:)))+((2*h*A22*Tinf)/(RHO(31,:)*A11*delta_x*C(31,:)))+(egen_test/(
RHO(31,:)*C(31,:))));

    %node 32

T32n=T(32,:)+delta_t*(((K(32,:)*T(31,:))/((delta_x^2)*RHO(32,:)*C(32,:)
))+((2*k_a2*A2*Tdien)/((L_die)*RHO(32,:)*A1*delta_x*C(32,:)))-
(((2*K(32,:))/((delta_x^2)*RHO(32,:)*C(32,:)))+((2*k_a2*A2)/((L_die)*RH
O(32,:)*A1*delta_x*C(32,:))))*T(32,:)+((K(32,:)*T(33,:))/((delta_x^2)*R
HO(32,:)*C(32,:)))+(egen_clamp/(RHO(32,:)*C(32,:))));

    %node 33

T33n=T(33,:)+delta_t*(((K(33,:)*T(32,:))/((delta_x^2)*RHO(33,:)*C(33,:)
))+((2*k_a2*A2*Tdien)/((L_die)*RHO(33,:)*A1*delta_x*C(33,:)))-
(((2*K(33,:))/((delta_x^2)*RHO(33,:)*C(33,:)))+((2*k_a2*A2)/((L_die)*RH
O(33,:)*A1*delta_x*C(33,:))))*T(33,:)+((K(33,:)*T(34,:))/((delta_x^2)*R
HO(33,:)*C(33,:)))+(egen_clamp/(RHO(33,:)*C(33,:))));

    %node 34

T34n=T(34,:)+delta_t*(((K(34,:)*T(33,:))/((delta_x^2)*RHO(34,:)*C(34,:)
))+((2*k_a2*A2*Tdien)/((L_die)*RHO(34,:)*A1*delta_x*C(34,:)))-
(((2*K(34,:))/((delta_x^2)*RHO(34,:)*C(34,:)))+((2*k_a2*A2)/((L_die)*RH
O(34,:)*A1*delta_x*C(34,:))))*T(34,:)+((K(34,:)*T(35,:))/((delta_x^2)*R
HO(34,:)*C(34,:)))+(egen_clamp/(RHO(34,:)*C(34,:))));

    %node 35

T35n=T(35,:)+delta_t*(((K(35,:)*T(34,:))/((delta_x^2)*RHO(35,:)*C(35,:)
))+((2*k_a2*A2*Tdien)/((L_die)*RHO(35,:)*A1*delta_x*C(35,:)))-
(((2*K(35,:))/((delta_x^2)*RHO(35,:)*C(35,:)))+((2*k_a2*A2)/((L_die)*RH
O(35,:)*A1*delta_x*C(35,:))))*T(35,:)+((K(35,:)*T(36,:))/((delta_x^2)*R
HO(35,:)*C(35,:)))+(egen_clamp/(RHO(35,:)*C(35,:))));

    %node 36
```

```
T36n=T(36,:)+delta_t*(((K(36,:)*T(35,:))/((delta_x^2)*RHO(36,:)*C(36,:)
))+((2*k_a2*A2*Tdien)/((L_die)*RHO(36,:)*A1*delta_x*C(36,:)))-
(((2*K(36,:))/((delta_x^2)*RHO(36,:)*C(36,:)))+((2*k_a2*A2)/((L_die)*RH
O(36,:)*A1*delta_x*C(36,:))))*T(36,:)+((K(36,:)*T(37,:))/((delta_x^2)*R
HO(36,:)*C(36,:)))+(egen_clamp/(RHO(36,:)*C(36,:))));

    %node 37

T37n=T(37,:)+delta_t*(((K(37,:)*T(36,:))/((delta_x^2)*RHO(37,:)*C(37,:)
))+((2*k_a2*A2*Tdien)/((L_die)*RHO(37,:)*A1*delta_x*C(37,:)))-
(((2*K(37,:))/((delta_x^2)*RHO(37,:)*C(37,:)))+((2*k_a2*A2)/((L_die)*RH
O(37,:)*A1*delta_x*C(37,:))))*T(37,:)+((K(37,:)*T(38,:))/((delta_x^2)*R
HO(37,:)*C(37,:)))+(egen_clamp/(RHO(37,:)*C(37,:))));

    %node 38

T38n=T(38,:)+delta_t*(((K(38,:)*T(37,:))/((delta_x^2)*RHO(38,:)*C(38,:)
))+((2*k_a2*A2*Tdien)/((L_die)*RHO(38,:)*A1*delta_x*C(38,:)))-
(((2*K(38,:))/((delta_x^2)*RHO(38,:)*C(38,:)))+((2*k_a2*A2)/((L_die)*RH
O(38,:)*A1*delta_x*C(38,:))))*T(38,:)+((K(38,:)*T(39,:))/((delta_x^2)*R
HO(38,:)*C(38,:)))+(egen_clamp/(RHO(38,:)*C(38,:))));

    %node 39

T39n=T(39,:)+delta_t*(((K(39,:)*T(38,:))/((delta_x^2)*RHO(39,:)*C(39,:)
))+((2*k_a2*A2*Tdien)/((L_die)*RHO(39,:)*A1*delta_x*C(39,:)))-
(((2*K(39,:))/((delta_x^2)*RHO(39,:)*C(39,:)))+((2*k_a2*A2)/((L_die)*RH
O(39,:)*A1*delta_x*C(39,:))))*T(39,:)+((K(39,:)*T(40,:))/((delta_x^2)*R
HO(39,:)*C(39,:)))+(egen_clamp/(RHO(39,:)*C(39,:))));

    %node 40

T40n=T(40,:)+delta_t*(((K(40,:)*T(39,:))/((delta_x^2)*RHO(40,:)*C(40,:)
))+((2*k_a2*A2*Tdien)/((L_die)*RHO(40,:)*A1*delta_x*C(40,:)))-
(((2*K(40,:))/((delta_x^2)*RHO(40,:)*C(40,:)))+((2*k_a2*A2)/((L_die)*RH
O(40,:)*A1*delta_x*C(40,:))))*T(40,:)+((K(40,:)*T(41,:))/((delta_x^2)*R
HO(40,:)*C(40,:)))+(egen_clamp/(RHO(40,:)*C(40,:))));

    %node 41

T41n=T(41,:)+delta_t*(((K(41,:)*T(40,:))/(((delta_x^2)/2)*RHO(41,:)*C(4
1,:)))-
((K(41,:)/(((delta_x^2)/2)*RHO(41,:)*C(41,:)))+((2*k_a2*w)/((L_die)*RHO
(41,:)*A1*C(41,:)))+((h*t*w)/(RHO(41,:)*A1*(delta_x/2)*C(41,:))))*T(41,
:)+((2*k_a2*w*Tdien)/((L_die)*RHO(41,:)*A1*C(41,:)))+((h*t*w*Tinf)/(RHO
(41,:)*A1*(delta_x/2)*C(41,:)))+(egen_clamp/(RHO(41,:)*C(41,:))));

    %store results in matrix
    Temperature(i,:)=[T1n T2n T3n T4n T5n T6n T7n T8n T9n T10n T11n
T12n T13n T14n T15n T16n T17n T18n T19n T20n T21n T22n T23n T24n T25n
```

```
T26n T27n T28n T29n T30n T31n T32n T33n T34n T35n T36n T37n T38n T39n
T40n T41n];
    Die_temp(i,:)=Tdien;
    Density(i,:)=[RHO(1,:) RHO(2,:) RHO(3,:) RHO(4,:) RHO(5,:) RHO(6,:)
RHO(7,:) RHO(8,:) RHO(9,:) RHO(10,:) RHO(11,:) RHO(12,:) RHO(13,:)
RHO(14,:) RHO(15,:) RHO(16,:) RHO(17,:) RHO(18,:) RHO(19,:) RHO(20,:)
RHO(21,:) RHO(22,:) RHO(23,:) RHO(24,:) RHO(25,:) RHO(26,:) RHO(27,:)
RHO(28,:) RHO(29,:) RHO(30,:) RHO(31,:) RHO(32,:) RHO(33,:) RHO(34,:)
RHO(35,:) RHO(36,:) RHO(37,:) RHO(38,:) RHO(39,:) RHO(40,:) RHO(41,:)];
    Conductivity(i,:)=[K(1,:) K(2,:) K(3,:) K(4,:) K(5,:) K(6,:) K(7,:)
K(8,:) K(9,:) K(10,:) K(11,:) K(12,:) K(13,:) K(14,:) K(15,:) K(16,:)
K(17,:) K(18,:) K(19,:) K(20,:) K(21,:) K(22,:) K(23,:) K(24,:) K(25,:)
K(26,:) K(27,:) K(28,:) K(29,:) K(30,:) K(31,:) K(32,:) K(33,:) K(34,:)
K(35,:) K(36,:) K(37,:) K(38,:) K(39,:) K(40,:) K(41,:)];
    H_capacity(i,:)=[C(1,:) C(2,:) C(3,:) C(4,:) C(5,:) C(6,:) C(7,:)
C(8,:) C(9,:) C(10,:) C(11,:) C(12,:) C(13,:) C(14,:) C(15,:) C(16,:)
C(17,:) C(18,:) C(19,:) C(20,:) C(21,:) C(22,:) C(23,:) C(24,:) C(25,:)
C(26,:) C(27,:) C(28,:) C(29,:) C(30,:) C(31,:) C(32,:) C(33,:) C(34,:)
C(35,:) C(36,:) C(37,:) C(38,:) C(39,:) C(40,:) C(41,:)];
    Resistivity(i,:)=[RHOE(1,:) RHOE(2,:) RHOE(3,:) RHOE(4,:) RHOE(5,:)
RHOE(6,:) RHOE(7,:) RHOE(8,:) RHOE(9,:) RHOE(10,:) RHOE(11,:)
RHOE(12,:) RHOE(13,:) RHOE(14,:) RHOE(15,:) RHOE(16,:) RHOE(17,:)
RHOE(18,:) RHOE(19,:) RHOE(20,:) RHOE(21,:) RHOE(22,:) RHOE(23,:)
RHOE(24,:) RHOE(25,:) RHOE(26,:) RHOE(27,:) RHOE(28,:) RHOE(29,:)
RHOE(30,:) RHOE(31,:) RHOE(32,:) RHOE(33,:) RHOE(34,:) RHOE(35,:)
RHOE(36,:) RHOE(37,:) RHOE(38,:) RHOE(39,:) RHOE(40,:) RHOE(41,:)];
    Die_dens(i,:)=rho_a2;
    Die_conduct(i,:)=k_a2;
    Time(i,:)=i*delta_t;

    %display simulation time remaining
    if i==bb*3000
        display(['Simulation time remaining: ', num2str(length_t-
i*delta_t),' (s)'])
        bb=bb+1;
     end

    i=i+1;   %increment storage array index

    %reset node temperature based off of new calculated temperature
    T(1,:)=T1n;
    T(2,:)=T2n;
    T(3,:)=T3n;
    T(4,:)=T4n;
    T(5,:)=T5n;
    T(6,:)=T6n;
    T(7,:)=T7n;
    T(8,:)=T8n;
    T(9,:)=T9n;
    T(10,:)=T10n;
    T(11,:)=T11n;
    T(12,:)=T12n;
    T(13,:)=T13n;
```

```
    T(14,:)=T14n;
    T(15,:)=T15n;
    T(16,:)=T16n;
    T(17,:)=T17n;
    T(18,:)=T18n;
    T(19,:)=T19n;
    T(20,:)=T20n;
    T(21,:)=T21n;
    T(22,:)=T22n;
    T(23,:)=T23n;
    T(24,:)=T24n;
    T(25,:)=T25n;
    T(26,:)=T26n;
    T(27,:)=T27n;
    T(28,:)=T28n;
    T(29,:)=T29n;
    T(30,:)=T30n;
    T(31,:)=T31n;
    T(32,:)=T32n;
    T(33,:)=T33n;
    T(34,:)=T34n;
    T(35,:)=T35n;
    T(36,:)=T36n;
    T(37,:)=T37n;
    T(38,:)=T38n;
    T(39,:)=T39n;
    T(40,:)=T40n;
    T(41,:)=T41n;
    Tdie=Tdien;

    %calculate new sheet properties based off of current node
temperature

    %density (sheet)
    for mmm=1:1:41
        RHO(mmm,:)=-0.1414*T(mmm,:)+1821.9;
    end

    %thermal conductivity (sheet)
    for uuu=1:1:41
        K(uuu,:)=0.1011*T(uuu,:)+49.557;
    end

    %heat capacity (sheet)
    for rrr=1:1:41
        C(rrr,:)=0.7779*T(rrr,:)+777.64;
    end

    %electrical resistivity (sheet)
    for sss=1:1:41
        RHOE(sss,:)=(2*10^-10)*T(sss,1)+(4*10^-8);
    end
```

```
    %calculate new die properties based off of current die temperature

    %density (A2 dies)
    rho_a2=-0.3032*Tdie+7951.5;

    %themal conductivity (A2 dies)
    k_a2=0.0058*Tdie+24.252;

end
%=========================================================================
```

E.1.2 - Thermal Model Uniform Deformation

```
%1D transient finite difference model of sheet metal dogbone
temperature profile
%Includes: joule heating, conduction to dies, and convection to
environment
%Includes: Uniform Deformation*********

%Assumptions
%1)1D model and HT is equal across specimen thickness and width
%2)There are 41 nodes across the length of the specimen (spacing = 5mm)
%3)The material is homogeneous and isotropic
%5)Electrical resistivity of the dies is not temperature dependent*
%6)Specific heat of the dies is not temperature dependent*
%7)The environmental properties are an assumption (h value)
%8)Radiation effects is lumped into the convection coefficient - h
combined
%9)Sheet metal dogbone does not account for fillets from the test
region to the grip region
%10)Deformation in the model assumes isotropy and uniform deformation

%*not a large temperature chance in dies so it is a good approximation

%Notes
%1)Left side of specimen is node 1
%2)Right side of specimen is node 41
%3)Center of specimen is node 21
%4)Nodes 1-10 and 32-41 are in the clamping region - conduct directly
into dies
%5)Nodes 1 and 41 have convection effects on the end edge of the
specimen
%6)Nodes 11-31 have convection effects to environment
%7)All nodes are linked by conduction
%8)The thermal conductivity, heat capacity, and density of the sheet
are temperature dependent in the model
%9)The dies increases in temperature over time from joule heating when
current is applied - analyzed as a lumped mass
%10)47.5 of the specimen is clamped @ each end
%11) Platen Speed is 0.1"/min
```

```
%=========================================================================

%Variables
%=========================================================================

%environment properties
Tinf=273+26;                              %room temperature [=] K
h=20;                                   %convection coefficient [=] W/m^2-K
Tinitial=273+26;                          %initial material temperature
[=] K

%sheet geometry (Mg)
L=200/1000;                             %specimen length [=] m
Ld=(47.5/1000)*2;                       %specimen length under dies [=] m
Lt=L-Ld;                                %specimen length in test region [=]
m
w=20/1000;                              %specimen width in grip region [=]
m
w1=12.5/1000;                           %specimen width in test region [=]
m
t=1/1000;                               %specimen thickness [=] m

%sheet material properties (Mg)
rho=-0.1414*Tinitial+1821.9;            %density of MgAZ31B [=] kg/m^3
k=0.1011*Tinitial+49.557;               %thermal conductivity of MgAZ31B
[=] W/m-K
c=0.779*Tinitial+777.64;                %heat capacity [=] J/kg-K
rhoe=(2*10^-10)*Tinitial+(4*10^-8);     %electrical resistivity of MgAZ31B
[=] ohm-m

%die geometry (A2)
As_die=0.029832;                        %die surface area [=] m^2
V_die=0.000305837;                      %die volume [=] m^3

%die material properties (A2)
rho_a2=-0.3032*Tinitial+7951.5;         %density of A2 [=] kg/m^3
k_a2=0.0058*Tinitial+24.252;            %thermal conductivity of A2 dies
[=] W/m-K
c_a2=460;                               %heat capacity
rhoe_a2=6*10^-7;                        %electrical resistivity of A2 [=]
ohm-m

%element properties
delta_x=(L/40);                         %node spacing [=] m
A1=t*w;                                 %conduction area in die region [=]
m^2
A11=t*w1;                               %conduction area in test region [=]
m^2
A2=delta_x*w;                           %conduction area into dies [=] m^2
A22=delta_x*w1;                         %convection area in test region [=]
m^2
```

```
A3=w*(47.5/1000);                    %full conduction area into dies [=]
m^2
L_die=t/2;                           %die conduction length

%element deformation properties
def_rate=0.1*25.4/1000;              %deformation rate (in/min to m/min)

%=========================================================================

%Internal Energy Generation
%=========================================================================

%pulsing parameters
I=500;                          %applied current magnitude (square wave)
[=] A
PSeff=0.7;                      %Power Supply effiency
period=60;                      %period for pulsing [=] s
duration=1;                     %length of pulse [=] s
duty=(duration/period)*100;     %duty cycle in percent

%specimen resistance (sheet in clamp region)
R_clamp=rhoe*Ld/(w*t);                  %specimen resistance in clamp
region [=] ohm

%joule heating (sheet in clamp region)
egen_clamp_initial=((I^2)*R_clamp)/(Ld*w*t);    %heat generation per
unit volume in clamp region [=] W/m^3

%joule heating (A2 die)
L1=0.04445;                             %height of section current flow
goes into die [=] m
L2=0.0381;                              %width of section current flow
goes into die [=] m
egen_die_initial=((I^2)*rhoe_a2)/((L1*L2)^2);   %heat generation per
unit volume in die [=] W/m^3

%=========================================================================

%Explicit Solution - Node Equations
%=========================================================================

%time step
delta_t=.01;                        %time step [=] s

%simulation length
length_t=10*60;                      %simulation length [=] s

%preallocate arrays for performance and memory allocation
Temperature=zeros(length_t/delta_t,41);
Die_temp=zeros(length_t/delta_t,1);
Density=zeros(length_t/delta_t,41);
```

```
Conductivity=zeros(length_t/delta_t,41);
H_capacity=zeros(length_t/delta_t,41);
Resistivity=zeros(length_t/delta_t,41);
Die_dens=zeros(length_t/delta_t,1);
Die_conduct=zeros(length_t/delta_t,1);
Time=zeros(length_t/delta_t,1);
T=zeros(41,1);
RHO=zeros(41,1);
K=zeros(41,1);
C=zeros(41,1);
RHOE=zeros(41,1);
Delta_S=zeros(length_t/delta_t,1);
Delta_S_Element=zeros(length_t/delta_t,1);
Delta_X_Test=zeros(length_t/delta_t,1);
A11_Def=zeros(length_t/delta_t,1);
A22_Def=zeros(length_t/delta_t,1);
Width_Test=zeros(length_t/delta_t,1);
Thickness_Test=zeros(length_t/delta_t,1);
Length_Test=zeros(length_t/delta_t,1);
Strain_L=zeros(length_t/delta_t,1);
Strain_W=zeros(length_t/delta_t,1);
R_Test_Def=zeros(length_t/delta_t,1);
Egen_Test_Def=zeros(length_t/delta_t,1);
Egen_Clamp=zeros(length_t/delta_t,1);
Egen_Test=zeros(length_t/delta_t,1);
Egen_Die=zeros(length_t/delta_t,1);


%set initial conditions (room temperature)

%node temperatures (row1=node1 ... row 41=node41)
for u=1:1:41
    T(u,:)=Tinitial;
end

%density (sheet) (row1=node1 ... row 41=node41)
for mm=1:1:41
    RHO(mm,:)=rho;
end

%thermal conductivity (sheet) (row1=node1 ... row 41=node41)
for uu=1:1:41
    K(uu,:)=k;
end

%heat capacity (sheet) (row1=node1 ... row 41=node41)
for rr=1:1:41
    C(rr,:)=c;
end

%electrical resistivity (sheet) (row1=node1 ... row 41=node41)
for ss=1:1:41
```

```
    RHOE(ss,:)=rhoe;
end

%die temperature
Tdie=Tinitial;

%nodal solution
i=1;     %temperature array index
bb=1;    %time remaining display index
for j=delta_t:delta_t:length_t

    %calcuate deformation parameters
    delta_s=def_rate*j/60;  %def amount in total in test region (min-
sec conversion) [=] m
    test_elements=21;       %elements/nodes in test region (11-31)
    delta_s_element=delta_s/test_elements;  %def per time step per
element [=] m
    delta_x_test=delta_x+delta_s_element; %new element length in test
region due to deformation
    A11_def=A11*delta_x/delta_x_test;   %new conduction area in test
region [=] m^2
    strain_l=log((delta_s+Lt)/Lt);  %strain in the length axis
    strain_t=-0.5*strain_l; %strain in the thickness axis
    strain_w=-0.5*strain_l; %strain in the width axis
    length_test=Lt+delta_s; %new sheet length [=] m
    thickness_test=t*exp(strain_t); %new sheet thickness, assumes
istropy [=] m
    width_test=w1*exp(strain_w); %new sheet  width, assumes istropy [=]
m
    A22_def=delta_x_test*width_test;    %new convection area in test
region [=] m^2

    %specimen resistance (sheet in test region)
    R_test_def=rhoe*length_test/(width_test*thickness_test);
%specimen resistance in test region [=] ohm

    %joule heating (sheet in test region)

egen_test_def=((I^2)*R_test_def)/(length_test*width_test*thickness_test
);     %heat generation per unit volume in test region [=] W/m^3

    %joule heating arrays applied
    egen_clamp=egen_clamp_initial*egen_clamp_array(i,:)*PSeff;
    egen_test=egen_test_def*egen_test_array(i,:)*PSeff;
    egen_die=egen_die_initial*egen_die_array(i,:)*PSeff;

    %die temperature calculations as a function of joule heating and
conduction back into dies (die temperature changes)

    %average Mg specimen temperature under dies for conduction into
dies
```

```
    Tavg_mg=mean([T(1,:) T(2,:) T(3,:) T(4,:) T(5,:) T(6,:) T(7,:)
T(8,:) T(9,:) T(10,:) T(32,:) T(33,:) T(34,:) T(35,:) T(36,:) T(37,:)
T(38,:) T(39,:) T(40,:) T(41,:)]);

    %calculate new die temperature

Tdien=Tdie+delta_t*(((h*As_die*Tinf)/(rho_a2*V_die*c_a2))+((2*k_a2*A3*T
avg_mg)/(rho_a2*V_die*c_a2*L_die))-
(((h*As_die)/(rho_a2*V_die*c_a2))+((2*k_a2*A3)/(rho_a2*V_die*c_a2*L_die
)))*Tdie+(egen_die/(rho_a2*c_a2)));

    %node 1

T1n=T(1,:)+delta_t*(((K(1,:)*T(2,:))/(((delta_x^2)/2)*RHO(1,:)*C(1,:)))
-
((K(1,:)/(((delta_x^2)/2)*RHO(1,:)*C(1,:)))+((2*k_a2*w)/((L_die)*RHO(1,
:)*A1*C(1,:)))+((h*t*w)/(RHO(1,:)*A1*(delta_x/2)*C(1,:))))*T(1,:)+((2*k
_a2*w*Tdien)/((L_die)*RHO(1,:)*A1*C(1,:)))+((h*t*w*Tinf)/(RHO(1,:)*A1*(
delta_x/2)*C(1,:)))+(egen_clamp/(RHO(1,:)*C(1,:))));

    %node 2

T2n=T(2,:)+delta_t*(((K(2,:)*T(1,:))/((delta_x^2)*RHO(2,:)*C(2,:)))+((2
*k_a2*A2*Tdien)/((L_die)*RHO(2,:)*A1*delta_x*C(2,:)))-
(((2*K(2,:))/((delta_x^2)*RHO(2,:)*C(2,:)))+((2*k_a2*A2)/((L_die)*RHO(2
,:)*A1*delta_x*C(2,:))))*T(2,:)+((K(2,:)*T(3,:))/((delta_x^2)*RHO(2,:)*
C(2,:)))+(egen_clamp/(RHO(2,:)*C(2,:))));

    %node 3

T3n=T(3,:)+delta_t*(((K(3,:)*T(2,:))/((delta_x^2)*RHO(3,:)*C(3,:)))+((2
*k_a2*A2*Tdien)/((L_die)*RHO(3,:)*A1*delta_x*C(3,:)))-
(((2*K(3,:))/((delta_x^2)*RHO(3,:)*C(3,:)))+((2*k_a2*A2)/((L_die)*RHO(3
,:)*A1*delta_x*C(3,:))))*T(3,:)+((K(3,:)*T(4,:))/((delta_x^2)*RHO(3,:)*
C(3,:)))+(egen_clamp/(RHO(3,:)*C(3,:))));

    %node 4

T4n=T(4,:)+delta_t*(((K(4,:)*T(3,:))/((delta_x^2)*RHO(4,:)*C(4,:)))+((2
*k_a2*A2*Tdien)/((L_die)*RHO(4,:)*A1*delta_x*C(4,:)))-
(((2*K(4,:))/((delta_x^2)*RHO(4,:)*C(4,:)))+((2*k_a2*A2)/((L_die)*RHO(4
,:)*A1*delta_x*C(4,:))))*T(4,:)+((K(4,:)*T(5,:))/((delta_x^2)*RHO(4,:)*
C(4,:)))+(egen_clamp/(RHO(4,:)*C(4,:))));

    %node 5

T5n=T(5,:)+delta_t*(((K(5,:)*T(4,:))/((delta_x^2)*RHO(5,:)*C(5,:)))+((2
*k_a2*A2*Tdien)/((L_die)*RHO(5,:)*A1*delta_x*C(5,:)))-
(((2*K(5,:))/((delta_x^2)*RHO(5,:)*C(5,:)))+((2*k_a2*A2)/((L_die)*RHO(5
,:)*A1*delta_x*C(5,:))))*T(5,:)+((K(5,:)*T(6,:))/((delta_x^2)*RHO(5,:)*
C(5,:)))+(egen_clamp/(RHO(5,:)*C(5,:))));
```

```
    %node 6

T6n=T(6,:)+delta_t*(((K(6,:)*T(5,:))/((delta_x^2)*RHO(6,:)*C(6,:)))+((2
*k_a2*A2*Tdien)/((L_die)*RHO(6,:)*A1*delta_x*C(6,:)))-
(((2*K(6,:))/((delta_x^2)*RHO(6,:)*C(6,:)))+((2*k_a2*A2)/((L_die)*RHO(6
,:)*A1*delta_x*C(6,:))))*T(6,:)+((K(6,:)*T(7,:))/((delta_x^2)*RHO(6,:)*
C(6,:)))+(egen_clamp/(RHO(6,:)*C(6,:))));

    %node 7

T7n=T(7,:)+delta_t*(((K(7,:)*T(6,:))/((delta_x^2)*RHO(7,:)*C(7,:)))+((2
*k_a2*A2*Tdien)/((L_die)*RHO(7,:)*A1*delta_x*C(7,:)))-
(((2*K(7,:))/((delta_x^2)*RHO(7,:)*C(7,:)))+((2*k_a2*A2)/((L_die)*RHO(7
,:)*A1*delta_x*C(7,:))))*T(7,:)+((K(7,:)*T(8,:))/((delta_x^2)*RHO(7,:)*
C(7,:)))+(egen_clamp/(RHO(7,:)*C(7,:))));

    %node 8

T8n=T(8,:)+delta_t*(((K(8,:)*T(7,:))/((delta_x^2)*RHO(8,:)*C(8,:)))+((2
*k_a2*A2*Tdien)/((L_die)*RHO(8,:)*A1*delta_x*C(8,:)))-
(((2*K(8,:))/((delta_x^2)*RHO(8,:)*C(8,:)))+((2*k_a2*A2)/((L_die)*RHO(8
,:)*A1*delta_x*C(8,:))))*T(8,:)+((K(8,:)*T(9,:))/((delta_x^2)*RHO(8,:)*
C(8,:)))+(egen_clamp/(RHO(8,:)*C(8,:))));

    %node 9

T9n=T(9,:)+delta_t*(((K(9,:)*T(8,:))/((delta_x^2)*RHO(9,:)*C(9,:)))+((2
*k_a2*A2*Tdien)/((L_die)*RHO(9,:)*A1*delta_x*C(9,:)))-
(((2*K(9,:))/((delta_x^2)*RHO(9,:)*C(9,:)))+((2*k_a2*A2)/((L_die)*RHO(9
,:)*A1*delta_x*C(9,:))))*T(9,:)+((K(9,:)*T(10,:))/((delta_x^2)*RHO(9,:)
*C(9,:)))+(egen_clamp/(RHO(9,:)*C(9,:))));

    %node 10

T10n=T(10,:)+delta_t*(((K(10,:)*T(9,:))/((delta_x^2)*RHO(10,:)*C(10,:))
)+((2*k_a2*A2*Tdien)/((L_die)*RHO(10,:)*A1*delta_x*C(10,:)))-
(((2*K(10,:))/((delta_x^2)*RHO(10,:)*C(10,:)))+((2*k_a2*A2)/((L_die)*RH
O(10,:)*A1*delta_x*C(10,:))))*T(10,:)+((K(10,:)*T(11,:))/((delta_x^2)*R
HO(10,:)*C(10,:)))+(egen_clamp/(RHO(10,:)*C(10,:))));

    %node 11

T11n=T(11,:)+delta_t*(((K(11,:)*T(10,:))/((delta_x_test^2)*RHO(11,:)*C(
11,:)))-
(((2*K(11,:))/((delta_x_test^2)*RHO(11,:)*C(11,:)))+((2*h*A22_def)/(RHO
(11,:)*A11_def*delta_x_test*C(11,:))))*T(11,:)+((K(11,:)*T(12,:))/((del
ta_x_test^2)*RHO(11,:)*C(11,:)))+((2*h*A22_def*Tinf)/(RHO(11,:)*A11_def
*delta_x_test*C(11,:)))+(egen_test/(RHO(11,:)*C(11,:))));

    %node 12

T12n=T(12,:)+delta_t*(((K(12,:)*T(11,:))/((delta_x_test^2)*RHO(12,:)*C(
```

```
12,:)))-
(((2*K(12,:))/((delta_x_test^2)*RHO(12,:)*C(12,:)))+((2*h*A22_def)/(RHO
(12,:)*A11_def*delta_x_test*C(12,:))))*T(12,:)+((K(12,:)*T(13,:))/((del
ta_x_test^2)*RHO(12,:)*C(12,:)))+((2*h*A22_def*Tinf)/(RHO(12,:)*A11_def
*delta_x_test*C(12,:)))+(egen_test/(RHO(12,:)*C(12,:))));

    %node 13

T13n=T(13,:)+delta_t*(((K(13,:)*T(12,:))/((delta_x_test^2)*RHO(13,:)*C(
13,:)))-
(((2*K(13,:))/((delta_x_test^2)*RHO(13,:)*C(13,:)))+((2*h*A22_def)/(RHO
(13,:)*A11_def*delta_x_test*C(13,:))))*T(13,:)+((K(13,:)*T(14,:))/((del
ta_x_test^2)*RHO(13,:)*C(13,:)))+((2*h*A22_def*Tinf)/(RHO(13,:)*A11_def
*delta_x_test*C(13,:)))+(egen_test/(RHO(13,:)*C(13,:))));

    %node 14

T14n=T(14,:)+delta_t*(((K(14,:)*T(13,:))/((delta_x_test^2)*RHO(14,:)*C(
14,:)))-
(((2*K(14,:))/((delta_x_test^2)*RHO(14,:)*C(14,:)))+((2*h*A22_def)/(RHO
(14,:)*A11_def*delta_x_test*C(14,:))))*T(14,:)+((K(14,:)*T(15,:))/((del
ta_x_test^2)*RHO(14,:)*C(14,:)))+((2*h*A22_def*Tinf)/(RHO(14,:)*A11_def
*delta_x_test*C(14,:)))+(egen_test/(RHO(14,:)*C(14,:))));

    %node 15

T15n=T(15,:)+delta_t*(((K(15,:)*T(14,:))/((delta_x_test^2)*RHO(15,:)*C(
15,:)))-
(((2*K(15,:))/((delta_x_test^2)*RHO(15,:)*C(15,:)))+((2*h*A22_def)/(RHO
(15,:)*A11_def*delta_x_test*C(15,:))))*T(15,:)+((K(15,:)*T(16,:))/((del
ta_x_test^2)*RHO(15,:)*C(15,:)))+((2*h*A22_def*Tinf)/(RHO(15,:)*A11_def
*delta_x_test*C(15,:)))+(egen_test/(RHO(15,:)*C(15,:))));

    %node 16

T16n=T(16,:)+delta_t*(((K(16,:)*T(15,:))/((delta_x_test^2)*RHO(16,:)*C(
16,:)))-
(((2*K(16,:))/((delta_x_test^2)*RHO(16,:)*C(16,:)))+((2*h*A22_def)/(RHO
(16,:)*A11_def*delta_x_test*C(16,:))))*T(16,:)+((K(16,:)*T(17,:))/((del
ta_x_test^2)*RHO(16,:)*C(16,:)))+((2*h*A22_def*Tinf)/(RHO(16,:)*A11_def
*delta_x_test*C(16,:)))+(egen_test/(RHO(16,:)*C(16,:))));

    %node 17

T17n=T(17,:)+delta_t*(((K(17,:)*T(16,:))/((delta_x_test^2)*RHO(17,:)*C(
17,:)))-
(((2*K(17,:))/((delta_x_test^2)*RHO(17,:)*C(17,:)))+((2*h*A22_def)/(RHO
(17,:)*A11_def*delta_x_test*C(17,:))))*T(17,:)+((K(17,:)*T(18,:))/((del
ta_x_test^2)*RHO(17,:)*C(17,:)))+((2*h*A22_def*Tinf)/(RHO(17,:)*A11_def
*delta_x_test*C(17,:)))+(egen_test/(RHO(17,:)*C(17,:))));

    %node 18
```

```
T18n=T(18,:)+delta_t*(((K(18,:)*T(17,:))/((delta_x_test^2)*RHO(18,:)*C(
18,:)))-
(((2*K(18,:))/((delta_x_test^2)*RHO(18,:)*C(18,:)))+((2*h*A22_def)/(RHO
(18,:)*A11_def*delta_x_test*C(18,:))))*T(18,:)+((K(18,:)*T(19,:))/((del
ta_x_test^2)*RHO(18,:)*C(18,:)))+((2*h*A22_def*Tinf)/(RHO(18,:)*A11_def
*delta_x_test*C(18,:)))+(egen_test/(RHO(18,:)*C(18,:))));

    %node 19

T19n=T(19,:)+delta_t*(((K(19,:)*T(18,:))/((delta_x_test^2)*RHO(19,:)*C(
19,:)))-
(((2*K(19,:))/((delta_x_test^2)*RHO(19,:)*C(19,:)))+((2*h*A22_def)/(RHO
(19,:)*A11_def*delta_x_test*C(19,:))))*T(19,:)+((K(19,:)*T(20,:))/((del
ta_x_test^2)*RHO(19,:)*C(19,:)))+((2*h*A22_def*Tinf)/(RHO(19,:)*A11_def
*delta_x_test*C(19,:)))+(egen_test/(RHO(19,:)*C(19,:))));

    %node 20

T20n=T(20,:)+delta_t*(((K(20,:)*T(19,:))/((delta_x_test^2)*RHO(20,:)*C(
20,:)))-
(((2*K(20,:))/((delta_x_test^2)*RHO(20,:)*C(20,:)))+((2*h*A22_def)/(RHO
(20,:)*A11_def*delta_x_test*C(20,:))))*T(20,:)+((K(20,:)*T(21,:))/((del
ta_x_test^2)*RHO(20,:)*C(20,:)))+((2*h*A22_def*Tinf)/(RHO(20,:)*A11_def
*delta_x_test*C(20,:)))+(egen_test/(RHO(20,:)*C(20,:))));

    %node 21

T21n=T(21,:)+delta_t*(((K(21,:)*T(20,:))/((delta_x_test^2)*RHO(21,:)*C(
21,:)))-
(((2*K(21,:))/((delta_x_test^2)*RHO(21,:)*C(21,:)))+((2*h*A22_def)/(RHO
(21,:)*A11_def*delta_x_test*C(21,:))))*T(21,:)+((K(21,:)*T(22,:))/((del
ta_x_test^2)*RHO(21,:)*C(21,:)))+((2*h*A22_def*Tinf)/(RHO(21,:)*A11_def
*delta_x_test*C(21,:)))+(egen_test/(RHO(21,:)*C(21,:))));

    %node 22

T22n=T(22,:)+delta_t*(((K(22,:)*T(21,:))/((delta_x_test^2)*RHO(22,:)*C(
22,:)))-
(((2*K(22,:))/((delta_x_test^2)*RHO(22,:)*C(22,:)))+((2*h*A22_def)/(RHO
(22,:)*A11_def*delta_x_test*C(22,:))))*T(22,:)+((K(22,:)*T(23,:))/((del
ta_x_test^2)*RHO(22,:)*C(22,:)))+((2*h*A22_def*Tinf)/(RHO(22,:)*A11_def
*delta_x_test*C(22,:)))+(egen_test/(RHO(22,:)*C(22,:))));

    %node 23

T23n=T(23,:)+delta_t*(((K(23,:)*T(22,:))/((delta_x_test^2)*RHO(23,:)*C(
23,:)))-
(((2*K(23,:))/((delta_x_test^2)*RHO(23,:)*C(23,:)))+((2*h*A22_def)/(RHO
(23,:)*A11_def*delta_x_test*C(23,:))))*T(23,:)+((K(23,:)*T(24,:))/((del
ta_x_test^2)*RHO(23,:)*C(23,:)))+((2*h*A22_def*Tinf)/(RHO(23,:)*A11_def
*delta_x_test*C(23,:)))+(egen_test/(RHO(23,:)*C(23,:))));
```

```
    %node 24

T24n=T(24,:)+delta_t*(((K(24,:)*T(23,:))/((delta_x_test^2)*RHO(24,:)*C(
24,:)))-
(((2*K(24,:))/((delta_x_test^2)*RHO(24,:)*C(24,:)))+((2*h*A22_def)/(RHO
(24,:)*A11_def*delta_x_test*C(24,:))))*T(24,:)+((K(24,:)*T(25,:))/((del
ta_x_test^2)*RHO(24,:)*C(24,:)))+((2*h*A22_def*Tinf)/(RHO(24,:)*A11_def
*delta_x_test*C(24,:)))+(egen_test/(RHO(24,:)*C(24,:))));

    %node 25

T25n=T(25,:)+delta_t*(((K(25,:)*T(24,:))/((delta_x_test^2)*RHO(25,:)*C(
25,:)))-
(((2*K(25,:))/((delta_x_test^2)*RHO(25,:)*C(25,:)))+((2*h*A22_def)/(RHO
(25,:)*A11_def*delta_x_test*C(25,:))))*T(25,:)+((K(25,:)*T(26,:))/((del
ta_x_test^2)*RHO(25,:)*C(25,:)))+((2*h*A22_def*Tinf)/(RHO(25,:)*A11_def
*delta_x_test*C(25,:)))+(egen_test/(RHO(25,:)*C(25,:))));

    %node 26

T26n=T(26,:)+delta_t*(((K(26,:)*T(25,:))/((delta_x_test^2)*RHO(26,:)*C(
26,:)))-
(((2*K(26,:))/((delta_x_test^2)*RHO(26,:)*C(26,:)))+((2*h*A22_def)/(RHO
(26,:)*A11_def*delta_x_test*C(26,:))))*T(26,:)+((K(26,:)*T(27,:))/((del
ta_x_test^2)*RHO(26,:)*C(26,:)))+((2*h*A22_def*Tinf)/(RHO(26,:)*A11_def
*delta_x_test*C(26,:)))+(egen_test/(RHO(26,:)*C(26,:))));

    %node 27

T27n=T(27,:)+delta_t*(((K(27,:)*T(26,:))/((delta_x_test^2)*RHO(27,:)*C(
27,:)))-
(((2*K(27,:))/((delta_x_test^2)*RHO(27,:)*C(27,:)))+((2*h*A22_def)/(RHO
(27,:)*A11_def*delta_x_test*C(27,:))))*T(27,:)+((K(27,:)*T(28,:))/((del
ta_x_test^2)*RHO(27,:)*C(27,:)))+((2*h*A22_def*Tinf)/(RHO(27,:)*A11_def
*delta_x_test*C(27,:)))+(egen_test/(RHO(27,:)*C(27,:))));

    %node 28

T28n=T(28,:)+delta_t*(((K(28,:)*T(27,:))/((delta_x_test^2)*RHO(28,:)*C(
28,:)))-
(((2*K(28,:))/((delta_x_test^2)*RHO(28,:)*C(28,:)))+((2*h*A22_def)/(RHO
(28,:)*A11_def*delta_x_test*C(28,:))))*T(28,:)+((K(28,:)*T(29,:))/((del
ta_x_test^2)*RHO(28,:)*C(28,:)))+((2*h*A22_def*Tinf)/(RHO(28,:)*A11_def
*delta_x_test*C(28,:)))+(egen_test/(RHO(28,:)*C(28,:))));

    %node 29

T29n=T(29,:)+delta_t*(((K(29,:)*T(28,:))/((delta_x_test^2)*RHO(29,:)*C(
29,:)))-
(((2*K(29,:))/((delta_x_test^2)*RHO(29,:)*C(29,:)))+((2*h*A22_def)/(RHO
(29,:)*A11_def*delta_x_test*C(29,:))))*T(29,:)+((K(29,:)*T(30,:))/((del
```

```
ta_x_test^2)*RHO(29,:)*C(29,:)))+((2*h*A22_def*Tinf)/(RHO(29,:)*A11_def
*delta_x_test*C(29,:)))+(egen_test/(RHO(29,:)*C(29,:))));

    %node 30

T30n=T(30,:)+delta_t*(((K(30,:)*T(29,:))/((delta_x_test^2)*RHO(30,:)*C(
30,:)))-
(((2*K(30,:))/((delta_x_test^2)*RHO(30,:)*C(30,:)))+((2*h*A22_def)/(RHO
(30,:)*A11_def*delta_x_test*C(30,:))))*T(30,:)+((K(30,:)*T(31,:))/((del
ta_x_test^2)*RHO(30,:)*C(30,:)))+((2*h*A22_def*Tinf)/(RHO(30,:)*A11_def
*delta_x_test*C(30,:)))+(egen_test/(RHO(30,:)*C(30,:))));

    %node 31

T31n=T(31,:)+delta_t*(((K(31,:)*T(30,:))/((delta_x_test^2)*RHO(31,:)*C(
31,:)))-
(((2*K(31,:))/((delta_x_test^2)*RHO(31,:)*C(31,:)))+((2*h*A22_def)/(RHO
(31,:)*A11_def*delta_x_test*C(31,:))))*T(31,:)+((K(31,:)*T(32,:))/((del
ta_x_test^2)*RHO(31,:)*C(31,:)))+((2*h*A22_def*Tinf)/(RHO(31,:)*A11_def
*delta_x_test*C(31,:)))+(egen_test/(RHO(31,:)*C(31,:))));

    %node 32

T32n=T(32,:)+delta_t*(((K(32,:)*T(31,:))/((delta_x^2)*RHO(32,:)*C(32,:)
))+((2*k_a2*A2*Tdien)/((L_die)*RHO(32,:)*A1*delta_x*C(32,:)))-
(((2*K(32,:))/((delta_x^2)*RHO(32,:)*C(32,:)))+((2*k_a2*A2)/((L_die)*RH
O(32,:)*A1*delta_x*C(32,:))))*T(32,:)+((K(32,:)*T(33,:))/((delta_x^2)*R
HO(32,:)*C(32,:)))+(egen_clamp/(RHO(32,:)*C(32,:))));

    %node 33

T33n=T(33,:)+delta_t*(((K(33,:)*T(32,:))/((delta_x^2)*RHO(33,:)*C(33,:)
))+((2*k_a2*A2*Tdien)/((L_die)*RHO(33,:)*A1*delta_x*C(33,:)))-
(((2*K(33,:))/((delta_x^2)*RHO(33,:)*C(33,:)))+((2*k_a2*A2)/((L_die)*RH
O(33,:)*A1*delta_x*C(33,:))))*T(33,:)+((K(33,:)*T(34,:))/((delta_x^2)*R
HO(33,:)*C(33,:)))+(egen_clamp/(RHO(33,:)*C(33,:))));

    %node 34

T34n=T(34,:)+delta_t*(((K(34,:)*T(33,:))/((delta_x^2)*RHO(34,:)*C(34,:)
))+((2*k_a2*A2*Tdien)/((L_die)*RHO(34,:)*A1*delta_x*C(34,:)))-
(((2*K(34,:))/((delta_x^2)*RHO(34,:)*C(34,:)))+((2*k_a2*A2)/((L_die)*RH
O(34,:)*A1*delta_x*C(34,:))))*T(34,:)+((K(34,:)*T(35,:))/((delta_x^2)*R
HO(34,:)*C(34,:)))+(egen_clamp/(RHO(34,:)*C(34,:))));

    %node 35

T35n=T(35,:)+delta_t*(((K(35,:)*T(34,:))/((delta_x^2)*RHO(35,:)*C(35,:)
))+((2*k_a2*A2*Tdien)/((L_die)*RHO(35,:)*A1*delta_x*C(35,:)))-
(((2*K(35,:))/((delta_x^2)*RHO(35,:)*C(35,:)))+((2*k_a2*A2)/((L_die)*RH
O(35,:)*A1*delta_x*C(35,:))))*T(35,:)+((K(35,:)*T(36,:))/((delta_x^2)*R
HO(35,:)*C(35,:)))+(egen_clamp/(RHO(35,:)*C(35,:))));
```

```
    %node 36

T36n=T(36,:)+delta_t*(((K(36,:)*T(35,:))/((delta_x^2)*RHO(36,:)*C(36,:)
))+((2*k_a2*A2*Tdien)/((L_die)*RHO(36,:)*A1*delta_x*C(36,:)))-
(((2*K(36,:))/((delta_x^2)*RHO(36,:)*C(36,:)))+((2*k_a2*A2)/((L_die)*RH
O(36,:)*A1*delta_x*C(36,:))))*T(36,:)+((K(36,:)*T(37,:))/((delta_x^2)*R
HO(36,:)*C(36,:)))+(egen_clamp/(RHO(36,:)*C(36,:))));

    %node 37

T37n=T(37,:)+delta_t*(((K(37,:)*T(36,:))/((delta_x^2)*RHO(37,:)*C(37,:)
))+((2*k_a2*A2*Tdien)/((L_die)*RHO(37,:)*A1*delta_x*C(37,:)))-
(((2*K(37,:))/((delta_x^2)*RHO(37,:)*C(37,:)))+((2*k_a2*A2)/((L_die)*RH
O(37,:)*A1*delta_x*C(37,:))))*T(37,:)+((K(37,:)*T(38,:))/((delta_x^2)*R
HO(37,:)*C(37,:)))+(egen_clamp/(RHO(37,:)*C(37,:))));

    %node 38

T38n=T(38,:)+delta_t*(((K(38,:)*T(37,:))/((delta_x^2)*RHO(38,:)*C(38,:)
))+((2*k_a2*A2*Tdien)/((L_die)*RHO(38,:)*A1*delta_x*C(38,:)))-
(((2*K(38,:))/((delta_x^2)*RHO(38,:)*C(38,:)))+((2*k_a2*A2)/((L_die)*RH
O(38,:)*A1*delta_x*C(38,:))))*T(38,:)+((K(38,:)*T(39,:))/((delta_x^2)*R
HO(38,:)*C(38,:)))+(egen_clamp/(RHO(38,:)*C(38,:))));

    %node 39

T39n=T(39,:)+delta_t*(((K(39,:)*T(38,:))/((delta_x^2)*RHO(39,:)*C(39,:)
))+((2*k_a2*A2*Tdien)/((L_die)*RHO(39,:)*A1*delta_x*C(39,:)))-
(((2*K(39,:))/((delta_x^2)*RHO(39,:)*C(39,:)))+((2*k_a2*A2)/((L_die)*RH
O(39,:)*A1*delta_x*C(39,:))))*T(39,:)+((K(39,:)*T(40,:))/((delta_x^2)*R
HO(39,:)*C(39,:)))+(egen_clamp/(RHO(39,:)*C(39,:))));

    %node 40

T40n=T(40,:)+delta_t*(((K(40,:)*T(39,:))/((delta_x^2)*RHO(40,:)*C(40,:)
))+((2*k_a2*A2*Tdien)/((L_die)*RHO(40,:)*A1*delta_x*C(40,:)))-
(((2*K(40,:))/((delta_x^2)*RHO(40,:)*C(40,:)))+((2*k_a2*A2)/((L_die)*RH
O(40,:)*A1*delta_x*C(40,:))))*T(40,:)+((K(40,:)*T(41,:))/((delta_x^2)*R
HO(40,:)*C(40,:)))+(egen_clamp/(RHO(40,:)*C(40,:))));

    %node 41

T41n=T(41,:)+delta_t*(((K(41,:)*T(40,:))/(((delta_x^2)/2)*RHO(41,:)*C(4
1,:)))-
((K(41,:)/(((delta_x^2)/2)*RHO(41,:)*C(41,:)))+((2*k_a2*w)/((L_die)*RHO
(41,:)*A1*C(41,:)))+((h*t*w)/(RHO(41,:)*A1*(delta_x/2)*C(41,:))))*T(41,
:)+((2*k_a2*w*Tdien)/((L_die)*RHO(41,:)*A1*C(41,:)))+((h*t*w*Tinf)/(RHO
(41,:)*A1*(delta_x/2)*C(41,:)))+(egen_clamp/(RHO(41,:)*C(41,:))));

    %store results in matrix
```

```
    Temperature(i,:)=[T1n T2n T3n T4n T5n T6n T7n T8n T9n T10n T11n
T12n T13n T14n T15n T16n T17n T18n T19n T20n T21n T22n T23n T24n T25n
T26n T27n T28n T29n T30n T31n T32n T33n T34n T35n T36n T37n T38n T39n
T40n T41n];
    Die_temp(i,:)=Tdien;
    Density(i,:)=[RHO(1,:) RHO(2,:) RHO(3,:) RHO(4,:) RHO(5,:) RHO(6,:)
RHO(7,:) RHO(8,:) RHO(9,:) RHO(10,:) RHO(11,:) RHO(12,:) RHO(13,:)
RHO(14,:) RHO(15,:) RHO(16,:) RHO(17,:) RHO(18,:) RHO(19,:) RHO(20,:)
RHO(21,:) RHO(22,:) RHO(23,:) RHO(24,:) RHO(25,:) RHO(26,:) RHO(27,:)
RHO(28,:) RHO(29,:) RHO(30,:) RHO(31,:) RHO(32,:) RHO(33,:) RHO(34,:)
RHO(35,:) RHO(36,:) RHO(37,:) RHO(38,:) RHO(39,:) RHO(40,:) RHO(41,:)];
    Conductivity(i,:)=[K(1,:) K(2,:) K(3,:) K(4,:) K(5,:) K(6,:) K(7,:)
K(8,:) K(9,:) K(10,:) K(11,:) K(12,:) K(13,:) K(14,:) K(15,:) K(16,:)
K(17,:) K(18,:) K(19,:) K(20,:) K(21,:) K(22,:) K(23,:) K(24,:) K(25,:)
K(26,:) K(27,:) K(28,:) K(29,:) K(30,:) K(31,:) K(32,:) K(33,:) K(34,:)
K(35,:) K(36,:) K(37,:) K(38,:) K(39,:) K(40,:) K(41,:)];
    H_capacity(i,:)=[C(1,:) C(2,:) C(3,:) C(4,:) C(5,:) C(6,:) C(7,:)
C(8,:) C(9,:) C(10,:) C(11,:) C(12,:) C(13,:) C(14,:) C(15,:) C(16,:)
C(17,:) C(18,:) C(19,:) C(20,:) C(21,:) C(22,:) C(23,:) C(24,:) C(25,:)
C(26,:) C(27,:) C(28,:) C(29,:) C(30,:) C(31,:) C(32,:) C(33,:) C(34,:)
C(35,:) C(36,:) C(37,:) C(38,:) C(39,:) C(40,:) C(41,:)];
    Resistivity(i,:)=[RHOE(1,:) RHOE(2,:) RHOE(3,:) RHOE(4,:) RHOE(5,:)
RHOE(6,:) RHOE(7,:) RHOE(8,:) RHOE(9,:) RHOE(10,:) RHOE(11,:)
RHOE(12,:) RHOE(13,:) RHOE(14,:) RHOE(15,:) RHOE(16,:) RHOE(17,:)
RHOE(18,:) RHOE(19,:) RHOE(20,:) RHOE(21,:) RHOE(22,:) RHOE(23,:)
RHOE(24,:) RHOE(25,:) RHOE(26,:) RHOE(27,:) RHOE(28,:) RHOE(29,:)
RHOE(30,:) RHOE(31,:) RHOE(32,:) RHOE(33,:) RHOE(34,:) RHOE(35,:)
RHOE(36,:) RHOE(37,:) RHOE(38,:) RHOE(39,:) RHOE(40,:) RHOE(41,:)];
    Die_dens(i,:)=rho_a2;
    Die_conduct(i,:)=k_a2;
    Time(i,:)=i*delta_t;
    Delta_S(i,:)=delta_s;
    Delta_S_Element(i,:)=delta_s_element;
    Delta_X_Test(i,:)=delta_x_test;
    A11_Def(i,:)=A11_def;
    A22_Def(i,:)=A22_def;
    Width_Test(i,:)=width_test;
    Thickness_Test(i,:)=thickness_test;
    Length_Test(i,:)=length_test;
    Strain_L(i,:)=strain_l;
    Strain_W(i,:)=strain_w;
    R_Test_Def(i,:)=R_test_def;
    Egen_Test_Def(i,:)=egen_test_def;
    Egen_Clamp(i,:)=egen_clamp;
    Egen_Test(i,:)=egen_test;
    Egen_Die(i,:)=egen_die;

    %display simulation time remaining
    if i==bb*3000
        display(['Simulation time remaining: ', num2str(length_t-
i*delta_t),' (s)'])
        bb=bb+1;
     end
```

```
    i=i+1;   %increment storage array index

    %reset node temperature based off of new calculated temperature
    T(1,:)=T1n;
    T(2,:)=T2n;
    T(3,:)=T3n;
    T(4,:)=T4n;
    T(5,:)=T5n;
    T(6,:)=T6n;
    T(7,:)=T7n;
    T(8,:)=T8n;
    T(9,:)=T9n;
    T(10,:)=T10n;
    T(11,:)=T11n;
    T(12,:)=T12n;
    T(13,:)=T13n;
    T(14,:)=T14n;
    T(15,:)=T15n;
    T(16,:)=T16n;
    T(17,:)=T17n;
    T(18,:)=T18n;
    T(19,:)=T19n;
    T(20,:)=T20n;
    T(21,:)=T21n;
    T(22,:)=T22n;
    T(23,:)=T23n;
    T(24,:)=T24n;
    T(25,:)=T25n;
    T(26,:)=T26n;
    T(27,:)=T27n;
    T(28,:)=T28n;
    T(29,:)=T29n;
    T(30,:)=T30n;
    T(31,:)=T31n;
    T(32,:)=T32n;
    T(33,:)=T33n;
    T(34,:)=T34n;
    T(35,:)=T35n;
    T(36,:)=T36n;
    T(37,:)=T37n;
    T(38,:)=T38n;
    T(39,:)=T39n;
    T(40,:)=T40n;
    T(41,:)=T41n;
    Tdie=Tdien;

    %calculate new sheet properties based off of current node
temperature

    %density (sheet)
    for mmm=1:1:41
```

```
        RHO(mmm,:)=-0.1414*T(mmm,:)+1821.9;
    end

    %thermal conductivity (sheet)
    for uuu=1:1:41
        K(uuu,:)=0.1011*T(uuu,:)+49.557;
    end

    %heat capacity (sheet)
    for rrr=1:1:41
        C(rrr,:)=0.7779*T(rrr,:)+777.64;
    end

    %electrical resistivity (sheet)
    for sss=1:1:41
        RHOE(sss,:)=(2*10^-10)*T(sss,1)+(4*10^-8);
    end

    %calculate new die properties based off of current die temperature

    %density (A2 dies)
    rho_a2=-0.3032*Tdie+7951.5;

    %themal conductivity (A2 dies)
    k_a2=0.0058*Tdie+24.252;

end
%=========================================================================
```

E.1.3 - Thermal Model Diffuse Deformation

```
%1D transient finite difference model of sheet metal dogbone
temperature profile
%Includes: joule heating, conduction to dies, and convection to
environment
%Includes: Diffuse Deformation*********

%Assumptions
%1)1D model and HT is equal across specimen thickness and width
%2)There are 41 nodes across the length of the specimen (spacing = 5mm)
%3)The material is homogeneous and isotropic
%5)Electrical resistivity of the dies is not temperature dependent*
%6)Specific heat of the dies is not temperature dependent*
%7)The environmental properties are an assumption (h value)
%8)Radiation effects is lumped into the convection coefficient - h
combined
%9)Sheet metal dogbone does not account for fillets from the test
region to the grip region
%10)Deformation in the model assumes isotropy and experimental strain
data
%is used to caluclate elements sizes in the test region as a fuction of
%time (used linear assumption of strain to measured fracture strain)
```

```
%*not a large temperature chance in dies so it is a good approximation

%Notes
%1)Left side of specimen is node 1
%2)Right side of specimen is node 41
%3)Center of specimen is node 21
%4)Nodes 1-10 and 32-41 are in the clamping region - conduct directly
into dies
%5)Nodes 1 and 41 have convection effects on the end edge of the
specimen
%6)Nodes 11-31 have convection effects to environment
%7)All nodes are linked by conduction
%8)The thermal conductivity, heat capacity, and density of the sheet
are temperature dependent in the model
%9)The dies increases in temperature over time from joule heating when
current is applied - analyzed as a lumped mass
%10)47.5 of the specimen is clamped @ each end
%11) Platen Speed is 0.1"/min

%=========================================================================
===

%Variables
%=========================================================================
===

%environment properties
Tinf=273+26;                              %room temperature [=] K
h=20;                                   %convection coefficient [=] W/m^2-K
Tinitial=273+26;                          %initial material temperature
[=] K

%sheet geometry (Mg)
L=200/1000;                             %specimen length [=] m
Ld=(47.5/1000)*2;                       %specimen length under dies [=] m
Lt=L-Ld;                                %specimen length in test region [=]
m
w=20/1000;                              %specimen width in grip region [=]
m
w1=12.5/1000;                           %specimen width in test region [=]
m
t=1/1000;                               %specimen thickness [=] m

%sheet material properties (Mg)
rho=-0.1414*Tinitial+1821.9;            %density of MgAZ31B [=] kg/m^3
k=0.1011*Tinitial+49.557;               %thermal conductivity of MgAZ31B
[=] W/m-K
c=0.779*Tinitial+777.64;                %heat capacity [=] J/kg-K
rhoe=(2*10^-10)*Tinitial+(4*10^-8); %electrical resistivity of MgAZ31B
[=] ohm-m
```

```
%die geometry (A2)
As_die=0.029832;                    %die surface area [=] m^2
V_die=0.000305837;                  %die volume [=] m^3

%die material properties (A2)
rho_a2=-0.3032*Tinitial+7951.5;     %density of A2 [=] kg/m^3
k_a2=0.0058*Tinitial+24.252;        %thermal conductivity of A2 dies
[=] W/m-K
c_a2=460;                           %heat capacity
rhoe_a2=6*10^-7;                    %electrical resistivity of A2 [=]
ohm-m

%element properties
delta_x=(L/40);                     %node spacing [=] m
A1=t*w;                             %conduction area in die region [=]
m^2
A11=t*w1;                           %conduction area in test region [=]
m^2
A2=delta_x*w;                       %conduction area into dies [=] m^2
A22=delta_x*w1;                     %convection area in test region [=]
m^2
A3=w*(47.5/1000);                   %full conduction area into dies [=]
m^2
L_die=t/2;                          %die conduction length

%element deformation properties
def_rate=0.1*25.4/1000;             %deformation rate (in/min to m/min)

%=========================================================================
===

%Internal Energy Generation
%=========================================================================
===

%pulsing parameters
I=800;                          %applied current magnitude (square wave)
[=] A
PSeff=0.7;                      %Power Supply effiency
period=60;                      %period for pulsing [=] s
duration=0.3;                     %length of pulse [=] s
duty=(duration/period)*100;     %duty cycle in percent

%joule heating (A2 die) - rhoe_a2 assumed constant as a result of small
temperature change
L1=0.04445;                             %height of section current flow
goes into die [=] m
L2=0.0381;                              %width of section current flow
goes into die [=] m
egen_die_initial=((I^2)*rhoe_a2)/((L1*L2)^2);   %heat generation per
unit volume in die [=] W/m^3
```

```
%=========================================================================
===

%Explicit Solution - Node Equations
%=========================================================================
===

%time step
delta_t=.01;                        %time step [=] s

%simulation length
length_t=10*60;                      %simulation length [=] s

%preallocate arrays for performance and memory allocation
Temperature=zeros(length_t/delta_t,41);
Die_temp=zeros(length_t/delta_t,1);
Density=zeros(length_t/delta_t,41);
Conductivity=zeros(length_t/delta_t,41);
H_capacity=zeros(length_t/delta_t,41);
Resistivity=zeros(length_t/delta_t,41);
Die_dens=zeros(length_t/delta_t,1);
Die_conduct=zeros(length_t/delta_t,1);
Time=zeros(length_t/delta_t,1);
T=zeros(41,1);
RHO=zeros(41,1);
K=zeros(41,1);
C=zeros(41,1);
RHOE=zeros(41,1);
Delta_S=zeros(length_t/delta_t,1);
Length_Test=zeros(length_t/delta_t,1);
Length_Element=zeros(length_t/delta_t,21);
Width_Element=zeros(length_t/delta_t,21);
Thickness_Element=zeros(length_t/delta_t,21);
A11_Def=zeros(length_t/delta_t,21);
A22_Def=zeros(length_t/delta_t,21);
R_Test_Def=zeros(length_t/delta_t,21);
Egen_Test_Def=zeros(length_t/delta_t,21);
Egen_Clamp=zeros(length_t/delta_t,1);
Egen_Test=zeros(length_t/delta_t,21);
Egen_Die=zeros(length_t/delta_t,1);

%set initial conditions (room temperature)

%node temperatures (row1=node1 ... row 41=node41)
for u=1:1:41
    T(u,:)=Tinitial;
end

%density (sheet) (row1=node1 ... row 41=node41)
for mm=1:1:41
    RHO(mm,:)=rho;
end
```

```
%thermal conductivity (sheet) (row1=node1 ... row 41=node41)
for uu=1:1:41
    K(uu,:)=k;
end

%heat capacity (sheet) (row1=node1 ... row 41=node41)
for rr=1:1:41
    C(rr,:)=c;
end

%electrical resistivity (sheet) (row1=node1 ... row 41=node41)
for ss=1:1:41
    RHOE(ss,:)=rhoe;
end

%die temperature
Tdie=Tinitial;

%nodal solution
i=1;     %temperature array index
bb=1;    %time remaining display index
for j=delta_t:delta_t:length_t

    %calcuate deformation parameters
    delta_s=def_rate*j/60;  %def amount in total in test region (min-
sec conversion) [=] m
    length_test=Lt+delta_s; %new sheet length [=] m

    length_element=delta_x*exp(Length_Strain_Matrix(i,:));   %new
element length in test region due to deformation [=] m (varies along
length)
    width_element=w1*exp(Width_Strain_Matrix(i,:));  %new element width
in test region due to deformation [=] m (varies along length)
    thickness_element=t*exp(Thickness_Strain_Matrix(i,:));   %new
element thickness in test region due to deformation [=] m (varies along
length)

    A11_def=thickness_element.*width_element;   %conduciton area
(vector that varies along length of test region and corresponds to
elements)
    A22_def=length_element.*width_element;  %convection area (vector
that varies along length of test region and corresponds to elements)

   %individual element resistance (sheet in test region)

R_test_def=transpose(RHOE(11:31,:)).*length_element./(width_element.*th
ickness_element);   %specimen resistance in test region [=] ohm

    %joule heating (sheet in test region)
```

```
egen_test_def=((I^2)*R_test_def)./(length_element.*width_element.*thick
ness_element);     %heat generation per unit volume in test region [=]
W/m^3

    %average rhoe for sheet in clamped region  used to update rhoe for
egen update during process
    rhoe_clamp_average=mean([RHOE(1,:) RHOE(2,:) RHOE(3,:) RHOE(4,:)
RHOE(5,:) RHOE(6,:) RHOE(7,:) RHOE(8,:) RHOE(9,:) RHOE(10,:) RHOE(32,:)
RHOE(33,:) RHOE(34,:) RHOE(35,:) RHOE(36,:) RHOE(37,:) RHOE(38,:)
RHOE(39,:) RHOE(40,:) RHOE(41,:)]);

    %specimen resistance (sheet in clamp region)
    R_clamp=rhoe_clamp_average*Ld/(w*t);                    %specimen
resistance in clamp region [=] ohm

    %joule heating (sheet in clamp region)
    egen_clamp=((I^2)*R_clamp)/(Ld*w*t);    %heat generation per unit
volume in clamp region [=] W/m^3

    %joule heating arrays applied
    egen_clamp=egen_clamp*egen_clamp_array(i,:)*PSeff;
    egen_test=egen_test_def*egen_test_array(i,:)*PSeff;
    egen_die=egen_die_initial*egen_die_array(i,:)*PSeff;

    %die temperature calculations as a function of joule heating and
conduction back into dies (die temperature changes)

    %average Mg specimen temperature under dies for conduction into
dies
    Tavg_mg=mean([T(1,:) T(2,:) T(3,:) T(4,:) T(5,:) T(6,:) T(7,:)
T(8,:) T(9,:) T(10,:) T(32,:) T(33,:) T(34,:) T(35,:) T(36,:) T(37,:)
T(38,:) T(39,:) T(40,:) T(41,:)]);

    %calculate new die temperature

Tdien=Tdie+delta_t*(((h*As_die*Tinf)/(rho_a2*V_die*c_a2))+((2*k_a2*A3*T
avg_mg)/(rho_a2*V_die*c_a2*L_die))-
(((h*As_die)/(rho_a2*V_die*c_a2))+((2*k_a2*A3)/(rho_a2*V_die*c_a2*L_die
)))*Tdie+(egen_die/(rho_a2*c_a2)));

    %node 1

T1n=T(1,:)+delta_t*(((K(1,:)*T(2,:))/(((delta_x^2)/2)*RHO(1,:)*C(1,:)))
-
((K(1,:)/(((delta_x^2)/2)*RHO(1,:)*C(1,:)))+((2*k_a2*w)/((L_die)*RHO(1,
:)*A1*C(1,:)))+((h*t*w)/(RHO(1,:)*A1*(delta_x/2)*C(1,:))))*T(1,:)+((2*k
_a2*w*Tdien)/((L_die)*RHO(1,:)*A1*C(1,:)))+((h*t*w*Tinf)/(RHO(1,:)*A1*(
delta_x/2)*C(1,:)))+(egen_clamp/(RHO(1,:)*C(1,:))));

    %node 2
```

```
T2n=T(2,:)+delta_t*(((K(2,:)*T(1,:))/((delta_x^2)*RHO(2,:)*C(2,:)))+((2
*k_a2*A2*Tdien)/((L_die)*RHO(2,:)*A1*delta_x*C(2,:)))-
(((2*K(2,:))/((delta_x^2)*RHO(2,:)*C(2,:)))+((2*k_a2*A2)/((L_die)*RHO(2
,:)*A1*delta_x*C(2,:))))*T(2,:)+((K(2,:)*T(3,:))/((delta_x^2)*RHO(2,:)*
C(2,:)))+(egen_clamp/(RHO(2,:)*C(2,:))));

    %node 3

T3n=T(3,:)+delta_t*(((K(3,:)*T(2,:))/((delta_x^2)*RHO(3,:)*C(3,:)))+((2
*k_a2*A2*Tdien)/((L_die)*RHO(3,:)*A1*delta_x*C(3,:)))-
(((2*K(3,:))/((delta_x^2)*RHO(3,:)*C(3,:)))+((2*k_a2*A2)/((L_die)*RHO(3
,:)*A1*delta_x*C(3,:))))*T(3,:)+((K(3,:)*T(4,:))/((delta_x^2)*RHO(3,:)*
C(3,:)))+(egen_clamp/(RHO(3,:)*C(3,:))));

    %node 4

T4n=T(4,:)+delta_t*(((K(4,:)*T(3,:))/((delta_x^2)*RHO(4,:)*C(4,:)))+((2
*k_a2*A2*Tdien)/((L_die)*RHO(4,:)*A1*delta_x*C(4,:)))-
(((2*K(4,:))/((delta_x^2)*RHO(4,:)*C(4,:)))+((2*k_a2*A2)/((L_die)*RHO(4
,:)*A1*delta_x*C(4,:))))*T(4,:)+((K(4,:)*T(5,:))/((delta_x^2)*RHO(4,:)*
C(4,:)))+(egen_clamp/(RHO(4,:)*C(4,:))));

    %node 5

T5n=T(5,:)+delta_t*(((K(5,:)*T(4,:))/((delta_x^2)*RHO(5,:)*C(5,:)))+((2
*k_a2*A2*Tdien)/((L_die)*RHO(5,:)*A1*delta_x*C(5,:)))-
(((2*K(5,:))/((delta_x^2)*RHO(5,:)*C(5,:)))+((2*k_a2*A2)/((L_die)*RHO(5
,:)*A1*delta_x*C(5,:))))*T(5,:)+((K(5,:)*T(6,:))/((delta_x^2)*RHO(5,:)*
C(5,:)))+(egen_clamp/(RHO(5,:)*C(5,:))));

    %node 6

T6n=T(6,:)+delta_t*(((K(6,:)*T(5,:))/((delta_x^2)*RHO(6,:)*C(6,:)))+((2
*k_a2*A2*Tdien)/((L_die)*RHO(6,:)*A1*delta_x*C(6,:)))-
(((2*K(6,:))/((delta_x^2)*RHO(6,:)*C(6,:)))+((2*k_a2*A2)/((L_die)*RHO(6
,:)*A1*delta_x*C(6,:))))*T(6,:)+((K(6,:)*T(7,:))/((delta_x^2)*RHO(6,:)*
C(6,:)))+(egen_clamp/(RHO(6,:)*C(6,:))));

    %node 7

T7n=T(7,:)+delta_t*(((K(7,:)*T(6,:))/((delta_x^2)*RHO(7,:)*C(7,:)))+((2
*k_a2*A2*Tdien)/((L_die)*RHO(7,:)*A1*delta_x*C(7,:)))-
(((2*K(7,:))/((delta_x^2)*RHO(7,:)*C(7,:)))+((2*k_a2*A2)/((L_die)*RHO(7
,:)*A1*delta_x*C(7,:))))*T(7,:)+((K(7,:)*T(8,:))/((delta_x^2)*RHO(7,:)*
C(7,:)))+(egen_clamp/(RHO(7,:)*C(7,:))));

    %node 8

T8n=T(8,:)+delta_t*(((K(8,:)*T(7,:))/((delta_x^2)*RHO(8,:)*C(8,:)))+((2
*k_a2*A2*Tdien)/((L_die)*RHO(8,:)*A1*delta_x*C(8,:)))-
(((2*K(8,:))/((delta_x^2)*RHO(8,:)*C(8,:)))+((2*k_a2*A2)/((L_die)*RHO(8
```

```
,:)*A1*delta_x*C(8,:))))*T(8,:)+((K(8,:)*T(9,:))/((delta_x^2)*RHO(8,:)*
C(8,:)))+(egen_clamp/(RHO(8,:)*C(8,:))));

    %node 9

T9n=T(9,:)+delta_t*(((K(9,:)*T(8,:))/((delta_x^2)*RHO(9,:)*C(9,:)))+((2
*k_a2*A2*Tdien)/((L_die)*RHO(9,:)*A1*delta_x*C(9,:)))-
(((2*K(9,:))/((delta_x^2)*RHO(9,:)*C(9,:)))+((2*k_a2*A2)/((L_die)*RHO(9
,:)*A1*delta_x*C(9,:))))*T(9,:)+((K(9,:)*T(10,:))/((delta_x^2)*RHO(9,:)
*C(9,:)))+(egen_clamp/(RHO(9,:)*C(9,:))));

    %node 10

T10n=T(10,:)+delta_t*(((K(10,:)*T(9,:))/((delta_x^2)*RHO(10,:)*C(10,:))
)+((2*k_a2*A2*Tdien)/((L_die)*RHO(10,:)*A1*delta_x*C(10,:)))-
(((2*K(10,:))/((delta_x^2)*RHO(10,:)*C(10,:)))+((2*k_a2*A2)/((L_die)*RH
O(10,:)*A1*delta_x*C(10,:))))*T(10,:)+((K(10,:)*T(11,:))/((delta_x^2)*R
HO(10,:)*C(10,:)))+(egen_clamp/(RHO(10,:)*C(10,:))));

    %node 11

T11n=T(11,:)+delta_t*(((K(11,:)*T(10,:))/((length_element(:,1)^2)*RHO(1
1,:)*C(11,:)))-
(((2*K(11,:))/((length_element(:,1)^2)*RHO(11,:)*C(11,:)))+((2*h*A22_de
f(:,1))/(RHO(11,:)*A11_def(:,1)*length_element(:,1)*C(11,:))))*T(11,:)+
((K(11,:)*T(12,:))/((length_element(:,1)^2)*RHO(11,:)*C(11,:)))+((2*h*A
22_def(:,1)*Tinf)/(RHO(11,:)*A11_def(:,1)*length_element(:,1)*C(11,:)))
+(egen_test(:,1)/(RHO(11,:)*C(11,:))));

    %node 12

T12n=T(12,:)+delta_t*(((K(12,:)*T(11,:))/((length_element(:,2)^2)*RHO(1
2,:)*C(12,:)))-
(((2*K(12,:))/((length_element(:,2)^2)*RHO(12,:)*C(12,:)))+((2*h*A22_de
f(:,2))/(RHO(12,:)*A11_def(:,2)*length_element(:,2)*C(12,:))))*T(12,:)+
((K(12,:)*T(13,:))/((length_element(:,2)^2)*RHO(12,:)*C(12,:)))+((2*h*A
22_def(:,2)*Tinf)/(RHO(12,:)*A11_def(:,2)*length_element(:,2)*C(12,:)))
+(egen_test(:,2)/(RHO(12,:)*C(12,:))));

    %node 13

T13n=T(13,:)+delta_t*(((K(13,:)*T(12,:))/((length_element(:,3)^2)*RHO(1
3,:)*C(13,:)))-
(((2*K(13,:))/((length_element(:,3)^2)*RHO(13,:)*C(13,:)))+((2*h*A22_de
f(:,3))/(RHO(13,:)*A11_def(:,3)*length_element(:,3)*C(13,:))))*T(13,:)+
((K(13,:)*T(14,:))/((length_element(:,3)^2)*RHO(13,:)*C(13,:)))+((2*h*A
22_def(:,3)*Tinf)/(RHO(13,:)*A11_def(:,3)*length_element(:,3)*C(13,:)))
+(egen_test(:,3)/(RHO(13,:)*C(13,:))));

    %node 14

T14n=T(14,:)+delta_t*(((K(14,:)*T(13,:))/((length_element(:,4)^2)*RHO(1
```

```
4,:)*C(14,:)))-
(((2*K(14,:))/((length_element(:,4)^2)*RHO(14,:)*C(14,:)))+((2*h*A22_de
f(:,4))/(RHO(14,:)*A11_def(:,4)*length_element(:,4)*C(14,:))))*T(14,:)+
((K(14,:)*T(15,:))/((length_element(:,4)^2)*RHO(14,:)*C(14,:)))+((2*h*A
22_def(:,4)*Tinf)/(RHO(14,:)*A11_def(:,4)*length_element(:,4)*C(14,:)))
+(egen_test(:,4)/(RHO(14,:)*C(14,:))));

    %node 15

T15n=T(15,:)+delta_t*(((K(15,:)*T(14,:))/((length_element(:,5)^2)*RHO(1
5,:)*C(15,:)))-
(((2*K(15,:))/((length_element(:,5)^2)*RHO(15,:)*C(15,:)))+((2*h*A22_de
f(:,5))/(RHO(15,:)*A11_def(:,5)*length_element(:,5)*C(15,:))))*T(15,:)+
((K(15,:)*T(16,:))/((length_element(:,5)^2)*RHO(15,:)*C(15,:)))+((2*h*A
22_def(:,5)*Tinf)/(RHO(15,:)*A11_def(:,5)*length_element(:,5)*C(15,:)))
+(egen_test(:,5)/(RHO(15,:)*C(15,:))));

    %node 16

T16n=T(16,:)+delta_t*(((K(16,:)*T(15,:))/((length_element(:,6)^2)*RHO(1
6,:)*C(16,:)))-
(((2*K(16,:))/((length_element(:,6)^2)*RHO(16,:)*C(16,:)))+((2*h*A22_de
f(:,6))/(RHO(16,:)*A11_def(:,6)*length_element(:,6)*C(16,:))))*T(16,:)+
((K(16,:)*T(17,:))/((length_element(:,6)^2)*RHO(16,:)*C(16,:)))+((2*h*A
22_def(:,6)*Tinf)/(RHO(16,:)*A11_def(:,6)*length_element(:,6)*C(16,:)))
+(egen_test(:,6)/(RHO(16,:)*C(16,:))));

    %node 17

T17n=T(17,:)+delta_t*(((K(17,:)*T(16,:))/((length_element(:,7)^2)*RHO(1
7,:)*C(17,:)))-
(((2*K(17,:))/((length_element(:,7)^2)*RHO(17,:)*C(17,:)))+((2*h*A22_de
f(:,7))/(RHO(17,:)*A11_def(:,7)*length_element(:,7)*C(17,:))))*T(17,:)+
((K(17,:)*T(18,:))/((length_element(:,7)^2)*RHO(17,:)*C(17,:)))+((2*h*A
22_def(:,7)*Tinf)/(RHO(17,:)*A11_def(:,7)*length_element(:,7)*C(17,:)))
+(egen_test(:,7)/(RHO(17,:)*C(17,:))));

    %node 18

T18n=T(18,:)+delta_t*(((K(18,:)*T(17,:))/((length_element(:,8)^2)*RHO(1
8,:)*C(18,:)))-
(((2*K(18,:))/((length_element(:,8)^2)*RHO(18,:)*C(18,:)))+((2*h*A22_de
f(:,8))/(RHO(18,:)*A11_def(:,8)*length_element(:,8)*C(18,:))))*T(18,:)+
((K(18,:)*T(19,:))/((length_element(:,8)^2)*RHO(18,:)*C(18,:)))+((2*h*A
22_def(:,8)*Tinf)/(RHO(18,:)*A11_def(:,8)*length_element(:,8)*C(18,:)))
+(egen_test(:,8)/(RHO(18,:)*C(18,:))));

    %node 19

T19n=T(19,:)+delta_t*(((K(19,:)*T(18,:))/((length_element(:,9)^2)*RHO(1
9,:)*C(19,:)))-
(((2*K(19,:))/((length_element(:,9)^2)*RHO(19,:)*C(19,:)))+((2*h*A22_de
```

```
f(:,9))/(RHO(19,:)*A11_def(:,9)*length_element(:,9)*C(19,:))))*T(19,:)+
((K(19,:)*T(20,:))/((length_element(:,9)^2)*RHO(19,:)*C(19,:)))+((2*h*A
22_def(:,9)*Tinf)/(RHO(19,:)*A11_def(:,9)*length_element(:,9)*C(19,:)))
+(egen_test(:,9)/(RHO(19,:)*C(19,:))));

    %node 20

T20n=T(20,:)+delta_t*(((K(20,:)*T(19,:))/((length_element(:,10)^2)*RHO(
20,:)*C(20,:)))-
(((2*K(20,:))/((length_element(:,10)^2)*RHO(20,:)*C(20,:)))+((2*h*A22_d
ef(:,10))/(RHO(20,:)*A11_def(:,10)*length_element(:,10)*C(20,:))))*T(20
,:)+((K(20,:)*T(21,:))/((length_element(:,10)^2)*RHO(20,:)*C(20,:)))+((
2*h*A22_def(:,10)*Tinf)/(RHO(20,:)*A11_def(:,10)*length_element(:,10)*C
(20,:)))+(egen_test(:,10)/(RHO(20,:)*C(20,:))));

    %node 21

T21n=T(21,:)+delta_t*(((K(21,:)*T(20,:))/((length_element(:,11)^2)*RHO(
21,:)*C(21,:)))-
(((2*K(21,:))/((length_element(:,11)^2)*RHO(21,:)*C(21,:)))+((2*h*A22_d
ef(:,11))/(RHO(21,:)*A11_def(:,11)*length_element(:,11)*C(21,:))))*T(21
,:)+((K(21,:)*T(22,:))/((length_element(:,11)^2)*RHO(21,:)*C(21,:)))+((
2*h*A22_def(:,11)*Tinf)/(RHO(21,:)*A11_def(:,11)*length_element(:,11)*C
(21,:)))+(egen_test(:,11)/(RHO(21,:)*C(21,:))));

    %node 22

T22n=T(22,:)+delta_t*(((K(22,:)*T(21,:))/((length_element(:,12)^2)*RHO(
22,:)*C(22,:)))-
(((2*K(22,:))/((length_element(:,12)^2)*RHO(22,:)*C(22,:)))+((2*h*A22_d
ef(:,12))/(RHO(22,:)*A11_def(:,12)*length_element(:,12)*C(22,:))))*T(22
,:)+((K(22,:)*T(23,:))/((length_element(:,12)^2)*RHO(22,:)*C(22,:)))+((
2*h*A22_def(:,12)*Tinf)/(RHO(22,:)*A11_def(:,12)*length_element(:,12)*C
(22,:)))+(egen_test(:,12)/(RHO(22,:)*C(22,:))));

    %node 23

T23n=T(23,:)+delta_t*(((K(23,:)*T(22,:))/((length_element(:,13)^2)*RHO(
23,:)*C(23,:)))-
(((2*K(23,:))/((length_element(:,13)^2)*RHO(23,:)*C(23,:)))+((2*h*A22_d
ef(:,13))/(RHO(23,:)*A11_def(:,13)*length_element(:,13)*C(23,:))))*T(23
,:)+((K(23,:)*T(24,:))/((length_element(:,13)^2)*RHO(23,:)*C(23,:)))+((
2*h*A22_def(:,13)*Tinf)/(RHO(23,:)*A11_def(:,13)*length_element(:,13)*C
(23,:)))+(egen_test(:,13)/(RHO(23,:)*C(23,:))));

    %node 24

T24n=T(24,:)+delta_t*(((K(24,:)*T(23,:))/((length_element(:,14)^2)*RHO(
24,:)*C(24,:)))-
(((2*K(24,:))/((length_element(:,14)^2)*RHO(24,:)*C(24,:)))+((2*h*A22_d
ef(:,14))/(RHO(24,:)*A11_def(:,14)*length_element(:,14)*C(24,:))))*T(24
,:)+((K(24,:)*T(25,:))/((length_element(:,14)^2)*RHO(24,:)*C(24,:)))+((
```

```
2*h*A22_def(:,14)*Tinf)/(RHO(24,:)*A11_def(:,14)*length_element(:,14)*C
(24,:)))+(egen_test(:,14)/(RHO(24,:)*C(24,:))));

    %node 25

T25n=T(25,:)+delta_t*(((K(25,:)*T(24,:))/((length_element(:,15)^2)*RHO(
25,:)*C(25,:)))-
(((2*K(25,:))/((length_element(:,15)^2)*RHO(25,:)*C(25,:)))+((2*h*A22_d
ef(:,15))/(RHO(25,:)*A11_def(:,15)*length_element(:,15)*C(25,:))))*T(25
,:)+((K(25,:)*T(26,:))/((length_element(:,15)^2)*RHO(25,:)*C(25,:)))+((
2*h*A22_def(:,15)*Tinf)/(RHO(25,:)*A11_def(:,15)*length_element(:,15)*C
(25,:)))+(egen_test(:,15)/(RHO(25,:)*C(25,:))));

    %node 26

T26n=T(26,:)+delta_t*(((K(26,:)*T(25,:))/((length_element(:,16)^2)*RHO(
26,:)*C(26,:)))-
(((2*K(26,:))/((length_element(:,16)^2)*RHO(26,:)*C(26,:)))+((2*h*A22_d
ef(:,16))/(RHO(26,:)*A11_def(:,16)*length_element(:,16)*C(26,:))))*T(26
,:)+((K(26,:)*T(27,:))/((length_element(:,16)^2)*RHO(26,:)*C(26,:)))+((
2*h*A22_def(:,16)*Tinf)/(RHO(26,:)*A11_def(:,16)*length_element(:,16)*C
(26,:)))+(egen_test(:,16)/(RHO(26,:)*C(26,:))));

    %node 27

T27n=T(27,:)+delta_t*(((K(27,:)*T(26,:))/((length_element(:,17)^2)*RHO(
27,:)*C(27,:)))-
(((2*K(27,:))/((length_element(:,17)^2)*RHO(27,:)*C(27,:)))+((2*h*A22_d
ef(:,17))/(RHO(27,:)*A11_def(:,17)*length_element(:,17)*C(27,:))))*T(27
,:)+((K(27,:)*T(28,:))/((length_element(:,17)^2)*RHO(27,:)*C(27,:)))+((
2*h*A22_def(:,17)*Tinf)/(RHO(27,:)*A11_def(:,17)*length_element(:,17)*C
(27,:)))+(egen_test(:,17)/(RHO(27,:)*C(27,:))));

    %node 28

T28n=T(28,:)+delta_t*(((K(28,:)*T(27,:))/((length_element(:,18)^2)*RHO(
28,:)*C(28,:)))-
(((2*K(28,:))/((length_element(:,18)^2)*RHO(28,:)*C(28,:)))+((2*h*A22_d
ef(:,18))/(RHO(28,:)*A11_def(:,18)*length_element(:,18)*C(28,:))))*T(28
,:)+((K(28,:)*T(29,:))/((length_element(:,18)^2)*RHO(28,:)*C(28,:)))+((
2*h*A22_def(:,18)*Tinf)/(RHO(28,:)*A11_def(:,18)*length_element(:,18)*C
(28,:)))+(egen_test(:,18)/(RHO(28,:)*C(28,:))));

    %node 29

T29n=T(29,:)+delta_t*(((K(29,:)*T(28,:))/((length_element(:,19)^2)*RHO(
29,:)*C(29,:)))-
(((2*K(29,:))/((length_element(:,19)^2)*RHO(29,:)*C(29,:)))+((2*h*A22_d
ef(:,19))/(RHO(29,:)*A11_def(:,19)*length_element(:,19)*C(29,:))))*T(29
,:)+((K(29,:)*T(30,:))/((length_element(:,19)^2)*RHO(29,:)*C(29,:)))+((
2*h*A22_def(:,19)*Tinf)/(RHO(29,:)*A11_def(:,19)*length_element(:,19)*C
(29,:)))+(egen_test(:,19)/(RHO(29,:)*C(29,:))));
```

```
    %node 30

T30n=T(30,:)+delta_t*(((K(30,:)*T(29,:))/((length_element(:,20)^2)*RHO(
30,:)*C(30,:)))-
(((2*K(30,:))/((length_element(:,20)^2)*RHO(30,:)*C(30,:)))+((2*h*A22_d
ef(:,20))/(RHO(30,:)*A11_def(:,20)*length_element(:,20)*C(30,:))))*T(30
,:)+((K(30,:)*T(31,:))/((length_element(:,20)^2)*RHO(30,:)*C(30,:)))+((
2*h*A22_def(:,20)*Tinf)/(RHO(30,:)*A11_def(:,20)*length_element(:,20)*C
(30,:)))+(egen_test(:,20)/(RHO(30,:)*C(30,:))));

    %node 31

T31n=T(31,:)+delta_t*(((K(31,:)*T(30,:))/((length_element(:,21)^2)*RHO(
31,:)*C(31,:)))-
(((2*K(31,:))/((length_element(:,21)^2)*RHO(31,:)*C(31,:)))+((2*h*A22_d
ef(:,21))/(RHO(31,:)*A11_def(:,21)*length_element(:,21)*C(31,:))))*T(31
,:)+((K(31,:)*T(32,:))/((length_element(:,21)^2)*RHO(31,:)*C(31,:)))+((
2*h*A22_def(:,21)*Tinf)/(RHO(31,:)*A11_def(:,21)*length_element(:,21)*C
(31,:)))+(egen_test(:,21)/(RHO(31,:)*C(31,:))));

    %node 32

T32n=T(32,:)+delta_t*(((K(32,:)*T(31,:))/((delta_x^2)*RHO(32,:)*C(32,:)
))+((2*k_a2*A2*Tdien)/((L_die)*RHO(32,:)*A1*delta_x*C(32,:)))-
(((2*K(32,:))/((delta_x^2)*RHO(32,:)*C(32,:)))+((2*k_a2*A2)/((L_die)*RH
O(32,:)*A1*delta_x*C(32,:))))*T(32,:)+((K(32,:)*T(33,:))/((delta_x^2)*R
HO(32,:)*C(32,:)))+(egen_clamp/(RHO(32,:)*C(32,:))));

    %node 33

T33n=T(33,:)+delta_t*(((K(33,:)*T(32,:))/((delta_x^2)*RHO(33,:)*C(33,:)
))+((2*k_a2*A2*Tdien)/((L_die)*RHO(33,:)*A1*delta_x*C(33,:)))-
(((2*K(33,:))/((delta_x^2)*RHO(33,:)*C(33,:)))+((2*k_a2*A2)/((L_die)*RH
O(33,:)*A1*delta_x*C(33,:))))*T(33,:)+((K(33,:)*T(34,:))/((delta_x^2)*R
HO(33,:)*C(33,:)))+(egen_clamp/(RHO(33,:)*C(33,:))));

    %node 34

T34n=T(34,:)+delta_t*(((K(34,:)*T(33,:))/((delta_x^2)*RHO(34,:)*C(34,:)
))+((2*k_a2*A2*Tdien)/((L_die)*RHO(34,:)*A1*delta_x*C(34,:)))-
(((2*K(34,:))/((delta_x^2)*RHO(34,:)*C(34,:)))+((2*k_a2*A2)/((L_die)*RH
O(34,:)*A1*delta_x*C(34,:))))*T(34,:)+((K(34,:)*T(35,:))/((delta_x^2)*R
HO(34,:)*C(34,:)))+(egen_clamp/(RHO(34,:)*C(34,:))));

    %node 35

T35n=T(35,:)+delta_t*(((K(35,:)*T(34,:))/((delta_x^2)*RHO(35,:)*C(35,:)
))+((2*k_a2*A2*Tdien)/((L_die)*RHO(35,:)*A1*delta_x*C(35,:)))-
(((2*K(35,:))/((delta_x^2)*RHO(35,:)*C(35,:)))+((2*k_a2*A2)/((L_die)*RH
O(35,:)*A1*delta_x*C(35,:))))*T(35,:)+((K(35,:)*T(36,:))/((delta_x^2)*R
HO(35,:)*C(35,:)))+(egen_clamp/(RHO(35,:)*C(35,:))));
```

```
    %node 36

T36n=T(36,:)+delta_t*(((K(36,:)*T(35,:))/((delta_x^2)*RHO(36,:)*C(36,:)
))+((2*k_a2*A2*Tdien)/((L_die)*RHO(36,:)*A1*delta_x*C(36,:)))-
(((2*K(36,:))/((delta_x^2)*RHO(36,:)*C(36,:)))+((2*k_a2*A2)/((L_die)*RH
O(36,:)*A1*delta_x*C(36,:))))*T(36,:)+((K(36,:)*T(37,:))/((delta_x^2)*R
HO(36,:)*C(36,:)))+(egen_clamp/(RHO(36,:)*C(36,:))));

    %node 37

T37n=T(37,:)+delta_t*(((K(37,:)*T(36,:))/((delta_x^2)*RHO(37,:)*C(37,:)
))+((2*k_a2*A2*Tdien)/((L_die)*RHO(37,:)*A1*delta_x*C(37,:)))-
(((2*K(37,:))/((delta_x^2)*RHO(37,:)*C(37,:)))+((2*k_a2*A2)/((L_die)*RH
O(37,:)*A1*delta_x*C(37,:))))*T(37,:)+((K(37,:)*T(38,:))/((delta_x^2)*R
HO(37,:)*C(37,:)))+(egen_clamp/(RHO(37,:)*C(37,:))));

    %node 38

T38n=T(38,:)+delta_t*(((K(38,:)*T(37,:))/((delta_x^2)*RHO(38,:)*C(38,:)
))+((2*k_a2*A2*Tdien)/((L_die)*RHO(38,:)*A1*delta_x*C(38,:)))-
(((2*K(38,:))/((delta_x^2)*RHO(38,:)*C(38,:)))+((2*k_a2*A2)/((L_die)*RH
O(38,:)*A1*delta_x*C(38,:))))*T(38,:)+((K(38,:)*T(39,:))/((delta_x^2)*R
HO(38,:)*C(38,:)))+(egen_clamp/(RHO(38,:)*C(38,:))));

    %node 39

T39n=T(39,:)+delta_t*(((K(39,:)*T(38,:))/((delta_x^2)*RHO(39,:)*C(39,:)
))+((2*k_a2*A2*Tdien)/((L_die)*RHO(39,:)*A1*delta_x*C(39,:)))-
(((2*K(39,:))/((delta_x^2)*RHO(39,:)*C(39,:)))+((2*k_a2*A2)/((L_die)*RH
O(39,:)*A1*delta_x*C(39,:))))*T(39,:)+((K(39,:)*T(40,:))/((delta_x^2)*R
HO(39,:)*C(39,:)))+(egen_clamp/(RHO(39,:)*C(39,:))));

    %node 40

T40n=T(40,:)+delta_t*(((K(40,:)*T(39,:))/((delta_x^2)*RHO(40,:)*C(40,:)
))+((2*k_a2*A2*Tdien)/((L_die)*RHO(40,:)*A1*delta_x*C(40,:)))-
(((2*K(40,:))/((delta_x^2)*RHO(40,:)*C(40,:)))+((2*k_a2*A2)/((L_die)*RH
O(40,:)*A1*delta_x*C(40,:))))*T(40,:)+((K(40,:)*T(41,:))/((delta_x^2)*R
HO(40,:)*C(40,:)))+(egen_clamp/(RHO(40,:)*C(40,:))));

    %node 41

T41n=T(41,:)+delta_t*(((K(41,:)*T(40,:))/(((delta_x^2)/2)*RHO(41,:)*C(4
1,:)))-
((K(41,:)/(((delta_x^2)/2)*RHO(41,:)*C(41,:)))+((2*k_a2*w)/((L_die)*RHO
(41,:)*A1*C(41,:)))+((h*t*w)/(RHO(41,:)*A1*(delta_x/2)*C(41,:))))*T(41,
:)+((2*k_a2*w*Tdien)/((L_die)*RHO(41,:)*A1*C(41,:)))+((h*t*w*Tinf)/(RHO
(41,:)*A1*(delta_x/2)*C(41,:)))+(egen_clamp/(RHO(41,:)*C(41,:))));

    %store results in matrix
```

```
    Temperature(i,:)=[T1n T2n T3n T4n T5n T6n T7n T8n T9n T10n T11n
T12n T13n T14n T15n T16n T17n T18n T19n T20n T21n T22n T23n T24n T25n
T26n T27n T28n T29n T30n T31n T32n T33n T34n T35n T36n T37n T38n T39n
T40n T41n];
    Die_temp(i,:)=Tdien;
    Density(i,:)=[RHO(1,:) RHO(2,:) RHO(3,:) RHO(4,:) RHO(5,:) RHO(6,:)
RHO(7,:) RHO(8,:) RHO(9,:) RHO(10,:) RHO(11,:) RHO(12,:) RHO(13,:)
RHO(14,:) RHO(15,:) RHO(16,:) RHO(17,:) RHO(18,:) RHO(19,:) RHO(20,:)
RHO(21,:) RHO(22,:) RHO(23,:) RHO(24,:) RHO(25,:) RHO(26,:) RHO(27,:)
RHO(28,:) RHO(29,:) RHO(30,:) RHO(31,:) RHO(32,:) RHO(33,:) RHO(34,:)
RHO(35,:) RHO(36,:) RHO(37,:) RHO(38,:) RHO(39,:) RHO(40,:) RHO(41,:)];
    Conductivity(i,:)=[K(1,:) K(2,:) K(3,:) K(4,:) K(5,:) K(6,:) K(7,:)
K(8,:) K(9,:) K(10,:) K(11,:) K(12,:) K(13,:) K(14,:) K(15,:) K(16,:)
K(17,:) K(18,:) K(19,:) K(20,:) K(21,:) K(22,:) K(23,:) K(24,:) K(25,:)
K(26,:) K(27,:) K(28,:) K(29,:) K(30,:) K(31,:) K(32,:) K(33,:) K(34,:)
K(35,:) K(36,:) K(37,:) K(38,:) K(39,:) K(40,:) K(41,:)];
    H_capacity(i,:)=[C(1,:) C(2,:) C(3,:) C(4,:) C(5,:) C(6,:) C(7,:)
C(8,:) C(9,:) C(10,:) C(11,:) C(12,:) C(13,:) C(14,:) C(15,:) C(16,:)
C(17,:) C(18,:) C(19,:) C(20,:) C(21,:) C(22,:) C(23,:) C(24,:) C(25,:)
C(26,:) C(27,:) C(28,:) C(29,:) C(30,:) C(31,:) C(32,:) C(33,:) C(34,:)
C(35,:) C(36,:) C(37,:) C(38,:) C(39,:) C(40,:) C(41,:)];
    Resistivity(i,:)=[RHOE(1,:) RHOE(2,:) RHOE(3,:) RHOE(4,:) RHOE(5,:)
RHOE(6,:) RHOE(7,:) RHOE(8,:) RHOE(9,:) RHOE(10,:) RHOE(11,:)
RHOE(12,:) RHOE(13,:) RHOE(14,:) RHOE(15,:) RHOE(16,:) RHOE(17,:)
RHOE(18,:) RHOE(19,:) RHOE(20,:) RHOE(21,:) RHOE(22,:) RHOE(23,:)
RHOE(24,:) RHOE(25,:) RHOE(26,:) RHOE(27,:) RHOE(28,:) RHOE(29,:)
RHOE(30,:) RHOE(31,:) RHOE(32,:) RHOE(33,:) RHOE(34,:) RHOE(35,:)
RHOE(36,:) RHOE(37,:) RHOE(38,:) RHOE(39,:) RHOE(40,:) RHOE(41,:)];
    Die_dens(i,:)=rho_a2;
    Die_conduct(i,:)=k_a2;
    Time(i,:)=i*delta_t;
    Delta_S(i,:)=delta_s;
    Length_Test(i,:)=length_test;
    Length_Element(i,:)=length_element;
    Width_Element(i,:)=width_element;
    Thickness_Element(i,:)=thickness_element;
    A11_Def(i,:)=A11_def;
    A22_Def(i,:)=A22_def;
    R_Test_Def(i,:)=R_test_def;
    Egen_Test_Def(i,:)=egen_test_def;
    Egen_Clamp(i,:)=egen_clamp;
    Egen_Test(i,:)=egen_test;
    Egen_Die(i,:)=egen_die;

   %display simulation time remaining
    if i==bb*3000
        display(['Simulation time remaining: ', num2str(length_t-
i*delta_t),' (s)'])
        bb=bb+1;
     end

    i=i+1;   %increment storage array index
```

```
    %reset node temperature based off of new calculated temperature
    T(1,:)=T1n;
    T(2,:)=T2n;
    T(3,:)=T3n;
    T(4,:)=T4n;
    T(5,:)=T5n;
    T(6,:)=T6n;
    T(7,:)=T7n;
    T(8,:)=T8n;
    T(9,:)=T9n;
    T(10,:)=T10n;
    T(11,:)=T11n;
    T(12,:)=T12n;
    T(13,:)=T13n;
    T(14,:)=T14n;
    T(15,:)=T15n;
    T(16,:)=T16n;
    T(17,:)=T17n;
    T(18,:)=T18n;
    T(19,:)=T19n;
    T(20,:)=T20n;
    T(21,:)=T21n;
    T(22,:)=T22n;
    T(23,:)=T23n;
    T(24,:)=T24n;
    T(25,:)=T25n;
    T(26,:)=T26n;
    T(27,:)=T27n;
    T(28,:)=T28n;
    T(29,:)=T29n;
    T(30,:)=T30n;
    T(31,:)=T31n;
    T(32,:)=T32n;
    T(33,:)=T33n;
    T(34,:)=T34n;
    T(35,:)=T35n;
    T(36,:)=T36n;
    T(37,:)=T37n;
    T(38,:)=T38n;
    T(39,:)=T39n;
    T(40,:)=T40n;
    T(41,:)=T41n;
    Tdie=Tdien;

    %calculate new sheet properties based off of current node
temperature

    %density (sheet)
    for mmm=1:1:41
        RHO(mmm,:)=-0.1414*T(mmm,:)+1821.9;
    end

    %thermal conductivity (sheet)
```

```
    for uuu=1:1:41
        K(uuu,:)=0.1011*T(uuu,:)+49.557;
    end

    %heat capacity (sheet)
    for rrr=1:1:41
        C(rrr,:)=0.7779*T(rrr,:)+777.64;
    end

    %electrical resistivity (sheet)
    for sss=1:1:41
        RHOE(sss,:)=(2*10^-10)*T(sss,1)+(4*10^-8);
    end

    %calculate new die properties based off of current die temperature

    %density (A2 dies)
    rho_a2=-0.3032*Tdie+7951.5;

    %themal conductivity (A2 dies)
    k_a2=0.0058*Tdie+24.252;

end
%=========================================================================
```

E.2 - Deformation Model Codes

E.2.1 - Deformation Model Main Code

```
%Notes************
%where "strain" is given this is along the axial length unless noted

%variables
nodes=21;
node_spacing=5/1000; %node spacing [=] m
mult=2000; %iterations

delta_t=0.5; %[=] s (.01 is temp model)
def_rate=(0.1*25.4/60)/1000; %deformation rate [=] m/s
delta_d=delta_t*def_rate; %deformation step [=] m
def_length=mult*delta_d; %deformation length [=] m

%For Mg AZ31B (empirical material constants)
K1=-1.9529;
K2=500.68;
K3=931.06;
K4=-0.01;
n1=-0.000364;
n2=0.1909;
n3=-0.0009;
n4=0.2713;
```

```
s1=0.00008;
s2=-0.0357;
s3=3.1162;
Kbase=457.72; %Room temperature constant
nbase=.1818; %Room temperature constant

%preallocate arrays for memory and speed
t=zeros(1,nodes);
w=zeros(1,nodes);
L=zeros(1,nodes);
A=zeros(1,nodes);
T=zeros(1,nodes);
K=zeros(1,nodes);
n=zeros(1,nodes);
s=zeros(1,nodes);
stress=zeros(1,nodes);
strain=zeros(1,nodes);
strain_array=zeros(def_length/delta_d,nodes);
tot_elem_strain_array=zeros(def_length/delta_d,nodes);
tot_elem_strain_w_array=zeros(def_length/delta_d,nodes);
tot_elem_strain_t_array=zeros(def_length/delta_d,nodes);
tot_elem_L_array=zeros(def_length/delta_d,nodes);
tot_elem_w_array=zeros(def_length/delta_d,nodes);
tot_elem_t_array=zeros(def_length/delta_d,nodes);
tot_elem_A_array=zeros(def_length/delta_d,nodes);
tot_elem_V_array=zeros(def_length/delta_d,nodes);
K_array=zeros(def_length/delta_d,nodes);
n_array=zeros(def_length/delta_d,nodes);
s_array=zeros(def_length/delta_d,nodes);
A_array=zeros(def_length/delta_d,nodes);
L_array=zeros(def_length/delta_d,nodes);
strain_w_array=zeros(def_length/delta_d,nodes);
strain_t_array=zeros(def_length/delta_d,nodes);
w_array=zeros(def_length/delta_d,nodes);
t_array=zeros(def_length/delta_d,nodes);
V_array=zeros(def_length/delta_d,nodes);
stress1_array=zeros(def_length/delta_d,nodes);
force2_array=zeros(def_length/delta_d,nodes);
disp_array=zeros(def_length/delta_d,1);
Lo_array=zeros(1,nodes);
Ao_array=zeros(1,nodes);
tot_elem_strain=zeros(1,nodes);

Temp=zeros(mult,21);

%input thermal array
    %test array
    for y=1:mult
        Temp(y,1)=22+273.15;
        Temp(y,2)=22+273.15;
        Temp(y,3)=22+273.15;
        Temp(y,4)=22+273.15;
        Temp(y,5)=22+273.15;
```

```
        Temp(y,6)=22+273.15;
        Temp(y,7)=22+273.15;
        Temp(y,8)=22+273.15;
        Temp(y,9)=22+273.15;
        Temp(y,10)=22+273.15;
        Temp(y,11)=22+273.15;
        Temp(y,12)=22+273.15;
        Temp(y,13)=22+273.15;
        Temp(y,14)=22+273.15;
        Temp(y,15)=22+273.15;
        Temp(y,16)=22+273.15;
        Temp(y,17)=22+273.15;
        Temp(y,18)=22+273.15;
        Temp(y,19)=22+273.15;
        Temp(y,20)=22+273.15;
        Temp(y,21)=22+273.15;
    end

%initial geometry
to=1/1000; %initial thickness [=] m
wo=12.5/1000; %initial width [=] m
Lo=5/1000; %initial length [=] m
Ao=to*wo; %initial area [=] m^2

%apply initial conditions
for q=1:nodes
    t(1,q)=to;
    w(1,q)=wo;
    L(1,q)=Lo;
    Lo_array(1,q)=Lo;
    Ao_array(1,q)=Ao;
    A(1,q)=Ao;
end

%loop index
u=1;
bb=1;
check=1;

for j=delta_d:delta_d:def_length

    %Determination of flow constants using temperature
    %Note: input temperature (K) and converted to C
    for i=1:nodes

        %Temp conversion to C
        T(:,i)=Temp(u,i)-273.15;

        %Coefficient determination for K and n
        if T(:,i)<=25 %at room temperature
            K(:,i)=Kbase;
            n(:,i)=nbase;
```

```
        elseif T(1,i)<150 %linear interperation from 22C to 150C as no
exp data
            K(:,i)=K1*T(:,i)+K2;
            n(:,i)=n1*T(:,i)+n2;
        else %calcuate off of elevated temp exp constants
            K(:,i)=K3*exp(K4*T(:,i)); %strength term
            n(:,i)=n3*T(:,i)+n4; %hardening term
        end

        %piecewise relation for softening term (parabolic)
        if T(:,i)<120 %no effect below 120C
            s(:,i)=0;
        elseif T(:,i)<=327 %parabolic relation between limits
            s(:,i)=s1*T(:,i)^2+s2*T(:,i)+s3;
        else %no effect above 327C
            s(:,i)=0;
        end
    end

    %strain guess vector
    if j==delta_d; %first time step use uniform straining for guess
        strain(:,1)=.000003;
        strain(:,2)=.000003;
        strain(:,3)=.000003;
        strain(:,4)=.000003;
        strain(:,5)=.000003;
        strain(:,6)=.000003;
        strain(:,7)=.000003;
        strain(:,8)=.000003;
        strain(:,9)=.000003;
        strain(:,10)=.000003;
        strain(:,11)=.000003;
        strain(:,12)=.000003;
        strain(:,13)=.000003;
        strain(:,14)=.000003;
        strain(:,15)=.000003;
        strain(:,16)=.000003;
        strain(:,17)=.000003;
        strain(:,18)=.000003;
        strain(:,19)=.000003;
        strain(:,20)=.000003;
        strain(:,21)=.000003;

        %solve first iteration using uniform strain guess

[strain,f]=NewtonRaphson(strain',K',n',s',A',L',delta_d,nodes,tot_elem_
strain);
        strain=strain';
        check=check+1;
    else
        %solve subsequent iterations using prior strain as guess
        [strain,f]=NewtonRaphson(strain_array(u-
1,:)',K',n',s',A',L',delta_d,nodes,tot_elem_strain);
```

```
        strain=strain';
    end

    %note: strain solved for is incremental strain and use to find new
    %length of element

    %Calculate new values based off of solved axial strain in each
element
    strain_w=-0.5*strain;
    strain_t=-0.5*strain;
    L=L.*exp(strain);
    w=w.*exp(strain_w);
    t=t.*exp(strain_t);
    A=w.*t;
    V=w.*t.*L;

    %calculate total element strain from initial length at beginning
    tot_elem_strain=log(L/Lo);
    tot_elem_strain_w=-0.5*tot_elem_strain;
    tot_elem_strain_t=-0.5*tot_elem_strain;

    %calculate total length of element from total element strain
    tot_elem_L=Lo*exp(tot_elem_strain);
    tot_elem_w=wo*exp(tot_elem_strain_w);
    tot_elem_t=to*exp(tot_elem_strain_t);
    tot_elem_A=tot_elem_w.*tot_elem_t;
    tot_elem_V=tot_elem_L.*tot_elem_w.*tot_elem_t;

    stress1=(K.*tot_elem_strain.^n).*exp(tot_elem_strain.*s);

    force2=stress1.*tot_elem_A*10^6;
    %store values (21 columns) by simulation length
    strain_array(u,:)=strain;
    strain_w_array(u,:)=strain_w;
    strain_t_array(u,:)=strain_t;
    tot_elem_strain_array(u,:)=tot_elem_strain;
    tot_elem_strain_w_array(u,:)=tot_elem_strain_w;
    tot_elem_strain_t_array(u,:)=tot_elem_strain_t;
    tot_elem_L_array(u,:)=tot_elem_L;
    tot_elem_w_array(u,:)=tot_elem_w;
    tot_elem_t_array(u,:)=tot_elem_t;
    tot_elem_A_array(u,:)=tot_elem_A;
    tot_elem_V_array(u,:)=tot_elem_V;
    K_array(u,:)=K;
    n_array(u,:)=n;
    s_array(u,:)=s;
    A_array(u,:)=A;
    L_array(u,:)=L;
    w_array(u,:)=w;
    t_array(u,:)=t;
    V_array(u,:)=V;
    stress1_array(u,:)=stress1;
```

```
    force2_array(u,:)=force2;
    disp_array(u,1)=j;
    f_array(:,u)=f;

    %display simulation time remaining
    if u==bb*10
        display(['Simulation length remaining: ', num2str((def_length-
u*delta_d)*1000),' (mm)'])
        bb=bb+1;
    end

    u=u+1;
end
```

E.2.2 - Deformation Model Newton-Raphson

```
function[x,f]=NewtonRaphson(x,K,n,s,A,L,delta_d,nodes,tot_elem_strain)
%performs the newton raphson method to find the unknown variables of
system

%initial conditions
res=1;
ii=1;

%loop till error very small
while (res>1e-10)
    f=compute_f(x,K,n,s,A,L,delta_d,nodes,tot_elem_strain); %send to
evaluate function at current values
    J=compute_J(x,K,n,s,A,L,delta_d,tot_elem_strain); %send to evaluate
jacobian at current values
    res=norm(f); % Euclidean length calculation for f "norm"
    %x_save(ii,:)=x'; %store guesses
    %f_save(ii,:)=f'; %store result
    %res_save(ii,1)=res; %store Euclidean length
    x_aug=rref([J,-f+J*x]); %solve linear system
    x=x_aug(:,nodes+1);

    ii=ii+1; %iterate
end
```

E.2.3 - Deformation Model Compute f

```
function[f]=compute_f(x,K,n,s,A,L,delta_d,nodes,tot_elem_strain)
%computes the function values at the given time step

%x is a vector with x variables at given time step (guesses)

%x equations with x variables

for m=1:nodes-1

f_eq1(m,:)=log(K(m)/K(m+1))+log(A(m)/A(m+1))+n(m)*log(tot_elem_strain(m
```

```
)+x(m))-n(m+1)*log(tot_elem_strain(m+1)+x(m+1))+x(m)*(s(m)-
1)+x(m+1)*(1-s(m+1))+tot_elem_strain(m)*s(m)-
tot_elem_strain(m+1)*s(m+1);
end

for w=1:nodes
    f_eq2array(:,w)=L(w)*(exp(x(w))-1);
end

f_eq2=sum(f_eq2array)-delta_d;

f=[f_eq1;f_eq2];

%returns the function values at given time step
```

E.2.4 - Deformation Model Compute J

```
function[J]=compute_J(x,K,n,s,A,L,delta_d,tot_elem_strain)
%computes the Jacobian at the given time step

%x is a vector with x variables at given time step (guesses)

syms x1 x2 x3 x4 x5 x6 x7 x8 x9 x10 x11 x12 x13 x14 x15 x16 x17 x18 x19
x20 x21

f1=log(K(1)/K(2))+log(A(1)/A(2))+n(1)*log(tot_elem_strain(1)+x1)-
n(2)*log(tot_elem_strain(2)+x2)+x1*(s(1)-1)+x2*(1-
s(2))+tot_elem_strain(1)*s(1)-tot_elem_strain(2)*s(2);
f2=log(K(2)/K(3))+log(A(2)/A(3))+n(2)*log(tot_elem_strain(2)+x2)-
n(3)*log(tot_elem_strain(3)+x3)+x2*(s(2)-1)+x3*(1-
s(3))+tot_elem_strain(2)*s(2)-tot_elem_strain(3)*s(3);
f3=log(K(3)/K(4))+log(A(3)/A(4))+n(3)*log(tot_elem_strain(3)+x3)-
n(4)*log(tot_elem_strain(4)+x4)+x3*(s(3)-1)+x4*(1-
s(4))+tot_elem_strain(3)*s(3)-tot_elem_strain(4)*s(4);
f4=log(K(4)/K(5))+log(A(4)/A(5))+n(4)*log(tot_elem_strain(4)+x4)-
n(5)*log(tot_elem_strain(5)+x5)+x4*(s(4)-1)+x5*(1-
s(5))+tot_elem_strain(4)*s(4)-tot_elem_strain(5)*s(5);
f5=log(K(5)/K(6))+log(A(5)/A(6))+n(5)*log(tot_elem_strain(5)+x5)-
n(6)*log(tot_elem_strain(6)+x6)+x5*(s(5)-1)+x6*(1-
s(6))+tot_elem_strain(5)*s(5)-tot_elem_strain(6)*s(6);
f6=log(K(6)/K(7))+log(A(6)/A(7))+n(6)*log(tot_elem_strain(6)+x6)-
n(7)*log(tot_elem_strain(7)+x7)+x6*(s(6)-1)+x7*(1-
s(7))+tot_elem_strain(6)*s(6)-tot_elem_strain(7)*s(7);
f7=log(K(7)/K(8))+log(A(7)/A(8))+n(7)*log(tot_elem_strain(7)+x7)-
n(8)*log(tot_elem_strain(8)+x8)+x7*(s(7)-1)+x8*(1-
s(8))+tot_elem_strain(7)*s(7)-tot_elem_strain(8)*s(8);
f8=log(K(8)/K(9))+log(A(8)/A(9))+n(8)*log(tot_elem_strain(8)+x8)-
n(9)*log(tot_elem_strain(9)+x9)+x8*(s(8)-1)+x9*(1-
s(9))+tot_elem_strain(8)*s(8)-tot_elem_strain(9)*s(9);
f9=log(K(9)/K(10))+log(A(9)/A(10))+n(9)*log(tot_elem_strain(9)+x9)-
n(10)*log(tot_elem_strain(10)+x10)+x9*(s(9)-1)+x10*(1-
s(10))+tot_elem_strain(9)*s(9)-tot_elem_strain(10)*s(10);
```

```
f10=log(K(10)/K(11))+log(A(10)/A(11))+n(10)*log(tot_elem_strain(10)+x10
)-n(11)*log(tot_elem_strain(11)+x11)+x10*(s(10)-1)+x11*(1-
s(11))+tot_elem_strain(10)*s(10)-tot_elem_strain(11)*s(11);
f11=log(K(11)/K(12))+log(A(11)/A(12))+n(11)*log(tot_elem_strain(11)+x11
)-n(12)*log(tot_elem_strain(12)+x12)+x11*(s(11)-1)+x12*(1-
s(12))+tot_elem_strain(11)*s(11)-tot_elem_strain(12)*s(12);
f12=log(K(12)/K(13))+log(A(12)/A(13))+n(12)*log(tot_elem_strain(12)+x12
)-n(13)*log(tot_elem_strain(13)+x13)+x12*(s(12)-1)+x13*(1-
s(13))+tot_elem_strain(12)*s(12)-tot_elem_strain(13)*s(13);
f13=log(K(13)/K(14))+log(A(13)/A(14))+n(13)*log(tot_elem_strain(13)+x13
)-n(14)*log(tot_elem_strain(14)+x14)+x13*(s(13)-1)+x14*(1-
s(14))+tot_elem_strain(13)*s(13)-tot_elem_strain(14)*s(14);
f14=log(K(14)/K(15))+log(A(14)/A(15))+n(14)*log(tot_elem_strain(14)+x14
)-n(15)*log(tot_elem_strain(15)+x15)+x14*(s(14)-1)+x15*(1-
s(15))+tot_elem_strain(14)*s(14)-tot_elem_strain(15)*s(15);
f15=log(K(15)/K(16))+log(A(15)/A(16))+n(15)*log(tot_elem_strain(15)+x15
)-n(16)*log(tot_elem_strain(16)+x16)+x15*(s(15)-1)+x16*(1-
s(16))+tot_elem_strain(15)*s(15)-tot_elem_strain(16)*s(16);
f16=log(K(16)/K(17))+log(A(16)/A(17))+n(16)*log(tot_elem_strain(16)+x16
)-n(17)*log(tot_elem_strain(17)+x17)+x16*(s(16)-1)+x17*(1-
s(17))+tot_elem_strain(16)*s(16)-tot_elem_strain(17)*s(17);
f17=log(K(17)/K(18))+log(A(17)/A(18))+n(17)*log(tot_elem_strain(17)+x17
)-n(18)*log(tot_elem_strain(18)+x18)+x17*(s(17)-1)+x18*(1-
s(18))+tot_elem_strain(17)*s(17)-tot_elem_strain(18)*s(18);
f18=log(K(18)/K(19))+log(A(18)/A(19))+n(18)*log(tot_elem_strain(18)+x18
)-n(19)*log(tot_elem_strain(19)+x19)+x18*(s(18)-1)+x19*(1-
s(19))+tot_elem_strain(18)*s(18)-tot_elem_strain(19)*s(19);
f19=log(K(19)/K(20))+log(A(19)/A(20))+n(19)*log(tot_elem_strain(19)+x19
)-n(20)*log(tot_elem_strain(20)+x20)+x19*(s(19)-1)+x20*(1-
s(20))+tot_elem_strain(19)*s(19)-tot_elem_strain(20)*s(20);
f20=log(K(20)/K(21))+log(A(20)/A(21))+n(20)*log(tot_elem_strain(20)+x20
)-n(21)*log(tot_elem_strain(21)+x21)+x20*(s(20)-1)+x21*(1-
s(21))+tot_elem_strain(20)*s(20)-tot_elem_strain(21)*s(21);

f21=L(1)*(exp(x1)-1)+L(2)*(exp(x2)-1)+L(3)*(exp(x3)-1)+L(4)*(exp(x4)-
1)+L(5)*(exp(x5)-1)+L(6)*(exp(x6)-1)+L(7)*(exp(x7)-1)+L(8)*(exp(x8)-
1)+L(9)*(exp(x9)-1)+L(10)*(exp(x10)-1)+L(11)*(exp(x11)-
1)+L(12)*(exp(x12)-1)+L(13)*(exp(x13)-1)+L(14)*(exp(x14)-
1)+L(15)*(exp(x15)-1)+L(16)*(exp(x16)-1)+L(17)*(exp(x17)-
1)+L(18)*(exp(x18)-1)+L(19)*(exp(x19)-1)+L(20)*(exp(x20)-
1)+L(21)*(exp(x21)-1)-delta_d;

J=jacobian([f1,f2,f3,f4,f5,f6,f7,f8,f9,f10,f11,f12,f13,f14,f15,f16,f17,
f18,f19,f20,f21],[x1 x2 x3 x4 x5 x6 x7 x8 x9 x10 x11 x12 x13 x14 x15
x16 x17 x18 x19 x20 x21]);
%J is the Jacobian matrix which gets evaluated
J=subs(J,{x1,x2,x3,x4,x5,x6,x7,x8,x9,x10,x11,x12,x13,x14,x15,x16,x17,x1
8,x19,x20,x21},{x(1),x(2),x(3),x(4),x(5),x(6),x(7),x(8),x(9),x(10),x(11
),x(12),x(13),x(14),x(15),x(16),x(17),x(18),x(19),x(20),x(21)});

J=double(J);
%returns the evaluated Jacobian at current x values
```

E.2.5 - Deformation Model Elevated Temperature Flow Stress Model

```
function [ output ] = ETFM_F(strain,T)
%ETFM_F=Elevated Temperature Flow Model Function(output MPa)
%Inputs - material property constants, strain, and temperature (K)
%Note: input temperature (K) and converted to C
%Note: strain cannot be zero if n is negative*****

%For Mg AZ31B (empirical material constants)
K1=-1.9529;
K2=500.68;
K3=931.06;
K4=-0.01;
n1=-0.000364;
n2=0.1909;
n3=-0.0009;
n4=0.2713;
s1=0.00008;
s2=-0.0357;
s3=3.1162;
Kbase=457.72; %Room temperature constant
nbase=.1818; %Room temperature constant

%Temp conversion to C
T=T-273.15;

%Coefficient determination for K and n
if T<=25 %at room temperature
    K=Kbase;
    n=nbase;
elseif T<150 %linear interperation from 22C to 150C as no exp data
    K=K1*T+K2;
    n=n1*T+n2;
else %calcuate off of elevated temp exp constants
    K=K3*exp(K4*T); %strength term
    n=n3*T+n4; %hardening term
end

%piecewise relation for softening term (parabolic)
if T<120 %no effect below 120C
    s=0;
elseif T<=327 %parabolic relation between limits
    s=s1*T^2+s2*T+s3;
else %no effect above 327C
    s=0;
end

%calculate flow stress
flow=K*(strain^n)*exp(strain*s); %MPa
%return flow stress value in MPa
output=flow;
end
```

E.3 - Multiphysics Model Codes

E.3.1 - Multiphysics Model Main Code

```
%Sheet Deformation Model
%J. Jones

%Notes************
%where "strain" is given this is along the axial length unless noted

%START DEF MODEL
%%%%%%%%%%%%%%%%%%%%%%%%%%%%%%%%%%%%%%%%%%%%%%%%%%%%%%%%%%%%%%%%%%%%%%%%%%%%%%%
%variables
nodes=21;
node_spacing=5/1000; %node spacing [=] m
mult=60000; %iterations

delta_t=0.01; %[=] s (.01 is temp model)
def_rate=(0.1*25.4/60)/1000; %deformation rate [=] m/s
delta_d=delta_t*def_rate; %deformation step [=] m
def_length=mult*delta_d; %deformation length [=] m

%For Mg AZ31B (empirical material constants)
K1=-1.9529;
K2=500.68;
K3=931.06;
K4=-0.01;
n1=-0.000364;
n2=0.1909;
n3=-0.0009;
n4=0.2713;
s1=0.00008;
s2=-0.0357;
s3=3.1162;
Kbase=457.72; %Room temperature constant
nbase=.1818; %Room temperature constant

%preallocate arrays for memory and speed
t=zeros(1,nodes);
w=zeros(1,nodes);
L=zeros(1,nodes);
A=zeros(1,nodes);
% T=zeros(1,nodes);
K_def=zeros(1,nodes);
n=zeros(1,nodes);
s=zeros(1,nodes);
stress=zeros(1,nodes);
strain=zeros(1,nodes);
strain_array=zeros(def_length/delta_d,nodes);
tot_elem_strain_array=zeros(def_length/delta_d,nodes);
tot_elem_strain_w_array=zeros(def_length/delta_d,nodes);
tot_elem_strain_t_array=zeros(def_length/delta_d,nodes);
```

```
tot_elem_L_array=zeros(def_length/delta_d,nodes);
tot_elem_w_array=zeros(def_length/delta_d,nodes);
tot_elem_t_array=zeros(def_length/delta_d,nodes);
tot_elem_A_array=zeros(def_length/delta_d,nodes);
tot_elem_V_array=zeros(def_length/delta_d,nodes);
K_array=zeros(def_length/delta_d,nodes);
n_array=zeros(def_length/delta_d,nodes);
s_array=zeros(def_length/delta_d,nodes);
A_array=zeros(def_length/delta_d,nodes);
L_array=zeros(def_length/delta_d,nodes);
strain_w_array=zeros(def_length/delta_d,nodes);
strain_t_array=zeros(def_length/delta_d,nodes);
w_array=zeros(def_length/delta_d,nodes);
t_array=zeros(def_length/delta_d,nodes);
V_array=zeros(def_length/delta_d,nodes);
stress_array=zeros(def_length/delta_d,nodes);
force_array=zeros(def_length/delta_d,nodes);
disp_array=zeros(def_length/delta_d,1);
Lo_array=zeros(1,nodes);
Ao_array=zeros(1,nodes);

%initial geometry
to=1/1000; %initial thickness [=] m
wo=12.5/1000; %initial width [=] m
Lo=5/1000; %initial length [=] m
Ao=to*wo; %initial area [=] m^2

%apply initial conditions
for q=1:nodes
    t(1,q)=to;
    w(1,q)=wo;
    L(1,q)=Lo;
    Lo_array(1,q)=Lo;
    Ao_array(1,q)=Ao;
    A(1,q)=Ao;
end
%%%%%%%%%%%%%%%%%%%%%%%%%%%%%%%%%%%%%%%%%%%%%%%%%%%%%%%%%%%%%%%%%%%%%%%%%%%%
%END DEF MODEL

%START TEMP MODEL
%Variables
%=========================================================================

%environment properties
Tinf=273+26;                              %room temperature [=] K
h=20;                                    %convection coefficient [=] W/m^2-K
Tinitial=273+26;                          %initial material temperature
[=] K

%sheet geometry (Mg)
L_spec=200/1000;                            %specimen length [=] m
Ld=(47.5/1000)*2;                        %specimen length under dies [=] m
```

```
Lt=L_spec-Ld;                                %specimen length in test
region [=] m
w_temp=20/1000;                              %specimen width in grip region
[=] m
w1=12.5/1000;                           %specimen width in test region [=]
m
t_temp=1/1000;                               %specimen thickness [=] m

%sheet material properties (Mg)
rho=-0.1414*Tinitial+1821.9;            %density of MgAZ31B [=] kg/m^3
k=0.1011*Tinitial+49.557;               %thermal conductivity of MgAZ31B
[=] W/m-K
c=0.779*Tinitial+777.64;                %heat capacity [=] J/kg-K
rhoe=(2*10^-10)*Tinitial+(4*10^-8); %electrical resistivity of MgAZ31B
[=] ohm-m

%die geometry (A2)
As_die=0.029832;                        %die surface area [=] m^2
V_die=0.000305837;                      %die volume [=] m^3

%die material properties (A2)
rho_a2=-0.3032*Tinitial+7951.5;         %density of A2 [=] kg/m^3
k_a2=0.0058*Tinitial+24.252;            %thermal conductivity of A2 dies
[=] W/m-K
c_a2=460;                               %heat capacity
rhoe_a2=6*10^-7;                        %electrical resistivity of A2 [=]
ohm-m

%element properties
delta_x=(L_spec/40);                         %node spacing [=] m
A1=t_temp*w_temp;                                 %conduction area in die
region [=] m^2
A11=t_temp*w1;                               %conduction area in test
region [=] m^2
A2=delta_x*w_temp;                           %conduction area into dies [=]
m^2
A22=delta_x*w1;                         %convection area in test region [=]
m^2
A3=w_temp*(47.5/1000);                       %full conduction area into
dies [=] m^2
L_die=t_temp/2;                              %die conduction length

%element deformation properties
%def_rate=0.1*25.4/1000;              %deformation rate (in/min to
m/min)

%=========================================================================

%Internal Energy Generation
%=========================================================================

%pulsing parameters
```

```
I=500;                          %applied current magnitude (square wave)
[=] A
PSeff=0.7;                      %Power Supply effiency
period=60;                      %period for pulsing [=] s
duration=1;                     %length of pulse [=] s
duty=(duration/period)*100;     %duty cycle in percent

%joule heating (A2 die) - rhoe_a2 assumed constant as a result of small
temperature change
L1=0.04445;                             %height of section current flow
goes into die [=] m
L2=0.0381;                              %width of section current flow
goes into die [=] m
egen_die_initial=((I^2)*rhoe_a2)/((L1*L2)^2);   %heat generation per
unit volume in die [=] W/m^3

%=========================================================================

%Explicit Solution - Node Equations
%=========================================================================

%time step
delta_t=.01;                        %time step [=] s

%simulation length
length_t=10*60;                      %simulation length [=] s

%preallocate arrays for performance and memory allocation
Temperature=zeros(length_t/delta_t,41);
Die_temp=zeros(length_t/delta_t,1);
Density=zeros(length_t/delta_t,41);
Conductivity=zeros(length_t/delta_t,41);
H_capacity=zeros(length_t/delta_t,41);
Resistivity=zeros(length_t/delta_t,41);
Die_dens=zeros(length_t/delta_t,1);
Die_conduct=zeros(length_t/delta_t,1);
Time=zeros(length_t/delta_t,1);
T=zeros(41,1);
RHO=zeros(41,1);
K=zeros(41,1);
C=zeros(41,1);
RHOE=zeros(41,1);
Delta_S=zeros(length_t/delta_t,1);
Length_Test=zeros(length_t/delta_t,1);
Length_Element=zeros(length_t/delta_t,21);
Width_Element=zeros(length_t/delta_t,21);
Thickness_Element=zeros(length_t/delta_t,21);
A11_Def=zeros(length_t/delta_t,21);
A22_Def=zeros(length_t/delta_t,21);
R_Test_Def=zeros(length_t/delta_t,21);
Egen_Test_Def=zeros(length_t/delta_t,21);
Egen_Clamp=zeros(length_t/delta_t,1);
```

```
Egen_Test=zeros(length_t/delta_t,21);
Egen_Die=zeros(length_t/delta_t,1);

%set initial conditions (room temperature)

%node temperatures (row1=node1 ... row 41=node41)
for ur=1:1:41
    T(ur,:)=Tinitial;
end

%density (sheet) (row1=node1 ... row 41=node41)
for mm=1:1:41
    RHO(mm,:)=rho;
end

%thermal conductivity (sheet) (row1=node1 ... row 41=node41)
for uu=1:1:41
    K(uu,:)=k;
end

%heat capacity (sheet) (row1=node1 ... row 41=node41)
for rr=1:1:41
    C(rr,:)=c;
end

%electrical resistivity (sheet) (row1=node1 ... row 41=node41)
for ss=1:1:41
    RHOE(ss,:)=rhoe;
end

%die temperature
Tdie=Tinitial;

%%%%%%%%%%%%%%%%%%%%%%%%%%%%%%%%%%%%%%%%%%%%%%%%%%%%%%%%%%%%%%%%%%%%%%%%%%%
%END TEMP MODEL

%loop index
u=1; %index def model
bb=1; %index for simulation remaining
check=1; %check for def model
stopper=1; %check no complex results

i=1;     %temperature array index

%j is def
%jj is time

for jj=delta_t:delta_t:length_t %delta_d:delta_d:def_length
    j=jj*def_rate;
 if stopper==0
        break
```

```
 else
     %START DEF MODEL
     %%%%%%%%%%%%%%%%%%%%%%%%%%%%%%%%%%%%%%%%%%%%%%%%%%%%%%%%%%%%%%%%%%%%%%%
    Temp_transpose=T';
    Temp=Temp_transpose(:,11:31);
    %Determination of flow constants using temperature
    %Note: input temperature (K) and converted to C
    for ij=1:nodes

        %Temp conversion to C
        Temp(:,ij)=Temp(:,ij)-273.15;

        %Coefficient determination for K and n
        if Temp(:,ij)<=25 %at room temperature
            K_def(:,ij)=Kbase;
            n(:,ij)=nbase;
        elseif Temp(1,ij)<150 %linear interperation from 22C to 150C as
no exp data
            K_def(:,ij)=K1*Temp(:,ij)+K2;
            n(:,ij)=n1*Temp(:,ij)+n2;
        else %calcuate off of elevated temp exp constants
            K_def(:,ij)=K3*exp(K4*Temp(:,ij)); %strength term
            n(:,ij)=n3*Temp(:,ij)+n4; %hardening term
        end

        %piecewise relation for softening term (parabolic)
        if Temp(:,ij)<120 %no effect below 120C
            s(:,ij)=0;
        elseif Temp(:,ij)<=327 %parabolic relation between limits
            s(:,ij)=s1*Temp(:,ij)^2+s2*Temp(:,ij)+s3;
        else %no effect above 327C
            s(:,ij)=0;
        end
    end

    %strain guess vector
    if j==delta_d; %first time step use uniform straining for guess
        strain(:,1)=.000003;
        strain(:,2)=.000003;
        strain(:,3)=.000003;
        strain(:,4)=.000003;
        strain(:,5)=.000003;
        strain(:,6)=.000003;
        strain(:,7)=.000003;
        strain(:,8)=.000003;
        strain(:,9)=.000003;
        strain(:,10)=.000003;
        strain(:,11)=.000003;
        strain(:,12)=.000003;
        strain(:,13)=.000003;
        strain(:,14)=.000003;
        strain(:,15)=.000003;
```

```
        strain(:,16)=.000003;
        strain(:,17)=.000003;
        strain(:,18)=.000003;
        strain(:,19)=.000003;
        strain(:,20)=.000003;
        strain(:,21)=.000003;

        %solve first iteration using uniform strain guess

[strain,f]=NewtonRaphson(strain',K_def',n',s',A',L',delta_d,nodes);
        strain=strain';
        check=check+1;
    else
        %solve subsequent iterations using prior strain as guess
        [strain,f]=NewtonRaphson(strain_array(u-
1,:)',K_def',n',s',A',L',delta_d,nodes);
        strain=strain';
    end

    %note: strain solved for is incremental strain and use to find new
    %length of element

    %Calculate new values based off of solved axial strain in each
element
    strain_w=-0.5*strain;
    strain_t=-0.5*strain;
    L=L.*exp(strain);
    w=w.*exp(strain_w);
    t=t.*exp(strain_t);
    A=w.*t;
    V=w.*t.*L;

    %calculate total element strain from initial lenght at beginning
    tot_elem_strain=log(L/Lo);
    tot_elem_strain_w=-0.5*tot_elem_strain;
    tot_elem_strain_t=-0.5*tot_elem_strain;

    %calculate total length of element from total element strain
    tot_elem_L=Lo*exp(tot_elem_strain);
    tot_elem_w=wo*exp(tot_elem_strain_w);
    tot_elem_t=to*exp(tot_elem_strain_t);
    tot_elem_A=tot_elem_w.*tot_elem_t;
    tot_elem_V=tot_elem_L.*tot_elem_w.*tot_elem_t;

    %use flow stress function evaluate stress in each element
    for v=1:nodes
        stress(:,v)=ETFM_F(strain(:,v),Temp(:,v)+273.15);
    end

    stress1=(K_def.*tot_elem_strain.^n).*exp(tot_elem_strain.*s);

    %calcuate force in each element
```

```
    force=stress.*tot_elem_A*10^6; %[=] N

    force1=Ao*stress.*exp(-tot_elem_strain)*10^6;
    force2=stress1.*tot_elem_A*10^6;
    %store values (21 columns) by simulation length
    strain_array(u,:)=strain;
    strain_w_array(u,:)=strain_w;
    strain_t_array(u,:)=strain_t;
    tot_elem_strain_array(u,:)=tot_elem_strain;
    tot_elem_strain_w_array(u,:)=tot_elem_strain_w;
    tot_elem_strain_t_array(u,:)=tot_elem_strain_t;
    tot_elem_L_array(u,:)=tot_elem_L;
    tot_elem_w_array(u,:)=tot_elem_w;
    tot_elem_t_array(u,:)=tot_elem_t;
    tot_elem_A_array(u,:)=tot_elem_A;
    tot_elem_V_array(u,:)=tot_elem_V;
    K_array(u,:)=K_def;
    n_array(u,:)=n;
    s_array(u,:)=s;
    A_array(u,:)=A;
    L_array(u,:)=L;
    w_array(u,:)=w;
    t_array(u,:)=t;
    V_array(u,:)=V;
    stress_array(u,:)=stress;
    stress1_array(u,:)=stress1;
    force_array(u,:)=force;
    force1_array(u,:)=force1;
    force2_array(u,:)=force2;
    disp_array(u,1)=j;
    f_array(:,u)=f;

    %%%%%%%%%%%%%%%%%%%%%%%%%%%%%%%%%%%%%%%%%%%%%%%%%%%%%%%%%%%%
    %END DEF MODEL

    %START TEMP MODEL
    %%%%%%%%%%%%%%%%%%%%%%%%%%%%%%%%%%%%%%%%%%%%%%%%%%%%%%%%%%%%
    %calcuate deformation parameters
    delta_s=def_rate*j/60;  %def amount in total in test region (min-
sec conversion) [=] m
    length_test=Lt+delta_s; %new sheet length [=] m

    length_element=L; %delta_x*exp(Length_Strain_Matrix(i,:));   %new
element length in test region due to deformation [=] m (varies along
length)
    width_element=w; %w1*exp(Width_Strain_Matrix(i,:));  %new element
width in test region due to deformation [=] m (varies along length)
    thickness_element=t; %t*exp(Thickness_Strain_Matrix(i,:));   %new
element thickness in test region due to deformation [=] m (varies along
length)
```

```
    A11_def=thickness_element.*width_element;   %conduciton area
(vector that varies along length of test region and corresponds to
elements)
    A22_def=length_element.*width_element;  %convection area (vector
that varies along length of test region and corresponds to elements)

   %individual element resistance (sheet in test region)

R_test_def=transpose(RHOE(11:31,:)).*length_element./(width_element.*th
ickness_element);   %specimen resistance in test region [=] ohm

    %joule heating (sheet in test region)

egen_test_def=((I^2)*R_test_def)./(length_element.*width_element.*thick
ness_element);     %heat generation per unit volume in test region [=]
W/m^3

    %average rhoe for sheet in clamped region  used to update rhoe for
egen update during process
    rhoe_clamp_average=mean([RHOE(1,:) RHOE(2,:) RHOE(3,:) RHOE(4,:)
RHOE(5,:) RHOE(6,:) RHOE(7,:) RHOE(8,:) RHOE(9,:) RHOE(10,:) RHOE(32,:)
RHOE(33,:) RHOE(34,:) RHOE(35,:) RHOE(36,:) RHOE(37,:) RHOE(38,:)
RHOE(39,:) RHOE(40,:) RHOE(41,:)]);

    %specimen resistance (sheet in clamp region)
    R_clamp=rhoe_clamp_average*Ld/(w_temp*t_temp);
%specimen resistance in clamp region [=] ohm

    %joule heating (sheet in clamp region)
    egen_clamp=((I^2)*R_clamp)/(Ld*w_temp*t_temp);    %heat generation
per unit volume in clamp region [=] W/m^3

    %joule heating arrays applied
    egen_clamp=egen_clamp*egen_clamp_array(i,:)*PSeff;
    egen_test=egen_test_def*egen_test_array(i,:)*PSeff;
    egen_die=egen_die_initial*egen_die_array(i,:)*PSeff;

    %die temperature calculations as a function of joule heating and
conduction back into dies (die temperature changes)

    %average Mg specimen temperature under dies for conduction into
dies
    Tavg_mg=mean([T(1,:) T(2,:) T(3,:) T(4,:) T(5,:) T(6,:) T(7,:)
T(8,:) T(9,:) T(10,:) T(32,:) T(33,:) T(34,:) T(35,:) T(36,:) T(37,:)
T(38,:) T(39,:) T(40,:) T(41,:)]);

    %calculate new die temperature

Tdien=Tdie+delta_t*(((h*As_die*Tinf)/(rho_a2*V_die*c_a2))+((2*k_a2*A3*T
avg_mg)/(rho_a2*V_die*c_a2*L_die))-
```

```
(((h*As_die)/(rho_a2*V_die*c_a2))+((2*k_a2*A3)/(rho_a2*V_die*c_a2*L_die
)))*Tdie+(egen_die/(rho_a2*c_a2)));

    %node 1

T1n=T(1,:)+delta_t*(((K(1,:)*T(2,:))/(((delta_x^2)/2)*RHO(1,:)*C(1,:)))
-
((K(1,:)/(((delta_x^2)/2)*RHO(1,:)*C(1,:)))+((2*k_a2*w_temp)/((L_die)*R
HO(1,:)*A1*C(1,:)))+((h*t_temp*w_temp)/(RHO(1,:)*A1*(delta_x/2)*C(1,:))
))*T(1,:)+((2*k_a2*w_temp*Tdien)/((L_die)*RHO(1,:)*A1*C(1,:)))+((h*t_te
mp*w_temp*Tinf)/(RHO(1,:)*A1*(delta_x/2)*C(1,:)))+(egen_clamp/(RHO(1,:)
*C(1,:))));

    %node 2

T2n=T(2,:)+delta_t*(((K(2,:)*T(1,:))/((delta_x^2)*RHO(2,:)*C(2,:)))+((2
*k_a2*A2*Tdien)/((L_die)*RHO(2,:)*A1*delta_x*C(2,:)))-
(((2*K(2,:))/((delta_x^2)*RHO(2,:)*C(2,:)))+((2*k_a2*A2)/((L_die)*RHO(2
,:)*A1*delta_x*C(2,:))))*T(2,:)+((K(2,:)*T(3,:))/((delta_x^2)*RHO(2,:)*
C(2,:)))+(egen_clamp/(RHO(2,:)*C(2,:))));

    %node 3

T3n=T(3,:)+delta_t*(((K(3,:)*T(2,:))/((delta_x^2)*RHO(3,:)*C(3,:)))+((2
*k_a2*A2*Tdien)/((L_die)*RHO(3,:)*A1*delta_x*C(3,:)))-
(((2*K(3,:))/((delta_x^2)*RHO(3,:)*C(3,:)))+((2*k_a2*A2)/((L_die)*RHO(3
,:)*A1*delta_x*C(3,:))))*T(3,:)+((K(3,:)*T(4,:))/((delta_x^2)*RHO(3,:)*
C(3,:)))+(egen_clamp/(RHO(3,:)*C(3,:))));

    %node 4

T4n=T(4,:)+delta_t*(((K(4,:)*T(3,:))/((delta_x^2)*RHO(4,:)*C(4,:)))+((2
*k_a2*A2*Tdien)/((L_die)*RHO(4,:)*A1*delta_x*C(4,:)))-
(((2*K(4,:))/((delta_x^2)*RHO(4,:)*C(4,:)))+((2*k_a2*A2)/((L_die)*RHO(4
,:)*A1*delta_x*C(4,:))))*T(4,:)+((K(4,:)*T(5,:))/((delta_x^2)*RHO(4,:)*
C(4,:)))+(egen_clamp/(RHO(4,:)*C(4,:))));

    %node 5

T5n=T(5,:)+delta_t*(((K(5,:)*T(4,:))/((delta_x^2)*RHO(5,:)*C(5,:)))+((2
*k_a2*A2*Tdien)/((L_die)*RHO(5,:)*A1*delta_x*C(5,:)))-
(((2*K(5,:))/((delta_x^2)*RHO(5,:)*C(5,:)))+((2*k_a2*A2)/((L_die)*RHO(5
,:)*A1*delta_x*C(5,:))))*T(5,:)+((K(5,:)*T(6,:))/((delta_x^2)*RHO(5,:)*
C(5,:)))+(egen_clamp/(RHO(5,:)*C(5,:))));

    %node 6

T6n=T(6,:)+delta_t*(((K(6,:)*T(5,:))/((delta_x^2)*RHO(6,:)*C(6,:)))+((2
*k_a2*A2*Tdien)/((L_die)*RHO(6,:)*A1*delta_x*C(6,:)))-
(((2*K(6,:))/((delta_x^2)*RHO(6,:)*C(6,:)))+((2*k_a2*A2)/((L_die)*RHO(6
,:)*A1*delta_x*C(6,:))))*T(6,:)+((K(6,:)*T(7,:))/((delta_x^2)*RHO(6,:)*
C(6,:)))+(egen_clamp/(RHO(6,:)*C(6,:))));
```

```
    %node 7

T7n=T(7,:)+delta_t*(((K(7,:)*T(6,:))/((delta_x^2)*RHO(7,:)*C(7,:)))+((2
*k_a2*A2*Tdien)/((L_die)*RHO(7,:)*A1*delta_x*C(7,:)))-
(((2*K(7,:))/((delta_x^2)*RHO(7,:)*C(7,:)))+((2*k_a2*A2)/((L_die)*RHO(7
,:)*A1*delta_x*C(7,:))))*T(7,:)+((K(7,:)*T(8,:))/((delta_x^2)*RHO(7,:)*
C(7,:)))+(egen_clamp/(RHO(7,:)*C(7,:))));

    %node 8

T8n=T(8,:)+delta_t*(((K(8,:)*T(7,:))/((delta_x^2)*RHO(8,:)*C(8,:)))+((2
*k_a2*A2*Tdien)/((L_die)*RHO(8,:)*A1*delta_x*C(8,:)))-
(((2*K(8,:))/((delta_x^2)*RHO(8,:)*C(8,:)))+((2*k_a2*A2)/((L_die)*RHO(8
,:)*A1*delta_x*C(8,:))))*T(8,:)+((K(8,:)*T(9,:))/((delta_x^2)*RHO(8,:)*
C(8,:)))+(egen_clamp/(RHO(8,:)*C(8,:))));

    %node 9

T9n=T(9,:)+delta_t*(((K(9,:)*T(8,:))/((delta_x^2)*RHO(9,:)*C(9,:)))+((2
*k_a2*A2*Tdien)/((L_die)*RHO(9,:)*A1*delta_x*C(9,:)))-
(((2*K(9,:))/((delta_x^2)*RHO(9,:)*C(9,:)))+((2*k_a2*A2)/((L_die)*RHO(9
,:)*A1*delta_x*C(9,:))))*T(9,:)+((K(9,:)*T(10,:))/((delta_x^2)*RHO(9,:)
*C(9,:)))+(egen_clamp/(RHO(9,:)*C(9,:))));

    %node 10

T10n=T(10,:)+delta_t*(((K(10,:)*T(9,:))/((delta_x^2)*RHO(10,:)*C(10,:))
)+((2*k_a2*A2*Tdien)/((L_die)*RHO(10,:)*A1*delta_x*C(10,:)))-
(((2*K(10,:))/((delta_x^2)*RHO(10,:)*C(10,:)))+((2*k_a2*A2)/((L_die)*RH
O(10,:)*A1*delta_x*C(10,:))))*T(10,:)+((K(10,:)*T(11,:))/((delta_x^2)*R
HO(10,:)*C(10,:)))+(egen_clamp/(RHO(10,:)*C(10,:))));

    %node 11

T11n=T(11,:)+delta_t*(((K(11,:)*T(10,:))/((length_element(:,1)^2)*RHO(1
1,:)*C(11,:)))-
(((2*K(11,:))/((length_element(:,1)^2)*RHO(11,:)*C(11,:)))+((2*h*A22_de
f(:,1))/(RHO(11,:)*A11_def(:,1)*length_element(:,1)*C(11,:))))*T(11,:)+
((K(11,:)*T(12,:))/((length_element(:,1)^2)*RHO(11,:)*C(11,:)))+((2*h*A
22_def(:,1)*Tinf)/(RHO(11,:)*A11_def(:,1)*length_element(:,1)*C(11,:)))
+(egen_test(:,1)/(RHO(11,:)*C(11,:))));

    %node 12

T12n=T(12,:)+delta_t*(((K(12,:)*T(11,:))/((length_element(:,2)^2)*RHO(1
2,:)*C(12,:)))-
(((2*K(12,:))/((length_element(:,2)^2)*RHO(12,:)*C(12,:)))+((2*h*A22_de
f(:,2))/(RHO(12,:)*A11_def(:,2)*length_element(:,2)*C(12,:))))*T(12,:)+
((K(12,:)*T(13,:))/((length_element(:,2)^2)*RHO(12,:)*C(12,:)))+((2*h*A
22_def(:,2)*Tinf)/(RHO(12,:)*A11_def(:,2)*length_element(:,2)*C(12,:)))
+(egen_test(:,2)/(RHO(12,:)*C(12,:))));
```

```
    %node 13

T13n=T(13,:)+delta_t*(((K(13,:)*T(12,:))/((length_element(:,3)^2)*RHO(1
3,:)*C(13,:)))-
(((2*K(13,:))/((length_element(:,3)^2)*RHO(13,:)*C(13,:)))+((2*h*A22_de
f(:,3))/(RHO(13,:)*A11_def(:,3)*length_element(:,3)*C(13,:))))*T(13,:)+
((K(13,:)*T(14,:))/((length_element(:,3)^2)*RHO(13,:)*C(13,:)))+((2*h*A
22_def(:,3)*Tinf)/(RHO(13,:)*A11_def(:,3)*length_element(:,3)*C(13,:)))
+(egen_test(:,3)/(RHO(13,:)*C(13,:))));

    %node 14

T14n=T(14,:)+delta_t*(((K(14,:)*T(13,:))/((length_element(:,4)^2)*RHO(1
4,:)*C(14,:)))-
(((2*K(14,:))/((length_element(:,4)^2)*RHO(14,:)*C(14,:)))+((2*h*A22_de
f(:,4))/(RHO(14,:)*A11_def(:,4)*length_element(:,4)*C(14,:))))*T(14,:)+
((K(14,:)*T(15,:))/((length_element(:,4)^2)*RHO(14,:)*C(14,:)))+((2*h*A
22_def(:,4)*Tinf)/(RHO(14,:)*A11_def(:,4)*length_element(:,4)*C(14,:)))
+(egen_test(:,4)/(RHO(14,:)*C(14,:))));

    %node 15

T15n=T(15,:)+delta_t*(((K(15,:)*T(14,:))/((length_element(:,5)^2)*RHO(1
5,:)*C(15,:)))-
(((2*K(15,:))/((length_element(:,5)^2)*RHO(15,:)*C(15,:)))+((2*h*A22_de
f(:,5))/(RHO(15,:)*A11_def(:,5)*length_element(:,5)*C(15,:))))*T(15,:)+
((K(15,:)*T(16,:))/((length_element(:,5)^2)*RHO(15,:)*C(15,:)))+((2*h*A
22_def(:,5)*Tinf)/(RHO(15,:)*A11_def(:,5)*length_element(:,5)*C(15,:)))
+(egen_test(:,5)/(RHO(15,:)*C(15,:))));

    %node 16

T16n=T(16,:)+delta_t*(((K(16,:)*T(15,:))/((length_element(:,6)^2)*RHO(1
6,:)*C(16,:)))-
(((2*K(16,:))/((length_element(:,6)^2)*RHO(16,:)*C(16,:)))+((2*h*A22_de
f(:,6))/(RHO(16,:)*A11_def(:,6)*length_element(:,6)*C(16,:))))*T(16,:)+
((K(16,:)*T(17,:))/((length_element(:,6)^2)*RHO(16,:)*C(16,:)))+((2*h*A
22_def(:,6)*Tinf)/(RHO(16,:)*A11_def(:,6)*length_element(:,6)*C(16,:)))
+(egen_test(:,6)/(RHO(16,:)*C(16,:))));

    %node 17

T17n=T(17,:)+delta_t*(((K(17,:)*T(16,:))/((length_element(:,7)^2)*RHO(1
7,:)*C(17,:)))-
(((2*K(17,:))/((length_element(:,7)^2)*RHO(17,:)*C(17,:)))+((2*h*A22_de
f(:,7))/(RHO(17,:)*A11_def(:,7)*length_element(:,7)*C(17,:))))*T(17,:)+
((K(17,:)*T(18,:))/((length_element(:,7)^2)*RHO(17,:)*C(17,:)))+((2*h*A
22_def(:,7)*Tinf)/(RHO(17,:)*A11_def(:,7)*length_element(:,7)*C(17,:)))
+(egen_test(:,7)/(RHO(17,:)*C(17,:))));

    %node 18
```

```
T18n=T(18,:)+delta_t*(((K(18,:)*T(17,:))/((length_element(:,8)^2)*RHO(1
8,:)*C(18,:)))-
(((2*K(18,:))/((length_element(:,8)^2)*RHO(18,:)*C(18,:)))+((2*h*A22_de
f(:,8))/(RHO(18,:)*A11_def(:,8)*length_element(:,8)*C(18,:))))*T(18,:)+
((K(18,:)*T(19,:))/((length_element(:,8)^2)*RHO(18,:)*C(18,:)))+((2*h*A
22_def(:,8)*Tinf)/(RHO(18,:)*A11_def(:,8)*length_element(:,8)*C(18,:)))
+(egen_test(:,8)/(RHO(18,:)*C(18,:))));

    %node 19

T19n=T(19,:)+delta_t*(((K(19,:)*T(18,:))/((length_element(:,9)^2)*RHO(1
9,:)*C(19,:)))-
(((2*K(19,:))/((length_element(:,9)^2)*RHO(19,:)*C(19,:)))+((2*h*A22_de
f(:,9))/(RHO(19,:)*A11_def(:,9)*length_element(:,9)*C(19,:))))*T(19,:)+
((K(19,:)*T(20,:))/((length_element(:,9)^2)*RHO(19,:)*C(19,:)))+((2*h*A
22_def(:,9)*Tinf)/(RHO(19,:)*A11_def(:,9)*length_element(:,9)*C(19,:)))
+(egen_test(:,9)/(RHO(19,:)*C(19,:))));

    %node 20

T20n=T(20,:)+delta_t*(((K(20,:)*T(19,:))/((length_element(:,10)^2)*RHO(
20,:)*C(20,:)))-
(((2*K(20,:))/((length_element(:,10)^2)*RHO(20,:)*C(20,:)))+((2*h*A22_d
ef(:,10))/(RHO(20,:)*A11_def(:,10)*length_element(:,10)*C(20,:))))*T(20
,:)+((K(20,:)*T(21,:))/((length_element(:,10)^2)*RHO(20,:)*C(20,:)))+((
2*h*A22_def(:,10)*Tinf)/(RHO(20,:)*A11_def(:,10)*length_element(:,10)*C
(20,:)))+(egen_test(:,10)/(RHO(20,:)*C(20,:))));

    %node 21

T21n=T(21,:)+delta_t*(((K(21,:)*T(20,:))/((length_element(:,11)^2)*RHO(
21,:)*C(21,:)))-
(((2*K(21,:))/((length_element(:,11)^2)*RHO(21,:)*C(21,:)))+((2*h*A22_d
ef(:,11))/(RHO(21,:)*A11_def(:,11)*length_element(:,11)*C(21,:))))*T(21
,:)+((K(21,:)*T(22,:))/((length_element(:,11)^2)*RHO(21,:)*C(21,:)))+((
2*h*A22_def(:,11)*Tinf)/(RHO(21,:)*A11_def(:,11)*length_element(:,11)*C
(21,:)))+(egen_test(:,11)/(RHO(21,:)*C(21,:))));

    %node 22

T22n=T(22,:)+delta_t*(((K(22,:)*T(21,:))/((length_element(:,12)^2)*RHO(
22,:)*C(22,:)))-
(((2*K(22,:))/((length_element(:,12)^2)*RHO(22,:)*C(22,:)))+((2*h*A22_d
ef(:,12))/(RHO(22,:)*A11_def(:,12)*length_element(:,12)*C(22,:))))*T(22
,:)+((K(22,:)*T(23,:))/((length_element(:,12)^2)*RHO(22,:)*C(22,:)))+((
2*h*A22_def(:,12)*Tinf)/(RHO(22,:)*A11_def(:,12)*length_element(:,12)*C
(22,:)))+(egen_test(:,12)/(RHO(22,:)*C(22,:))));

    %node 23

T23n=T(23,:)+delta_t*(((K(23,:)*T(22,:))/((length_element(:,13)^2)*RHO(
```

```
23,:)*C(23,:)))-
(((2*K(23,:))/((length_element(:,13)^2)*RHO(23,:)*C(23,:)))+((2*h*A22_d
ef(:,13))/(RHO(23,:)*A11_def(:,13)*length_element(:,13)*C(23,:))))*T(23
,:)+((K(23,:)*T(24,:))/((length_element(:,13)^2)*RHO(23,:)*C(23,:)))+((
2*h*A22_def(:,13)*Tinf)/(RHO(23,:)*A11_def(:,13)*length_element(:,13)*C
(23,:)))+(egen_test(:,13)/(RHO(23,:)*C(23,:))));

    %node 24

T24n=T(24,:)+delta_t*(((K(24,:)*T(23,:))/((length_element(:,14)^2)*RHO(
24,:)*C(24,:)))-
(((2*K(24,:))/((length_element(:,14)^2)*RHO(24,:)*C(24,:)))+((2*h*A22_d
ef(:,14))/(RHO(24,:)*A11_def(:,14)*length_element(:,14)*C(24,:))))*T(24
,:)+((K(24,:)*T(25,:))/((length_element(:,14)^2)*RHO(24,:)*C(24,:)))+((
2*h*A22_def(:,14)*Tinf)/(RHO(24,:)*A11_def(:,14)*length_element(:,14)*C
(24,:)))+(egen_test(:,14)/(RHO(24,:)*C(24,:))));

    %node 25

T25n=T(25,:)+delta_t*(((K(25,:)*T(24,:))/((length_element(:,15)^2)*RHO(
25,:)*C(25,:)))-
(((2*K(25,:))/((length_element(:,15)^2)*RHO(25,:)*C(25,:)))+((2*h*A22_d
ef(:,15))/(RHO(25,:)*A11_def(:,15)*length_element(:,15)*C(25,:))))*T(25
,:)+((K(25,:)*T(26,:))/((length_element(:,15)^2)*RHO(25,:)*C(25,:)))+((
2*h*A22_def(:,15)*Tinf)/(RHO(25,:)*A11_def(:,15)*length_element(:,15)*C
(25,:)))+(egen_test(:,15)/(RHO(25,:)*C(25,:))));

    %node 26

T26n=T(26,:)+delta_t*(((K(26,:)*T(25,:))/((length_element(:,16)^2)*RHO(
26,:)*C(26,:)))-
(((2*K(26,:))/((length_element(:,16)^2)*RHO(26,:)*C(26,:)))+((2*h*A22_d
ef(:,16))/(RHO(26,:)*A11_def(:,16)*length_element(:,16)*C(26,:))))*T(26
,:)+((K(26,:)*T(27,:))/((length_element(:,16)^2)*RHO(26,:)*C(26,:)))+((
2*h*A22_def(:,16)*Tinf)/(RHO(26,:)*A11_def(:,16)*length_element(:,16)*C
(26,:)))+(egen_test(:,16)/(RHO(26,:)*C(26,:))));

    %node 27

T27n=T(27,:)+delta_t*(((K(27,:)*T(26,:))/((length_element(:,17)^2)*RHO(
27,:)*C(27,:)))-
(((2*K(27,:))/((length_element(:,17)^2)*RHO(27,:)*C(27,:)))+((2*h*A22_d
ef(:,17))/(RHO(27,:)*A11_def(:,17)*length_element(:,17)*C(27,:))))*T(27
,:)+((K(27,:)*T(28,:))/((length_element(:,17)^2)*RHO(27,:)*C(27,:)))+((
2*h*A22_def(:,17)*Tinf)/(RHO(27,:)*A11_def(:,17)*length_element(:,17)*C
(27,:)))+(egen_test(:,17)/(RHO(27,:)*C(27,:))));

    %node 28

T28n=T(28,:)+delta_t*(((K(28,:)*T(27,:))/((length_element(:,18)^2)*RHO(
28,:)*C(28,:)))-
(((2*K(28,:))/((length_element(:,18)^2)*RHO(28,:)*C(28,:)))+((2*h*A22_d
```

```
ef(:,18))/(RHO(28,:)*A11_def(:,18)*length_element(:,18)*C(28,:))))*T(28
,:)+((K(28,:)*T(29,:))/((length_element(:,18)^2)*RHO(28,:)*C(28,:)))+((
2*h*A22_def(:,18)*Tinf)/(RHO(28,:)*A11_def(:,18)*length_element(:,18)*C
(28,:)))+(egen_test(:,18)/(RHO(28,:)*C(28,:))));

    %node 29

T29n=T(29,:)+delta_t*(((K(29,:)*T(28,:))/((length_element(:,19)^2)*RHO(
29,:)*C(29,:)))-
(((2*K(29,:))/((length_element(:,19)^2)*RHO(29,:)*C(29,:)))+((2*h*A22_d
ef(:,19))/(RHO(29,:)*A11_def(:,19)*length_element(:,19)*C(29,:))))*T(29
,:)+((K(29,:)*T(30,:))/((length_element(:,19)^2)*RHO(29,:)*C(29,:)))+((
2*h*A22_def(:,19)*Tinf)/(RHO(29,:)*A11_def(:,19)*length_element(:,19)*C
(29,:)))+(egen_test(:,19)/(RHO(29,:)*C(29,:))));

    %node 30

T30n=T(30,:)+delta_t*(((K(30,:)*T(29,:))/((length_element(:,20)^2)*RHO(
30,:)*C(30,:)))-
(((2*K(30,:))/((length_element(:,20)^2)*RHO(30,:)*C(30,:)))+((2*h*A22_d
ef(:,20))/(RHO(30,:)*A11_def(:,20)*length_element(:,20)*C(30,:))))*T(30
,:)+((K(30,:)*T(31,:))/((length_element(:,20)^2)*RHO(30,:)*C(30,:)))+((
2*h*A22_def(:,20)*Tinf)/(RHO(30,:)*A11_def(:,20)*length_element(:,20)*C
(30,:)))+(egen_test(:,20)/(RHO(30,:)*C(30,:))));

    %node 31

T31n=T(31,:)+delta_t*(((K(31,:)*T(30,:))/((length_element(:,21)^2)*RHO(
31,:)*C(31,:)))-
(((2*K(31,:))/((length_element(:,21)^2)*RHO(31,:)*C(31,:)))+((2*h*A22_d
ef(:,21))/(RHO(31,:)*A11_def(:,21)*length_element(:,21)*C(31,:))))*T(31
,:)+((K(31,:)*T(32,:))/((length_element(:,21)^2)*RHO(31,:)*C(31,:)))+((
2*h*A22_def(:,21)*Tinf)/(RHO(31,:)*A11_def(:,21)*length_element(:,21)*C
(31,:)))+(egen_test(:,21)/(RHO(31,:)*C(31,:))));

    %node 32

T32n=T(32,:)+delta_t*(((K(32,:)*T(31,:))/((delta_x^2)*RHO(32,:)*C(32,:)
))+((2*k_a2*A2*Tdien)/((L_die)*RHO(32,:)*A1*delta_x*C(32,:)))-
(((2*K(32,:))/((delta_x^2)*RHO(32,:)*C(32,:)))+((2*k_a2*A2)/((L_die)*RH
O(32,:)*A1*delta_x*C(32,:))))*T(32,:)+((K(32,:)*T(33,:))/((delta_x^2)*R
HO(32,:)*C(32,:)))+(egen_clamp/(RHO(32,:)*C(32,:))));

    %node 33

T33n=T(33,:)+delta_t*(((K(33,:)*T(32,:))/((delta_x^2)*RHO(33,:)*C(33,:)
))+((2*k_a2*A2*Tdien)/((L_die)*RHO(33,:)*A1*delta_x*C(33,:)))-
(((2*K(33,:))/((delta_x^2)*RHO(33,:)*C(33,:)))+((2*k_a2*A2)/((L_die)*RH
O(33,:)*A1*delta_x*C(33,:))))*T(33,:)+((K(33,:)*T(34,:))/((delta_x^2)*R
HO(33,:)*C(33,:)))+(egen_clamp/(RHO(33,:)*C(33,:))));

    %node 34
```

```
T34n=T(34,:)+delta_t*(((K(34,:)*T(33,:))/((delta_x^2)*RHO(34,:)*C(34,:)
))+((2*k_a2*A2*Tdien)/((L_die)*RHO(34,:)*A1*delta_x*C(34,:)))-
(((2*K(34,:))/((delta_x^2)*RHO(34,:)*C(34,:)))+((2*k_a2*A2)/((L_die)*RH
O(34,:)*A1*delta_x*C(34,:))))*T(34,:)+((K(34,:)*T(35,:))/((delta_x^2)*R
HO(34,:)*C(34,:)))+(egen_clamp/(RHO(34,:)*C(34,:))));

    %node 35

T35n=T(35,:)+delta_t*(((K(35,:)*T(34,:))/((delta_x^2)*RHO(35,:)*C(35,:)
))+((2*k_a2*A2*Tdien)/((L_die)*RHO(35,:)*A1*delta_x*C(35,:)))-
(((2*K(35,:))/((delta_x^2)*RHO(35,:)*C(35,:)))+((2*k_a2*A2)/((L_die)*RH
O(35,:)*A1*delta_x*C(35,:))))*T(35,:)+((K(35,:)*T(36,:))/((delta_x^2)*R
HO(35,:)*C(35,:)))+(egen_clamp/(RHO(35,:)*C(35,:))));

    %node 36

T36n=T(36,:)+delta_t*(((K(36,:)*T(35,:))/((delta_x^2)*RHO(36,:)*C(36,:)
))+((2*k_a2*A2*Tdien)/((L_die)*RHO(36,:)*A1*delta_x*C(36,:)))-
(((2*K(36,:))/((delta_x^2)*RHO(36,:)*C(36,:)))+((2*k_a2*A2)/((L_die)*RH
O(36,:)*A1*delta_x*C(36,:))))*T(36,:)+((K(36,:)*T(37,:))/((delta_x^2)*R
HO(36,:)*C(36,:)))+(egen_clamp/(RHO(36,:)*C(36,:))));

    %node 37

T37n=T(37,:)+delta_t*(((K(37,:)*T(36,:))/((delta_x^2)*RHO(37,:)*C(37,:)
))+((2*k_a2*A2*Tdien)/((L_die)*RHO(37,:)*A1*delta_x*C(37,:)))-
(((2*K(37,:))/((delta_x^2)*RHO(37,:)*C(37,:)))+((2*k_a2*A2)/((L_die)*RH
O(37,:)*A1*delta_x*C(37,:))))*T(37,:)+((K(37,:)*T(38,:))/((delta_x^2)*R
HO(37,:)*C(37,:)))+(egen_clamp/(RHO(37,:)*C(37,:))));

    %node 38

T38n=T(38,:)+delta_t*(((K(38,:)*T(37,:))/((delta_x^2)*RHO(38,:)*C(38,:)
))+((2*k_a2*A2*Tdien)/((L_die)*RHO(38,:)*A1*delta_x*C(38,:)))-
(((2*K(38,:))/((delta_x^2)*RHO(38,:)*C(38,:)))+((2*k_a2*A2)/((L_die)*RH
O(38,:)*A1*delta_x*C(38,:))))*T(38,:)+((K(38,:)*T(39,:))/((delta_x^2)*R
HO(38,:)*C(38,:)))+(egen_clamp/(RHO(38,:)*C(38,:))));

    %node 39

T39n=T(39,:)+delta_t*(((K(39,:)*T(38,:))/((delta_x^2)*RHO(39,:)*C(39,:)
))+((2*k_a2*A2*Tdien)/((L_die)*RHO(39,:)*A1*delta_x*C(39,:)))-
(((2*K(39,:))/((delta_x^2)*RHO(39,:)*C(39,:)))+((2*k_a2*A2)/((L_die)*RH
O(39,:)*A1*delta_x*C(39,:))))*T(39,:)+((K(39,:)*T(40,:))/((delta_x^2)*R
HO(39,:)*C(39,:)))+(egen_clamp/(RHO(39,:)*C(39,:))));

    %node 40

T40n=T(40,:)+delta_t*(((K(40,:)*T(39,:))/((delta_x^2)*RHO(40,:)*C(40,:)
))+((2*k_a2*A2*Tdien)/((L_die)*RHO(40,:)*A1*delta_x*C(40,:)))-
(((2*K(40,:))/((delta_x^2)*RHO(40,:)*C(40,:)))+((2*k_a2*A2)/((L_die)*RH
```

```
O(40,:)*A1*delta_x*C(40,:))))*T(40,:)+((K(40,:)*T(41,:))/((delta_x^2)*R
HO(40,:)*C(40,:)))+(egen_clamp/(RHO(40,:)*C(40,:))));

    %node 41

T41n=T(41,:)+delta_t*(((K(41,:)*T(40,:))/(((delta_x^2)/2)*RHO(41,:)*C(4
1,:)))-
((K(41,:)/(((delta_x^2)/2)*RHO(41,:)*C(41,:)))+((2*k_a2*w_temp)/((L_die
)*RHO(41,:)*A1*C(41,:)))+((h*t_temp*w_temp)/(RHO(41,:)*A1*(delta_x/2)*C
(41,:))))*T(41,:)+((2*k_a2*w_temp*Tdien)/((L_die)*RHO(41,:)*A1*C(41,:))
)+((h*t_temp*w_temp*Tinf)/(RHO(41,:)*A1*(delta_x/2)*C(41,:)))+(egen_cla
mp/(RHO(41,:)*C(41,:))));

    %store results in matrix
    Temperature(i,:)=[T1n T2n T3n T4n T5n T6n T7n T8n T9n T10n T11n
T12n T13n T14n T15n T16n T17n T18n T19n T20n T21n T22n T23n T24n T25n
T26n T27n T28n T29n T30n T31n T32n T33n T34n T35n T36n T37n T38n T39n
T40n T41n];
    Die_temp(i,:)=Tdien;
    Density(i,:)=[RHO(1,:) RHO(2,:) RHO(3,:) RHO(4,:) RHO(5,:) RHO(6,:)
RHO(7,:) RHO(8,:) RHO(9,:) RHO(10,:) RHO(11,:) RHO(12,:) RHO(13,:)
RHO(14,:) RHO(15,:) RHO(16,:) RHO(17,:) RHO(18,:) RHO(19,:) RHO(20,:)
RHO(21,:) RHO(22,:) RHO(23,:) RHO(24,:) RHO(25,:) RHO(26,:) RHO(27,:)
RHO(28,:) RHO(29,:) RHO(30,:) RHO(31,:) RHO(32,:) RHO(33,:) RHO(34,:)
RHO(35,:) RHO(36,:) RHO(37,:) RHO(38,:) RHO(39,:) RHO(40,:) RHO(41,:)];
    Conductivity(i,:)=[K(1,:) K(2,:) K(3,:) K(4,:) K(5,:) K(6,:) K(7,:)
K(8,:) K(9,:) K(10,:) K(11,:) K(12,:) K(13,:) K(14,:) K(15,:) K(16,:)
K(17,:) K(18,:) K(19,:) K(20,:) K(21,:) K(22,:) K(23,:) K(24,:) K(25,:)
K(26,:) K(27,:) K(28,:) K(29,:) K(30,:) K(31,:) K(32,:) K(33,:) K(34,:)
K(35,:) K(36,:) K(37,:) K(38,:) K(39,:) K(40,:) K(41,:)];
    H_capacity(i,:)=[C(1,:) C(2,:) C(3,:) C(4,:) C(5,:) C(6,:) C(7,:)
C(8,:) C(9,:) C(10,:) C(11,:) C(12,:) C(13,:) C(14,:) C(15,:) C(16,:)
C(17,:) C(18,:) C(19,:) C(20,:) C(21,:) C(22,:) C(23,:) C(24,:) C(25,:)
C(26,:) C(27,:) C(28,:) C(29,:) C(30,:) C(31,:) C(32,:) C(33,:) C(34,:)
C(35,:) C(36,:) C(37,:) C(38,:) C(39,:) C(40,:) C(41,:)];
    Resistivity(i,:)=[RHOE(1,:) RHOE(2,:) RHOE(3,:) RHOE(4,:) RHOE(5,:)
RHOE(6,:) RHOE(7,:) RHOE(8,:) RHOE(9,:) RHOE(10,:) RHOE(11,:)
RHOE(12,:) RHOE(13,:) RHOE(14,:) RHOE(15,:) RHOE(16,:) RHOE(17,:)
RHOE(18,:) RHOE(19,:) RHOE(20,:) RHOE(21,:) RHOE(22,:) RHOE(23,:)
RHOE(24,:) RHOE(25,:) RHOE(26,:) RHOE(27,:) RHOE(28,:) RHOE(29,:)
RHOE(30,:) RHOE(31,:) RHOE(32,:) RHOE(33,:) RHOE(34,:) RHOE(35,:)
RHOE(36,:) RHOE(37,:) RHOE(38,:) RHOE(39,:) RHOE(40,:) RHOE(41,:)];
    Die_dens(i,:)=rho_a2;
    Die_conduct(i,:)=k_a2;
    Time(i,:)=i*delta_t;
    Delta_S(i,:)=delta_s;
    Length_Test(i,:)=length_test;
    Length_Element(i,:)=length_element;
    Width_Element(i,:)=width_element;
    Thickness_Element(i,:)=thickness_element;
    A11_Def(i,:)=A11_def;
    A22_Def(i,:)=A22_def;
    R_Test_Def(i,:)=R_test_def;
```

```
    Egen_Test_Def(i,:)=egen_test_def;
    Egen_Clamp(i,:)=egen_clamp;
    Egen_Test(i,:)=egen_test;
    Egen_Die(i,:)=egen_die;

    i=i+1;   %increment storage array index

    %reset node temperature based off of new calculated temperature
    T(1,:)=T1n;
    T(2,:)=T2n;
    T(3,:)=T3n;
    T(4,:)=T4n;
    T(5,:)=T5n;
    T(6,:)=T6n;
    T(7,:)=T7n;
    T(8,:)=T8n;
    T(9,:)=T9n;
    T(10,:)=T10n;
    T(11,:)=T11n;
    T(12,:)=T12n;
    T(13,:)=T13n;
    T(14,:)=T14n;
    T(15,:)=T15n;
    T(16,:)=T16n;
    T(17,:)=T17n;
    T(18,:)=T18n;
    T(19,:)=T19n;
    T(20,:)=T20n;
    T(21,:)=T21n;
    T(22,:)=T22n;
    T(23,:)=T23n;
    T(24,:)=T24n;
    T(25,:)=T25n;
    T(26,:)=T26n;
    T(27,:)=T27n;
    T(28,:)=T28n;
    T(29,:)=T29n;
    T(30,:)=T30n;
    T(31,:)=T31n;
    T(32,:)=T32n;
    T(33,:)=T33n;
    T(34,:)=T34n;
    T(35,:)=T35n;
    T(36,:)=T36n;
    T(37,:)=T37n;
    T(38,:)=T38n;
    T(39,:)=T39n;
    T(40,:)=T40n;
    T(41,:)=T41n;
    Tdie=Tdien;

    %calculate new sheet properties based off of current node
temperature
```

```
    %density (sheet)
    for mmm=1:1:41
        RHO(mmm,:)=-0.1414*T(mmm,:)+1821.9;
    end

    %thermal conductivity (sheet)
    for uuu=1:1:41
        K(uuu,:)=0.1011*T(uuu,:)+49.557;
    end

    %heat capacity (sheet)
    for rrr=1:1:41
        C(rrr,:)=0.7779*T(rrr,:)+777.64;
    end

    %electrical resistivity (sheet)
    for sss=1:1:41
        RHOE(sss,:)=(2*10^-10)*T(sss,1)+(4*10^-8);
    end

    %calculate new die properties based off of current die temperature

    %density (A2 dies)
    rho_a2=-0.3032*Tdie+7951.5;

    %themal conductivity (A2 dies)
    k_a2=0.0058*Tdie+24.252;
    %%%%%%%%%%%%%%%%%%%%%%%%%%%%%%%%%%%%%%%%%%%%%%%%%%%%%%%%%%%%%%%%
    %END TEMP MODEL



    %display simulation time remaining
    if u==bb*10
        display(['Simulation length remaining: ', num2str((def_length-
u*delta_d)*1000),' (mm)'])
        bb=bb+1;
    end

    u=u+1;

    stopper=isreal(strain);

  end
end
```

E.3.2 - Multiphysics Model Newton-Raphson

```
function[x,f]=NewtonRaphson(x,K,n,s,A,L,delta_d,nodes)
%performs the newton raphson method to find the unknown variables of
system

%initial conditions
res=1;
ii=1;

%loop till error very small
while (res>1e-10)
    f=compute_f(x,K,n,s,A,L,delta_d,nodes); %send to evaluate function
at current values
    J=compute_J(x,K,n,s,A,L,delta_d); %send to evaluate jacobian at
current values
    res=norm(f); % Euclidean length calculation for f "norm"
    %x_save(ii,:)=x'; %store guesses
    %f_save(ii,:)=f'; %store result
    %res_save(ii,1)=res; %store Euclidean length

    x_aug=rref([J,-f+J*x]); %solve linear system
    x=x_aug(:,nodes+1);
%     x=x-(J\f);
    ii=ii+1; %iterate
end
```

E.3.3 - Multiphysics Model Compute f

```
function[f]=compute_f(x,K,n,s,A,L,delta_d,nodes)
%computes the function values at the given time step
%x is a vector with x variables at given time step (guesses)
%x equations with x variables

for m=1:nodes-1
    f_eq1(m,:)=log(K(m)/K(m+1))+log(A(m)/A(m+1))+n(m)*log(x(m))-
n(m+1)*log(x(m+1))+x(m)*(s(m)-1)+x(m+1)*(1-s(m+1));
end

for w=1:nodes
    f_eq2array(:,w)=L(w)*(exp(x(w))-1);
end

f_eq2=sum(f_eq2array)-delta_d;
f=[f_eq1;f_eq2];
%returns the function values at given time step
```

E.3.4 - Multiphysics Model Compute J

```
function[J]=compute_J(x,K,n,s,A,L,delta_d)
%computes the Jacobian at the given time step
%x is a vector with x variables at given time step (guesses)
```

```
syms x1 x2 x3 x4 x5 x6 x7 x8 x9 x10 x11 x12 x13 x14 x15 x16 x17 x18 x19
x20 x21

f1=log(K(1)/K(2))+log(A(1)/A(2))+n(1)*log(x1)-n(2)*log(x2)+x1*(s(1)-
1)+x2*(1-s(2));

f2=log(K(2)/K(3))+log(A(2)/A(3))+n(2)*log(x2)-n(3)*log(x3)+x2*(s(2)-
1)+x3*(1-s(3));

f3=log(K(3)/K(4))+log(A(3)/A(4))+n(3)*log(x3)-n(4)*log(x4)+x3*(s(3)-
1)+x4*(1-s(4));

f4=log(K(4)/K(5))+log(A(4)/A(5))+n(4)*log(x4)-n(5)*log(x5)+x4*(s(4)-
1)+x5*(1-s(5));

f5=log(K(5)/K(6))+log(A(5)/A(6))+n(5)*log(x5)-n(6)*log(x6)+x5*(s(5)-
1)+x6*(1-s(6));

f6=log(K(6)/K(7))+log(A(6)/A(7))+n(6)*log(x6)-n(7)*log(x7)+x6*(s(6)-
1)+x7*(1-s(7));

f7=log(K(7)/K(8))+log(A(7)/A(8))+n(7)*log(x7)-n(8)*log(x8)+x7*(s(7)-
1)+x8*(1-s(8));

f8=log(K(8)/K(9))+log(A(8)/A(9))+n(8)*log(x8)-n(9)*log(x9)+x8*(s(8)-
1)+x9*(1-s(9));

f9=log(K(9)/K(10))+log(A(9)/A(10))+n(9)*log(x9)-
n(10)*log(x10)+x9*(s(9)-1)+x10*(1-s(10));

f10=log(K(10)/K(11))+log(A(10)/A(11))+n(10)*log(x10)-
n(11)*log(x11)+x10*(s(10)-1)+x11*(1-s(11));

f11=log(K(11)/K(12))+log(A(11)/A(12))+n(11)*log(x11)-
n(12)*log(x12)+x11*(s(11)-1)+x12*(1-s(12));

f12=log(K(12)/K(13))+log(A(12)/A(13))+n(12)*log(x12)-
n(13)*log(x13)+x12*(s(12)-1)+x13*(1-s(13));

f13=log(K(13)/K(14))+log(A(13)/A(14))+n(13)*log(x13)-
n(14)*log(x14)+x13*(s(13)-1)+x14*(1-s(14));

f14=log(K(14)/K(15))+log(A(14)/A(15))+n(14)*log(x14)-
n(15)*log(x15)+x14*(s(14)-1)+x15*(1-s(15));

f15=log(K(15)/K(16))+log(A(15)/A(16))+n(15)*log(x15)-
n(16)*log(x16)+x15*(s(15)-1)+x16*(1-s(16));

f16=log(K(16)/K(17))+log(A(16)/A(17))+n(16)*log(x16)-
n(17)*log(x17)+x16*(s(16)-1)+x17*(1-s(17));
```

```
f17=log(K(17)/K(18))+log(A(17)/A(18))+n(17)*log(x17)-
n(18)*log(x18)+x17*(s(17)-1)+x18*(1-s(18));

f18=log(K(18)/K(19))+log(A(18)/A(19))+n(18)*log(x18)-
n(19)*log(x19)+x18*(s(18)-1)+x19*(1-s(19));

f19=log(K(19)/K(20))+log(A(19)/A(20))+n(19)*log(x19)-
n(20)*log(x20)+x19*(s(19)-1)+x20*(1-s(20));

f20=log(K(20)/K(21))+log(A(20)/A(21))+n(20)*log(x20)-
n(21)*log(x21)+x20*(s(20)-1)+x21*(1-s(21));

f21=L(1)*(exp(x1)-1)+L(2)*(exp(x2)-1)+L(3)*(exp(x3)-1)+L(4)*(exp(x4)-
1)+L(5)*(exp(x5)-1)+L(6)*(exp(x6)-1)+L(7)*(exp(x7)-1)+L(8)*(exp(x8)-
1)+L(9)*(exp(x9)-1)+L(10)*(exp(x10)-1)+L(11)*(exp(x11)-
1)+L(12)*(exp(x12)-1)+L(13)*(exp(x13)-1)+L(14)*(exp(x14)-
1)+L(15)*(exp(x15)-1)+L(16)*(exp(x16)-1)+L(17)*(exp(x17)-
1)+L(18)*(exp(x18)-1)+L(19)*(exp(x19)-1)+L(20)*(exp(x20)-
1)+L(21)*(exp(x21)-1)-delta_d;

J=jacobian([f1,f2,f3,f4,f5,f6,f7,f8,f9,f10,f11,f12,f13,f14,f15,f16,f17,
f18,f19,f20,f21],[x1 x2 x3 x4 x5 x6 x7 x8 x9 x10 x11 x12 x13 x14 x15
x16 x17 x18 x19 x20 x21]);
%J is the Jacobian matrix which gets evaluated
J=subs(J,{x1,x2,x3,x4,x5,x6,x7,x8,x9,x10,x11,x12,x13,x14,x15,x16,x17,x1
8,x19,x20,x21},{x(1),x(2),x(3),x(4),x(5),x(6),x(7),x(8),x(9),x(10),x(11
),x(12),x(13),x(14),x(15),x(16),x(17),x(18),x(19),x(20),x(21)});

J=double(J);


%returns the evaluated Jacobian at current x values
```